16th Symposium on Application of Plasma Processes

SAPP

Workshop on Research of Plasma Physics and Applications in Visegrad Countries

Visegrad Fund

Book of Abstracts

Podbanské, Slovakia
January, 20-25, 2007

Edited by J. Matúška, Š. Matejčík, J.D. Skalný

An Eulogy to Hannspeter Winter 1941-2006

The scientific community lost a great friend and colleague with the sudden and unexpected death of Professor Hannspeter Winter on November 8 2006.

Following his Ph.D. degree obtained 1970 at the Vienna University of Technology, Hannspeter initiated his professional career in 1970 as a Research Scientist at the Austrian Nuclear Research Center Seibersdorf and as an Assistant Professor at the TU Wien. During this time he spent 1973-1975 as Visiting Scientist at the Gesellschaft für Schwerionenforschung in Darmstadt and 1976/77 as Senior Visiting Scientist at FOM in Amsterdam. His considerable talent and exceptional energy led to an extremely productive period in this time and earned him a University Professorship for Plasma Physics in 1980 at the TU Vienna. He was one of the leaders instrumental in developing a plasma and atomic physics program that quickly achieved international recognition leading also to a full professorship in 1990 at the Institut für Allgemeine Physik at the TU Vienna. Winter's institute and own research group was extremely productive, making important contributions to plasma physics, atomic and molecular physics, surface physics and fusion technology leading to more than 270 papers in refereed journals.

In addition to this prolific publication record, Hannspeter also carried out a number of other activities serving since 1996 as Head of the Research Unit of the Austrian Association to the EURATOM Fusion Program, 1989-1990 as Chairman of the Austrian Physical Society, 1997-199 as Vice Chairman of the IUPAP Commission C-15, 1998-2001 as Chairman of EPS Atomic and Molecular Physics Division, 1995-2001 as Board Member of EPS Plasma Physics Division, 1990-1992 as Chairman of the Austrian University professors Union, 1991-2001 as Vice Chairman of the Österreichische Universitätsprofessorenkonferenz, and since 2000 as Council Member for the Austrian Universities of Applied Sciences and as Co-editor of "Plasma Physics and Controlled Fusion" and "Europhysics Letters".

His scientific achievements were recognized in 1998 by the election as Corresponding Member of the Austrian Academy of Sciences, in 2000 by the receipt of the Österreichische Ehrenkreuz für Wissenschaft und Kunst 1.Klasse and in 2003 by the receipt of the German Alexander von Humboldt Research Prize.

Hannspeter's interests were broad and varied. In addition to his research and teaching he had a lively appreciation of art and music. He was a vigorous person physically. He was an avid jogger and a regular

mountaineer, taking part recently in Vienna's half marathon and climbing one of Tirol's highest mountain the Zuckerhütl with 3507 m.

Hannspeter's extraordinary joy of living and deep insight into science made his friendship a rewarding and memorable experience. He will be sorely missed.

Tilmann Märk

Innsbruck, December 2006

CONTENTS

SPONSORS


HIDEN
ANALYTICAL


Lao


PFEIFFER VACUUM


Swagelok


Visegrad Fund

Plasma Characterisation

The Hiden *EQP* and *PSM* advanced mass/energy analysers provide detailed plasma analysis for plasma reaction kinetics, characterisation and enhanced process understanding.

EQP/PSM

Features include:

- High Sensitivity: Sub PPM detection of ions, neutrals and radicals.
- Ion Energy Analysis: Ion energy distributions of plasma ions are acquired in seconds. 100 and 1000eV versions available.
- Time-Resolved Studies: Programmable signal gating module provides fully integrated and software controlled timing circuitry with 100 nanosec resolution for pulsed plasma applications.
- Positive and Negative Ion Measurement: Pre-set software modes for switching between analysis modes.
- Neutral and Radical Detection: Integral electron impact analyser provides analysis of neutral and radical species.
- Electron Attachment: Soft ionisation technique for analysis of electronegative species in plasma.
- Wide Pressure Range: 2 and 3 stage molecular beam sampling inlets for high pressure plasma diagnostics

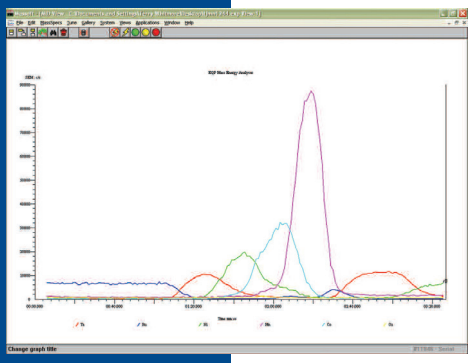

MID Mode: Multi-Ion Detection

EQP: Mass/Energy Analyser

www.HidenAnalytical.com

HIDEN ANALYTICAL

surface science | vacuum analysis | gas analysis | plasma diagnostics

HIDEN ANALYTICAL

Hiden Analytical Ltd.
420 Europa Boulevard, Warrington
WA5 7UN, ENGLAND

Tel +44 (0)1925 445 225
Fax +44 (0)1925 416 518
Email: info@hiden.co.uk

LAO PRŮMYSLOVÉ SYSTÉMY, S.R.O.

VĚDECKÉ APLIKACE - LASERY, LASEROVÁ TECHNIKA, OPTIKA, OPTOELEKTRONIKA
VĚDECKÉ PŘÍSTROJE A SYSTÉMY

Lasery, laserové systémy a příslušenství
Realizace optické dráhy a vedení světla
Detekční systémy: CCD a ICCD detektory, fotodiody, fotonásobiče, spec. kamery a další
Měřící systémy: online plazma monitorovací systémy spektrometry, spektrografy, reflektometry elipsometry, streak kamery a další

Naši hlavní dodavatelé: **Coherent, Lasos, Quantel, Melles Griot, Hamamatsu, LOT-Oriel, Andor, Electrophysics, Zygo, Ocean Optics**

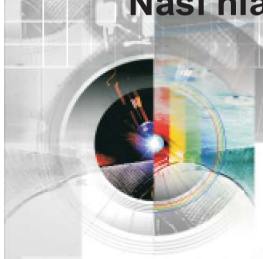

Na Floře 1328/4, 143 00 Praha 4, tel.: 241 046 800
e-mail: **laser@lao.cz**, **www.lao.cz**

www.tuv.com TÜV TÜV Rheinland Group ID:9105032609
ISO 9001:2001

World class Turbopumps with pumping speed of 10 – 500 l/s

- Dependable Operation
- Low Cost of Ownership
- Wide Variety of Applications

PFEIFFER VACUUM
Austria & C.E. Europe

Pfeiffer-Vacuum Austria, office Prague, Czech Rep.
Novodvorská 1010/14B, 142 01 Praha 4 · Phone: +420-257 923 888 · Fax: +420-257 923 014 · office@pfeiffer-vacuum.cz

PT 0116 PE

www.pfeiffer-vacuum.net

Swagelok

Tube fittings , VCO and VCR fittings, quick connects, hoses, valves and other fluid components for super clean, general and heavy industy applications from one source.

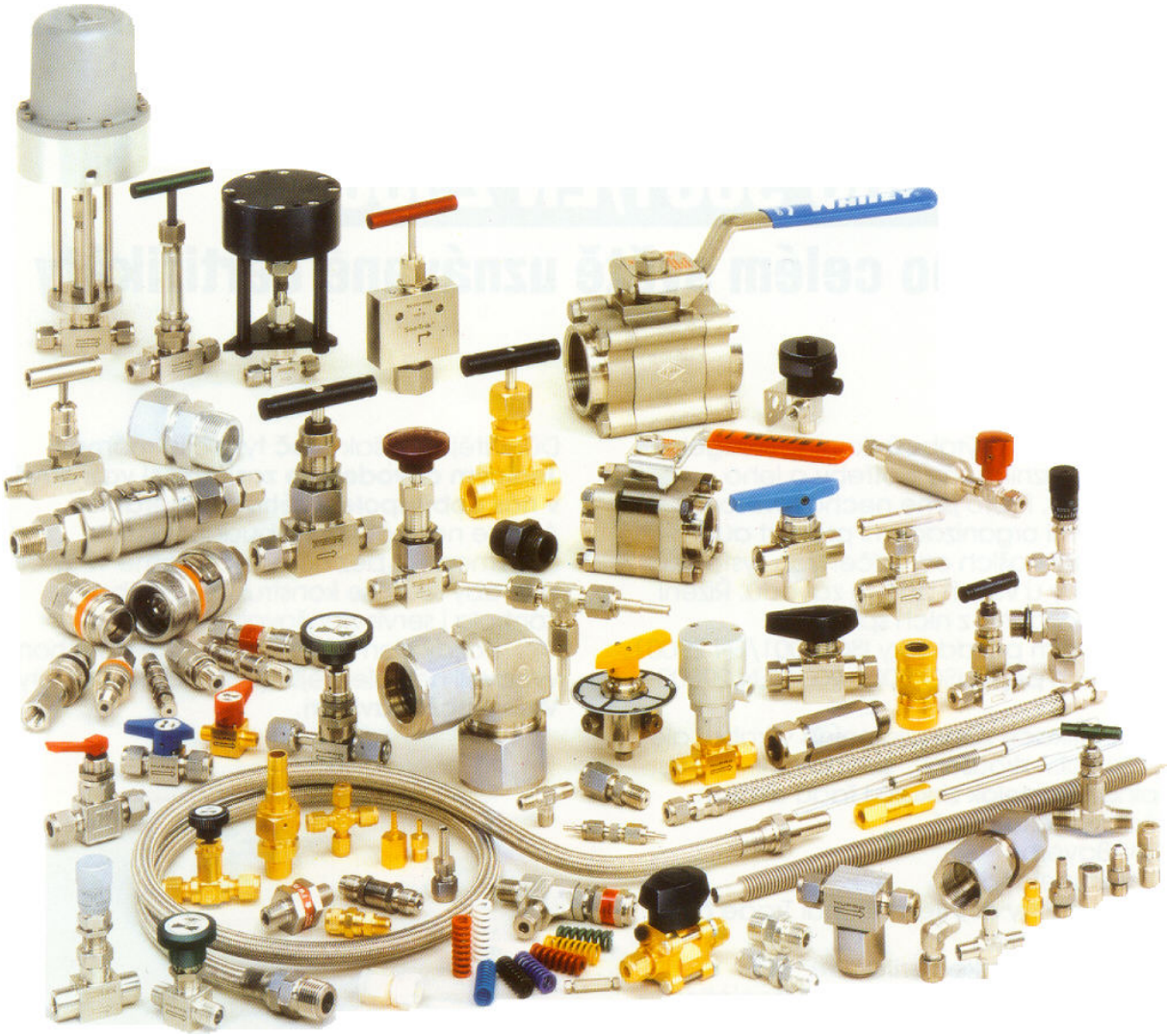

Ventil a Fiting Bratislava spol. s r.o.
Dubovského 1035/2
901 01 Malacky, Slovakia

tel. 00421 34 7743020, fax 7725626, e-mail: ventil@fiting.sk, www.fiting.sk
www.swagelok.com

Workshop on Research of Plasma Physics and Applications in Visegrad Countries

Invited Lectures

Low-Cost and High-Speed Plasma Surface Treatments at Atmospheric Pressure

M. Černák[1, 3], D. Kováčik [1], A. Buček [1], Ľ. Černáková [2], A. Zahoranová [1], J. Ráheľ [1, 3], P. Sťahel[3]

[1]Department of Experimental Physics, Comenius University, Mlynská dolina, 842 48 Bratislava, Slovakia
[2]Department of Plastics, Faculty of Chemical and Food Technology, Slovak University of Technology, Radlinského 9, 812 37 Bratislava
[3]Department of Physical Electronics, Masaryk University, Kotlářská 2, 611 37 Brno, Czech Republic
e-mail: cernak@fmph.uniba.sk

Abstract

The lecture will report on a novel atmospheric-pressure plasma source; a Diffuse Coplanar Surface Barrier Discharge (DCSBD), which is capable of generating macroscopically uniform high-power-density diffuse plasmas in any working gas, including pure atmospheric-pressure oxygen, without the use of He or Ar. DCSBD is a type of dielectric barrier discharge generated on the surface of a dielectric barrier with embedded electrodes, which appears to be advantageous to surface treatment and deposition processes. Preliminary results on polypropylene and PLA nonwoven fabrics activation, nanopowder immobilization onto a polypropylene fabric, glass and aluminium surface cleaning, paper and wood surface treatment, and photoresist ashing will be presented.

Introduction

Nonequilibrium electric plasmas are central to many surface treating and coating processes. Although vacuum plasma processes are well understood and are used extensively, e.g., in the semiconductor industry, the fact that vacuum conditions are necessary makes low-pressure plasma impractical to use in industries requiring high rates of throughput, e.g., the textile and paper industries. Atmospheric plasma treatment, on the other hand, is well suited for continuous processing of low-cost materials, and the development of atmospheric pressure plasma sources to replace costly plasma processing in vacuum system is a current trend in industrial plasma engineering [1].

A common shortcoming of a great majority of atmospheric pressure plasma sources applied for surface treatments and plasma depositions is that a helium-containing plasma gas is required to prevent the appearance of filaments or sparks that are detrimental to the treatment uniformity and can lead to the undesirable plasma thermalization. Thus the challenge is to avoid the helium while maintaining plasma stability and reactivity. This task is complicated even more by the fact that to facilitate an in-line atmospheric-pressure plasma treatment, it is usually desirable to reduce the plasma exposure time below 1 sec. by enhancing the concentrations of charged particles and reactive species generated. This can be most conveniently approached by increasing the plasma power density to the order of 10 W/cm^3. However, increasing the atmospheric-pressure plasma density above of some 1 – 10 W/cm^3 the generated plasma will normally undergo glow-to-arc transition and evolve into an arc or spark discharge [2,3].

Results and discussion

To fulfill the above requirements collaborating Czech and Slovakian university teams have recently developed an innovative plasma source, the so-called Diffuse Coplanar Surface Barrier Discharge (DCSBD) [4-6]. The DCSBD plasma sources have unique properties, which clearly differentiate them from the other atmospheric pressure plasma sources studied for surface treatments:

1. Very high plasma power densities can be achieved (~100 W/cm^3), which allows for short plasma exposure times on the order of 0.1 sec. and, consequently, high treatment speeds.
2. The high-power-density plasma can be generated in any working gas. To our best knowledge, DCSBD is the only known plasma source capable of generating the high-density diffuse plasma in atmospheric-pressure oxygen.
3. The homogeneity of the plasma increases with increasing discharge power density. Note that normally, the homogeneity of atmospheric pressure discharges decreases with increased power because of the streamer formation, gas heating and sparking.
4. The electrode system, where the plasma is not in contact with metallic electrodes, is very durable and high power density diffuse plasmas can be generated in any, even strongly reactive gas without any degradation of the electrodes.
5. The system is very safe and robust. The contact of human body to the electrode system and the high-density DCSBD plasma is not dangerous, not even unpleasant (see Fig.1). The system is

mechanically robust and, consequently, the samples being treated can be pressed to the electrode system surface, which is important, i.e., for treatment soft materials with surface irregularities as thick fabrics.

6. The DCSBD is operable in dusty and humid environment typical for, e.g., the textile finishing and papermaking industries and scalable to large area (square meters).
7. The DCSBD can comply with clean room operation requirements.

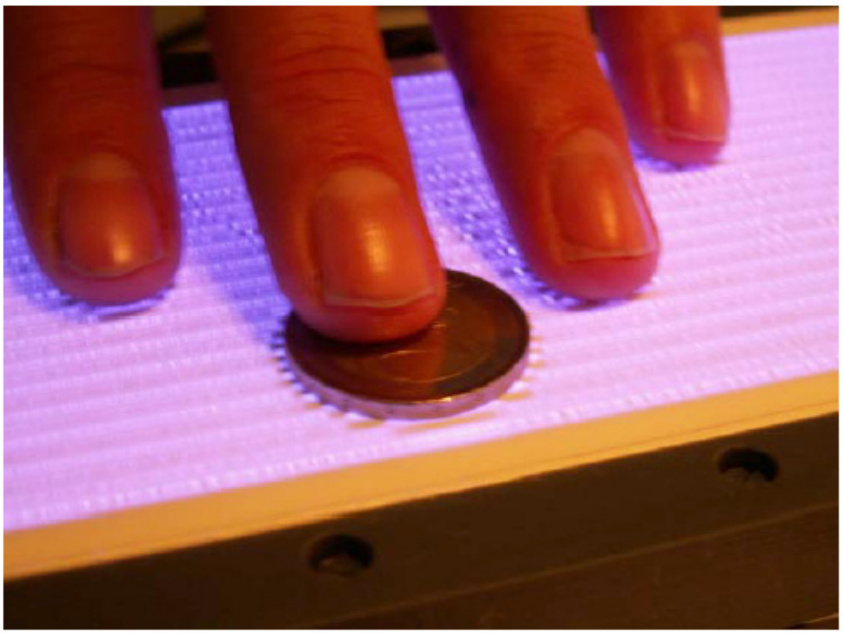

Figure 1: An illustration of diffusivity and safety of DCSBD plasma generated in laboratory air.

The reader is referred to video records available on [7], illustrating DCSBD properties and its application for fabric treatment and glass surface cleaning.

The lecture will discuss the above DCSBD properties in details together with the applications of DCSBD for polypropylene and PLA nonwoven fabrics activation, nanopowder immobilization onto a polypropylene fabric, glass and aluminum surface cleaning, paper and wood surface treatment, and photoresist ashing.

Acknowledgements

This work was supported by VEGA grant No. 1/1011/04 and by APVV grants No. 20-033004, No. 20/P01505, No. 99/035004.

References

[1] J.R. Roth, *Industrial Plasma Engineering, Vol. 2: Applications to Nonthermal Plasma Processing*, Inst. of Phys. Publishing, Bristol and Philadelphia, 2001
[2] A. Schutze, J. Y. Jeong, S. E. Babayan, J. Park, G. S. Selwyn, and R. F. Hicks, *IEEE Trans. Plasma Sci.* (1998), pp. 1685-1694
[3] A.P. Napartovich, *Plasmas and Polymers* 6 (2001), 1-1
[4] M. Šimor, J. Ráheľ, P. Vojtek, A. Brablec, M. Černák, *Appl. Phys. Lett.* 81 (2002), pp. 2716-2718
[5] M.Černák, J.Ráheľ, D. Kováčik, M. Šimor. A. Brablec, *Contributions to Plasma Physics* 44 (2004), pp. 492-495
[6] M. Černák, "Method and apparatus for treatment of textile materials" *US Patent Appl.* 2004/0194223
[7] http://gimmel.ip.fmph.uniba.sk/glass, http://gimmel.ip.fmph.uniba.sk/treaters

Modeling of Dual-Frequency Capacitive Discharges

Z. Donkó

Research Institute for Solid State Physics and Optics of the Hungarian Academy of Sciences
H-1121 Budapest, Konkoly Thege Miklós str. 29-33, Hungary
e-mail: donko@sunserv.kfki.hu

Abstract

Particle-in-cell (PIC/MCC) simulations of capacitively-coupled Ar discharges excited simultaneously by two sources of different frequencies are presented. The properties and the formation mechanism of the flux-energy distribution of the Ar^+ ions reaching the electrodes is analyzed in detail. It is demonstrated that the ion energy and the ion flux can nearly independently be controlled by properly choosing the excitation frequencies and the operating pressure of the discharge.

Introduction

Radio-frequency capacitively coupled plasma (CCP) sources have widely been used in technological steps of modern integrated circuit fabrication [1]. In particular CCPs are applied for etching of the dielectrics, where high ion energies are required. The control of plasma properties in these applications is of primary importance. During the last couple of years it has been recognized that the plasma maintenance and ion properties may be controlled independently from each other using plasma sources excited by two different radio frequencies [2-4]. In such plasma sources one generator is used to produce the plasma and the other to extract and accelerate the ions. Properties of capacitively coupled radio-frequency (CCRF) discharges driven by two frequencies have been explored based on different approaches, by developing analytical, as well as computational models [5-14]. While in industrial applications reactive gases are primarily used, the physics of dual frequency-excited discharges can readily been studied using e.g. argon as a buffer gas. The need for the understanding of the details of the operation of these discharges has motivated the studies presented here.

Simulation model

Radio-frequency argon discharges formed in a symmetrical reactor are described here by a one-dimensional (1d3v) bounded plasma particle-in-cell model, complemented with Monte Carlo treatment of collision processes (PIC/MCC). The electrodes are assumed to be plane and parallel, and separated by a distance of L = 2 cm. In the present implementation of the PIC simulation method one of the electrodes is driven by a voltage $V(t) = V_{HF}\sin(2\pi f_{HF} t) + V_{LF}\sin(2\pi f_{LF} t)$, while the other electrode is grounded. V_{HF} and V_{LF} , and $f_{HF} >> f_{LF}$ are the amplitudes and the frequencies, respectively, of the driving (High-Frequency and Low-Frequency) voltages. The secondary electron yield at the electrodes is assumed to be zero.

The characteristics of the discharges are analyzed in the pressure range between 25 mTorr and 100 mTorr. It is well known that at such low pressures in RF argon discharges driven by 13.56 MHz (i) the distribution function of the electrons (EDF) can be characterized by two temperatures [15] and (ii) a very high number of superparticles is needed in PIC simulations to obtain a correct temperature for the slow electron group and to describe properly the discharge characteristics [16]. In this work the high frequency is chosen to be f_{HF} = 100 MHz, where the sensitivity of the calculated discharge characteristics on the number of superparticles used in the simulation is less pronounced. For such conditions the number of superparticles used in the present simulations, $N \sim 10^5$, is expected to provide acceptable accuracy.

Results and discussion

The central quantities in the present study are the flux and energy distribution of the Ar^+ ions arriving at the electrodes. In the forthcoming analysis the dependence of these characteristics on the values of the high- and low-frequency driving voltages, as well as on the values of the lower and higher driving frequencies, and the gas pressure is presented and discussed. Special attention is devoted to the analysis of the formation of the flux-energy distribution of ions.

The flux-energy distribution of Ar^+ ions reaching the powered electrode is displayed in Figure 1 for different discharge conditions. The high-frequency is chosen to be 100 MHz, with an amplitude V_{HF} = 60V. The first series of data (left column) demonstrates the effect of the value of *low-frequency voltage* for the case of discharges operated at 100 MHz / 1 MHz frequencies. At single frequency operation, V_{LF} = 0, the

distribution sharply peaks at the energy ≅ 40 eV, the time-averaged value of the sheath potential. As V_{LF} is increased the distribution extends towards higher energies, and exhibits a characteristic saddle shape. The range of ion energies significantly increases with increasing V_{LF}. At 25 mTorr the ion transit time in shorter than $1/f_{LF}$ and, as the sheaths are nearly collisionless, the energy of ions reaching the electrodes at a given time strongly correlates with the difference of the instantaneous plasma potential and the potential of the powered electrode. (Taking $\sigma \sim 5\times10^{-15}$ cm^2 as the total cross section of Ar^+ collisions with Ar, the mean free path at 25 mTorr pressure is $\lambda \cong 0.25$cm, which is comparable to the length of the sheath at $V_{LF} = 0$.) As the electrode sheaths are not completely collisionless we observe a flux of low-energy (< 40 eV) ions, as well. Their flux gradually increases with V_{LF}, as the sheath extends with increasing V_{LF}. The effect of the *value of the lower frequency* f_{LF} (at constant V_{LF}) is illustrated by the second set of data (middle column of Figure 1). At f_{LF} values higher than 1 MHz we observe multiple peaks in the energy spectrum. The number of peaks increases with increasing f_{LF} and also the high-energy side cutoff of the distribution is shifted towards lower ion energies. This is explained by the fact that at these conditions the ion transit time through the sheath becomes greater than $1/f_{LF}$, i.e. the ions cross the sheath during a couple to several low-frequency cycles. The right column in Figure 1 shows again the effect of *low-frequency voltage,* but a four time higher pressure (100 mTorr) compared to the previous cases. The flux-energy distributions of the ions peak around zero energy and fall nearly exponentially due to the increased number of collisions they experience in the electrode sheath.

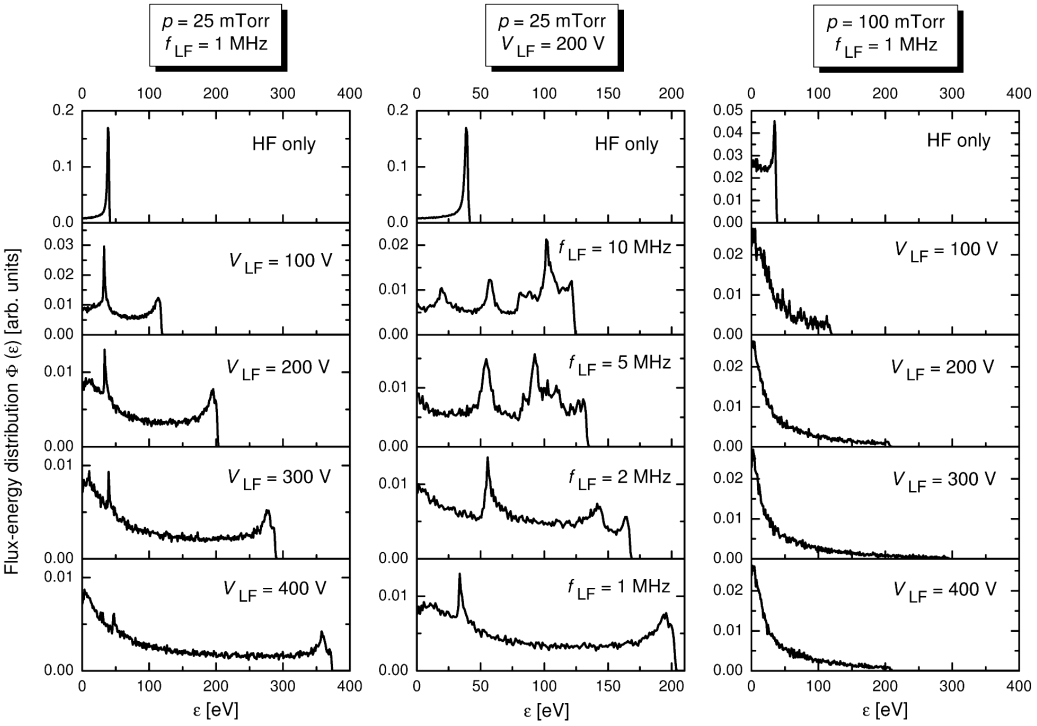

Figure 1. Flux-energy distributions of Ar^+ ions upon arrival at the electrodes. Left column: effect of the voltage of the low-frequency source at $p = 25$ mTorr, $f_{LF} = 1$ MHz. Center column: effect of the value of the value of the low frequency at $p = 25$ mTorr, $V_{LF} = 200$ V. Right column: effect of the voltage of the low frequency source at $p = 100$ mTorr, $f_{LF} = 1$ MHz. The high-frequency voltage is $V_{HF} = 60$ V @ $f_{HF} = 100$ MHz for all cases.

The formation of the distributions shown in Figure 1 is further analyzed for selected cases in Figure 2. Figures 2(a), (c) and (e) display the joint temporal and energy distribution of the arriving Ar^+ ions for three different sets of discharge conditions: dots on the energy – time plane correspond to individual ions reaching the powered electrode. Figures 2(b), (d) and (f) show the corresponding values of the time-dependent plasma potential and the time-dependent low-frequency excitation signal. The data plotted in Figures 2 (a) and (b) for the 100 MHz / 1 MHz discharge at 25 mTorr clearly show that the energy of most of the Ar^+ ions at the powered electrode follows the difference between the plasma potential and the instantaneous value of the applied low-frequency voltage $V_{LF}(t)$ (i.e. the "accelerating potential"). We observe a "phase shift" between the energy distribution of the ions and the accelerating voltage (the highest ion energies are observed subsequent to the occurrence the maximum of the accelerating potential). This delay originates from finite ion transit time through the sheath. In the case of the above discharge conditions many of the ions acquire the highest possible energy (the dots are concentrated at the envelope of the distribution shown in Figure 2(a)),

although we observe ions with lower energies as well, in accordance with the corresponding flux-energy (time-integrated) distribution displayed in Figure 1. At higher pressure the spread of the energy becomes greater, as indicated by the data shown in Figure 2(c), for 100 mTorr. The maximum energy of the ions, however, still follows the time-dependent accelerating voltage. When the value of the lower excitation frequency is increased the distribution becomes more complex (c.f. the distributions having several peaks in Figure 1). This effect is illustrated in Figure 2(e) for 100 MHz / 10 MHz excitation. At these conditions, as the ion transit time is longer than $1/f_{LF}$, the maximum energy is roughly independent of the phase of the low frequency voltage, and is correlated with the time-average of the difference between the plasma potential and $V_{LF}(t)$ (see Figure 2(f)). Figure 2(e) indicates that there exist several, nearly monoenergetic streams of ions in the sheath.

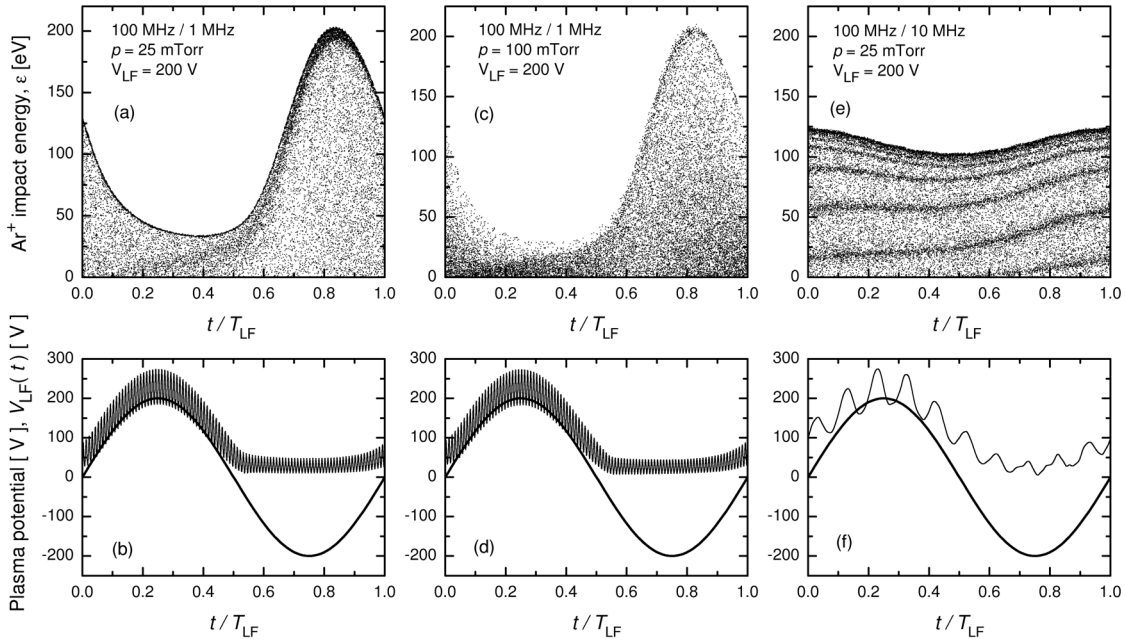

Figure 2. Temporal and energy distribution of Ar^+ ions falling on the surface of the powered electrode at V_{LF} = 200 V. Dots correspond to individual Ar^+ ions, their positions in the plots correspond to their energy and the time of arrival during a low-frequency cycle. (a) 100 MHz /1 MHz, 25 mTorr; (c) 100 MHz /1 MHz, 100 mTorr; (e) 100 MHz /10 MHz, 25 mTorr. (b), (d) and (f): corresponding time-dependent plasma potential (thin lines) and low-frequency excitation voltage $V_{LF}(t) = 200\ V \sin(2\pi t / T_{LF})$ (heavy lines).

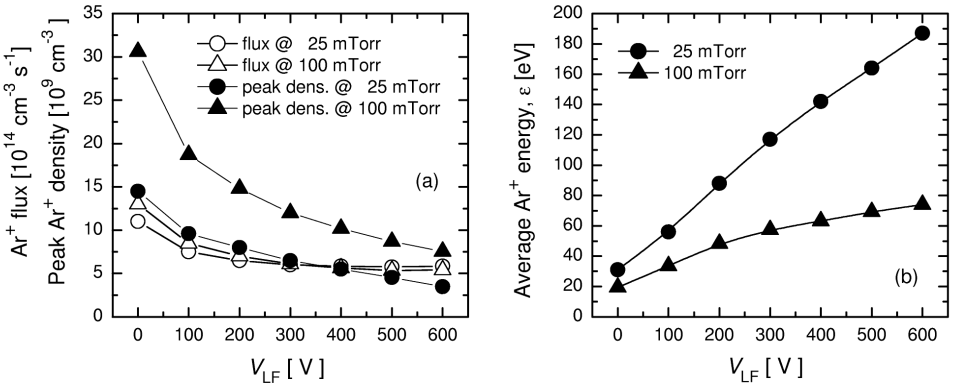

Figure 3. (a) Ion flux and peak value of ion density, and (b) average energy of Ar^+ ions reaching the electrodes as a function of the *low-frequency voltage* in 100 MHz / 1 MHz discharges at V_{HF} = 60 V.

So far we have observed that at (i) great ratios of the high frequency to the low frequency applied for the excitation of the discharge and (ii) having a sufficiently low pressure, the flux-energy distribution of the ions can be tuned by the low-frequency voltage. In Figure 3 it is demonstrated that this can be achieved at a nearly constant flux of the ions when V_{LF} is fixed. At p = 25 mTorr we indeed observe that while the peak ion density in the discharge decays with increasing V_{LF}, after an initial decrease the flux of ions remains nearly constant when the low-frequency voltage is increased. Meanwhile, the average energy of Ar^+ ions increases considerably, as displayed in Figure 3(b). At the higher pressure studied (100 mTorr, as already predictable from the earlier discussion) the average energy saturates with increasing low-frequency voltage.

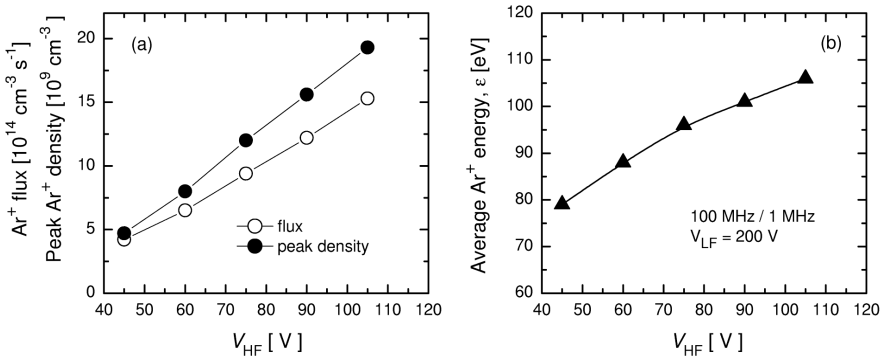

Figure 4. (a) Ion flux and peak value of ion density, and (b) average energy of Ar^+ ions reaching the electrodes as a function of the *high-frequency voltage* in the 100 MHz / 1 MHz discharge at p = 25 mTorr and V_{LF} = 200 V.

The density and the flux of ions, on the other hand, can be controlled by the high-frequency voltage, as illustrated in Figure 4. We observe a nearly linear increase of these quantities with increasing V_{HF}, as seen in Figure 4(a). At the same time, the increase of V_{HF} changes only slightly the average energy of ions (see Figure 4(b)). These observations confirm that the dual-frequency excitation, when operating conditions are properly chosen, makes it possible to realize a nearly independent control of the ion energy and flux in low-pressure plasma sources.

This work has been supported by the Hungarian Scientific Research Fund through the grant OTKA-T-48389.

References

[1] M.A. Liberman,A.J. Lichtenberg, *Principles of Plasma Discharges and Materials Processing*, Wiley and Sons, New York, 1994.
[2] T. Kitajima, Y. Takeo, Z. Lj. Petrović, T. Makabe, *Appl. Phys. Lett*., 77 (2000) 489.
[3] T. Fujita, T. Makabe, *Plasma Sources Sci. Technol*., 11 (2002) 142.
[4] T. Denda, Y. Miyoshi, Y. Komukai, T. Goto, Z. Lj. Petrović, T. Makabe, *J. Appl. Phys*., 95 (2004) 870.
[5] J. Robiche, P.C. Boyle, M.M. Turner, A.R. Ellingboe, *J. Phys. D: Appl. Phys*., 36 (2003) 1810.
[6] G. Wakayama, K. Nanbu, *IEEE Trans. Plasma Sci*. 31 (2003) 638.
[7] V. Georgieva, A. Bogaerts, R. Gijbels, *J. Appl. Phys.* 93 (2003) 2369; J. *Appl. Phys*. 94 (2003) 3748.
[8] P.C. Boyle, A.R. Ellingboe, M.M. Turner, *J. Phys. D: Appl. Phys*. 37 (2004) 697; *Plasma Sources Sci. Technol*. 13 (2004) 493.
[9] F.A. Haas, *J. Phys. D: Appl. Phys*. 37 (2004) 3117.
[10] K. Denpoh, G. Wakayama, K. Nanbu, *Jpn. J. Appl. Phys.* 43 (2004) 5533.
[11] H.C. Kim, J.K. Lee, *J. Vac. Sci. Technol. A* 23 (2005) 651; *Phys. Plasmas* 12 (2005) 053501.
[12] A. Salabas, R.P. Brinkmann, *Plasma Sources Sci. Technol*. 14 (2005) S53.
[13] Z.-Q. Guan, Z.-L. Dai, Y.-N. Wang, *Phys. Plasma*s 12 (2005) 123502.
[14] Z. Donkó, Z. Lj. Petrović, *Jpn. J. Appl. Phys*. 45 (2006) 8151.
[15] V.A. Godyak, R.B. Piejak, *Phys. Rev. Lett*. 65 (1990) 996.
[16] M.M. Turner, *Phys. Plasmas* 13 (2006) 033506.

Atmospheric Pressure Microwave Plasma Sources for Gas Treatment

M. Jasinski, Z. Zakrzewski, J. Mizeraczyk

Centre for Plasma and Laser Engineering, The Szewalski Institute of Fluid-Flow Machinery,
Polish Academy of Sciences, Fiszera 14, 80-231Gdansk, Poland
e-mail: mj@imp.gda.pl

Abstract

In this paper, atmospheric pressure microwave discharge methods and sources used for producing the non-thermal plasmas for gas treatment are presented. Two types of new microwave plasma sources (MPSs), i.e. a waveguide-based nozzle-type MPS and waveguide-based cylinder-type MPS are described. The important advantages of the presented MPSs are: stable operation in gases, including air, at high flow rates, lack of a special cooling system, no need for a 3-stub tuner, and discharge initiation and operation without any admixture of a noble gas.

1. Introduction

The emission of SO_2, NO_x (NO, NO_2), CO, CO_2, volatile organic compounds (VOCs) and other gaseous pollutants to the atmosphere influence heavily our environment. They cause acid rains, depletion of the ozone layer, greenhouse effect, etc. Human beings, animals and plants suffer due to direct and indirect influence of the gaseous pollutants.

Therefore, efficient methods for the control and reduction of gaseous pollutant emission are strongly required. Nowadays, conventional methods, e.g. adsorption, absorption, catalytic combustion seem not to be efficient enough. Recently, potential of the atmospheric pressure thermal (e.g. DC torches from plasmatrons, RF torches) and non-thermal (e.g. electron beam, DC and pulsed corona discharges, corona discharges in packed-bed reactors, dielectric barrier discharges, surface discharges, microwave discharges) plasma methods for the abatement of gaseous pollutants have been tested [1, 2, 3]. Majority of the non-thermal plasma methods have been tested for destruction of gaseous pollutants (SO_x, NO_x, VOCs) of a relatively low concentration [up to 1000 ppm (0.1 %)] in the working gas [3]. The nozzle-type microwave discharge method (e.g. [4]) has been used for destruction of gaseous pollutants [mainly VOCs] of relatively high concentration [up to tens %)].

Microwave discharges at atmospheric pressure can be classified as a non-thermal plasma at elevated gas temperature (up to 4000 K). This temperature is too low to form the local thermal equilibrium (LTE) of the plasma, however it is helpful in the decomposition of stable VOC molecules.

In this paper we deal with new MPSs, i.e. waveguide-based nozzle-type MPS and waveguide-based cylinder-type MPS, which we propose for the treatment of gases, in particular of pollutants.

2. Atmospheric pressure MPSs

The nozzle-type MPSs first appeared as structures based on microwave coaxial line components (e.g. [5]). In these coaxial-line-based MPSs, the microwave plasma was induced in the form of a plasma “flame” at the open end of a rigid coaxial line, at the tip of its inner conductor. The power-handling capability of coaxial-line-based microwave discharges is generally limited to much less than 1 kW due to the low thermal strength of the coaxial line components.

Parallel with the coaxial-line-based nozzle-type MPSs the so-called waveguide-based nozzle-type MPSs have been developed (e.g. [6-8]). In these applicators the microwave plasma is also induced in the form of a plasma flame at the tip of a field-shaping structure that is similar to that of the coaxial-line based MPSs. However, the microwave power is fed into this structure from a waveguide, usually rectangular at 2.45 GHz. In the advanced devices, the microwave power is delivered to the field-shaping structure in the form of a conductor with a conical nozzle through a waveguide with a reduced-height section [8].

Since both microwave discharges, the coaxial-line-based and waveguide-based one, are gas flowing systems, they are particularly suitable for processing various gases or materials carried by gases.

Recently, a new MPS was presented (e.g. [9-11] based on the rectangular waveguide with a reduced-height section, where the discharge is generated inside of a dielectric cylinder with a swirl flow of the working gas. There is not any nozzle in such a system.

In this paper we present the performance of both systems, the waveguide-based nozzle-type MPS and waveguide-based (nozzleless) cylinder-type MPS. The both MPSs were equipped with a swirl gas flow

supplying system.

3. Experimental

The main parts of two experimental setups used in this investigation were a microwave generator (magnetron), microwave plasma source (MPS), microwave supplying and measuring system, and gas supplying system. The microwave (2.45 GHz) power was supplied to the MPS from a magnetron via WR-284 rectangular waveguide with a reduced-height section. The MPSs were: the waveguide-based nozzle-type MPS (chapter 3.1) and waveguide-based (nozzleless) cylinder-type MPS (chapter 3.2). In both MPSs the plasma generated inside the glass discharge cylinder was stabilized by forming an additional swirl gas flow (nitrogen) in the cylinder, which stabilized the discharge in the center of the cylinder and protected the cylinder wall from the heat [9]. Initiation of the microwave discharge in the both cylinders was realized by insertion of a metal wire into the discharge zone.

The important advantages of the presented MPSs are: initiation of the discharge without any admixture of a noble gas, stable operation in gases at high flow rates, lack of a cooling system and no need for a 3-stub tuner.

3.1. Waveguide-based nozzle-type MPS

The photo and the sketch of the waveguide-based nozzle-type MPS are shown in Fig. 1a and 1b, respectively. Two flows were formed in the cylinder: central flow (air) and a swirl flow (nitrogen). The air flow was introduced centrally to the discharge zone through a conical nozzle. The nitrogen flow was supplied tangentially through the four inlets, as shown in Fig. 1b, creating a spiral vortex flow in the glass cylinder.

A disadvantage of the presented waveguide-based nozzle-type MPS is the use of the nozzle, which exposed to erosion. Such a disadvantage has been avoided in the waveguide-based (nozzleless) cylinder-type MPS presented below.

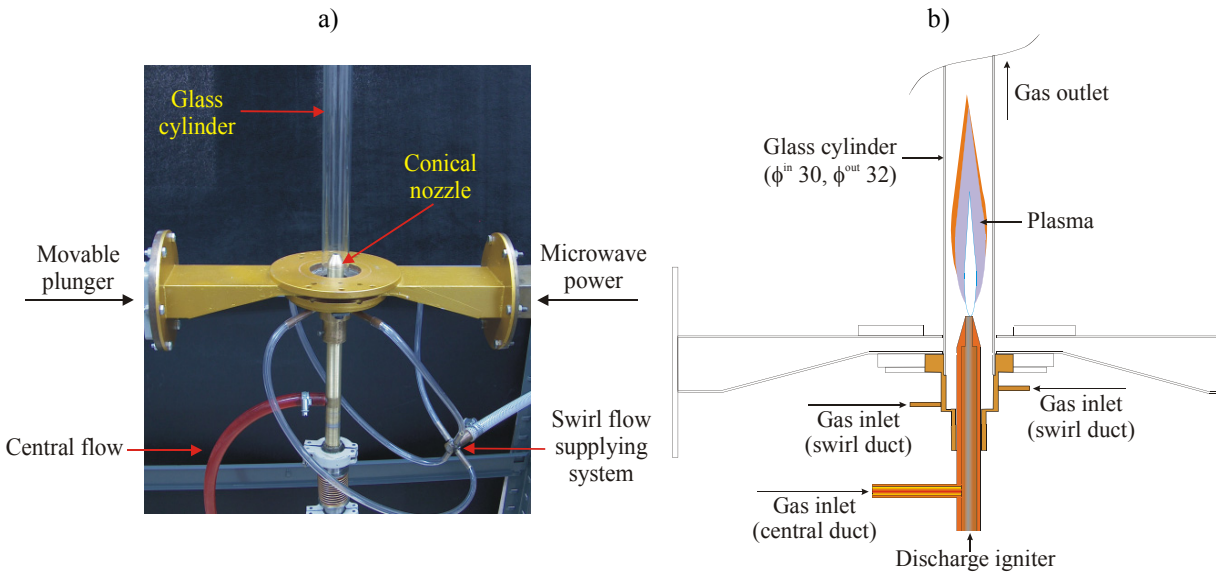

Fig. 1. Photo (a) and sketch (b) of the waveguide-based nozzle-type MPS.

3.2. Waveguide-based (nozzleless) cylinder-type MPS

The photo and the sketch of the waveguide-based cylinder-type MPS are shown in Fig. 2a and 2b, respectively. There is not any nozzle in this MPS. As shown in Fig. 2b, two flows were formed in the cylinder: central flow (air) and a swirl flow (nitrogen).

4. Results and discussion

The performance of the both MPSs was tested in a wide range of the gas flow rate and microwave input power. The both MPSs exhibited stable operation at microwave power from 600 W up to 6000 W, provided that the gas flow was sufficiently large (200 l/min and more).

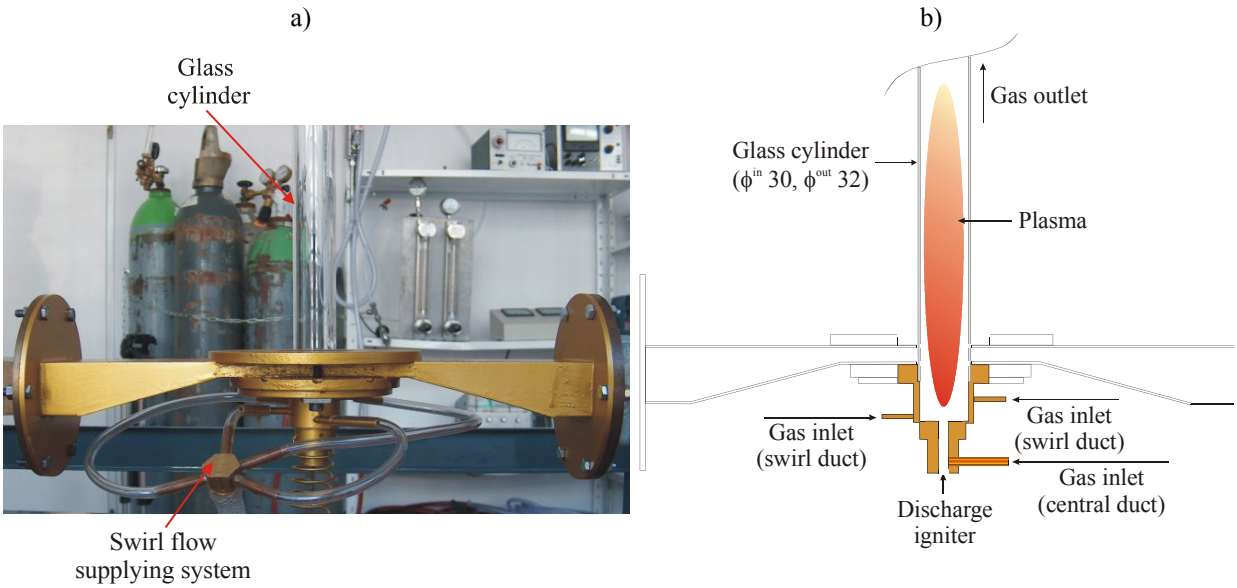

Fig. 2. Photo (a) and sketch (b) of the waveguide-based cylinder-type MPS.

4.1. Waveguide-based nozzle-type MPS

The photo of the waveguide-based nozzle-type discharge is shown in Fig. 3. The metal shielding chamber protected personnel and instrumentation from microwave radiation. The absorbed microwave power, central flow (air) and swirl flow (nitrogen) were 2000 W, 50 l/min and 200 l/min, respectively. At this condition the discharge length was about 20 cm.

The dependence of the reflection coefficient P_R/P_I (P_R - reflected microwave power, P_I - incident microwave power) on incident microwave power P_I for different nitrogen swirl flow rates (Q^{swirl}) is shown in Fig. 4 at the optimum matching (the best position of the movable plunger). For this position of the movable plunger, the best matching corresponds to P_I = 2000 W. The reflection coefficient was almost independent of the nitrogen swirl flow rate.

The reflected microwave power was negligible for the incident microwave power of about 2000 W. At higher values of the incident microwave power P_I, the reflected microwave power P_R was lower than 20 % of the value of P_I.

Fig. 3. Photo of the nozzle-type discharge.

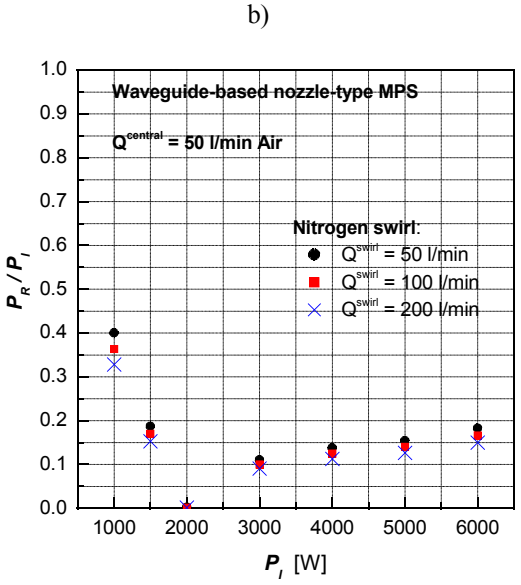

Fig. 4. The reflection coefficient versus incident power.

4.2. Waveguide-based (nozzleless) cylinder-type MPS

The photo of the waveguide-based cylinder-type discharge is shown in Fig. 5. The absorbed microwave power, central flow (air) and swirl flow (nitrogen) were 2000 W, 50 l/min and 200 l/min, respectively. At this

conditions the discharge length was about 20 cm.

The dependence of the reflection coefficient P_R/P_I on incident microwave power P_I for different nitrogen swirl flow rates (Q^{swirl}) is shown in Fig. 6. As seen, the reflection coefficient was almost independent of the nitrogen swirl flow rate. The reflected microwave power was negligible for the incident microwave power less than about 2500 W. At higher incident microwave power, the P_R/P_I can reach 30 %.

a)

Fig. 5. Photo of the cylinder-type discharge.

b)

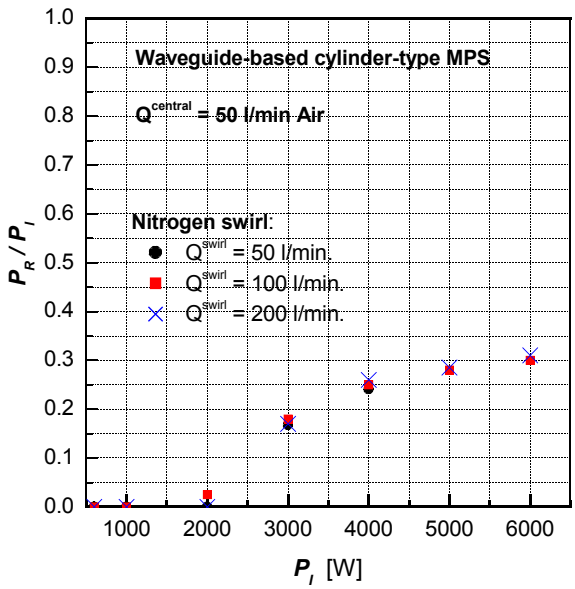

Fig. 6 The reflection coefficient versus incident power.

Acknowledgements

This research was supported by the Ministry of Science and Higher Education (MNiSW) under the programme 3020/T02/2006/31 and by the Szewalski Institute of Fluid-Flow Machinery PAS.

References

[1] K.H. Becker, U. Kogelschatz, K.H. Schoenbach, R.J. Barker, Eds., *Non-Equilibrium Air Plasmas at Atmospheric Pressure*, IOP Publishing Ltd, Bristol, UK, (now: Taylor & Francis, CRC Press), 2004 pp. 621-642.

[2] E.M. Van Veldhuizen, *Electrical Discharges for Environmental Purposes: Fundamentals and Applications*, Nova Science Publisher, Inc., 2000, pp. 221-427.

[3] K. Urashima, J.S. Chang, *IEEE Transactions on Dielectrics and Electrical Insulation*, 7(5), 2000, pp. 602-614.

[4] M. Jasiński, J. Mizeraczyk, Z. Zakrzewski, T. Ohkubo, J.S. Chang, *J. Phys. D: Appl. Phys.*, 35, 2002, pp. 2274-2280.

[5] J.D. Cobine, D.A. Wilbur, *J. Appl. Phys*., 22, 1951, pp. 835-841.

[6] M. Yamamoto, S. Murayama, *Spectrochim. Acta A*, 23, 1967, pp. 773-776.

[7] M. Moisan, G. Sauve, Z. Zakrzewski, J. Hubert, *Plasma Sources Sci. Technol.,* 3, 1994, pp.584-592.

[8] M. Moisan, Z. Zakrzewski, J.C. Rostaining, *Plasma Sources Sci. Technol*., 10, 2001, pp. 387-394.

[9] H.S. Uhm, Y.C. Hong, D.H. Shin, *Plasma Sources Sci. Technol.,* 15, 2006, pp. S26-S34.

[10] Y.C. Hong, H.S. Uhm, H.S. Kim, M.J. Han, S.C. Ko, S.K. Park, *IEEE Transactions on Plasma Science*, 33, 2005, pp. 958-963.

[11] K.M. Green, M.C. Borras, P.P. Woskow, G.J. Flores, K. Hadidi, P. Thomas, *IEEE Transactions on Plasma Science*, 29, 2001, pp. 399-406.

Electrical Discharges in Water

P. Lukeš, M. Člupek, V. Babický, P. Šunka

Department of Pulse Plasma Systems, Institute of Plasma Physics, Academy of Sciences of the Czech Republic, Za Slovankou 3, Praha 182 00, Czech Republic
e-mail: lukes@ipp.cas.cz

Abstract

Fundamentals of electrical discharges in water, the principles of breakdown phenomena in the liquid, the physical and chemical processes initiated by the pulsed electrical discharges in water and their application for degradation of chemical compounds and inactivation of microorganisms in water are presented.

Introduction

Recently, different types of liquid phase electrical discharge reactors have been investigated, and are being developed, since non-thermal plasma generated by electrical discharges initiate various chemical and physical processes in water that can be potentially utilized in different environmental, biological or medical applications. These processes include high electric field, intense ultraviolet radiation, overpressure shock waves and, of particular importance, formation of various reactive chemical species such as radicals (OH, H, O) and molecular species (H_2O_2, H_2, O_2, O_3). It has been demonstrated that these physical and chemical processes are capable to destroy or degrade biological cells and chemical compounds dissolved in water when the magnitudes of the various contributions of these processes strongly depend upon the type and the power of the discharge and also on water conductivity [1]. In this paper basic principles of electrical discharges in water are presented with particular emphasis to the pulsed (electrohydraulic) discharges and the physical and chemical effects initiated by these discharges in water.

Formation of electrical discharge in water

The breakdown phenomena in liquids have been studied for a long time, in particular to their importance in electrical transmission processes and their practical application to the design and the insulation of high voltage pulsed power systems. However, the detailed mechanism of the initiation of the discharges in water is still not fully understood compared to the understanding of the gas phase discharges. Such difference is caused mainly by the substantially higher density of water leading to much higher collision frequency and lower mobility of charges as the mobility of ions is much less than that of electrons. In addition, water is a highly polar liquid with large electrical permittivity and specific conductivity [2].

Since very high-localized electric field of the order of 1 MV/cm is needed for electrical breakdown of water, the pulsed high voltage is often used to generate electrical (electrohydraulic) discharge in water. Discharges are generated either directly in the water or in the gas phase in close proximity to the liquid surface or in both phases simultaneously. Consequently, AC and DC electric fields are also used to initiate discharge. Concerning pulsed electric discharges there are two of the basic types that differ primarily by the amount of energy deposited in the system and they can be classified into “partial“ electrical discharges (streamer discharges) where the discharge current flows from one electrode, however, it does not reach the counter electrode, and arc or spark discharge. In the partial discharge with the energy of the order 1J/pulse (called also “streamer corona“ or “corona-like“) the current is transferred by ions. It is evident that in such situation the solution conductivity plays an important role in parameters of the generated plasmas. Higher conductivity (a higher concentration of ions) results in a larger discharge current, and, on the other hand, in shortening of the streamer length (faster compensation of the space charge electric fields on the head of the streamer). This results in a higher power density in the channel (a higher power dissipated in a smaller volume) resulting in an increase in the plasma density, in a higher temperature of the plasma. Spark and arc discharges (energy of ~ 1kJ/pulse) are quite different from the “partial” discharges. The current between electrodes is transferred here by electrons. Due the relatively high breakdown electric field of water, a small inter electrode gap is necessary and the discharge current heats a small volume of plasma that results in generation of almost thermal plasma. The spark and arc discharges differ only in their durations. Temperatures of the spark and arc discharges plasmas are above 10 000 K and high power UV and also strong shock waves are generated [1].

For generation of electrical discharge in water electrode systems producing a highly non-uniform electric field are used (point-plate, wire-cylinder, hole-plate, rod-rod, ring-cylinder, etc.) [1,3]. Among them point-to-plane geometry has most typically been studied where the needle, used as point electrode, is connected to the high voltage and the plane is earthed. In this case the point electrode with appropriate insulation, where only

a tip of the electrode is in direct contact with water, makes possible to form a concentrated electric field. Another approach is to bubble gas through the hypodermic needle since gas bubbles in the discharge region significantly facilitate the plasma formation due to lower electrical breakdown of gas (typically ~ 30 kV/cm) than of water. However, one of the major problems of the point-to-plane geometry is that the very large electric field at the high voltage electrode, necessary to produce the discharge, causes extensive wear on the electrode [4]. As the radius of curvature increases at the tip, the field decreases and the discharge reaches a condition where it can no longer be sustained.

In order to overcome this limitation, porous ceramic-coated metal electrodes have been recently developed that can be used in a wide variety of geometrical configurations, including wire cylinder or planar systems [5]. Porous ceramic coatings (layer thickness 0.2-0.3 mm, open porosity 2%-5%, pore dimension 1-10 μm) were deposited on the surface of metal electrode by thermal plasma spraying technology. Powders of natural raw minerals such as aluminum oxide Al_2O_3 or iron aluminum silicate (almandine) $Fe_3Al_2(SiO_4)_3$ are used for preparation of the coatings. The role of ceramic layer is to enhance the electric field on the surface of the wire electrode by its redistribution due to different permittivity and conductivity of the porous ceramic layer and water. Using such design a large number of discharge channels, distributed almost homogenously along the whole surface of the ceramic layer, can be generated from the pores at relatively moderate applied voltage of 20-30 kV. Design of the composite discharge electrode corresponds to a limiting case of the diaphragm discharge (or pinhole), which is another type of discharge reactor configuration, where the perforated dielectric sheet is placed between the electrodes [6]. In this case the pre-discharge current is concentrated in small hole(s) and leads to strong thermal effects, causing bubble formation and breakdown. Possible advantage of such system is that discharge is initiated in the liquid outside of the electrodes; however, in this case wear problems are also associated with the pinhole in the diaphragm layer [7].

Processes initiated by the electrical discharges in water

The pulsed high voltage discharges in water generate non-thermal plasma that initiate a variety of physical and chemical effects as high electric field, intense ultraviolet radiation, overpressure shock waves and, especially, formation of reactive chemical species acting on biological cells and chemical compounds dissolved in water. These effects have various important roles in different application regions in the liquid and the magnitude of their contributions strongly depends upon the energy of the discharge.

Physical processes

In discharges with the pulse power in the range of MW a large part of the energy is consumed in the formation of a high temperature plasma channel, which emits light in a wide range of wavelengths. Temperature of the spark discharge plasma initiated in water by exploding fine wires has been estimated to be several tens of thousands of degrees Kelvin [8]. The discharge channel thus functions as a blackbody radiation source with maximum in the vacuum ultraviolet (VUV) region. This radiation can cause photolysis effect, leading to dissociation of water molecules and formation of hydroxyl radicals. In addition, the expansion of the plasma channel against the surrounding water generates an intense shock wave with pressure on the order of hundreds of MPa. The resulting shockwave can induce pyrolytic and free radical reactions indirectly via electrohydraulic cavitation [1,9].

The radiation from pulsed streamer discharges in water with the pulse power in the range of kW is lower intensity. The results obtained using the emission spectroscopy showed a radiation from pulsed corona discharge in the range of 200-1000 nm, which is dominated by the spectral lines of hydrogen (peaks at 434, 486, 656 nm) and oxygen atom (771 nm) and by emission from OH· radical (309 nm). Electron density above 10^{18} cm^{-3} in the streamer has been determined from the H_α spectral line profile. Comparing the measured fine structure of the OH spectral band with the computed one, a rotational temperature above 2000 K of the OH radicals has been estimated. However, with increase in water conductivity a higher electron density and more intensive emission spectrum of the discharge with broader spectral lines was determined [1,2]. In addition, the generation of UV light from the pulsed corona discharge in water has been demonstrated by means of chemical actinometry technique. Strong increase of intensity of UV radiation from the discharge has been measured with increasing solution conductivity [10]. Furthermore, thermal effects and shock waves generation by corona-like discharge were determined in highly conductive liquids [11].

Chemical processes

Production of various reactive chemical species such as radicals (OH·, H·, O·, HO_2·) and molecular species (H_2O_2, H_2, O_2) has been reported for the pulsed electrical discharges in water with power of kW/pulse, like pulsed streamer corona discharge, among which hydroxyl radicals and hydrogen peroxide are the most important for oxidation processes. Generation of OH, H and O radicals has been proven by

emission optical spectroscopy. There is also evidence about production of OH, H and HO_2 radicals and hydrogen peroxide by chemical methods [1-3]. The generation of molecular hydrogen and oxygen was measured by gas chromatography [12].

It is expected that the primary chemical activity of electrical discharges in water is associated largely with the initial production of OH and H radicals from the dissociation and/or ionization of water molecules by high energetic electrons. The mechanisms of their formation is assumed to be similar to those in radiolytic processes such as γ-radiation, electron beam radiation, pulse radiolysis and photochemical processes:

a) direct electron dissociation of water to form H· and OH· radicals

$$e^- + H_2O \rightarrow H\cdot + OH\cdot + e^- \quad (1)$$

b) ionization of water to form H_2O^+, which by rapid reaction with another water molecule produces H_3O^+ and the OH· radical.

$$e^- + H_2O \rightarrow H_2O^+ + 2\,e^- \quad (2)$$
$$H_2O^+ + H_2O \rightarrow H_3O^+ + OH\cdot \quad (3)$$

Considering the ionization of water molecules that requires quite high electron energies (12.62 eV), electron impact dissociation of water (6.4 eV) seems to be the more feasible process. However, there are also models [1] proposing electric field-assisted dissociation/ionization of water that would require significantly lower energy levels for processes in Eqs. 1 and 2.

$$H\cdot + H\cdot \rightarrow H_2 \quad (4)$$
$$OH\cdot + OH\cdot \rightarrow H_2O_2 \quad (5)$$
$$H\cdot + OH\cdot \rightarrow H_2O \quad (6)$$

Consequently, the OH and H radicals may in dependence of the energy distribution of electrons in the streamer head either react with each other to form product molecules H_2 and H_2O_2 or reform water (Eqs. 4-6) or diffuse away from each other and to be available to react with solutes.

Applications of electrical discharges in water

Pulsed electrical discharges in water have been shown to be effective at degrading a number of small organic compounds including phenols, TCE, biphenyls, organic dyes etc., at deactivating of microorganisms in water and also in the modification of surface properties of polymeric materials [1-3]. The mechanism of degradation of organic compounds was found to be attributed mainly to the oxidation by hydroxyl radicals produced directly by the discharge and it can be described by the first order kinetics. The removal efficiency of the discharge can be significantly enhanced in the presence of iron due to Fenton's reaction, where hydrogen peroxide produced by the discharge reacts with ferrous ions to produce hydroxyl radicals. There is also evidence about contribution of reductive species HO_2 and H radicals in the removal of chemical compounds by the discharge in water [1-3,13]. Plasma chemical activity of electrical discharge in water can be further enhanced by the addition of solid particles into the discharge reactor. Several types of materials have been tested such as activated carbon, silica gel, alumina, titanium oxide or zeolites. These materials can affect chemical activity of the discharge in various ways including, in addition to the simple adsorption processes, also plasma induced catalytic reactions on their surface.

Consequently, a number of studies have utilized gas phase discharge generated over the water surface to produce in the gas or at the gas-liquid interface strongly oxidative species, such as OH· radicals, O atoms and their reaction products (O_3, H_2O_2), that can dissolve into the water to initiate oxidation processes [1]. The hybrid gas-liquid electrical discharge reactors that combine gas phase non-thermal plasma formed above the water surface with direct liquid phase corona-like discharge in the water have been demonstrated to significantly enhance overall plasmachemical activity of the discharge compared to the single-liquid phase discharge reactor due to simultaneous oxidation of organic compounds by chemically active species produced by the liquid phase discharge and the gas phase discharge above the liquid. It was shown that depending on used gas atmosphere above water, e.g. phenol degradation was mainly caused by the attack of OH· radicals produced by the liquid phase discharge directly in water and OH· radicals and ozone produced by the gas phase discharge above the liquid. At high pH phenol was degraded, in addition to the direct attack by ozone, also through indirect reactions of OH· radicals formed via Peroxone process by the decomposition of dissolved ozone by hydrogen peroxide produced by the liquid phase discharge [14,15].

On the other hand, less is known about mechanism of sterilization by means of electrical discharge in water although it was successfully applied to the inactivation a number of microorganisms in water such as bacteria, viruses or yeast [1]. Apparently, living matter represents much more complex system where various factors such as a type of microorganism, its morphology, cell wall strength and structure, but also a type of aqueous medium supporting microorganism, play significant role in the efficiency of the inactivation process. Survivor curves of different shapes including single-slope or two-slope with initial lag-phase are usually reported for inactivation kinetics of various microorganisms compared to usually first order kinetic of plasmachemical decomposition of chemical compounds. In general, it is evident that, in addition to the chemical effects caused by produced reactive species (e.g. OH radicals, H_2O_2 and O_3), the physical processes such as high electric field and ultraviolet radiation from the discharge also contribute in the inactivation process. This was proved for example on inactivation of bacteria *Escherichia coli* by the pulsed corona discharge in water when significant effect of UV radiation from the discharge has been determined and its contribution was estimated to be about 30% in overall inactivation activity of the discharge [16]. Consequently, lethal activity of hydrogen peroxide produced by the discharge on *E. coli* was significantly enhanced under influence of high electric field. This was caused more likely by electroporation effect induced by electric field in the discharge that polarizes bacteria cell and can enhance penetration of H_2O_2 through the cell membrane and cause damage inside of the cell via *in-vivo* produced OH radicals. The role of shockwaves produced by the discharge in water should be also considered. Their effect has been demonstrated in highly conductive liquids when a focused cylindrical pressure wave produced by a multichannel discharge at a composite anode has been shown effectively damage cancer cell membranes in the soft tissues. There is also possibility that local thermal effects accompanying the cavitation collapse and production of chemical radicals may also play role in the cell destruction [11].

Acknowledgement

Work was supported by the Academy of Sciences of the Czech Republic under contract No. K2043105.

References

[1] B.R. Locke, M. Sato, P. Sunka, M.R. Hoffmann, J.-S. Chang, *Ind. Eng. Chem. Res*., 45 (2006) 882.
[2] P. Sunka, *Phys. Plasmas*, 8 (2001) 2587.
[3] M.A. Malik, A. Ghaffar, S.A. Malik, *Plasma Sources Sci. Technol*., 10 (2001) 82.
[4] P. Lukes, M. Clupek, V. Babicky, P. Sunka, J.D. Skalny, M. Stefecka, J. Novak, Z. Malkova, *Czech. J. Phys.,* 56 (2006) B916.
[5] P. Sunka P., V. Babicky, M. Clupek, P. Lukes, M. Simek, J. Schmidt, M. Cernak, *Plasma Sources Sci. Technol*., 8 (1999) 258.
[6] P. Sunka, V. Babicky, M. Clupek, M. Fuciman, P. Lukes, M. Simek, J. Benes, B.R. Locke, Z. Majcherova, *Acta Phys. Slovaca,* 54 (2004) 135.
[7] Z. Stara, F. Krcma, *Czech. J. Phys.,* 54 (2004) C1050.
[8] J.W. Robinson, M. Ham, A.N. Balaster, *J. Appl. Phys*., 44 (1973) 72.
[9] N. Karpel Vel Leitner, G. Syonen, H. Romat, K. Urashima, J.-S. Chang, *Water Res*., 39 (2005) 4705.
[10] P. Lukes, *Water treatment by pulsed streamer corona discharge in water*, IPP AS CR, Prague, 2001.
[11] P. Sunka, V. Stelmashuk, V. Babicky, M. Clupek, J. Benes, P. Pouckova, J. Kaspar, M. Bodnar, *IEEE Trans. Plasma Sci*., 34 (2006) 1382.
[12] M.J. Kirkpatrick, B.R. Locke, *Ind. Eng. Chem. Res*., 44 (2005) 4243.
[13] M. Sahni, B.R. Locke, *Plasma Process. Polym.*, 3 (2006) 342.
[14] P. Lukes, B.R. Locke, *J. Phys. D: Apl. Phys.,* 38 (2005) 4074.
[15] P. Lukes, B.R. Locke, *Ind. Eng. Chem. Res.,* 44 (2005) 2921.
[16] T. Vykouk, M. Clupek, P. Lukes, *HAKONE X – Contributed Papers*, (2006) 229.

Progress Reports

Plasma Based Energetic Particle Treatment of UHMWPE

A. Tóth, M. Mohai, I. Bertóti

Institute of Materials and Environmental Chemistry, Chemical Research Center, Hungarian Academy of Sciences, H-1025 Budapest, Pusztaszeri út 59-67, Hungary
e-mail: totha@chemres.hu

Abstract

Medical grade ultra-high molecular weight polyethylene (UHMWPE) samples were treated by plasma immersion ion implantation in H_2, He and N_2 plasma gases. Voltages (U) between 15 and 30 kV, fluences (F) between 1×10^{17} and 3×10^{17} cm^{-2} and fluence rates (FR) between 3×10^{13} and 7×10^{13} cm^{-2} s^{-1} were varied systematically. Alterations in the mean surface roughness (R_a), the bulk plasmon loss energy of the C 1s peak (E_p) and the macroscopic surface temperature (T) were studied for each treatment. R_a increased from the value of the untreated material (20 nm) up to 108 and 187 nm respectively in H_2 and N_2, while in He a maximum value of about an order of magnitude higher (1422 nm) was obtained. E_p increased from 19 eV up to 25.2 and 25.0 eV respectively in H_2 and N_2, while in He to 27.2 eV, implying a significantly enhanced densification in He. The pronounced increase in roughness and enhanced densification obtained in He were attributed to the very high T developed in this plasma and to the inert, atomic nature of He.

Introduction

Plasma-based energetic particle treatment is a relatively simple, efficient and cost-effective way of surface modification of solids in general and of polymeric materials in particular. Fast atom beam (FAB) treatment for instance – in which the positively charged plasma ions are usually accelerated to relatively low energies and then neutralised – do not lead to significant surface charging and can induce substantial changes in such properties of polymers like gas permeability and selectivity [1-3], mechanical and other properties [4-6]. Another, relatively new related technique is plasma based ion implantation (PBII) called also plasma immersion ion implantation (PIII or PI^3), which is alternative to conventional ion-implantation. With this method even irregularly shaped objects can be uniformly treated, enhancing their surface properties. PIII proved to be a viable way of modifying the surface chemical and mechanical properties and increasing the wear resistance of ultra-high molecular weight polyethylene (UHMWPE) [7-16], which is a frequently applied cup material of hip joints applied in human implantology. In this work UHMWPE samples were treated by PIII in various plasma gases. The main process parameters like acceleration voltage, fluence and fluence rate were varied systematically and alterations in the properties like surface roughness, bulk plasmon loss energy and macroscopic surface temperature were studied and compared.

Results and discussion

The mean surface roughness R_a of the untreated and the PIII-treated UHMWPE samples was determined from topographic curves obtained by a NanoTest 600 equipment. Fig. 1 shows the evolution of R_a in various plasma gases as a function of voltage U and fluence rate FR. For comparison, the ordinate is scaled to similar values for each treatment. In general, R_a increased for each treatment, showing a dependence mainly on U, while the influence of FR and F was not pronounced under the conditions applied. However, a spectacular difference can be observed in the extents of the increase of R_a in the various gases: in case of H_2 and N_2 it increased from the value of the untreated material (20 nm) up to the highest values of 108 and 187 nm, respectively, while in case of He it increased much more strongly, reaching a maximum value of as high as 1422 nm.

In order to obtain a deeper insight into the background of this effect, the surfaces of the samples were studied by X-ray photoelectron spectroscopy (XPS), using a Kratos XSAM800 spectrometer. From the detailed study of the C 1s region the bulk plasmon loss energy E_p could be determined. E_p was found to increase from 19 eV of the untreated sample up to values reaching 25.2 and 25.0 eV for samples treated in H_2 and N_2, respectively. After treatment in He, however, E_p was usually higher, reaching the highest value of 27.2 eV. This implies a significant increase in the mass density upon PIII-treatment, especially in case of treatment in He, since (for similar materials) E_p is known to be proportional to the square root of the valence electron density and thereby to the mass density. Thus, upon treatment in He, the pronounced increase of R_a was accompanied by an enhanced densification.

The temperature T developed in the stainless steel sample holder was also studied as a function of the PIII parameters. The aim was to estimate the possible temperature effect to which the UHMWPE samples could be exposed. T was calculated based on the ion current and calibrated by small pieces of various low melting

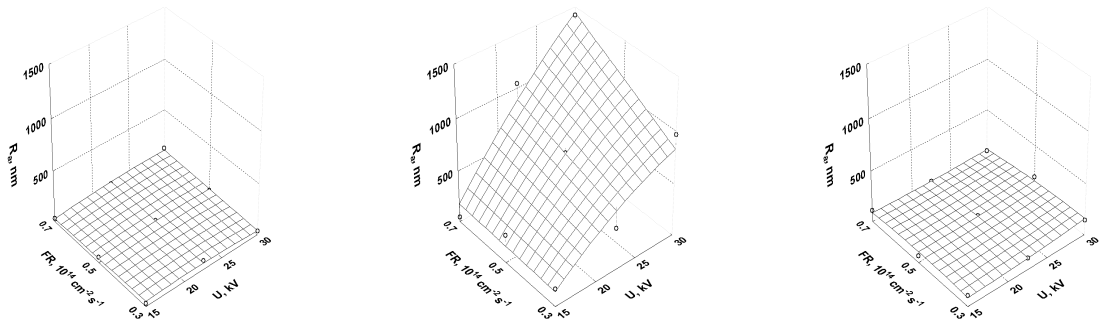

Fig. 1 Mean roughness developed as a result of PIII-treatment in H_2 (left), He (middle) and N_2 (right)

point metals. The results showed that *T* always increased upon PIII-treatment. As a general trend, it increased mainly with the increase of *U* and *FR*. When similar process parameters were applied, similar *T* values were obtained in H_2 and N_2. At the same time, the corresponding values obtained in He were always higher. Also, the highest *T* developed in He (239 °C) was much higher than that obtained in H_2 (149 °C) or in N_2 (143 °C). This can be a possible explanation for the pronounced increase in R_a and the enhanced densification in He.

In case of treatment in H_2 or N_2, a significant portion of ions can be present in the form of molecular ions. Upon collisions with the surface they are expected to dissociate and share their total energy, which is not the case with He. This will influence the energy distribution and thus the *T* values developed upon treatment.

Finally, monoatomic hydrogen and nitrogen particles are reactive and can block a portion of the radicals created upon energy deposition. In fact, in case of treatment in N_2, XPS shows a strong incorporation of N. Oppositely, He particles are not reactive, can not block radicals, thus the ablation-type reactions may proceed in He plasma gas without obstacle.

Conclusions

The mean surface roughness developed in He PIII-treatment is about an order of magnitude higher than that obtained in H_2 or in N_2 under similar conditions. This can be attributed to the very high *T* developed in this plasma and to the inert, atomic nature of He.

Acknowledgement

The first author thanks the Visegrad Fund for the financial support of his participation at the 16th SAPP.

References

[1] Hungarian Patent 211 184 (1993) and Russian Patent 2 072 890 (1993).
[2] A. Tóth, V.S. Khotimsky, I. Bertóti, G. Marletta, *J. Appl. Polym. Sci.* 60 (1996) 1883.
[3] A. Tóth, I. Bertóti, V.S. Khotimsky, G. Marletta, J.L. Sullivan, S.O. Saied, *Nucl. Instrum. Methods B* 122 (1997) 547.
[4] T. Ujvári, A. Tóth, I. Bertóti, P.M. Nagy, A. Juhász, *Solid State Ionics* 141-142 (2001) 225.
[5] A. Tóth, T. Ujvári, I. Bertóti, E. Szilágyi, T. Keszthelyi, A. Juhász. *Surf. Interface Anal.* 36 (2004) 1041.
[6] S. Tóth, M. Füle, M. Veres, I. Pócsik, M. Koós, A. Tóth, T. Ujvári, I. Bertóti, *Thin Solid Films* 497 (2006) 279.
[7] H. Dong, T. Bell, C. Blawert, B.L. Mordike*, J. Mater. Sci. Lett.* 19 (2000) 1147.
[8] W. Shi, X.Y. Li, H. Dong, *Wear* 250 (2001) 544.
[9] A. Kondyurin, V. Karmanov, R. Guenzel, *Vacuum* 64 (2002) 105.
[10] H. Dong, *Trans. Nonferrous Met. Soc. China,* 14 (2004) 36.
[11] K.G. Kostov, M. Ueda, I.H. Tan, N.F. Leite, A.F. Beloto, G.F. Gomes, *Surf. Coat. Technol.* 186 (2004) 287.
[12] A.R. Marcondes, M. Ueda, K.G. Kostov, A.F. Beloto, N.F. Leite, G.F. Gomes, C.M. Lepienski*, Braz. J. Phys.,* 34 (2004) 1667.
[13] A. Tóth, M. Mohai, T. Ujvári, I. Bertóti, *Surf. Interface Anal.* 38 (2006) 898.
[14] A. Tóth, I. Bertóti, M. Mohai, T. Ujvári, *Mater. Sci. Forum* 537-538 (2007) 255.

Double Hollow Cathode Plasma Jet System Applied for Deposition of Thin Films

P. Virostko[1,2], Z. Hubička[1], J. Olejníček[1], P. Adámek[3], M. Tichý[2]

[1]Institute of Physics, Academy of Sciences of the Czech Republic, Na Slovance 2, 182 21 Prague 8, Czech Republic
[2]Charles University in Prague, Faculty of Mathematics and Physics, Department of Electronics and Vacuum Physics, V Holešovičkách 2, 180 00 Prague 8, Czech Republic
[3]University of South Bohemia, Department of Physics, Jeronýmova 10, 371 15 České Budějovice, Czech Republic
e-mail: virostko@fzu.cz

Abstract

The presented work describes measurement of plasma parameters that are important for the control of the deposition process in the double hollow cathode plasma jet system. Time-resolved Langmuir probe technique was used for determination of electron distribution, electron density, and effective electron temperature in the position of the substrate at deposition conditions. Ratio of the sputtered particles, especially Ba and Sr atoms and ions, was controlled by optical emission spectroscopy. Measurements of the positive ion flux to the negatively biased substrate during deposition were performed.

Introduction

One of the promising plasma jet deposition systems is the low temperature low pressure hollow cathode plasma jet [1]. It was successfully used for many PVD thin films depositions, as for example TiN, ZnO, $LiCoO_x$, or $Pb(Zr_xTi_{1-x})O_3$ thin films. Recently, the $Ba_xSr_{1-x}TiO_3$ (BSTO) thin films were deposited using the RF hollow cathode plasma jet system [2]. For deposition of gradient BSTO films, which are interesting due to their dielectric properties, the double hollow cathode plasma jet system was developed.

Results and discussion

A schematic view of double hollow cathode plasma jet system for deposition of gradient BSTO films can be seen in Fig. 1.

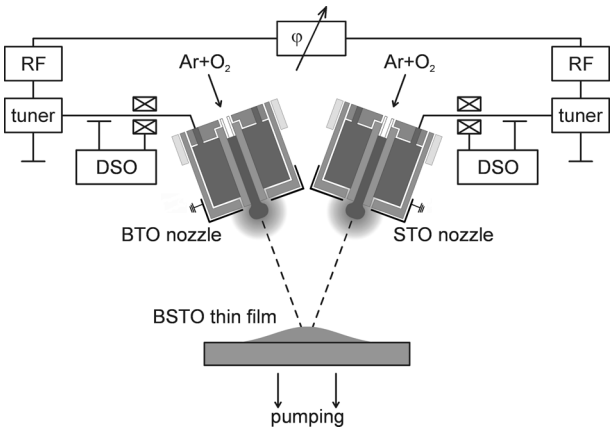

Figure 1. The double hollow cathode plasma jet system for BSTO thin films deposition.

Two nozzles were reactively sputtered by intensive pulse-modulated RF hollow cathode discharge. One nozzle was made of $BaTiO_3$ (BTO) ceramics and the other was made of $SrTiO_3$ (STO) ceramics. The working pressure was $p = 5$ Pa. The active part of the modulation pulse for the BTO nozzle followed right after the active part of modulation pulse for the STO nozzle. Then the afterglow part of the modulation pulse followed. The length of active part of modulation pulse was varied independently on both nozzles to vary their sputtering rates. By changing the sputtering rates of BTO and STO nozzles, it was possible to deposit gradient $Ba_xSr_{1-x}TiO_3$ films with varying parameter x along the axis perpendicular to the substrate.

Time evolution of electron energy probability function (EEPF) measured by the Langmuir probe in the position of substrate is depicted in Fig. 2. It can be seen from Fig. 2 that the electron distributions were similar in both active parts of the STO and BTO nozzles. It means that the plasma conditions were successfully set to be similar in both nozzles. Subsequently, the composition of the deposited films can be varied by varying the lengths of the active parts on each nozzle.

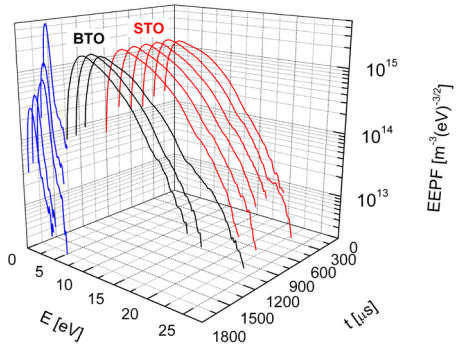

Figure 2. EEPF measured in the position of substrate in double hollow cathode plasma jet system for deposition of gradient BSTO films.

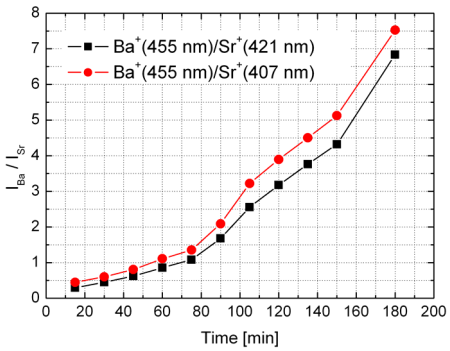

Figure 3. Controlling the composition of deposited film – the ratio of ion emission line intensities measured during deposition of a gradient BSTO film.

To control the composition of films, the ratio of optical emission spectral line intensities of particular ion emission lines was measured during the deposition, see Fig. 3. As we have shown before [3], the depicted ratio of the spectral line intensities is proportional to the ratio of Ba and Sr atoms in the deposited films. Subsequently, we can expect that the profile of Ba/Sr concentration ratio in the film will have qualitatively similar shape as the dependence depicted in Fig. 3.

The substrate was biased by pulse modulated DC source to a negative voltage with respect to the bulk plasma. The repetition frequency of the modulation was 40 kHz and the duty cycle 70%. The ion current through the substrate was measured on the resistor connected between the DC source and the substrate. The measured ion currents for different deposition conditions are in Table 1.

Table 1. Ion current to the substrate for different deposition conditions.

Sample	Discharge power [W]	DC bias [V]	Ion current [mA]
1	50	-80	12
2	100	-80	21
3	150	-80	29
4	200	-20	25
5	200	-35	26
6	200	-50	28
7	200	-65	31
8	200	-80	34

It can be seen from Table 1 that the ion current to the substrate rises with rising discharge power. This is due to the higher density of positive ions for higher power absorbed in the discharge, and it was confirmed by the Langmuir probe measurements. The ion current is also rising with rising amplitude of applied negative DC voltage for the same discharge power. Since the negatively biased substrate can be viewed as a planar probe working in ion saturation current region, one would expect no dependence of the ion current on the DC voltage. The discrepancy can be explained by the edge effect, i.e. the substrate is not an infinite plane and the sheath collecting area rises on its edge with the voltage. The other source of higher ion current can be additional ionization of the plasma around the substrate which would be higher for higher applied DC bias.

Acknowledgements

This work was financially supported by the research plan MSM 1M06002 of MSMT of the Czech Republic.

References

[1] L. Bárdoš, S. Berg, H. Baránková, *J. Vac. Sci. Technol.*, A 11 (1993) 1486.
[2] Z. Hubička, J. Olejníček, M. Čada, P. Virostko, H. Šíchová, A. Deyneka, L. Jastrabík, D. Chvostová, M. Šícha, *Ferroelectrics*, 317 (2005) 193.
[3] J. Olejníček, Z. Hubička, P. Virostko, A. Deyneka, L. Jastrabík, D. Chvostová, H. Šíchová, J. Pokorný, *Integr. Ferroelectr.*, 81 (2006) 1.

Numerical Experiments on Complex Plasmas

P. Hartmann[1], Z. Donkó[1], G. J. Kalman[2]

[1]Laser Physics Department, Research Institute for Solid State Physics and Optics of the Hungarian Academy of Sciences, H-1525 Budapest, P.O.B. 49, Hungary
[2]Department of Physics, Boston College, Chestnut Hill, MA 02467, USA
e-mail: hartmann@sunserv.kfki.hu

Abstract

A wide range of complex (dusty) plasma phenomena can be modeled with many-particle systems interacting through the Yukawa pair-potential. We present molecular dynamics simulation results for 2D Yukawa systems including structural, thermodynamic and collective dynamic (wave dispersion) properties.

Introduction

Complex (dusty) plasmas are systems where micron sized particles are immersed in gas discharges [1]. The (typically noble gas) glow discharge can be direct current (d.c.) or radio frequency (r.f.) driven and serves primarily as a charging medium for the (typically spherical, dielectric) particles. The dust particles collect the free electrons and ions from the discharge plasma, until a dynamic equilibrium is reached, where their net electric charge can be in the order of 10,000 electron charges. The interaction of these particles with their environment can be manifold: gravitation, Lorenz force, ion drag force, neutral drag force, thermophoretic effects, etc. [2]. The dominance of the different force contributions can be tuned by adjusting the experimental conditions (microgravity, flowing gas, etc.). In this paper we focus our attention to systems where the particles are levitated in a horizontal plane-parallel electrode configuration r.f. discharge. In this case the gravitation is compensated by the vertical electric field of the plasma sheath, and the particles settle in a single quasi-2D layer near the lower electrode. Other effects, like ion- and neutral drag forces act also mainly perpendicular to the particle plane, therefore influence only the equilibrium position of this layer. The remaining in-plane forces can be well approximated by a simple Yukawa type interaction, originating from the Coulomb repulsion of the charged dust particles and the polarizability (screening property) of the surrounding discharge plasma [3].

2D many-particle systems interacting through the Yukawa interaction can be characterized by two dimensionless quantities: (i) the Coulomb coupling (or non-ideality) parameter $\Gamma = Q^2 / k_B T a$, where Q is the charge of the dust particle, k_B is the Boltzmann constant, T is the temperature and a is the Wigner-Seitz (or ion sphere) radius given by $a = 1/\sqrt{np}$, where n is the areal density of the dust particles; (ii) the Yukawa screening parameter $\kappa = a / l_D$, where λ_D is the Debye screening length. Charged many-particle systems characterized with $\Gamma \geq 1$ are called *strongly coupled plasmas*. Depending on the coupling strength the system shows liquid like properties or may even crystallize at sufficiently high Γ [4].

The aim of this paper is to present some results achieved by investigating the static, thermodynamic and collective properties of 2D Yukawa systems by means of molecular dynamics simulations [5].

The numerical model

In our molecular dynamics (MD) simulations we use rectangular simulation box with periodic boundary conditions to emulate the infinite size of the system. To investigate the static and thermodynamic properties of the many-particle systems we use N = 63,360 particles in the simulation box. To determine the collective dynamic behavior, longer time-averaging is necessary which limits the particle number to N = 3,960 in these cases. The force calculation is performed between all particle pairs separated by less then a cutoff distance R_c, which is chosen to provide an accuracy of at least six digits. The particles are initially released with random velocities samples from a Maxwellian distribution from random or hexagonal lattice positions. The system is thermalized in the first simulation period by continuous rescaling of the particles' momenta according to the prescribed system temperature. Measurements of the physical quantities start after this thermalization period, when the particles move without any artificial intervention.

The particle simulation provides position and velocity data of each particle in every timestep, like in real dusty plasma experiments, where the same raw data is obtained from digital video sequences. Based on this primary data we perform a series of statistical analysis, and calculate quantities like the pair correlation function $g(r)$, bond order parameter G_Θ, thermodynamic pressure and internal energy P and E, inverse compressibility L, Einstein frequencies ω_E (oscillation frequencies of a single particle in the frozen

environment of the other particles), longitudinal and transverse current fluctuation spectra $L(\omega)$ and $T(\omega)$, velocity autocorrelation function, etc. These quantities provide the insight into the structural and dynamical properties in the investigated many-particle systems.

Results and discussion

In this section we present results for some of the above listed quantities to demonstrate the versatility of the numerical technique.

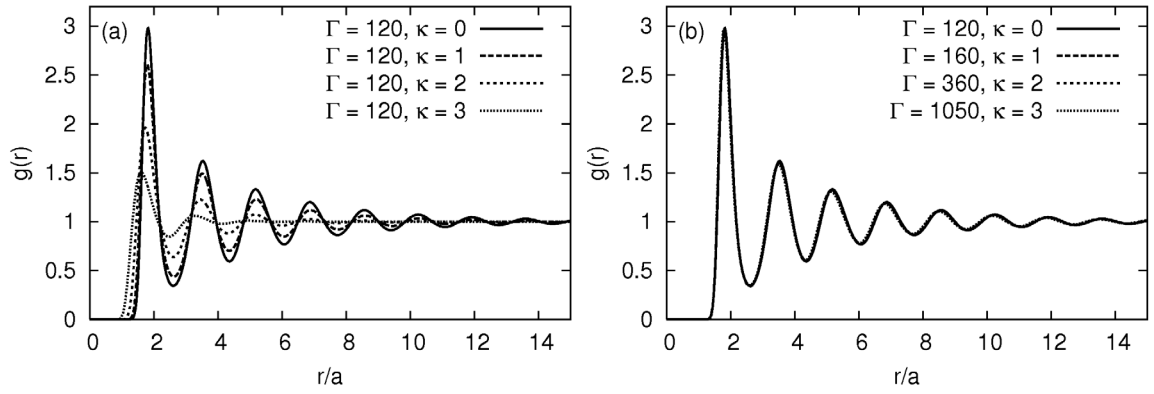

Figure 1. *Pair correlation functions for a series of Yukawa screenings κ (a) for Γ = 120 and (b) for Γ_{eff} = 120.*

Structural studies based on the pair correlation function $g(r)$ show the dominance of the hexagonal structure in the liquid and solid phases, as it can be obtained from the peak positions and amplitudes of the graphs in Figure 1a, where a series of $g(r)$ functions is plotted for different κ values at Γ = 120. We have found, that for every value of κ one can find a value of Γ, where the static structure of the system will very nearly map the structure of a corresponding Coulomb (κ = 0) system with a given coupling Γ*, as demonstrated in Figure 1b. This observation leads us to the definition of an effective coupling for 2D Yukawa systems: Γ_{eff} is the coupling parameter of a 2D Coulomb system which has the same first-peak amplitude as the investigated Yukawa system described with the parameters Γ and κ. This relationship can be expressed with the fitted formula:

$$\Gamma_{eff} = \Gamma f(k), \quad \text{where } f(k) = 1 - 0.388k^2 + 0.138k^3 - 0.0138k^4 \quad (1)$$

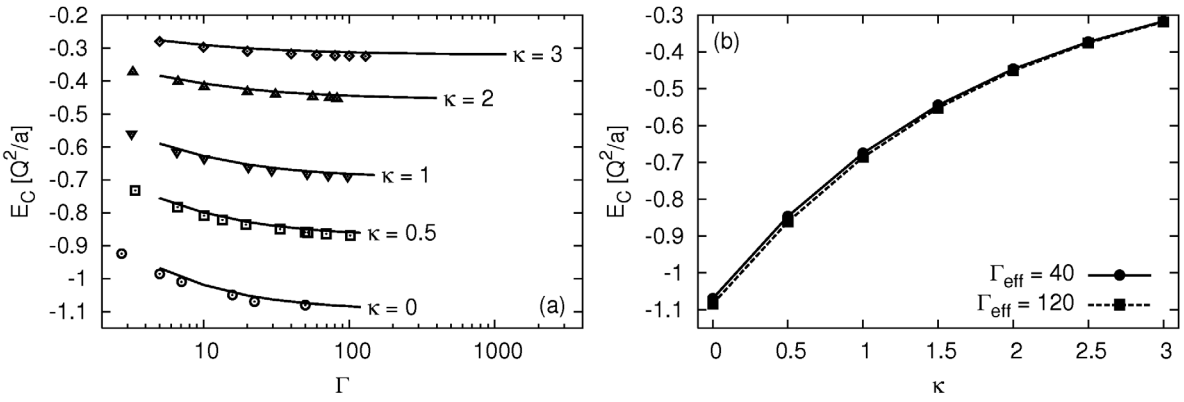

Figure 2. *Correlational energy (a) vs. Γ for a series of κ (lines: present data, symbols: data taken from [6]), and (b) vs. κ for Γ_{eff} = 40 and 120.*

Thermodynamic quantities like pressure, internal energy and compressibility are given as functionals of the pair correlation function. The internal energy, for example, can be split in three contributions: (i) the thermal energy $E_0 = k_B T$, (ii) the Hartree part representing the polarizable background $E_H = Q^2/ak$ and (iii) the non-trivial correlational part:

$$E_C = \frac{Q^2}{a}\int_0^\infty [g(r) - 1] e^{-\kappa r}\, dr \quad (2)$$

An interesting phenomena in 2D systems in general is the phase transition between the solid and the liquid phases. It has been theoretically proven that exact long-range order does not even exist for finite

temperatures [7]. However, it is expected, that the system undergoes a transition from the solid (quasi-long-range order) to the liquid (short-range order) phase while the temperature is increased. In 3D Coulomb systems this is a clear first-order phase transition [8], while in 2D the KTHNY theory [9] predicts a two-stage melting scenario with a so called *hexatic* phase, where the position order already reduces, but the orientational order of the inter-particle bounds is still quasi-long-ranged. This theoretical prediction has been, for some time, a matter of intense controversy. The temperature domain of the hexatic phase is expected to be very narrow, therefore it seems to be difficult to access it by the usual techniques due to the natural fluctuation level in every finite particle number simulation or dusty plasma experiment. Nevertheless we have investigated the variation of several physical quantities in the regime of the expected melting temperature.

Figure 3 shows the values of the bond-order parameter G_Θ (3) and the Einstein oscillation mean frequency ω_E. Each point represents a separate simulation for a prescribed temperature. The Γ values are calculated from the measured average temperatures, error bars indicate the $\pm\sigma$ standard deviation of the fluctuating quantities.

The bond-order parameter is calculated using:

$$G_\Theta = \frac{1}{N}\left|\sum_{k=1}^{N}\frac{1}{6}\sum_{m=1}^{6}\exp\left(i6\Theta_{k,m}\right)\right|, \qquad (3)$$

where k runs over all particles, m runs over the six nearest neighbors of the k-th particle. $\Theta_{k,m}$ is the angle between a predefined (e.g. x) direction and the vector connecting k-th and m-th particles.

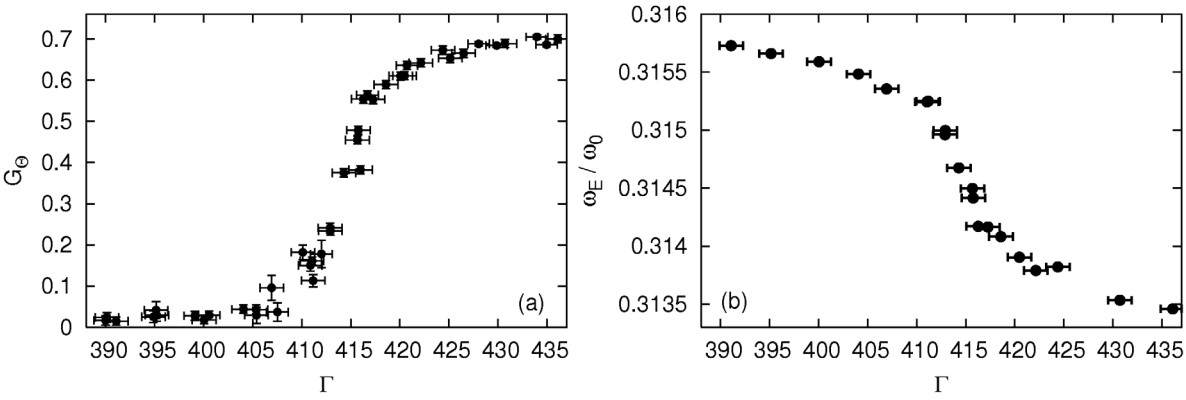

Figure 3. *(a) G_Θ bond-order parameter and (b) ω_E mean Einstein frequency vs. Γ for $\kappa = 2$ simulations.*

Both quantities show well defined transitions in the range of $\Gamma = 415\pm5$, which corresponds to an effective Coulomb coupling of $\Gamma_{eff} = 137.5\pm2$ [see Eq. (1)] in very good agreement with the widely accepted, experimentally obtained value $\Gamma_m = 137\pm15$ [10]. On the other hand, the limitation of these simulations is also visible: the temperature fluctuation of the $N = 63{,}360$ particle simulation has a standard deviation ($\sigma = 1.2$ in this Γ range) comparable with the width of the transition region itself, which makes the resolution of the details of this transition not possible. In fact, we observe a slight shift of the transition temperature to higher Γ values while investigating the quasi-long-range positional order, but this shift is in the order of the statistical fluctuation as well.

Wave dispersion properties are investigated through the $L(k,\omega)$ and $T(k,\omega)$ longitudinal and transverse current fluctuation spectra [11]. Figure 4 shows the power spectra of the $\Gamma = 360$, $\kappa = 2$ system in the strongly coupled liquid domain.

$L(k,\omega)$ and $T(k,\omega)$ are calculated from the Fourier transforms

$$L(k,\omega) = \frac{1}{2\pi N}\lim_{\Delta t\to\infty}\frac{1}{\Delta t}\left|F\left\{\lambda(k,t)\right\}\right|^2 \text{ and } T(k,\omega) = \frac{1}{2\pi N}\lim_{\Delta t\to\infty}\frac{1}{\Delta t}\left|F\left\{\tau(k,t)\right\}\right|^2 \qquad (4)$$

of the microscopic currents

$$\lambda(k,t) = k\sum_j v_{jx}\exp\left(ikx_j\right) \quad \text{and} \quad \tau(k,t) = k\sum_j v_{jy}\exp\left(ikx_j\right), \qquad (5)$$

where the index j runs over all particles and Δt in (4) is the duration of data recording. The $\omega(k)$ dispersion curves represent the peaks of the fluctuation spectra, frequencies are given in units of the nominal

2D plasma frequency $\omega_0 = \sqrt{2p\ Q^2 n/ma}$, where m is the mass of the dust particles.

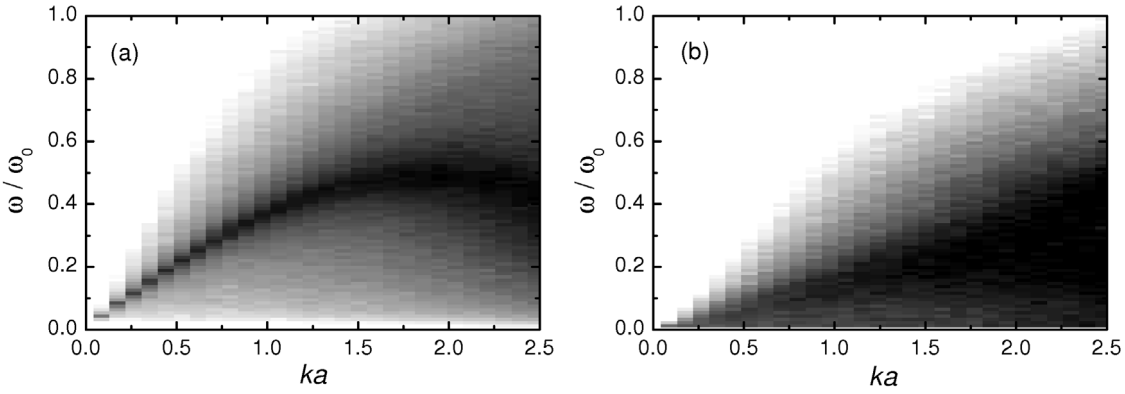

Figure 4. *(a) Longitudinal and (b) transverse current fluctuation spectra for Γ = 360, κ = 2.*

The longitudinal mode exhibits a quasi-acoustic behavior, $\omega \propto \sqrt{k}$, with an acoustic (linear) portion at small wave numbers [12]. Transverse dispersions feature finite $k_{\text{cut-off}}$ wave numbers in the liquid domain. This can be explained by the fact, that liquids are not able to sustain long-wavelength shear modes. Comparison with the theoretical Quasi-Localized Charge Approximation (QLCA) - which is based on the separability of the particle oscillation and the diffusion time scales in the strongly coupled domain [13] - is shown in Fig. 5.

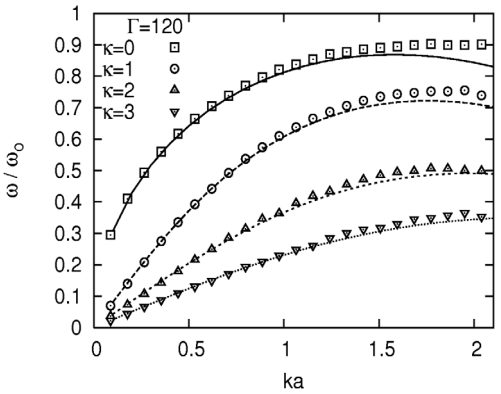

Figure 5. Comparison of MD (symbol) and QLCA (lines) longitudinal dispersions for Γ = 120 and κ = 0,1,2 and 3.

Acknowledgements

This work was supported by the Hungarian Grants OTKA-T-48389, OTKA-PD-049991, MTA-OTKA-90/46140 and NSF Grant PHY-0206695 as well as DOE Grant DE-FG02-03ER54716 in the USA.

References

[1] R. L. Merlino, J. A. Goree, *Physics Today,* **57** (2004) 32
[2] B. Liu, J. Goree, V. Nosenko, *Physics of Plasmas,* **10** (2003) 9
[3] U. Konopka, G.E. Morfill, L. Ratke, *Phys. Rev. Lett.*, **84** (2000) 891
[4] M. H. Thoma, M. Kretschmer, H. Rothermel, H. M. Thomas, G. E. Morfill, *Am. J. Phys.,* **73** (2005) 420
[5] D. Frenkel, B. Smit, *Understanding Molecular Simulation*, Academic Press, 1996
[6] H. Totsuji, M. S. Liman, C. Totsuji, K. Tsuruta, *Phys. Rev. E,* **70** (2004) 016405
[7] P. C. Hohenberg, *Phys. Rev.,* **158** (1966) 383; N. D. Mermin, *Phys. Rev.,* **176** (1968) 250
[8] W. T Farouki and S. Hamaguchi, *J. Chem. Phys.,* **101** (1994) 9885
[9] D. R. Nelson, B. I. Halperin, *Phys. Rev. B,* **19** (1979) 2457
[10] C. C. Grimes, G. Adams, *Phys. Rev. Lett.*, **42** (1975) 795
[11] P. Hartmann, Z. Donkó, K. Kutasi, G. J. Kalman, *Phys. Rev. E,* **72** (2005) 026409
[12] G. J. Kalman, P. Hartmann, Z. Donkó, M. Rosenberg, *Phys. Rev. Lett.*, **92** (2004) 065001
[13] K. I. Golden, G. J. Kalman, *Physics of Plasmas,* **7** (2000) 14

Structure and Properties of Superhard TiB_2 Coatings Prepared by DC Magnetron Sputtering

B. Grančič[1], M. Mikula[2], V. Buršíková[3], A. Csuba[2], T. Plecenik[1], M. Držík[4], I. Vávra[5], A. Plecenik[1] and P. Kúš[1]

[1]*Department of Experimental Physics FMPI CU, Mlynská dolina Bratislava, Slovakia*
[2]*Institute of Materials and Machine Mechanics SAS, Račianska 75 Bratislava, Slovakia*
[3]*Department of Physical Electronics MU, Kotlářska 2 Brno, Czech Republic*
[4]*Laboratory of Applied Optics ILC, Ilkovičova 3 Bratislava, Slovakia*
[5]*Institute of Electrical Engineering SAS Dúbravská cesta 9 Bratislava, Slovakia*

TiB_2 coatings were deposited onto Si(001), high speed steel and tungsten carbide substrates by nonreactive sputtering using unbalanced DC magnetron. All TiB_2 coatings exhibited high values of hardness more than 40 GPa, high Young´s modulus and high compressive residual stresses caused by ion bombardment during deposition. XRD analysis showed hexagonal TiB_2 structure with (0001) preffered orientation. The microstructure of TiB_2 coatings was depended on applying of different substrate bias U_s and substrate temperature T_s. Transmission electron microscopy TEM and Atomic force microscopy AFM was used to investigate of growth mechanism of TiB_2 coatings. Glow discharge optical spectroscopy GDOES was used to evaluate chemical composition depth profile. Mechanical properties were evaluated from loading/unloading curves measured by a computer-controlled Fischerscope H100 microhardness tester.

Dissociative Electron Attachment to Amino Acids - Theoretical Study

P. Papp[1], O. Ingolfsson[2], Š. Matejčík[1]

[1]Department of Experimental Physics, Comenius University, Mlynská dolina, Bratislava 842 45, Slovakia
[2]University of Iceland, Science Institute, Dunhaga 3, 107 Reykjavik, Iceland
e-mail: papp@fmph.uniba.sk

Abstract

Using a crossed electron/molecule beams technique the dissociative electron attachment to gas phase L-valine ($(CH_3)_2CHCH(NH_2)COOH$ = Val) was studied by the means of mass spectrometric detection of the product anions. Additionally, *ab initio* calculations of the structure and energies of the anions and neutral fragments have been carried out at G3MP2 [1] and B3LYP/6-311+G(2d,2p) [2,3] level. The dominant negative ion $(Val-H)^-$ (m/Z=116) was observed at electron energy of 1.12 eV. This ion is the major reaction product at electron energies below 5 eV. Additional fragment ions with m/Z = 100, 72, 56, 45, 26 and 17 have been detected. At higher incident electron energies the fragment anions are formed via core excited resonances at about 5.5 and 8.0-9.0 eV.

Introduction

Dissociative electron attachment (DEA) is one of the processes contributing to the toxicity of halocarbons, where an electron attached to the halogenated molecule starts the dissociation of the negative temporary anion into a reactive radical and a halide ion. DEA may play also an important role in the radical formation in the living organism as a result of interaction with ionization radiation. The kinetic energy of secondary electrons is sufficient to induce electron impact ionization and dissociative electron impact ionization. These reactions are responsible for the formation of negative and positive ions in the medium and may play important role in the radical formation of amino acids. The main part of this contribution will be oriented to experimental and theoretical investigation of fragmentation reactions on L-valine amino acid.

Results and discussion

Due to the fact that L-valine has a metastable anionic state it is possible to detect several anionic fragments with different m/Z ratios using the mass spectrometric technique. The most pronounced of the fragments is the dehydrogenated molecular ion with m/Z = 116 (Fig.1 a). This anion is predominantly formed via a low energy resonance, reflected in the ion yield curve by an intensity maximum at about 1.2 eV. According to present calculations energetically most favorable is the H cleavage from the carboxylic group (reaction enthalpy of 1.112 eV in Tab.1). Hydrogen cleavage from α carbon, side chain carbon or the amino group occurs according to present calculations at higher energies. The m/Z = 100 anion has an energy resonance at 1.6 eV which belong to the direct cleavage of the hydroxyl group (Fig.1 b). The anionic structure formed via direct dissociation of OH is energetically less favorable with threshold of 4.0 eV whilst the rearrangement of this structure to *tert-butyl* anion ($HN\text{-}CtBut\text{-}O^-$) gives a reaction enthalpy at 1.712 eV. The next channel of m/Z = 72 with cleavage of the COOH group and rearrangement of the anionic structure to $(CH_3)_3C\text{-}NH^-$ on theoretical level underestimates the threshold energy of about 6.7 eV and the core excited resonance at approx. 8.0 eV with the reaction enthalpy of 4.138 eV. For the m/Z = 56 a high energy resonance at approx. 9.0 eV was observed, again a weak agreement with theoretical calculations for several possible anionic structures leading to reaction enthalpies of 3.810 and 5.517 eV for two stable calculated anions $C_3H_4O^-$ and $C_3H_6N^-$ respectively. For the channel m/Z = 26 we calculate the electron affinity of COOH to be about 1.5 eV, which results in a reaction enthalpy for formation

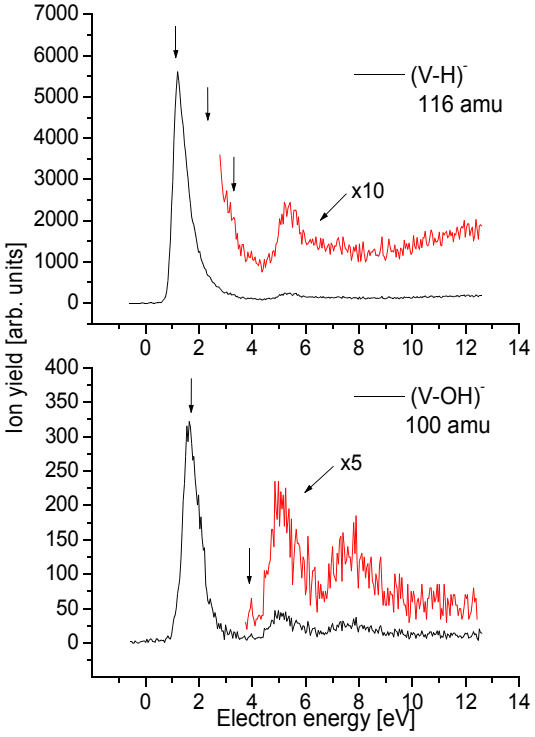

Figure 6**:** Ion yields for two product ions formed via DEA to valine

of $COOH^-$ of 2.35 eV. The 0.2 eV resonance in the spectrum should therefore not be accessible through this channel but there is a second less intensive peak at 2.5 eV. The neutral precursor to the formic ion $CHOO^-$ on the other hand possesses the appreciable electron affinity of 3.5 eV, which could lead to the reaction enthalpy about 0.35 eV. The m/Z = 26 channel which can be unambiguously assigned to the CN^- has a lot of possibilities in radical and neutral species formed via this dissociation and it is still being investigated. Finally for the OH^- with m/Z =17 the calculated reaction enthalpy from direct cleavage is 2.895 eV, which is in contrast with the experimental value with the strong core excited resonances at above 5.0 eV.

		Reaction enthalpies (eV)	
m/z	Anionic fragments	B3LYP	G3MP2
116	$(CH_3)_2CH\text{-}CHNH_2\text{-}COO^-$	1,040	1,112
	$(CH_3)_2CH\text{-}CNH_2\text{-}COOH^-$	2,198	2,351
	$(CH_3)_2C\text{-}CHNH_2\text{-}COOH^-$	3,642	3,360
100	HN-C-tBut-O^-	1,548	1,712
	$(CH_3)_2CH\text{-}CHNH_2\text{-}CO^-$	3,761	3,991
72	$(CH_3)_3C\text{-}NH^-$	3,746	4,138
56	$C_4H_3O^-$	3.173	3.810
	$C_3H_6N^-$	4.734	5.517
45	$COOH^-$	1,834	2,349
17	OH^-	2,621	2,895

Table 1: The calculated reaction enthalpies for the six different fragmentation channels of L-valine amino acid to the anionic species listed in the table and the contributing radicals. The values in the last two columns are for B3LYP/6-311+G(2d,2p) and G3MP2 methods.

Conclusions

The DEA to gas phase L-valine leads to the formation of at least 7 fragment anions over four distinct resonances appearing at 0.2 eV, 1-2eV, 5-6eV and 8-9 eV. The most abundant anion appearing at sub-excitation energies, i.e. below 5 eV, is formed by hydrogen detachment which is assigned to the decay of the π^* resonance of the -COOH group. The ion yield around 5 and 8 eV is assigned to core excited resonances. In this electron energy range the OH^- and $COOH^-$ are the most abundant products. The comparison of DEA to valine with the previously studied DEA reactions of the aliphatic amino acids glycine and alanine indicates that there exist very common features. In all cases DEA at low electron energies is dominated by the hydrogen detachment formation and by the properties of the -COOH group. Also, the fragmentation patterns of these amino acids are very similar. However, what is striking when comparing our calculations with our experimental results is that the majority of the DEA products from valine are apparently formed through considerable rearrangement and not through direct dissociation.

Acknowledgment

This research project was partially supported by by the Slovak Research and development agency, project Nr. APVT-20-007504, ESF projects COST P9 and EIPAM.

References

[1] L.A. Curtiss, K. Raghavachari, P.C. Redfern, V. Rassolov and J.A. Pople. *J. Chem. Phys.* 109 (1998) 7764

[2] A. D. Becke, *Phys. Rev. A*, 38 (1988) 3098

[3] C. Lee, W. Yang, R. G. Parr, *Phys. Rev. B*, 37 (1988) 785

Dissociative Electron Attachment to the Chloro- and Bromo- Substituted Hydrocarbons

W. Barszczewska

Department of Chemistry, University of Podlasie, ul.3 Maja 54, 08-110 Siedlce, Poland
e-mail: wbar@ap.siedlce.pl

This paper deals with thermal electron capture processes by some halocarbons in the gas phase. The kinetic data from various laboratories differ quite often by more than an order of magnitude and new data and some theoretical analysis are required to find the correct values [1-4].

The rate constant for the thermal electron capture strongly depends on the extent of overlap between the shape and position of the dissociative electron attachment (DEA) cross-section peak and the Maxwell-Boltzman distribution of both electron and molecules energies [1-3]. The thermal attachment rate constant can be measured in a swarm experiment. The resonance peak can be represented by electron capture negative ion spectra obtained in beam experiment or vertical attachment energy (VAE) obtained from electron transmission spectroscopy (ETS) as in reference1. These data describe the same process and should be interconnected.

Moreover, the important question for understanding electron attachment processes is the dependence between the structure of the molecule and the mechanism and the rate constant of the process. We have proposed an empirical correlation between the rate constant for the electron capture and the polarizability of the attaching center. As an attaching center we consider that part of the molecule which is immediately connected with the attachment process.

This work presents joint effort of Siedlce and Bratislava groups to measure dissociative electron attachment for the same compounds using the same samples.

In the present work the dissociative electron attachment (DEA) to the chloro- and bromo- substituded hydrocarbons has been studied in the gas phase at ambient temperature. Two experimental techniques has been used:

1. electron swarm method with ionization chamber and carbon dioxide as a carrier gas to measure kinetics of the thermal electron attachment processes. The experimental procedure has been described in [5]. We have found that all the investigated compounds attach electrons in two-body processes. Corresponding rate constants have been determined.

2. crossed electron/molecule beams technique. The apparatus has been described in detail in [6]. In contrast to the swarm method we were able to extend the electron energy range up to 10 eV and we were also able to analyse the products of the reactions using the mass spectrometer. In this case the main interest of the investigation was to measure the yields of the negative ions Cl^- and Br^- formed in the DEA. The ion yields were measured in the electron energy range from 0 to about 9 eV. The negative ion mass spectra of the molecules at different electron energies have been studied.

The correlation between rate constants (k_{th}), polarizability of the attaching center (α_{center}) position of the DEA peaks and vertical attachment energy (VAE) has been demonstrated .

Acknowledgements

This research was supported from scientific founds for the years 2005-2007 under Grant 3 T09A 111 29 and by the the EIPAM Program.

References

[1] G.A. Gallup, K. Aflatooni, P.D. Burrow, J. Chem. Phys. **118**, 2562 (2003)
[2] W. Barszczewska, J. Kopyra, J. Wnorowska, I. Szamrej, J. Phys. Chem. A **107**, 11427 (2003)
[3] W. Barszczewska, J. Kopyra, J. Wnorowska, I. Szamrej, Int. J. Mass Spectrom. **233**, 199 (2004)
[4] L.G. Christophorou, Z. Phys. Chem. **195**, 195 (1996)
[5] A. Rosa, W. Barszczewska, M. Foryś, I. Szamrej, Int. J. Mass Spectrom. **205**, 85 (2001)
[6] S. Matejcik, V. Foltin, M. Stano, J.D. Skalny, Int. J. Mass Spect. **223–224,** 9 (2003)

Water Remediation with Streamer Discharges

M. Dors, E. Metel, J. Mizeraczyk

Centre for Plasma and Laser Engineering
The Szewalski Institute of Fluid Flow Machinery, Polish Academy of Sciences
Fiszera 14, 80-231 Gdańsk, Poland
e-mail: mdors@imp.gda.pl

Abstract

In this paper, results of phenol degradation in water induced by a positive pulsed streamer corona discharge are presented. A novelty of this work is studying an influence of the pulsed streamer corona discharge enhanced with the Fenton reaction on phenol degradation in the tap water. To our knowledge, the tap water has never been used before in such studies. The positive pulsed streamer discharge was generated between a stressed needle and a cylinder, both immersed in the water contaminated with phenol, to which $FeSO_4$ was added. The iron ions formed from $FeSO_4$ were supposed to enhance the phenol degradation through the Fenton reaction. The initial concentration of phenol was 0.62 mM. It was found that Fenton's reaction enhanced significantly phenol degradation rate (from 42% to 78%) only in the distilled water of low conductivity. In the tap water Fenton's reaction was weak and had to be initiated by changing initial pH from alkaline to acidic. In the tap water without iron ions and acidic pH there was no phenol oxidation. When phenol was oxidized the water acidity increased as a result of phenol degradation into organic acids with dihydroxyphenols as intermediates.

Experimental set-up

The pulsed positive streamer discharge was generated between a stressed stainless steel needle electrode and a grounded brass cylinder electrode. The needle-cylinder spacing was 55 mm. The electrodes were placed in a glass parallelepiped reactor (12.0 cm × 3.6 cm × 14.4 cm), which was filled with phenol-polluted water. The water was either distilled or tap water. Conductivity of the water was 1 μS/cm (pure distilled water), 200 μS/cm (distilled water with addition of NaCl) and 600 μS/cm (tap water). Initial concentration of phenol was 0.62 μM. For studying an influence of Fenton reaction on phenol decomposition, iron salt (Fe_2SO_4) to produce iron ions was added to the phenol-polluted water. Initial concentration of Fe_2SO_4 was 0.08 mM. The water flowed through the reactor and the external heat exchanger to keep the water temperature in the range of 20-25°C. The positive polarity high voltage pulses of 30 kV were applied to the needle electrode from a discharge capacitor (2 nF), through a rotary spark with repetition rate of 50 Hz. The concentration of phenol and hydrogen peroxide in the water was measured by a gas chromatograph and a pertitanic acid formation method, respectively.

Results and discussion

Generally, phenol oxidation efficiency decreased when the water conductivity increased. This effect is known and is attributed to the lower production of OH radicals in the water of higher conductivity [1, 2]. In our experiment, when the phenol-polluted water (without iron ions) was processed by the pulsed streamer corona discharge the concentration of phenol in the water decreased during 90-minutes processing time by 42% and 10% in the distilled water of a conductivity 1 μS/cm and 200 μS/cm, respectively. In the tap water, the conductivity of which was 600 μS/cm, no phenol oxidation was observed (Fig. 1a).

The presence of iron ions, added to the water in the form of Fe_2SO_4 (0.08 mM), improved the phenol oxidation efficiency due to enhanced OH radical production via the Fenton reaction (1). However, again the water conductivity influenced the phenol oxidation process.

In the presence of iron ions the phenol concentration decreased by 78% and 52% in the distilled water of conductivity 1 μS/cm and 200 μS/cm, respectively (Fig. 1b). However, our first processing of the phenol-polluted tap water, with iron ions showed no phenol oxidation at all. This was because the initial pH of tap water was 7.6, i.e. much far from the pH range of 3-6, in which the Fenton reaction works. In order to initiate the Fenton reaction, the initial pH was lowered to 4.1 by addition of H_2SO_4. As can be seen in Fig. 1b, in such a water, phenol oxidation efficiency was 20%.

Unfortunately, in our experiment we were not able to detect directly organic acids in the water. However, due to organic acids we observed an increase in acidity of the water. The decrease in pH corresponded to the amount of oxidized phenol. When there was no iron ions in the distilled water of conductivity 1 μS/cm decrease in phenol concentration was relatively high, so pH decreased from initial 6.3 to 4.9. In the distilled

water of conductivity 200 μS/cm, change in the phenol concentration was lower and consequently pH decreased only to 6.0. Since in the tap water without iron ions there was no decrease in the phenol concentration, there was no change in the pH too.

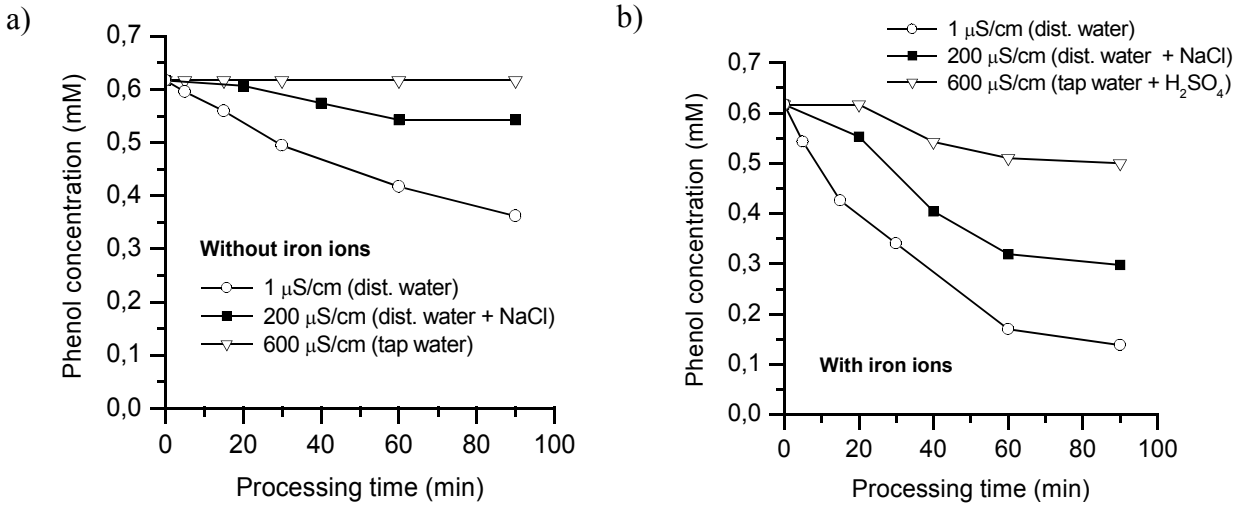

Fig. 1. Concentration of phenol in the phenol-polluted water (without iron ions) of different conductivities: 1 μS/cm, 200 μS/cm, 600 μS/cm. Initial phenol concentration 0.6 mM. Water amount 500 cm^3. Pulse energy 0.7 J.

In the water with iron ions more phenol molecules were decomposed to organic acids and consequently the pH was lower than in the water without iron ions. In contradiction to the case without iron ions, the pH decreased not linearly but with a rapid drop at the beginning of the processing and then with the slower decrease. A very similar shape of the pH curve in the water with iron ions was predicted by the numerical model developed by Grymonpré et al. [3]. In our experiment, such a behaviour concerns the distilled water of conductivity 1 μS/cm and 200 μS/cm. In the case of the tap water with phenol and iron ions, the initial pH was decreased artificially to 4.1 by addition of H_2SO_4, what allowed to initiate the Fenton reaction. The pH drop observed after initiation of the Fenton reaction was 0.2 only, i.e. to 3.9, and corresponded to the relatively small amount of oxidized phenol.

According to the Fenton reaction most of H_2O_2 molecules formed during the discharge are supposed to be converted into OH radicals which are dominant oxidants of phenol. Therefore, H_2O_2 molecules are indirectly responsible for the phenol degradation. This is consistent with our results, which show that the concentration of H_2O_2 in the water containing iron ions, i.e. with the Fenton reaction present, during the streamer corona discharge processing is much lower than in the water without iron ions.

Conclusions

In this paper, results of the investigation of iron ions influence on phenol oxidation in both the distilled and tap water by pulsed positive streamer corona discharge are presented. To our knowledge, the tap water has never been used before in such studies. Thus, a novelty of this work is presenting an influence of the pulsed streamer corona discharge in combination with the Fenton reaction on phenol degradation in the tap water. A general conclusion arises from the above experiment that the Fenton reaction combined with the pulsed streamer corona discharge is not effective in the purification of drinking water. Thus, other chemical activators or other types of discharges are needed for this purpose.

References

[1] B.R. Locke, M. Sato, P. Sunka, M.R. Hoffmann, J.S. Chang, *Ind. Eng. Chem. Res.*, 45 (2006) 882-905.

[2] P. Sunka, V. Babicky, M. Clupek, P. Lukes, M. Simek, J. Schmidt, M. Cernak, *Plasma Sources Sci. Technol*., 8 (1999) 258–265.

[3] D.R. Grymonpré, A.K. Sharma, W.C. Finney, B.C. Locke, *Chemical Engineering Journal*, 82 (2001) 189–207.

Removal of Organic Dyes from Water Solutions by the Diaphragm Discharge

Z. Stará[1], F. Krčma[1], M. Nejezchleb[1]

[1]Institute of Physical and Applied Chemistry, Faculty of Chemistry, Brno University of Technology, Purkyňova 118, 612 00 Brno, Czech Republic
e-mail: stara@fch.vutbr.cz

Abstract

This work was focused on the diaphragm discharge generated by DC non-pulsed high voltage in water solutions containing organic dye Direct Red 79 and selected electrolytes. The dye decomposition as a function of discharge conditions (discharge polarity, input power, etc.) and an influence of solution properties on the dye removal was investigated. The dye degradation went much faster in the negative discharge, dye concentration dropped to approximately 20 % after the first 10 minutes of the discharge treatment. The increasing input power enhanced the dye removal almost linearly. The strong influence of electrolysis on the dye decomposition was confirmed, as well as the added electrolyte kind and its concentration. Optimal solution conductivity should be adjusted for the most efficient process operation.

Introduction

Electrical discharges generated in water initiate various physical and chemical processes that are responsible for, for example, degradation of organic molecules [1]. Decomposition of organic molecule in electrical discharge can be caused by several mechanisms, mainly by UV radiation, electrolytic oxidation (in the case of DC non-pulsed discharge) and by various reactive species such as radicals, ions and some molecules that are formed in water by the discharge [2]. Diaphragm discharge that was investigated in this work is created in a small pin-hole in the dielectric diaphragm dividing two electrode spaces. Due to the application of DC voltage, two different plasma regions are formed on each side of the diaphragm [3]. An obvious analogy with the corona discharge created in the point-to-plane electrode configuration can describe the structure of this system – on the side with the positive electrode, the pin-hole behaves like a negatively charged point and therefore so-called negative plasma streamers propagate to the anode. On the other side with the cathode, the pin-hole behaves like a positive point and so-called positive streamers are created. Thus this discharge configuration enables a simultaneous study of processes in both discharge polarities.

Results and discussion

Organic dye Direct Red 79 dissolved in water solution of selected electrolyte (NaCl) was decomposed in the diaphragm discharge. Absorption spectra representing the dye concentration decrease in the discharge time are given in Fig. 1 for both electrode spaces. It is obvious that the dye decoloration went faster in the part with the anode, e.g. where the negative streamers are created.

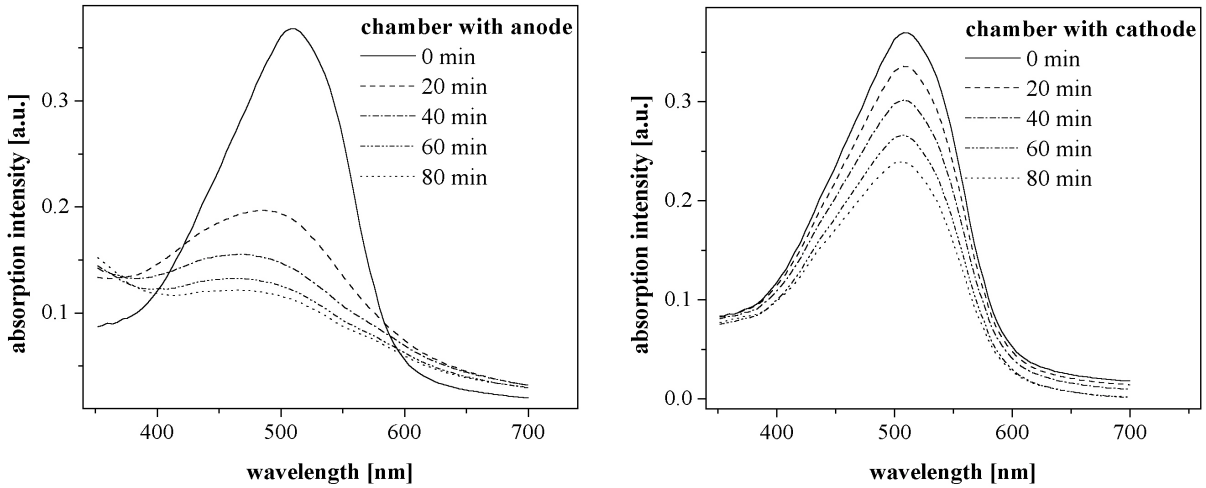

Fig. 1: Decrease of the dye absorption intensity during the diaphragm discharge in 5 mM NaCl solution (Direct Red 79, initial concentration of 12 mg·l^{-1}, input power of 120 W).

Comparison of the dye concentration decrease caused by the diaphragm discharge and by pure electrolysis is shown in Fig. 2, also for both electrode chambers. It is evident that the electrolytic effect significantly contributed to the dye removal and in the part with anode, it caused almost 50 % of the dye

overall destruction. The influence of the electrolyte and its concentration (given by solution conductivity) on the dye final concentration after the discharge is presented in Fig. 3. Optimal conditions for the dye decomposition were in NaCl or NaBr solutions with the conductivity of about 600 $\mu S \cdot cm^{-1}$.

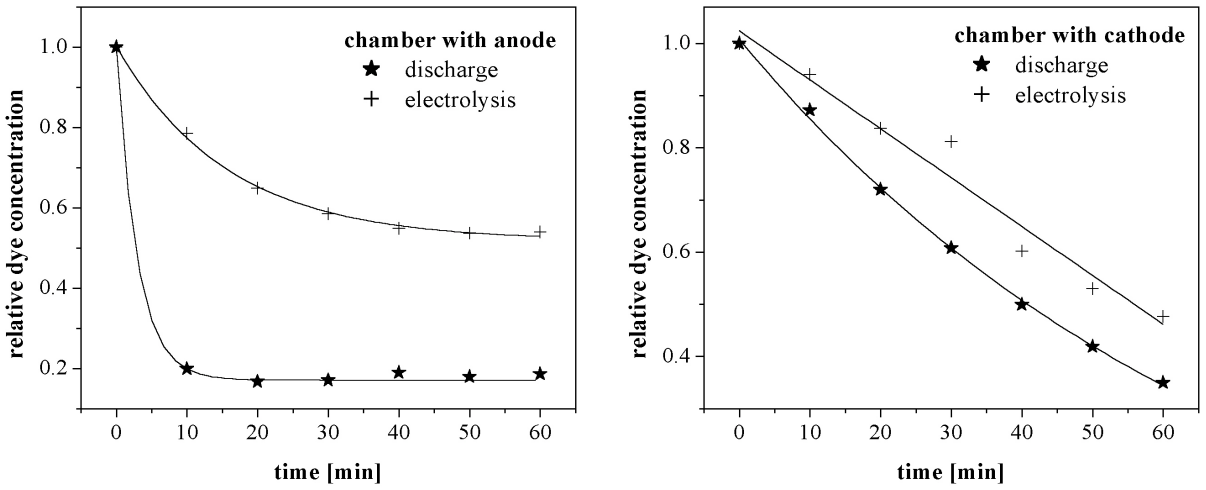

Fig. 2: Comparison of the dye decomposition by the diaphragm discharge and by the electrolysis in two discharge regions – in the part with the anode (left) and with the cathode (right) in 5 mM NaCl solution (Direct Red 79, initial concentration of 12 $mg \cdot l^{-1}$, electrical current of 100 mA).

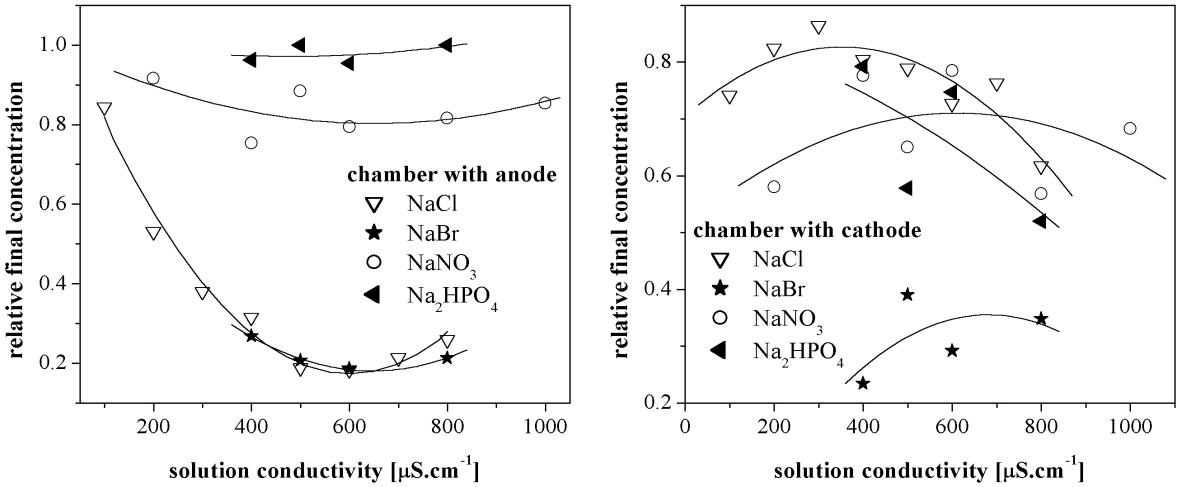

Fig. 3: Dye concentration after 40 minutes of the discharge treatment in two discharge regions, given for four electrolyte solutions as a function of the initial conductivity (Direct Red 79, initial concentration of 12 $mg \cdot l^{-1}$, input power of 160 W).

Conclusions

Organic dye Direct Red 79 was decomposed by the DC diaphragm discharge in water solutions of selected electrolytes. The dye decoloration strongly depended on the discharge polarity and input power. The influence of electrolysis on the dye removal was confirmed. Presence of electrolyte giving particular solution conductivity was necessary for the efficient discharge treatment. The best results were achieved in NaCl and NaBr solutions with the conductivity of 600 $\mu S \cdot cm^{-1}$.

References

[1] A.T. Sugiarto et. al., *J. Electrostat.,* **58** (2003) 135
[2] B. Sun et. al., *J. Phys. D: Appl. Phys.,* **39** (2006) 3814
[3] I. P. Kuzhekin, *Proc. 9th Int. Symp. High Volt. Eng.*, Graz 1995, 8073-1

This work was supported by the Czech Science Foundation, contract No. 202/03/H162.

16th Symposium on Application of Plasma Processes

Invited Lectures

Microplasmas: Scientific Challenges, Technological Applications and Limitations

K. Becker

Department of Physics and Engineering Physics and Center for Environmental Systems,
Stevens Institute of Technology, Hoboken, NJ 07030, USA

Abstract

Spatially confining atmospheric-pressure, non-equilibrium plasmas to dimensions of 1 mm or less is a promising approach to the generation and maintenance of stable, glow discharges at atmospheric pressure. Such microdischarges or microplasmas represent systems with new and fascinating challenges for plasma science such as the possible breakdown of "*pd* scaling" and the increasing dominance of boundary-dominated phenomena. Pulsed excitation on a sub-microsecond time scale results in microplasmas with significant shifts in both the temperatures and energy distribution functions of ions and electrons. This allows for the selective production of chemically reactive species and opens the door to a wide range of new applications of microplasmas in areas such as environmental remediation, biology and biomedicine, intense light sources in the ultraviolet and vacuum ultraviolet, and gas and surface analysis. This paper addresses some of the scientific challenges and technological opportunities afforded by microplasmas and point to some limitations of their use.

I. Introduction and Background

High-pressure plasmas represent an environment where collisions and radiative processes are dominated by (i) step-wise processes and by (ii) three-body collisions. The dominance of collisional and radiative processes beyond binary collisions involving ground-state species allows for many applications of high-pressure plasmas such as high power lasers, opening switches, novel plasma processing applications and sputtering, electromagnetic absorbers and reflectors, remediation of gaseous pollutants, medical sterilization and biological decontamination, and excimer lamps and other non-coherent vacuum-ultraviolet (VUV) light sources [1]. However, self-sustained diffuse plasmas are unstable at high pressure due to their susceptibility to filamentation and the transition to an arc, which limits their practical utility. A promising approach to generate stable high-pressure plasmas is based on the recognition that plasmas confined to critical dimensions below about 1 mm, so-called "microplasmas", display a remarkable stability towards arcing. There are several factors that contribute to the stabilization of microplasmas, not all of them fully understood at this point in time.

Microdischarges generated in spatially confined cavities appeared first in the literature in the mid-1990s. Schoenbach et al. [2] reported the stable atmospheric-pressure operation of a microdischarge in a cylindrical hollow cathode geometry (fig. 1a). These authors coined the term "Microhollow Cathode Discharge (MHCD)" for this microdischarge, which was also used by other groups [3-8]. The phrase "hollow cathode" historically refers to a specific mode of discharge operation, in which the sustaining voltage drops as the current increases, i.e. the discharge has a "negative differential resistance" (hollow cathode mode). Nowadays, MHCDs are often not operated in the hollow cathode mode, but as normal or abnormal glow discharges. Thus, the phrase 'hollow cathode' in the name MHCD is misleading. Others have been referring to these discharges as "Microdischarges" or "Microstructured Electrode Arrays". In an effort to emphasize the distinction between discharge device geometry and operational characteristics, we adopt the general terms "microplasma", "microcavity plasma", or "microdischarge". Figs. 1b and 1c show two other frequently used microcavity plasma sources, the Capillary Plasma Electrode Discharge (CPED, fig. 1b) and a Cylindrical Dielectric Barrier Discharge (C-DBD, fig. 1c). A variety of other microplasma sources have been developed in the meantime, often leveraging rapid advances in microfabication techniques.

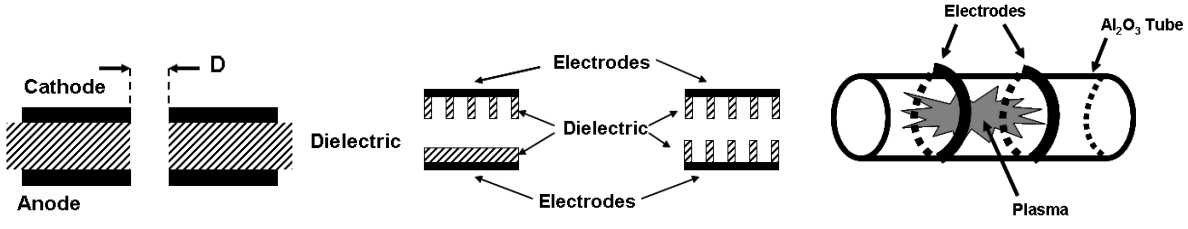

Fig. 1: Schematic diagram of (a) a microhollow cathode discharge (MHCD), (b) a capillary plasma electrode (CPE) discharge, and (c) a cylindrical dielectric barrier discharge (C-DBD).

II. Diagnostics of Microplasma and Microplasma Properties

Extensive diagnostics studies of various microplasmas have been carried out using a variety of established techniques (electrical characterization, optical diagnostics methods, plasma mass spectrometry). These include time-averaged as well as time-resolved studies. Because of the small spatial extent of most microplasmas, the vast majority of these studies yielded results averaged over the size of the microplasma. Recently, there have been two examples of spatially resolved microplasma diagnostics studies. Wagner and coworkers [9] reported the result of spatially and temporally resolved optical diagnostics studies of an isolated filamentary discharge in a DBD using cross correlation spectroscopy. Donnelly and collaborators [10] used optical emission spectroscopy with a 6 μm spatial resolution to determine the gas temperature profile across a 200 μm wide atmospheric-pressure He microplasma.

Microplasmas in various configurations can be excited by direct current (dc), pulsed dc, alternating current (ac), and radio frequency (rf), and microwave sources. Pulsed excitation of microdischarges reduces the thermal load on the electrodes at higher currents. Pulsed excitation with sub-μs pulse widths causes significant changes in the plasma parameters and a noticeable increase in the excimer emission intensity as observed in Ar and Xe microdischarges, which is attributed to pulsed electron heating [11]. The electron temperature is increased during the short pulse, but the change in the gas temperature is insignificant. The shift in the electron energy distribution function leads to an increase in the ionization and excitation rate coefficients.

Measurements of the electron temperature in rare gas microplasmas have been carried out using emission spectroscopy. An electron temperature of about 1 eV was obtained in Ar from line intensity measurements in a dc microdischarge, twice that value for pulsed operation. It is important to realize that measurements which provide information on average electron energies only yield rather low values. The simple fact that microplasmas are efficient sources of excimer radiation points to the presence of a significant fraction of high-energy electrons (with energies exceeding the excitation and ionization energies of the rare gas atoms, i.e. above at least 12 eV in Xe and more than 21 eV in He). Thus, the electron energy distribution function must be highly non-Maxwellian and contains a large fraction of energetic ("beam") electrons. Electron densities in microplasmas in Ar were found to exceed 5 x 10^{14} cm^{-3} and increased slightly with current. When excited by 10 ns pulses of 600 V, the electron densities increased to 5 x 10^{16} cm^{-3} [12].

Gas temperature measurements in rare gas and in air microdischarges using optical emission spectroscopy or absorption spectroscopy revealed values in atmospheric-pressure air from 1700 K to 2000 K for discharge currents between 4 and 12 mA, but only about 400 K in a Ne microplasma at 400 Torr at 1 mA. This indicates that the gas temperature depends strongly on the nature of the gas, (as well as on the pressure and geometry of the microcavity in which the microplasma is generated). In general, temperatures are highest for molecular gases incl. air and lower for rare gases.

III. Applications of Microplasmas

Microdischarges and microplasmas have made an enormous impact on applications. The diversity of applications, in which microplasmas are being employed, renders it impossible to provide a detailed account of all microplasma applications here. Only a limited selection is given below. Two sources for further information on microplasma applications are the recent J Phys D Cluster Issue on Microplasmas (volume 38, 2005) and chapter 9 of the book "Non-equilibrium Air Plasmas at Atmospheric Pressure (IOP Publishing, 2004; editors: K.H. Becker, U. Kogelschatz, K.H. Schoenbach and R.J. Barker). Both sources contain a large number of references to other microplasma applications.

III.1 Microplasmas for Environmental Applications

Non-thermal plasma devices have been used in numerous environmental applications such as NO_x and SO_x remediation and the destruction of volatile organic compounds (VOCs) for more than 20 years. High energy electron beams, corona discharges, dielectric barrier discharges, and various surface-type discharges, sometimes with packed beds of ferroelectric pellets, have been widely utilized discharge configurations for the generating non-thermal plasmas in the environmental field. Koutsospyros and co-workers [13-15] carried out comprehensive studies of VOC destruction in the context of exploring the use of non-thermal microplasmas for use in Advanced Life Support (ALS) systems designs for controlled cabin environments (submarine, aircraft, spacecraft, and space station). The destruction of several prototypical aliphatic (ethylene, heptane, octane) and aromatic (benzene, toluene, ethylbenzene, xylene) compounds as well as ammonia were studied. Initial contaminant concentrations varied between 75 and 1500 ppm(v) (parts per million in volume) in ambient air with comparatively low gas flow rates between 1 and 10 liters per minute (l/m), which are typical for ALS systems.

III.2. Biological Applications of Microplasmas.

The interaction of plasmas with biological systems falls generally into two areas. Most of the work has been focused on applications such as inactivation, bio-decontamination, and sterilization, where lethal plasma intensities are applied to initiate cell death. Some work has also been done in which a non-lethal plasma dosage was used to change the cell response in a controlled way. The inactivation of individual microorganisms by plasmas has received much attention in recent years. Particular emphasis has been on the utilization of atmospheric-pressure plasmas as they do not require operation in costly vacuum enclosures and thus facilitate the convenient and low-cost treatment of large surface areas. Spore-forming bacteria, in particular bacteria of the genera *Bacillus*, are among the most resistant individual microorganisms. The species *Bacillus subtilis* has received particular attention, as these bacteria are easy to grow in a reproducible fashion under chemically well-defined conditions and are considered a non-lethal surrogate for the lethal *Bacillus anthracis*, which causes Anthrax.

III.3 Microdischarges as Vacuum Ultraviolet (VUV) and Ultraviolet (UV) Radiation Sources

The presence of a significant number of energetic "beam" electrons in the electron energy distribution functions of all microplasmas in conjunction with the stable operation of these discharges at high pressure favors three body collisions, and thus enables processes such as ozone generation and excimer formation. The latter effect has been extensively studied for the rare gases He and for some rare gas halide mixtures which generated ArF excimer radiation. Efficiencies of up to 8% have been reported for Xe excimer formation in microplasma sources, lower efficiencies for heavier rare gases. For rare gas halide mixtures, efficiencies of the order of a few percent have been measured.

In addition to being efficient sources of excimer radiation, microplasmas in various geometries have also been shown to emit atomic line radiation with high efficiency, e.g., the emission of the atomic hydrogen Lyman-α (121.6 nm) and Lyman-β (102.5 nm) lines from respectively a high-pressure MHCD abd a C-DBD.

III. 4 Microplasmas for Gas and Surface Analysis

Microcavity plasmas at atmospheric pressure are nowadays used as a promising miniaturized ionization source for mass spectrometry and optical spectrometry. The power density that can be achieved is about 1MW/cm^3 for an input power of 1 W. The discharge operates at atmospheric pressure, primarily with He as the carrier gas. Another configuration uses a small-volume corona discharge as ion source in air in an atmospheric-pressure chemical ionization mass spectrometer (AP-CIMS) where the ions from sample gases are formed by ion molecule reactions. The corona discharge operates at 5kV dc with a discharge current of about 5 μA.

The utility of dielectric barrier discharges for analytical purposes was investigated by Miclea et al. [16]. A plasma column was generated by two electrodes (coated by dielectric layers of 20 μm), 50 mm long and 0.7 mm wide with a gap of 1 mm. The discharge operated in He or Ar (10 – 100 hPa, 1000 ml/min) with an rectangular voltage of 5 – 20 kHz and a peak-to-peak voltage of 400 – 900 V. Halogenated and sulfur-containing hydrocarbons were investigated by element selective diode laser absorption spectroscopy using the good absorption properties of the "long" plasma column with detection limits in the pg/s range. A geometrical similar long plasma column can be generated as a capacitively coupled 13.56 MHz discharge in a 200μm x 500 μm channel with the length of a few centimeters in a quartz wafer. The parallel plate electrodes are positioned on the outer bottom of the quartz plate that contains the plasma channel and on the outer surface of the upper quartz plate. This atmospheric-pressure discharge has great potential as a detector for a miniaturized gas chromatography system.

References

[1] see e.g. "Non-Equilibrium Air Plasmas at Atmospheric Pressure", eds. K.H. Becker, U. Kogelschatz, K.H. Schoenbach, and R. Barker, IOP Publ., Bristol, UK (2004), chapter 9 "Applications of Atmospheric-Pressure Air Plasmas"

[2] K.H. Schoenbach et al., Appl. Phys. Lett. 68, 13 (1996)

[3] P. Kurunczi, H. Shah, and K. Becker, J. Phys. B. 32, L651 (1999)

[4] I. Petzenhauser et al., Appl. Phys. Lett. 83, 4297 (2003)

[5] D.D. Hsu and D.B. Graves, J. Phys. D 36, 2898 (2003)

[6] H.I. Park, T.I. Lee, K.W. Park, and H.K. Baik, Appl. Phys. Lett. 82, 3191 (2003)

[7] Y.-B. Guo and F.C.-N. Hong, Appl. Phys. Lett. 82, 337 (2003)

[8] F. Adler, E. Kindel and E. Davliatchine, J. Phys. D, 35**,** 2291 (2002)

[9] R. Brandenburg et al., J. Phys. D 38, 1649 (2005) and references therein to earlier publications

[10] Q. Wang, I. Koleva, V.M. Donnelly, and D. Economou, J. Phys. B 38, 1690 (2005)
[11] R.H. Stark and K.H. Schoenbach, J. Appl. Phys. 89, 3568 (2001)
[12] M. Moselhy et al., J. Phys. D: Appl. Phys. 36**,** 2922 (2003)
[13] A. Koutsospyros et al., Int. J. Mass Spectrom. 233, 305 (2004)
[14] A. Koutsospyros et al., IEEE Trans. Plasma Sci, 33, 42 (2005)
[15] K. Becker et al., Plasma Phys. Control. Fusion 47, B513 (2005)
[16] M. Miclea et al., Spectrochim. Acta B 56, 37 (2001)

Elementary Plasma Reactions Revisited: Electron Ionization and Ion Surface Reactions Relevant for Fusion Plasmas

L. Feketeova[1], S. Feil[1], V. Grill[1], N. Endstrasser[1], B. Rasul[1], W. Schustereder[2], A. Bacher[1], S. Matt-Leubner[1], F. Zappa[1], P. Scheier[1] and T. D. Märk[1,3]

[1]Institut für Ionenphysik und Angewandte Physik, Leopold Franzens Universität, Technickerstr.25, A-6020 Innsbruck, Austria

[2]Max-Planck-Institut für Plasmaphysik, EURATOM Assoziation, Boltzmannstraße 2, D-85748 Garching, Germany

[3]Department of Plasma Physics, Comenius University, Mlynská dolina, Bratislava 842 45, Slovakia

e-mail: Tilmann.Maerk@uibk.ac.at

Introduction

Collisions between electrons and atomic targets (atoms, molecules, ions) have been the subject of intense experimental and theoretical studies since the early days of atomic collision physics. They are of importance in environments such as low-temperature plasmas, fusion plasmas, planetary and cometary atmospheres, and mass spectrometry. Besides these volume processes also reactions between plasma particles and the corresponding plasma vessel walls are of relevance for controlling and modelling plasma reactors. In order to understand and elucidate the role of these processes in the plasma, it is essential to have available detailed and quantitative knowledge on the corresponding elementary reactions proceeding in the volume and at the wall. Today's situation in terms of accurate data on these processes is still far from satisfying.

In order to provide quantitative information on collision processes involving various plasma constituents (in particular hydrocarbons) we have carried out the past years a series of studies with a variety of techniques in our laboratory including

(i) Experimental studies about electron ionization of neutrals and ions and electron attachment to molecules (differential, partial and total cross sections, appearance energies, etc)

(ii) Theoretical studies about electron ionization of neutrals and ions (total cross sections) and

(iii) Reactive interaction of molecular ions with surfaces (surface induced dissociation, surface induced reactions, charge exchange reactions).

The study of ion-surface reactive collisions is a research area, which has undergone rapid growth in the past twenty years. Considerable interest has been devoted to studying selected physical and chemical processes stimulated by the impact of slow ions containing collision energies up to 100 eV [1,2]. In this energy regime the relative collision energy (and the energy transferred) is of the same order of magnitude or somewhat larger than energies observed in chemical bonds. Thus, slow ion-surface interaction studies can provide useful information regarding the nature of both, the projectile and the surface, as well as the characteristics of ion-surface interactions. Reactive collisions of slow ions have been studied here in an effort to characterize molecular ions and to investigate the ion-surface interaction processes, i.e. surface-induced dissociation (SID), charge exchange reactions (CER) and surface-induced reactions (SIR) and the concomitant energy transfer in ion surface collisions.

Besides being of fundamental importance, ion-surface collisions are also relevant in the terrestrial ionosphere and interstellar medium and for technological applications, such as plasma-wall interactions in electrical discharges and fusion plasmas [3]. Hyperthermal plasma particles may collide with solid surfaces such as limiters and divertors in fusion devices, eroding the material by chemical and physical processes. Charged and neutral particles emitted from the surface may interact with the plasma and hit the surfaces again.

Experimental

Experiments were carried out on the one hand with a two sector field mass spectrometer including a modified Nier type electron impact ions source and on the other hand with a tandem mass spectrometer apparatus BESTOF described in detail in our earlier paper [4]. It consists of a double focusing two-sector-field mass spectrometer (reversed BE geometry), a Surface chamber combined with a linear Time-Of-Flight mass spectrometer. Projectile ions were produced either in a low-pressure Nier-type electron impact ion source, at elevated pressures in a Colutron gas discharge source or in a cluster source. The ions produced were extracted from the ion source region and accelerated to 3 keV for mass (and energy) analysis by a double-focusing two-sector-field mass spectrometer. After passing the mass spectrometer exit slit, the ions were refocused by an Einzel lens and decelerated to the required collision energy by a system of deceleration lenses before interacting with the target surface. The incident impact angle of the projectile ions was kept at

45° and the scattering angle (defined as a deflection from the incident beam direction) was fixed at 91°.

The collision energy of ions impacting on the surface is defined by the potential difference between the ion source and the surface. The potential difference (hence, the collision energy) can be varied from about zero to about 2 keV with a typical resolution of about 200 meV (full width at half maximum) in the case of the Nier type and cluster ion source and of about 1 eV in the case of the Colutron type ion source.

A fraction of the product ions formed at the surface exited the shielded chamber through a 1 mm diameter orifice. The ions were then subjected to a pulsed extraction-and-acceleration field that initiated the time-of-flight analysis of the ions.

Results

Results obtained to be presented here include (i) the interaction of electrons with various hydrocarbons (including the determination of differential, partial and total ionization cross sections also as a function of target temperature) and (ii) the interaction of various singly and doubly charged hydrocarbon ions (including C_1, C_2 and C_3 group ions) and cluster ions (including carbon aggregates) with a number of targets including stainless steel, carbon tile, diamond surfaces (O-terminated and H-terminated) and plasma sprayed tungsten maintained under ultra high vacuum conditions (below 10^{-9} Torr) in a bakeable turbo-pump evacuated target collision chamber. Secondary mass spectra at different incident collision energies are converted to collision energy resolved mass spectra (CERMS) plots covering usually the energy range from about 0 to 100 eV thereby yielding after proper analysis desired information on the energetics, kinetics and mechanisms of the various ion surface reactions studied.

It is a pleasure to acknowledge valuable cooperation with Z.Herman, Praha and J.Skalny and S.Matejcik, Bratislava.

References

[1] R.G.Cooks, T.Ast, and M.D.A.Mabud, Int. J. Mass Spectrom. Ion Process., **100**, 209 (1990).
[2] L. Hanley, ed., *Polyatomic Ion Surface Interactions*, Int. J. Mass Spectrom. Ion Process. **174** (1998).
[3] W. O. Hofer and J. Roth, eds., *Physical Processes of the Interaction of Fusion Plasmas with Solids* (Academic, San Diego, 1996).
[4] A.Qayyum, Z.Herman, T.Tepnual, C.Mair, S.Matt-Leubner, P.Scheier and T.D.Märk, J.Phys.Chem, **108**, 1 (2004).

Collisions of Slow Hydrocarbon Ions with Room-Temperature and Heated Carbon and Tungsten Surfaces

Z. Herman, J. Žabka, A. Pysanenko

V. Čermák Laboratory, J. Heyrovský Institute of Physical Chemistry,
Academy of Sciences of the Czech Republic, Dolejškova 3, 182 23 Prague 8, Czech Republic
e-mail: zdenek.herman@jh-inst.cas.cz

Abstract

Results of scattering experiments on collisions of slow (15-45 eV) C1 and C2 hydrocarbon ions with room-temperature and heated (600^0C) carbon and tungsten surfaces are described. From mass spectra, translational energy and angular distributions of product ions conclusions about survival probability, energy transfer and fragmentation and chemical reactions at surfaces could be made.

Introduction

Studies of surface collisions of ions provide information of interest for both chemistry and physics. Considerable attention has been devoted during the last decade to collisions of slow molecular ions of energies 10 –100 eV [1-5]. Besides the basic importance of describing details of elementary processes in single ion-surface encounters, these studies are of interest for activation of polyatomic molecular projectile ions in surface collisions (novel methods of analysis of organic and bioorganic ions), and for information on collision processes relevant to plasma-wall interaction in low temperature plasmas and fusion systems.

We undertook a systematic beam scattering study of interaction of slow (15 – 50 eV) hydrocarbon ions C_1 – C_3 with carbon (highly-oriented pyrolytic graphite, samples of Tokamak tiles) [2-5] and tungsten at room-temperature (covered with hydrocarbons) and heated to about 600^0 C. Information on ion survival probability, energy transfer, fragmentation and chemical reactions of the projectile ions at surfaces were obtained from measurements of mass spectra, translational energy and angular distributions of product ions, studied in dependence on the incident energy of the projectile ions and incident angle.

Experimental

Mass spectra, translational energy and angular distributions of the product ions were measured in the scattering experiments using the Prague apparatus EVA II modified to study ion collisions with surfaces (Fig. 1). Briefly, projectile ions were formed by bombardment by 120 eV electrons of simple hydrocarbon molecules (methane, acetylene, ethane (or their deuterated variants) at an ion source pressure of about 3.10^{-5} Torr. The ions were extracted, accelerated to about 150 - 200 eV, mass analyzed by a 90^0 permanent magnet, and decelerated to a required energy in a multi-element deceleration lens. The narrow beam was directed towards the carbon target surface under a pre-adjusted incident angle Φ_N. Ions scattered from the surface passed through a detection slit into a stopping potential energy analyzer. After energy analysis the ions were focused and accelerated into a detection mass spectrometer (a magnetic sector instrument), and detected with a Galileo channel multiplier. The primary beam - target section could be rotated about the scattering center with respect to the detection slit to obtain angular distributions.

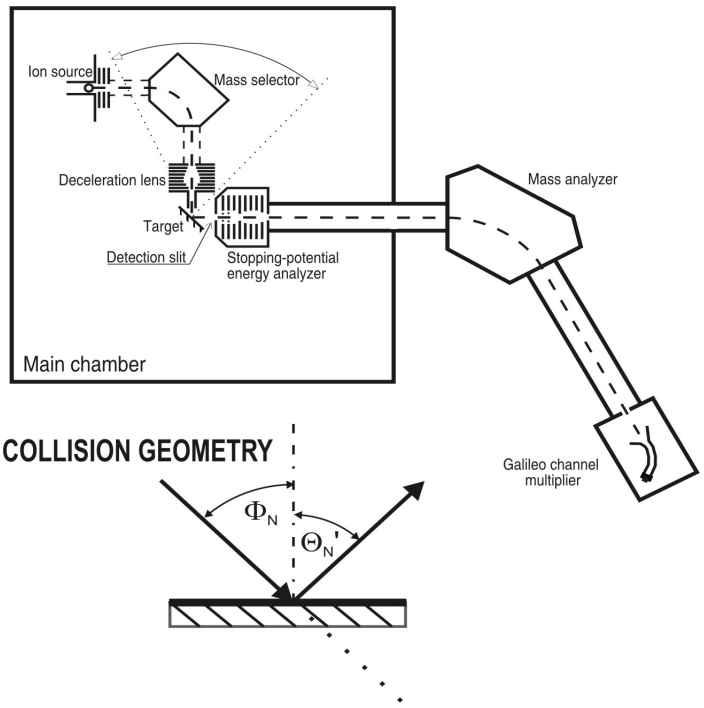

Fig. 1

Results and discussion

1.*Collisions with carbon surfaces*

Scattering studies of C_1 hydrocarbon ions (CD_5^+, $CD_4^{+\bullet}$, CD_3^+ and their labeled isotopic variants) [2] and $C_2X_n^+$ (X=H,D; n=2-5) [4] impinging on room-temperature HOPG surfaces showed both surface-induced dissociation of the projectiles and chemical reactions with the surface material (Fig. 2). The projectiles showed formation of $C_2X_3^+$ (X=H,D) in interaction of C1 projectiles with terminal CH_3-groups of surface-adsorbed hydrocarbons, as shown by analysis of the results with labeled projectile ions. In collisions of both C1 and C2 hydrocarbon ions a small amount of C_3 product ions was formed. Collisions of $CD_4^{+\bullet}$ led, in addition, to the formation of CD_4H^+ in a H-atom transfer reaction with hydrogen of surface hydrocarbons. The surface collisions were inelastic, with 41-55% of the incident energy in product ion translation.

Heating of the surface to 600^0 C practically removed the surface hydrocarbon layer as indicated by the absence of products of the efficient H-atom transfer reaction. Interactions of the projectiles

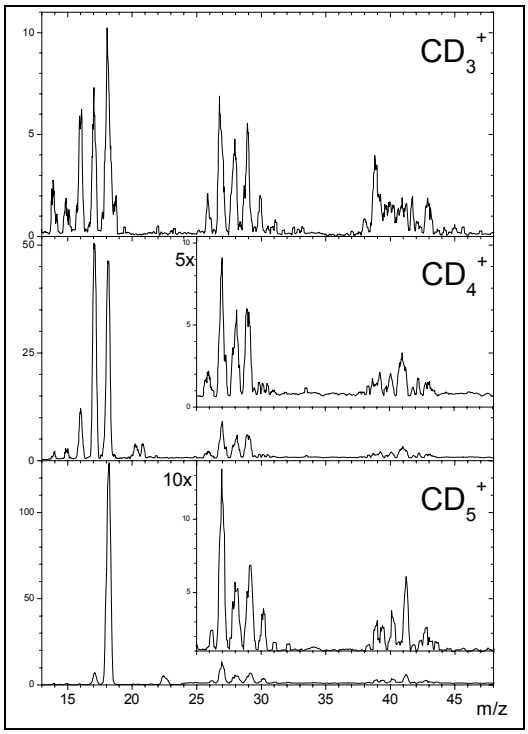

Fig. 2

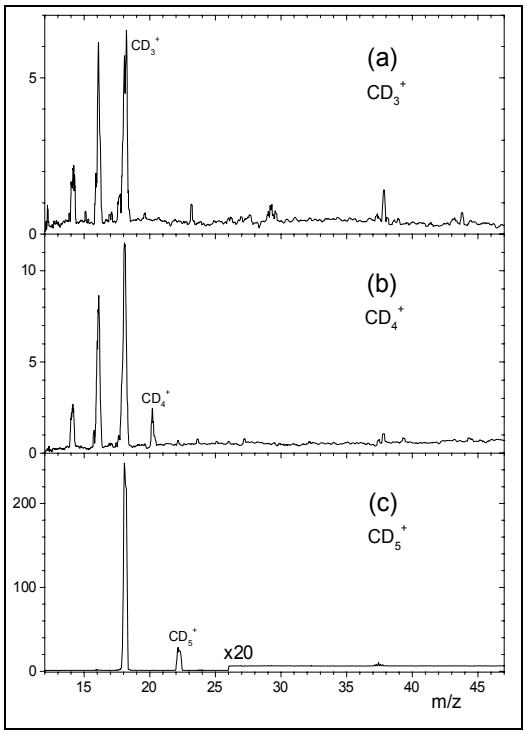

Fig. 3

with the heated surface showed only fragmentation of the projectile ions (no chemical reactions) in inelastic collisions with up to 75 % of the incident energy in product ion translation.

The absolute survival probability was defined as the sum of intensities of all product ions, scattered from the surface, to the intensity of the incident projectile ion beam. It varied from a few tenths of percent for ions CH_3^+ and CH_4^+ to several tens of percent for closed shell ions CH_5^+ , and it was smaller for radical cations $C_2H_2^+$ and $C_2H_4^+$ than for the respective closed-shell cations $C_2H_3^+$ and $C_2H_5^+$ (see Table I).

2. Collisions with tungsten surfaces

The tungsten surface target was a 5x6 mm sample of 99.9% tungsten sheet 0.05 mm thick. Before placing it into vacuum, the surface was either mechanically or electrochemically polished. The tungsten target surfaces in the experiments were kept either at room temperature or at an elevated temperature of about 600^0 C. For this purpose, the sample could be resistively heated up to almost 1000^0 C and its temperature measured by a thermocouple and by a pyrometer. Practical absence of chemical reactions with surface hydrocarbons indicated that heating the surface to 600^0C or higher decreased the concentration of hydrocarbons on the surface more that 100-times. At sample temperatures above about 500^0C an emission of K^+ ions from the sample, increasing with temperature, was observed.

When the tungsten sample was first placed into vacuum, the mass spectrum at room temperature showed, besides the product ions, an ion current of incident projectile ions having the full incident energy and the narrow energy distribution of the incident ions. Because their energy was higher than the energy of the scattered product ions, their apparent mass depended on the incident energy and appeared in the mass spectra

at a slightly higher apparent mass that increased with increasing energy. This component with a new, unheated W- sample was about 5% of the incident ion intensity. Heating the sample and cooling it to room-temperature decreased this projectile ion component to 0.05 % of the incident ion intensity. We interpret this component as a fraction of the incident beam deflected in front of the surface by surface charge and not making collision with the surface at all.

XPS analysis of the tungsten employed surfaces was carried out. The mechanically or electrochemically cleaned W-sample placed into vacuum at room –temperature (unheated) showed presence of oxides and small amount of tungsten carbide and C-H groups on the surface (evidently adsorbed hydrocarbons). Heating or repeated heating the W-sample to 600^0 C led to a clear decrease of the W-oxides and to a sharp increase of tungsten carbide peaks (about 2.5-times with respect to unheated sample) in the XPS spectra. It appears, therefore, that heating the sample leads to degradation of the surface hydrocarbons and formation of substantial amount of tungsten carbides on the surface.

We believe that these observations indicate that islands of insulating tungsten oxides cause a fraction of projectile ions to be deflected with full energy by surface charges without hitting the surface. Heating the sample decreases the amount of surface oxides and strongly increases the amount of non-insulating tungsten carbides. The incident projectile beam may then collide to a significant extent with carbon atoms on the surface.

The collision of investigated radical cations CD_4^+ and $C_2D_4^+$ with room-temperature W surface showed both fragmentation processes and chemical reactions of the projectile ion. The chemical reactions were H-atom transfer to the projectile ion and fragmentation of the protonated product and, to a smaller extent, C-atom build-up reactions. Collisions with the closed-shell ions showed only fragmentation processes. In this sense, the processes were very similar to those occurring on the investigated carbon surfaces, and indicated that the surface was largely covered at room temperature with a layer of hydrocarbons. Collisions with the heated surface showed only fragmentation of the projectile ions, again similarly to observations on heated carbon surfaces.

The translational energy distributions of the product ions showed peaking of the product ions at about the same velocity indicating decomposition after interaction with the surface. Recalculated to the energy of the scattered undissociated projectile ion, the translational energy distributions peaked mostly at

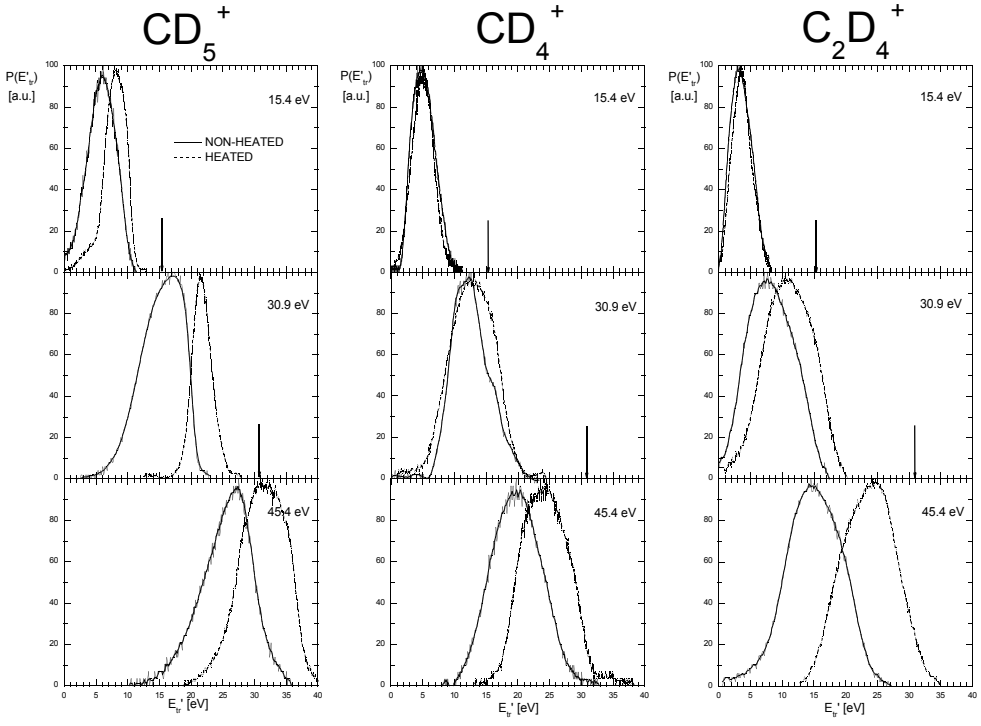

Fig. 4

30-40 % of the incident energy on room-temperature surfaces and at 40-60% of the incident energy on W-surfaces heated to 600^0 C, with a slow increase with increasing incident energy. Several examples are given in Fig. 4 for CD_4^+, CD_5^+, and $C_2D_4^+$, respectively.

The ion survival probability on tungsten surfaces was smaller than on carbon surfaces. Table 1 summarizes the results of estimation of the absolute survival probability (the ratio of the sum of intensities of

all product ions divided by the intensity of the projectile ion beam incident on the surface) for collisions with both room temperature and heated (to 600^0C) surfaces of carbon (HOPG) and tungsten.

Table 1
Survival probability, S_a(%), in collisions of hydrocarbon ions with carbon and tungsten surfaces

	Surface	15.4 eV	30.9 eV	45.4 eV
ROOM-TEMPERATURE				
CD_4^+	W	0.05	0.05	0.12
	HOPG	0.37	0.34	0.27
CD_5^+	W	5.8	0.8	1.2
	HOPG	12.5	12	18
$C_2D_4^+$	W	0.17	0.17	-
	HOPG	(2.3)	1.0	0.4
$C_2H_5^+$	W	2.7	1.6	0.85
	HOPG	1.1	1.0	0.3
HEATED				
CD_4^+	W	0.03	0.02	0.02
	HOPG	0.5	0.23	-
CD_5^+	W	1.1	0.5	0.5
	HOPG	-	-	(23)
$C_2D_4^+$	W	-	0.1	-
	HOPG	-	0.4	-
$C_2H_5^+$	W	0.56	0.32	0.24
	HOPG	-	-	-

References

[1] J. Žabka, Z. Dolejšek, J. Roithová, V. Grill, T.D. Märk, Z. Herman, Int. J. Mass Spectrom. **213** (2002) 145.
[2] J. Roithová, J. Žabka, Z. Dolejšek, Z. Herman, J. Phys. Chem. B **106** (2002) 8293
[3] Z. Herman, J. Am. Soc. Mass Spectrom. **14** (2003) 1360.
[4] J. Jašík, J. Žabka, L. Feketeová, A. Pysanenko, I. Ipolyi, T.D. Märk, Z. Herman, J. Phys. Chem. A **109** (2005) 10208.
[5] Z. Herman, T.D. Märk in "Data for molecular processes in edge plasmas", I.A.E.A. TechDoc, I.A.E.A., Vienna (in print).

Investigation of Electron-Induced Reactions in the Condensed Phase by Thermal Desorption Spectrometry

P. Swiderek[1], E. Burean[1], I. Ipolyi[1]

[1]Institut für Angewandte und Physikalische Chemie, Fachbereich 02, Universität Bremen, Leobener Str., NW2, 28359 Bremen, Germany
e-mail: swiderek@uni-bremen.de

Abstract

Electrons with low kinetic energy are omnipresent in plasmas. When plasmas are applied in processes for surface modification, low-energy electrons contribute to the chemical reactions that occur. In organic materials, electron-induced reactions are efficient at particularly low electron energies. Thus, it is important to study the effect of low-energy electrons on organic molecules adsorbed or condensed as thin films on surfaces. This contribution presents measurements on low-energy electron-induced reactions in such systems using thermal desorption spectrometry (TDS). The experiments aim at obtaining both cross sections and an insight into the mechanisms of the observed reactions.

Introduction

Low-energy electrons, which constitute an important component of plasmas, are known to induce chemical reactions not only in gaseous molecules but also in molecules adsorbed or condensed as thin film on surfaces. The interaction of electrons with surfaces thus contributes to the modifications occuring under plasma treatment. In order to understand in detail the effect of low-energy electrons in surface modification processes, it is necessary to investigate these reactions within well-defined ranges of incident energies and to aim at both a conprehensive identification of the reaction products and the measurement of cross sections for their formation.

We have recently demonstrated that thermal desorption spectrometry (TDS) is a valubale tool to study reactions induced by low-energy electrons in adsorbates and thin molecular films. Using this method we have observed the formation of larger products from simple molecules in both condensed films of acetaldehyde [1] and acetonitrile as well as mixtures of acetonitrile with ethane [2]. These samples are simple model systems that provide insight in the elementary processes of electron-induced reactions in the condensed phase. Here we demonstrate the capability of TDS to provide cross sections for low-energy electron-induced reactions in thin films and present new results concerning reactions in thin films of hexamethyldisiloxane (HMDSO) which serves as model to understand electron-induced chemistry in siloxane coatings.

Experimental

The TDS experiments were performed in an ultrahigh vacuum (UHV) chamber pumped by a turbomolecular pump to a pressure of about 10^{-10} Torr. If necessary, additional pumping can be provided by a titanium sublimator. Low-energy electron-induced reactions of samples condensed at 35 K onto a polycrystalline Au sheet were monitored by thermal desorption spectrometry (TDS) using a Quadrupole Mass Spectrometer (QMS) residual gas analyser (Stanford, 200 amu) with electron impact ionization at 70 eV. The temperature was measured using a thermocouple type E press-fitted to the Au substrate. A commercial floadgun with an estimated resolution of the order of 0.5 - 1 eV delivering currents of the order of a few $\mu A/cm^2$ as measured at the substrate was used for electron exposure.

Acetaldehyde (CH_3CHO, stated purity of 99.95%) and HMDSO (NMR grade, 99.9%) used in the experiments were purchased from Fluka and ABCR, respectively. For the experiments, thin molecular films were deposited on the Au substrate held at cryogenic temperatures by a closed-cycle Helium refrigerator. To produce these films, gases or vapours were introduced via a gas handling manifold consisting of precision leak valves and a small calibrated volume where the absolute pressure is measured with a capacitance manometer. For each film deposition, a calibrated amount of gas or vapour was leaked via a stainless steel capillary whose end is located just in front of the metal substrate. The film thickness of acetaldehyde was estimated previously [1] by recording TDS curves for increasing coverage. Acetaldehyde desorption shows a weak but characteristic peak that rapidly saturates and is ascribed to the first layer on the Au and a second peak at slightly lower temperature that starts to increase upon saturation of the monolayer peak. The TDS of HMDSO is discussed together with the first results on electron-induced reactions in this contribution.

Electron-induced reactions are monitored in an exposure-TDS experiment. A thin molecular film is

exposed to electrons of specific energy (E_0) until a certain accumulated charge is reached. Subsequently, the sample temperature is increased at a rate of 1 K/s. This leads to desorption of the remaining initial products and of new species formed as a results of exposure. Comparison of TDS experiments performed without and after exposure yields information about the reactions induced by electron exposure.

Measurement of cross sections using TDS

Electron-induced reactions in thin molecular films produce species that lead to new stable molecules immediately or upon subsequent increase of the substrate temperature (TDS experiment). Each specific molecule can be identified in a TDS curve corresponding to a characteristic molecular mass by the temperature at which desorption from the surface occurs. Assuming that overlapping signals due to other molecules with fragment of identical mass do not occur, the intensity of the desorption peak is proportional to the amount of its neutral precursor molecule on the surface. Experiments performed on CH_3CHO demonstrate the ability of our TDS experiment to yield data that can be used to determine reaction cross sections not only for the decomposition of the initial sample but also the production of new species.

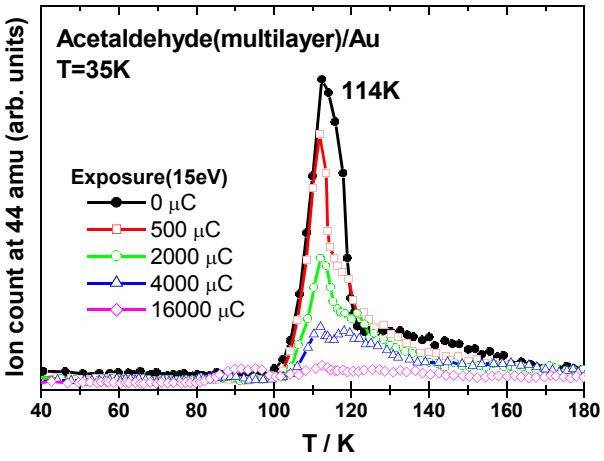

Fig. 1:
TDS curves for multilayer films of CH_3CHO recorded at 44 amu after increasing exposure to electrons at E_0 = 15 eV.

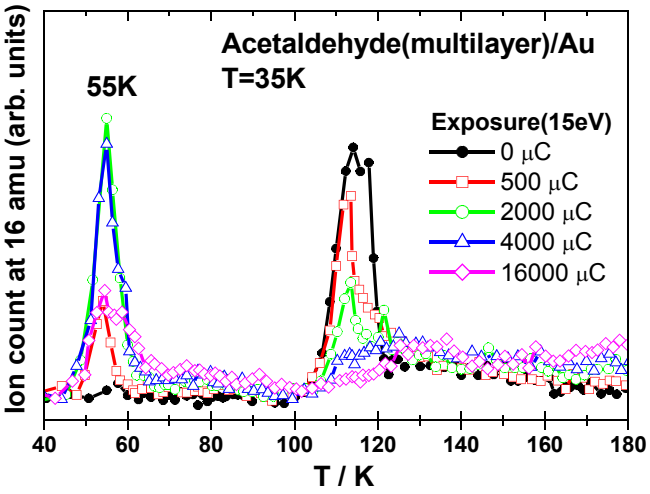

Fig. 2:
TDS curves for multilayer films of CH_3CHO recorded at 16 amu after increasing exposure to electrons at E_0 = 15 eV.

Fig. 1 shows a representative set of desorption curves obtained by measuring the intensity of the 44 amu signal as function of the substrate temperature. CH_3CHO desorption peaks at 114 K with the intensity decreasing continuously with increasing exposure at E_0 = 15 eV. Analyzing this decrease as quantified from the integral desorption peaks in terms of first order kinetics and taking into account the irradiated area of the sample yields a cross section of 7.2×10^{-17} cm^2 for the loss of acetaldehyde at this energy.

CH_3CHO typically releases CO upon exposure to electrons above E_0 = 10 eV [1]. From stochiometric arguments, this must be accompanied by formation of other species. We previously identified CH_4 and CH_3CH_2CHO as products and suggested a mechanism for their formation [1]. The production of these species was demonstrated by recording TDS curves at characteristic masses. As an example, Fig. 2 shows TDS curves recorded at 16 amu to monitor the production of CH_4 which desorbs at 55 K.

The amount of the product was quantified by comparing with the integral desorption signal of CH_4 in reference samples consisting of CH_3CHO mixed with specific percentages of CH_4 as shown in Fig. 3. To account for possible variations of the absolute intensities, the peak areas obtained both after electron exposure and for the non-exposed reference mixtures are normalized to the intensity of the 44 amu signal of CH_3CHO. From this analysis, we find an astonishingly small cross section for the formation of CH_4 of 4.1×10^{-18} cm^2, while a similar analysis for CO which desorbs at 48 K yields a value of 6.6×10^{-17} cm^2. While the latter value compares closely with the cross section found previously for the production of CO from acetone (CH_3COCH_3) [3], this result demonstrates that other hydrocarbon species must be formed to a significant amount. Among those, CH_3CH_2CHO is produced with a cross section below 10^{-18} cm^2 as deduced from the quantitative analysis.

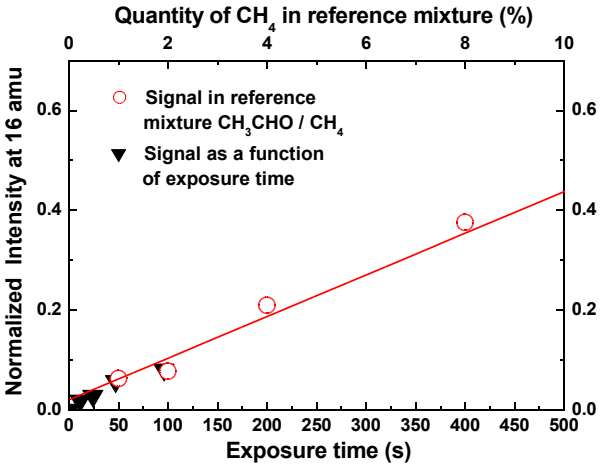

Fig. 3:
Integral intensity at 16 amu as function of exposure at E_0 = 15 eV and compared to the same quantity for reference mixtures containing increasing amounts of CH_4.

Low-energy electron-induced chemistry in HMDSO

TDS curves of HMDSO recorded using the most intense signal at 147 amu reveal an interesting feature. Upon increasing coverage, the maximum desorption temperature first shifts from values above 160 K at monolayer coverage down to 149 K where a distinct peak appears at multilayer coverage. Above a certain deposited amount of vapour, which is already well above the dose required for monolayer formation, a second peak appears at 158 K. This may be explained by assuming that a minimum film thickness is required to produce crystalline domaines from the supposedly amorphous as-deposited films upon annealing during the TDS run. Interestingly, electron exposure affects the high temperature multilayer desorption signal much more strongly than the signal at 149 K. While the former completely disappears after an exposure of only 500 µC, the latter does not decrease and even remains visible after 2000 µC. Loss of HMDSO is obvious at and above E_0 = 11 eV (Fig. 4). We suggest that this effect is related to quenching effects near the metal surface so that the material remaining after electron exposure is not sufficient to produce a crystalline structure.

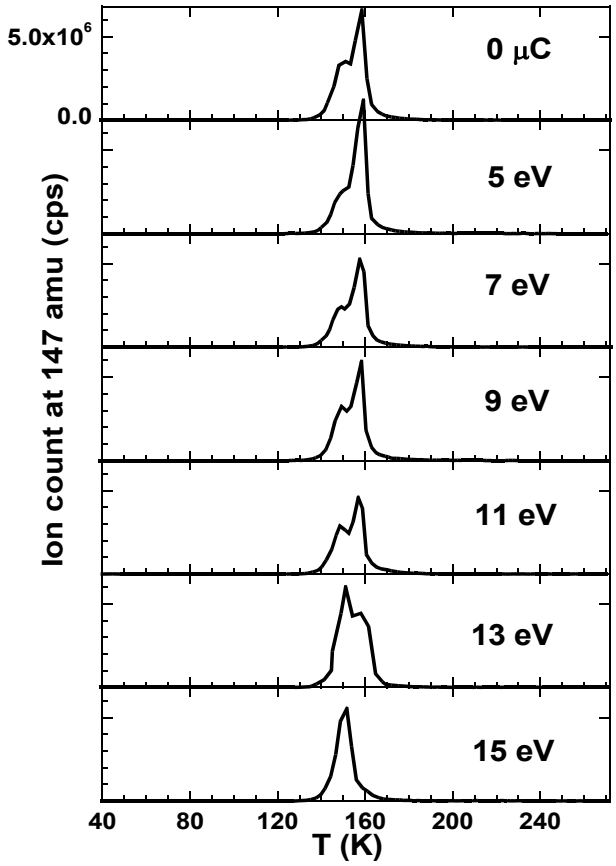

Fig. 4:
TDS curves for multilayer films of HMDSO recorded at 147 amu on a fresh film and after electron exposure of 500 µC at various E_0.

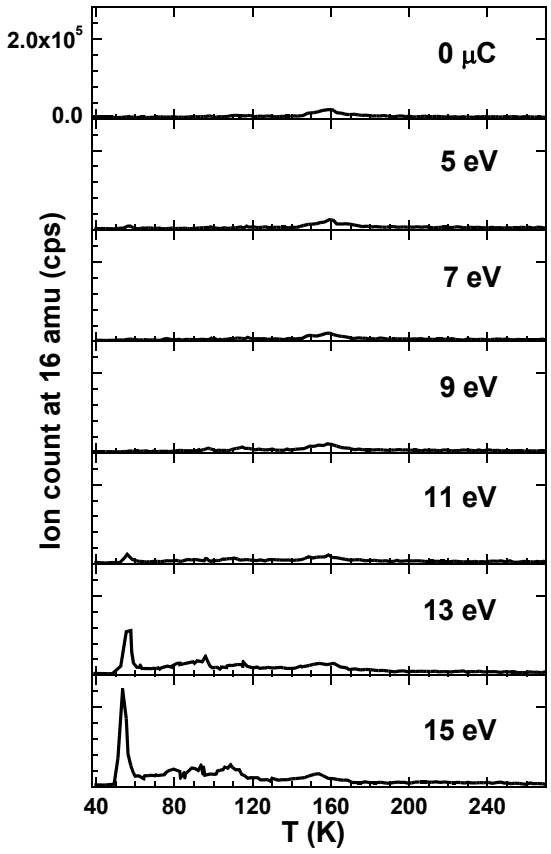

Fig. 5:
TDS curves for multilayer films of HMDSO recorded at 16 amu on a fresh film and after electron exposure of 500 μC at various E_0.

Additional experiments aimed at the identification of products formed in films of HMDSO upon exposure to low-energy electrons. As an example, Fig. 5 shows TDS curves recorded at 16 amu. Formation of CH_4 becomes detectible at E_0 = 11 eV and increases at higher E_0 in accord with the energy-dependence for loss of HMDSO. CH_4 production may hint towards crosslinking of the molecules within the film in this energy range.

Conclusions

We have demonstrated that thermal desorption spectrometry is a valuable tool for studying reactions induced by low-energy electrons in thin molecular films. Cross sections for the formation of various products can be obtained rapidly as shown for CH_4, CO, and CH_3CH_2CHO produced in CH_3CHO. Also, for the case of HMDSO, we observe a complex desorption process involving formation of phases with different desorption temperature and find evidence for differences in reaction rate that hint towards quenching effects at the metal surface. Finally, loss of HMDSO taking place above approximately 10 eV is accompanied by production of CH_4.

References

[1] P.Swiderek, C.Jäggle, D.Bankmann, E.Burean, J.Phys.Chem.B, in print.
[2] I.Ipolyi, W.Michaelis, P.Swiderek, PCCP **2007**, *8*, 182.
[3] M.Lepage, M.Michaud, and L.Sanche, J.Chem.Phys. **2000**, *113*, 3602.

Carbon Ion Irradiation of Astronomical Ices

A. Dawes[1], A. Hunniford[2], P. D. Holtom[1], R. J. Mikerji[1], R. W. McCullough[2] and N. J. Mason[1]

[1]Department of Physics and Astronomy, The Open University, Walton Hall, Milton Keynes, MK6 7AA, United Kingdom. Fax: +44 1908 654192; Tel: +44 1908 655132; n.j.mason@open.ac.uk

[2]International Research Centre for Experimental Physics, Queen's University of Belfast, Belfast, Northern Ireland, BT7 1NN, United Kingdom. Fax: +44 28 9097 3110; Tel: +44 0 28 9097 3709; rw.mccullough@Queens-Belfast.AC.UK

1. Introduction;

Ion processing plays an important role in the chemical and physical modification of ice surfaces in astrophysical environments. Magnetospheric ions surrounding the Gas Giants in the outer Solar System impinge upon and modify the icy satellite surfaces creating new chemical species, including elements not originally present in the local ice composition. These may be formed via ion induced dissociative or reactive processes.

Carbon is the fourth most abundant element in the interstellar medium (ISM) and plays an important role in many chemical networks both in the ISM and in our own Solar System. In our Solar System most of the carbon ions present in planetary magnetospheres are thought to originate from the slow component of the solar wind with charge states ranging from 4^+ to 6^+ and energies in the low keV range. However surface sputtering and atmospheric ionisation of local satellites can also give rise to carbon ions with different charge state contributions. For example, the extraction of carbon bearing species e.g. CH_4 from the atmosphere of Titan, may lead to the enrichment of Saturnian magnetospheric plasma with carbon ions and carbon containing molecular ions. Similarly the detection of CO_2 on the surface of the Galilean moons Io, Europa, Ganymede and Callisto and the surface of the Uranian satellite Ariel, suggests the presence of CO_2^+, CO^+ and C^+ ions in the local planetary magnetospheres. Recent results from Cassini's Cosmic Dust analyser, which measured Jovian and Saturnian stream particles, have revealed C^+ as a dominant component in the mass spectra.

Outside the solar system, carbon ions are expelled in the stellar wind from carbon stars and are expected, in some regions of the ISM, to interact with the molecular clouds containing ice covered interstellar dust grains. A recent experimental study has also shown that 30 keV He^+ (a cosmic ray mimic) may release carbon ions from these dust grains into their ice mantles where they react with water ice to form CO and CO_2.

However, despite such evidence for the important role of carbon ions in interstellar and planetary chemistry, to date only a few studies of carbon ion irradiation of water ice have been carried out. In this talk I will discuss recent results on the interaction of low energy (4 keV) singly and doubly charged carbon ions with amorphous ice films at 30 K and 90 K. Such experiments are providing intriguing insights into the role of ion reactions in astrochemistry.

2. Experimental

A schematic diagram of the experimental setup is shown in Figure 1. Water ice samples were prepared in situ in an ultra-high vacuum chamber by directed vapour deposition onto a 20 mm diameter transmitting zinc selenide (ZnSe) substrate which was in thermal contact with a continuous flow open cycle cryostat. Control of the sample temperature over the range 20 – 400 K was achieved using a temperature controller with a resistive heater. The sample temperature was derived from thermocouples positioned close to the substrate. Beams of $^{13}C^{q+}$ (q = 1 or 2) ions were extracted from a 9.0 – 10.5 GHz Electron Cyclotron Resonance (ECR) ion source held at a potential V_S and coupled to a low energy accelerator of 'floating beamline' design whose potential was maintained at -4 kV. This allowed the production of low energy ($V_S \times q$ keV) beams incident upon the sample area whilst maintaining a high ion energy for beam analysis. The ion source was fed with high purity, isotopically labelled, ^{13}CO ensuring that the carbonaceous species produced in the ice originated from the incident ion beam and not from any background contaminant (which will be derived from ^{12}C).

Analysis of the irradiated water ice was carried out using in situ infrared spectroscopy derived from a purged Thermo-Nicolet Nexus 670 FTIR spectrometer. Spectra were acquired in the range from 4000 to 650 cm^{-1} at 1 cm^{-1} resolution. The sample was positioned with the infrared and the ion beams perpendicular to one another and both at 45° to the substrate surface.

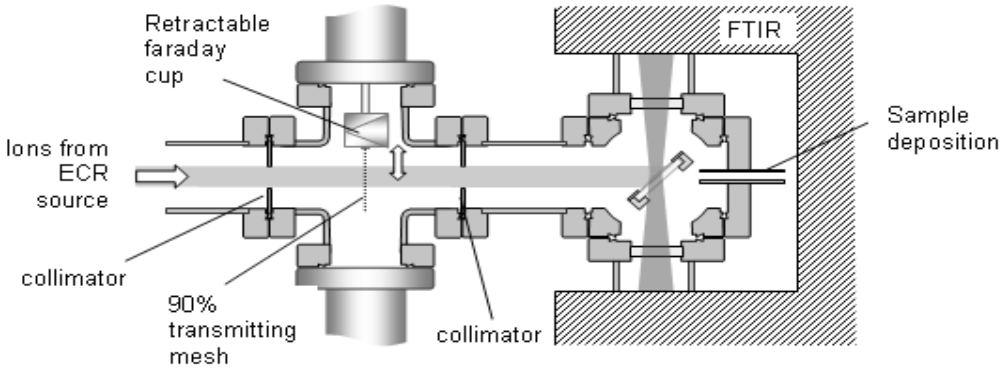

Figure . 1 Schematic diagram of the experimental set-up.

The ion current was measured before irradiating the sample using a Faraday cup placed in the path of the ion beam prior to the sample chamber. During irradiation the beam current was continuously monitored using a 90% transmitting mesh placed in the beam path in place of the Faraday cup. The thickness, *D*, of the deposited water ice films was determined from the measured infrared spectrum. The column density, [H_2O], of water was calculated using the following equation:

$$\left[\mathrm{H_2O}\right] = \frac{\int \tau(\nu)\,\mathrm{d}\,\nu}{\mathrm{A}}$$

where $\int\tau(\nu)$ is the area of the infrared absorption band on an optical depth scale with $\tau(\nu) = ln(10) \times Absorbance$, and *A* is the integrated absorption coefficient associated with this infrared feature. A typical column density of a deposited water ice sample was 5.5×10^{17} molecules cm^{-2}, equivalent to an average ice thickness of 160 nm. These ice films were sufficiently thick to ensure that all of the carbon ions were stopped within the sample and so the substrate had no influence on the results.

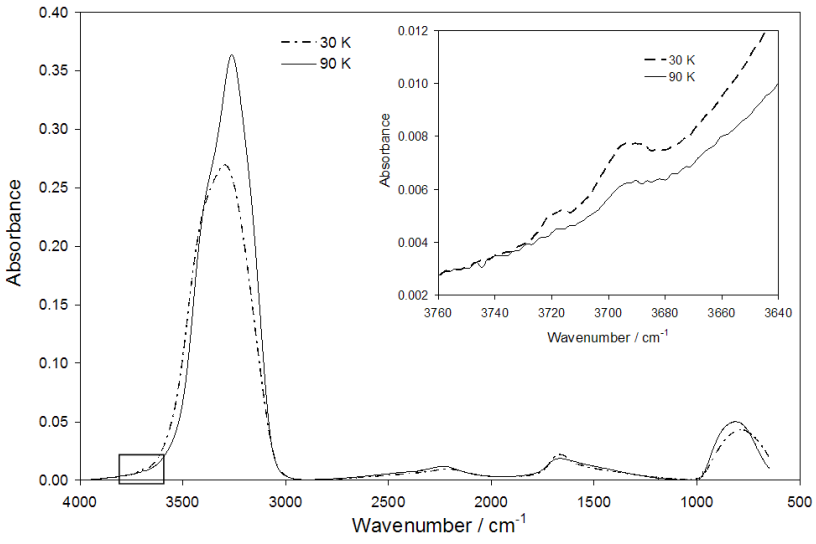

Figure 2; FTIR spectra of 160 nm H_2O films at 30 and 90 K. Inset shows the signature of the dangling OH bonds in the ice matrix indicating that the 30 K sample has greater porosity.

3. Results

Spectra of pristine 160 nm thick H_2O ice films at 30 and 90 K are shown in Figure 2. The spectra clearly illustrate that the morphology of solid H_2O is considerably different at 30 and 90 K. While both samples are amorphous, the spectrum of the 90 K sample shows a sharper and redshifted O-H stretching band around 3300 cm^{-1} indicating a more ordered structure and increased hydrogen bonding. The inset in Figure 2 shows a signature of OH dangling bond vibrations found between 3730 and 3670cm^{-1}. The presence of dangling OH bonds indicates that the degree of porosity in the amorphous ice film is larger for the 30 K sample than the 90 K sample.

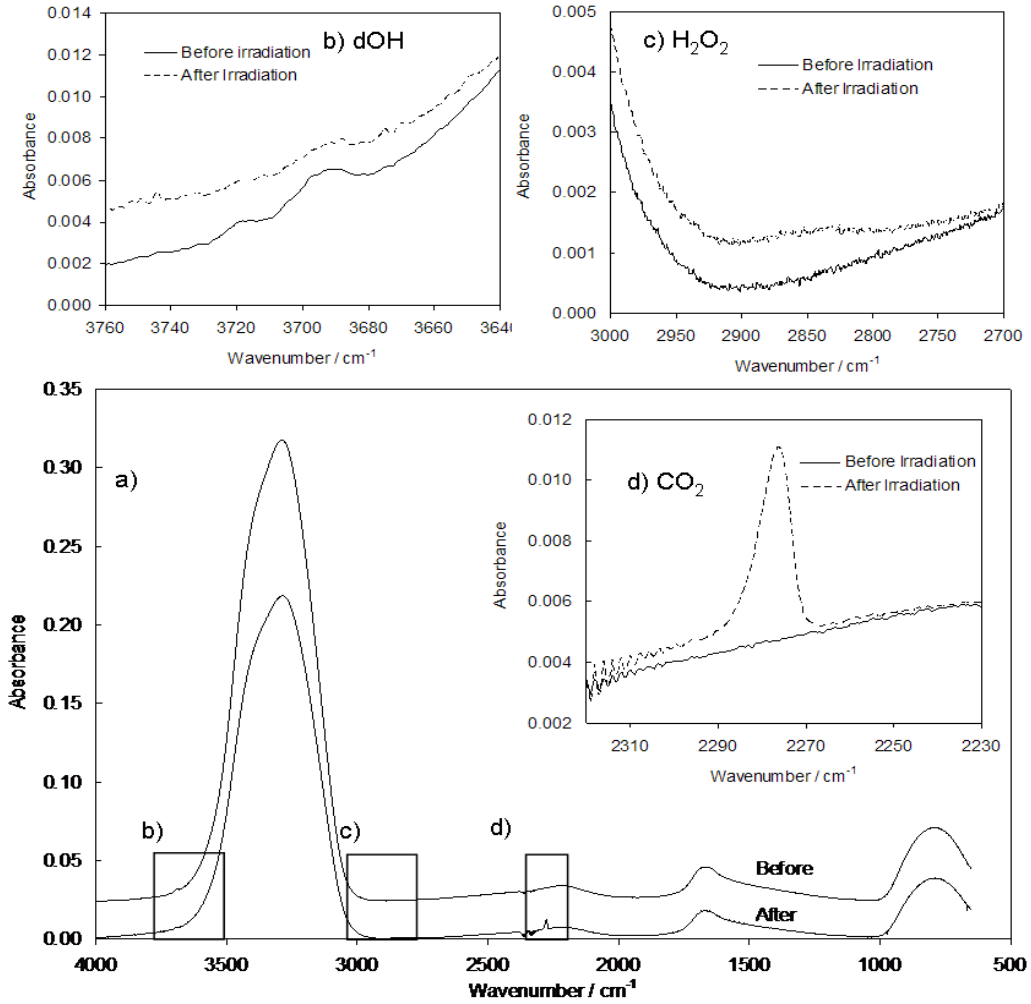

Figure 3 FTIR spectra of 160 nm H_2O films at 30 and 90 K after irradiation by carbon ions.

After irradiation with singly and doubly charged 4 keV carbon ions, several changes were observed in the measured FTIR spectra (Figure 3). Two new bands were observed at 2276 cm^{-1} and 2860 cm^{-1} which were assigned to $^{13}CO_2$ (Figure 3d) and H_2O_2 (Figure 3c) respectively. The dangling bond features between 3730 and 3670 cm^{-1} diminished considerably after irradiation (Figure 3b). The reduction in intensity of these bands can be interpreted in terms of pore collapse during irradiation. The formation of CO but the lack of any CO is noteworthy since one would expect CO to form by sequential reactions through the CO intermediate.

Figure 4 shows the $^{13}CO_2$ column density as a function of $^{13}C^+$ ion fluence for ice temperatures of 30 and 90 K. For both singly and doubly charged ions we observe a higher $^{13}CO_2$ yield in the 30 K ice compared to 90 K. The difference in yields may be explained by variations in mobility caused by sample temperature and morphology. Clear differences are also observed in the shapes of the $^{13}CO_2$ growth curves during irradiation with $^{13}C^+$ and $^{13}C^{2+}$ ions. The former follows a typical pseudo-first-order reaction trend whereas the growth curve in the latter appears to contain two distinct components. Details of these observations and possible mechanims will be discussed in the conference presentation.

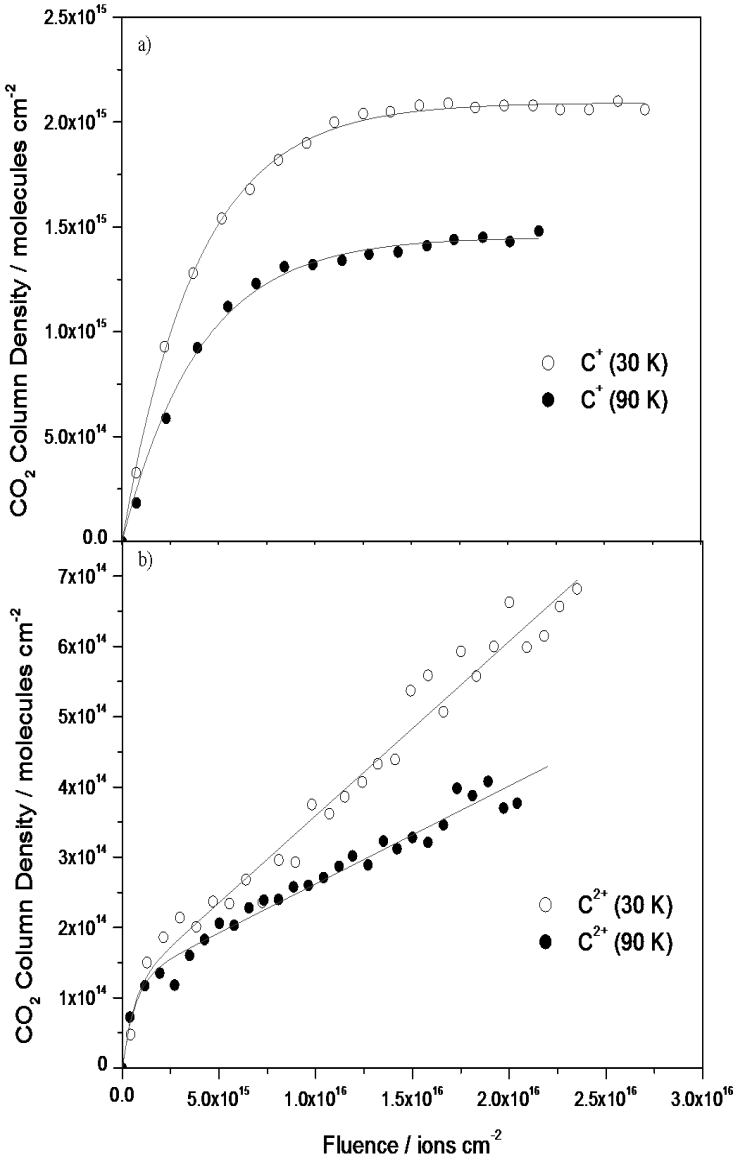

Figure 4 Growth of the $^{13}CO_2$ band as a function of ion fluence using 4 keV a) $^{13}C^+$ and b) $^{13}C^{2+}$ in on H_2O ice at 30 and 90K

Acknowledgements

This experiment has been performed at the distributed LEIF-infrastructure at Queen's University Belfast as part of the European project HPRI-CT-2005-026015. The support of the International Research Centre for Experimental Physics in providing a Distinguished Visiting Fellowship for N. J. Mason is gratefully acknowledged. AH acknowledges the award of a PhD studentship from the Department of Education and Learning (Northern Ireland).

Cavity-Hollow Cathode as Sputtering Source

R. Schrittwieser[1], C. Ionita[1], D. Luca[2], D. Alexandroaei[2], R. Apetrei[2], V. Anita[2], G. Popa[2], P. C. Balan[1], S. B. Olenici[1], A. Murawski[1],

[1]Institute of Ion Physics and Applied Physics, Leopold-Franzens University of Innsbruck, A-6020 Innsbruck, Austria

[2]Faculty of Physics, Alexandru-Ioan-Cuza University of Iasi, RO-700506 Iasi, Romania

e-mail: roman.schrittwieser@uibk.ac.at

Abstract

A cavity-hollow cathode post-discharge can be used as versatile, low-cost sputtering source. Results of measurements with electrical and optical emission spectroscopy diagnostics are presented, which were performed in the discharge plasma inside and in front of the cathode for parameters relevant for sputter-deposition of ferromagnetic (Ni,Fe) and non-ferromagnetic materials. Thin films of titanium suboxides and nickel were deposited on amorphous and single-crystal substrates and their morphology was investigated by AFM, XRD and EDX. The operation of the source was tested in both stationary and pulsed regimes. In the latter case, experimental conditions were sought to operate in self-oscillating and pulsed regimes. The results are useful to find the operating conditions for implementing a highly versatile sputtering source.

Introduction

In spite of the great success of magnetron sputtering sources for deposition techniques, the search for novel sputtering configurations is still of interest in many fields, such as the design of metal ion sources and for film growth [1-3]. **H**ollow **c**athode discharge-based **s**puttering **s**ources (HCSS), where ionization is enhanced by electron confinement inside the cathode chamber, turned out to be promising alternative options.

The simple, low cost, high-efficiency metal vapour source described in [4] utilizes a hollow cathode post-discharge geometry in the 0,01 mbar range to grow TiN_xO_y thin films. Good quality thin films of TiN, Ni and Fe were up to now successfully produced by various groups [5,6]. Nevertheless this configuration needs further characterization, as demonstrated in the devices used to manufacture low-temperature aggregation metallic/oxidic cluster sources [7]. Moreover, due to the fact that the dc regime is much better understood [8], the pulsed regime of a HCSS was presented only very recently [9].

The main advantage of the HCSS configuration lies in the chance to overcome the specific problems of sputtering ferromagnetic materials in conventional magnetron configurations [10]. Moreover, improved film quality is ensured by intense ion bombardment of the substrate during deposition. To improve the performances of this configuration regarding the control of film parameters (vapour fluency, growth rate, film uniformity, energy of ions impinging on the substrate, size of the sputtered aggregates, elemental composition), further characterization of the HCSS is necessary. Here, we present and discuss results regarding plasma diagnostics and their impact on the characteristics of some metal and oxide thin films.

Experimental set-up and diagnostics

A schematic diagram of the sputtering source is shown in Fig. 1a. Two specifically shaped equi-potential metallic disks, 25 mm in diameter are separated by a glass spacer, 18 mm in diameter, 6 mm high. The disks confine a 1,4 cm^3 cylindrical cathode chamber, visible through the glass spacer for optical and spectral measurements. The additional cylindrical cavity (5 mm diameter) inside the lower disk further enhances the ionization rate in the hollow cathode [4]. The cathode ensemble is introduced into a cylindrical glass cover. The grounded wall of the 1 liter discharge chamber (not shown in Fig. 1(a)) plays the role of the anode. In certain experiments, an additional 30 mm diameter ring anode, placed 6-20 mm in front of the cathode nozzle was used, with the ring serving also as substrate holder.

After evacuation to a base pressure of 10^{-6} mbar, Ar gas is employed in front of the nozzle through three inlets. A conical glowing plasma jet exits from the cathode nozzle, its shape being determined by electrical and pressure gradients. In the pulsed regime (Fig. 1b) the dc power supply is substituted by either an *R-L* circuit (whose elements are adjusted for adequate current pulse repetition rate) or by an externally pulsed current source. In the self-oscillatory regime a slight thermal drift due to electrode heating destabilizes the discharge with the time. Therefore, a second configuration was tested to pulse the source externally. With this arrangement, current pulses up to 200 mA with 1 ms duration (or shorter) and frequencies up to 1 kHz were obtained.

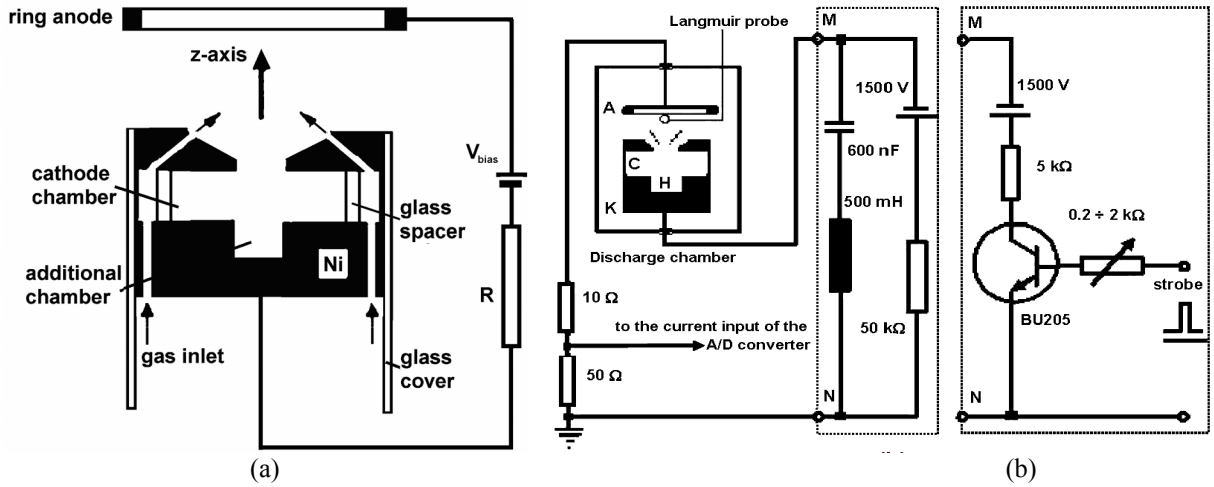

Fig. 1: (a) Schematic view of the dc-operated hollow-cathode source; (b) Electronic circuits used to operate it in the pulsed regime.

The current-voltage (*I-V*) characteristic of the discharge, both in dc and pulsed regimes, were first used to derive the connection between the operation parameters and film parameters. The plasma parameters, such as electron temperature (T_e), electron distribution function (EEDF), electron (plasma) density (n_e), and plasma potential (Φ_{pl}) were derived from the Langmuir probe characteristics of a cylindrical probe (tungsten, 0.05 mm diameter). The ion velocity distribution function (IVDF) in the same region was derived from the *I-V* characteristic of a movable four-grid retarding-field energy analyzer (RFEA). Using an analogue box-car technique, time-resolved measurements were also performed to record the Langmuir probe characteristics correlated with the temporal evolution of the discharge current pulse.

Optical measurements were performed using a collimated optical fibre and a photodiode sensor to measure the light intensity in a plane perpendicular to the symmetry axis *z* of the discharge. The intensity was measured at different axial positions between the two cathode disks and in the nozzle-anode region, for pressures ranging between 0,4 and 0,95 mbar and a discharge current of 10 mA. The current was chosen sufficiently low for a low density plasma so that the plasma emission profile (which is proportional to the electron density) could be determined performing an Abel inversion.

Spectral data were acquired using an optical fibre, a monochromator and a photomultiplier. The spatial distribution of a certain wavelength was mapped inside the cathode chamber and between the anode and cathode. The light intensity (giving information about the species inside the plasma) was measured for wavelength of 434,8 nm and 341,4 nm, corresponding to the de-excitation of Ar^{II} and Ni^{I} between the energy levels of 19,49 eV to 16,64 eV, and $3d^9(^2D)4p$ (3,65 eV) to $3d^9(^2D)4s$ (0,03 eV), respectively [11].

In addition, optical spectra or certain individual lines were recorded by time-resolved measurements in correlation with the temporal evolution of the current pulse using the photon counting technique. A monochromator, followed by a Stanford Research SR-400 gated photon counter and a low-noise photomultiplier were used to sequentially count the photons emitted by the transient plasma (correlated with the temporal evolution of discharge current).

Results and discussion

The dc regime:

In this regime the sputtering source was tested up to discharge currents of 300 mA (corresponding to 125 W). A set of current-voltage characteristics is shown in Fig. 2, and in Fig. 3 a typical visual aspect of the conically-shaped high-current discharge in front of the cathode. The HCSS is operated in the low-voltage, high-current domain of the *I-V* characteristics. The pressure ranged between 0,01 and 0,1 mbar, and the current between 20 and 50 mA. Previous probe measurements [5] have shown that the electron temperature on the cathode axis decreases from around 1 eV in the exit plane of the nozzle to 0,65 eV at 2 cm in front of it (i.e. on the substrate site). Under low-pressure conditions, the plasma potential profile remains almost constant along the axis. This tendency turns to a monotonous decrease for p = 0,07 mbar. A similar behaviour is evident in corresponding plots of plasma density profiles. On the other hand, the peak value of the EEDF remains practically unchanged over 2 cm in front of the exit nozzle under these conditions, while it shows a clear tendency to shift towards lower values over the same distance under higher pressures.

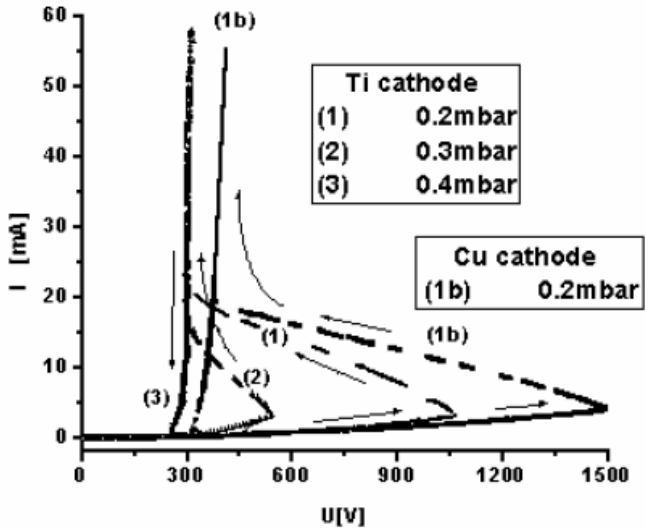

Fig. 2: dc-operated current-voltage characteristics of the source for different discharge conditions.

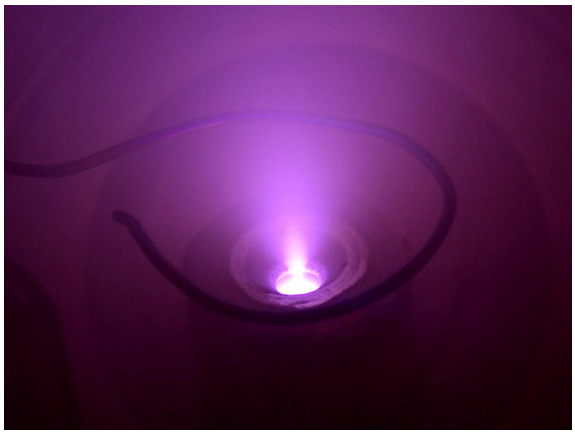

Fig. 3: A typical view of the plasma jet.

To check these results, optical measurements of the plasma emission were carried out. For a homogeneous optically thin plasma, the integral light intensity registered by the photo diode depends on: (a) the depth x of the measured plasma chord along the diode's line of sight, (b) the distance y between the discharge axis and the chord, (c) the local plasma emission ε. Then ε at a distance r from the axis of symmetry can be expressed by:

$$\varepsilon(r) = -\frac{1}{\pi}\int_r^R \frac{\mathrm{d}I(y)}{\mathrm{d}y}\frac{\mathrm{d}y}{\left(y^2 - r^2\right)^{1/2}}, \quad (1)$$

where R is the radius where $\varepsilon(r)$ vanishes [10]. The recorded light intensity curves, $I(y)$, were first fitted to Gaussian functions. Then an Abel inversion was applied to the fitted curves to obtain $\varepsilon(r)$ according to Eq. (1). In the cathode-anode region the plasma emission decreases monotonically in radial direction, with the highest dropping rate in the region closest to the cathode nozzle. This tendency becomes less evident for approaching the anode ring. This is associated with an evident decrease of the length of the plasma jet in the higher pressure range and with a flattening of the ion velocity distribution functions along the cathode-anode axis [6]. The conical shape (Fig. 3) of the plasma jet results in the axial distribution of the plasma emission. For this cathode geometry and gas pressure of 0,4 mbar, the plasma emission decreases by a factor of six over a distance of 14 mm in front of the nozzle. For a pressure of 0,9 mbar it is about two times smaller between 0 and 3 mm in front of the nozzle.

By comparing these results with those from Langmuir probe diagnostics, where an almost linear decrease of plasma density was found [8], we may conclude that the light emission originates from a beam of high-energy electrons exiting from the cathode [12] (while actually, the mean electron energy is only about 1 eV). The cross section of this beam is correlated to the electric field line distribution in the conical nozzle region and on the electron confinement degree inside the cathode chamber.

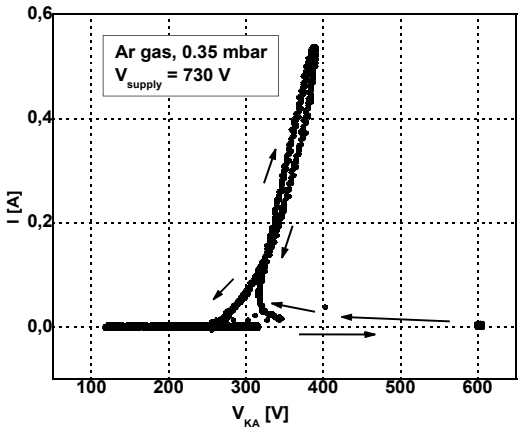

Fig. 4: Dynamic current-voltage characteristic of the discharge (with an Fe-cathode) in pulsed operation. The arrows show the temporal evolution of the current.

The pulsed regime:

In the pulsed regime, dynamical *I-V* characteristics (Fig. 4) were recorded. Using the reactive elements mentioned in Fig. 1b (left side) and supply voltages up to 1500 V, relaxation oscillations with repetition rates in the 1 – 20 Hz range were observed. In the pulsed regime, at a repetition rate of 25 Hz and a duty cycle of 0,18, peak currents of 1.8 A and power values of 720 W were tested. Unfortunately, the operation pressure range was rather narrow (2 – 20 mbar), but further research can lead to a widening of this range.

During each current pulse, the voltage on the discharge rises exponentially from the low value, specific for the high-impedance discharge regime, until an ignition value, where the current starts increasing

drastically. This leads to the rapid discharge of the capacitor through the discharge interval, and the process repeats periodically. The inductance *L* coupled in series with the capacitor *C* is used to increase the current pulse duration, thus making it comparable with the eigen period of free oscillation of the *LC* circuit. Similar *I-V* characteristics were obtained for gas pressures ranging between 0,2 and 0,8 mbar. The differential resistance of the discharge ranged between 150 and 180 Ω. Maximum currents of 1,8 A were routinely achieved without water cooling.

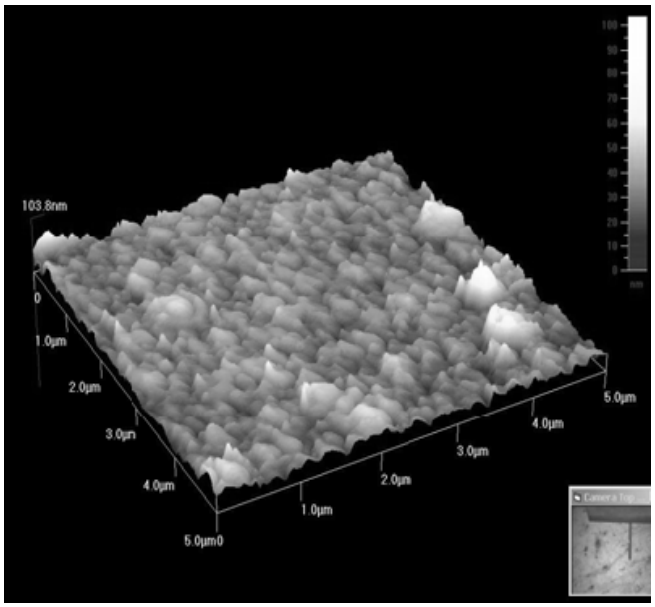

Fig. 5: A typical AFM image of a TiO_2 film deposited in the dc operated HCSS.

Production of thin titanium films:

Thin films of Ti and TiO_2 with a thickness of 100 nm were grown at a substrate temperature of 300°C, using the described source operated in dc mode. Polished (100)Si and microscope glass slides were used as substrates. The Ar partial pressure was maintained at 0,22 mbar. An additional atmosphere of oxygen (partial pressure 0,08 mbar) was added to ensure a reactive discharge regime and thus prepare titanium dioxide films. Current values of 700 mA were used. A typical AFM image of film's surface is shown in Fig. 5.

Conclusion

A low-cost, high-efficiency sputtering source, based on the cavity hollow cathode post-discharge (the HCSS) operated in both dc and pulsed regimes was investigated. Langmuir probe and OES measurements were performed to characterize the HCSS. Good correlations between local plasma parameters such as electron temperature, density and electron velocity distribution function and the total light emission were found. This is useful since the measurement of light emission is easier and less perturbing. By monitoring certain spectral lines of both buffer gas and sputtered metal, the distribution of atomic species both inside the hollow cathode and in the anode-cathode interspace, data for the design of an adequate geometry for film deposition were gathered. Time-resolved measurements of optical emission spectra and Langmuir probe characteristics allowed us to find appropriate values of the circuit elements, gas pressure, and discharge current for pulsed operation. The results demonstrate that this device is useful, either in dc or pulse operation, for substrate bombardment with energetic particles during deposition.

References

[1] N. Gavrilov, G. Mesyats, G. Radkovski, V. Bersenev, *Surf. Coat. Technol.*, **96** (1997) 81.
[2] K. Ishii, K. Amano, H. Hamakake, *J. Vac. Sci. Technol.*, **A17** (1999) 310.
[3] E.M. Oks, A. Anders, I.G. Brown, *Rev. Sci. Instrum.*, **75** (2004) 1030.
[4] M.H. Kazemeini, A.A. Berezin, N. Fukuhara, *Thin Solid Films*, **372** (2000) 70.
[5] P.C. Balan, R. Apetrei, D. Luca, C. Ionita, R. Schrittwieser, G. Popa, *J. Optoel. Adv. Mater*, 7 (2005) 2459.
[6] S. Guruvenket, G. Mohan Rao, *J. Vac. Sci. Technol.*, **A20** (2002) 678.
[7] D. Luca, D. Alexandroaei, R. Apetrei, V. Anita, G. Popa, *unpublished results*.
[8] R. Apetrei, D. Alexandroaei, D. Luca, P. Balan, C. Ionita, R. Schrittwieser, G. Popa, Japan. *J. Appl. Phys.*, **45** (2006) 8128.
[9] R. Apetrei, D. Alexandroaei, D. Luca, P. Balan, C. Ionita, R. Schrittwieser, G. Popa, Japan. *J. Appl. Phys.*, **45** (2006) 8132.
[10] D. Luca, *Rom. Reports in Phys.*, **47** (1996) 768.
[11] W. Lochte-Holtgreven, *Plasma Diagnostic*, North-Holland, Amsterdam, 1968, p 134.
[12] G. Popa, M. Sanduloviciu, P. Croitoru, and C. Moldovan: *J. Phys.*, **40** (1979) 187.

High-Power Pulsed Magnetron Discharges for Ionized High-Rate Sputtering of Films

J. Vlček, P. Kudláček, K. Burcalová, A. D. Pajdarová and J. Musil

Department of Physics, University of West Bohemia, Univerzitní 22, 306 14 Plzeň, Czech Republic
e-mail: vlcek@kfy.zcu.cz

Abstract

Recently, novel high-power pulsed dc magnetron systems have been used for sputtering of films [1-7]. The target power loading in a pulse of these discharges with a peak value up to several kW/cm^2 is considerably higher than a typical maximum target power loading (usually less than 20W/cm^2) applied in conventional dc magnetron sputtering. Consequently, film deposition can be carried out at highly ionized fluxes of sputtered atoms. This is of great interest for directional deposition into high aspect ratio trench and via structures, and for ion-assisted growth of films.

To master new advantages of high-power pulsed dc sputtering requires an understanding of the physical basis of the generation and behaviour of the high-power pulsed dc magnetron discharges. However, these discharges are very complex environments with a highly nonuniform structure, fast sheath dynamics and temporal changes in diffusion mechanisms and plasma composition during pulses.

High-power pulsed magnetron sputtering of copper and titanium films was systematically investigated. The depositions were performed using a strongly unbalanced magnetron system with a target of 100mm in diameter. The repetition frequency of the pulsed dc power supply (with a maximum voltage and current of 1kV and 120A, respectively) was 1kHz at a 20% duty cycle and an argon pressure of 0.5Pa.

Time evolutions of the magnetron voltage, the target current density (up to 1.5 A/cm^2) and the ion current density on the substrate (up to 0.45A/cm^2) were measured to provide information on absorption of energy in the discharge plasma and on transfer of arising ions to the substrate at a target power density in a pulse up to 950W/cm^2. The deposition rate and the substrate ion current density per average target power density were determined to investigate efficiency of magnetron sputtering, and formation and transfer of ions to the substrate, respectively. Time-resolved plasma diagnostics was carried out to understand complex time-dependent processes in pulsed magnetron discharges. Time-averaged mass spectroscopy was performed at the substrate position to characterize ion energy distributions and composition of total ion fluxes to the substrate.

A completely different trend in measured values of the deposition rate per average target power density obtained for these two technologically interesting materials and the same trend in their values of the ionized fraction of sputtered atoms in the flux onto the substrate (up to 56% for copper and 81% for titanium) were explained on the basis of model predictions. We present a qualitative model based on that developed recently by Christie [8]. The original model was modified and supplemented by a balance equation for secondary electrons near the sputtered target. This makes it possible to evaluate the fraction of ionized sputtered atoms directed back to the target to sustain the magnetron discharge under the experimental conditions investigated. The effects of self-sputtering of target material, losses of the target material ions during transport to the substrate and additional ionization of sputtered atoms in a plasma bulk on the deposition rate per average target power density and on the ionized fraction of sputtered atoms in the flux onto the substrate are shown.

Acknowledgment

This work was supported by the Ministry of Education of the Czech Republic under Project No. MSM 4977751302.

References

[1] V. Kouznetsov, K. Macák, J. M. Schneider, U. Helmersson and I. Petrov, *Surf. Coat. Technol*. 122 (1999) 290.
[2] K. Macák, V. Kouznetsov, J. Schneider, U. Helmersson and I. Petrov, *J. Vac. Sci. Technol. A* 18 (2000) 1533.
[3] A. P. Ehiasarian, P. Eh. Hovsepian, L. Hultman. and U. Helmersson, *Thin Solid Films* 457 (2004) 270.
[4] J. Vlček, A. D. Pajdarová and J.Musil, *Contrib. Plasma Phys*. 44 (2004) 426.
[5] P. Vašina, M. Meško, M. Ganciu, J. Bretagne, C. Boisse-Laporte, L. de Poucques and M. Touzeau, *Europhys. Lett*. 72 (2005) 390.
[6] S. Konstantinidis, J. P. Dauchot, M. Ganciu, A. Ricard and M. Hecq, *J. Appl. Phys*. 99 (2006) 013307.

[7] J. Vlček, P. Kudláček, K. Burcalová and J. Musil, *J. Vac. Sci. Technol. A* 25 (2007), in print.
[8] D. J. Christie, *J. Vac. Sci. Technol. A* 23 (2005) 330.

Deposition of Thin Superconducting Coatings by Means of Ultra-High Vacuum Arc Facilities

M. J. Sadowski[1], P. Strzyzewski[1] and S. Tazzari[2]

[1] The Andrzej Soltan Institute for Nuclear Studies (IPJ), 05-400 Otwock-Swierk n. Warsaw, Poland
[2] Tor Vergata University – INFN Roma 2, Rome, Italy
e-mail: msadowski@ipj.gov.pl

Abstract

This paper presents systems used for deposition of thin coatings by means of arc discharges performed under ultra-high vacuum (UHV) conditions. It also reports on progress achieved in the UHV arc technology.

Introduction

The deposition of thin layers upon surfaces of various materials is of great importance for the material science and engineering. Such a process can be performed by means of different techniques, e.g. plasma vacuum deposition (PVD), magnetron sputtering, etc. [1]. In modern technology, e.g. in the construction of RF-type accelerators, there appears interest in the use of superconducting materials. Since pure niobium (Nb) is expensive, the application of Cu-cavities coated with a thin Nb-layer may reduce costs considerably. For this purpose, the use was made of the magnetron sputtering technique [2], but quality of the deposited Nb-layers has not been the best one. To improve adhesion and to reduce amount of impurities, a new technique based on arc discharges under UHV conditions was proposed several years ago [3].

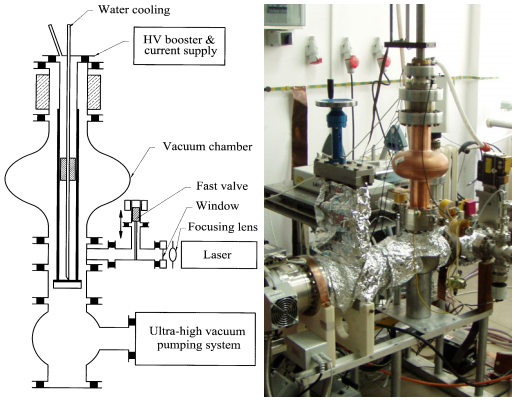

Fig.1. Scheme and view of UHV cylindrical-arc facility constructed at IPJ in Swierk.

Experimental facilities and results

The Polish-Italian team developed UHV arc devices of two different configurations: so-called UHV linear-arc facilities equipped with a cylindrical cathode (see Fig.1) and UHV planar-arc devices equipped with a planar cathode. Several UHV linear-arc facilities were constructed and modified step by step [4]. To optimize the operational conditions, samples (made of sapphire or Cu) were coated within a chamber of dimensions similar to the TESLA-type cavity. The samples coated by UHV linear-arc discharges showed that the deposited Nb-layers have good characteristics: a relatively high RRR (the record was 48) and the good composition, but the main problem constitute micro-droplets.

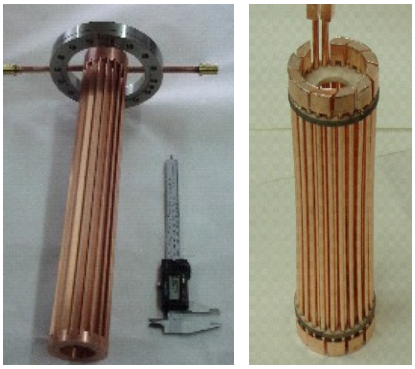

Fig.3. Venetian-type filter (left) and a new one (right) consisted of many thin current-carrying

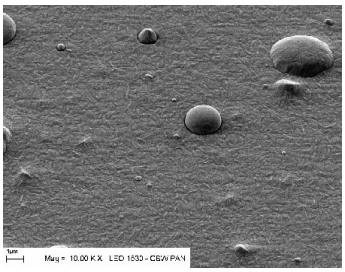

Fig.2. SEM image of the Nb-layer with micro-droplets.

The structure of the deposited Nb-layers was investigated by means of a scattering electron microscope (SEM) and scattered ion mass spectroscopy (SIMS) techniques. The SIMS profiles showed that the deposited layer contains mainly pure Nb, but SEM pictures demonstrated micro-droplets of different sizes. It was observed that such micro-droplets are immersed into the Nb-layer or deposited upon its surface (Fig.2). To reduce the number of micro-droplets, there were designed special cylindrical filters. The first filter was a concentric system of the Venetian blinds cooled at the end, while the second one consisted of many thin Cu-tubes carrying magnetizing currents and cooling-water flow simultaneously (Fig.3). Test of these filters have already been performed and characterization of the coated samples is realized [4].

During recent years there were also constructed several UHV planar-arc facilities [4]. In fact they were equipped with Nb cathodes of the truncated-cone shape (see Fig.4). Similar to the linear-arc systems, the arcs

within the UHV planar-arc devices were also initiated with a laser beam focused on the cathode surface. In order to investigate the Nb deposition, the samples made of sapphire and copper were placed inside the vacuum chamber upon a special holder, which enabled the application of polarization voltage. Using different coating times and different values of the substrate bias, the Tor Vergata team produced Nb-layers of 1 μm to 3.5 μm in thickness, with the RRR values ranging from 26 to 50 for the bias above - 40 V. Recently, attention was paid a dependence of the of an Nb-layer quality on an angle of the exposition to the arc discharge, as shown in Fig.5. The main problem appeared also to be micro-droplets.

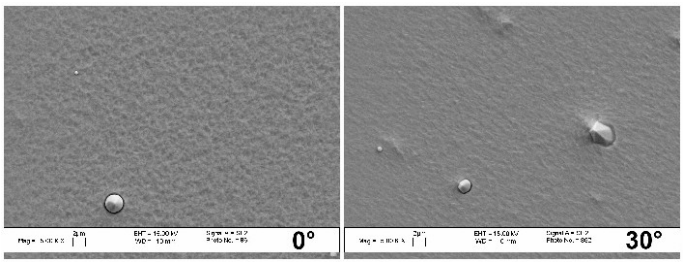

Fig.5. SEM pictures of Nb-layers deposited at different angles within an UHV planar-arc device without filtering.

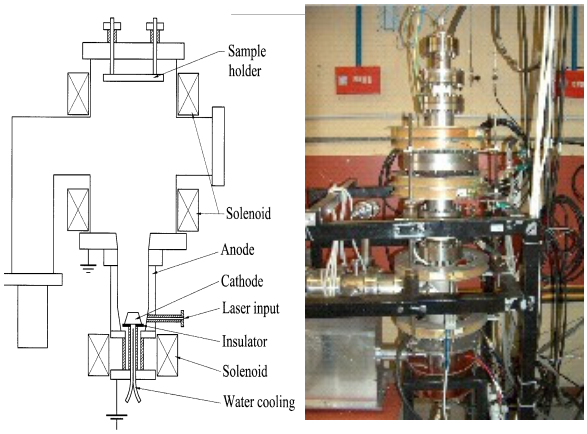

Fig.4. Scheme and view of UHV planar-arc device at Tor Vergata University in Rome.

To reduce the number of the micro-droplets, the IPJ and Tor Vergata teams designed and constructed special magnetic filters. The idea was to deflect the arc column and to allow the heavy micro-droplets (moving along almost straight lines) to be deposited upon walls of a special channel. Theoretical modeling of such magnetic filters (see Fig.6) and laboratory tests enabled the optimum configuration to be found [5]. In 2006 a new UHV planar-arc device with a T-type filter was put into operation and optimized. Characterization of Nb-layers deposited upon Cu samples was performed by means of FEG-SEM and XRD techniques. It was shown that the deposited layers have smooth surfaces and lattice parameters very similar to those of bulk Nb [6].

Fig.6. Distribution of B-field lines in a T-type filter.

It should also be added that the UHV planar-arc device with a magnetic filter has recently been applied also for the deposition of pure lead (Pb) layers which can be used as photo-cathodes in modern electron injectors [7].

Conclusions

In conclusions it can be stated that the UHV planar- and linear-arc facilities with laser triggering systems, as described above, provide very clean conditions for thin-film deposition processes. Such facilities have already been used for the deposition of superconducting Nb-films, which showed properties similar to the bulk Nb. In general, the UHV cathodic-arc devices are powerful tools for the deposition of pure metallic and super-conducting films, but efficiency of the micro-droplet filtering must still be improved.

Acknowledgement: We acknowledge a support of the EC - Research Infrastructure Activity under the FP6 "Structuring the European Research Area" program (CARE, contract number RII3-CT-2003-506395).

References

[1] R.L. Boxman, et al., *Handbook of vacuum arc science and technology,* Noyes, Park Ridge, NJ, 1995.
[2] C. Benvenuti, et al., *Physica* **C 351** (2001) 421-425.
[3] J.Langner, et al., Czech. J. Phys. **52**, Suppl. D (2002) D829-D835.
[4] M.J. Sadowski, et al., *Proc. Workshop on Thin Films*, INFN-Legnaro, Italy, Sept. 2006, p. 51.
[5] P. Strzyzewski, et al., Physica Scripta **T123** (2006) 135-139.
[6] R. Russo, et al., *Proc. Workshop on Thin Films,* INFN-Legnaro, Italy, Sept. 2006, p. 52.
[7] P. Strzyzewski, et al., *Proc. EPAC 2006,* Edinburgh, Scotland, June 2006, pp. 3205-3205.

A New Multi-Cathode High Current Pulsed Cathodic Arc Thin Film Deposition System

M. Bilek[1], R. S. de Castro[1], D. Andruczyk[1], L. Ryves[1], R. Tarrant[1], J. Pigott[1]

[1]Applied and Plasma Physics Group, School of Physics, University of Sydney, NSW 2006, Australia

Abstract

We have developed a high current pulsed cathodic arc which contains up to 4 cathode materials, able to be fired in any desired sequence. A unique centre triggering method ensures uniform erosion of the cathodes and thereby highly repeatable fluxes from pulse to pulse. The high current operation delivers low ion current fluctuations and very low macroparticle emissions. Due to the highly repeatable plasma pulses and computer control allowing easy preprogramming of pulse sequences the system is ideal for producing precision multilayered films with layer thicknesses on the sub-nanometer scale and also for producing alloys with precise control of stochiometry. We have successfully fabricated soft magnetic layers suitable for high density recording media and epitaxial MAX phase thin films with this system to date. We have also performed extensive plasma diagnostics using Langmuir probes, microwave interferometry and mirnov coils in order to characterise the plasma.

Introduction

The cathodic vacuum arc is an attractive technique for thin film deposition because of the highly ionized (almost 100%) plasma flux it produces. Because the film forming species are delivered as ions their arrival energies at the growth surface can be controlled using electric fields providing a handle for the control of stress and microstructure in the thin films deposited [1,2]. Cathodic arcs can be triggered on most conducting materials. The highly ionized plasma plumes of cathodic arcs are created in micron sized ablation regions known as cathode spots. The high energy density dissipated at the spots ejects highly ionized vapour of the cathode material. The stochastic nature of the spot formation and motion causes large fluctuations in the plasma flux generated as a function of time. Such fluctuations are detrimental if highly controlled stochiometry or fine scale layering in thin films is required. Uneven cathode erosion is also typically a feature of most common implementations of cathodic arcs. This leads to changing deposition rates as a function of time which is also detrimental to the production of layers needing fine control of depth profiles or multi-element stoichiometry.

In this paper, we describe a newly developed system which exploits the use of multiple cathode spots to smooth out fluctuations in plasma production and centre triggering in combination with the phenomenon of retrograde motion to ensure deposition rate stability as the cathodes erode. Plasma characterization using a variety of diagnostic methods is reported together with some recent thin film results which demonstrate the system's efficacy.

Results and discussion

Figure 1a is a schematic diagram showing our two cathode assembly and magnetic macroparticle filter. Once ignited by the centre trigger pins shown, the plasma is injected into an internally mounted solenoid coil. A capacitor bank power supply capable of currents up to 5 kA, powers the pulsed discharge after triggering. Microwave interferometry and electrostatic probe measurements show that plasma densities up to 10^{19} m^{-3} are readily achieved at the substrate position at exit of the curved filter (shown in the schematic as a straight section for simplicity). A typical plasma profile in the filter coil is shown in Figure 1b.

Key design features which exploit the physics of cathode spots are the high current operation and centre triggering. The high current insures that there are multiple cathode spots on the cathode surface at any one time and if they are ignited at the centre of the cathode their retrograde (repulsive) motion can be exploited to drive them evenly and reproducibly outwards along radii of the cathode, leading to uniform erosion, as shown in Figure 2. These features will be discussed at length in the presentation together with a plasma diagnostics characterization of the plasma produced.

Applications of this system to the creation of multi-component materials which are sensitive to composition as well as to structures needing high depth resolution will be presented to demonstrate its capabilities.

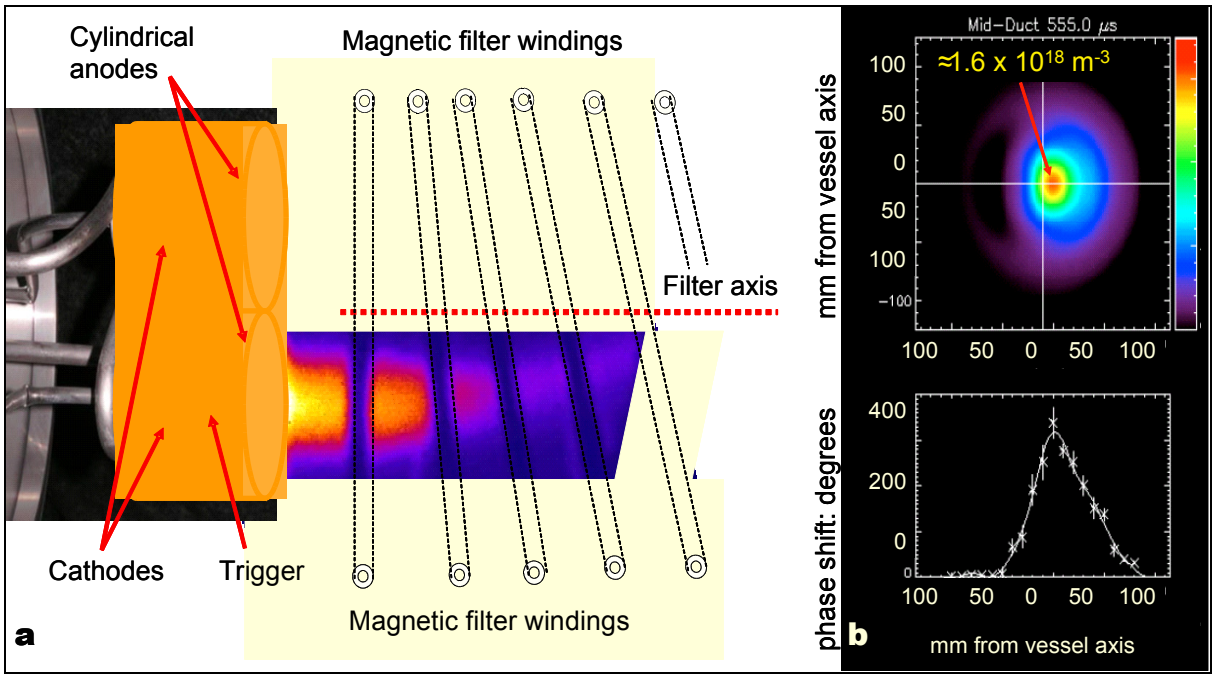

Figure 1: a) A diagrammatic representation of the cathode and anode assemblies and the position of the magnetic filter. b) A tomographic reconstruction of the electron density approximately mid-way between the cathodes and the substrate obtained using a 2 mm quasi-optical interferometer.

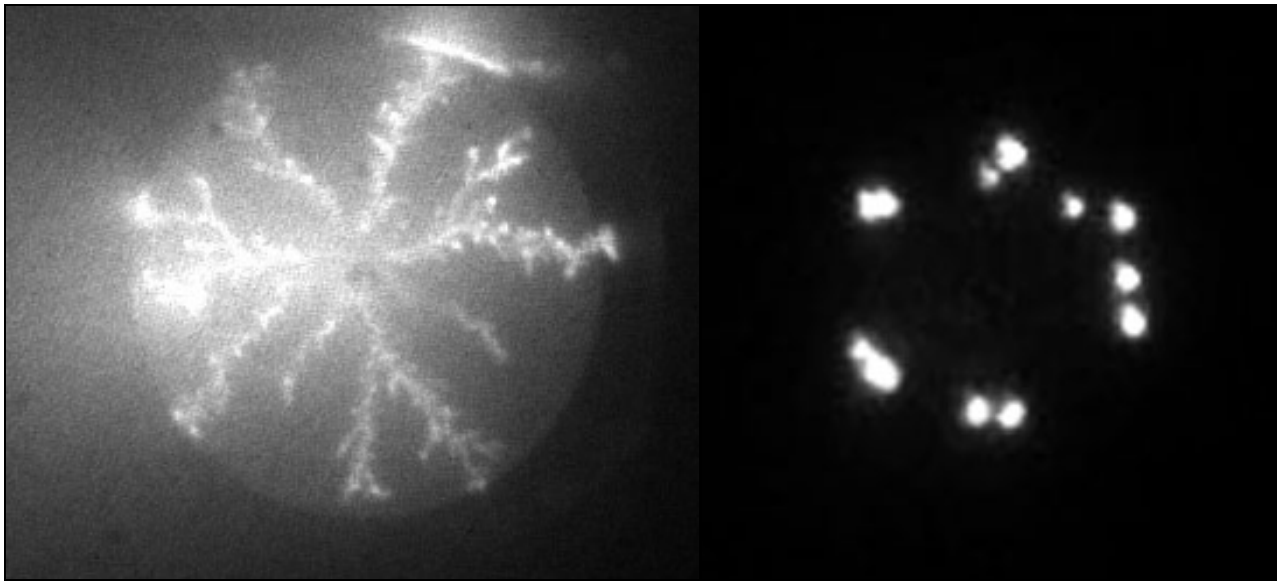

Figure 2: Fast framing camera images showing a) cathode spot paths from the triggering location at the cathode centre to the cathode edge taken in time lapse mode – the phenomena of branching and extinction of spots are clearly visible - and b) a single frame depicting the position of spots at a single time in the pulse. Roughly twelve spots travelling from inside to outside of the cathode in a ring formation are clearly visible.

Conclusions

We have developed a plasma deposition system based on the pulsed cathodic arc to produce highly controlled fluxes of multiple elements during a single thin film deposition. The system's capabilities are demonstrated by the results of recent thin film synthesis experiments as well as by the extensive plasma diagnostics we have preformed. Both will be presented in this talk.

References

[1] M.M.M. Bilek, D.R. McKenzie, *Surf. Coat. Tech.*, 200 (2006) 4345.
[2] M.M.M. Bilek, D.R. McKenzie, W. Moeller, *Surf. Coat. Tech.*, 186 (2004) 21.

Progress Reports

High Resolution Laser Spectroscopy of Ions

P. Hlavenka[1], J. Varju[1], R. Plašil[1], I. Korolov[1], T. Kotrík[1], O. Votava[2], J. Glosík[1]

[1]Charles University in Prague, Faculty of Mathematics and Physics, Prague, Czech Republic
[2]J. Heyrovský Institute of Physical Chemistry, Academy of Sciences Czech Republic, Prague, Czech Republic
e-mail: Juraj.Glosik@mff.cuni.cz

Abstract

Reported are results of measurements of H_3O^+ spectra in the first OH stretching overtone region. At least 30 absorption lines of H_3O^+ were found in near infrared region 6900 to 6960 cm^{-1} using a very sensitive time resolved continuous wave cavity ringdown spectrometer (cw-CRDS). H_3O^+ ions were produced in pulsed microwave plasma discharge in He/H_2O mixture. A technique based on time resolved absorption has been used to distinguish the absorption lines of short living ions from longer living radicals and water vapors.

Introduction

Hydronium ion, H_3O^+, is one of the key ionic species in the both gas and condensed phases. Besides its importance in both chemistry and astrophysics, H_3O^+ also serves as an important model system for benchmark theoretical predictions. Due to its small size high level theoretical treatment is possible for this molecule. H_3O^+ is isoelectronic with ammonia, NH_3, and shares number of important characteristics with this molecule. Thus the theoretical tools developed for characterization of ammonia can be put to an independent test when applied to H_3O^+. High resolution spectroscopy provides some of the most accurate experimental data, which can be used to test the theoretical predictions. Vibrational spectroscopy of the H_3O^+ ion has therefore attracted substantial attention [1,2,3,4]. Accurate calculation of the large inversion splitting in H_3O^+ has indeed proved a challenge for theorists. Only the most recent full dimensional ab initio calculations of the potential energy surface, coupled with variational evaluation of the vibrational states yielded satisfactory agreement with experiment in the fundamental and several low lying combination bands [5,6]. While the agreement between theories based on the full dimensional ab-initio PES and the available data is very good, there is presently a clear lack of experimental data that would test the PES at higher energies that are crucial for detailed understanding the chemical properties of the H_3O^+ ion. Molecular overtone spectroscopy is inherently a probe into those parts of molecular potential energy surfaces and thus it is capable provide critical information on the chemically relevant energy levels.

In this report we present first results in search of the H_3O^+ spectra in the first OH stretching overtone region. The experiments were made possible by use of a very high sensitivity spectroscopic technique based on time resolved cw cavity ringdown scheme coupled with AC microwave discharge absorption cell. Based on the time evolution of the absorption signals it is possible to distinguish the weak ionic absorptions from those of much stronger signals originating from the stable or metastable species in the gas mix.

The H_3O^+ ions are formed in microwave discharge in He/H_2O mixture at pressure of 5 mbar (see Fig. 1). The cw cavity ringdown spectrometer had been used in past for the time resolved absorption measurements of H_3^+, H_2D^+ and D_2H^+ ions using weak second overtone transitions (for details see [7,8,9,10]). The apparatus consists of the discharge tube with two highly reflective mirrors on each end of the tube, making up an optical cavity (see Fig. 1). To increase the sensitivity and to simplify the assignment of the observed absorption lines, synchronous detection scheme has been applied.

Results and discussion

The first OH stretching overtone region of H_3O^+ ion in NIR was scanned with CRD spectrometer in the region 6900 – 6960 cm^{-1} with approximately 80% coverage. An example of obtained spectra is plotted in Fig. 2. The upper line is the spectrum corresponding to the 'discharge ON' window and the lover line (slightly shifted downwards for clarity) is the spectrum obtained during the late afterglow ('discharge OFF'). It can be seen that indeed certain spectral lines are observed with virtually the same intensity both in the active discharge and in the late afterglow, indicating that they belong to stable species, while others exhibit vastly different intensities in the active discharge and afterglow, indicating they belong to discharge generated species. The details of the time evolution obtained at each laser wavelengths are used to distinguish in more detail between the stable (H_2O), the long-lived metastable species (such as the OH radical), and the short lived ionic species such as the H_3O^+.

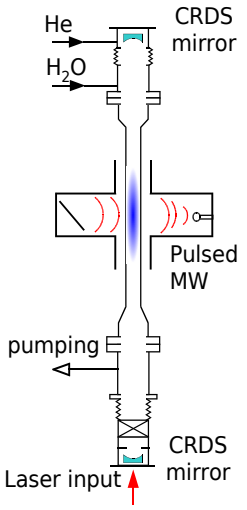

Fig. 1. The discharge tube with CRDS. The mirrors of the cavity are mounted inside the vacuum.

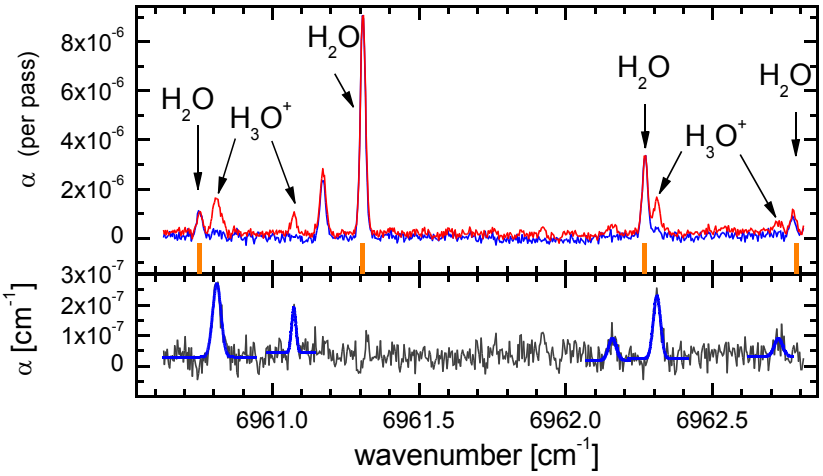

Fig. 2. The example of absorption spectra obtained by CRDS using synchronous detection. Upper panel shows the absorbance (the relative loss of light intensity per pass) in discharge and background time windows. For H_2O, the both curves are overlapping, in contrast to H_3O^+, which is populated during the discharge period only. Lower panel shows the absorbance spectrum with subtracted baseline.

Conclusions

The position of OH stretching overtone band of H_3O^+ ion has been estimated in the region 6900 – 6960 cm^{-1} using CRDS spectrometer. For higher sensitivity the concentration modulation technique have been used together with time resolved measurement. It was demonstrated, that this technique is essential in this kind of experiments to distinguish the short-lived H_3O^+ from metastable radicals (OH) and stable molecules (H_2O). The assignment of H_3O^+ lines is in progress.

Acknowledgments: This work is a part of the research plan MSM 0021620834 that are financed by the Ministry of Education of the Czech Republic and partly was supported GACR (205/05/0390, 202/05/P095) and GAUK-278/2004 /B-FYZ/MFF.

References

[1] M. H. Begemann, C. S. Gudeman, J. Pfaff, R. J. Saykally, *Phys. Rev. Lett.* **51** (1983) 554.
[2] D. Uy, E. T. White, T. Oka, *J. Mol. Spectr.* **183** (1997) 240.
[3] V. Spirko and W. P. Kraemer, *J. Mol. Spectr.* **134** (1989) 72.
[4] J. Tang and T. Oka, *J. Mol. Spectr.* **196** (1999) 120.
[5] T. Rajamaki, A. Miani, L. Halonen, *J. Chem. Phys.* **118** (2003) 10929.
[6] X. Huang, S. Carter, J. M. Bowman, J. Phys. Chem. B **106** (2002) 8182.
[7] P. Macko, G. Bánó, P. Hlavenka, R. Plašil, V. Poterya, A. Pysanenko, O. Votava, R. Johnsen, J. Glosík, *Int. J. Mass Spectrom.* **233 1-3** (2004) 299.
[8] P. Hlavenka, R. Plašil, G. Bánó, I. Korolov, D. Gerlich, J. Ramanlal, J. Tennyson, J. Glosík, *Int. J. Mass Spectom.* **255-256** (2006) 170.
[9] P. Hlavenka, I. Korolov, R. Plašil, J. Varju, T. Kotrík, J. Glosík, *Czech. J. Phys.* **56 Suppl. B** (2006) 749.
[10] R. Plašil, P. Hlavenka, P. Macko, G. Bánó, A. Pysanenko, J. Glosík, *Journal of Physics: Conference Series* **4** (2005) 118.

Temporary Anion States and Dissociative Electron Attachment to Nitrobenzene Derivatives

S. A. Pshenichnyuk[1], I. A. Pshenichnyuk[1], V. G. Lukin[1], A. Modelli[2], Š. Matejčk[3],N. L. Asfandiarov[1]

[1]Institute of Physics of Molecules and Crystals, Ufa Research Center of RAS, October Prospect, 151, Ufa 450075, Russia,

[2]Dipartimento di Chimica "G. Ciamician", Università di Bologna, Via Selmi 2, 40126 Bologna, Italy

[3]Department of Experimental Physics, Comenius University, Mlynska dolina F2, 84248 Bratislava, Slovak Republik

e-mail: nail@anrb.ru

The nitrobenzene derivatives 1,2-nitrotoluene; 1,3-nitrotoluene; 1,2-fluoronitrobenzene; 1,3-fluoronitrobenzene; 1,4-fluoronitrobenzene; 1,2-chloronitrobenzene; 1,3-chloronitrobenzene; and 1,4-chloronitrobenzene, are investigated by means of Electron Transmission Spectroscopy (ETS), Dissociative Electron Attachment Spectroscopy (DEAS), and Negative Ion Mass Spectrometry (NIMS). The observed vertical electron attachment energies (VAEs) to π* MOs are satisfactorily reproduced by scaling with empirical linear equations the corresponding virtual orbital energies (VOEs) supplied by HF/6-31G and B3LYP/6-31G* calculations for the neutral molecules. In the chloro derivatives three main negative ion (NI) species (long-lived M^-, Cl^-, and NO_2^-) are observed, M^- and NO_2^- being the dominant NIs in the other investigated compounds. The detection of metastable NIs corresponding to the process $M^{*-} \rightarrow R^- + (M\text{-}R)^{\cdot}$ suggests that the molecular NIs formed near thermal electron energies dissociate on a microsecond time-scale. The breakdown curves as a function of electron energy and the mean autodetachment lifetimes of the molecular NI are also estimated.

Typical ETS, DEAS and NIMS results for 1,3-chloronitrobenzene are present in the Figure. The ET spectrum is displayed in the upper left panel. The VAEs obtained from the HF/6-31G VOEs are also represented as vertical lines above the spectrum. The middle left panel shows the high resolution DEA spectrum. The peak of the M^- current is observed at thermal electron energy in all compounds under investigation. There is a close energy correspondence between the π^*_3 temporary negative ion (TNI) state observed in ET spectra at ~1 eV and the maxima of the Cl^- and NO_2^- currents in high resolution DEA spectra, although these dissociation channels are forbidden by symmetry reasons in the equilibrium geometry of the neutral molecules. Also the core excited TNI state observed at ~3.6 eV in ET spectra has a counterpart in the DEA spectra. Similar correlations have been noted in a previous ETS and DEAS study of nitrobenzene. So, interpretation of the ET spectra gives insight into the localization properties of the temporary anion states leading to anion dissociation. The bottom left panel reports the low resolution NIMS spectrum. The differences between the high and low resolution DEA results arise from three main factors: i) different energy resolutions of the incident electron beams; ii) different time scales; and iii) different temperatures. The high resolution DEA spectrometer provides a more correct profile of the DEA cross section as a function of incident electron energy. In addition to the dissociation processes detected in high resolution DEAS (Cl^-, and NO_2^-) many low-intensity dissociation channels leading to deep fragmentation of the parent anion, including ring cleavage and rearrangement processes, are observed with the more sensitive low-resolution DEA apparatus. These low-intensity rearrangement processes indicate that a significant part of internal degrees of freedom of the anion are excited and play a role in sharing the anion excess energy. So-called metastable (with respect to *dissociation*) anions have also been detected. In the present molecules, formation of the Cl^- and NO_2^- fragment anions at low energies is extremely slow with respect to nuclear motion. It is thus possible to describe these processes in the framework of a statistical approximation. The results of theoretical calculations of $\ln(R^-/M^-)$ as a function of incident electron energy are shown in the upper right panel. The middle right panel shows the logarithm of these ratios obtained from the high resolution experiment, in qualitative agreement with calculations. The bottom right panel represents the energy dependence of the molecular NI lifetime.

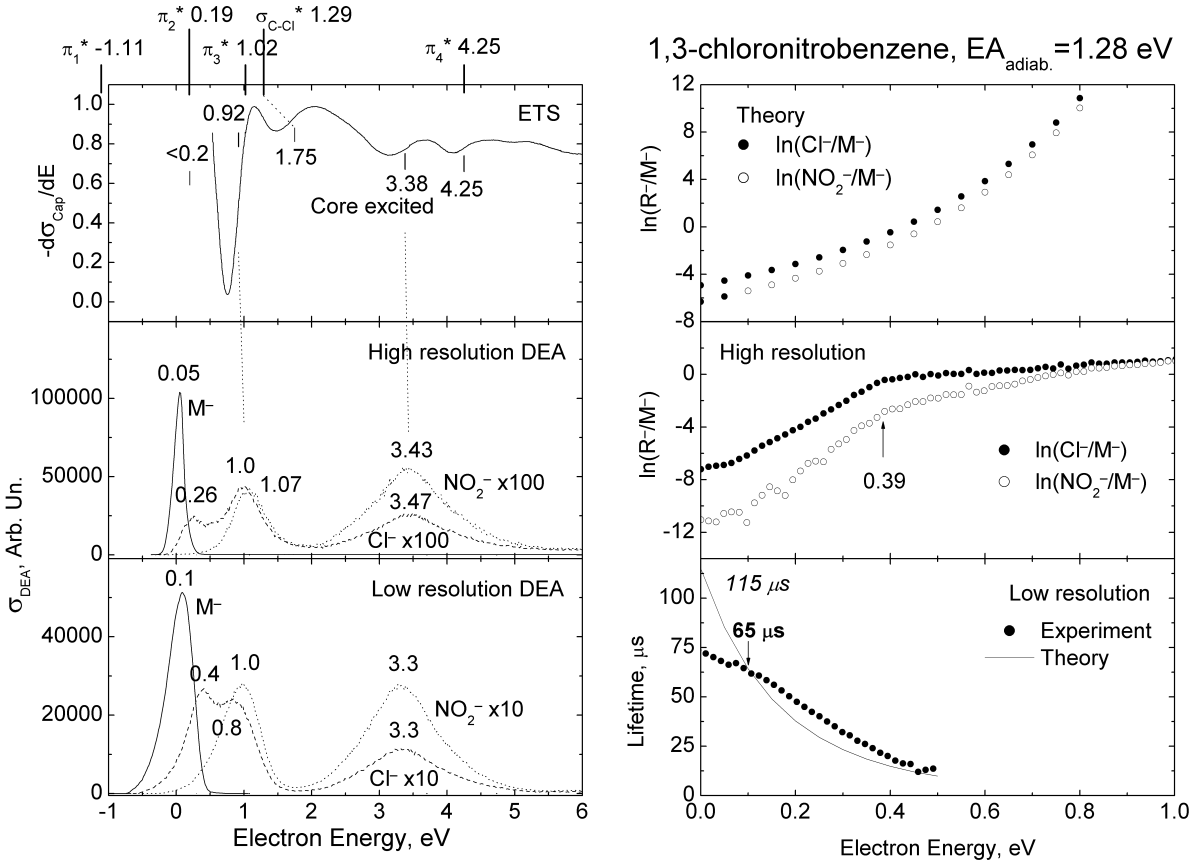

Figure. Left column: ET spectrum, high- and low-resolution DEA spectra of 1,3-chloronitrobenzene. Right column: theoretical and experimental ln(R^-/M^-), experimental and theoretical molecular NI lifetime as a function of electron energy.

Conclusions

A series of nitrobenzene derivatives are investigated using the ETS, DEAS, and NIMS techniques. The ET spectra are interpreted using quantum chemical calculations at the HF/6-31G and B3LYP/6-31G* levels. Correlations are found between VAEs measured in ETS and NIs peaks in DEA cross section. Competition between autodetachment and dissociation controls the DEA cross section. Metastabe anions associated with Cl^- and NO_2^- production indicate that these dissociation channels take place on a microsecond time-scale in the low (0-0.5 eV) electron energy range. Analysis of the decay curves and comparison with model kinetic calculations suggest that in 1,3-, 1-4-fluoronitrobenznes and the chloronitrobenzenes dissociation of the π_2^* anion occurs through the ground electronic state.

Acknowledgements

This work was partially supported by Russian Foundation for Basic Research, Grant No. 06-03-32059-a and by Slovak Science and Technology Assistance Agency under the contract No. APVT-20-007504.

DNA Damage by Low Energy Electrons: Dissociative Electron Attachment to Gas Phase Biomolecules

I. Bald, J. Kopyra, C. König, I. Dąbkowska and E. Illenberger

Institut für Chemie und Biochemie Physikalische und Theoretische Chemie Freie Universität Berlin Takustrasse 3, D-14195 Berlin, Germany.

e-mail: ibald@zedat.fu-berlin.de

After deposition of living cells to ionising radiation low energy electrons (LEE, < 20 eV) are produced along the radiation track in great quantities. Temporary negative ion states generated by low energy electron attachment are hence believed to be precursor states of DNA strand breaks. Dissociative electron attachment (DEA) is an appropriate mechanism to describe the resonant features in fragmentation yield curves observed in experiments using plasmid DNA [1] and shorter oligonucleotides [2]. It is, however, not clear where the extra charge is initially localized and if charge transfer to the phosphate unit is an important process.

In this progress report we present a study of dissociative electron attachment to different gas phase building blocks of DNA and RNA. This includes the RNA sugar D-ribose and its isotope labeled analogues, phosphate esters but also more complex model systems. We found that, in addition to nucleobases, both the sugar unit and the phosphate group are efficiently decomposed by electrons with energies in the range 0-11 eV.

Dibutylphosphate ($(C_4H_9O)_2PO(OH)$, DBP) was used as a model compound for the phosphate group in DNA that is bound to two sugar units [3]. Besides a strong abundance of the $(DBP-H)^-$ ion at 1 eV we observed different fragments that are associated with P-O and C-O bond breaking. A single butyl group is excised creating the negative ion $(DBP-C_4H_9)^-$ in the energy regions 2-4 eV and 7-9 eV that directly corresponds to a single strand break in DNA.

In D-ribose we found effective abstraction of neutral water molecules and selective excision of neutral C5 containing fragments very close to 0 eV, i.e. a decomposition of the ring system with the negative charge remaining on the C1 fragment [4]. As an improved model system we investigated peracetylated ribose [5] as this molecule possesses a five membered ring structure and no free hydroxy groups. The phosphate groups and the nucleobase are mimicked by acetyl groups as CH_3COO possesses a similar electron affinity like the PO_3 and (Thymine-H) radicals, respectively.

Furthermore a new approach is presented to study dissociative electron attachment to larger building blocks of DNA in the gas phase like whole nucleotides. For this purpose an electron gun and quadrupole mass spectrometer is combined with a laser desorption source. The new system will be described and first measurements will be discussed.

[1] F. Martin, P. D. Burrow, Z. Cai, P. Cloutier, D. Hunting, and L. Sanche, Phys. Rev. Lett. 93 (2004) 068101.
[2] Y. Zheng, J. R. Wagner, and L. Sanche, Phys. Rev. Lett. 96 (2006) 208101.
[3] C. König, J. Kopyra, I. Bald and E. Illenberger, Phys. Rev. Lett. 97 (2006) 018105.
[4] I. Bald, J. Kopyra, and E. Illenberger, Angew. Chem. Int. Ed. 45 (2006) 4851.
[5] Ilko Bald, Janina Kopyra, Iwona Dąbkowska, Egill Antonsson and Eugen Illenberger, submitted.

Resonant Excitation of Multi-Frequency Nonlinear Oscillations

V. Yu. Novokshenov

Institute of Mathematics, Ufa Science Center RAS

e-mail: novokshenov@yahoo.com

The oscillating frequency of a nonlinear, Duffing-like oscillator changes with amplitude. If you excite such an oscillator by driving it at its linear frequency, the oscillator's amplitude will grow only marginally before its shifting frequency causes it to go out of phase with the drive, after which the oscillator's amplitude will beat back down to zero. By measuring the oscillator's instantenuous frequency and phase, you could use feedback to grow the oscillator's amplitude arbitrarily. But how can you grow the oscillator to high amplitude without feedback?

A general property of weakly driven, nonlinear oscillator is that, under certain conditions, they *automatically* stay in resonance with their drives even if the parameters of the system vary in time and/or space. This phenomenon is called autoresonance. For example, consider an oscillator whose frequency increases with the amplitude. Assume that the oscillator is initially locked to its drive. In autoresonance, sweeping the drive frequency upwards or downwards will cause corresponding increase or decrease of the oscillation amplitude, so that the nonlinear frequency just matches the drive frequency (see [1], [2]).

A number of applications in physics and technology has been known since 1930-s, exploiting autoresonant effect. The most famous are autogenerators of radio frequency and cyclotron acceleration of relativistic particles [1]. In recent time more applications has been found in astronomy and plasma physics [2].

One can easily see a resemblance of the phase locking effect in autoresonant oscillator with adiabatic deformations of completely integrable Hamiltonian systems. The KAM-theory proves this deformation to conserve the motion over Lioville tori of the system for almost all initial data. The Lioville tori, in its turn, are governed by the first integrals, which depend now on a slow variable $\tau = \varepsilon t$. An analytic desciption of the motion is done by the well-known Kuzmak-Whitham (or Bogolyubov-Mitropolskii) method [3]. Here the phase shifts of the quasi-periodic oscillations are strongly matched to the driving frequences, while the first integral's evolution is controlled by an averages of the driving force over basic periods. The latter is done through the solutions of the Whitham equations, which provide elimination of the "secular" terms for the higher-order approximations (see [4]).

Note that for a Hamiltonian system reduced to canonical action-angle variables $(I,\phi) = (I_1,...,I_n,\phi_1,...,\phi_n)$,

$$\begin{cases} \dot{I} = \varepsilon f(I,\phi,\varepsilon), \\ \dot{\phi} = \phi_0 + \varepsilon g(I,\phi,\varepsilon), \end{cases} \tag{1}$$

this procedure is equivalent to classical multi-phase averaging method, ascending to H.Poincaré.

Apply now multi-phase averaging for integrable systems in a reverse way, namely, for some given deformation of n-periodic solution find small driving force, implementing the deformation. More precisely, assume some deformation of the action-angle variables, which transforms initial n-periodic motion to a given m-periodic motion during finite slow time interval ($t: \ O(\varepsilon^{-1})$). In general, this will cause the drive not to be small, moreover the Hamiltonian structure will fail. To avoid this, restrict the class of deformations to those satisfying Whitham equations. Now the resulting driving force appears to be small and is explicitely controlled by boundary conditions for the Whitham equations. An auxiliary constraints on the angle variables demonstrate specific autoresonant features – the phase locking and synchronization with driving force frequences.

Note that the procedure is essentially multi-phase, which was not known for physically interesting systems. For example, it is possible to drive in adiabatic way a top-like oscillator from a stable state to some given n-periodic rotation [5].

The finite-gap integration theory provides a unified approach to the linearization of the phase flow and is based on the Lax form of the equations of motion:

$$\frac{dL(\lambda)}{dt}+[L(\lambda),A(\lambda)]=0, \qquad (2)$$

where $L,A,\Psi=\cdot(\lambda,I,\phi)$ are $l\times l$ matrices, polynomial in λ. Equation (2) provides an unperturbed system (0.1), e.g., $\dot I=0,\ \dot\phi=\phi_0$. As soon as the Lax representation is found, one should construct the Ψ -function, also called the Baker-Akhiezer function, which is a solution of the linear system,

$$L(\lambda)\Psi=\mu\Psi,$$
$$\frac{d\Psi}{dt}=A(\lambda)\Psi.$$

This function can be found from its analytic properties implied by the form of the matrices L and A constituting the Lax pair. The Ψ -function is constructed explicitly in terms of theta functions of the Riemann surface Γ determined by the equation $\det(L(\lambda)-\mu I)=0$. This yields explicit formulas for the dynamical variables of the original nonlinear system. The language of the Ψ -function is well suited for the perturbation theory of equation (1) with respect to an additional parameter. Note that the original version of the finite-gap integration method implied this very kind of construction: if x is the deformation parameter, then the right-hand side of equation (2) is equal to $\partial_x A$ and equation (2) takes the form $\Psi_x=L(\lambda)\Psi$. In this case the Ψ -function remains qualitatively unchanged, because the winding vector $tV+D$ in the argument of the corresponding theta function is merely replaced by $tV+xU+D$. This fact makes it possible to consider small deformations of equation (2) that destroy neither its Liouville torus $\mathrm{Jac}(\Gamma)$ nor the quasi-periodic winding on $\mathrm{Jac}(\Gamma)$. In the following we construct a class of right-hand sides for (2) of the form of $\varepsilon F(A,L),\ \ \varepsilon<1$, such that the quasi-periodic winding on the deformed torus $\mathrm{Jac}(\Gamma)$ fills it without "gaps" and the deformation of the torus progresses smoothly at a rate of $O(\varepsilon)$. Since the Jacobian of the surface Γ and the curve itself are determined by the branch points λ_k , which are the zeros of $\det(L(\lambda)-\mu I)$, it is convenient to describe the deformation in terms of λ_k. It turns out that the dynamics of $\lambda_k=\lambda_k(\tau),\tau=\varepsilon t$, is determined by the Whitham equations (see [4]), and that under quite general conditions on the zeros λ_k (e.g., for real λ_k) it can be proved that

$$\Gamma(\tau)\,|_{\tau=\tau^+}=\Gamma_+,\qquad \Gamma(\tau)\,|_{\tau=\tau^-}=\Gamma_-,$$

where Γ_+ and Γ_- are some given surfaces of the same genus. Then the leading term of asymptotics of Ψ is given explicitly by the similar formula as for unperturbed case with respect to the “moving" surface $\Gamma(\tau)$ (see [5]).

[1] Veksler V., JETP v.9 (1946) 143
[2] Friedland L., Shagalov A.G., Phys.Rev. Lett., **90**, (2003) 1123
[3] Whitham J., Linear and Nonlinear Waves, Academic Press, New York, 1965.
[4] Kuksin S.B., *Amer. Math. Soc. Transl. (***2***),* (2004) 237
[5] Novokshenov V.Yu., Theor.Math.Phys., (2007) (to appear)

Tribological Properties and Characterization of the Nanostructured Carbon Thin Films Deposited by Thermionic Vacuum Arc Technology

R. Vladoiu[1], V. Ciupina[1], C. Surdu-Bob[2], C. P. Lungu[2], J. D. Skalny[4], V. Bursikova[5], J. Bursik[6], G. Musa[1]

[1]Department of Physics, Ovidius University, Constanta, Romania,
[2]National Institute of Plasma Physics and Laser Radiation, Bucharest-Magurele, Romania
[3]Department of Plasma Physics, FMPI, Comenius University, Bratislava, Slovak Republic
[4]Deparment of Physics, Masaryk University, Brno, Czech Republic
[5]Institute of Physics of Materials, Academy of Sciences of the Czech republic, Brno, Czech republic
e-mail: rvladoiu@univ-ovidius.ro

Introduction

The amorphous carbon thin films have a widespread application in areas as: nanoelectronics, novel optical devices, integrated digital circuits, protective coatings. A great interest of the researchers is devoted to possible applications as protective coatings of amorphous carbon in order to improve the mechanical properties like: hardness, fracture toughness, elastic modulus and resistance against indentation. [1-3]

The aim of the present paper is to investigate the properties of the Diamond Like Carbon (DLC) film condensation from the carbon plasma generated by Thermionic Vacuum Arc (TVA) method. The substrate materials used for deposition by Thermionic Vacuum Arc were: glass and Silicon.

Experimental arrangement

Thermionic Vacuum Arc (TVA) is an externally heated cathode arc, which can be established, in high vacuum conditions, in vapors of the anode material. Thermionic Vacuum Arc is ignited between a heated cathode surrounded by an electron-focusing Wehnelt cylinder and an anode, in our case a carbon rod which would be deposited. [4,5] The carbon film is bombarded during its deposition by energetic carbon ions with established value of directed energy. Because this system can heat at elevated temperature any material, it is one of the most adequate technologies for the deposition of refractory metals with high melting points (over 3000 K).The pressure for arc discharge inside of the vacuum vessel was maintained around 10^{-6} mbar.

The indentation tests were performed using the Fischerscope H100 DSI tester equipped with Vickers indenter. The applied load L ranges from 0.4mN to 1N and the accuracy of the depth measurement is of about ±1nm.The SEM images were made using a JEOL JSM 6460 apparatus with an accelerating voltage of 20kV.

Results and Discussions

A number of increasing loads ranging from 1 to 1000 mN were applied to each sample to obtain the hardness and elastic modulus as a functions of load and indentation depth (See Figures 1 and 2.) This enabled us to study the influence of the substrate on the measured material parameters. The loading time was 20 s. The maximum load was kept constant 5s. The subsequent unloading part lasted 20 s. Each indentation test was repeated at least nine times, the results of the hardness and elastic modulus were averaged calculated and the 95% confidence level was determined. In case of the indentation testing of thin films, the measured properties depend on the indentation depth due to combined response of the coating and the substrate. The thickness of studied films was too low to obtain the so-called critical indentation depth, where the substrate influence may be neglected. Therefore, the measured elastic modulus and hardness values were corrected for the substrate influence.

The combined effect of the film and substrate on the measured values of composite hardness H_c was modelled according to Battacharya and Nix [4] by

$$H_c = H_s + (H_f - H_s)\exp\left[-\alpha_n\left(\frac{h}{t}\right)^n\right] \quad (1)$$

where h is the indentation depth and t is the film thickness, α_n, and n are fitting parameters. The film hardness is marked with suffix f and the substrate hardness is marked with suffix s. The calculated film hardness H_f was 13.4±0.4 GPa for film H31 and 11.5±0.5 GPa for film H30. The obtained hardness values indicate suitable values for data storage applications.

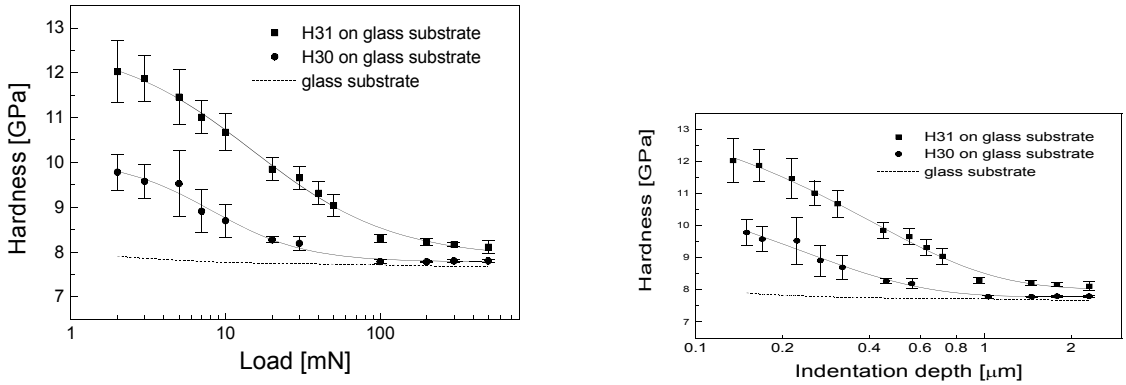

Fig.1. The composite hardness of the film-substrate systems (H31 on glass, H30 on glass) and the hardness of the glass substrate as a function of the load (left) and of the indentation depth (right).

Both films exhibited indentation induced delamination at higher loads (~500mN). The relationship (1) does not take the influence of the fracture into account, so the experimental data were fitted only up to 500 mN, where the interfacial fracture and delamination begun.

Conclusions

Amorphous diamond-like carbon films were deposited on glass and single crystal silicon substrates using thermionic vacuum arc method. Mechanichal tests, TEM and SEM investigation of the film surface after nanoindentation test were used for characterization of the amorphous carbon thin films. The hardness of the deposited films was found in the range from 10 to 14 GPa and the elastic modulus was found in the range from 100 to 125 GPa The operating parameters such as the arc current, the intensity of the heating current of the filament, the applied voltage and the sample-anode distance were higher in case of the film H31 than in case of film H30. Film H31 showed higher hardness and elastic modulus, than film H30, however its adhesion especially to silicon substrate was worse than in case of film H30. Nanometer-sized diamond crystallites were found on all samples, with high sp^3 content and relatively low growth stress. The results show that TVA has been proved to be a very suitable method for the preparation of diamond like nanostructured coatings, as well as other types of coatings.

References

[1]. J. Robertson, *Mater. Sci. and Engineering*, R 37 (2002) 129-181
[2]. S.Aisemberg, R. Chabot, *J.Appl. Phys*.42 (1971) 2953
[3] Y. Lifshitz, *Diamond and Relat. Mater.*,8 (1999) , 1659-1676
[4]. A. K. Battacharya, W. D. Nix, Int. J. Solids Struct. 38 (2001) 335.

Transition to Chaos by a Cascade of Period-Doubling Bifurcations in Plasma

D. G. Dimitriu[1], M. Aflori[2], L. M. Ivan[1], C. Ionita[3], R. Schrittwieser[3]

[1]Faculty of Physics, "Al. I. Cuza" University, 11 Carol I Blvd., Iasi 700506, Romania
[2]Romanian Academy, "Petru Poni" Institute of Macromolecular Chemistry, Aleea Gr. Ghica Voda 41A, Iasi 700487, Romania
[3]Institute of Ion Physics and Applied Physics, Leopold-Franzens University, Innsbruck 6020, Austria
e-mail: dimitriu@uaic.ro

Abstract

Experimental results are presented on the transition to chaos of a plasma conductor by a cascade of period-doubling bifurcations (Feigenbaum scenario), related to the complex nonlinear dynamics of a multiple double layer structure.

Introduction

Multiple double layers are complex nonlinear potential structures in plasma consisting of two or more concentric double layers attached to the anode of a glow discharge [1,2] or to a positively biased electrode immersed into plasma [3]. The axial profile of the plasma potential has a stair step shape, with potential jumps close to the ionization potential of the used gas. At high values of the voltage applied to the electrode the multiple double layer structure evolves into a dynamic state, consisting of periodic disruptions and re-aggregations of the constituent double layers.

Here we present experimental results which show that the plasma conductor passes into a chaotic state through a cascade of period-doubling bifurcations (Feigenbaum scenario [4]) when the voltage on the electrode increases.

Results and discussion

The experiments were performed in a hot filament discharge plasma diode. The plasma was pulled away from equilibrium by gradually increasing the voltage applied to an electrode, under the following experimental conditions: argon pressure $p = 5 \times 10^{-3}$ mbar, plasma density $n_{pl} \approx 10^8$-10^9 cm^{-3}. When the voltage on the electrode with respect to ground reaches $V_E \approx 180$ V, a multiple double layer structure consisting of 8 luminous plasma shells appears in front of the electrode. By a further increase of the voltage on the electrode, the current collected by it becomes time dependent (Fig. 1a-c). These oscillations appear because the multiple double layer structure passes into dynamic state. The constituent double layers pass into dynamic state one by one, starting with the innermost one because the current density is hoghest through it. When the second double layer starts its own dynamics, a period-doubling bifurcation is observed (Fig. 1d-f). By further increasing the electrode voltage, a cascade of period-doubling bifurcations appear (Fig. 1g-o), simultaneously with the transition of each double layer into a dynamic state. Finally, the plasma system passes into a chaotic state (Fig. 1p-r), determined by the uncorrelation between the individual dynamics of the constituent double layers.

Conclusions

Experimental results are presented emphasizing the Feigenbaum scenario of transition to chaos by a cascade of period-doubling bifurcations in plasma, related to the nonlinear dynamics of a multiple double layer structure.

Acknowledgments

This work was supported in part by the Leopold-Franzens University of Innsbruck and the Romanian Ministry of Education – National Authority for Scientific Research, under the excellence grant cod ET 69.

References

[1] L. Conde, L. Leon, *Phys. Plasmas*, 1 (1994) 2441.
[2] O.A. Nerushev *et al.*, *Phys. Rev. E*, 58 (1998) 4897.
[3] C. Ionita, D.G. Dimitriu, R. Schrittwieser, *Int. J. Mass Spectrom.*, 233 (2004) 343.
[4] M.J. Feigenbaum, *Los Alamos Science*, 1 (1980) 4.

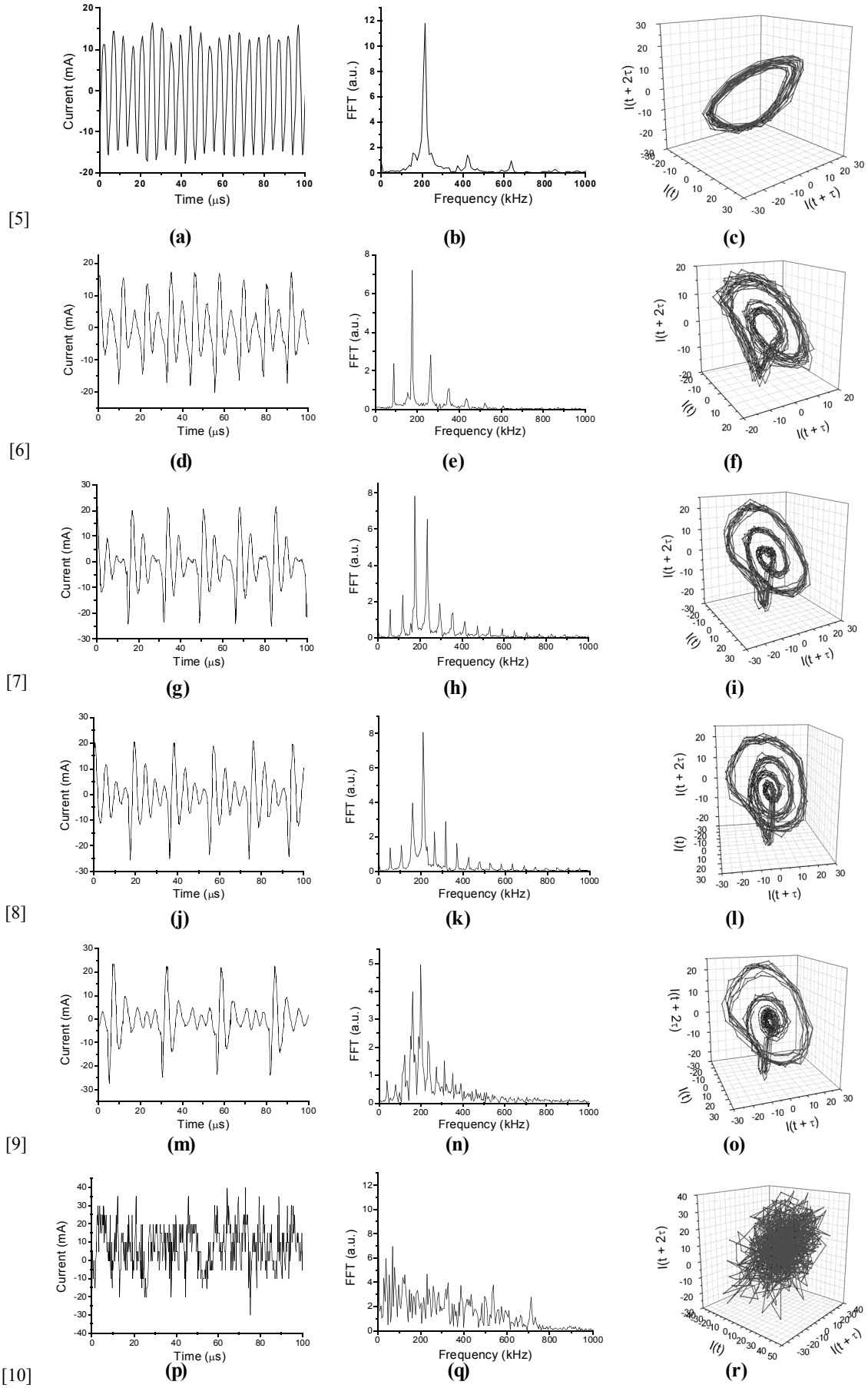

[5]

[6]

[7]

[8]

[9]

[10]

Fig.1: Oscillations of the current (first column), their FFT's (second column) and the reconstructed attractor of the plasma system dynamics (third column), at different increasing values of the voltage applied to the electrode

Hard X-ray Generation and Particle Acceleration in Short-Pulse Laser Target Interactions

J. Limpouch

Czech Technical University in Prague, Faculty of Nuclear Sciences and Physical Engineering, Břehová 7, 115 19 Praha 1, Czech Republic
e-mail: limpouch@ishtar.fjfi.cvut.cz

Abstract

Short introduction into the interaction physics of high-power femtosecond lasers with targets is presented. Generation is revealed of subpicosecond hard X-ray pulses that can be used for ultrafast X-ray diffraction measurements. Electron and ion acceleration mechanisms are reviewed and the possible construction of table-top particle accelerators is discussed. Our novel particle-in-cell (PIC) simulation results of laser-target interactions are presented.

Introduction

The advent of chirped pulse amplification (CPA) of ultrashort laser pulses in 1985 opened path to an unprecedented boom in research of interaction of intense laser radiation with matter. Presently, table-top lasers in ordinary university laboratories reach relativistic intensities with repetition rates from 10 Hz up 1 kHz while several PW high energy lasers are operated or being completed in large national laboratories. Several multi-PW lasers are under construction or in preparation and the construction of EW laser is proposed. There are lots of demonstrated and potential applications of femtosecond laser interactions. However, we shall concentrate here only on generation of short pulses of hard X-rays for ultrafast X-ray crystallography and on acceleration of charged particles.

Physics of laser-target interaction

Energy of femtosecond laser is basically transferred to energetic electrons via collisionless absorption. The basic electron acceleration mechanism for non-relativistic intensities is resonance absorption of p-polarized obliquely incident wave when the electric field component parallel to the density gradient skinning from the reflection surface resonantly excites plasma wave at the critical surface. In case of a very high contrast of laser pulse, the density scale length L is extremely short and resonance absorption transforms to so called "vacuum heating", when electron is accelerated into vacuum in one laser half-period and it is returned into the target in the second laser half-period, it transits extremely narrow skin layer without any deceleration and it carries off a part of laser energy to the target interior. At relativistic intensities, electrons are accelerated into the target by $\vec{v}\times\vec{B}$ force even for normal incidence. Very high current of fast electrons flying into the target has to be neutralized by return current of thermal electrons. Extremely high magnetic fields up to ~100 MG may be generated due to the curl of the ambipolar electric field.

Generation of ultra-short hard X-ray pulses

When electrons accelerated at the surface propagate into the dense target, they produce vacancies in the K-shell of the target atoms. The vacancy is filled in less than 10 fs and either Auger electron or characteristic photon is released. K-α emission is produced when the vacancy is filled by an L-shell electron. Only K-α photons generated in the target surface layer of thickness less than 100 μm may escape out of the target, and the pulse duration is determined by the fast electron transit through this target surface layer. Consequently, ultrashort K-α pulses are emitted. It is a non-coherent line emission and high ($>10^{-4}$) conversion efficiencies of laser energy into K-α pulse may be achieved. Using pulse-probe set-up, X-ray diffraction techniques with subpicosecond temporal resolution have been demonstrated. The best ever time resolution of 250 fs was reached in diffraction measurements of ultrafast melting [1]. When laser with 1 kHz repetition rate is used, even subtle reversible changes on the crystal surface may be detected with subpicosecond and micron resolution [2].

Our simulations use relativistic one-dimensional PIC code with all three velocity components (1D3V) for modeling of laser-plasma interaction at the target surface and 3D time resolved Monte Carlo code tracks the propagation of fast electrons into the target and K-α photon emission. We have shown [3] that the shortest X-ray pulse may be only about 60 fs longer than the laser pulse and that moderate laser intensities of order $10^{16} – 10^{17}$ W/cm^2 are optimal for the generation of ultrashort K-α pulses. The impact of ionization processes on K-α emission is studied here using our novel 1D3V PIC code [4] including optical field and collisional

ionization, and elastic collisions. It is shown that the experimental results in MBI Berlin where K-α emission from copper foils irradiated by 5 mJ 45 fs laser pulses was measured [5], may be explained only when pre-plasma formation by amplified spontaneous emission, and ionization processes are taken into account.

Electron acceleration

Gas jet is usually used to produce long underdense plasma for electron acceleration. Recently, high quality quasi-monoenergetic 200 MeV electron beams were produced [6] by bubble acceleration mechanism. Our numerical simulations of electron acceleration by a laser beam with a central intensity minimum are presented.

Ion acceleration

The most important scheme is the target normal sheath acceleration (TNSA) when hot electrons accelerated by the laser at the front side into a thin foil escape out of the target rear side and they form there a strong electrostatic sheath that accelerates ions in the direction normal to the target surface. Unless special precautions are taken, the accelerated ions are protons as they have the best q/m ratio and they are present in contaminations at the target surface. The accelerated ion beam has usually a very high current and excellent angular characteristics, but the effort to achieve monoenergetic ion beams has been successful only very recently [7, 8].

The interaction of low-energy intense laser beams with massive targets is not very efficient as the energy delivered to the charged particles spreads out quickly over large distances and it is redistributed among many secondary particles. One possibility to limit this undesirable energy spread is to use so called mass-limited targets (MLT) [9], for example droplets, big clusters and small foil sections with the transverse target dimensions comparable to the focal spot diameter. The results of our newly developed two-dimensional (2D3V) relativistic PIC code [10] are presented and a significant increase in the energy of accelerated ions for an infinite cylindrical wire (2D model of a droplet) compared to a foil of the same thickness is demonstrated. The difference in the formed sheath for material with two ion species (water droplet – H^+, O^{6+}) compared with pure hydrogen target is shown. We search here for a suitable regime when monoenergetic ion beam is formed using a target material with two ion species.

Conclusions

Applications of high-power femtosecond laser pulses for hard X-ray generation and particle acceleration are reviewed and results of our numerical simulations are presented.

References

[1] T. Feurer, A. Morak, I. Uschmann, Ch. Ziener, H. Schwoerer, E. Förster, R. Sauerbrey, *Appl. Phys. B*, 72 (2001) 15.

[2] M. Bargheer, N. Zhavoronkov, Y. Gritsai, J.C. Woo, D.S. Kim, M. Woerner, T. Elsaesser, *Science*, 306 (2004) 1771.

[3] J. Limpouch, O. Klimo, V. Bína, S. Kawata, *Laser & Particle Beams*, 22 (2004) 147.

[4] O. Klimo, J. Limpouch, *33rd EPS Conference on Plasma Phys. Rome, 19-23 June 2006*, *European Conference Abstracts*, 30I (2006) P-5.023.

[5] N. Zhavoronkov, Y. Gritsai, M. Bargheer, M. Woerner, T. Elsaesser, F. Zamponi, I. Uschmann, E. Förster, *Opt. Lett.*, 30 (2005) 1737.

[6] J. Faure, Y. Glinec, A. Pukhov, S. Kiselev, S. Gordienko, E. Lefebvre, J.-P. Rousseau, F. Burgy, V. Malka, *Nature*, 431 (2004) 541.

[7] B.M. Hegelich, B.J. Albright, J. Cobble, K. Flippo, S. Letzring, M. Paffett, H. Ruhl, J. Schreiber, R.K. Schulze, J. C. Fernández, *Nature*, 439 (2006), 441.

[8] H. Schwoerer, S. Pfotenhauer, O. Jäckel, K.-U. Amthor, B. Liesfeld, W. Ziegler, R. Sauerbrey, K.W.D. Ledingham, T. Esirkepov, *Nature*, 439 (2006), 445.

[9] M. Schnurer, S. Ter-Avetisyan, S. Busch, E. Risse, M.P. Kalachnikov, W. Sandner, P.V. Nickles, Laser & Particle Beams 23 (2005), 337.

[10] J. Pšikal, J. Limpouch, S. Kawata, A.A. Andreev, *Cz. J. Phys.*, 56 (2006) B515.

Nano-Crystalline Diamond Coatings - a Basic Technology for Various Applications

H. Drexel, H. Sternschulte, G. Denifl, D. Steinmüller, D. Steinmüller-Nethl
rho-BeSt coating GmbH, Exlgasse 20a, 6020 Innsbruck, Austria, www.rhobest.com

Abstract

Nano-crystalline diamond (NCD) and ultra-nano-crystalline diamond (UNCD) films offer the same outstanding physical properties as natural diamond and hence provide a tremendous rich field of new applications. Additionally the nano-structure enhances the surface-to-volume ratio drastically and surface properties can be improved and tailored to meet the demands of applications. Since 1994 rho-BeSt coating developed and improved a technology to produce ultranano-crystalline diamond film (grain sizes 5 – 15 nm, thickness: 100nm – 100μm)) with high quality on silicon, tungsten carbide, glass, quartz, titanium, sapphire etc.. The nano-structured surface exhibits a large amount of surface atoms leading to interesting surface properties in addition to the intrinsic diamond properties. rho-BeSt diamond technology opens a world of intriguing possibilities for applications in biotechnology and electronics. UNCD is a bio-active material with a surface that can be engineered to carry different and very specific (bio-)chemical functionalities. The combination of these properties renders diamond a favourite candidate for bio-sensing applications. Three examples of use demonstrating the high potential of such carbon nano-material will be presented:

Introduction

Diamond is a unique material with extraordinary physical and chemical properties like

properties	diamond	comments
Chemical reactivity	**extremely low**	
Melting point [°C]	3800°C	Si: 1413°C; GaAs: 1238°C
Hardness [kg*mm^{-2}]	10000	cBN: 4500; SiC: 4000
Thermal Conductivity [Wcm^{-1}K^{-1}]	**20**	Ag: 4.3; Cu: 4.0; BeO: 2.2
Tensile Strength [psi]	0.5*10^{6}	14*10^{6} (theoretical)
Compressive Strength [psi]	14*106	80*10^{6} (theoretical)
Thermal Expansion Coeff. [°K]	0.8*10^{-6} (300K)	SiO_2: 0.5*10^{-6}
Refractive Index	2.41@590nm	Glass 1.4-1.8
Transitivity	**225 nm - far IR**	Widest known
Coeff. of Friction	0.05 (dry)	Teflon: 0.05
Electrical Resistivity [Ωcm]	1*10^{16} (natural)	AlN: 1*10^{14};Al_2O_3: 1*10^{15}
Density [gm*cm^{-3}]	3.51	Ge: 5.4; Si: 2.42
Young Modulus [GPa]	**1140**	W: 344; Si: 110; Steel: 200
Poisson ratio	0.0691-0.29	
Molar Heat Capacity [J*mol^{-1}°C^{-1}]	6.19 (298K)	Ag: 25.5; Cu: 24.5; H_2O: 4.22
Sound Velocity [km*s^{-1}]	**18**	B: 15, SiC: 11.4, Si: 7.5
Band gap [eV]	**5.45-I**	Si: 1.1-I; GaAs: 1.43-D
Breakdown Field [V/cm]	**□1*10^{7}**	Si: 5*10^{6}; GaAs: 6*10^{6}
Electrical Resistivity [Ωcm]	1*10^{16}	Si: 1*10^{3}; GaAs: 1*10^{8}
Work Function [eV]	4.8/NEA	Si: 4.8; GaAs: 4,7
Dielectric Constant	**5.5**	Si: 11; GaAs: 12.5
Lattice Constant [Å]	3.57	Si: 5.42; GaAs: 5.65

Of utmost importance for the presented applications are: highest hardness, high Young's Modulus, high chemical and thermal stability, large electrochemical potential window, surface termination: hydrophilic - hydrophobic, biocompatibility, conductivity controllable by doping. Taking advantage of the tremendous capability offered by the combination of the intrinsic properties of diamond and the features of the NCD/UNCD films we were able to realise new and promising applications.

Results and discussion

i) Bio-sensors

UNCD possesses superb electrochemical properties (physicochemical stability, large electrochemical potential window, chemical sensitivity). These properties in combination with bio-functionalisation of proteins like enzymes, antibodies etc. (still bio-active) makes UNCD an excellent candidate as transducer material for applications in bio- and chemo-sensors.

Latest results will be presented, the large potential of such applications will be demonstrated [1, 2].

ii) MEMS/NEMS

Scaling down mechanical UNCD-resonators to the nanoscale opens a wide range of applications e.g. the detection of small masses (< attogramm), RF-NEMS [3] etc. Mechanical properties of diamond like high Young's Modulus, low density or low energy loss at the surface allow UNCD access to attractive device-realisation like FBAR mass sensor or FPW Biosensor, both demonstrated in the presentation [4, 5].

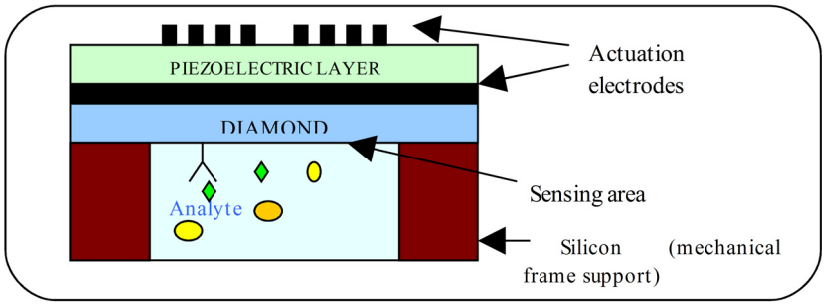

iii) Nano-cell-technology, implants

The influence and interaction of the UNCD-surface on different cell types as well as bio-functionalisation with proteins, like growth factors (still biologically active) was examined. Fundamental insights into binding mechanisms like physisorption were gained. Results of in vitro and in vivo studies of proteins to promote osteogenic cell adhesion and osseointegration will be illustrated [6].

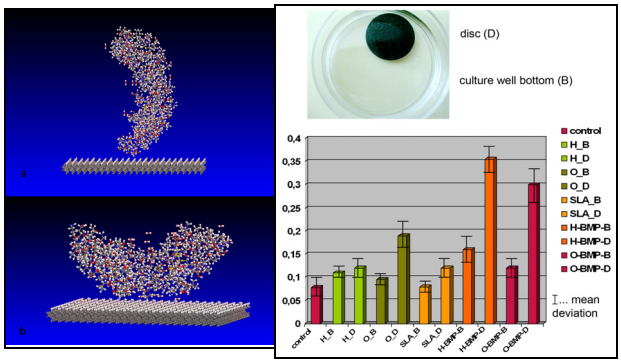

Conclusions

Nano-crystalline diamond films have been tailored in order to meet the demands of various electronic and bio applications. First prototypes for bio-sensors, NEMS and implants have been realised. The results achieved encourage further investigations which in turn will lead to tremendous contributions for new and sophisticated applications. Due to the industrial rho-BeSt process possibilities UNCD can compete with established technologies.

References

[1] Protein-modified nanocrystalline diamond thin films for biosensor applications, Nature Materials 3 (10) (2004), 736-742

[2] Synthetic Nanocrystalline Diamond as a Third-Generation Biosensor Support, Jorge Rubio-Retama, Jorge Hernando, Beatriz López-Ruiz, Andreas Härtl, Doris Steinmüller, Martin Stutzmann, Enrique López-Cabarcos, and José Antonio Garrido, Langmuir, ASAP Article 10.1021/la060167r S0743-7463(06)00167-3

[3] http://www.wirelessdesignonline.com/content/news/article.asp?DocID=%7b2C655084-21DD-426F-B169-799634070F5E%7d&Bucket=&Featured=&VNETCOOKIE=NO

[4] Theoretical investigation of Nanocrystalline diamond Thin Film Bulk Acoustic Resonator (FBAR) for Mass Sensing Application, L.A. Francis et al., to be published in Sensor IEEE

[5] Non-destructive dynamic characterization of nanocrystalline diamond membranes for flexural plate wave sensors, L. A. Francis, A. Kromka, D. Steinmüller-Nethl, P. Bertrand, and C. Van Hoof, IEEE Sensors Journal 6 (4), 916 – 923 (2006)

[6] Strong binding of bioactive BMP-2 to nanocrystalline diamond by physisorption, Steinmuller-Nethl D, Kloss FR, Najam-Ul-Haq M, Rainer M, Larsson K, Linsmeier C, Kohler G, Fehrer C, Lepperdinger G, Liu X, Memmel N, Bertel E, Huck CW, Gassner R, Bonn G, Biomaterials 27 (2006), 4547 – 4556

Investigation of the Coplanar Dielectric Barrier Discharge in Air at Atmospheric Pressure by Cross-Correlation Spectroscopy

T. Hoder[1], M. Šíra[1], K. V. Kozlov[2,3], H. E. Wagner[2]

[1]Department of Physical Electronics, Masaryk University, Kotlářská 2, Brno 611 37, Czech Republic
[2]Institute of Physics, Ernst-Moritz-Arndt University, Domstrasse 10a, D-17489 Greifswald, Germany
[3]Department of Chemistry, Moscow State University, Leninskie Gory 1, str.9, 119899 Moscow, Russia
e-mail: hoder@physics.muni.cz

Abstract

The evolution of the luminosity of the coplanar barrier discharge in the single-filament mode was studied by the technique of cross-correlation spectroscopy. The one-dimensional spatio-temporally resolved luminosity of the first negative (at 391.5 nm) and the second positive (at 337.1 nm) system of molecular nitrogen was recorded. From these experimental data the propagation of the cathode- and anode-directed streamer is described. Based on the interpretation of the above mentioned luminosities distributions as the electric field and electron density distribution the qualitative description of the discharge is made.

Introduction

Due to favorable one-sided geometry and atmospheric pressure working area of the coplanar dielectric barrier discharge (CDBD or simply CD) is this representative of non-thermal plasmas useful for the surface treatment of textile and/or paper materials [1]. Despite the fact that several numerical simulations of the coplanar discharge have been made so far [2], the systematic experimental study of its ignition, progress and extinction phases are still missing. In order to observe these, a close temporally resolved measurement is needed, as the time scale of the phenomena is in the order of units of nanoseconds. The use of cross-correlation spectroscopy (CCS) technique has been already found to be a powerful tool in the case of the volume barrier discharge [3,4,5]. This paper reports our initial work and presents current results in the field of coplanar discharge CCS measurements.

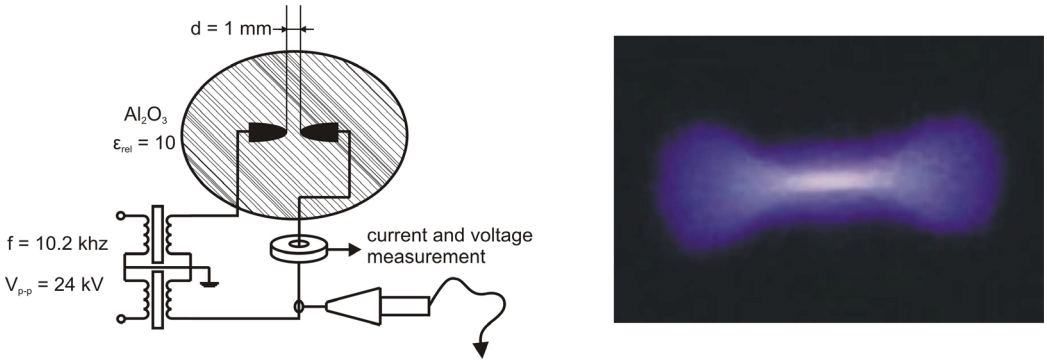

Figure 1. The experimental setup for the coplanar discharge cell is shown left. Right: photo of the coplanar discharge in single-filament mode burning above the dielectric in the synthetic air at atmospheric pressure (exposure time 1/30 s).

Experimental setup

The technique of cross-correlation spectroscopy (CCS) is already described in detail in [3]. The CCS technique used here allowed us to measure with the temporal resolution of 0.1 ns. For these measurements the discharge has to be both periodical and spatially well localized. In order to fulfill these requirements the pin-to-pin coplanar electrode configuration was used (Fig.1). The tips' curvature was r = 0.25 mm for both electrodes. The mutual distance of electrodes was 1 mm. The circulating transformer oil was applied to electrically insulate both electrodes. The electrodes were situated on the one side of 0.7 mm thick alumina ceramic (96% pure Al_2O_3), discharge plasma was generated on the opposite side. The coplanar discharge cell was driven by 24 kV_{p-p} voltage operating at 10.2 kHz frequency. The cell was situated inside the stainless steel reactor described in [3,4]. The synthetic air (20% O_2 and 80% N_2) with the flow rate of 500 sccm was used during this experiment.

The time between the synchronization signal (corresponding to the moment of maximum optical emission of the discharge event) and spectrally and spatially resolved single-photon count was measured.

Consequently a time histogram of more then 10^4 counted photons for each position was created. This is supposed to correspond to the actual light emission of single microdischarge filament.

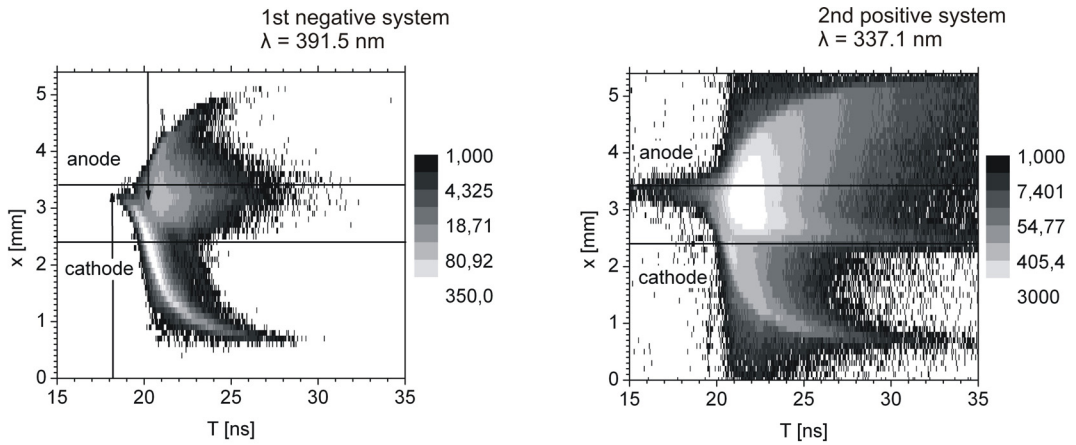

Figure 2. The spatio-temporal distribution of the luminosity of the first negative (left) and second positive (right) system of nitrogen. The gray-scale denotes the number of counted photons, intensity is plotted in the logarithmic scale. The position of the electrodes under the ceramic is denoted. As one can see the active discharge area is not only between the electrodes.

Results and discussion

In figure 2 the spatio-temporally resolved distributions of the luminosities of the selected spectral bands is shown. The cathode-directed streamer as well as anode-directed streamer is visible from the luminosity evolution for λ = 391.5 nm. The black arrows denote the starting points of the streamers. The cathode-directed streamer starts above the anode edge and with increasing velocity reaches the area above the cathode edge where the velocity is maximal. This value $1.1 \cdot 10^6$ ms^{-1} is at the same level as in the volume barrier discharge (see [3,4]). After that the electric field gradient decreases its magnitude and the velocity as well. The streamer extincts far from the cathode edge, about 2 mm outward. Based on the earlier results of the CCS measurements for the volume dielectric barrier discharge [3] the signal distribution at 391.5 nm and 337.1 nm can be approximately considered as the spatio-temporal distribution of the electric field and electron density respectively. According to this interpretation high electric field can be recognized in the streamer propagation phase (see figure 2 left). Additionally, no high magnitude of the electric field is observed near the cathode after the streamer extinction. The luminosity distribution of the signal at 337.1 nm detects the area of high electron density mainly above the inter-electrode space and the anode.

Conclusions

The spatio-temporally resolved luminosity of the selected bands of molecular nitrogen was recorded. Breakdown starts with the cathode directed streamer as well as by the volume discharge. The velocity is in the same order of magnitude as for the volume discharge. Nevertheless 2 ns after the positive streamer the negative (anode-directed) streamer follows and propagates above the anode. The active discharge area extends almost 2 mm over the ceramic edge of both electrodes.

References

[1] M. Simor, J. Rahel, P. Vojtek, A. Brablec, M. Cernak *Applied Physics Letters* 81 (2002) 15 2716
[2] V. I. Gibalov and G. J. Pietsch *J. Phys. D: Appl. Phys., 37 (2004) 2082*
[3] K.V. Kozlov, H.-E. Wagner, R. Brandenburg and P. Michel *J. Phys. D: Appl. Phys.*, 34 (2001) 3164
[4] K.V. Kozlov, R. Brandenburg, H.-E. Wagner, A. M. Morozov and P. Michel *J. Phys. D: Appl. Phys.*, 38 (2005) 518
[5] H.-E. Wagner, R. Brandenburg, K.V. Kozlov, A.M. Morozov and P. Michel *Contrib. Plasma Phys.,* 45 (2005), No. 5 – 6, 338

Physical Properties and Plasma-Chemical Effects of Microdischarges in Porous Ceramics

K. Hensel[1], M. Janda[1], M. Leštinský[1], Z. Machala[1], V. Martišovitš[1], P. Tardiveau[2], A. Mizuno[3]

[1]Department of Astronomy, Earth Physics and Meteorology, Comenius University, Bratislava 842 45, Slovakia
[2]Laboratoire de Physique des Gaz et des Plasmas, Université Paris-Sud, 91400 Orsay, France
[3]Department of Ecological Engineering, Toyohashi University of Technology, 441858 Toyohashi, Japan
e-mail: hensel@fmph.uniba.sk

Abstract

Physical properties of microdischarges inside porous ceramics have been investigated by means of electrical and optical measurements. The plasma-chemical effects of the microdischarges were evaluated by absorption spectrometry. The effects of pore size, discharge power, gas mixture composition and gas flow on the discharge properties and its plasma-chemical activity were examined.

Introduction

Non-thermal plasmas generated by various types of electrical discharges (mostly streamer and pulsed coronas, and various types of barrier discharges) are widely applied for various environmental applications. These discharges are typical with non-equilibrium character and a large amount of thin filamentary channels, called microdischarges. The chemical effect of the discharges can be enhanced if they are combined with catalysts (e.g. of pellet bed or honeycomb structure). Several works dealing with the generation of microdischarges in narrow cavities and capillaries of porous dielectrics and catalysts by pulsed power were published recently [1-3]. We have found the microdischarges can also be generated with a DC and an AC power [4, 5]. The objective of the presented research was the investigation of the physical properties of the microdischarges inside porous ceramics and the test of their plasma chemical efficiency. The methods of the investigations consisted of oscilloscopic measurements and optical emission and absorption spectroscopy. Pore size, gas flow rate, gas composition and discharge power were tested to determine the optimal conditions of the discharge generation.

Experimental Set-up

The detailed description of the experimental setup consisting of a discharge reactor and electric and optical measuring circuits can be found elsewhere [5, 6]. The pore size of the ceramics was 0.8 - 200 μm, their diameter and thickness were 31 and 7 mm, respectively. AC high voltage power supply was used to ignite the discharge. The discharge voltage and current were measured by probes linked to the oscilloscope. Emission spectroscopy optical system consisted of a dual fiber-optic compact spectrometer with CCD detector. Besides, the photographs of the discharge were taken by a digital camera with adjustable aperture and exposure time. The experiments were carried out in various mixtures of oxygen and nitrogen at the atmospheric pressure and at room temperature. The total gas flow rate ranged from 0.4 to 2.0 l/min.

Results and Discussion

In the previous work [5] we have commented on the effect of the pore size, discharge power, and gas mixture on the discharge properties based on the electrical measurements and visual observation (mainly a digital photography) of the discharge. In this paper, we summarize the main results and add more information obtained from the optical emission spectroscopic measurements.

Generation of microdischarges inside the ceramics was possible only at the specific discharge power depending on the pore size of the ceramics. At a small voltage a surface discharge over the surface of the ceramics may be observed. With the increase of the applied voltage, however, microdischarges inside the ceramics are formed. The onset voltage of the microdischarges increased with the decreasing pore size. For a very small pore size (less than 2 μm) only a surface discharge can be observed. The results are in the agreement with what can theoretically be derived from the Paschen's law. Upon the transition from the surface discharge to the microdischarges, the slope of the I-U characteristics increases. The bigger is the pore size the bigger is the slope, as the result of the increase of the discharge current. The amplitude of the current pulses increased with the applied voltage and discharge current, the maximal observed with 50 and 80 μm pore size ceramics.

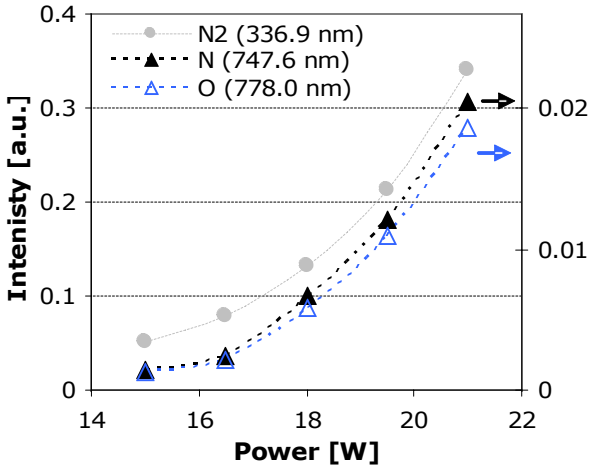

Fig 1: Emission intensity as a function of total power (5% O_2 in N_2, Q = 1.0 l/min).

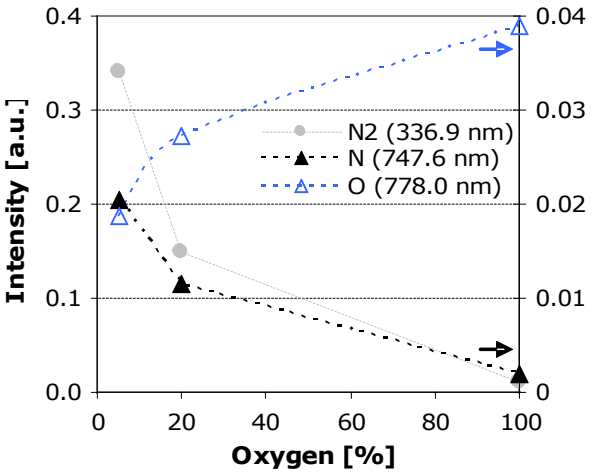

Fig 2: Emission intensity as a function of O_2 content (P= 17.5 W, Q = 1.0 l/min)

The optical observations by photography and emission spectroscopy showed the spatial and temporal distribution of channels was not steady, but changed randomly in time. Light emission increased with the discharge power (Fig.1). In pure nitrogen the light emission was homogenously distributed over the whole surface of the ceramics. Oxygen in the mixture caused the channels concentrated mainly at the outer circumference of the ceramics. The effect of oxygen on the emission intensity can be seen on Fig.2. In nitrogen and air, the 2nd positive system of N_2 in the violet region corresponding to the transition $C^3\Pi_u - B^3\Pi_g$ of N_2 excited states, the 1st positive system of N_2 corresponding to the transition $B^3\Pi_g - A^3\Sigma_u^+$ and atomic N and O lines were observed. Their presence indicated relatively cold plasmas with a high level of non-equilibrium. Non-equilibrium conditions were confirmed also by calculated vibrational (T_V) and rotational (T_R) temperatures, obtained by fitting the experimental spectra (using SpecAir simulation program [7]). The typical measured temperatures in pure nitrogen are T_R = 350-400 K, T_V = 1100-1250 K, gradually increasing with the contents of oxygen in a mixture. Many other unidentified bands have been observed in the spectra and they may be due to the material of the ceramics, which besides alumina and silica includes compounds containing Ca, Mg and Na. The further investigation and interpretation of the bands in needed.

Plasma-chemical effects of microdischarges were studied too. Generation of ozone and oxidation of nitrous oxide were tested to evaluate the chemical efficiency of the discharges [5, 6].

Conclusions

Physical properties and plasma-chemical effects of microdischarges in porous ceramics generated by AC high voltage power have been investigated. The effect of the pore size, discharge power and gas mixture was described. The obtained were in the agreement with those obtained by DC power. The microdischarges present a novel way to generate the stable atmospheric pressure plasmas in hybrid plasma-catalyst reactors and can be effectively used for flue gas treatment.

The research has been supported by Science and Technology Assistance Agency Grants APVT 20-032404 and SK-FR 00506 and Slovak Grant Agency VEGA 1/3041/06.

References

[1] N. Gherardi et al., *Plasma Sources Sci. Technol.* 9 (2000) 340-346.
[2] N. Blin-Simiand et al., *Plasma Proc. Polym.* 2 (2005) 256-262.
[3] N. Jidenko, M. Petit, J-P. Borra, *J. Phys. D: Appl. Phys.* 39 (2006) 281-293.
[4] K. Hensel, S. Katsura, A. Mizuno, *IEEE Trans. Plasma Sci.*, 33 (2005) 574- 575.
[5] K. Hensel et al., Electrical and Optical Properties of AC Microdischarges in Porous Ceramics, *10th Symposium on HP LT Plasma Chemistry HAKONE X*, Saga, Japan, September 4-8 (2006) 277-283.
[6] M. Leštinský et al., Ozone Generation by Microdischarges in Porous Ceramics, *16th Symposium on Applications of Plasma Processes SAPPXVI*, Podbanské, Slovakia, January 20-25 (2007) in this book.
[7] C.O. Laux, Radiation and Nonequilibrium Collisional Radiative Models, von Karman Institute for Fluid Dynamics, Lecture Series 200207, Rhode SaintGenese, Belgium (2002).

Electron-Driven Reactions in Van der Waals Clusters

J. Langer, I. Martin and E. Illenberger

Freie Universität Berlin, Institut für Chemie und Biochemie-Physikalische und Theoretische Chemie-Takustrasse. 3, D-14195 Berlin, Germany

e-mail: langerj@chemie.fu-berlin.de

The interaction of low energy electrons (0-15eV) with single molecules can result in the formation of *temporary negative ion* (TNI) states at characteristic energies. Once the thermodynamically unstable TNI is created, two relaxation processes are available: a) reemission of the initially attached electron and b) decomposition into an anion X^- and one or more neutral fragments R (radicals, molecules). This so-called *dissociative electron attachment* (DEA) process can be described as:

$e^- (\varepsilon) + M \rightarrow M^{-\#}$ (TNI) $\rightarrow X^- + R$

The ionic products formed (X^-) are analyzed mass spectrometrically and recorded as a function of the incident electron energy in a crossed electron/molecular beam experiment.

In a van der Waals cluster, the molecule does no longer exist as an independent particle but it is coupled to neighboring molecules by weak van der Waals interactions. The coupling to the environment allows energy dissipation and charge transfer to the neighboring particles. This results in a reactivity change with manifold consequences and the corresponding DEA process may not proceed with the same efficiency as in single molecules. Instead, stabilization of intact negative parent molecules M^- and aggregates M_n^- (*associative electron attachment*) as well as the formation of ion-molecule complexes $X^{-}\cdot M_n$ also occur. The branching ratio between M^- and $X^{-}\cdot M$ reflects the fast dissociation dynamics in the very early time slot of the reaction. As an example we present results on the C_2F_3I molecule which is so rapidly stabilized in the cluster that the selective decay observed in single molecules does no longer dominate the process in clusters[1]. Electrons can also be scattered inelastically from one molecule in the cluster by electronic excitation (ε >5eV). A second molecule in the same cluster captures the slowed down electron and decomposes efficiently into X^-. These self-scavenging processes become visible in the ion yield of X^- (I^-/C_2F_5I [2], M^-/CF_3COCF_3). In some specific cases, anionic (I_2^-/C_2F_3I [1], $(CF_3CO)_2O^-/CF_3COOH$[3]) and neutral products (H_2O/CF_3COOH[3]) resulting from intermolecular intra-cluster reactions induced by sub-excitation energy electron are observed.

References:

[1] J. Langer, PhD Thesis 2003, Freie Universität Berlin.
[2] J. Langer, S. Matejcik, E. Illenberger, Int. J. Mass Spectrom. 220 (2002) 211.
[3] J. Langer, I. Martin, G. Karwasz, E. Illenberger, Int. J. Mass Spectrom. 249/250 (2006) 477.

Carbon Plasmas as a Source of Novel Carbon Nanostructures

A. Huczko[1], W. W. Płotczyk[1], R. Stankiewicz[1], M. Bystrzejewski[1], H. Lange[1], M. Ruemmeli[2], T. Pichler[2], G.Soucy[3], B. Rybicki[4], R. Wycisk[4]

[1]Department of Chemistry, Warsaw University, 02-093 Warsaw, Poland
[2]IFW Dresden, D-01171 Dresden, Germany
[3]Plasma Technology Research Center, University of Sherbrooke, G7H 2B1 Sherbrooke, Canada
[4]CARBO-GRAF, Ltd., 47-400 Racibórz, Poland
e-mail: ahuczko@chem.uw.edu.pl

Rapid quench of carbon vapors can lead to the formation of novel carbon nanostructures otherwise difficult to obtain using the conventional methods. However, due to the extremely high sublimation point of carbon element (close to 4000 ^{o}C) only plasma heating of carbon-bearing reactants can ensure such conditions. Different plasmas have been tried in the present study, those including DC (Direct Current) plasma jet and carbon arc, (Radio Frequency) RF plasma, HCGD (Hollow Cathode Glow Discharge) and laser ablation of solid carbon. The morphology and characterization of collected solid soot-like products were analyzed using different techniques, e.g., SEM and TEM observations, Raman spectroscopy and wet chemistry. Different, both powdered or rod-like solid carbons (amorphous and crystalline) and gas hydrocarbons (acetylene, methane) were plasma processed. Single-walled and multi-walled carbon nanotubes (SWCNTs and MWCNTs), fullerenes, carbon onions and nanoencapsulates containing magnetic nanocrystallites have been efficiently produced. The use of catalysts (mostly iron-group metals) resulted in formation of SWCNTs instead of MWCNTs.

1. DC plasma jet

Using a direct current plasma jet solid carbon (graphite rods 6 mm dia. with addition of 1.2% Ni and 0.4% Ce and rods 10 mm dia. made of carbon black) were transformed into carbon gas. Ar/H_2 mixtures were used as a plasma gas while arc discharge power ranged between 13.4 – 18.7 kW. The condensation and coalescence of gaseous carbon result in formation of novel carbon nanostructures, e.g., carbon nanotubes (Fig. 1).

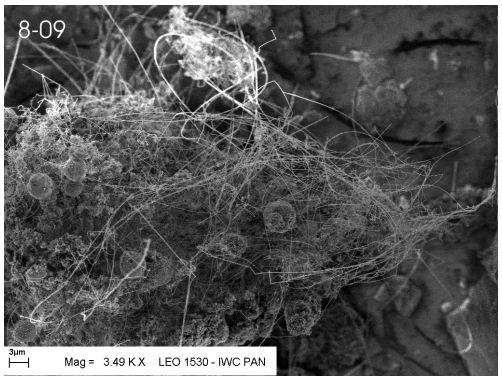

Fig. 1. Carbon nanotubes formed in the DC plasma jet system

2. DC carbon arc

Various carbon-bearing reactants (carbon rods with different graphitization degree) were arc-sublimated in Ar/H_2 atmosphere. Both SWCNTs and MWCNTs were detected in the collected soot, with the highest content of SWNTs for starting amorphous carbons. Also, the diagnostics of arc plasma under conditions of carbon nanostructures formation was performed by optical emission spectroscopy to identify intermediate species and determine temperature and carbon vapor pressure distribution within the arc gap. The emphasis was mainly on carbon dimmers, C_2, since theses species are readily detected and are considered to be the initial nuclei of carbon vapor condensation and soot formation. The quantitative information on the carbon gas composition was obtained using the self-absorption effect which usually is well- pronounced within the 0-0 Swan band (516.5 nm).

3. RF plasma

Large scale production of Fe, Fe_3C and NdC_2 carbon-encapsulated magnetic nanoparticles (CEMNPs)

using RF thermal plasma was carried out. The formation of CEMNPs in this method is based on the high temperature transformation of magnetic powder and decomposition of carbon precursor (CH_4 or C_2H_2) with further quenching and condensation leading to graphene-encapsulated solid nanocrystalline phases. Electron microscopy studies showed that the obtained structures have core-shell structure, with the core diameter between 10 and 30 nm (Fig. 2). X-ray diffraction and Raman spectroscopy showed defects and crystallization degree of the carbon coatings. The thickness and the basal plane diameter of the carbon coating were also estimated by using these techniques. Magnetic measurements revealed that all products exhibit ferromagnetic properties at room temperature.

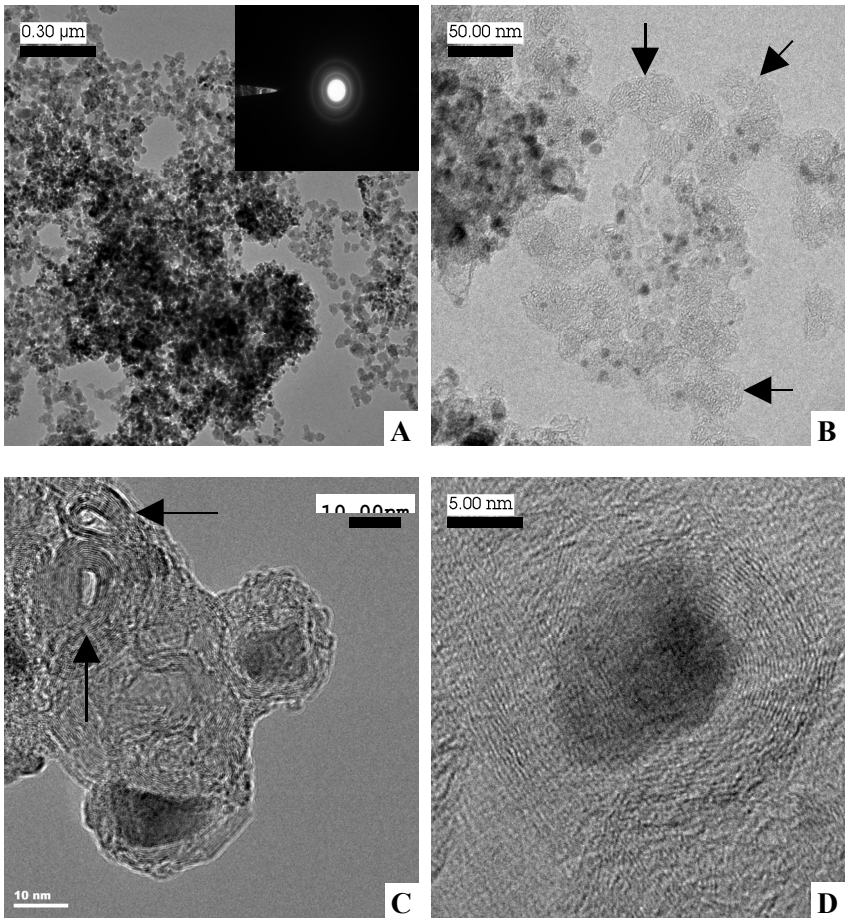

Fig. 2. Graphene-encapsulated magnetic nanoparticles formed in the RF plasma system

4. Laser ablation

Laser ablation synthesis of SWCNTs is a reliable means to produce SWCNTs with narrow diameter distributions and consistent properties. Further, the technique is an excellent platform for the systematic investigation of the synthesis parameters and hence in improved understanding of the growth mechanisms. Our recent laser ablation studies have shown that oxygen can enable non-standard catalysts to yield SWCNTs. The data suggest that oxygen may act as a growth promoter consistent with other results. The reported studies center on exploring the role of H_2O, O_2 and H_2 in the synthesis of SWCNT via laser ablation of carbon-bearing starting materials.

Acknowledgement

This work was supported by the Ministry of Science and Education through the Department of Chemistry, Warsaw University under Grant No. N204 096 31/2160.

Plasma Polymer Coatings from Sputtering Processes

H. Biederman, D. Slavinska, A. Choukourov, J. Hanuš, J. Kousal, M. Drabik

Charles University, Faculty of Mathematics and Physics, Department of Macromolecular Physics, V Holesovickach 2, 18000 Prague 8, Czech Republic

e-mail: bieder@kmf.troja.mff.cuni.cz

Abstract

Deposition process using RF sputtering of PTFE and basic characterization of fluorocarbon plasma polymer films are described. In addition, hydrocarbon plasma polymer films from RF sputtering of PE, PP, LDPE, PIB and PI are addressed. In conclusion nanocomposite films composed of SiO_x inclusions in plasma polymer matrix are concisely introduced.

Introduction

In late 1960s P. J. Harrop with co-workers were probably the first investigators who attempted RF sputtering of polytetrafluoroethylene (PTFE) with the aim to prepare thin polymeric films of useful electrical properties [1] So-called self sputtering mode was applied: sputtering in argon was started and performed for a short time, then argon supply was shut off and sputtering continued in PTFE volatile fragments. Low friction coatings were deposited on steel and glass. They were found to be comparable to bulk PTFE.

After the early beginnings, i.e. after 1980 and especially after 1990, some more polymer targets were used for RF sputtering (for review see [2]). In this contribution the following polymers will be considered for sputtering: PTFE, polyethylene (PE), polypropylene (PP), low-density polyethylene (LDPE), polyisobutylene (PIB) and polyimide (PI).

Fluorocarbon plasma polymer films from RF sputtering of PTFE

The sputtering process can be described as follows. Positive ions bombard with sufficient energy the surface of the target; this results in breaking the polymeric chains into small fragments that are emitted into the plasma volume. These serve as precursors of a plasma polymerization process. As a result, fluorocarbon plasma polymer film is deposited on the substrate. The deposition rate of the film increases within the first 5 min. after the start of sputtering. After 4-6 min. it reaches a constant value and then it decreases. The increase is caused by the rising target temperature while the later decrease by carbonization of the target surface (altered layer) [3].

The deposition process was subjected to the corpuscular diagnostics by means of Hidden Analytical EQP300 spectrometer. CF_4, C_2F_4, C_2F_8 and C_3F_8 stable gases and Ar as a working gas were observed and also CF/CF_2 fragments were found at a concentrations higher than the former species [4]. In an early study [5] based on decomposition of PTFE in He gas in a microwave discharge it was proposed that C_2F_4 is the most abundant specie.

The structure of the film depends on the substrate temperature and on Ar working gas pressure [6]. In the former case a columnar structure is found at decreased temperatures (below the room temperature). In the latter case both chemical composition as obtained by XPS and roughness of the films change. On increasing the pressure from 10 to 50 Pa the contact angle of water of deposited films increases to 140 °. Superhydrophobic coatings may be an application.

Hydrocarbon plasma polymers RF sputtered from PE, PP, LDPE and PIB and PI

Polyethylene was RF sputtered using an unbalanced magnetron [7] with a rate of about 4 nm/min that was several times lower than the sputtering rate of PTFE target. Later PE target 1 mm thick was RF sputtered by means of balanced magnetron (80 mm in diameter) on substrates placed 50 mm above it [7]. When the RF power was increased above 100 W "co-evaporation" from the place of the erosion zone of the target took place. The mentioned power threshold 100 W depends on the magnetic field strength generated by the magnetic circuit of the magnetron. Clear co-evaporation was observed at RF power values around 200 W. Hydrocarbon plasma polymer film was deposited at the rate of 120 nm/min that, according to FTIR (DRIFT) spectra, was much more alike the parent PE. The film deposited at lower RF power values (below 100 W) was found to be a hydrocarbon plasma polymer with a lot of OH and CO groups.

Similarly to the case of PE the RF sputtering of PP, LDPE and PIB at a certain RF power becomes assisted by co-evaporation from the erosion zone. The power thresholds for the same magnetron were decreasing in the above mentioned order.

Recently, a study of RF magnetron sputtering of polyimide in working gases such as argon, nitrogen and

in a self-sputtering mode was performed [8]. At the beginning sputtering caused an abrupt release of hydroxyls, which originated likely from water absorbed by the polyimide material. When the RF power applied exceeded a certain threshold a co-evaporation of PI again occurred.

Nanocomposite films with plasma polymer matrix prepared by RF magnetron sputtering

Nanocomposite films of SiO_x/fluorocarbon plasma polymer were prepared by RF magnetron sputtering using Ar at a pressure of 5 Pa and a flow rate 24 cm^3STP/min from two independently powered balanced magnetrons with SiO_2 and PTFE targets powered in the range of 25 – 160 W and 35 –145 W, respectively. Substrates were oscillating 40 mm above the magnetrons with the frequency 1 Hz. Equivalent filling factors of SiO_x ranged from 0 to 0.7. The calculated values of microhardness decreased in the above range from 720 to 3200 N/mm^2 while the contact angle of water changed from 68° to 40°. At higher SiO_x contents the composite films have a heterogeneous structure as shown by TEM. Nanocomposite films may be generally described as a fluorocarbon plasma polymer, which was partly oxidized, with SiO_x inclusions as shown by FTIR and RBS/ERDA. Nanocomposites in many respects similar to the former case may be obtained by SiO_2 and PE or PP sputtering that results in deposition of SiO_x/hydrocarbon plasma polymer films [9]. Nanocomposites prepared by RF sputtering of SiO_2 and PI have very recently been examined [10].

Conclusions

RF sputtering of polymer targets is a promising process that results in the deposition of corresponding plasma polymers. Fluorocarbon plasma polymer films were proposed for various applications such as low friction coating, protective and non-wettable films and barrier coatings. Optical properties were examined and the films were also destined for application as a dielectric film. RF sputtered polyimide films were proposed for mechanical applications as a low friction and wear resistant coatings. RF sputtered polyethylene and polypropylene films were considered as protective and hard coatings.

Composite SiO_x/plasma polymer films represent part of a new class of nanocomposite materials with a very broad range of properties and possible applications.

Acnowledgements

This work is part of the research plan MSM 0021620834 that is financed by the Ministry of Education, Youth and Sports of the Czech Republic.

References

[1] R.Harrop, P. J. Harrop, *Thin Solid Films*, 3 (1969) 109.
[2] H. Biederman, V. Stelmashuk, I. Kholodkov, A. Choukourov, D. Slavinska, *Surface and Coatings Technology*, 174-175 (2003) 27-32.
[3] H. Biederman, M. Zeuner, J. Zalman, P. Bílková, D. Slavínská, V. Stelmasuk, A. Boldyreva, *Thin Solid Films*, 392 (2001) 208.
[4] Zeuner M., Hirsch D., Neumann H., Zalman J. and Biederman H., *Proc. of ISPC 14*, Vol.III, eds. Hrabovský M., Konrád M. and Kopecký V.,(Institute of Plasma Physics AS CR, Prague, Czech Republic 1999) 1527.
[5] E. Mathias, G. H. Miller, *Journal of Physical Chemistry*, 71 (1967) 2671.
[6] V. Stelmashuk, H. Biederman, D. Slavínská, J. Zemek, and M.Trchová, *Vacuum* 77 (2005) 131.
[7] E. Mathias, G. H. Miller, *Journal of Physical Chemistry*, 71 (1967) 2671.
[8] A. Choukourov, J. Hanuš, J. Kousal, A. Grinevich,Y. Pihosh, D. Slavínská, H. Biederman, *Vacuum*, 81 (2006) 517.
[9] Y. Pihosh, H. Biederman, D. Slavinska, A. Choukourov, M. Trchova, J. Kousal, A. Mackova, A. Boldyreva, *Vacuum*, 81 (2006) 32.
[10] Drabik et al, Vacuum 2006/2007 in print

Indium Tin Oxide Thin Films Properties Deposited by Reactive Dual Magnetron Sputtering

A. Kolitsch, A. Rogozin, M. Vinnichenko, N. Shevchenko,

Ion Technology Division, Institute for Ion Beam Physics and Materials Research, Forchungszentrum Dresden-Rossendorf, P.O. Box 510119, 01314 Dresden, Germany

e-mail: A.Kolitsch@fzd.de

A certain design of the dual-magnetron system, e.g. when magnetrons are aimed on the substrate edges, can offer an additional advantage of the investigation of the plasma influence on the ITO film properties. In this case, plasma parameters have essentially inhomogeneous spatial distribution. It can lead to a strong variation of the film properties at homogeneous film thickness distribution along the substrate. Therefore, the aim of the present research is to investigate the influence of the magnetron plasma on the properties and structure of the growing ITO films. Tin-doped indium oxide (ITO) films were deposited by sputtering of metallic In (90%) - Sn (10%) alloy targets in atmosphere of Ar and O_2 mixture by using pulsed dual magnetron system in the unipolar mode. The films were prepared on SiO_2 covered (500 nm) Si (100) wafers and fused silica substrates at deposition parameters which provide simultaneously lowest resistivity and high optical transmittance. The substrates were not intentionally heated and were at floating potential.

The spatial distribution of plasma parameters during the deposition was characterized in situ by means of Langmuir probe method and optical emission spectroscopy. The film deposition process was monitored by using in situ spectroscopic ellipsometry (SE). Post deposition characterization of the ITO layer optical properties included combination of SE and optical transmittance measurements. The XRD patterns were recorded at different angles of grazing incidence. The film structure was studied by cross sectional TEM. Stoichiometry of the films was checked by elastic recoil detection analysis (ERDA). The ITO film surface morphology was examined by AFM.

The film properties distribution along the substrates is related to the space distribution of the plasma flows escaping from the magnetrons. It was shown that the plasma streams assist the deposition of the ITO films by neutral particles and significantly influence the film properties. It has been observed that the ITO layers demonstrate grading of optical constants through the film thickness. It is related to an increase of the ITO film crystallinity in direction from the ITO-substrate interface to the film surface due to XRD results. This conclusion is also confirmed by cross sectional TEM data which revealed columnar structure near the film surface which gradually changes to amorphous layer near the ITO-substrate interface. AFM and the TEM data analysis demonstrated that even films which are mainly amorphous due to XRD have crystallites in the near surface layer. These crystallites comprise the ITO film surface roughness. ERDA demonstrated grading of oxygen and metal (In and Sn) content through the film. Such grading of ITO film characteristics through the thickness is related mainly to local heating of the substrate by the plasma streams escaping magnetrons.

It is shown that the formation of an ITO film takes place on the substrate due to oxidation of the incident atoms and ions. A film growth mechanism is proposed taking into account the processes of adsorption, oxide formation, resputtering, and thermal desorption of adatoms. The competition of all these processes, depending on the temperature, results in two regimes of film formation, with the highest growth rate occurring at about 270 °C. The evolution of the microstructure is consistent with the well-known structure zone model in the literature. The temperature dependence of the film texture is described with consideration of the interplay of the shadowing and surface diffusion processes. Films with a pronounced (222) texture form at 400 and 510 °C. These films exhibit the lowest resistance as well as a high free carrier concentration and mobility. The high concentration of free carriers results from the activation of the Sn donor impurity.

The post deposition isothermal annealing of films was performed in vacuum at different temperatures. The evolution of the film structure and properties were characterized by combination of four complementary *in situ* techniques: synchrotron X-ray diffraction analysis, spectroscopic ellipsometry, recoil detection analysis (ERDA) and resistivity measurements. The as-deposited films have amorphous structure which is transformed to crystalline during annealing. ERDA results show a considerable decrease in oxygen quantity taken place before crystallisation as well as a decrease in the film resistivity. The following crystallization leads to further decrease of the resistivity. Increase of the annealing temperature leads to decrease of the time of crystallization onset and the total time of amorphous-to-crystalline transformation.

The film resistivity decreases by the factor of ten as a result of annealing. The resistivity and optical properties depend non-linearly on the crystalline fraction.

As a new method of indium tin oxide (ITO) annealing in vacuum, direct electric current flow through the film is proposed. During annealing at constant electric power, the film resistance, free electron density and structure evolution were monitored in situ. Compared to conventional isothermal annealing, the current annealing is more efficient with a noticeable reduction of the thermal budget and a decrease of the kinetic exponent of the crystallization. Electrical inhomogenities of the film, which produce locally overheated regions, are discussed as potential reason for the acceleration of the crystallization process.

Properties of Plasma of the Electrical Discharge in the Air Channel with a Water Wall

V. Ya. Chernyak[1], S. Matejcik[2], V. V. Yukhymenko[1], J. D. Skalny[2], I. V. Prisyazhnevich[1], V. V. Naumov[3], M. Sabo[2]

[1]Faculty of Radiophysics, Dept. of Physical Electronics, Taras Shevchenko Kyiv National University, Prospect Acad. Glushkova 2/5, 03127 Kyiv, Ukraine

[2]Faculty of mathematics, physics and informatics, Comenius University Bratislava, Mlynska dolina F2, 84248 Bratislava, Slovak Republic

[3]Institute of Fundamental Problems for High Technology, Ukrainian Academy of Sciences Prospect Nauki 45, Kiev 03028, Ukraine

e-mail: chern@univ.kiev.ua; jan.skalny@uibk.ac.at; naumov@ifpht.kiev.ua

Abstract

The optical studies of the plasma-liquid system based on the electrical discharge in the gas channel with a water wall were carried out for different sections of the gas channel. The energy characteristics of the investigated discharge were determined. The population temperatures were calculated and non-isothermal character of the air plasma in the gas channel with a water wall was shown.

Introduction

Among the electrical discharges, which are used in plasma-liquid systems, the special attention is given to discharges at atmospheric pressure with large ratio of the surface of plasma-liquid contact to the plasma volume: diaphragm [1], capillary [2] etc. The electrical discharge in gas channel with a liquid wall is the least investigated among them. The principal discrepancy of this discharge from other discharge types mentioned above is the possibility of external control of plasma-created gas compound, which specifies its large potential opportunities in plasmachemical applications [3]. But plasma properties of this discharge have been not well studied until now.

Experimental set-up

The parameters of plasma in the air channel with a water wall were investigated. The schema of experimental system is shown on Fig.1. Small cylindrical electrodes are placed inside glass tubes. Gas (air) flows along electrodes. Electrodes are placed into the liquid, which level was supported constant. The air, which flows from the bottom and top electrodes, is colliding and forming the steady gas channel that connects two electrodes. The distance between electrodes is 10 mm. The discharge burns inside the gas channel with a liquid wall. The power supply of the discharge was a constant-current source.

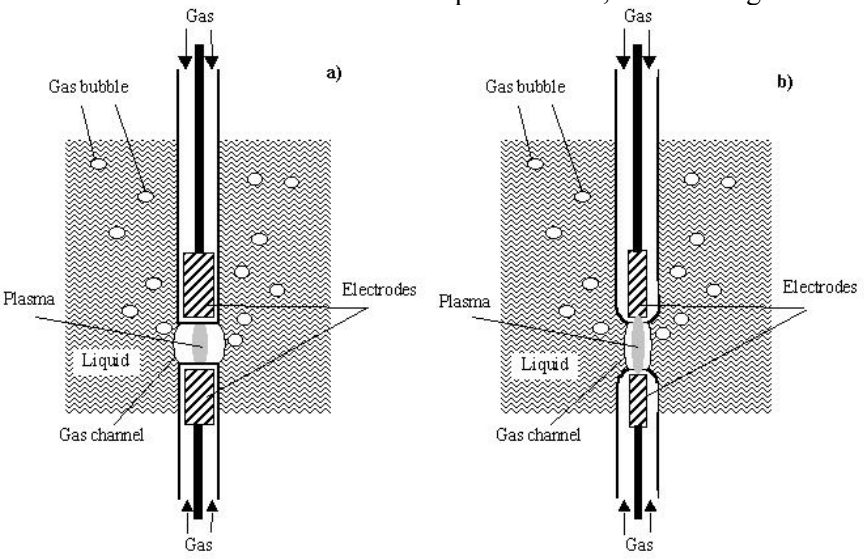

Fig. 1 Schema of experimental system

Plasma parameters of the discharge in the air channel with a water wall were investigated for different cross-sections. In one case electrodes of 6-mm diameter and of 25-mm length inside aperture glass tube of 7-mm diameter were used (a). In second case the diameter of electrodes was 3 mm, length – 40 mm and glass tube on the end was narrowed and its outlet was of 4-mm diameter (b). Velocity of airflow was G = 110 cm^3/s; the current of the discharge (I) changed from 80 up to 400 mA. The emission spectra of plasma were obtained by spectrometer SL-40 in the range of 200-1100 nm with spectral resolution ~ 0,75 nm.

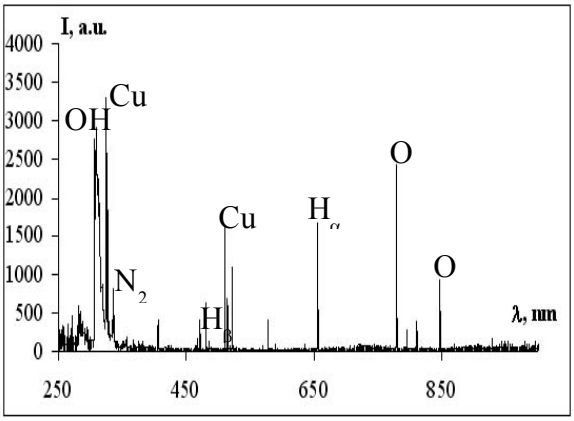

Fig.2 Typical emission spectrum of the air plasma in the gas channel with water wall.
G=110 cm^3/s, I=100 mA, n=600 ms.

Results and Discussion

The typical emission spectrum of plasma in the air channel with a water wall is represented on a Fig.2. The UV system of hydroxyl OH ($A^2\Sigma$-$X^2\Pi$); 2^+-system of nitrogen N_2 ($C^3\Pi_u$-$B^3\Pi_g$), atomic lines of hydrogen H_α, H_β, H_γ, oxygen OI and copper Cu were observed in spectra [4].

Increasing of the discharge current leads to the intensity increasing of all plasma components and is accompanied by intensity redistribution in spectra. The intensity of the OH band has been increased while the copper lines become less intensive. Such behaviour of the OH band intensity can be due to the pressure increasing of the saturated water vapour in plasma-created gas resulted from the current increasing.

Distributions of temperatures of excited electron levels population (T_e) of Cu, O, H atoms and exited vibration levels population (T_v) of N_2 molecule for different discharge currents are represented on Fig.3. It can be seen that obtained temperatures practically don't depend on discharge current and on the cross-sections of the gas channel. It was noticed that T_e of O and H atoms are almost in twice less than T_e of Cu (material of electrodes), and almost similarly distribution for different discharge currents. Such discrepancy between temperatures can be explained by different mechanisms of excitation of these atoms. From Fig.3.(b) can be seen that T_v value is slightly lower than T_e. It indicates the non-isothermal character of plasma in the gas channel with a water wall.

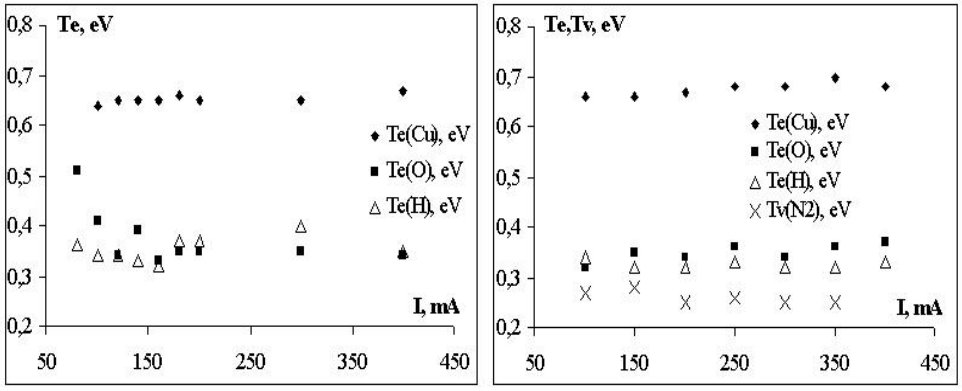

Fig. 3 Temperature distributions of excited electron level population of Cu, O, H atoms and exited vibration level population of N_2 molecule for different discharge current and different cross-sections of gas channel: a – the gas channel of a larger diameter, б– the gas channel of a smaller diameter.

Conclusions

- The optical researches of plasma of the electrical discharge in the air gas channel with a water wall were carried out. It was shown that basic components of emission spectrum of plasma of such discharge correspond to compounds of liquid, in which the gas channel is formed.
- It was shown that obtained T_e values of O and H atoms differ from T_e of Cu (material of electrodes) and the behaviour of its distribution is similar. It was supposed that temperature discrepancy deals with different mechanisms of excitation of these atoms.
- It was concluded that of plasma in the gas channel with a water wall is strongly non-equilibrium.

References

[1] I.K. Strojkova, A.I. Maximov, *Processes of solutions sterilisation under action decaying and low-voltage diaphragm discharges*, Proc. 3rd Intern. Symp. on Theor. and Appl. Plasma Chemistry (ISTAPC-2002), Plyos, Russia, V.2, (2002), p. 342-345. (in Russian).

[2] P. Bruggeman, C. Leys, J. Vierendeels, *Progress in the experimental study of DC electrical breakdown in bubbles*, Elec. Proc. of the Second Intern. Workshop Nonequilibrium Processes in Combustion and Plasma Based Technologies, Minsk, Belarus, (2006), 3p.

[3] Yu.P. Veremii, V.Ya. Chernyak et al., *Physicochemical properties of a plasma-liquid system with an electric discharge in a gas channel with a liquid wall*, Ukr. J. Phys, V.51, № 8, (2006), p. 769–774.

[4] R.W.B. Pears and A. G. Gaydon, *The identification of molecular spectra,* N.Y.: Chapman and Hall, 1976.

The Influence of Plasma Treatment and Plasma Polymerization on Adhesion of Polyester Cords to Rubber

I. Hudec[1], M. Jaššo[1], I. Amir[1], J. Široký[1], M. Černák[2] and S. Illisch[3]

[1] Institute of Polymer Materials, Department of Plastics and Rubber, Slovak University of Technology, Bratislava, Slovak Republic
[2] Institute of Physics , Comenius University, Bratislava
[3]Halle Institut of Science and Technology, Martin Luther University Halle-Wittenberg
e-mail: ivan.hudec@stuba.sk

The high-performance advanced polyester (PET) cords are superior to the conventional rubber reinforcing materials, because they have a very high strength, dimensional stability, toughness, fatigue resistance as well as lower specific weight. All those mentioned advantages are very important for the tire industry. However, in dynamic conditions, stresses acting on the rubber matrix are transmitting to the cords yarn across the interface. Consequently the sufficient interfacial adhesion strength between rubber matrix and fibre surface is necessary. The relatively inert chemical structure of PET shows many of desirable properties contributing adversely to their ability to bond to rubber compare with rayon and nylon [1]. The standard method for improvement of adhesion between polyester cords and rubber is established on surface modification of cords by RFL system. As a new method of surface modification plasma treatment and plasma polymerization of polyester cords for increasing of adhesion to rubber were applied [2, 3].

Plasma polymerization is a thin film forming process, where thin films deposit directly on surfaces of substrates. In this process, the growth of low-molecular weight molecules (monomers) into high-molecular weight molecules (polymers) occurs with the assistance of plasma energy, which involves activated electrons, ions and radicals [4]. These coatings offer the potential to alter the surface chemistry of solids in a controlled manner with thin and highly adherent plasma polymer while having a negligible influence upon the bulk properties of the cord material [5].

In this work different method of surface modification - plasma treatment and plasma polymerization of polyester reinforcing materials were observed. Plasma was generated by diffusion coplanar surface barrier discharge (DCSBD) at atmospheric pressure. Plasma polymerization was carried out in mixture of gases of propane-butane and nitrogen and plasma modification was carried out in ambient air and nitrogen.

The influence of plasma polymerization and plasma treatment on adhesion strength to rubber matrix (static adhesion strength and adhesion strength after dynamic stress – dynamic adhesion) was observed and compared with untreated and by resorcinol-formaldehyde latex (RFL system) modified cords. Adhesion strength to rubber blend was studied by the standard Henley test method according to STN 621464.

The results of estimation of static and dynamic adhesion strength to rubber compound for tested PET cords which were modified by plasma treatment in nitrogene or by plasma polymerization in admixture propane-butane with nitrogene are summarized in figure 1.

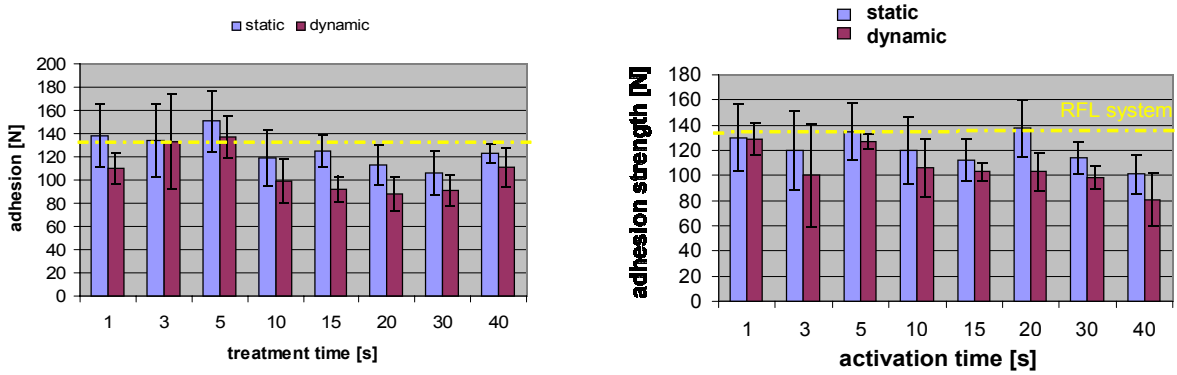

a - plasma treatment b – plasma polymerization

Fig. 1 **C**omparison of adhesion strength of plasma modified PET cords to rubber compound

From the experimental data of adhesion testing it is clear, that with plasma treatment in nitrogene and plasma polymerization technique is possible to obtain adhesion strength comparable with standard chemical way - RFL treatment (dashed line in figures), without any change of bulk mechanical properties of treated samples. Increasing of adhesion strength to rubber is result of chemical and morphological changes of surface layer of polyester cords material.

Chemical composition of plasma deposited layer or the modified surface of PET cords by plasma treatment was measured by XPS analysis (Tab. 1.).

Sample	C (at%)	N (at.%)	O (at.%)	O/C	N/C
Untreated PET	73,3	0,0	25.0	0,341	0,000
Plasma polymerized PET	83,0	10,6	6,4	0,077	0,127
Plasma treated PET - air, 10s	67,6	3,2	27,4	0,406	0,047
Plasma treated PET – N_2, 5s	64,7	3,9	28,6	0,442	0,060

Tab. 1 Composition of surface layer plasma modified polyester cords

From XPS results it is possible to allege that new layer created during plasma polymerization is amorphous very high crosslinked polymer that is indicated with the extension of primary peak of C1s spectrum. Chemical structure of the layer is largely represented with C-C, C=C, C-N, and C=N bonds. Very low content of polar oxygen groups predict poor hydrophilic properties of deposited polymer layer, what was verify also contact angle measurements and wettability (Tab. 2.).

Sample	γ_{total} [mJ/m^2]	$\gamma_{disperse}$ [mJ/m^2]	γ_{polar} [mJ/m^2]	wettability (s)
Untreated PET	46,43	43,50	2,93	18
Plasma polymerized PET	36,71	34,89	1,81	23

Tab. 2 Surface energy and wettability of untreated and plasma polymerized samples

Table 2 shows decrease in surface energy of propane-butane coated PET cords. This decrease is also evident in longer time of wettability of distilled water into structure of PET cords.

For detailed approaching of morphological changes, the samples were investigated by means of SEM and AFM (Fig. 2). This results shows that deposited layer consists of powder-film like structure with increasing of roughness, what is particularly determined with plasma characteristics.

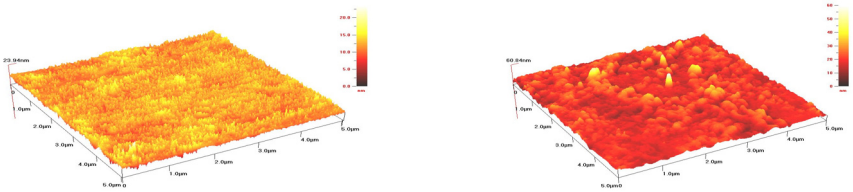

a) b)

Fig. 2 AFM 3D pictures of untreated (a) and plasma polymerized PET(b)

Conclusion

The main of this work to obtain more information about plasma treatment in ambient air and nitrogene and plasma polymerization of propane-butane on polyester cords surface. As it was shown, the plasma treatment of polyester cords in coplanar diffuse surface barier discharge (CDSBD) plasma reactor is the method seems to be available and suitable for improvement of polyester cords adhesion to rubber matrix as a results of chemical and morphological changes of the cords surface layer. In the case of plasma polymerisation deposited layer has more hydrophobic chemical structure as well as higher roughness.

Acknowledgement

This work was supported by Ministry of Education SR grant No.4/0003/05

References

[1] Janssen H., *Kautschuk Gummi Kunststoffe*, 48 (1995), pp. 622–624

[2] Hudec I., Jasso M., Cernak M., Krump H., Dayss E, Suriova V., Kautschuk Gummi Kunststoffe, 58(2005), pp. 525-528

[3] Krump H., Hudec I., Jaššo M, Dayss E., Luyt A.S., Applied Surface Science, 252(2006), pp. 4264-4278

[4] Imagaki N., Plasma Surface Modification and Plasma Polymerization, Technomic Publishing Company Book, Chapter 5, (1996), pp. 101-159

[5] Morgan R. A., Tran M. D., Polymer 40**,** (1999), pp. 5479-5488

Transient Negative ions of Hexafluoroacetone Azine ($(CF_3)_2CNNC(CF_3)_2$): Formation and Decay

O. Ingolfsson[1], I. Bald[2] and E. Illenberger[2]

[1]Science Institute, University of Iceland, Dunhagi 3, 107 Reykjavik, Iceland.
[2]Institute of Chemistry and Biochemistry - Physical and Theoretical Chemistry
Freie Universität Berlin Takustr. 3, 14195 Berlin, Germany.
e-mail: odduring@hi.is

Abstract

In this paper we present a crossed-beam study on the interaction of hexafluoroacetone azine ($(CF_3)_2CNNC(CF_3)_2$) with electrons in the energy range from few meV to about 12 eV. In this energy range dissociative electron attachment to hexafluoroacetone azine leads to the formation of at least five distinct negative ion fragments; F^-, CN^-, CF_3^-, $C(CF_3)_2^-$ and $(CF_3)_2CN^-$. The molecular ion is not observed within the time window of our experiment (about 100 μs). The ion yields for all fragments formed, except the CN^-, have in common two or more resonances above 2 eV, i.e., at about 3 eV, 4-5 eV and/or 8 eV. However, the $(CF_3)_2CN^-$ formation, which corresponds to the symmetric cleavage of the molecular ion, is the only fragment that is observed to any extends below 1 eV. The ion yield curves for CN^- show only one resonance with a maximum close to 1.4 eV and have apparently nothing in common with the ion yield curves of the other fragments.

Introduction

Hexafluoroacetone Azine (HFAA, Fig 1) possesses a number of properties which make it interesting with respect to electron attachment.

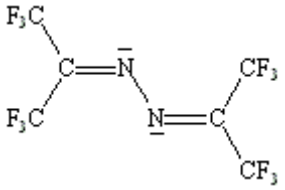

Hexafluoroacetone azine

It is a perfluorinated unsaturated compound with four CF_3 groups, thereby predestined to form F^- and CF_3^- through direct dissociation of the respective C-F or C-C bond with charge retention on the high electron affinity fragments F and CF_3 in the respective cases. It is an unsaturated compound with the LUMO being a low lying C=N π* orbital [1,2] which occupation may lead to the formation of CN^- through multiple bond ruptures. In addition HFAA has two lone-pairs residing in none-bonding orbital which may give rise to additional core excited resonances. To our knowledge there is no previously published work on electron attachment to either acetone azine or its perfluorinated analogue. However, a thorough study on the photoelectron and far-ultraviolet absorption spectra of acetone azine was conducted in the late seventies [2]. In this study the low lying nπ* and ππ* transitions were all assigned, which allows an interesting comparison with the appearance energies of the DEA fragments observed in this study. Though there have been no electron attachment studies on HFAA, there have been a number of studies on other molecules containing terminal CN-groups. These studies include molecules such as R-CN with R = CH_3 and CF_3 [3-5] and have revealed that the decay of the transient negative ion to form CN^- is characterized by low kinetic energy release as compared to systems such as CF_3I and CH_3I where the I^- formation proceeds via direct dissociation [6-9]. Also, the cross sections for the CN^- formation from CH_3CN and CF_3CN are about six orders of magnitude lower than for the I^- formation from the iodinated analogues. These observations are consistent with the excess electron occupying the C=N π* orbital and the CN^- formation proceeding via vibration pre-dissociation. In the case of hexafluoroacetone azine the situation is even more complex as multiple bond rupture is necessary for the CN^- formation.

Results and discussion

In this paper we present an experimental gas phase study on low energy electron attachment to hexafluoroacetone azine $(CF_3)_2C=N-N=C(CF_3)_2$ in the range from few meV to 12 eV. In this energy range low energy electron attachment to hexafluoroacetone azine leads to the formation of fragments with the mass

to charge ratio (m/Z): 164, 150, 69, 26 and 19. We attribute these to the fragments $(M/2)^-$, i.e., $(CF_3)_2CN^-$, $(CF_3)_2C^-$, CF_3^-, CN^- and F^-. Table I shows the location of the peak maxima in the ion yield curves for the individual fragments and the energetic of their formation.

Table I. Location of the peak maxima in the ion yield curves for the individual fragments and estimates of the energetics of their formation. The estimates for the bond dissociation energies are derived from the BDEs of similar compounds obtained from Ref. 6. Observed shoulders are denoted by (s). All values are in electron volts (eV)

m/z ratio	Fragm. Ion X^-	EA(X)	Σ D(R-X)	DH(X^-)	Peak Position
164	$(CF_3)_2CN^-$		≈ 3		0.1, 0.4, 2.8, 4.0(s)
150	$(CF_3)_2C^-$	≈0.6	≈ 5.7	≈ 5.1	4.5, 7.4
69	CF_3^-	1.8	≈ 3.7	≈ 1.9	3.0 (s), 4.0, 7.3
26	CN^-	3.82	≈ 8.3	≈ 4.5	1.4, 10.3
19	F^-	3.4	≈ 5.4	≈ 2	3.4, 5.2, 8.0(s), 10.7

The two most pronounced of these fragments are CF_3^- and $(CF_3)_2CN^-$. The $(CF_3)_2CN^-$ ion, which corresponds to a N-N bond rupture at the center of symmetry of the molecule, is the only fragment that is formed to any extend below 1.0 eV. This ion is formed through two distinct low energy resonances at about 0.1 eV and 0.4 eV, respectively and through a broader contribution with a maximum close to 2.8 eV and a shoulder at about 4 eV. One or both of these resonances appear in the ion yield curves for all other fragments, except for CN^-. The fragment CF_3^- appears through a broad structure with a maximum about 4 eV and a shoulder at about 3eV. The fragment $(CF_3)_2C^-$, is only formed through the higher energy resonance with a maximum close to 4.5 eV, but F^- shows two distinct contributions with maxima close to 3.4 and 5.2 eV respectively. In accordance with the combined photoelectron and far-ultraviolet absorption spectroscopy work from Vocelle et al., we assign the resonances above 2 eV as core excited resonances associated with the corresponding $\pi^* \leftarrow n_+$ and $\pi^* \leftarrow \pi$ transitions. For acetone azine Vocelle et al. located these transitions at about 4-4.1 eV, 5.2-5.5 eV and 6.2 eV respectively. The CN^- formation proceeds exclusively through a resonance at about 1.4 eV from which there is no trace in any of the other ion yield curves. Furthermore, despite the rough estimates for the binding energies given in table I, it is obvious that all fragments except CN^- may be formed through a single bond rupture, without new bonds being formed. This is especially true if one expects a transition from a single to a double bond between the nitrogen atoms of the neutral counterpart to the $(CF_3)_2C^-$ fragment. In the case of CN^- the energetics may only be explained if new bonds are formed in the process. In this case, the formation of hexafluoroethane from the two CF_3 groups cleaved from the carbon atom seems the most likely candidate.

References

[1] S.E. Bradforth, E.H. Kim, D.W. Arnold and D.M. Neumark, J. Chem Phys. 98 (1993) 800.
[2] D. Vocelle, A. Dargelos, R. Pottier and C. Sandorfy, J. Chem. Phys. 66(7) (1977) 2860.
[3] W. Sailer et al. Chem. Phys. Lett. 381 (2003) 216.
[4] M. Heni and E. Illenberger Int. J. Mass Spectrom. Ion Proc. 73 (1986) 127.
[5] M. Tronc and R. Azria, Chem. Phys. Lett. 85 (1982) 345.
[6] K. Nagesha, V. R.. Marathe and E. Krishnakumar, Int. J. Mass Spectrom. Ion Proc. 145 (1995) 89.
[7] C.W. Walter, B.G. Lindsay, K.A. Smith and F.B. Dunning, Chem. Phys. Lett. 154 (1989) 409.
[8] M. Heni and E. Illenberger, Chem. Phys. Lett. 131 (1986) 314.
[9] S. Marienfeld, I.I. Fabrikant, M. Braun, M.-W. Ruf and H. Hotop, J. Phys. B: At. Mol. Opt. Phys. 39 (2006) 105.
[10] *CRC Handbook of Chemistry and Physics,* David R. Lide, ed., Internet Version 2007, (87th Edition), <http:/www.hbcpnetbase.com> Taylor and Francis, Boca Raton, FL, 2007.

Acknowledgement

This work has been supported by the Deutsche Forschungsgemeinschaft (DFG) and the Freie Universität Berlin. IB is a fellow of the Studienstiftung des Deutschen Volkes and OI acknowledges support for a visit to Berlin by the European Union through the COST Action P9; on radiation damage to biologically relevant molecules.

Emissive Probe Diagnostics of Discharge Plasmas

C. Ioniță[1], R. Gstrein[1], A. Marek[2], M. Tichý[2], P. Kudrna[2], P. C. Balan,[1] S. B. Olenici[3], J. Adàmek[4], E. Martines[5], R. Schrittwieser,[1] J.Stöckel[4], G. van Oost[6]

[1]Institute for Ion Physics and Applied Physics, Leopold-Franzens University Innsbruck, A-6020 Innsbruck, Austria
[2]Charles University in Prague, Faculty of Mathematics and Physics, 18000 Prague, Czech Republic
[3]Al. I. Cuza University, Faculty of Physics, RO-700506, Iasi, Romania
[4]Institute of Plasma Physics, Academy of Sciences of the Czech Republic, Prague, Czech Republic
[5]Consorzio RFX, Padova, Italy
[6]Department of Applied Physics, University of Gent, Gent, Belgium

Electron-emissive probes are well-known diagnostic tools for direct measurements of the plasma potential. By emitting an electron current into the plasma, these probes make it possible to determine the plasma potential directly through their floating potential. We report on the basic principle of these probes and various effects which were recently investigated thoroughly. We found evidence that under certain conditions a deviation of the floating potential of the probe from the plasma potential can occur below *and* above the true value. These effects seem to be related to the formation of an electron space charge around the probe even in the case of a floating probe. We also report on methods to measure more complex plasma parameters, such as the electron temperature and the fluctuation-induced particle flux, by combinations of emissive and cold probes.

Posters

P 01

Mass-Spectrometry Investigations in Ar-H_2 Radio-Frequency Discharges

M. Aflori[1], D. G. Dimitriu[2]

[1]Romanian Academy, Petru Poni Intitute of Macromolecular Chemistry, Aleea Gr. Ghica Voda, 41A, Iasi 700487, Romania

[2] Faculty of Physics, "Al. I. Cuza" University, 11 Carol I Blvd., Iasi700506, Romania

email: maflori@icmpp.ro

Abstract

The mass-resolved ion energy distribution (IED) has been investigated at the grounded electrode of a capacitively coupled rf (13.56 MHz) discharge in argon-hydrogen mixture. The IED was determined for positive ions Ar^+, Ar^{++}, ArH^+, H^+, H_2^+, for different values of pressures and powers.

Introduction

Radio-frequency glow discharges are widely used in thin film and surface technology. They allow the homogeneous treatment of surface areas at rather low temperatures. Sputtering, anisotropic etching of semiconductor surfaces and the deposition of thin films are typical applications [1]. The fluxes of particles created in plasma or at its edge drive the interactions between plasma and surfaces. Mass spectrometry yields first the nature of ions created in the plasma and second, the corresponding ion energy distribution function. The reactions which take place in plasma have been discussed.

Experimental setup

The investigated rf plasma was confined in a plasma chamber of an asymmetrical industrial OTP Plasmalab 100 capacitively coupled system [1]. The mass-resolved IED was measured at the grounded electrode (included the chamber walls) which was much larger than the driven electrode. The top electrode diameter was 295 mm, inter-electrode spacing 50 mm and the driven electrode diameter was 205 mm. The pressure values were 50, 70 and 90 mTorr and the range of powers was 10 – 150 W. Ion and neutrals kinetic energy distributions were measured with a Hiden EQP Plasma probe which uses an electrostatic ion-energy analyser followed by a triple section quadrupole mass spectrometer for mass analysis.

Results and discussions

In Figure 1 the IEDs for positive ions are presented. For all ions, the intensity of IED is decreasing with increasing of pressure. The reactions which take place in argon-hydrogen plasma, with production of positive ions presented in figure 1, are listed in table 1 [2].

Table 1: Reactions with positive ions production

	Reaction	Cross section (m^2)
Ar^+	$Ar+e \rightarrow Ar^+ +2e$	1.7×10^{-20}
	$Ar^+ +Ar \rightarrow Ar+Ar^+$	4×10^{-19}
	$H_3^+ + Ar \rightarrow Ar^+ + H_2 + H$	3×10^{-20}
Ar^{++}	$Ar+e \rightarrow Ar^{++} +3e$	4.9×10^{-22}
	$Ar^{++} + Ar \rightarrow Ar + Ar^{++}$	8.7×10^{-20}
ArH^+	$H_2^+ + Ar \rightarrow ArH^+ + H$	2.4×10^{-19}
	$H_3^+ + Ar \rightarrow ArH^+ + H_2$	1.3×10^{-20}
	$Ar^+ + H_2 \rightarrow ArH^+ + H$	1.4×10^{-19}
H^+	$H_2 + e \rightarrow H^+ + H + 2e$	1×10^{-22}
	$H_2^+ + Ar \rightarrow H^+ + H + Ar$	1×10^{-22}
	$H^+ + H \rightarrow H + H^+$	4×10^{-19}
	$Ar^+ + H_2 \rightarrow H^+ + H + Ar$	2.5×10^{-21}
H_2^+	$H_2 + e \rightarrow H_2^+ + 2e$	9×10^{-21}
	$Ar^+ + H_2 \rightarrow H_2^+ + Ar$	9×10^{-21}
	$H^+ + H_2 \rightarrow H_2^+ + H$	1.1×10^{-19}
	$H_2^+ + H_2 \rightarrow H_2^+ + H_2$	5.4×10^{-21}

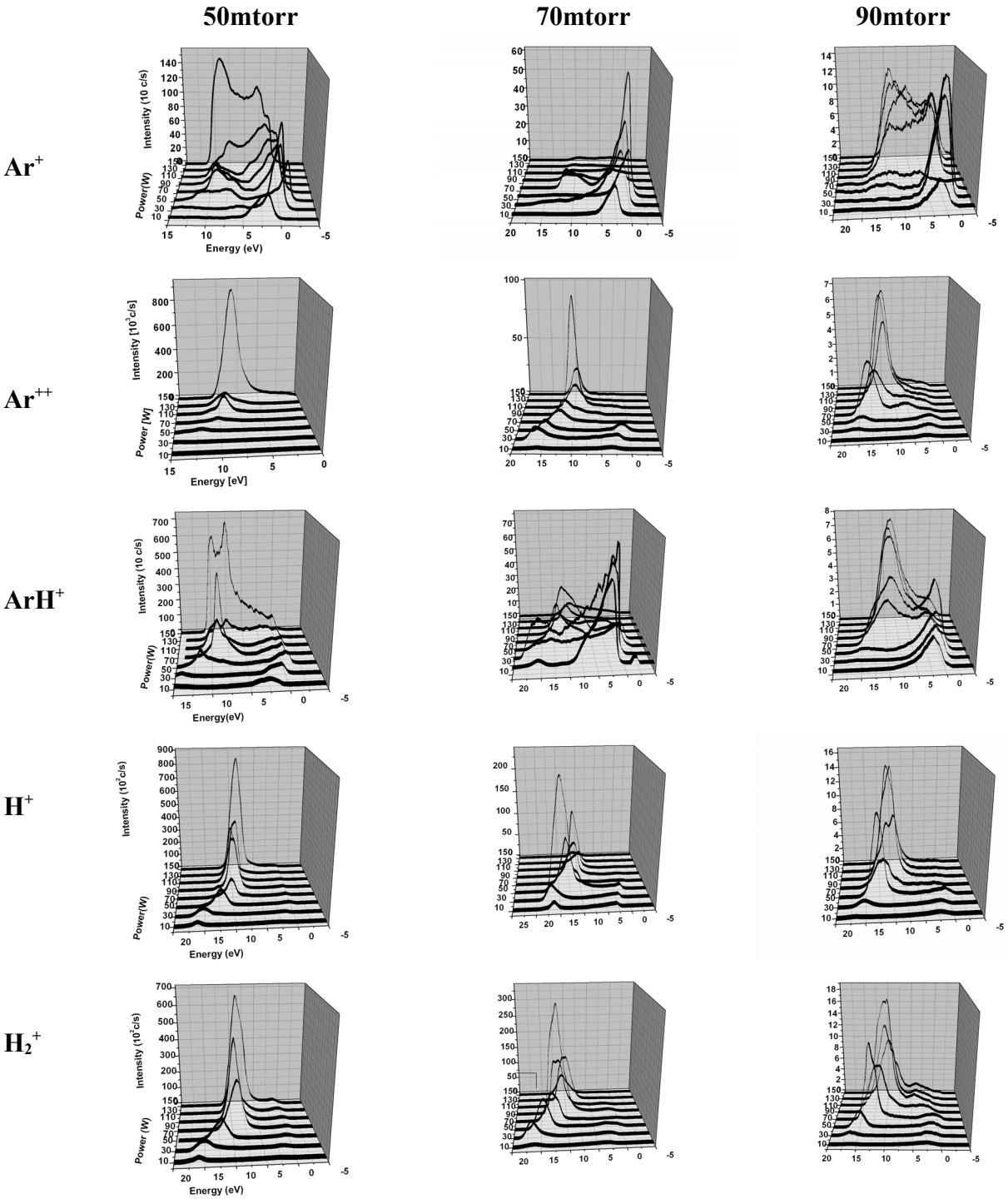

Fig. 1: IEDs for ions at different powers and pressures

Conclusions

In this article we experimentally investigated the energy distributions of positive ions inside an rf argon-hydrogen discharge plasma, at the grounded electrode of an asymmetrical capacitively-coupled device.

References

[1]C. C. Surdu-Bob, J. L. Sullivan, S. O. Saied, R. Layberry, M. Aflori, *Appl. Surf. Sci.*, 202 (2002) 183
[2]S.B. Radovanov, J.K. Olthoff, R.J. Van Brunt, S. Djurovic, *J. Appl. Phys.* 78 (1995) 746

P 02

Development of a Cluster Ion Source Based on High Pressure Electrical Discharge

L. K. H. K. Alwis, F. Zappa, A. Stamatovic, P. Scheier, T. D. Märk

Institut für Ionenphysik und Angewandte Physik, Leopold-Franzens-Universität Innsbruck, Technikerstrasse 25, A-6020 Innsbruck, Austria

e-mail: fabio.zappa@uibk.ac.at

It has been demonstrated that energetic beams of large clusters, with thousands of atoms, can be a powerful tool for surface modification [1, 2]. Normally ionized cluster beams are obtained by electron impact on neutral beams produced in a supersonic expansion [3].

At the University of Innsbruck we are pursuing the realization of a high current cluster ion source based on plasma sources. The idea is that the ionization should occur prior to the supersonic expansion thereby avoiding the need of subsequent electron impact. Furthermore, the ions should act as seeds for cluster growth and enhance by their increased interaction with neutral particles the yield of heavy cluster ions. In addition, all ions have roughly the same number of collisions with neutral atoms or molecules and thus the resulting cluster size distribution is expected to be rather narrow.

Presently, several different plasma production schemes are being tested, and in order to determine the cluster size distribution obtained in each case we have also constructed a custom-made time of flight mass spectrometer (TOF): In this work in particular we present a successful attempt of obtaining argon clusters from an arc discharge. In this mode of operation a plasma is formed in front of the nozzle of the cluster source. We have found that even at rather low gas pressures and at room temperature, effective cluster production takes place. This is remarkable, since usually conventional Van-der-Waals clusters are only obtained at stagnation pressures of several bars. Temperature naturally plays a key role also, i.e., better cluster conditions at temperatures close to the condensation point. Our results therefore serve as a proof-of-principle that much clustering can be obtained with pre-ionized gas (see also earlier work by Northby and coworkers [4]), and our future work will be devoted to obtaining plasmas and thus clusters at higher pressures and colder stagnation temperatures.

This work was supported by FFG and EU (ITS-LEIF). F.Z acknowledges support from Brazilian agency CNPq. We thank Prof. Dusan Skalny for helpful discussions about plasma science.

References

[1] Becker C., Gspann J. and Kramer R., Eur. Phys. J. D **16** (2001) 301–304

[2] Heck C, Seki T, Osawa T, Chikamatsu M, Tanigaki N, Hiraga T, Matsuo J, Nucl. Instrum. and Meth. in Phys. Res. B **242** (2006) 140.

[3] Seki T., Matsuo J., Nucl. Instrum. Meth. in Phys. Res. B **237** (2005) 455.

[4] Harris I.A., Kidwell R.S., Northby J.A., Physical Review Letters **53** (1984) 2390.

P 03

Space and Time Dependent Evolution of Microwave Discharge

Z. Bonaventura and D. Trunec

Department of Physical Electronic, Masaryk University, Kotlarska 2, Brno 611 37, Czech republic
e-mail: zbona@physics.muni.cz

Abstract

Let's have a plasma that is generated by electromagnetic plane wave of frequency $f = 9.379$ Ghz. Amplitude of electric field intenzity is $E_0 = 2$ kV/cm. Discharge chamber has a known linear dimension, that is equal to 16 times of wavelenght of incident wave. A microwave antenna is situated on the left hand side of this chamber and initial distribution of electron density is given. Space and time dependent evolution of distribution of electron density will be calculated on the frame of selfconsistent solution of continuity equation and a wave equation assuming a local field approximation.

Introduction

Propagation of electromagnetic plane wave is described by wave equation for electric field intensity [1] , [2]

$$\nabla^2 \boldsymbol{E} + K^2 \boldsymbol{E} = 0,$$

where

$$K^2 = K_0^2 (1 - j\frac{\sigma}{\omega \epsilon_0})$$

is a propagation constant, $K_0^2 = \omega^2 \epsilon_0 \mu_0$ is a propagation constant in a free space, σ is a complex plasma conductivity, ω and ϵ_0 are field angular frequency and permittivity of free space. Evolution of electron density is described by equation [3]

$$\frac{\partial n_e}{\partial t} = k_i n_e N + D_e \frac{\partial^2 n_e}{\partial z^2} - \nu_r n_e^2,$$

where k_i, D_e, ν_r are rate constant for ionization, electron diffusion coefficient and recombination frequency that is equal to 2×10^{-7} cm^3 s^{-1}. Parameters k_i, D_e, ν_r, σ are dependent on the local magnitude of electric field intensity, that is obtained by solving a wave equation, given above. The dependence of these parameters on the magnitude of electric field intensity was calculated by two term approximation of solution of Boltzmann kinetic equation. The value of ν_r was taken from ref. [4].

Results

System of equations given above is selfconsistently solved for pulses that last for 400 ns and are separated by 4 ms of decay. After several pulses the evolution of discharge reaches a stationary behavior. Spatial distribution of electron density and electric field magnitude at four different moments of a pulse is presented in Fig. 1. On the very beginning of a pulse, electron density distribution is given by the previous decay phase. After 100 ns can be seen that electric field is already absorbed after the plasma. At the consequent time can be seen that electron density is higher in the area that is closer to the antenna. As can be seen, electromagnetic wave is partially reflected back. At the end of the pulse, plasma is completely stick on the wall near the antenna. In the Fig. 2. , there is shown time dependent evolution of power reflection, transmission and absorption coefficients and the mean electron density computed along the whole discharge chamber. At the time 250 ns there is a maximum in the absorption and a consequent growth of the reflection. This is caused because the electron density is locally higher then the critical value n_c for a given wavelength of incident wave.

Conclusion

The evolution of microwave plasma pulse was simulated in the frame of local field approximation. Electron density and electric field magnitude was presented at the selected times. Global characteristics describing propagation of microwave power through the plasma: power transmission, reflection and absorption coefficients were calculated during the pulse.

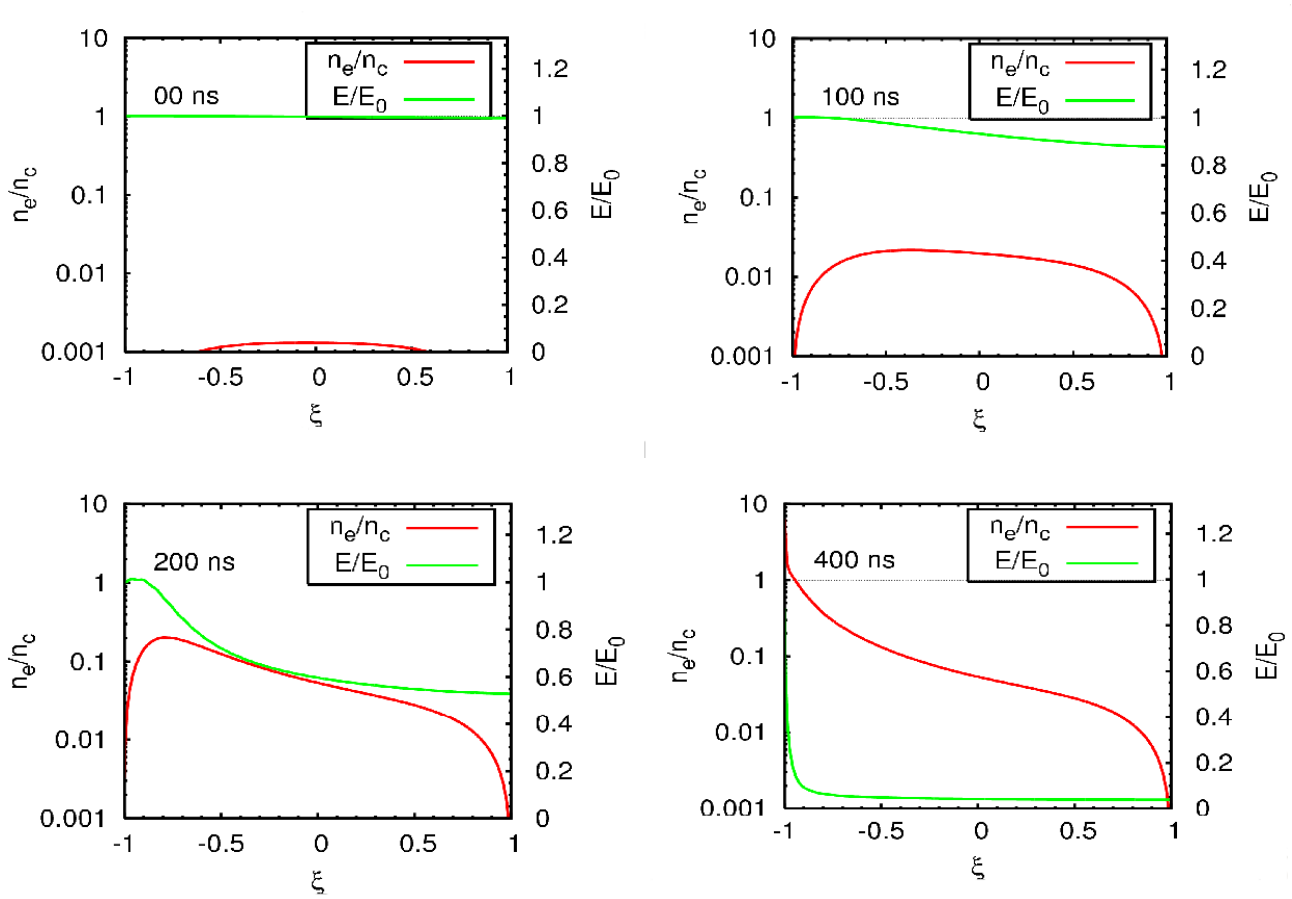

Fig. 1: Time dependence of distribution of magnitude of electric field intensity and electron density.

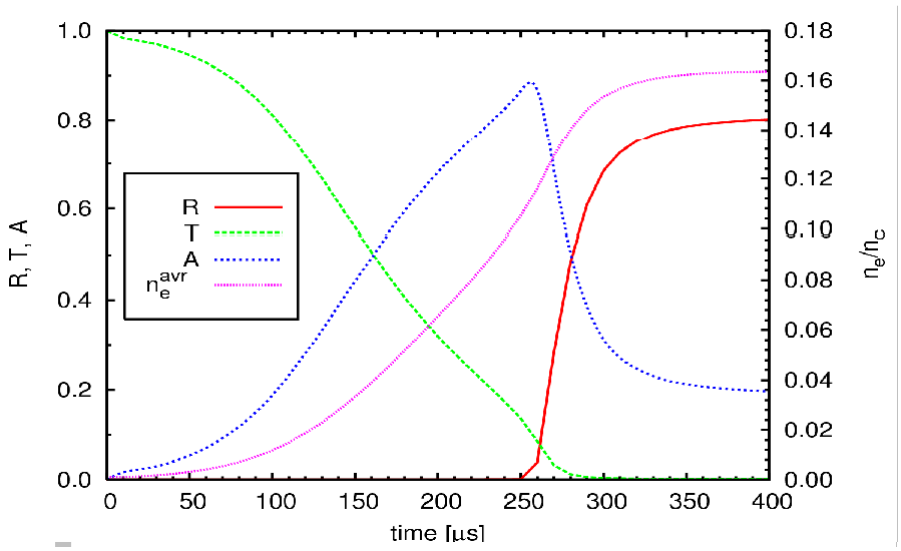

Fig. 2: Power reflection, transmission, and absorption coefficient and mean electron density.

References:

[1] M. Born and E.Wolf, Principles of Optics, Pergamon Press, 1965
[2] B. Sheldon et al, *Journal of the Optical Society of America,* **72**, (1982), 1049
[3] F. F. Chen, Úvod do fyziky plazmatu, ACADEMIA/PRAHA; 1984
[4] M. Mesko et al, *Plasma Sources Science Technology*, **13**:,2004, 562

P 04

Advanced Solvers of Poisson Equation in PIC-MC Metod

P. Bruna [1], R. Hrach [1,2], S. Novák [1]

[1] Department of Physics, Faculty of Science, J. E. Purkinje University
Ceske mladeze 8, 400 96 Usti nad Labem, Czech Republic
[2] Department of Electronics and Vacuum Physics, Faculty of Mathematics and Physics, Charles University
V Holesovickach 2, 180 00 Prague 8, Czech Republic
e-mail: pbruna@physics.ujep.cz\

Abstract

The main goal of this work is to develop a model of plasma-solid interaction based on the PIC-MC computational scheme and to find the most effective algorithm for a determination of the electric potential near the substrate immersed into a plasma.

Introduction

A surface of substrates immersed into a plasma is steadily bombarded by both charged and excited neutral particles. Consequently, they may occur a lot of various effects there. For example, particles can be absorbed on the electrode surface and create a thin film which has entirely different properties than the electrode. We can obtain a very hard surface or a surface which is good for the implantation into living organisms. Another example is the etching of substrates. In all these cases, we have to know which particles impinge the electrode, what is their energy distribution and the angle of impact.

This information can be obtained by various ways, experimentally and theoretically. Recently, with the further development of computer technologies, methods of computer analysis of experimental data become more important. There are two main approaches for solving this problem, the fluid modelling and the particle simulation approach. The fluid modelling is a relatively fast method, but the results give only limited information. On the other side, models based on the particle modelling give much deeper insight into the studied problems, but they are very slow and they have much higher requirements on the computer hardware. It is caused especially by the computation of forces acting between charged particles. There are several techniques to speed up their computation. The PIC-MC computational scheme [1] is one of these techniques. In this scheme, we first determine the electric potential from all charged particles and then we obtain the forces acting on the individual particles by a numeric derivation of this potential. In order to this computational scheme to be effective, it is necessary that the algorithms for determining of the electric potential are as effective as possible.

Computer experiment

In our group, we developed a self-consistent particle model of low-temperature plasma-solid interaction based on the PIC-MC computational scheme. Using this model we compared various methods for the solving of the Poisson equation to find the most effective one. In our model, we determine the spatial distribution of the electric potential and the spatial distribution of charged particles in the vicinity of a cylindrical probe (see **Fig. 1**). All simulations were performed in the plane of symmetry.

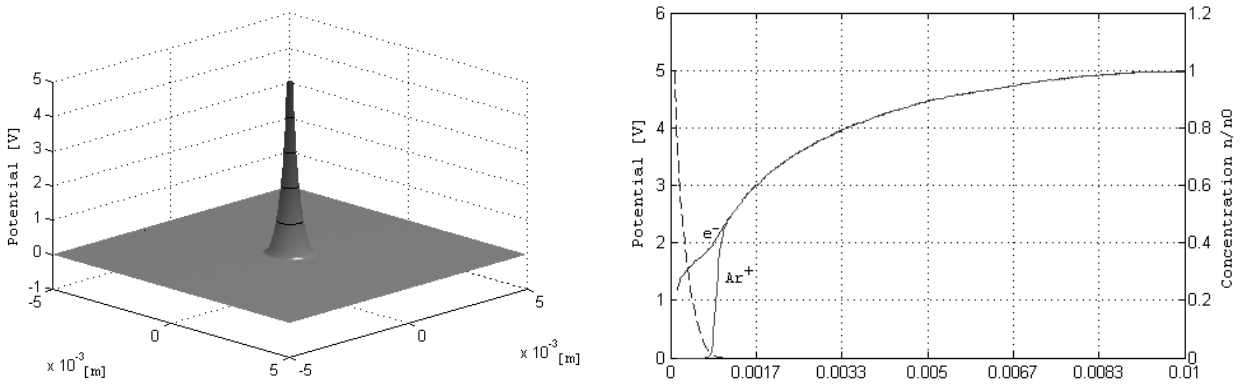

Fig. 1 Left – spatial distribution of electric potential near the cylindrical probe. Right – spatial distribution of charged particles and electic potontial (dashed line).Radius of cylindrical probe 100 μm, voltage bias +5 V, concentration of charged particles in undisturbed plasma 1×10^{15} m^{-3}.

Methods used

Successive overrelaxation method (SOR) – this is the basic and one of the simplest methods. It was used as a reference one, because it is easy to understand, it has low requirements on computer memory and the time needed for coding and debugging is very short. These advantages are restrained by a relatively slow (in the case of 3D models a very slow) convergence.

Conjugate gradients method (CG) – this method has a wider mathematic background than the SOR method. The method has a better convergence and its application is not difficult. A disadvantage of this method is the need of more computer memory, up to 5 times more then the SOR method.

Multigrid method – this is more like a recipe then an exact algorithm and this method always needs to be 'tailored' for a specific problem. On the other side, it is not limited for solving just one specific problem. In contrast to previous methods, which can be coded and debugged in minutes, this method needs much more time and effort. The requirements on computer memory depend on programming techniques. They are about 1.5 to 5.4 times more then the SOR method (faster computation, higher requirements)

Finite element method (FEM) – this is the last tested method and it is the most complex one. This method has a huge mathematic background and the theory is well covered. A big advantage of the FEM is its possibility to easy discretise the working area (we can easily use an arbitrary working area without the loss of accuracy on the boundaries). Another big advantage is the possibility to use most of the code for a large variety of problems.

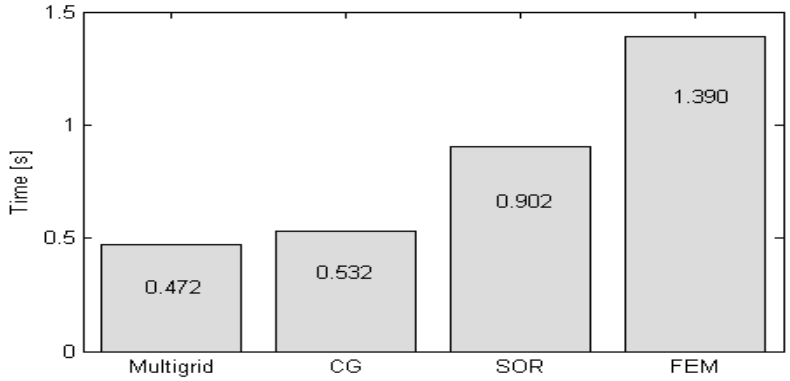

	Move	Scatter	Density	Poisson	Flux	All
Multigrid	0.218	0.097	0.128	0.014	0.014	0.472
CG	0.217	0.097	0.150	0.053	0.015	0.532
SOR	0.210	0.097	0.127	0.453	0.015	0.902
FEM	0.760	0.096	0.495	0.024	0.015	1.390

Table 1 Time consumption of selected parts in seconds

We divided our model in basic parts and tested their time consumption. These parts were: the particle mover (Move), the particle scattering (Scatter), determining density of charges on a grid (Density), solving the Poisson equation (Poisson), and the flux of particles (Flux). The results are summarized in table 1.

Acknowledgement

The authors acknowledge the support of the Ministry of Education of Czech Republic-Projects COST OC 143 and LC 06041.

The author P. B. thanks to support of Glaverbel a.s.

Reference

[1] R. W. Hockney, J. W. Eastwood: Computer Simulation Using Particles, Hilger, Bristol 1988.

[2] G. H. Golub, Ch. F. Van Loan: Matrix Computations, The Johns Hopkins University Press, Baltimore 1996.

P 05

Study of Attachment and Detachment Reactions in Flowing Afterglow via Computer Simulation

O. Brzobohatý and D. Trunec

Department of Physical Electronic, Masaryk University, Kotlářská 2, Brno 611 37, Czech Republic
e-mail: otobrzo@physics.muni.cz

Abstract

In the present contribution attachment and detachment reactions of electrons on C_6F_5Cl molecule at two temperatures 467 K and 550 K are studied These reactions were originally studied in so Flowing Afterglow Langmuir Probe (FALP) apparatus [1]. The measured data, *i. e.,* time evolution of the electron concentration, and the attachment/detachment coefficients determined from the experiments were compared with our simulation results.

Introduction

The FALP experiments were and still are often used for study of the attachment and/or the detachment processes. The result from these experiments is time evolution of the electron concentration (measured with the Langmuir probe) For the experimental arrangement see the Fig. 1.

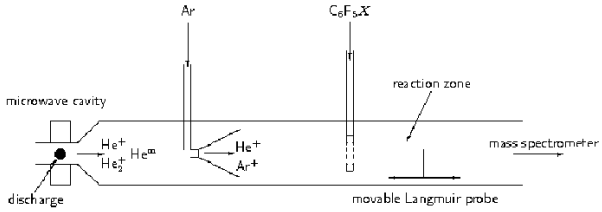

Figure 1: A schematic diagram of the FALP apparatus.

The interpretation of such data is not often an easy task. For the interpretation so called rate equations [1] are usually used. These equations are derived from the simple equation for ambipolar diffusion without consideration of Poisson equation. Therefore the more precise self-consistent model (diffusion equation - Poisson equation) was developed in order to simulate the studied afterglow. The model was 1D due to the cylindrical symmetry of the experiment [1] and it consists of following equations.

$$\frac{\partial n_i}{\partial t} = \nabla (n_i \mu_i \vec{E} - D_i \nabla n_i) + \frac{\delta n_i}{\delta t} \quad , \quad \Delta \varphi = \sum q_i n_i / \varepsilon_0 \quad , \quad \vec{E} = -\nabla \varphi \quad , \qquad (1)$$

where *i* denotes the particle type, *i. e*., electrons, positive ions (He^+ and Ar^+), negative ions $C_6F_5^-$, $C_6F_5Cl^-$, Cl^-. *n* is the concentration of the charged particles, μ is the mobility coefficient, *D* is the diffusion coefficient, $\vec{E}$ is the intensity of the electric field. The last terms of the first equation express the reactions, *e. g*., for electrons $\delta n_e / \delta t = -k_a n_r n_e + k_d n_{-1}$, where k_a is the attachment coefficient, k_d is the detachment coefficient , n_r is the concentration of reacting molecule C_6F_5Cl.

There is one reaction channel (attachment/detachment) at 467 K: $e + C_6F_5Cl \longleftrightarrow C_6F_5Cl^-$ and two reaction channels at 550 K: $e + C_6F_5Cl \longleftrightarrow C_6F_5Cl^-$, (f_1); $e + C_6F_5Cl \rightarrow C_6F_5 + Cl^-$, (f_2), $f_1 + f_2 = 1$ are branching fraction.

Results and discussion

The first case, *i. e*., T = 467 K, is not so complicated for the interpretation due to the one reaction channel. The values of attachment and detachment coefficients were in our simulation nearly the same (in the range of the precision of measurement) as in experiment. The more complicated case was for T = 550 K, where two types of negative ions are present (detaching $C_6F_5Cl^-$ and non-detaching Cl^-). The spatio-temporal distribution of the electric intensity and the temporal evolution of concentration of the charged particles determined in the axis of the tube are shown in the Fig. 2, Fig. 3. It can be seen that the electric field in the

sheath decreases in the vicinity of second electron concentration decay. This decay of the electric field is caused by transition of the electron - positive ions plasma to the negative – positive ions plasma. The values of mobilities are for the positive and the negative ions very similar and therefore the electric field in the sheath is diminished. Note that the electric field vanishes if the negative and positive ions have the same value of the mobility coefficient. The values of attachment/detachment coefficients and branching fraction were changed to fit the measured data. The influence of these coefficients on the temporal evolution of the system was studied too. The precision of the measurement was about 30% and therefore our calculated values of the attachment/detachment coefficients were again in agreement with the coefficients determined with simple model mentioned in the introduction; $k_a^{\exp}=10\,x\,10^{-14}\,m^3\,s^{-1}$, $k_a^s=9.5\,x\,10^{-14}\,m^3\,s^{-1}$, $k_d^{\exp}=4000\,s^{-1}$, $k_d^s=5000\,s^{-1}$ and $f_1^{\exp}=0.87$, $f_1^s=0.81$.

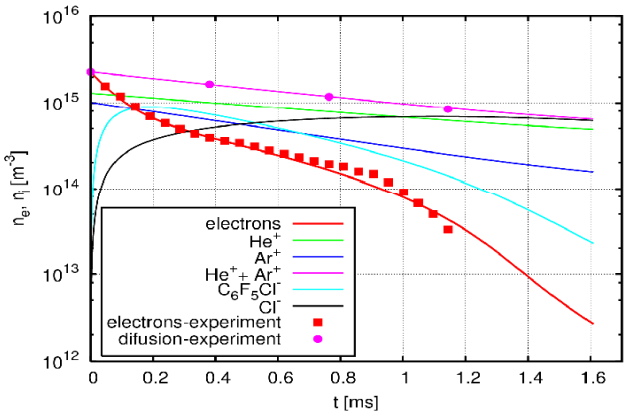

Figure 2: The temporal evolution of the concentration determined in the axis of the symmetry, i. e., in the axis of the tube.

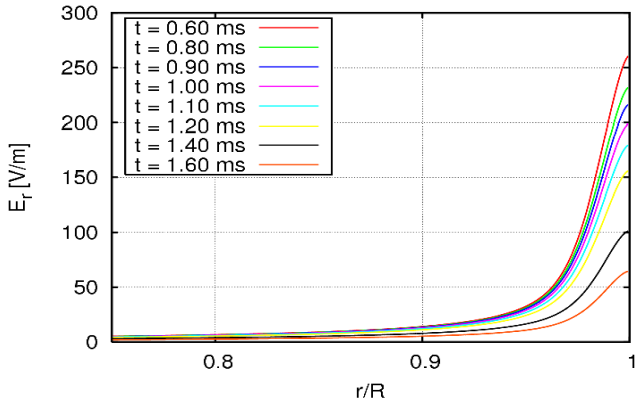

Figure 3: The spatio-temporal distribution of the electric intensity, in the time interval of second steep decay.

References

[1] T. M. Miller, A. A. Viggiano, *Phys. Rev A*, 1 (2004) 70.

P 06

Diffuse Coplanar Surface Barrier Discharge Surface Treatment of Glass

A. Buček[1], T. Homola[1], M. Aranyosiová[3], D. Velič[3], J. Havel[4], M. Černák[1, 2], A. Zahoranová[1]

[1]Department of Experimental Physics, Comenius University, Mlynská dolina, 842 48 Bratislava, Slovakia
[2]Department of Physical Electronics, Masaryk University, Kotlářská 2, 611 37 Brno, Czech Republic
[3]International Laser Center, Ilkovičova 3, 812 19 Bratislava, Slovakia
[4]Department of Analytical Chemistry, Masaryk University, Kotlářská 2, 611 37 Brno, Czech Republic
e-mail: cernak@fmph.uniba.sk

Abstract

Diffuse Coplanar Surface Barrier Discharge (DCSBD) is a novel type of atmospheric pressure plasma source capable of generating thin layers of high-density nonequilibrium plasmas in any gas, including atmospheric-pressure oxygen. Preliminary results presented on the DCSBD application for glass cleaning and activation indicate significant advantages over other plasma sources hitherto tested for the glass surface treatment

Introduction

Freshly cleaned glass surfaces have a high surface energy and are well wettable. They, however, have a tendency to adsorb organic contamination from the ambient environment. Adsorbed organic contaminant molecules, generally less than the full monolayer coverage, of order nm thickness, will generate a heterogeneous wettability. This may lead to non-uniform glass coatings, in particular if deposited from liquid media as in the case of widely used sol-gel coatings, silane coupling agent coatings, electroless metal plating, as well as in jetting fluid dispensing technology that is gaining popularity in the flat panel display manufacturing [1].

Glass cleaning processes using organic solvents are undesirable since they are implicated in ozone-depletion. Consequently, there is significant interest in dry cleaning processes such as plasma cleaning. Electrical plasmas generated at low gas pressures are widely used for glass surface cleaning and activation [2]. However, as e.g. in the flat panel display (FPD) manufacturing the glass substrate size is increased, it is difficult to generate low-pressure plasmas over the large substrate size and the fabrication of the equipment is very costly. This is of particular importance for the coatings onto large-size architectural glass plates.

As discussed in detail in [3], the use of atmospheric pressure plasma cleaning instead of the widely used low-pressure plasma cleaning can increase the handling capacity of large-area glass substrates, can increase the throughput by in-line processing under the atmospheric environment, and can decrease the equipment cost.

Several papers have been published on the glass cleaning using standard barrier discharge treaters [4], however, as discussed in [3, 5] such devices are not convenient for the glass surface cleaning, because of their low plasma power densities (less than 5 W/cm^3) resulting in long exposure times, typically 1 min. (see [4]). Moreover, such devices are not applicable for cleaning of glass substrates thicker that some 2 mm.

A more promising atmospheric-pressure plasma sources for the glass cleaning and activation are plasma jets [3,5], where the glass substrate is situated some 1 cm from the plasma source and is cleaned by a plasma flow, i.e., a plasma jet generated by the plasma source. A disadvantage is that working gas flow rates must be sufficiently high to carry the reactive species from the plasma source to the substrate at an acceptable rate (i.e., before they decay or recombine). As a consequence, a substantial part of the discharge power is uselessly dissipated in the plasma volume by, for example, recombination processes and gas heating. An additional disadvantage is that most commercial plasma jets and similar plasma sources applied for the glass cleaning as *APPJ*® [3,5], *APIS-F*^{TM} [6], and *Enercon* [7] use expensive helium-containing working gases [3,5,6] to stabilize the plasma at necessary power densities in the order of 10 W/cm^3. Moreover, it is difficult to comply a plasma jet with clean room conditions necessary, e.g., for FPD manufacturing.

Results and discussion

We have developed proprietary atmospheric pressure plasma cleaning illustrated by videos available on http://gimmel.ip.fmph.uniba.sk/glass/. The technique is based on the use of the Diffuse Coplanar Surface Barrier Discharge (DCSBD) and outperforms the existing plasma-jet based techniques in:

- ***extremely short plasma cleaning time***

As illustrated by preliminary results shown in Fig. 1, the glass surface becomes hydrophilic after some 1 - 3 sec. treatment, which enables an in-line continuous cleaning. The low contact angles are considered a good indication that organic contamination was, as verified by *MALDI* and *SIMS* measurements, virtually absent from the DCSBD plasma cleaned glass surface.

The results shown in Fig. 1 were obtained in laboratory air at a rather low plasma power density of 2.5 W/cm^2. By increasing the power density to proposed 10 W/cm^2 it will be possible to reduce the exposure time well below 1 sec.

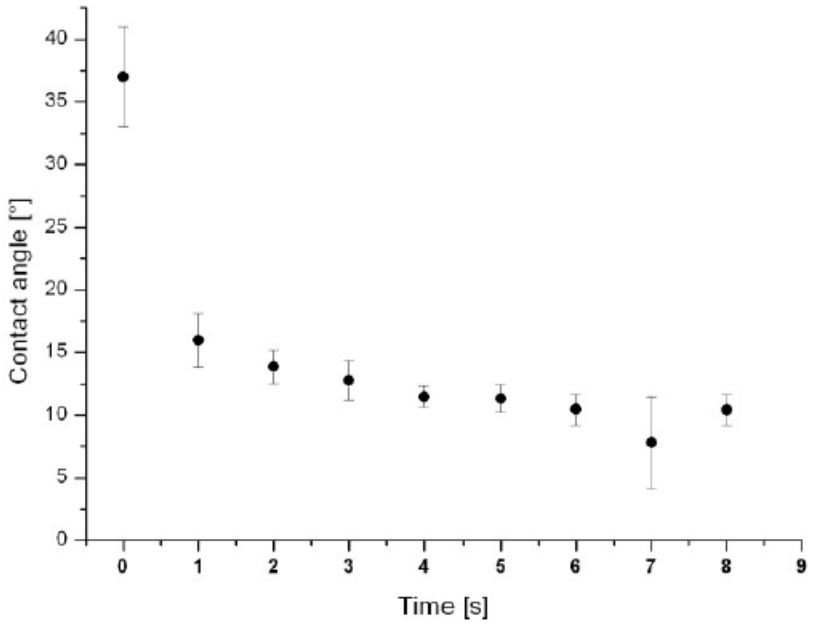

Figure 1: Effect of plasma exposure time on water contact angle. Glass samples of 200 cm^2 surface area was cleaned in ambient air at 2.5 W/cm^2 discharge power.

- ***extremely low energy consumption***

The energy consumption for the glass surface cleaning computed from the preliminary results in Fig. 1 of 5x10^3 W.sec /m^2 is of 1 to 2 orders less than in the case of the plasma jet cleaning with the corresponding reduction in nitrogen oxides and ozone generation.

Acknowledgement

This work was supported by VEGA grants No. 1/1011/04 and No. 1/4014/07.

References

[1] http://www.asymtek.com/news/articles/2005_12_advances_in_jet%20Dispensing_fpd.pdf
[2] http://www.samcointl.com/products/PC-1000.shtml
[3] H. Hermann et al., "Atmospheric Pressure Plasma Jet for Glass Processing", *Glass Processing Days* 2005, pp.1-3 - www.gpd.fi
[4] Changquan Wang, Xiangning He, "Preparation of hydrophobic coating on glass surface by dielectric barrier discharge using a 16 kHz power supply", *Applied Surface Science* (2005)
[5] http://www.apjet.com/aboutapjet.html
[6] http://www.semibank.net/nproduct/p_ap_apisf.html
[7] M. G. Mikhael, A.Yializis, Method and apparatus for applying material to glass, *USP Appl*. No. 20050045103

P 07

Conversion of Ethanol in Plasma of the Electrical Discharge in the Air Channel with Liquid Wall

V. Chernyak, V. Yukhymenko, Yu. Slyusarenko

Faculty of Radiophysics, Dept. of Physical Electronics, Taras Shevchenko Kyiv National University, Prospect Acad. Glushkova 2/5, 03127 Kyiv, Ukraine

e-mail: chern@univ.kiev.ua

Abstract

The results of researches of ethanol conversion in the electrical discharge with a liquid wall are presented in work. The emission analysis for investigation of discharge plasma was used. The mass-spectrometric technique for investigation of stable gas-core conversion products were used.

Introduction

Today one of the interesting applications of low-power (~ n *100 Wt) gas discharges is their use for plasma conversion of liquid fuels on vehicles for enrichment fuels by free hydrogen [1]. The conversion of ethanol in scantily investigated electrical discharges in the gas channel with a liquid wall is considered in this work [2].

Experimental set-up

Experimental set-up for reforming of liquid hydrocarbons is shown on Fig.1. It consists of a quartz tube from above tightly closed by a cover. The inner diameter of a quartz tube was 50 mm. Height of a tube was 100 mm. The discharge burned between the cylindrical copper cathode (∅ 5 mm, length 5 mm) and cylindrical molybdenum anode (∅ 1мм, length 5 mm). The cathode was located in end-wall glass tube with an inner diameter - 6 mm. The end -wall had an aperture with diameter - 3 mm. The volume of liquid was hold constant with the help of informed vessels system. The level of a liquid in a tube was 50 mm. The axis of electrode gap was on depth - 30 mm. On a tube with the cathode inlet the gas which formed the gas channel between the cathode and anode.

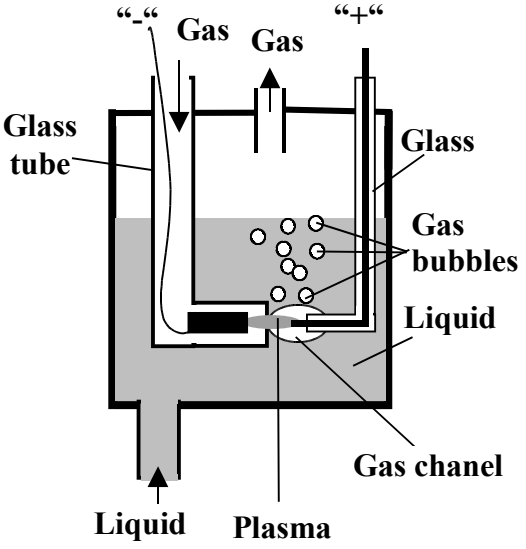

Fig.1. Experimental set-up.

Plasma radiation was measured by portable rapid PC-operated CCD-based multi-channel optical spectra analyser (MOSA), which has a wide wavelength survey (200-1100 nm) with spectral resolution (~0.75 nm).

The exhaust gas on polyethylene tube (inner diameter - 8 mm) was outlet in two consecutive condensers. The exhaust gases for the mass-spectrometric analysis were taken from the polyethylene channel through piezoelectric gate after cooling in condensers. Whole length of the outlet channel between an output from reactor and input in the mass - analyser was ~ 1 m..

The monopolar mass-spectrometer MX 7301 was used for the mass analysis. The pressure of residual gas in the analyser was not higher 5 10^{-6} torr. The pressure of gas in mass-spectrometer at the analysis of exhaust gases was 5 10^{-5} torr.

The argon and dry air were the gases which form the channel in a liquid. The flow of gas was 20 ml/s. The ethanol and mix of ethanol with water were treated liquids. The part of ethanol in a mix changed in a range 1/3 ÷ 1.

Results and discussion

The behaviour of volt-ampere characteristics of the discharge is essentially depends from the gas which forming the channel in a liquid. For Ar they had increasing character, for air from 100 up to 200 mA the plateau with the subsequent reduction of a voltage was observed at increase of a current.

The basic components of emission spectrum of plasma independently of a choice of gas which forming

the channel were the line of atomic hydrogen of a balmer series, lines of copper, band of molecules C_2, CN. At discharge currents ≥ 200 mA in a spectrum there were doublets of resonant lines natrium and potassium (components of a glass). At use of argon for formation of the gas channel in pure ethanol in a spectrum there was no radiation of OH. At the same time for mixes of ethanol with water independently of a choice of gas (Ar, air) and pure ethanol with the air channel there was a presence of radiation of OH.

The temperature of excited electron levels population (T_e) of H atoms slightly increases with discharge current increasing. Its value was nearly ≅ 0.4 eV under discharge current I=100 mA.

It was shown that increasing of quantity of water in a mix leads to the decreasing of hydrogen line H_a intensity. At the same time the relative share of hydrogen, in comparison with bands of C_2 and CN [2], considerably increases under practically constant temperature. At change of distillate concentration in a solution in a range from 0 up to 1 intensity of a hydrogen line decreases not considerably.

The main stable components of the exhaust gas of reactor were M/e = 2(H_2^+), 12 (C^+), 14, 16, 18 and 28 (CO^+ and N_2^+) under ethanol conversion. The presence of these components does not depend on choosing the gas, which creates the gas channel (Fig. 1, 2). Components of 40 (Ar^+) and 20 (Ar^{++}) appeared in mass-spectrum when Ar gas was used (Fig.2). A part of the hydrogen in mass-spectrum increases non-linear with increasing the discharge current and essentially increases with water adding.

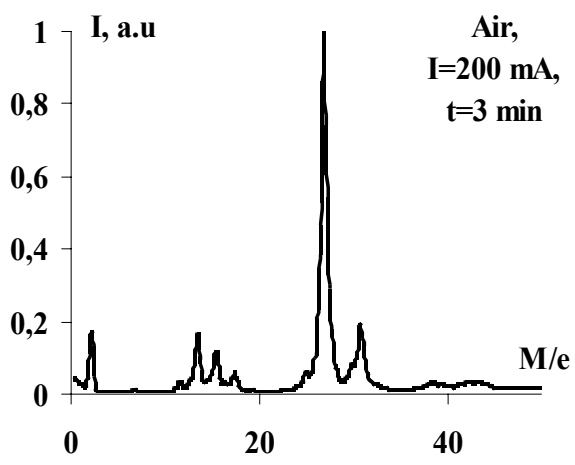

Fig. 2.

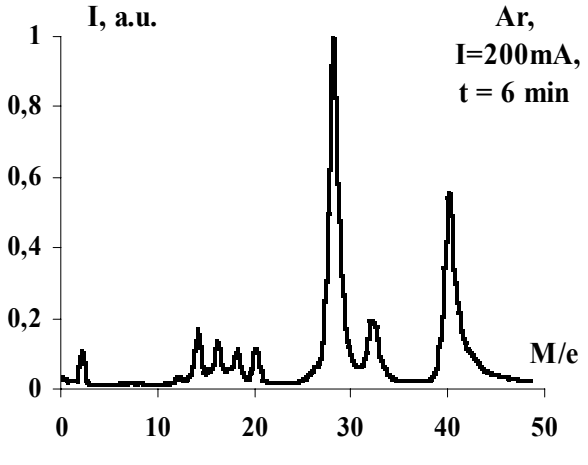

Fig.3.

Conclusions

- The behaviour of VAC of the discharge in gas channel with liquid ethanol wall essentially depends on gas, which creates the channel in liquid.
- The main components in emission spectra of plasma of this discharge are hydrogen H, copper Cu (material of electrodes) lines, molecular bands of C_2 and CN.
- Water adding into the ethanol leads to the increasing of hydrogen amount produced in the discharge.
- The main stable gas components in the outlet of the reactor are H_2, CO under ethanol conversion. The part of hydrogen is essentially increases under discharge current increasing.

References

[1]L. Bromberg, D.R. Cohn, A. Rabinovich, J. Heywood, *Emissions reductions using hydrogen from plasmatron fuel converters,* Int. Journal of Hydrogen Energy, v 26, (2001), pp. 1115-21 .

[2]Yu. Veremii, V. Chernyak, A. Trokhymchuk, Ya. Kondratyuk, V. Zrazhevskij, *Physicochemical properties of a plasma-liquid systems with an electric discharges in gas chanel with liquid wall,* Ukr. J. Phys., V.51, N8, (2006), pp.769-774.

P 08

Deposition of Thin TiO_x Layers Using Plasma Sources of Jet Types

M. Chichina[1,2], V. Straňák[1,2,3], O. Churpita[2], S. Kment[2], Z. Hubička[2], M. Tichý[1], P. Špatenka[3]

[1] Faculty of Mathematics and Physics, Charles University, V Holešovičkách 2, 180 00 Praha 8, Czech Republic

[2] Academy of Science of the Czech Republic, Institute of Physics, Na Slovance 2, 180 00 Prague 8, Czech Republic

[3] Department of Physics, University of South Bohemia, Jeronýmova 10, 371 15 České Budějovice, Czech Republic

e-mail: chichina@mbox.troja.mff.cuni.cz

Abstract

The contribution is focused on comparative diagnostics of deposited TiO_x thin films created by different plasma sources under different experimental conditions. The TiO_x layer were created from titanium isopropoxide vapours delivered into discharges zones of: **(i)** Ar/O_2 surfatron discharge, working at microwave frequency 2.45 GHz, operated at reduced pressure 200 Pa and **(ii)** He/N_2 pulsed RF driven barrier-torch discharge burning at open atmosphere. The layers were deposited on glass substrates and subsequently diagnosed by XRD before and also after thermal annealing and by AFM measurements.

Introduction

Low-temperature plasma is one of the essential tools in field of advanced technologies in biomedicine, microelectronic, micro-mechanics and other. Plasma produces energetic active species which can initiate physical changes or chemical reactions that can otherwise occur only with difficulty or not at all. Plasma deposition is one of the ways how to effectively replace ecologically unsuitable electrolytic coatings. Another advantage of plasma assisted deposition is the possibility to create layers of unique properties. Classical PVD deposition processes, e.g. using magnetron systems, are known for a long time. Hence, new PCVD (Plasma Chemical Vapour Deposition) processes, when a heterogeneous chemical reaction between plasma and one or more of the remaining three states of matter results in the deposition of thin film, are developed with great interest [1]. In our case the TiO_x layers were created using reaction of vapours of titanium isopropoxide and plasma generated by different ways - microwave and pulsed RF driven plasma sources.

Results and discussion

At first the TiO_x films were deposited by surfatron generated plasma generated with the microwave frequency 2.45 GHz. We used commercial (Sairem) surfatron and microwave generator 300 W (GMP 03). A quartz tube, 6 mm in inner diameter, was inserted into a surfatron cavity and working gas flew through it. The total flow rate of working gas mixture was kept with specific ratio 595 sccm of Ar and 5 sccm of reactive O_2. The vessel volume was pumped out by large rotary pump with the working pressure about 200 Pa. The microwave power was coupled from the surfatron cavity to the plasma via a thin slit and caused ionization of flowing gas in the quartz tube. Plasma created in this manner was sustained further downstream by a surface wave, which propagated along the plasma column [2]. Stable working conditions suitable for technological applications are mainly limited by pressure-power ratio, discussed in detail in [3]. The vapours of titanium isopropoxide were delivered into the plasma column and layer was deposited 60 minutes on glass

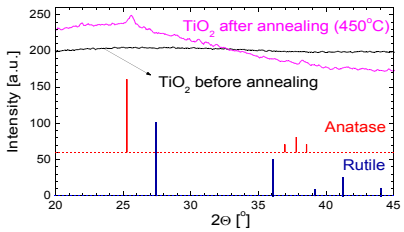

Fig.1. X-ray diffraction pattern of TiO_x (S) film on glass substrate and corresponding theoretical Anatase and Rutile patterns.

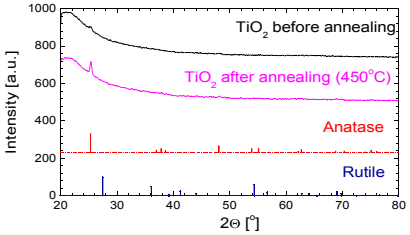

Fig.2. X-ray diffraction pattern of TiO_x (BTD) film on quartz glass substrate and corresponding theoretical Anatase and Rutile patterns.

substrate. Below in the text these layers are noticed as TiO_x(S) ; (S) = surfatron.

The atmospheric RF single barrier-torch plasma jet apparatus has been described in [4]. Plasma system excited by RF source worked in pulse modulated mode. The repetition frequency was 25.8 Hz with duty cycle 15%. The RF electrode was connected with the 13.56 MHz RF power generator (600W) via the matching unit. The ceramic nozzle with internal diameter 1.5 mm is surrounded by the stainless steel RF powered electrode. Titanium isopropoxide was placed into the container and kept at electronically stabilized temperature 47 °C. Precursor vapours were transferred into the plasma zone with help of working gasses (He 466 sccm and N_2 100 sccm). The layers were deposited 60 minutes on quartz glass substrate. Below in the text these layers are noticed as TiO_x(BTD) ; (BTD) = barrier torch discharge.

For understanding of the thin film structures we investigated the TiO_x thin films with help of X-Ray Diffraction (XRD) method, see Figs.1 and 2. X-Ray Diffraction analysis of TiO_x(S) thin films (Fig.1) showed that only the Anatase crystalline phase is present in films. Post-deposition annealing at temperature 450°C is required to produce the amorphous – Anatase transformation. The sloped part of the XRD spectra at lower Bragg angles is the effect of the amorphous substrate. In Fig. 2 it is shown that deposition using single barrier-torch discharge yields moderate amounts of Anatase phase already at room temperature.

Atomic force microscopy (AFM) technique allowed us to visualize surface structure of TiO_x thin films produced by both systems. The investigation was carried out in contact mode. Figs. 3 and 4 show AFM morphology of TiO_x(S) and TiO_x(BTD) thin films, respectively. The typical average surface roughness of TiO_x(S) films was about 50 nm and the size of patterns was around 5 μm; some grain-structure was observed. In case of BTD produced layer the average surface roughness was approximately 25 nm and the size of patterns was less than 1 μm; some voids were observed.

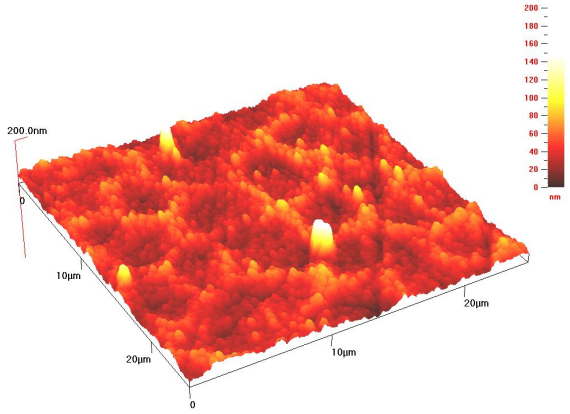

Fig.3. AFM morphology of surfatron produced TiO_x layer deposited at 200 Pa.

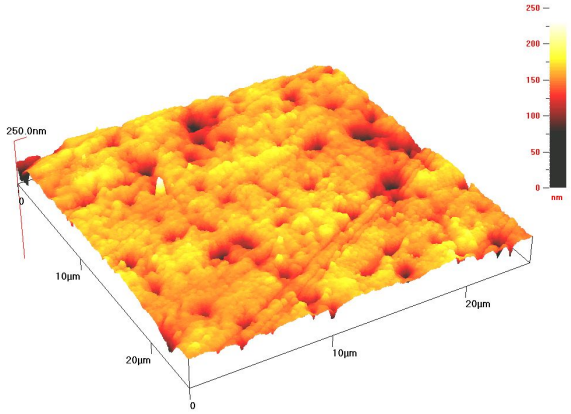

Fig.4. AFM morphology of barrier torch discharge produced TiO_x layer deposited at 100kPa.

Conclusion

The comparative investigation of TiO_x layers produced by different plasma sources – the microwave plasma source based on surfatron and the barrier torch discharge – was done. XRD measurements revealed Anatase crystalline phase in both cases. Morphology of surfatron produced layer structure measured by AFM showed higher roughness compared to that of BTD layer. On the other hand the surfatron produced layer seems to be more compact in comparison with that of BTD produced layer, which contains voids.

Acknowledgment

This work was financially supported by the research plan MSM 0021620834, financed by the Ministry of Education of the Czech Republic, and grants 202/05/2242 and 202/06/0776 of Czech Science Foundation.

References

[1] J. Roth, *Industrial Plasma Engineering* (Vol.2), IoP - Institute of Physics Publishing, Philadelphia, 2001.
[2] M. Moisan, J. Pelletier, *Microwave Excited Plasmas*, Elsevier, 1992.
[3] V. Straňák, P. Adámek, J. Blažek, M. Tichý, P. Špatenka, *Contrib. Plasma Phys*. 46, 5-6, (2006), 439.
[4] Z. Hubička, M. Čada, M. Šícha, et al, *Plasma Sources Science & Technology* 11, (2002), 195.

P 09

Visualization of Instabilities by Statistical Processing of Photographic Images of a Plasma Jet

O. Chumak, M. Hrabovsky

Department of Thermal Plasma Department, Institute of Plasma Physics
Za Slovankou 3, Prague 18200, Czech Republic

Summary

A statistical analysis of images of a plasma jet taken by a fast shutter camera was used for the visualization of a structure and stability of the jet. Short exposure time ensured imaging of the momentary state of the jet while analysis of a sequence of the images provided information on jet geometry and jet fluctuations. Frequency range of visualized instabilities was adjusted by the exposure time used for taking of the images.

A thermal plasma jet generated by a water stabilized arc plasma torch was studied. The slowest fluctuations are caused by an anode surface movement, they, however, have significant influence in the vicinity of the anode only. The most intensive fluctuations have frequency in the range 3.3 - 100 kHz. The plasma jet was investigated at different currents and anode positions.

Introduction

A common method of a generation of thermal plasma is driving of a plasma forming gas through a chamber where an arc burns. The gas heated and ionized by the arc flows out to an ambient atmosphere through a nozzle and forms plasma jet. The plasma jet is used to transfer energy to treated material in plasma spraying, melting, cutting, waste treatment technologies and so on. In order to describe a plasma process flow characteristics, like stability and structure, must be understood.

Short exposure photographic images of the plasma jet are used for giving of a conception about jet dynamics. A statistical analysis of the images of the plasma jet provides possibility for a simple description of the plasma jet. The set of the images can be used not only for evaluation of mean geometrical parameters of the jet but for characterization of plasma jet fluctuations.

Concept of the statistical image processing

Processing of an image set is schematically described by Fig. 1. The pictures demonstrate each step of processing and were obtained by application of the equations printed above them. All images are shown as

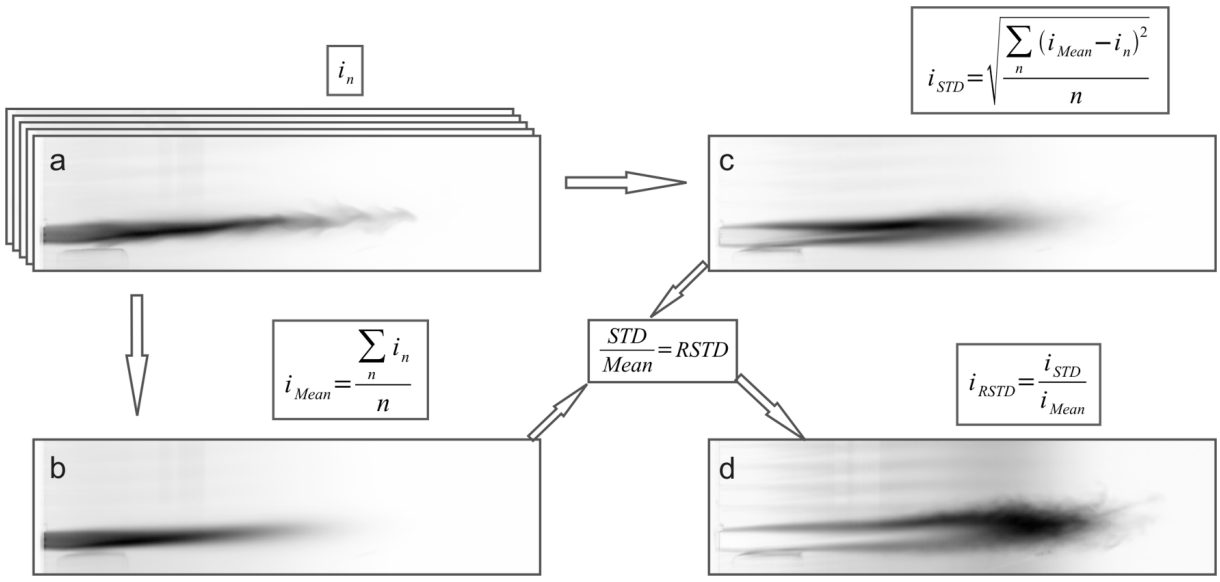

Fig. 1. Description of the statistical processing of the plasma jet images

negatives for better visibility.

The set of the photographic images of the plasma jet, taken without any synchronization, represents raw data (Fig. 1a). The mean jet image (Fig. 1b) is created by averaging of brightness in each pixel through the whole set of the images. The image of the standard deviation of brightness (STD image) is evaluated as the mean square deviation of brightness of each pixel of the whole set of the primary images (Fig. 1c). In the last step of the processing the standard deviation of brightness of each pixel is related to the average brightness value of the corresponded pixel. As the result (Fig. 1d) the image of distribution of relative standard deviation of brightness (RSTD image) was obtained. It is important to understand that an array of brightness of a particular pixel in all images of the set was evaluated independently in accordance with the equations. Mean jet image shows orientation and geometry of the plasma jet while the RSTD image visualizes plasma flow unsteadiness.

Example of experimental results

A thermal plasma jet generated by a water stabilized arc plasma torch was studied. The torch has an external copper anode which is visible on images as the block touching the bottom edge of the plasma jet (Fig. 2). Sequences of 500 plasma jet images were made with exposure times of 10 ms, 0.3 ms and 10 μs and RSTD images were evaluated (Fig 2a, b, c). An upper limit frequency of visualized fluctuations is inversely proportional to an exposure time and is approximately equal to 100 Hz, 3.3 kHz and 100 kHz for the images (a), (b), (c) respectively. Difference between image (b) and image (c) shows the fluctuations in the range from 100 Hz to 3.3 kHz (Fig. 2e). Difference between images (c) and (b) demonstrates fluctuations with frequencies limited in range 3.3 - 100 kHz (Fig. 2f).

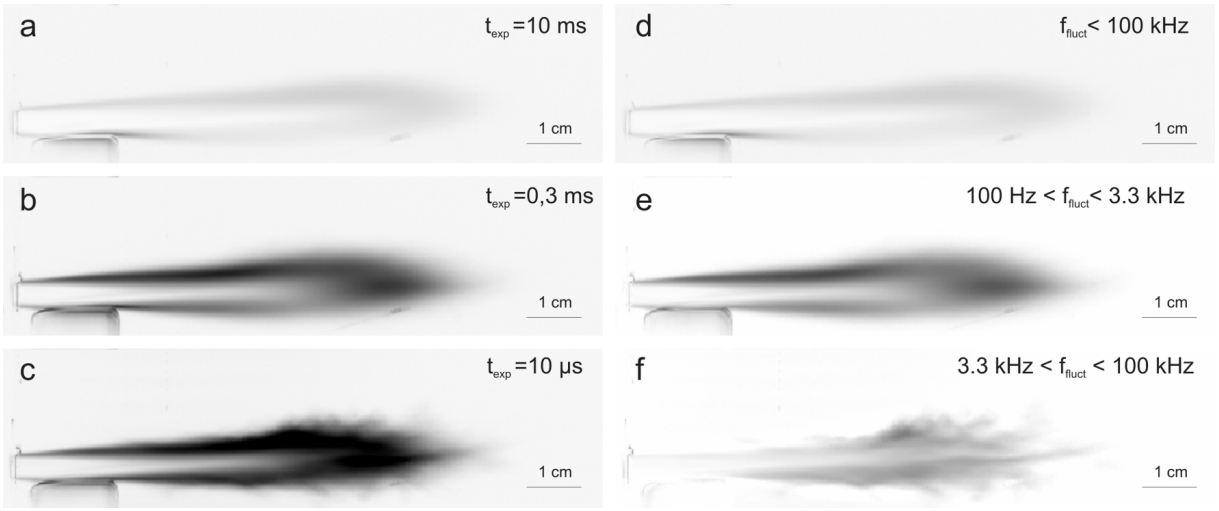

Fig. 2. Space distribution of the jet fluctuations in different frequency ranges

The first image (d) demonstrates the slow fluctuations caused by an anode surface movement which is known to have frequency of 50 Hz. The surface movement has considerable influence on the nearest part of the jet only, while downstream parts of the plasma jet are almost not affected.

The image in Fig. 2e shows fluctuations in the range 100 Hz - 3.3 kHz. It is the most contrasting among images (d)-(f) which means that in this frequency range the fluctuations are the strongest. The fluctuations on the anode surface are caused by the permanent displacement of the arc attachment on the anode surface. The particularly interesting phenomenon is the high intensity fluctuations at the top boundary of the plasma jet. They could be caused by the strong interaction of the plasma flow with ambient air as well as by an influence of the anode attachment.

Fig. 2f corresponds to fluctuations in the range 3.3-100 kHz. It turned out that 500 images were not enough for good visualization of these fluctuations. The differences in the image in Fig. 2e, however, are clear. The fastest fluctuations correspond to later development of the plasma jet. There are no fluctuations in the anode region and in the boundaries of the plasma jet. On the contrary, the fluctuations in the jet core prevail in the part of the jet from the nozzle exit to the end of the anode.

Acknowledgements

The work was supported by the Grant Agency of the Czech Republic under the project No. 202/05/0669.

P 10

The Influence of Emitting Layer on the Plasma Parameters of Atmospheric-Pressure Coplanar Barrier Discharge

J. Čech, P. Sťahel, M. Černák, A. Brablec

Department of Physical Electronics, Faculty of Science, Masaryk University, Kotlářská 2, 611 37 Brno, Czech Republic
e-mail: cech@physics.muni.cz

Abstract

The influence of emitting layer on the plasma parameters of coplanar barrier discharge in pure nitrogen or argon was studied. It was proved that the emitting layer composition has a significant effect on the discharge plasma properties. The vibrational temperature of 2^{nd} positive system of N_2 as a function of power dissipated in discharge and emitting layer composition was also calculated. The effect of emitting layer's roughness on the discharge properties was tested.

Introduction

The usefulness of atmospheric-pressure barrier discharges rises with rising demands on on-line, low-cost and environmental-friendly material plasma processing. Up to the present days many geometries and electrode configurations of atmospheric-pressure barrier discharges were used for plasma processing with various success. As the promising one planar configuration called Diffuse Surface Coplanar Barrier Discharge (CBD) was invited [2,3,5]. The energy efficiency of CBD plasma treatment as well as the overall quality of this treatment can be improved even optimized by the modification of dielectric barrier of CBD.

In this work the CBD in pure nitrogen or argon was studied. The variations of ignition, resp. extinction voltages of CBD for different emitting layers were measured. As the emitting layer these layers were used: bare alumina (Al_2O_3), N^+ dopped alumina, BaO and TiO_2, with RMS roughnesses of 0,5 ± 0,1 μm. For each emitting layer the vibrational temperature variations were estimated from 2^{nd} positive system of N_2 (Δ=-2) as the function of power dissipated in the discharge [1]. The effect of surface roughness on the ignition and extinction voltages was tested on bare alumina dielectric plates of roughnesses 0,5 μm and 1,8 μm.

Experimental

The experimental apparatus consisted of discharge electrode system (DES) in reaction chamber, power supply unit and diagnostic instruments. The DES was made of alumina plate (Al_2O_3) of 96% purity 0,5 mm thick with one surface serving as the emitting layer – coated or uncoated. From the other side of the plate the system of copper coplanar electrodes was placed. The distance between the electrode tips was set to 2,4 mm and fixed. For the voltage measurements narrow electrodes with round tips (5 mm in diameter) were used. For spectroscopy and photography of the discharge plasma a 30 mm wide electrodes with straight tips were used. The electrodes were dipped in insulating transformer oil bath. The reaction chamber's dimensions were 80x80x30 mm. The flow rate of 6 slpm of nitrogen, resp. 3 slpm of argon was kept in all experiments. The discharge was powered by high voltage (HV) power supply unit with frequency 8.5 kHz.

The emitting layer of alumina was modified by means of deposition of BaO or TiO_2 layer or nitrogen implantation. The roughness of alumina surface was modified by means of sand-blasting.

Electrical parameters were measured by a digital oscilloscope HP 54820A Infinium. Dissipated discharge power was then estimated from the HV current and voltage time evolution measurements. The spectra were recorded with monochromator Jobin-Yvon Triax 550 (grating 1200 gr/mm) equipped with liquid nitrogen cooled CCD detector. The vibrational temperature was calculated from the bands of second positive system of nitrogen (heads 0-2, 1-3, 2-4 and 3-5). Discharge images were taken by digital camera Olympus C-5050.

Results and discussion

Table 1 shows the variation of ignition voltage and extinction voltage amplitudes with respects to different emitting layers for pure nitrogen, resp. argon as a working gas. It is clear that the emitting layer influenced the ignition and/or extinction voltages. Most clearly for N^+ dopped alumina. The BaO and TiO_2 layers were able to reduce both ignition and extinction voltages, compared with uncoated alumina. In the case of N+ dopped alumina and roughened alumina both voltages increased. However it is interesting to look at the spatial behavior of the discharge plasma on different emitting layers, as it is shown on Fig. 1. Each picture was taken at approx. same excitation voltage amplitude of 15 kV and exposure time 1/25 s. One can see, that for BaO, resp. N^+ dopped alumina the inter-electrode part of plasma became much more dense, as

well as above-electrode diffuse part, that was much more extended over the electrodes in comparison with uncoated alumina. In the case of TiO_2 layer the geometry of the discharge plasma had completely changed.

gas / emitting layer		Al_2O_3	BaO	$N^+Al_2O_3$	TiO_2	roughened Al_2O_3
Argon	$U_{i\,max}$ [kV]	4,21 ± 0,13	4,24 ± 0,08	4,87 ± 0,07	5,23 ± 0,12	4,50 ± 0,11
	$U_{e\,max}$ [kV]	1,93 ± 0,05	2,04 ± 0,04	2,315 ± 0,04	2,31 ± 0,04	1,98 ± 0,04
Nitrogen	$U_{i\,max}$ [kV]	15,97 ± 0,08	15,62 ± 0,06	17,14 ± 0,05	15,58 ± 0,10	16,49 ± 0,05
	$U_{e\,max}$ [kV]	13,50 ± 0,07	13,28 ± 0,09	14,72 ± 0,09	13,36 ± 0,08	14,24 ± 0,05

Tab.1: Table of ignition and extinction voltage amplitudes for different emitting layers and gas compositions.

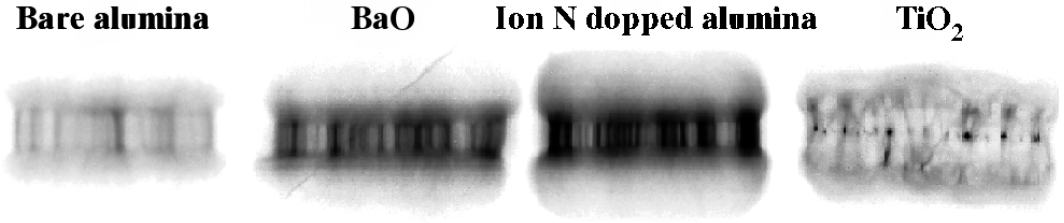

Fig. 1: Inverted images of the CBD burning above different emitting layers (U_{max}~15 kV).

The vibrational temperatures estimated as specified above increased linearly with the dissipated discharge power at least in the measured interval of 3-12 W (that is 1-4 W per cm of electrode length). The slope of the increase was highest for the BaO layer as well as the final temperature. The lowest slope and final temperature was obtained using TiO_2 layer. The linear fit regression coefficients of dependence of vibrational temperatures on dissipated discharge power is summed up in table 2.

	a [K]	Δa [K]	**b [K/W]**	Δb [K/W]	R	SD
Al_2O_3	**1971**	32	**53**	4	0,98	18
BaO	**1923**	26	**65**	3	0,99	18
Ion N^+	**2081**	43	**41**	9	0,85	31
TiO_2	**2103**	19	**16**	3	0,87	15

Tab. 2: Table of linear fit regression coefficients of vibrational temperatures vs. dissipated discharge power.

Conclusions

The influence of surface emitting layer's composition on the plasma properties and ignition as well as extinction voltages has been proved. It also has been shown that the vibrational temperature increases with increasing input power, and is dependent on emitting layer composition. Furthermore the emitting layer composition affects not only plasma parameters as vibrational temperature and discharge filament/diffuse ratio, but also the structure of the discharge. It turned out, that the surface layer roughness has an effect on the

Acknowledgement

This research has been supported by the grant No. 202/05/0777, Grant Agency of Czech Republic and Long-term intent project No. MSM0021622411, Ministry of Education, Czech Republic.

References

[1] J. Čech, A. Brablec, P. Sťahel and M. Černák, *Czechoslovak Journal of Physics, Vol.* 56 (2006) *Suppl.* D p. B1074-B1078
[2] M. Šimor, J. Rahel, P. Vojtek, A. Brablec, M. Černák: *Appl. Phys. Lett.* 81 (2002), p. 2716–2718
[3] M. Cernak, J. Rahel, D. Kovacik, M. Simor, A. Brablec, P. Slavicek: Contrib. Plasma *Phys.* 44 (2004) p. 504–507
[4] V.I. Gibalov, G.J. Pietsch: *J. Phys. D: Appl. Phys.* 37 (2004), p. 2093–2100
[5] M. Černák: *International Patent Application No. PCT/SK02/00008* (9 May 2002)

P 11

Chemical Compositions of Polypropylene Surfaces after Activation in Atmospheric–Pressure Air and Nitrogen Plasmas

Ľ. Černáková[1], A. Tóth[2], M. Černák[3], K. Kunovská[1]

[1]Institute of Polymer Material, Slovak University of Technology, Radlinského 9, Bratislava 812 37, Slovakia

[2]Institute of Materials and Enviromental Chemistry, Hungarian Academy of Sciences, Pusztaszeri út 59-67, Budapest H-1025, Hungary

[3]Department of Plasma Physics, Comenius University, Mlynská dolina, Bratislava 842 45, Slovakia

e-mail: ludmila.cernakova@stuba.sk

Abstract

Diffuse Coplanar Surface Barrier Discharge (DCSBD) burning in atmospheric-pressure nitrogen or air has been used for activation of polypropylene nonwoven (PPNW). The aim was to compare the chemical compositions of nitrogen and air plasma treated surfaces before subsequent immobilization of biomolecules like chitosan. The X-ray photoelectron spectroscopy was used for surface analysis. It was found that nitrogen plasma treatment resulted in relatively high oxygen incorporation about 9 atomic % and about 4 atomic % of nitrogen.

Introduction

Plasma modifications of polymer surfaces, particularly functionalization or plasma polymerization with functional group-carrying monomers are useful techniques to adjust the hydrophilicity, adsorption, and wetting properties of polymeric surfaces.

One of the major limitations of plasma technologies is the diversity of functional groups produced by the multitudes of chemical reactions that occur in the plasma. The plasma causes various homolytic bond fissions and ionization events, as well as secondary collisions. Subsequent molecular fragmentations, reactions, and ionizations processes result in spread of functionalities on the plasma treated or polymerized surfaces [1]. More controlled surface chemistries can be performed by grafting [2] or immobilization [3] a well defined chemical species onto a plasma activated surfaces. The identification and quantification of chemical groups at plasma treated surfaces defines the success of subsequent steps such as the immobilization .

Results and discussion

XPS was used to analyse the changes of chemical compositions on the polypropylene surface after activation by DCSBD at atmospheric pressure. Table 1 shows quantitative atomic percentage concentration of PPNW after the plasma treatment in air and nitrogen.

Table 1 Surface composition of the untreated and plasma treated polypropylene samples

Samples	C at %	O at %	N at %	O/C	N/C
PPNW untreated	98,3	1,7		0,02	
PPNW air plasma treated	90,0	8,3	1,7	0,09	0,02
PPNW nitrogen plasma treated	87,5	8,7	3,8	0,10	0,04

In both cases the plasma treatment significantly increased the O/C ratio from 0,02 to 0,10 what confirmed that polar functional groups containing oxygen were introduced on the PPNW surface.

In addition, the incorporation of nitrogen atoms was observed. In the nitrogen plasma activated samples

Samples	C at%	O at %	N at%	O/C	N/C
PPNW untreated	98.3	1.7		0.02	
PPNW air plasma treated	90.1	8.3	1.7	0.09	0.02
PPNW nitrogen plasma treated	87.5	8.7	3.8	0.10	0.04

the atomic percentage concentration of nitrogen was about 3,8 % i.e., roughly two times higher than in air. The oxygen content was higher than nitrogen content when both air and nitrogen were used as the plasma gas.

Conclusions

XPS analysis confirmed that in the nitrogen plasma treated samples the oxygen content is similar to that in polypropylene samples activated in air, but the chemical state of oxygen is different. The built in oxygen in this case was mainly in aliphatic C=O type bond, while in the air treated samples mainly in aliphatic C-O type bond.

References

[1] K.S.Siow, L.Britcher, S.Kumar, H.J. Griesser, *Plasma Processes and Polymers*, 3 (2006) 394.
[2] Ľ.Černáková, D.Kováčik, A.Zahoranová, M.Černák, M.Mazúr, *Plasma Chemistry and Plasma Processing* 25 (2005) 427
[3] Ľ.Černáková, K.Kunovská, D.Klimová, M.Mikulášová, Chitosan Coated Polypropylene Nonwoven with Antibacterial Properties, 3rdInternational Textile, Clothing&Design Conference, Dubrovnik, Croatia, 2006

P 12

Study of Plasma-Solid Interaction in Electronegative Gases

P. Černý[1], S. Novák[1], R. Hrach[1,2]

[1]Department of Physics, Faculty of Science, J. E. Purkinje University, České mládeže 8,
Ústí nad Labem 400 96, Czech Republic
[2]Faculty of Mathematics and Physics, Charles University, V Holešovičkách 2, 180 00 Prague 8, Czech Republic
e-mail: pav.cerny@email.cz

Abstract

In the paper we study low-temperature plasma-solid interaction using computer simulations. A one-dimensional model was created. It includes neutral atoms, electrons, positive argon ions Ar^+ and negative oxygen ions O^-. The main interest is paid to the development of the sheath in dependence on the concentration of the oxygen ions, in both, the steady and the dynamic state.

Introduction

The understanding of processes of plasma-solid interaction in low-temperature plasma is important for plasma-chemical technologies, as well as for probe diagnostics**.** Unfortunately, it is very difficult to find out and fully describe all of the processes and mechanisms that take place. The charged particles in the plasma are influenced by the intensity of the electric field at the solid surface immersed into the plasma. Due to this field, the energy of the particles changes and a so-called sheath appears. Recently it is shown, that the best and also the cheapest way to the understanding of this processes, is by computer simulations.

There are different ways how to simulate these processes. One of them is fluid modeling. With this kind of simulation we are able to study the plasma-solid interaction and obtain results (e.g. the distribution of the particle concentration, the intensity of the electric field). On the other hand, if we want further information concerning the charged particles, e.g. the energy distribution, etc. it is better to use particle-based computer simulations. The disadvantage of these methods is their higher time consumption. Another possible approach are hybrid methods, which combine continuous and particle modeling.

Using one of these techniques we can describe the behavior of charged particles for example by kinetic equations, or by using deterministic (Particle-in-Cell, PIC) or stochastic methods (Monte Carlo, MC). These methods are used to study the static as well as the dynamic state.

Computer experiment

In our laboratories we have developed several particle models of plasma-solid interaction, both self-consistent and non self-consistent. Models are based on the combination of deterministic molecular dynamics simulation of the movement of charged particles in both external and local electric fields, as well as stochastic Monte Carlo simulation of interactions of charged particles with neutral ones in plasma, i.e. on the PIC-MC simulation technique.

The particle model of plasma-solid interaction consists of the following parts:

- Source of particles: undisturbed plasma consisting of electrons, positive argon ions and argon atoms, negative oxygen ions and oxygen atoms
- Interactions: elastic collisions for electrons, elastic collisions and charge transfer interactions for ions.
- Trajectories of particles: between scattering simulated by the molecular dynamics method (Verlet velocity scheme)
- The scattering simulated by the Monte Carlo method and force calculations by the standard PIC-MC [1] technique in NGP modification.

Advanced computational techniques are used.

In the present contribution the results derived for electronegative plasma (O_2/Ar gas mixture) are presented. The input data was obtained from the literature [2].

Results and discussion

The simulation of plasma-solid interaction was performed for cylindrical probes of various radii. From the one-dimensional model a lot of useful results were achieved. In Fig.1, there is a distribution of the concentration of charged particles for the stable state in the sheath and pre-sheath area in fully electronegative plasma. Along that we obtained the energy and velocity distribution of the charged particles

in the proximity of the probe, the distribution of the potencial and the concentration of the particles in dependence on the fraction of negative ions in the plasma.

The main interest was paid to the dynamic state, whereat a rectangular signal at frequency of 1MHz on the electrode was used. From this we obtained information about the forming of a stable dynamic state (current plots of the particles are in Fig.2).

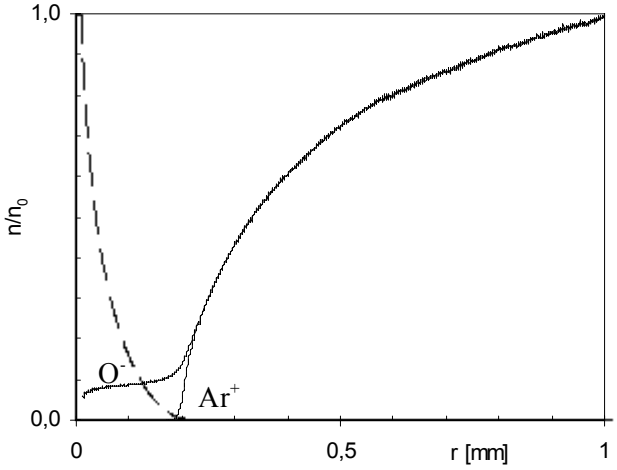

Fig. 1: Spatial distributions of charged species (solid lines) in the vicinity of cylindrical probe in electronegative plasma (oly negative and positive ions). Voltage bias +10 volts, radius of the probe 100 μm. By dashed lines is marked the distribution of electric potential in the sheath.

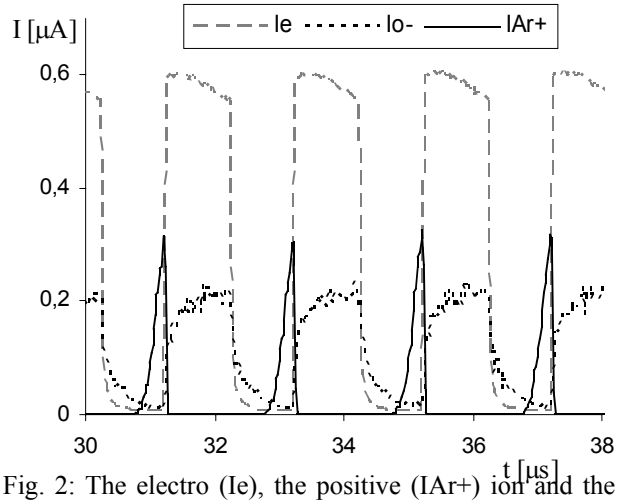

Fig. 2: The electro (Ie), the positive (IAr+) ion and the negative ion (Io-) current at the steady state. The values of the positive and negative ion current are multiplicated by the foctor of 250. The voltage changes with a frequency of 1MHz.

It is very time consuming to reach a steady state of the dynamic processes, especially for electronegative plasma (Fig. 2), where the negative ions cause the restraint, because of their small mobility. As you can see in Fig. 2, the negative ions reach the probe as well in a repulsive electric field, which is caused by the energy gained from the previous state at a positive bias, and so they can overcome the repulsive electric force. As you can see there is a difference in the behavior of positive (steeply descending at +10V) and negative (slowly descending at -10V) ions. This difference is caused by using different collision processes. The collision processes for oxygen at such low energies are not easily available and they are rather complicated. This problem has to be studied further.

Acknowledgements

The authors acknowledge the support of the Ministry of Education of Czech Republic-Projects COST OC 143 and LC 06041.

The author P. C. thanks to support of Glaverbel a.s.

References

[1] R. W. Hockney, J. W. Eastwood: *Computer Simulation Using Particles*, Hilger, Bristol 1988.

[2] S. C. Brown: *The Fundamental Data on Electrical Discharges in Gases, in Basic Data of Plasma Physics*, New York: AIP Press, 1994

P 13

Influence of Methane on Capacitively Coupled Oxygen Discharge

V. Doležal, P. Dvořák, J. Janča

Department of Physical Electronics, Masaryk University, Faculty of Science, Kotlářská 2, Brno, Czech republic
e-mail: vojta@physics.muni.cz

Abstract

In this work the mixture of oxygen and a small amount (0-5%) of methane was studied. The measurements were carried out in low-pressure (6.5 Pa) capacitively coupled radio frequency (RF) discharge. Positive ions and neutral particles were detected by mass spectrometer and ion energy analyzer.

O_2^+ was the dominating ion in the discharge. Its amount was significantly decreased when a small amount of methane was added. H_3O^+ and carbon containing ions as $C_2H_7^+$, CHO^+ ($C_2H_5^+$), CH_3^+ and CO^+ were consequently detected ions. The flux of neutral particles were composed of dominant O_2 which decreased with increasing amount of methane, and expected important product species as H_2O, CO_2 and CO.

Motivation

The focus of our studies lies in the changes of physical and chemical properties of a discharge in a main gas when we add small amount of another gas. In our previous paper we studied composition of capacitively coupled hydrogen plasma with small amount of methane [1]. Because we want to determine reaction constants between oxygen atom and hydrocarbons by flowing afterglow technique by means of Electron Spin Resonance technique [2], we would like to know more about how the admixture of methane changes the reactions and relative representations of species in the oxygen plasma. Such mixture of gases in low pressure RF plasma is not well investigated in literature due to the weak use in industry. The most comprehensive study till now is [3].

Experimental

The experiments were carried out in a spherical (i.d. approx. 33 cm) stainless steel reactor with two horizontally mounted, parallel, stainless steel electrodes of 80 mm diameter. The upper electrode, embedded in a grounded ring, was driven at the frequency of 13.56 MHz. The bottom electrode was grounded. Their distance was 40 mm. The reactor was evacuated by a turbomolecular pump backed by a membrane pump.

The plasma parameters were measured as functions of the relative methane flow rate. The total pressure was kept at a constant value of 6.5 Pa, the flow rate of methane varied within the range 0 - 0.5 sccm, the flow rate of oxygen within the range 10.4 – 10.0 sccm. The measurements were done for constant RF power of 35 W. The DC self-bias on the powered electrode was approximately -220 V demonstrating an asymmetric nature of the discharge due to grounded reactor parts.

The amount of positive ions and neutral particles flowing from the plasma were measured by Balzers Plasma Process Monitor PPM 421 (mass spectrometer with ion energy analyzer). The PPM was mounted parallel to the electrodes and its grounded extraction hood was placed at as the same height as the discharge center, 15 mm outside the space between the electrodes.

Results and discussion

The measured flux of neutral particles were composed of dominant O_2 , CH_4 (which we cannot distinguish from atomic oxygen O in the mass spectrum) and stable product species as H_2O, CO_2 and CO. Molecular oxygen partial pressure decreases immediately by a factor approx. 1.7 when methane was added.

In our experiment, where the neutral gas consists mainly of oxygen, the ion flux was dominated by O_2^+. Total ion flux steeply decreased when we added a small amount of methane. After that the total ion flux was nearly the same. Increasing methane gas flow results in an increase of the CH_4 partial pressure in the plasma. This also changes the ion flux, where we observed significant increase of H_3O^+ and carbon-carrying ions start to play significant role.

Up to the 3 % of the relative methane flow rate were the ion fluxes of CH_3^+ , COH^+ ($C_2H_5^+$) and $C_2H_7^+$ nearly the same. After that point exponentially growing $C_2H_7^+$ started to be dominant carbon-carrying ion.

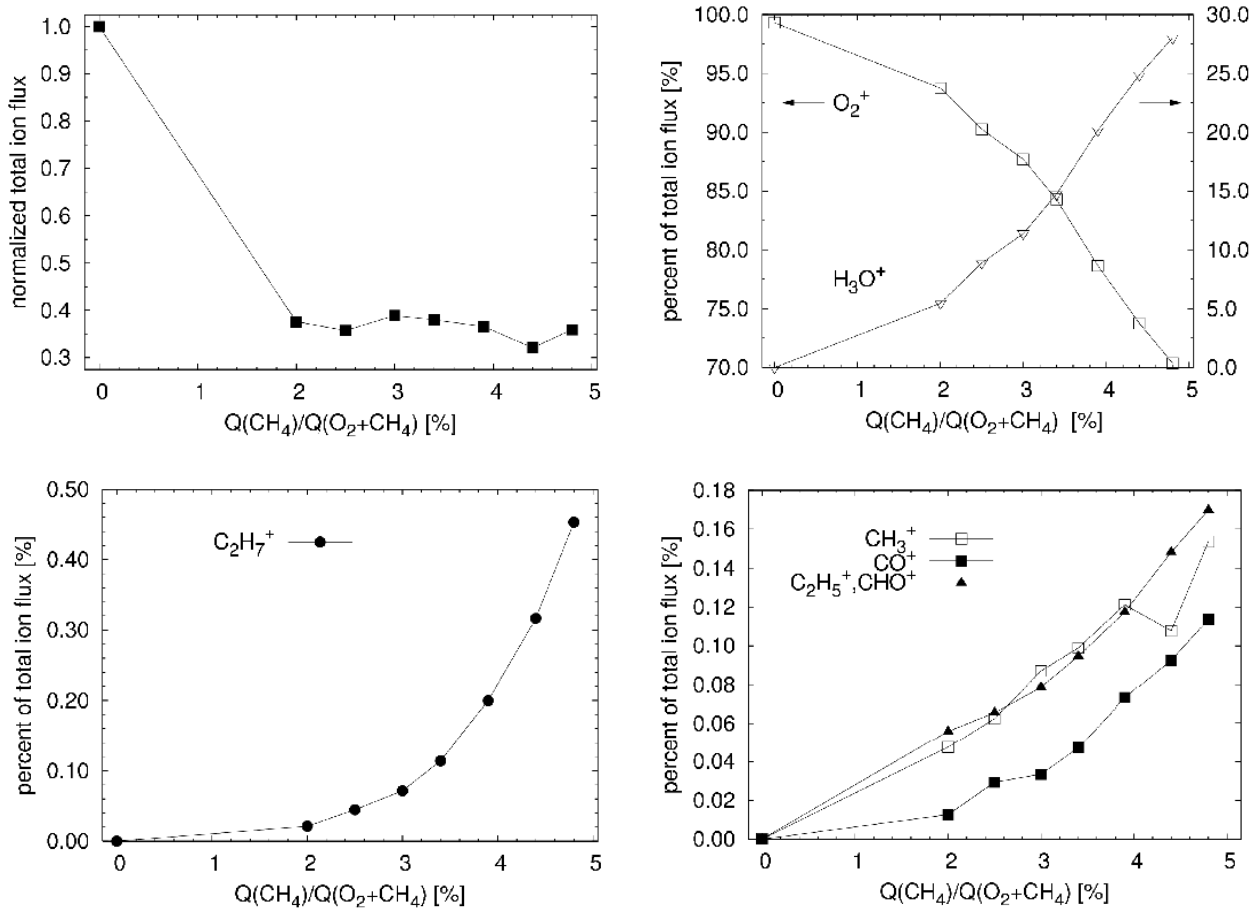

Fig. 3: Dependence of fluxes of main ions on the relative methane flow rate added to the discharge. P = 35 W, p = 6.5 Pa.

This shows important role of higher hydrocarbons in our experimental conditions. Even the ion C_3H^+ was detected. For heavier molecules it is rather difficult to derive the exact production channel. However, for lighter molecules, we suggest following reactions. CH_3^+ is the electron impact ionization product of CH_4. CHO^+ is created e. g. by the reaction $CH_3^+ + O \rightarrow CHO^+ + H_2$. Creation of $C_2H_5^+$ should be by the reaction between methyl ion and methane.

Acknowledgment

The present work was supported by grant GAČR 202/H3/162 and MSM 0021622411.

References

[1] V. Doležal, P. Dvořák, J. Janča, *Czechoslovak Journal of Physics B,* 56 (2006) 697
[2] V. Kudrle, V Doležal, A. Tálský, J. Janča, *Plasma Proc. and Polymers,* Wiley & VCH (2005) 95
[3] C. Busch, *PhD Dissertation* Ruhr University, Bochum (1999) 106-111

P 14

Production of Ozone and Hydrogen Peroxide Using the Hybrid Pulsed Streamer Discharge in the Water and to the Water Surface

M. Dors, E. Metel, J. Mizeraczyk

Centre For Plasma And Laser Engineering, The Szewalski Institute Of Fluid Flow Machinery
Polish Academy Of Sciences, Fiszera 14, 80-231 Gdańsk, Poland
e-mail: mdors@imp.gda.pl

Abstract

The production of strong oxidizers, such as ozone (O_3) and hydrogen peroxide (H_2O_2) has an application in a degradation of aqueous contaminants. Those processes have been studied for many years and are depended on kinds of discharge, reactor, power supply and solution [1,2]. Our previous investigations were conducted with two kinds of discharge, DC positive corona discharge to the water surface and pulsed positive streamer discharge in the water, with using distilled and phenol polluted water.

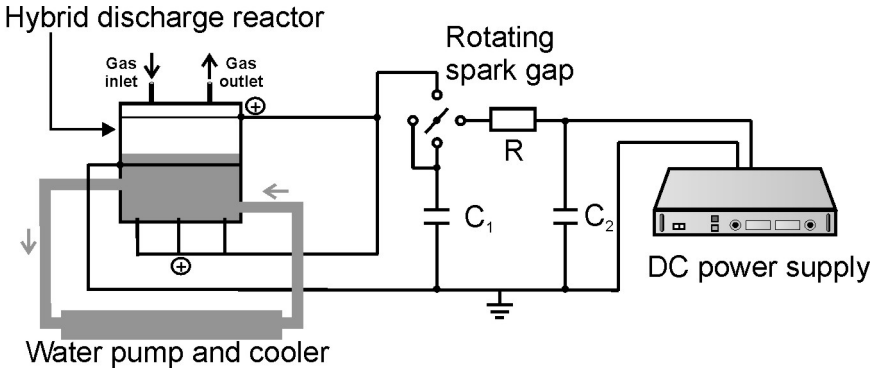

Fig. 1. The experimental setup.

In this work the production of ozone and hydrogen peroxide during the hybrid pulsed streamer discharge in the water and to the water surface is presented. The liquid phase pulsed streamer discharge was generated between three stressed stainless steel needle electrodes and the grounded stainless steel rod (the diameter of 4 mm) with electrodes distance of 60 mm (Fig. 1). The second high voltage wire electrode (diameter of 1 mm), giving the gas-phase discharge, was suspended 40 mm above the water surface. The reactor was filled with the water of different conductivity with and without phenol (0.62 mM). The water was either distilled or tap water. Conductivity of the water was varied in the range 0-200 μS/cm by addition of NaCl to the distilled water or using the tap water (conductivities 510 μS/cm and 700 μS/cm). Over the water surface dry air was flowing with a flow rate of 1 l/min. The positive high voltage pulses up to 58 kV were applied to electrodes from a discharge capacitor C_1 (2 nF) which was charged from DC power supply through a resistor (10 kΩ) and storage capacitor C_2 (22 nF). The repetition rate of the streamer pulses was 50 Hz.

The results of investigations showed that water conductivity influences H_2O_2 and O_3 production. In distilled water of conductivity 0 μS/cm the production of hydrogen peroxide was increasing with processing time up to 2.3 mM and was higher than in the water with higher conductivity (2.0 mM and 0.7 mM at 200 μS/cm and 510 μS/cm (tap water), respectively (Fig. 2a)). The same effect was reported by other researches [3,4]. The similar dependency was observed when phenol polluted water was used. Then the concentration of hydrogen peroxide was increasing with the processing time, but reached only 1.9 mM, 1.4 mM and 0.6 mM at conductivity of 6 μS/cm, 200 μS/cm and 700 μS/cm (tap water), respectively (Fig. 3a). The lower concentration, in this case, indicate the partial conversion of H_2O_2 to OH radicals, which react with phenol, causing its oxidation.

The gas-phase discharge produces gaseous ozone, which diffuse to aqueous phase. The increase of water conductivity decrease ozone concentration. In the distilled water with conductivity of 0 μS/cm and 200 μS/cm was observed high growth of O_3 concentration during 10 min of processing time up to 0.09 mM and after 10 min the concentration increased gradually up to 0.13 mM and 0.12 mM, respectively (Fig. 2b). Concentration of O_3 in the tap water increased linearly and it was lower than in the distilled water due to the high conductivity and pH, which was 7.4. The addition of phenol to distilled water give the same effect like in pure water but the concentration of ozone is a little higher, i.e. up to 0.15 mM and 0.14 mM at 6 μS/cm and 200 μS/cm, respectively (Fig. 3b). The reason can be the higher acidity of the water, which enhance

ozone diffusion from the gaseous phase. In the case of phenol-polluted tap water no ozone was found in the aqueous phase probably due to the high pH (7.6), at which ozone solubility in the water is weak.

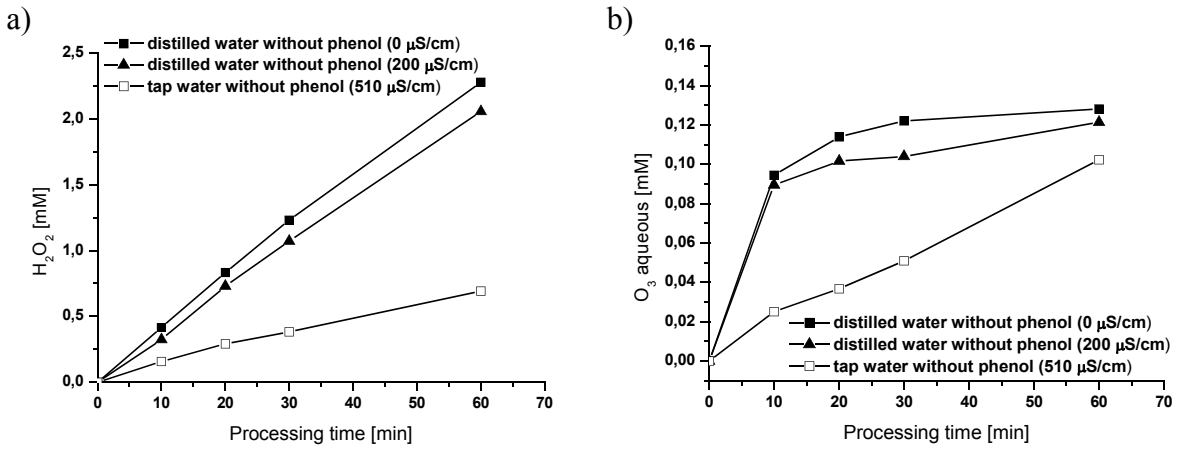

Fig. 2. The concentration of hydrogen peroxide (a) and ozone (b) in the distilled water of conductivities 0 μS/cm and 200 μS/cm and in the tap water of conductivity 510 μS/cm. The pulse properties: voltage 58 kV, 49 kV, 47 kV; current 1.8 A, 28 A, 35 A, FWHM of voltage pulse 18 μs, 2 μs, 1 μs, for conductivities of 0 μS/cm, 200 μS/cm, 510 μS/cm, respectively. Gas flow rate 1 l/min.

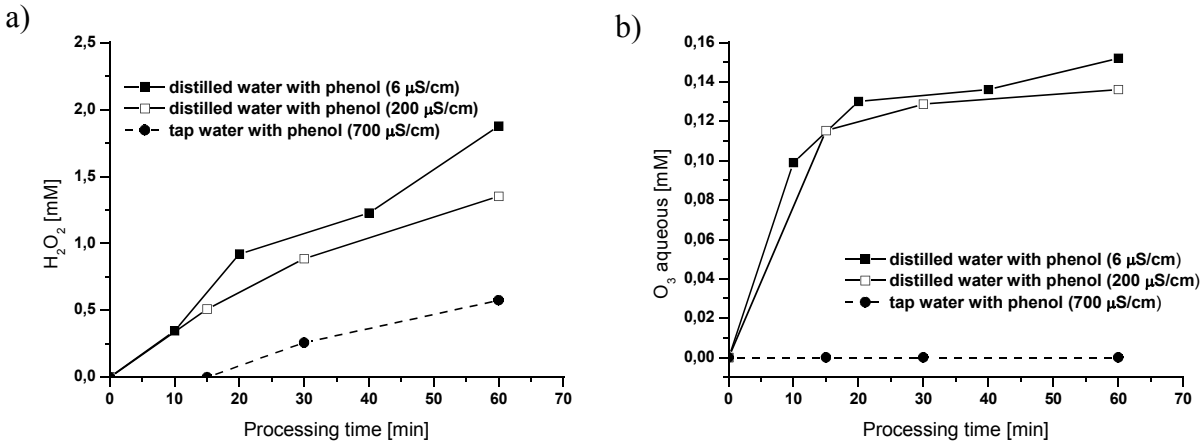

Fig. 3. The concentration of hydrogen peroxide (a) and ozone (b) in the phenol polluted distilled water of conductivities 6 μS/cm and 200 μS/cm and tap water of conductivity 700 μS/cm. The pulse properties: voltage 38 kV, 55 kV, 53 kV; current 2 A, 28 A, 30 A, FWHM of voltage pulse 8 μs, 2 μs, 1 μs, for conductivities of 6 μS/cm, 200 μS/cm, 700 μS/cm, respectively. Initial phenol concentration 0.62 mM. Gas flow rate 1 l/min.

References

[1] B.R. Locke, M. Sato, P. Sunka, M.R. Hoffman, J.-S. Chang, *Ind. Eng. Chem. Res.*, 45 (2006) 882-905.
[2] P. Lukes, B. Locke, *J. Phys. D: Appl. Phys.* 38 (2005) 4074-4081.
[3] M.J. Kirkpatrick, B.R. Locke, *Ind. Eng. Chem. Res.*, 44 (2005) 4243-4248.
[4] M. Sato, T. Ohgiyama, J.S. Clements, *IEEE Trans. Ind. Appl.*, 32 (1996) 106.

P 15

Hydrogen Dissociation Degree in Capacitively Coupled Discharge

P. Dvořák, J. Janča

Department of Physical Electronics, Masaryk University, Faculty of Science, Kotlářská 2, Brno, Czech republic
e-mail: pavel@chemi.muni.cz

Abstract

Results of optical emission spectroscopy of hydrogen low-pressure capacitively coupled RF discharge are presented. It was shown, that the dissociation degree of hydrogen molecules in the discharge was between 0.3 and 0.5 and it was sensitive to the sheath voltages. Further, the plasma temperatures were measured.

Introduction

Low-pressure capacitively coupled discharges have found their application in many branches of science and industry. This work focuses on the hydrogen discharge. Hydrogen plasma usually has a strong reduction and etching effects that are broadly used. An important role play the hydrogen radicals, that are created by the hydrogen dissociation. Here, the results of optical emission spectroscopy, that enables the estimation of the hydrogen dissociation degree, are published.

Experimental

The experiments were carried out in a spherical stainless steel reactor with two horizontally mounted, parallel, stainless steel electrodes of 80 mm diameter. The upper electrode, embedded in a grounded ring, was driven at the frequency of 13.56 MHz. The bottom electrode was grounded. Their distance was 40 mm. The reactor was exhausted by a turbomolecular pump with a membrane pump. For the optical emission spectroscopy the spectrometer Triax 550 Jobin Yvon - Spex was used. The spectra were recorded through a silica window located in the half of the reactor height.

Results and discussion

The optical emission spectroscopy enables the calculation of the dissociation degree of the hydrogen molecules. This method is based on the the comparison of the atomic (Balmer α) line intensity and the molecular line (Fulcher - $3d^3\Pi_u^- \rightarrow 2a^3\Sigma_g^+$, 2-2, Q1) intensity [1, 2]. The dissociation degree was calculated only in the case of sufficiently low pressure, where the results cannot be influenced by the collisions of excited particles.

The value of the dissociation degree was between 0.3 and 0.5. It was observed that the dissociation degree slightly decreases when the hydrogen pressure increases (fig. 1). According to approximate calculations, the dissociation rate constant steeply decreases by increasing pressure due to the fall of the electron energy. The decrease of the electron energy is demonstrated by the decrease of the excitation temperature of hydrogen atoms (T_b) shown in the fig. 2. Therefore the decrease of the dissociation degree can be accredited to the influence of the electron energy.

Fig. 1 shows that the dissociation degree was strongly reduced by the transition from the unconfined to the confined mode. The two modes, described in [3] and [4], differ mainly in the sheath potentials. By the mode transition the values of the electron concentration and energy in the discharge centre were not changed in that way, that could explain the sharp decrease of the dissociation degree. This means that an important part of the hydrogen molecules was dissociated in the sheaths or at the plasma - sheath boundaries, because the mode transition influenced above all the sheath characters. The sheath at the grounded electrode was enlarged and the sheath at the powered electrode was reduced by the transition. Since the dissociation degree decreased by the transition, it can be deduced that the sheath at the powered electrode had higher impact on the dissociation than the sheath at the grounded electrode. Taking into account that the sheath at the powered electrode was much bigger than the sheath at the grounded electrode this result is not surprising.

The optical emission spectroscopy also enables the measurement of the rotational temperature of hydrogen molecules in the ground state, that was an increasing function of pressure (fig. 3). A simple explanation for the rotational temperature growth is the increasing efficiency of the collisional processes that transform the energy of excited particles and ions to the translational and rotational energy of the neutral gas.

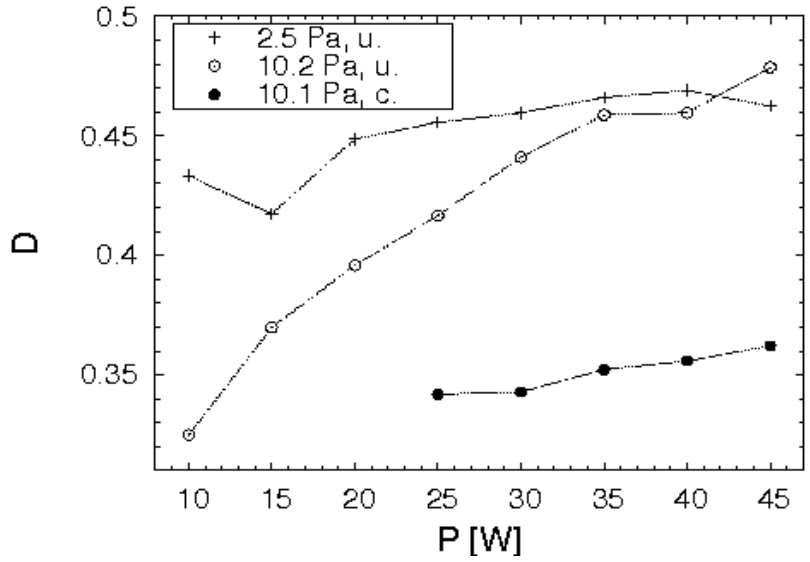

Fig 1: Dissociation degree (D) as a function of the RF power (P). The open symbols represent the unconfined mode, the closed symbols represent the confined mode.

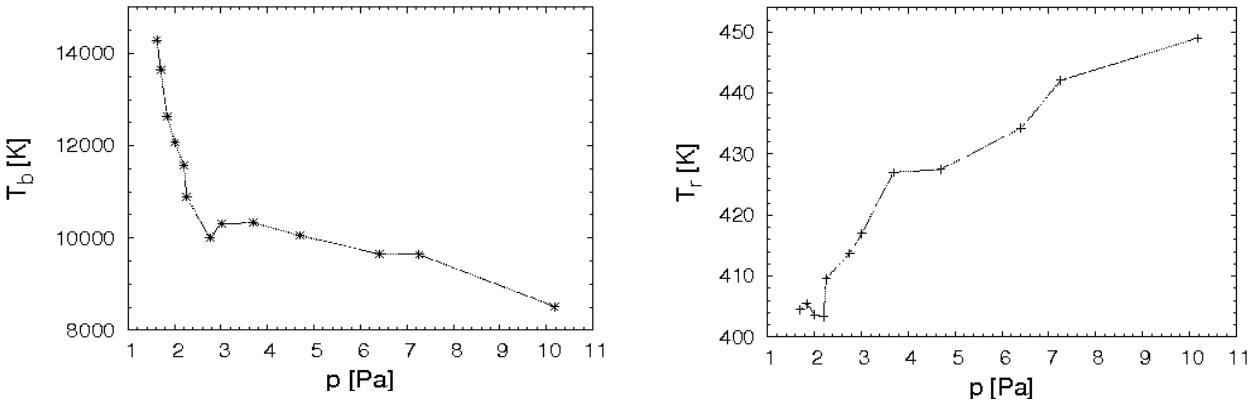

Fig. 2 and 3: The excitation (T_b) and rotational (T_r) temperature as functions of pressure.

References

[1] N. Lang, B.P. Lavrov, J. Röpcke, *Proceedings of Frontiers in Low Temprature Plasma Diagnostics IV,* (2001).
[2] B.P. Lavrov, A.V. Pipa, *Optics and Spectroscopy,* 92 (2002), 709-719.
[3] L. Zajíčková, P. Dvořák, V. Kudrle, R. Šmíd, *Czechoslovak Journal of Physics,* 52 (2002), 427-432.
[4] P. Dvořák, *doctoral thesis*, Masaryk University, Brno, 2006.

P 16

An Improved Pulsed-Power Source

E. Farshi, I. Alexeff, T. Anderson

Department of Electrical Engineering, University of Tennessee, USA
email: efarshi@ece.utk.edu

One of our objectives is to operate plasma antennas at high power. We have successfully operated plasma antennas at over 2 MegaWatts in the pulsed mode. What we now have developed is very simple technique of increasing the output power of the pulsed system by factors of two in an extremely simple fashion. This development may be of great use in electronic warfare.

The basic idea is that we have a high voltage system charging a coaxial cable. A spark gap connects this coaxial cable to another coaxial cable terminating in an antenna.

This system in our laboratory has been observed to radiate pulsed energy at over 2 MegaWatts. The problem is that in general, our power supply is voltage limited by sparkovers. The coaxial cable system, on the other hand, can stand enormous voltages on a short-time basis.

One way around the power supply voltage limitation is to charge a very low impedance line. The low impedance line discharges through a spark gap into a line with a tapered impedance. For example, if the line corresponds to an impedance of 10 Ohms, and the line increases in impedance to 300 ohms (Which matches the antenna to space.) the voltage rises by a factor of the square root of 30, and the power rises by a factor of 30 over that if the 300 Ohm line were charged directly by the power supply. Such a tapered line has been used successfully at the US Naval Research Laboratory to convert the output of a pulsed power supply from 10 MV at 100,000 A to 1 MV at 1 MA.

The basic problem in such a design is in fabricating the tapered line in a simple and inexpensive manner. Tapered lines are difficult to construct. We decided to simulate a tapered line with sections of untapered lines with periodic impedance changes. In the textbooks, there are open, shorted, and matched coaxial lines, but (To my knowledge.) no detailed discussion of intentionally miss-matched lines. We found that if the impedance were raised by a factor of 3, the voltage would rise by about 1.5, the power would increase by about a factor of 2, and about 30 % of the power would be reflected. This impedance transition can be repeated any number of times, increasing the power by a factor of 2 each time.

We have constructed a system of coaxial lines that are very long so that the experimental results may be viewed on a conventional oscilloscope. We have experimentally verified that the predicted voltage and power increases actually occur, and will exhibit these results at the meeting.

We have demonstrated a simple way of arbitrarily increasing the power in a pulsed power system, using only conventional coaxial lines. We consider this to be a significant advance in pulse-power technology, and we intend to use this technique in further experiments on our plasma antennas.

P 17

Reactive Interactions of Singly and Doubly Charged Molecular Ions with Surfaces

L. Feketeová[1-3], T. Tepnual[2], F. Zappa[2], V. Grill[2], P. Scheier[2], J. Žabka[3], J. Roithová[3], A. Pysanenko[3], J. Jašík[3], I. Ipolyi[3], Z. Herman[2,3] and T. D. Märk[2]

[1]Department of Physics and Astronomy, University of Aarhus, Ny Munkegade, Aarhus, 8000 C, Denmark
[2]Institut für Ionenphysik und Angewandte Physik, Leopold-Franzens Universität, Technikerstrasse 25, Innsbruck, 6020, Austria
[3]V. Čermák Laboratory, J. Heyrovský Institute of Physical Chemistry, Academy of Sciences of the Czech Republic, Dolejškova 3, Prague 8, 182 23, Czech Republic
e-mail: linda.feketeova@gmail.com

Abstract

Stainless steel (SS), highly oriented pyrolytic graphite (HOPG) and two different types of diamond (O-terminated (DO) and H-terminated (DH)) have been studied with respect to their effects on energy transfer, surface-induced dissociation and chemical reactions with various singly and doubly charged molecular ions.

Introduction

Interest in studying collisions of molecular ions with surfaces has been growing rapidly in the past twenty years. In the energy regime below 100 eV the relative collision energy and the energy transferred is within an order of magnitude of energies of chemical bonds. In our work, reactive collisions of slow ions have been studied in an effort to investigate the ion-surface interaction processes involving reflection, surface-induced dissociation (SID), charge exchange reactions (CER) and surface-induced reactions (SIR) and the concomitant energy transfer in ion-surface collisions.

Besides being of fundamental importance, ion-surface reactions are also relevant in such different fields as secondary ion mass spectrometry, reactions of ions with aerosols in the Earth's atmosphere, in the interstellar medium and in plasma processing of advanced materials and plasma-wall interactions in electrical discharges and fusion plasmas. In the latter detailed knowledge of the elementary processes of the interaction of gas phase particles with the plasma walls are necessary as an input for edge plasma modelling and diagnostic techniques.

Results and discussion

This work presents experimental data on several studies of singly and doubly charged ions ($SF_4^{2+/+}$ [1], $C_7H_8^{2+/+}$, $C_7H_7^{2+/+}$, $C_7H_6^{2+}$ [2,3] and $C_2X_n^+$ [4,5], where X=H, D and n=2-5) which interact with a number of targets including stainless steel, carbon tile and diamond surfaces in an energy regime below about 100 eV. These data resulted from a joint study between the Institut für Ionenphysik und Angewandte Physik in Innsbruck and the Čermák Laboratory in Prague. Employing a tandem mass spectrometer (BESTOF [6]) constructed in Innsbruck, the mass spectra of the product ions were measured at different collision energies of the projectile ions. The relative abundance of the product ions as a function of the incident projectile ion energy (so called CERMS curve – collision energy resolved mass spectra) was determined. An extension to this was performed in scattering experiments using a beam scattering machine (EVA II [7]) constructed in Prague. The mass spectra, translational energy distributions, and angular distributions of the product ions were measured. The survival probabilities for a range of incident energies and angles were estimated.

Fig. 1 presents the product ion mass spectra for the parent ion $C_2D_4^+$ upon impact on the SS, DO and DH surfaces at impact energy of 15 eV. Distinct differences are seen in the spectra. The parent ion $C_2D_4^+$ is highly abundant in the spectra of DH surface and dominates over the product ions observed in the spectra with its relative intensity, whereas for SS and DO we see an extensive fragmentation of the parent ion into $C_2D_3^+$ and $C_2D_2^+$. Note also that there are H-pick up reactions from contaminant hydrocarbons on the surface.

The spectra for the DH surface clearly show a difference in the production mechanism of an ion on its surface-induced fragmentation pattern. With the same projectile ions, produced in the same ion source, i.e. the projectiles with the same internal energies, the difference in the mass spectra probably result from a different energy transfer of kinetic energy into internal energy of the projectile.

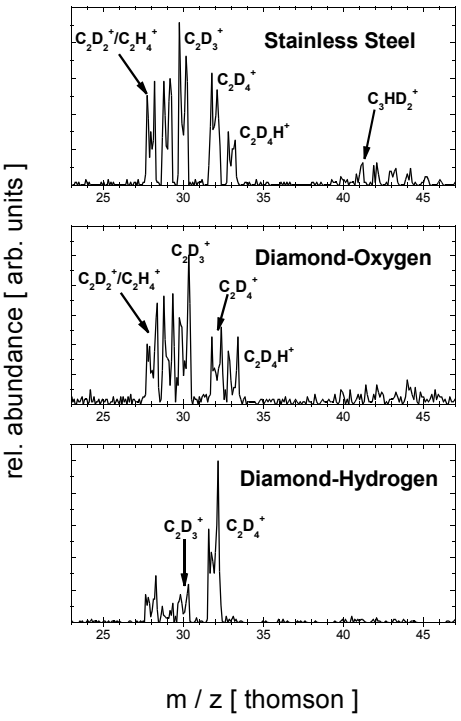

Fig. 1 The product ion mass spectra for the parent ion $C_2D_4^+$ at a collision energy of 15 eV upon impact on stainless steel, O-terminated diamond and H-terminated diamond surfaces, respectively.

The difference in the break up of $C_2D_4^+$ projectile ion after impacting on different surfaces is compared in fig. 2. The symbols indicate the effective survival probability, i.e. the yield of scattered parent ions divided by the total yield of all scattered ions. Depletion of $C_2D_4^+$ is characterized by a step (at half-hight) at about 11.3 eV for SS and DO surface, while in the case of the DH surface this step shifts to higher incident energy of 17.2 eV. This shift of approximately 6 eV results from the different interaction of parent ion with the surface.

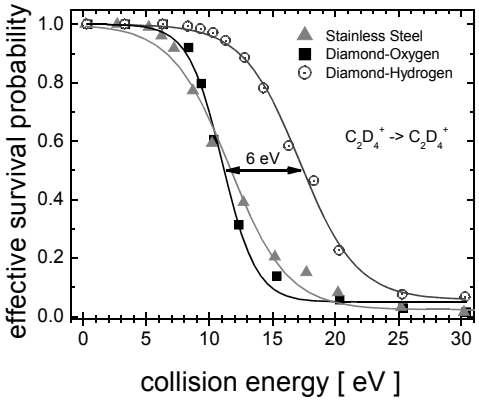

Fig. 2 Effective survival probability of $C_2D_4^+$ ions, i.e. the yield of scattered parent ions divided by the total yield of all scattered ions.

Conclusions

An overriding result of these studies is that the projectile ions, having the same internal energy content before surface impact, need a different kinetic energy to dissociate after impacting on the surface, i.e. the transfer of kinetic energy into internal energy of the projectile by surface impact differs clearly for the surfaces studied. Collisions with the DH surface show difference in: (i) reduced energy transfer, i.e. collisions with this HD are more elastic; (ii) suppression of chemical reaction with projectile ions; (iii) absorption of background hydrocarbons.

References

[1] L. Feketeová, F. Zappa, T. Tepnual, V. Grill, P. Scheier and T.D. Märk, *J. Phys. Chem.* (submitted 2006).
[2] J. Jašík, J. Roithová, J. Žabka, A. Pysanenko, L. Feketeová, I. Ipolyi, T. D. Märk and Z. Herman, *Int. J. Mass Spectrom.*, Chava Lifshitz Memorial Issue 249-250 (2006) 162.
[3] L. Feketeová, T. Tepnual, V. Grill, P. Scheier, J. Roithová, Z. Herman and T. D. Märk, *Int. J. Mass Spectrom.* (submitted 2006).
[4] J. Jašík, J. Žabka, L. Feketeová, I. Ipolyi, T. D. Märk and Z. Herman, *J. Phys. Chem. A* 109 (2005) 10208.
[5] L. Feketeová, F. Zappa, V. Grill, P. Scheier and T. D. Märk, *J. Chem. Phys.* (to be submitted 2006).
[6] C. Mair, T. Fiegele, F. Biasioli, R. Wörgötter, V. Grill, M. Lezius, T. D. Märk, *Plasma Source Sci. Technol.* 8 (1999) 191.
[7] Z. Herman, *J. Am. Soc. Mass Spectrom.* 14 (2003) 1360

P 18

Electric Properties of Positive Corona Discharge Fed by Mixture of Carbon Dioxide and Water Vapours

J. Országh[1], J. D. Skalný[1], N. J. Mason[2]

[1]Department of Experimental Physics, Faculty of Mathematics, Physics and Informatics, Comenius University, Mlynská dolina F-2, Bratislava

[2]Department of Physics and Astronomy, Open University, Milton Keynes, UK

e-mail: juraj.orszagh@googlemail.com

Abstract

Electrical characteristics of the positive corona discharge have been investigated. The reactor was equipped with coaxial stainless steel electrodes and was fed by mixture of carbon dioxide and small amount of water vapours (800 ppm). The experiments have been carried out in two regimes. In flowing regime the gas flow rate was kept constant and in flow-stopped regime it the reactor was closed by valves. The CV characteristics were registered in flowing regime. In flow-stopped regime, the voltage was constant and the time dependence of the discharge current was registered. The effect of ozone concentration on the onset voltage of the corona discharge has been found. The onset voltage is shifting to higher values with increasing ozone concentration.

Introduction

The modelling and simulating of processes active in the atmospheres of planets is an important part of astrophysics. To simulate such processes in the laboratory conditions various discharges like AC/DC corona or RF discharges are suitable [1], [2], [3]. Such experimental setup allows changing the gas mixture, its pressure and temperature to simulate the atmospheric conditions of investigated planet as faithfully as possible. The discharge provides environment in which the examined processes can be initiated. There are various published papers concerning with simulating atmospheric conditions of different planets including Mars [1], [3]. The Martian atmosphere is composed almost of 98 % of carbon dioxide. Recent results of the Mars Express mission have revealed the presence of significant amounts both molecular oxygen and ozone in the Martian atmosphere. Since the chemical formation of molecular oxygen and ozone is independent of the method by which initial oxygen atoms are formed in the atmosphere (by solar UV photolysis in the Martian atmosphere) an electrical discharge in pure carbon dioxide (allowing electron induced dissociation of CO_2) provides an excellent laboratory system for probing both oxygen and ozone production in the Martian atmosphere. The evidences of water in Martian atmosphere were given by recent mission Mars Global Surveyor. This can be active in formation of ozone and molecular oxygen.

Results and discussion

The positive corona discharge was generated in the reactor equipped with coaxial stainless steel electrodes. The gas mixture composed of carbon dioxide and 800 ppm water vapours. It was introduced into the reactor and then the discharge tube was closed by valves. The voltage of 7.4 kV was applied on the electrodes and the time dependence of discharge current was registered with sampling interval of 1 second. The whole measurement lasted 1800 seconds. In the flowing regime the same mixture was flowing through the reactor with constant flow rate of 300 cm^3/min. Then the current voltage characteristic of the discharge was measured. In both regimes the ozone concentration in the discharge tube has been measured by in line UV spectroscopy method.

The CV characteristic of the positive corona discharge in flowing regime and the time dependence of discharge current in flow stopped regime is shown in Fig. 1. In low-stopped regime the discharge was disrupted after few seconds of operation and then started again Fig. 2. Such effect was not observed in flowing regime at 800 ppm water vapours concentration but it was observed at higher concentrations (approximately 7000 ppm).

In positive corona discharge the secondary electrons are generated by photoionisation both in ionising and drift region. Secondary electrons formed beyond the ionising region of the positive corona discharge by primary avalanche are attached by CO_2 molecules at the boundary between ionising and drift region by dissociative attachment

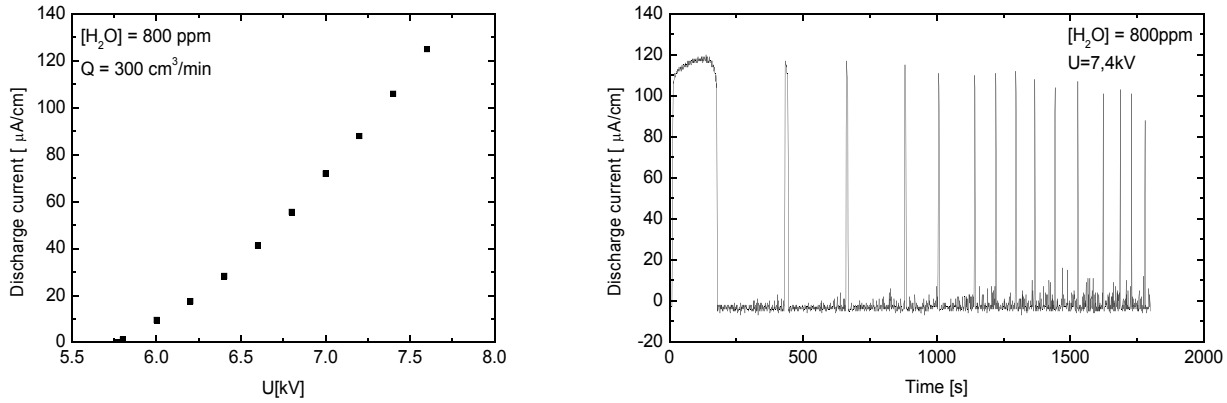

Fig. 1. Current-voltage characteristic of positive corona discharge fed by mixture of carbon dioxide and water in flowing regime (on the left side) and time dependence of discharge current fed by the same mixture in flow-stopped regime.

$e + CO_2 \rightarrow O^- + CO$ {1}

$k_1 = 3.6 \times 10^{-13}$ cm^3/sec [4] or $k_1 = 8.5 \times 10^{-12}$ cm^3/sec [5]

The process {1} exhibits the first sharp resonance at electron energy closed to 4.2 eV. Moreover, it is evident from two values of the rate constant that the process belongs to slow processes. Hence outside the ionising region the electron attachment is practically inactive. If the ozone is formed at voltages slightly above the onset voltage, (100-200) V, the concentration of secondary electrons can be reduced due to dissociative attachment to ozone molecule. There are two channels of such process, both of them having a sharp maximum at energy of electrons of 1 eV. The maximum of the total rate constant for process

$e + O_3 \rightarrow$ products (O^-, or O_2^-) {2}

reaches its maximum $k_2 = 2 \times 10^{-9}$ cm^3/sec deeply in the drift region where the reduced electric field E/N is low [6]. Therefore a part secondary electrons, which otherwise could contribute to sustaining a discharge, is converted to substantially less mobile negative ions. Thus the onset voltage in mixture $CO_2 + O_3$ is shifted to higher value and the discharge is extinguished after few seconds of discharge operation when sufficient amount of ozone is formed in discharge gap. The repeated onset of the discharge is caused by decrease of ozone concentration during the period when the discharge is extinguished.

Conclusion

The experiments confirmed an effect of ozone on the properties of the corona discharges in carbon dioxide. The onset voltage is shifted to higher values with increasing ozone concentration in the discharge gap due to dissociative electron attachment to the ozone molecule, which is reducing the amount of secondary electrons necessary to keep self-sustaining corona discharge. In flowing regime ozone concentration is kept at considerably lower value due to removal of this by flow of gas through the reactor.

Acknowledgements

This research project was partially supported by Slovak Grant Agency VEGA under project 1/1267/04, and ESF projects COST P9 and EIPAM. This work was also supported by Science and Technology Assistance Agency under the contract No. APVT-20-007504.

References

[1] Vušković, L., Ash, R. L., Shi, Z., Popović, S. and Dinh, T.: SAE Paper 972499 (1997).
[2] Ramírez, S. I., Navarro-Gonzáles, R., Coll, P. and Raulin, F.: Advances in Space Reseach **36**, (2005) 274.
[3] Gross, B. F.: Journal of Electrostatics **58** (2003) 147.
[4] O. Eichwald, M. Yousfi, A. Hennad, D. Benabdessadok: J. Appl. Phys. **82** (1997) 4781.
[5] H. Hokazono, M. Obara, K. Midorikawa, H. Tashiro: J. Appl. Phys. **69** (1991) 6850.
[6] J.M. Van Doren, T.M. Miller, S. Williams, A.A. Viggiano: Phys. Rev. Lett. 91 (2003) 223201-1.

P 19

Cavity Ring-Down Spectroscopy of Singlet Oxygen Generated in Microwave Plasma

T. Foldes[1], P. Čermák[1], M. Macko[2], V. Foltin[1], P. Veis[1], P. Macko[1]

[1]Department of Plasma Physics, Comenius University, Mlynská dolina, Bratislava 842 45, Slovakia
[2]Department of Computer Science, Comenius University, Mlynská dolina, Bratislava 842 45, Slovakia
e-mail: foldes.tomas@gmail.com

Abstract

The laser absorption spectrum of singlet molecular oxygen ($b^1\Sigma_g^+$–$a^1\Delta_g$) in the afterglow of a microwave discharge has been recorded by cw-CRDS using a DFB diode laser. The details of this method along with the recorded spectra are presented.

Introduction

Singlet oxygen is the common name used for the lowest excited electronic state of molecular oxygen. The energy difference between the triplet ground state and singlet oxygen corresponds to a transition in the near-infrared at ~1270 nm. In the isolated molecule this transition is strictly forbidden by spin, symmetry and parity selection rules. As a consequence, singlet oxygen in the gas phase is extremely long lived (72 minutes) however interaction with solvents significantly reduces this lifetime. Because of its noteworthy reactivity this state is important to a range of disciplines. It is a significant intermediate in the photoinduced degradation of polymers, in photodynamic therapies for cancer treatment and important to the radiative properties of the atmosphere.

Although oxygen transitions in the near-infrared ($a^1\Delta_g$ –$X^3\Sigma_g^-$) and visible ($b^1\Sigma_g^+$–$X^3\Sigma_g^-$) have been studied thoroughly there haven't been stratightforward methods for quantitative detection of singlet oxygen. Our sensitive absorption-based technique allows quantitative detection of singlet oxygen through the near-infrared $b^1\Sigma_g^+(v=0) – a^1\Delta_g(v=1)$ transition about which there is yet only few data available [1].

Results and discussion

The experimental setup is shown on Fig. 1. Singlet oxygen is generated in a 2,46 GHz microwave discharge pulsing at 50Hz with 1:1 duty cycle. The mean power coupled to the discharge is about 800W. The 200sccm flow of O_2 passes through the microwave cavity via a quartz tube. The ensuing plasma afterglow passes through the optical cavity of a cw-cavity ring-down setup (CRDS) to which the quartz tube is connected perpendicularly.

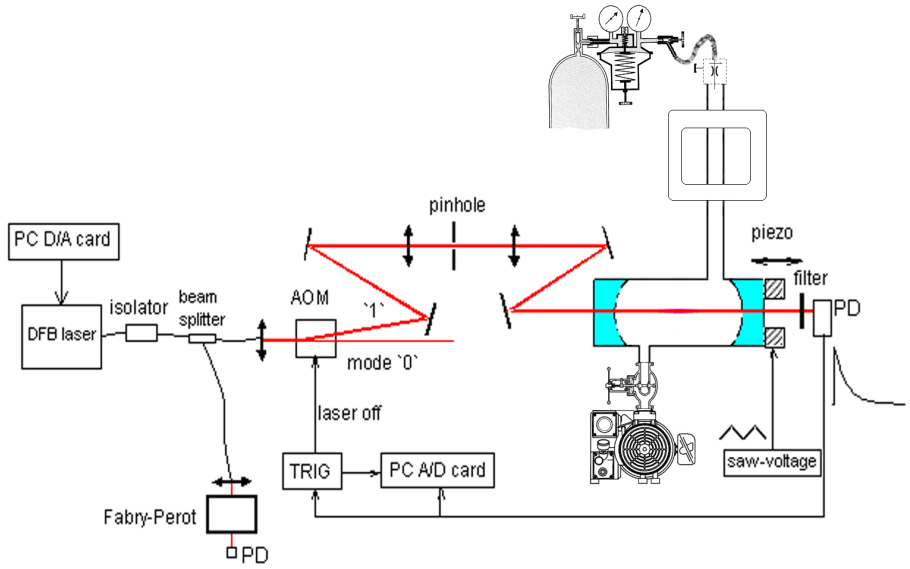

Fig.1. Schematic diagram of experimental setup

The CRDS setup (described previously in detail [2]) consists of a fibered butterfly-package distributed-feedback laser coupled into an optical cavity composed of 2 high reflectivity mirrors in a vacuum-tight glass

cell. The mirrors are mounted on tilt stages one including a piezo-electric tube for modulating the cavity length. The cavity is aligned and modulated in such a way, that light can be coupled into the cavity and inside the cavity is reflected many times between the mirrors. The laser is temperature tuned. Once the light is effectively coupled into the cavity an acousto-optic switch deflects the laser beam. The light leaking out of the cavity is focused into an InGaAs photodiode and from the measured time dependence of the intensity the rate of absorption can be obtained; the more the sample absorbs, the shorter the measured decay time. Recording the decay times as a function of the laser frequency one can easily calculate the absorption. The cavity and all open-air optics are placed on an L-shaped rail, which is lying on a marble tombstone. On-line data analysis, visualization and control of laser tuning are carried out using a PC A/D and a D/A card, employing LabView modules.

Fig.2 shows Q-branch transitions ($b^1\Sigma_g^+(v=0) - a^1\Delta_g(v=1)$) measured in the afterglow of O_2 microwave plasma at a pressure of 2.2torr and 200sccm. The ring-down event rate was ~1kHz. For each data point 500 ring-down decay frequencies have been averaged. The exact laser frequency and tuning rate were determined using known water absorption features (using the HITRAN database [3]) and a Fabry-Perot etalon.

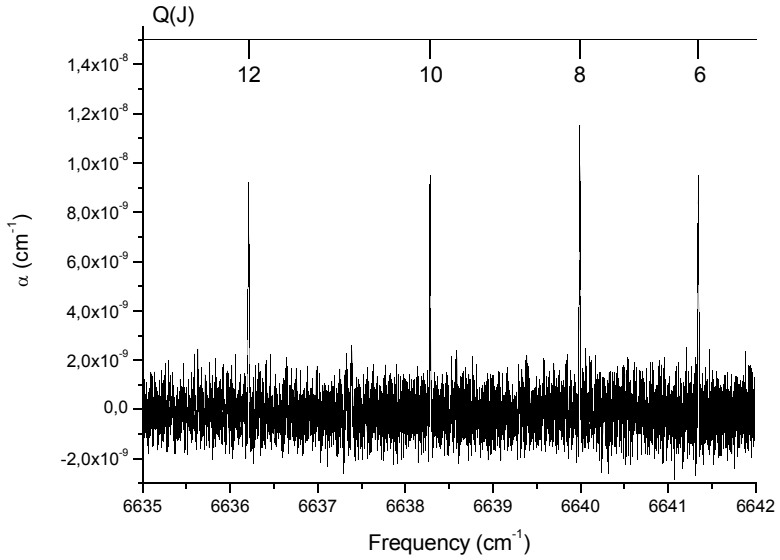

Fig.2. CRDS measurement of O_2 $a^1\Delta_g$ obtained by tuning the laser diode over selected Q-branch transitions at a 1kHz ring-down event rate. For each data point 500 ring-down decay frequencies have been averaged.

Conclusions

More than 10 well-resolved transitions have been already observed, that we assigned to the P- and Q-branches of the $b^1\Sigma_g^+$–$a^1\Delta_g$ system. From the line intensities we obtained a density of O_2 ($a^1\Delta_g$) $5x10^{15}$ cm^{-3} which means that 7% of O_2 molecules are in the singlet state. The observed line positions are in agreement with the predicted values.

This research was sponsored by the Science and Technology Assistance Agency under the contract No. APVT-20-020204, by the Scientific Grant Agency of Slovak Republic VEGA 1/1016/04, 1/2014/05, 1/4015/07 and by Comenius University UK/346/2006.

References

[1] S. Williams et al. Optics Letters, Volume 29, Issue 10, 1066-1068 (May 2004).
[2] T. Földes, *Diplomová práca*, Univerzita Komenského, Bratislava, 2005.
[3] L.S. Rothman et al. The HITRAN Molecular Spectroscopic Database, J. Quant. Spectrosc. Radiat. Transfer 82, 5–44, (2003)

P 20

Modeling and Diagnostics of Elementary Processes in a Collisionally Pumped Ne-, Ar-like Ions Plasma and Search of Optimal Plasma Parameters for X-ray Lasing

A. Glushkov[1], O. Khetselius[2]

[1]Department of Atomic Physics, Odessa Univ., P.O.Box 24a, Odessa-9, 65009, Ukraine
[2]Institute of Applied Mathematics, Odessa Univ., P.O.Box 24a, Odessa-9, 65009, Ukraine
e-mail: glushkov@paco.net

Abstract

We present the uniform energy approach, formally based on QED with using gauge invariant scheme of generation of the optimal one-electron representation to study, in a uniform manner, elementary processes responsible for emission-line formation in plasmas. The electron collision strengths and rate coefficients for electron-collisional excitation for some Ne- and Ar-like plasma ions are calculated.

Introduction

The X-ray laser problem has stimulated a great interest to development of theoretical methods for modelling the elementary processes in a collisionally pumped plasma. The shocking example is a scheme for accomplishing tabletop x-ray lasing in Li-like ion of Ne at 98A in an optically ionized plasma during recombination in the transient regime (Lawrence Livermore Nat. Lab.). The low temperature plasma sources show promise for producing lasing in the VUV and soft X-ray region. Two key problems must be solved to develop a special code and to predict necessary plasma parameters for X-ray lasing: i). Highly accurate definition of rate coefficients for plasma elementary processes that are responsible for forming emission lines spectra; ii).Developing new exact kinetics calculation schemes for defining level populations, gain coefficients at definite plasma parameters. The most consistent approach to these problems is based on QED. Here the QED energy approach in gauge invariant formulation [2] is used for description of elementary processes in collisionally pumped plasma. It is developed an optimal scheme for calculation of the electron-collision strength and rate coefficients for the de-excitation (excitation) processes in the multi charged ions plasma with estimating optimal plasma parameters for X-ray lasing. Detailes of the method are in ref. [2].

Results and discussion

We applied our approach to estimate of the electron collisional excitation cross-sections and strengths for Ne-and Ar-like ions. For example in table below we present calculated and measured electron-collisional excitation cross-sections σ for Ne-like Ba for two values of incident electron energy 5.69keV and 8.20 keV. For comparison we present the measured values σ and calculated ones within other theoretical schemes [2,3].

Level J	Measured Marrs etal [19]	Calculated Ivanov etal [5]	Calculated Zhang etal [20]	Calculated Reed [21]	Calculated Present paper
		E_{el}=5.69keV			
Sum (J=0)	2,50±0,35	2,48	2,58	2,60	2,51
$2p_{3/2}3d_{5/2}$ 1	3,98±0,56	3,20	3,44	3,56	3,25
$2p_{1/2}3d_{3/2}$ 1	2,12±0,30	1,78	2,42	2,00	1,84
		E_{el}=8.20keV			
Sum (J=0)	2,27±0,32	1,83	1,89	1,94	1,86
$2p_{3/2}3d_{5/2}$ 1	3,30±0,46	2,87	2,99	3,23	2,93
$2p_{1/2}3d_{3/2}$ 1	1,82±0,25	1,64	2,10	1,82	1,69

Note that the experimental information on the electron-collisional cross-sections for high-charged Ne-like ions is very scarce. Such experimental information for a few collisional excitations of the Ne-like barium ground state had been obtained in Ref.[3]. Our results are at the lower margin of experimental error as the corresponding data of ref.[3] with one exception: for the state $2p_{3/2}3d_{5/2}$ [J=1} our cross-section at collisional energy 5,69keV is a few percent lower. But one must understand that extraction of the cross section from the experiment is the most ambiguous for this level. There is physically reasonable agreement between theory and experiment. The collisional strengths are calculated for several values of the incident electron energy.

The comparison of our collisional rate coefficients for iron with those from refs. [2,3] is shown in Fig.1. Their dependence on the electron temperature is shown for three different transitions. The detailed designation of levels is presented in ref. [2]. The inclusion into consideration of Rydberg and autoionization Rydberg states of ions of the previous ionization stage definitely increase collisional cross-sections. We calculated the spectra of plasma, containing Ne- and Na-like ions with consistent account for Rydberg and autoionizing Rydberg series in the balance equations. The inclusion of Na-like states, accounting for diffusion-like processes, can increase the population inversion for the "lasing candidates" by at least a factor of two for a wide range of plasma conditions. We calculated the functions N_{el} , which describe the population distribution within each Rydberg series dependent on the Rydberg electron energy. These functions bear diagnostic information. Detailed calculations are done for the homogeneous steady-state Maxwellian plasma.

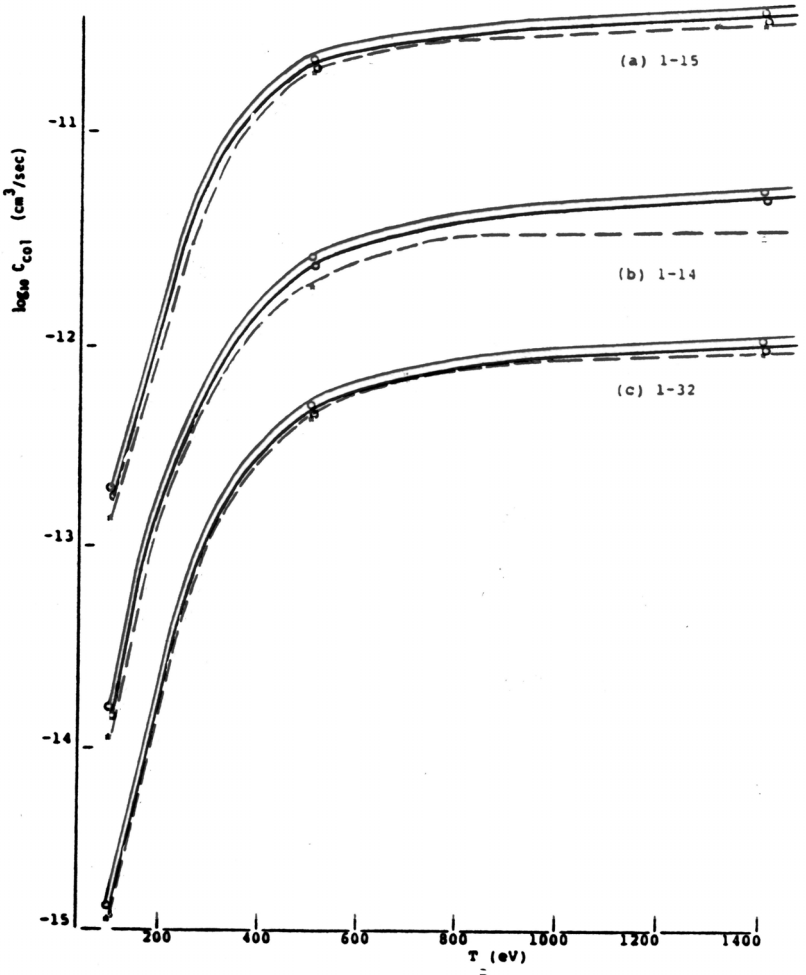

Fig.1. Temperature dependence of rate coefficients for electron-collisional excitation of Ne-like iron : solid line ~ calculation [3] ; dashes line ~ Ivanov et al [2] ; the solid line with dots ~ present calculation ;

Conclusions

We have used the uniform QED energy approach [2] to calculating the electron collision strengths and rate coefficients for electron-collisional excitation for some Ne-and Ar-like plasma ions.

References

[1]. Amendt P. etal, *Phys. Rev. Lett.* 66, 2589 (1991); Golt'z E.,Koshelev K. etal,*Phys.Lett.A.*119,359 (1987).

[2]. Glushkov A. *JETP. Lett.* 55, 97 (1992); Glushkov A., Ivanov L., *Phys.Lett.A.* 170,33 (1992); Ivanov L., Ivanova E., Knight L., *Phys.Rev.A.* 48,4365 (1993); A.V.Glushkov etal, In*: New Projects and New Lines of research in Nucl.Physics*. Eds. Fazio G. ,Hanappe F., World Publ. Singapore, 2003,p.142-158; *Int. Journ. Quant.Chem.* 99, 879 (2004); 99, 936 (2004); 105, 562 (2005); *J.Phys.CS.* 178, 188 (2005); 178, 199 (2005);

[3]. Marrs R. et al, J., *Phys.Rev.Lett.* 60,1715 (1988) ; H.Zhang H., Sampson D., Clark R., Mann J., *At.Dat.Nuc.Dat.Tabl.*37,17 (1987) ; Reed K.J., *Phys.Rev.A* 37,1791 (1988).

P 21

Atmospheric-Pressure Microwave Source of Microdischarge Based on Coaxial Line

M. Goch, M. Jasinski, Z. Zakrzewski, J. Mizeraczyk

Centre for Plasma and Laser Engineering, The Szewalski Institute of Fluid-Flow Machinery, Polish Academy of Sciences, Fiszera 14, 80-231 Gdańsk, Poland

e-mail: mj@imp.gda.pl

Abstract

In this paper we present a simple and cheap microwave microdischarge source (MMS) generated in argon at atmospheric pressure. The source of microdischarge consisted of a typical 2.45 GHz microwave magnetron generator and 50 Ω coaxial line terminated with a coaxial MMS. All experimental tests were performed with argon at a flow rate from 0.5 to 23 l/min and absorbed microwave power from 4 to 80 W. The microdischarge occurred in the form of a small plasma jet. The length and diameter of microdischarge ranged from 1.5 - 14 mm and 0.5 - 1.5 mm, respectively, depending on the discharge condition. The temperature of the microdischarge could be changed in the range of 30 - 1200 °C by changing the gas flow rate or/and absorbed microwave power.

Introduction

Nowadays, there is a growing interest in microdischarges at atmospheric pressure sources. They are needed for gas cleaning, microwelding, surface modification [1], light sources, atomic spectroscopy system [2]. They can be also used in the biomedical applications such as sterilization of medical instruments, high-precision surgery, cells treatment and deactivation of bacteria and viruses [3].

We present a new MMS based on a coaxial line. The main advantage of the presented microwave source is its simplicity and low cost. Our first model of MMS was described in [4]. Here we present its an advanced version.

Results and discussion

The structure of the presented MMS based on the coaxial line is shown in Fig. 1. The MMS operated stable at argon flow rates of 0.5 - 23 l/min and absorbed microwave powers of 4 - 80 W.

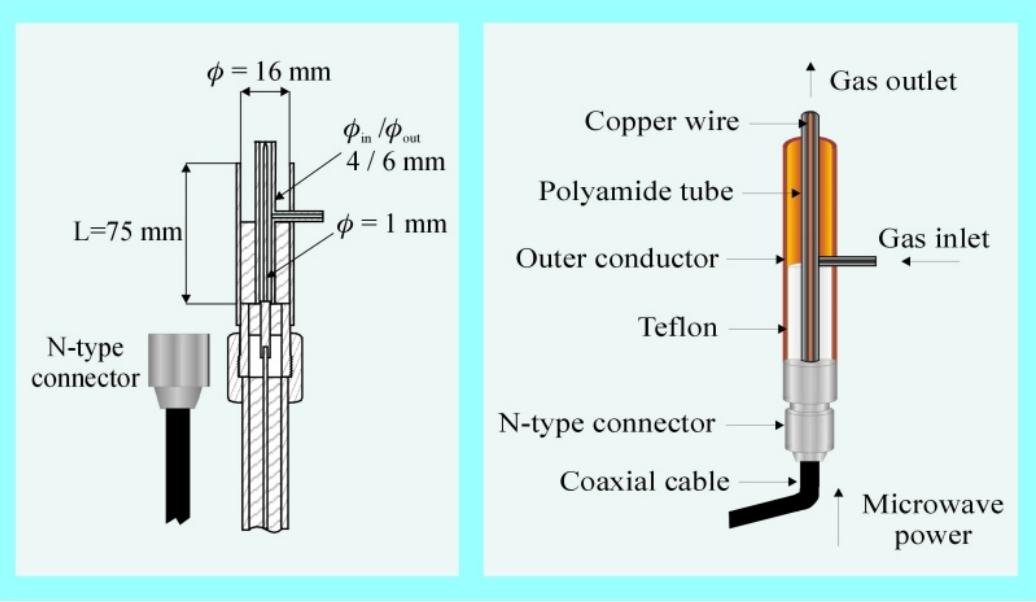

Fig. 1. The cross-sectional view of the 2.45 GHz atmospheric pressure MMS based on the coaxial line.

Due to the presence of an outer conductor the new MMS exhibited a better impedance matching (the lower reflected microwave power P_R) and lower incident microwave power P_I than the previous model MMS in [4].

The optimum length L of the outer conductor of MMS was chosen based on Fig. 2a. In Fig. 2a. the arrows

depict the best impedance matching, i.e. the lowest reflected microwave power, and hence the optimum length L of MMS. The dependence of reflection coefficient P_R/P_I on the length L of MMS changed periodically. The period of this changes was $\lambda/2$ (where λ is the wavelength in free space). No other impedance matching circuits were used in the MMS.

Influence of the incident microwave power P_I on the reflection coefficient P_R/P_I for different argon flow rates Q is shown in Fig. 2b. We can see that for the incident microwave power P_I higher than 10 W the reflection coefficient is relatively low and almost constant in the wide range of argon flow rates.

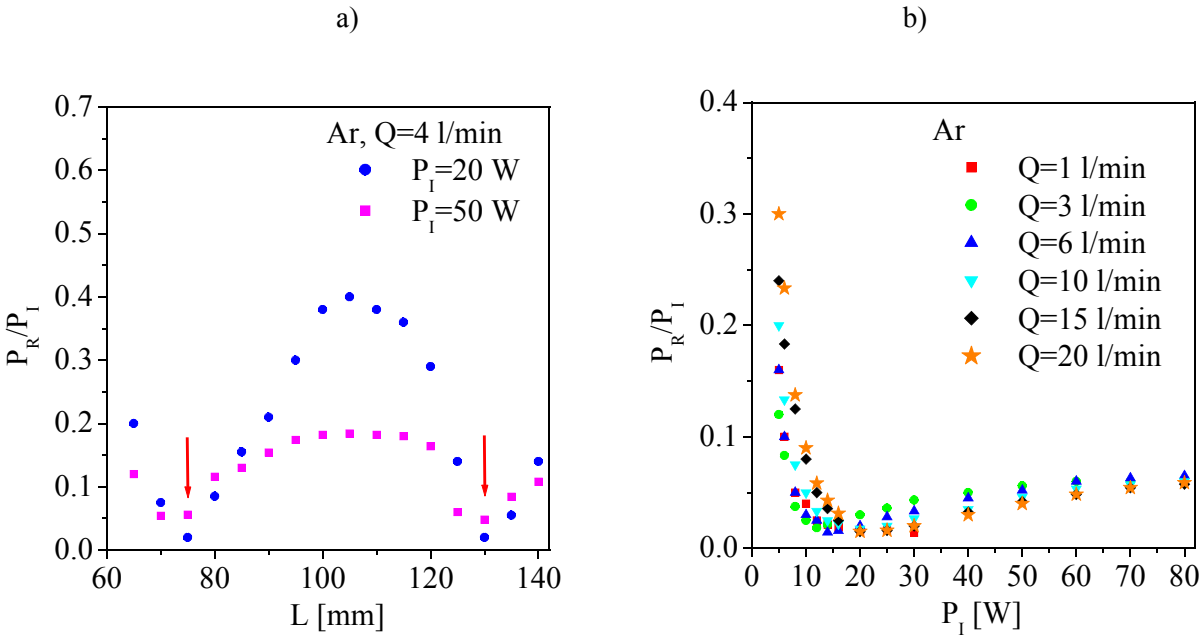

Fig. 2. Matching characteristics of MMS (a) and influence of the incident microwave power P_I on the reflection coefficient P_R/P_I for different argon flow rates (b).

The temperature of the microdischarge depends on gas flow rate and/or absorbed microwave power. When the gas flow rate increases and/or the absorbed microwave power decreases, the plasma temperature decreases. The gas temperature measured on the top of microdischarge ranged from 30 °C to 1200 °C. The wide range of temperature expands the area of MMS applications.

According to the our investigations we observed that the length and width of the microdischarge increases with increasing gas flow rate and absorbed microwave power. In other words, we can obtain different dimensions of the microdischarge by choosing operating conditions.

Conclusion

The simplicity and cost of the MMS, operation stability and parameters of the microdischarges allows the conclusion that the presented MMS can find practical applications in various fields.

References

[1] H. Yoshiki, *Jpn. J. Appl. Phys*., 45 (2006) 5618.

[2] A. M. Bilgic, U. Engel, E. Voges, M. Kuckelheim, J. A. C. Broekaert, *Plasma Sources Sci. Technol*., 9 (2000) 1.

[3] R. E. J. Sladek, E. Stoffels, *J. Phys. D: Appl. Phys*., 38 (2005) 1716.

[4] M. Goch, M. Jasinski, Z. Zakrzewski, J. Mizeraczyk, *Czech. J. Phys*., 56 (2006) 795.

P 22

Low Molecular Products Analysis of the Toluene Destruction in Gliding Arc Discharge

H. Grossmannova , F. Krcma

Faculty of Chemistry, Brno University of Technology, Purkynova 118, Brno 612 00, Czech Republic
e-mail: grossmannova@fch.vutbr.cz

Abstract

A DC atmospheric pressure gliding discharge was applied to the removal of volatile organic compounds (VOC). For an input concentration of 66 ppm, a removal fraction of nearly 97 % was obtained at a speciffic energy density of 445 J/l, total air flow rate of 2,8 l/min, carrier gas composition 40 % of N_2 and 60 % O_2. Detected NO concentration reaches from 170 up to 630 ppm and NO_2 from 27 up to 72 ppm for different specific energy densities for an input concentration of 232 ppm.

Introduction

We were focused on the plasma chemistry of a low temperature atmospheric gas discharge – gliding arc [1]. In previous work we demonstrated the experiments dealing with the high molecular analysis of VOC removal products [2]. In this paper, first results concerning the energy efficiencies, speciffic energy densities and formation of NO, NO_2, H_2, CO_2 as low molecular products of combustion in the plasma are presented. VOCs vapours are sometimes accidentally released into the environment, contribute to air pollution. Common artificial sources of VOCs include industrial processes, motor vehicles (outdoor) paint thinners, dry cleaning solvents (indoor). Conventional techniques for the abatement of VOC, such as thermal and catalytic oxidation of industrial waste gas are widely spread techniques because of their ability of total VOC destruction, although both suffer from low energy efficiency given the high operating temperatures. Technologies based on non-thermal plasmas could offer a good alternative [3]. Our plasma reactor closed in the discharge chamber consists of a single pair of diverging knife-shaped copper electrodes that are positioned in the fast gas flow.

Results and discussion

In our experiments combustion process of toluene is studied. The break-down parameters for the reactor were 825 V and 0,015 mA, the range of applied energy power was from 14,0 up to 30 J/s. Discharge was initiated in various gas mixtures of N_2/O_2 and just before entering the reactor was enriched by toluene. The main flow rate, controlled by a mass flow controller, was 2,8 and 4,0 l/min. Because of the typical concentration range of concern in air pollution problems, VOC inlet quantity was kept constant on two levels – 66 ppm, 232 ppm in our experiments.

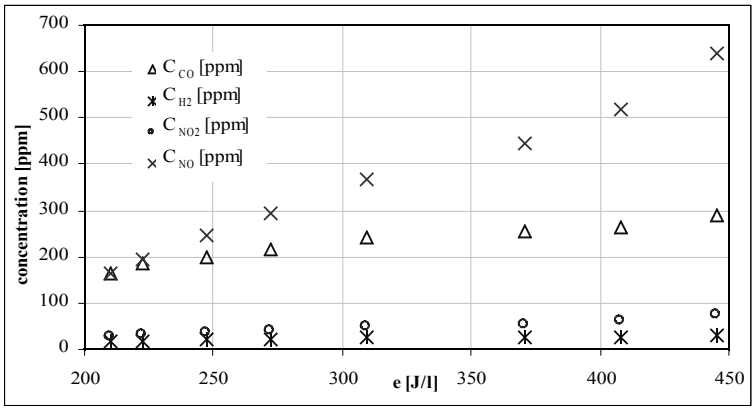

Figure 1. Concentrations versus speciffic energy density, toluene inlet concentration 232 ppm, flow rate 4 l/min, carrier gas composition 79 % of N_2 and 21 % O_2.

The outlet from the combustion chamber was analyzed by analytical equipment like GC/MS and combustion exhaust gas analyzer - TESTO 350 M/XL (quantitative H_2, CO_2, NO and NO_2 electrochemical sensors). High volumic power density may lead to the production of a significant amount of NO_x compounds, when working in N_2/O_2 air-like mixtures [4]. The experimental results showed NO and NO_2 emissions as well as CO_2 and H_2 is detected during the plasma treatment. Flow rate was constantly at 4 l/min

for experiments displayed on the figure 1. The NO concentration reaches from 170 up to 630 ppm and NO_2 from 27 up to 72 ppm for different specific energy densities, obtained at a constant flow rate by changing the electric power from 14,0 to 29,6 J/s. Similar linear relation was observed in the case of H_2 (18-30 ppm) and CO_2 (160-290 ppm) generation. Fig. 2 then shows that the higher specific electric energy affects the increasing of NO and NO_2 emissions. There is a maximum for each dependece, the highest NO generation was achieved at the oxygen content in carrier gas of 40 %.

The further series of experiments thus focuses on studying the removal efficiency and on energy consumption for single processes. The VOC removal efficiency was deduced from the ratio of the remaining VOC versus its initial concentration (toluene conversion is increasing up to 97 %). Energy efficiencies for the different N_2/O_2 mixtures were then calculated (Fig. 3), final values increased from 2,3 to 2,6 g/kWh.

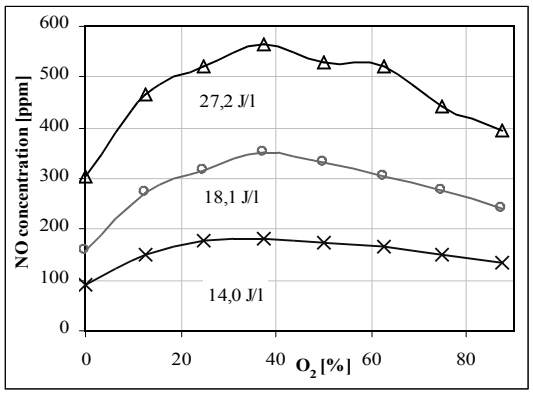

Figure 2. Production of NO as functions of the electric power and of the oxygen contect in gas, toluene inlet concentration 232 ppm, flow rate 4 l/min.

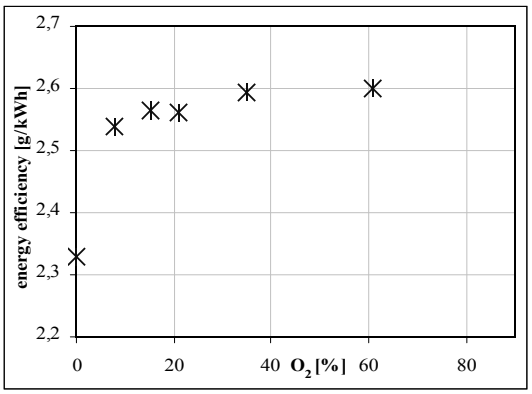

Figure 3. Energy efficiencies for the different N_2/O_2 mixtures, toluene inlet concentration 66 ppm, flow rate 2,8 l/min.

Conclusions

The energy cost, removal efficiency and H_2, CO_2, NO, NO_2 concentration for toluene decomposition with a plasma based on a DC atmospheric pressure glow discharge have been evaluated. The role of oxygen content in carrier gas and energy efficiency of the toluene removal process were investigated with the aim to operate the discharge reactor at a lower energy cost. We tried to explain some plasmochemical processes, such as significant generation of low molecular products like NO, NO_2 , H_2, CO_2. We expected to have a strong effect on the NO_x production during the plasma treatment of polluted gas. Both NO and NO_2 concentration increase lineary with the higher speciffic energy density of the process, as well as the H_2 and CO_2 concentration. The following experiments will be focused on the influence of an admixture of some other VOC compounds in different concentration on the production of NO_x.

References

[1] A. Czernichowski, A.. Ranaivosolarimanana, *Chem. Tech.* 26 (1996), pp. 45-49.
[2] H. Grossmannová, M. Ciganek, J. Prochazkova, F. Krcma, *Proceedings of HAKONE X* 2006, pp.255-258.
[3] H. Kim, *Plasma Proc. Polymers* 2 (2004) pp 91-110.
[4] A. Rousseau, A. Dantier, L. Gatilova, Y. Ionikh, J. Ropcke, Y. Tolmachev , *Plasma Sources Sci. Technol*, 14 (2005) pp. 70-75.

Acknowledgments

This work was supported by Czech Science Foundation, contract No. 202/03/H162.

P 23

Investigation of Plasma Composition During Carbon Nanotubes Synthesis

M. Guláš[1, 2], S. Farhat [3], P. Macko[1], P. Veis[1] and F. Le Normand[2]

[1] Department of Experimental Physics, Faculty of Mathematics, Physics and Informatics, Comenius University, Mlynská dolina, F2, 84248 Bratislava, Slovakia

[2] Groupe Surfaces and Interfaces, IPCMS, UMR 7504 CNRS, 23, rue du Loess, 67034 Strasbourg Cedex, France

[3] LIMHP, Université Paris Nord, Av. J.B. Clément, 93430 Villetaneuse, France

e-mail: gulas@fmph.uniba.sk

Abstract

In this contribution simulations of plasma during carbon nanotubes (CNTs) are presented. The plasma composition during plasma enhanced chemical vapor deposition method (PE CVD) and plasma enhanced hot-filament chemical vapour deposition (PE HF CVD) were studied and compared.

Introduction

Three ways of carbon nanotubes synthesis are generally used: electric arc discharge, laser ablation and chemical vapor deposition. In the first two methods CNTs are obtained after condensation of a hot carbon gas, while in the third case the growth of a CNT is determined by the presence of a catalyst. The advantages of CVD technique, besides large-scale production of CNTs are the relatively low temperature, less than 1100 K, needed for CNTs synthesis and the controlled and localized growth. This temperature could even be lowered using modifications of the incoming CVD gas mixture by plasma (plasma-enhanced catalytic CVD or PE CCVD), with hot-filaments associated or not with plasma CVD (PE HF CCVD)[1]. The advantage of using plasma (electric discharge) in the CNT growth process is based on the higher efficiency of electric excitation of the gas precursor, which is generally higher than either photonic or thermal excitations.

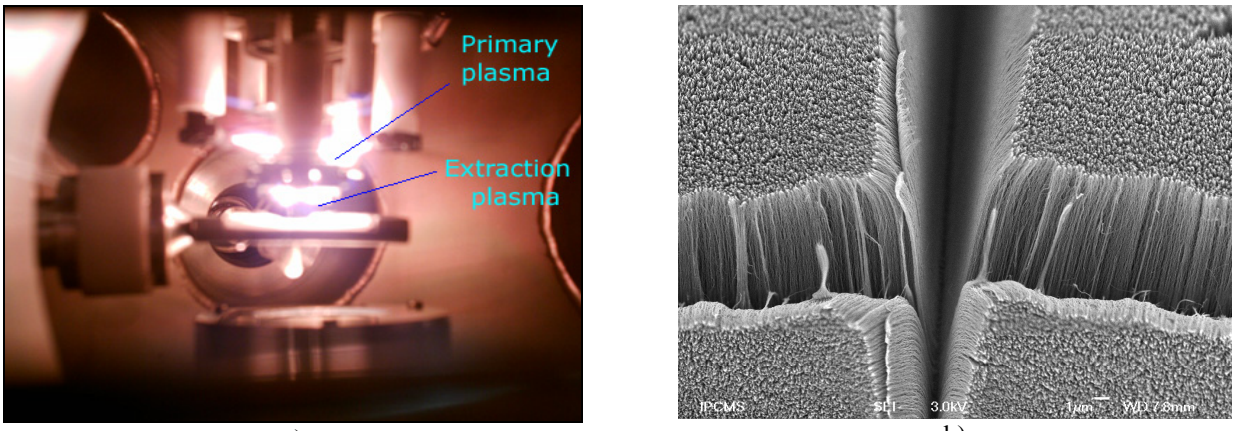

a) b)

Figure 1: a) Configuration of DC HF CVD reactor b) SEM image of film of carbon nanotubes

Results and discussion

For the plasma simulations software CHEMKIN [2] is used. This collection of software consists of various programs such as: AURORA which allows the simulation of electrons density, ion density for thermal or non-thermal plasma where temperature of gas T differs from temperature of electrons Te. CHEMKIN allows calculate the composition of gas at equilibrium in dependence of gas temperature, pressure, etc... This software works on the basis of thermodynamics data of entropy $S°$, enthalpy $H°$ and specific heat Cp. These three parameters are defined in temperature dependence by seven coefficients (a1,… a7) for every species which leads to thermodynamic database for simulation. The reaction mechanism is described by Arrhenius equation and three Arrhenius coefficients.

The parameters of plasma are taken from OES measurements [3].Reactions which assume to play the main role in this conditions are reactions neutral – neutral, ion – neutral (charge exchange), ionization and dissociative recombination [4, 5, 6]. For the plasma simulations of mixture $C_2H_2/H_2/NH_3$ (100 sccm, 20/79/01) 45 species and more than 240 reactions are used. These simulations are divided into two types (PE CVD and PE HF CVD). In the first approach, modelisation of plasma from low gas temperature is done. This simulation refers to PE CVD model, where preliminary thermal dissociation occurs at relatively low temperature. Second model refers to the simulations of plasma in PE HF CVD conditions, where incoming

gas pass through hot filaments (T_f = 2250 K). Comparison of the plasma composition in PE CVD and PE HF CVD (Figure 2) shows that concentration of species C and C_2 is higher in PE HF CVD. It is believed that these species play the most important role in carbon nanotubes growth.

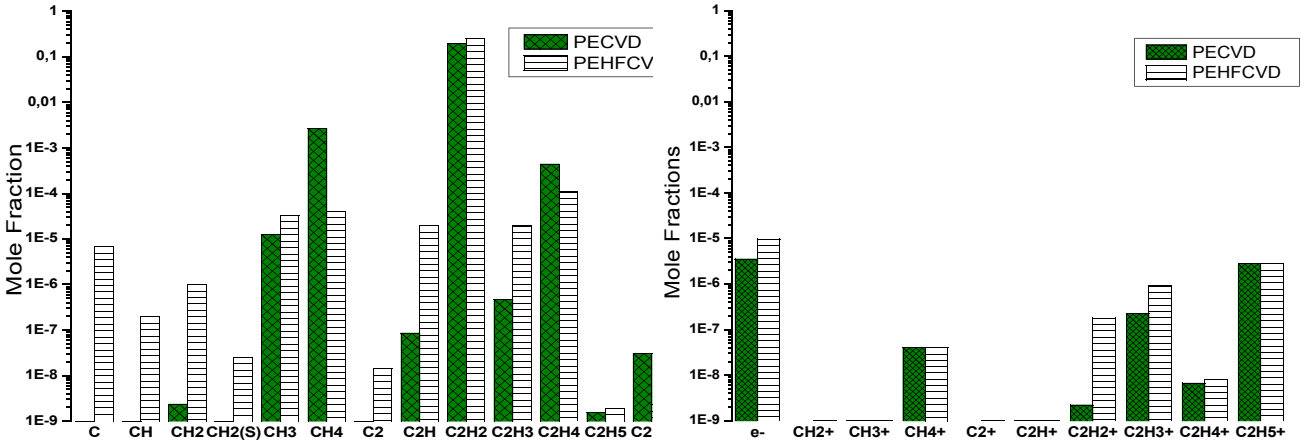

a) b)

Figure 2: Comparison of mole fraction in $C_2H_2/H_2/NH_3$ plasma between PE CVD and PE HF CVD a) molecules and radicals b) electrons and ions

Conclusion

CHEMKIN software allows plasma simulations in 0D with our approximation that thermodynamic data mentioned above are the same for the radicals and ions. These results of plasma modelisation in pure hydrogen atmosphere are in good agreement with results of Farhat [3] and Hash [7]. However, to our knowledge, there are no other results of ion concentration in DC C2H2/H2/NH3 plasma in these conditions to compare. But the concentration of electrons (1x10E-5 mole fraction ~ 5x10E+11/cm3) is typical for DC glow discharge. In continuation these results will be used in simulation of gas phase in PE HF CVD reactor with substrate reactions when whole process of growth of carbon nanotubes will be simulated in 1D model.

Acknowledgement

Part of this work was funded by Science and Technology Assistance Agency under the contract No. APVT-20-020204. We also acknowledge French Embassy in Slovakia and Government of France for funding research fellowship for one of the author (M.G) at IPCMS, CNRS, Strasbourg, FRANCE.

References

[1] C.S. Cojocaru, M. Larijani, D.S. Misra, M.K. Singh, P. Veis and F. Le Normand, *D&RM* , 13, 270, (2004)
[2] R. J. Kee, F. M. Rupley, et al. CHEMKIN Release 4.0.2, Reaction Design, San Diego, CA (2005)
[3] P.Veis, C.S.Cojocaru and F.Le Normand, *Acta Physica Universitatis Comenianae*, XLIV-XLV, 95-100, (2004)
[4] S.Farhat, F.Silva et al. 1997 *Joint International Meeting of the Electrochemical Society*, Paris, 1.9-5.9, (1997)
[5] Gregory P. Smith, David M. Golden et al. http://www.me.berkeley.edu/gri_mech/
[6] E Coda Zabetta, M. Hupa, http://www.abo.fi/fak/ktf/cmc, submitted to international scientific journal, 2006
[7] D.B. Hash, M. Meyyappan, *Journal of Applied Physics*, 93, 2003

P 24

Plasma Plume Diagnosis in High Fluence Laser Ablation

S. Gurliu[1], M. Ziskind[2] and C. Focsa[2]

[1]Al. I.Cuza University of Iasi, Faculty of Physics, B-dul Carol I Nr 11, Iasi, RO-6600, Romania
[2]Laboratoire de Physique des Lasers, Atomes et Molécules (UMR 8523), Centre d'Etudes et de Recherches Lasers et Applications (FR CNRS2416), Université des Sciences et Technologies de Lille, 59655 Villeneuve d'Ascq cedex, France

Abstract

The dynamics of a laser ablation plume from Cu and Al metals irradiated by 10 ns pulsed laser beam (λ = 532 nm) has been studied by means of optical and electrical methods.

Introduction

There is a high current interest in understanding the fundamentals of the complex pulsed laser desorption/ablation phenomena, due to their importance in a wide range of applications. The experimental technique used in this paper is based on a set-up developed mainly for analytical purposes and described in detail elsewhere [1]. At high laser pulse energy, the plume of ablated materials appears as a nearly spherical plasma blob [3-5] that has its origin in the non-equilibrium hot plasma produced at the impact point of the laser beam on the solid target.

Results and discussion

The formation and dynamics of the space charge structures have been studied by means the experimental set-up shown in figure1. Briefly, a 532 nm, 10 ns Nd:YAG laser beam has been focused by a f = 25 cm lens on an aluminum target placed in a vacuum chamber (base pressure < 10^{-7} Torr). The laser beam energy ranges from 10 to 80 mJ/pulse.

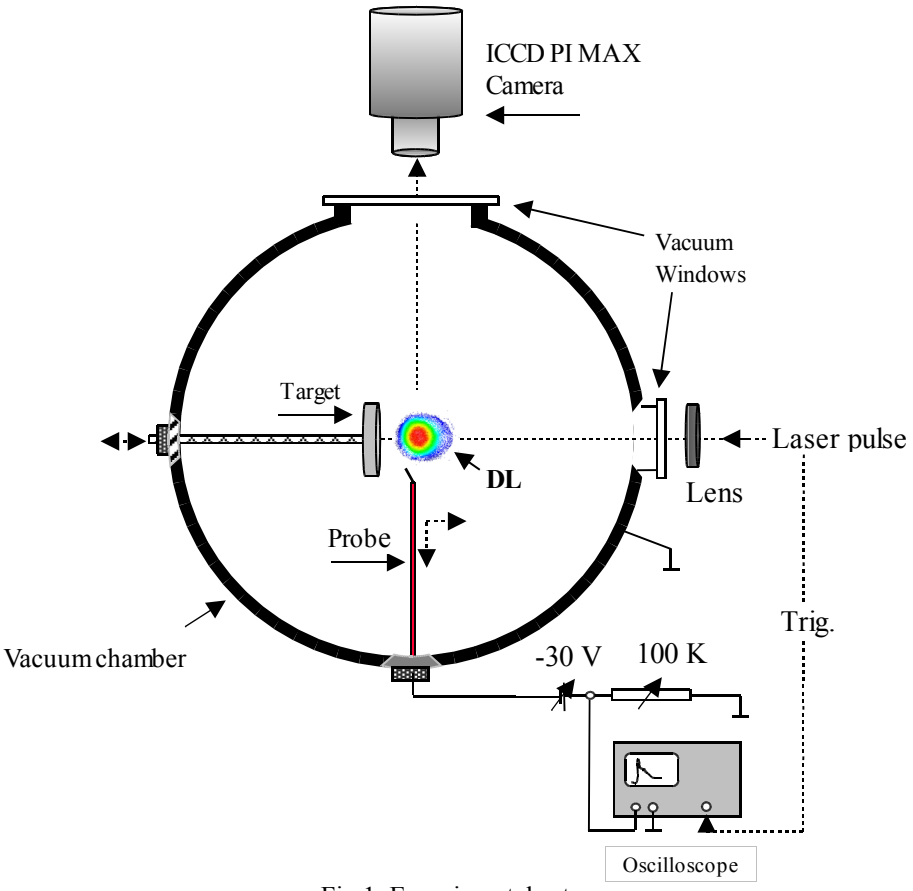

Fig.1. Experimental set-up

The total ionic current extracted from the high potential side of the nearly spherical space charge structure generated by the impact of the laser beam on the aluminum target was measured by means of a cylindrical Langmuir probe (stainless steel 0.8 mm in diameter and 5 mm in length) biased at negative voltage (-30 V,

stabilized dc power source), placed at different distances from the aluminum target. The transitory signals have been recorded by a 500 MHz digital oscilloscope (LeCroy 9350AM) and transferred to a PC for further analysis (LabView environment).The formation and dynamics of the space charge structures have been studied by means of an intensified CCD camera (PI MAX, 576X384 pixels, gating time 20ns) placed orthogonal to the plasma expansion direction. To image the plume region onto the camera a Nikon lens was used.

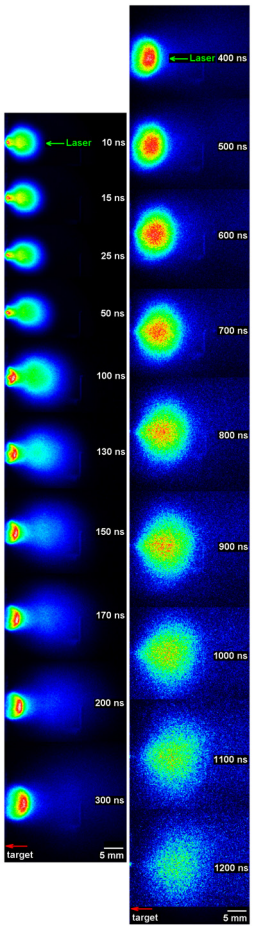

Figure2. The evolution of visible emission from the aluminium plume recorded using an ICCD PI MAX camera

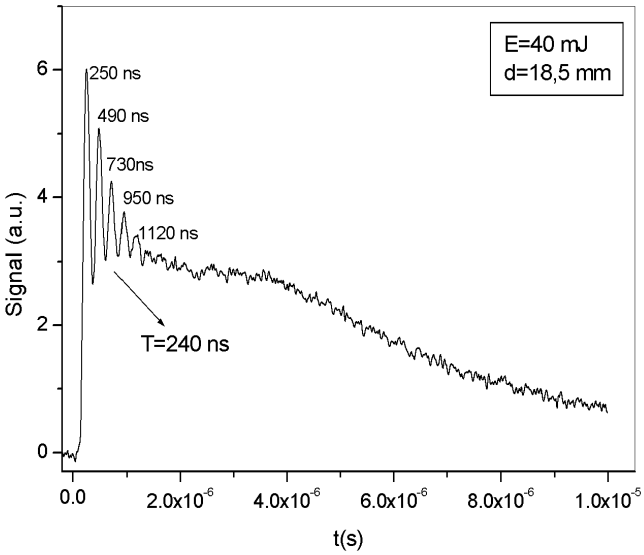

Figure 3. Transient (time-of-flight) signals recorded by Langmuir probes in a plasma plume created by 532 nm laser ablation of aluminum target. The distance from target to probe is 18.5 mm.

The images of these structures (Figure 2) reveal a splitting process of the plasma blobs. ICCD images of the plasma plume recorded at different time after each laser pulse evidenced two well-localized spherical plasma space charge structures. We evidenced the existence of periodic variations in the total ionic densities recorded by a Langmuir probe placed at 18.5 mm distance on the normal to the aluminium target.

Conclusions

This work studies the dynamics of the double layers obtained in laser ablation plumes by means optical and electrical diagnosis

References

[1] C. Focsa, C. Mihesan, M. Ziskind, B. Chazallon, E. Therssen, P. Desgroux and J. L. Destombes, J. Phys.: Condens. Matter, **18** (2006) S1357

[2] S. Gurlui, M. Sanduloviciu, M. Strat, G. Strat, C. Mihesan, M. Ziskind, and C. Focsa, J. of Optoelectr. and Adv. Mat., **8** (2006) 148

[3] N. M. Bulgakova, A.V. Bulgakov, and O.F. Bobrenok, Phys. Rev. **E 62** (2000) 5624

[4] S. Gurlui, M. Sanduloviciu, C. Mihesan, M. Ziskind, C. Focsa, AIP Conf. Proc., **812** (2006) 279

[5] S. S. Harilal, C.V. Bindhu, M.S. Tillack, F. Najmabadi and A.C. Gaeris, J. Phys. D: Appl. Phys. 35 (2002) 2935

P 25

Ozone Decomposition on Metallic Materials

G. Horváth[1], J. D. Skalný[1], J. Országh[1], V. Chernyak[2], I. Prisyazhnevich[2]

[1]Department of Experimental Physics, Faculty of Mathematics, Physics and Informatics, Comenius University, Mlynská dolina F-2, Bratislava

[2]Radiophysics Faculty, Taras Shevchenko University, Kyiv, Ukraine

e-mail: horesz@centrum.sk

The study of ozone decomposition is important form the different points of view. As the ozone is an exceptionally important filter of UV light in the Earth atmosphere and it is widely used in the industry ozone decomposition is an important topic [1]. In general the processes of ozone destruction can be divided into two groups

a) homogeneous reactions in the gas phase

b) heterogeneous reactions on the surface of materials in liquid or solid state.

In [1] the authors are concerned also in ozone decomposition. The coefficients of ozone decomposition on the surfaces of various materials (MgO, ZnO, steel, glass,…) at different temperatures (195 – 413 K) and pressures ($7x10^{-4}$ – 760 Torr) are shown in the table. Atyaksheva et al. [2] were interested in ozone decomposition in contact with fabric made of carbon fibres. They studied time dependence of ozone decomposition at different temperatures. With increasing temperature the ozone decomposition was decreasing. Kelichi Nashimoto was dealing with the production of ozone and NO_x in corona discharge generated in coaxial reactor [3]. The goal of the paper was to find out what is the influence wire material on production of these compounds. It was found out that ozone concentration decreases with the absolute value of ΔH_0 (highest standard heat of formation of oxides per oxygen atom) in positive corona discharge but no significant effect was found in negative polarity of the discharge. In 1992 Alebić-Juretić et al. published paper concerning with destruction of ozone on various kinds of powders (powders of silica-gel, alumina, sodium chloride, calcite, Saharan sand and wood ash) [4]. For different powders the ozone concentration has dropped to 25% for silica gel, 26% for alumina, 13% for wood ash, 30% for Saharan sand, 60% for calcite and 100% for NaCl. In our experiments we were interested in ozone decomposition (the rate of these processes) in the cylindrical cell made of aluminium, brass or stainless steel. The effects of material and cylinder radius were studied.

The ozone was produced by negative corona discharge fed by pure oxygen. The discharge tube with coaxial electrodes made of stainless steel was connected with the cell placed in the UV spectrometer by pipe. The cell was equipped by metallic cylindrical inner walls. Aluminium, stainless steel and brass cylinder used as walls in the cell with the diameter of 14 mm were used. One additional brass cylinder with the diameter of 7 mm was used to examine the effect of the metallic surface dimensions was used. When the cell was filled up by the mixture of ozone and oxygen from the discharge reactor, it was closed and the time dependence of ozone concentration has been measured. The rate of decomposition was calculated by linear fitting of measured points from the slope of the regressed line. The ozone decomposition has an exponential character which can be described by equation $[O_3] = [O_3]_0 \exp(-kt)$, where k is the rate constant given in [s^{-1}] and $[O_3]_0$ is the initial ozone concentration in [cm^{-3}]. The calculated rate constants of ozone decomposition are $k_s = 4.113 \times 10^{-4}$ s^{-1} for stainless steel, $k_a = 4.360 \times 10^{-4}$ s^{-1} for aluminium and $k_b = 4.113 \times 10^{-4}$ s^{-1} for brass. For the brass cylinder with diameter of 7 mm the rate constant is $k_{b7} = 1.088 \times 10^{-3}$ s^{-1}. In comparison with the results of [5] the difference for aluminium was approximately 12% and for stainless steel 45%. All the measurements were repeated several times to find out if any ageing of the metal surface is present. Only in case of brass surface the ageing effect has been observed. The rate constant was decreasing with repeated measurements. In the Figure 1 the time dependence of ozone concentration for the first and last (10^{th}) measurement is shown. The difference is approximately one order of magnitude. It can be suggested that thin layer of oxides if formed on the surface and ozone decomposes slower in contact with these oxides than in contact with clean brass.

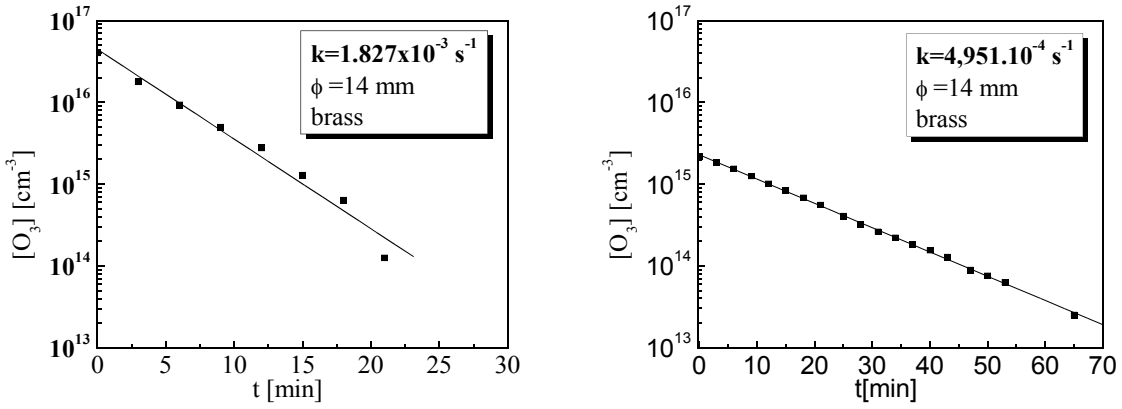

Fig. 1.Difference in the rate constant for the first and last measurement performed within the period around 120 hours.

Homogenous processes responsible for O_3 decomposition are active in the volume of the cell

$$M + O_3 \rightarrow O + O_2 + M \qquad k_1 = 2.28 \times 10^{-26}\ cm^3 s^{-1}\ (M = O_2)\ [6] \qquad (1)$$

Heterogeneous processes are active on the wall of the reactor or pipe

$$O_3 + \text{wall} \rightarrow \text{products} \qquad k_2 = 1.71 \times 10^{-5}\ s^{-1}\ [6] \qquad (2)$$

The rate of reaction (1) at ambient temperature is lower than rate of decomposition on the surface.

The following approximation has been considered. Let ΔN be the number of ozone molecules decomposed on the unit length of the cylindrical surface per second. It can be calculated if we presume that ozone molecules in thin layer at the surface are transported to the wall by thermal movement. Then let us presume that there is no gradient of ozone concentration n and that mean velocity v_s is determined by the temperature. Then equation

$$\frac{dn}{dt} = -\frac{\Delta N}{V} = -\frac{\Delta N}{\pi . R^2} = -\frac{1}{2}\frac{\gamma . v_s}{R} n \qquad \{1\}$$

where γ is the probability that ozone molecule is decomposed and V is the unit volume of the tube expresses the relation ship between rate of ozone decomposition and probability of O_3 molecule decomposition. The expression $\frac{1}{2}\frac{\gamma . v_s}{R}$ can contribute to the rate coefficient k as it can be considered in the form of $dn/dt = - k_d.n$. This way we can gain information concerning probability of ozone decomposition from the experimentally obtained rate constants.

The decomposition of ozone on the wall strongly depends on the wall material. Brass surface was found to be highly reactive in the ozone filled space but with repeating measurements it showed the quickest ageing. It caused decrease of the rate constant. Theoretical equation for calculation of the probability of O_3 decomposition on the surface was derived.

This research project was supported by Slovak Research and Development Agency SK-UA-01906 and by Slovak Grant Agency VEGA under project 1/1267/04.

[1] Lunin, V. V., Popovich, M. P., Tkatchenko, S. N.: Phizitcheskaya khimiya ozona, Izd. Moskovskogo Universiteta (1998).

[2] Atyaksheva, L. F., Emelyanova, G. I.: *Zhurnal Phizitcheskoj Khimii* **63** 2606-2609 (1989).

[3] Nashimoto, K.: *Journal of Imaging Science* **32** (1988).

[4] Alebić-Juretić, A., Cvitaš, T., and Klasinc, L.: *Ber. Bunsenges. Phys. Chem.* **96** No. 3 (1992).

[5] K. Yanallah, S. Hadj Ziane and A. Belasri. Ozone decomposition on walls. *Plasma Devices and Operations,* Vol. 14, No. 3, 215-222 (2006).

[6] Eliasson, B.: 1985, Electrical Discharge in Oxygen: Part 1. Basic Data, Rate Coefficients and Cross Sections. Report KLR 83/40 C, Brown Boveri Forschungszentrum, Baden-Dättwil, Switzerland.

P 26

Laboratory of High-Power Femtosecond Ti:Sapphire Laser at FNSPE CTU

R. Havliková, D. Klír, V. Kubeček, J. Limpouch, L. Pína, A. Zavadilová

Czech Technical University in Prague, Faculty of Nuclear Sciences and Physical Engineering, Břehová 7, 115 19 Praha 1, Czech Republic

e-mail: havlikov@troja.fjfi.cvut.cz

Abstract

Laboratory of high-power femtosecond laser (pulse energy 12 mJ, pulse duration 70 fs, repetition rate 10 Hz) has been opened at the Department of Physical Electronics of FNSPE CTU in Prague. The interaction area will include cylindrical vacuum chamber of radius 500 mm and height 400 mm and high-power capillary discharge. The planned program of the laboratory is briefly discussed.

Introduction

The advent of chirped pulse amplification (CPA) of ultrashort laser pulses in 1985 opened path to an unprecedented boom in research of interaction of intense laser radiation with matter. Thanks to the funds allocated in the frame of project LC528 "Laser Plasma Centre" supported by the Ministry of Education, Youth and Sports of the Czech Republic, we have been able to acquire small high-power 0.1 TW Ti:Sapphire femtosecond laser delivered by the French company "Amplitude Technologies". Presently, targets chambers are being prepared for experiments. This paper presents the facility and review experimental research plans.

Femtosecond laser

Laser system at FNSPE CTU in Prague (shown in Fig.1) consists of three boxes of 1200×600 mm, of two power supplies and of control unit. Ti:sapphire oscillator (Femtolasers GmbH) is pumped by 2 W of second harmonics of diode-pumped continuous wave Nd:vanadate laser. The oscillator average power in mode-locked regime is 130 mW (bandwidth 32 nm, pulse width below 60 fs, repetition rate 75 MHz). Higher pump power would extend the bandwidth and shorten the laser pulse. The output pulse train is sent to Offner type triplet on-axis stretcher with bandwidth 80 nm where it is extended to duration of approximately 200 ps before two-step amplification. The both Ti:sapphire amplifiers are pumped at repetition rate of 10 Hz by 120 mJ of second harmonic radiation from a flashlamp-pumped Nd:YAG laser. The first stage is a regenerative amplifier with contrast enhanced by two Pockels cells. The second stage is a multi-pass amplifier with Ti:sapphire crystal double side pumped. The single pulse energy after amplification is 20 mJ, which corresponds to 14 mJ energy and 63 fs pulse duration after optical compressor, The contrast ratio relative to a prepulse leaking through the regenerative amplifier 11 ns ahead of the main laser pulse is 1500, and the contrast during 20 ps before laser pulse is 10^7. The beam laser beam spatial profile is flat top with diameter of 12 mm, the beam quality $M^2 < 1.5$, central wavelength 802 nm, polarization 100:1 and energy stability <2% rms. A motorized shutter is available for single pulse operation. The focused intensities of few times 10^{16} W/cm^2 are expected.

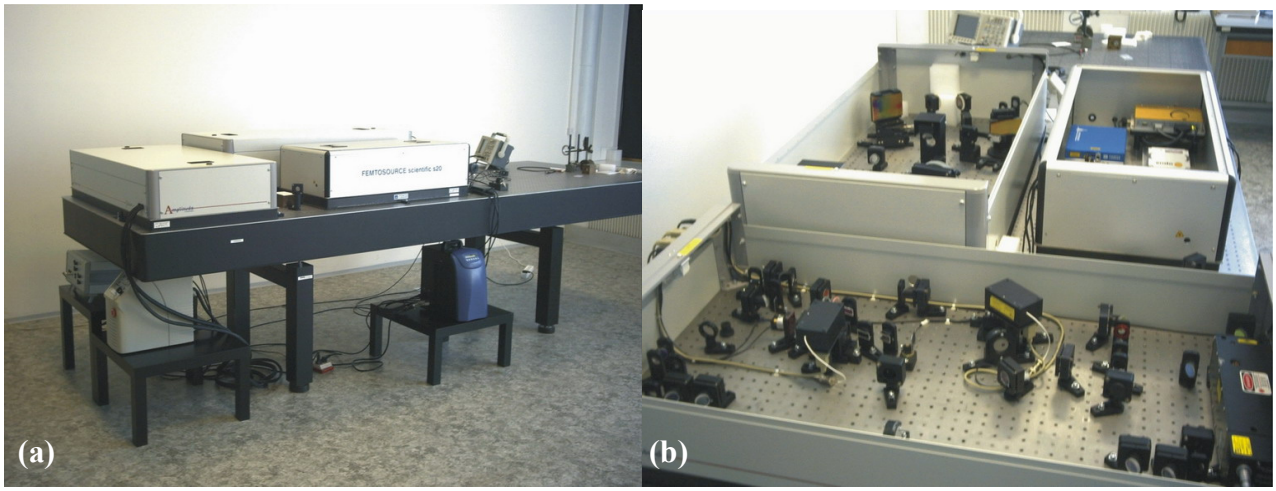

Fig. 1 Overall view (a) of Ti:Sapphire laser at FNSPE CTU in Prague, detailed view (b) into the three laser boxes, oscillator box (right), amplifier box (front) and stretcher and compressor (left).

Target areas

Two target areas are prepared for laser interaction experiments. The first one is the vacuum chamber for laser-target experiments and the second installation is planned for capillary discharge experiments.

The steel vacuum chamber for laser-target experiments is cylindrical with inner radius 500 mm and height 400 mm with fold back lid. Eight flanges of diameters 40, 100 and 160 mm are placed around the cylinder, one 100 mm flange is placed in the lid. The chamber will be pumped to 1 Pa for X-ray measurements and to 10^{-2} Pa for charged particle diagnostics.

Alternatively, laser may be focused to capillary discharge in the second installation which consisted of several parts including the vacuum chambers. This part will be pumped down to 10^{-2} Pa.

Both parts will be equipped with optical and X-ray diagnostics for imaging, spectroscopy, and time resolved measurements.

Experimental plans

High harmonics up to several hundreds may be generated in a gas cell or in a gas jet placed into the vacuum chamber. This coherent radiation may reach 13.5 nm range at our laser and attosecond pulses are generated due to phase-locking of different harmonics [1]. In principle, high harmonic radiation may be amplified in an amplifier pumped by capillary discharge, and high-power short wavelength laser may be constructed [2].

Intense short pulses of hard line X-ray K-α radiation are used for ultrafast X-ray crystallography [3] and dense plasma radiography, their applications in medical imaging have been proposed. Laser intensities in range 10^{16} – 10^{17} W/cm^2 are ideal for K-α emission from Al and Cu targets [4]. Detailed spectra of K-α emission from metal, dielectric and foam targets will be measured with a high spectral (> 5000) and spatial (< 10 μm) resolution using vertical Johann spectrograph with cylindrically bent crystals [5]. Laser prepulse, layered targets and low-density foams will be used for optimization of K-α yield.

Intense incoherent soft X-ray radiation in 13.5 nm range and in water window is emitted in femtosecond laser interaction with various materials [6]. This source will be used for testing and calibration of various X-ray optics systems. Confined microexplosions will be studied by focusing femtosecond laser pulse inside bulk transparent media. This interaction leads to the drastic transformations in a solid resulting in a void formation inside a dielectric [7]. Experiments oriented on biomedical applications of femtosecond lasers pulses are also anticipated [8].

For many applications, it is vital to extend the propagation of focused high-intensity laser beams over many Rayleigh lengths. Guiding of femtosecond laser pulses in gas-filled and ablation-filled capillary discharges has been already demonstrated [9] and used for improvement of electron wakefield acceleration [10] and for enhancement of transiently pumped XUV laser output [11]. Search for optimum regimes for guiding of laser beam in capillary discharge plasma is planned. We shall study various regimes that combine high-current fast capillary discharge and femtosecond laser pulse to improve characteristics of plasma XUV lasers.

Acknowledgements: This research is partially supported by the Ministry of Education, Youth and Sports of the Czech Republic within the project LC528 “Laser Plasma Centre”.

References

[1] P. Agostini, L.F. di Mauro, *Rep. Prog. Phys.*, 67 (2004) 813.
[2] P. Zeitoun, G. Faivre, S. Sebban, T. Mocek, A. Hallou, M. Fajardo *et al*., *Nature*, 431 (2004) 426.
[3] C. Rose-Petruck, R. Jimenez, T. Guo, A. Cavalleri, CW. Siders, F. Baksi *et al*., *Nature*, 398 (1999) 310.
[4] J. Limpouch, O. Klimo, V. Bína, S. Kawata, *Laser & Particle Beams*, 22 (2004) 147.
[5] O. Renner, T. Missalla, P. Sondhauss, E. Krousky, E. Förster *et al*., *Rev. Sci. Instrum.*, 68 (1997) 2393.
[6] U. Teubner, W. Theobald, C. Wulker, E. Förster, *Phys. Rev. E*, 50 (1994) R3334.
[7] E. Gamaly, S. Juodkazis, K. Nishimura, H. Misawa, B. Luther-Davies, *Phys. Rev. B*, 73 (2006) 214101.
[8] H. Jelinkova, T. Dostalova, M. Nemec, P. Koranda, P.Simunek *et al*., *Laser Phys. Lett.*, 3 (2006), 43.
[9] D.J. Spence, A. Butler, S.M. Hooker, *J. Phys. B*, 34 (2001), 4103.
[10] B. Hafizi, D.F. Gordon, A. Zigler, A. Ting, *Phys. Plasmas*, 10 (2003), 2545
[11] T. Mocek, C.M. McKenna, B. Cros, S. Sebban, D.J. Spence *et al*., *Phys. Rev. A*, 71 (2005), 013804.

P 27

Quantum Chemistry of Dissociative Electron Attachment to Adenine

N. Injan[1,3], M. Probst[1], S. Denifl[1], F. Zappa[1], J. Limtrakul[3], T. Märk[1,2], P. Scheier[1], J. Urban[2] and P. Mach[2]

[1] Institute of Ion Physics and Applied Physics, University of Innsbruck, 6020 Innsbruck, Austria
[2] Department of Nuclear Physics and Biophysics, Comenius University, Mlynská dolina, Bratislava 842 45, Slovakia
[3] Department of Chemistry and Center of Nanotechnology Kasetsart University, Bangkok 10900, Thailand
e-mail: michael.probst@uibk.ac.at

Abstract

We report calculations related to recent experiments of electron attachment to adenine and related derivatives of purine. The positions of hydrogen detachment are predicted by means of quantum thermochemical calculations. Attempts are made to model this process by identifying the relevant molecular orbitals and by calculating potential energy curves of the states which may play a role in the dissociation. The electrostatic potential of the molecules is used as a descriptor to explain the different detachment spectra of rather similar molecules.

Introduction

Dissociative electron attachment (DEA) of molecules is important for a variety of reasons. The general interest of understanding electron-driven processes is reinforced by the fact that such reactions are central to the mechanisms of radiation damage to living cells and of chemical reactions under astrophysical conditions. It is further reinforced by the fact that electron-molecule reactions play a major role in semiconductor industry, nanotechnology and in surface engineering. Ultimately, a detailed knowledge and understanding of electron-driven reactions might open a door towards fine-tuning chemical reactions in a similar way as electromagnetic radiation by means of ultrashort, customized laser pulses can already be used.

This presentation deals with the interaction of electrons with nucleic acids. Recent experiments carried out in Innsbruck [1] showed that electrons with low energies from about 0.5 eV upwards cause abstraction of a hydrogen atom from adenine, one of the bases that constitute DNA. These studies were augmented by experiments on slightly different molecules. All of these have two N-substituted fused rings, one six- and one five-membered and are members of the purine class of heterocycles.

Results and discussion

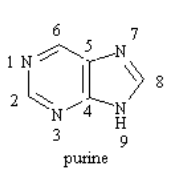

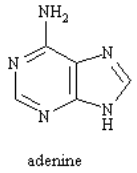

Structures of purine and adenine and the standard IUPAC numbering are shown to the right. Both molecules have hydrogen atoms at four positions of the ring if one regards the two hydrogens of the NH_2 group of adenine as equal. All purines studied by us have a negative electron affinity, their anions are thermodynamically less stable than the neutral molecule and a distant electron. Quantum thermochemical calculations allow reliable determination of the

BDE of H from	**Purine** neutral	anion
C2	4.91	3.42
N6	4.81	3.16
C8	5.20	2.33
N9	4.81	0.72

BDE of H from	**Adenine** neutral	anion
C2	4.74	3.63
N6	4.69	1.72
C8	5.06	2.53
N9	4.38	0.94

bond dissociation energies (BDEs) of the hydrogen atoms. The results for purine and adenine from G2(MP2) calculations are given in the tables above. For both molecules by far the smallest energy is – less than 1 eV - required for abstraction of H from the N9 position in the anionic case. Like in similar cases, the energy required for formation the $(M^{minus}H)^-$ anions is considerably less than the one needed for bond-breaking in the neutral case since closed-shell anions are energetically favored over neutral radicals The difference between neutral and anionic BDEs is equal to the electron affinity (EA) of $(M^{minus}H)$. For a detailed understanding of the reaction mechanism, knowledge of the relevant potential energy curves is prerequisite. Since hydrogen detaches from the N9 position, the approximation of a one-dimensional reaction coordinate seems justified.

In the equilibrium structure of the neutral molecule a metastable anion is less stable than the neutral species, but for large N9-H distance it is more stable, meaning that the neutral and anionic $E=f(r_{N9\text{-}H})$ curves cross each other. The calculation of the neutral potential energy curves poses only the general problem of an accurate description of homolytic bond breaking. The anionic ones are more interesting. In the region left of this crossing ($r_{N9\text{-}H} \sim\leq 1.4$) the anion not stable and therefore its energy cannot be calculated by standard quantum chemical methods. Life mentioned above, only the energy of the neutral species is retrieved in the limit of an infinite basis set. Second, it can be seen from the symmetry of the LUMO and the higher unoccupied molecular orbitals of the neutral species that the state that responsible for bond weakening/breaking is not the (stable or metastable) anionic ground state. The single electron of the anion at its lowest energy normally occupies a π-MO with a zero density in the molecular plane and therefore does not influence the N9-H bond. It is the lowest (or next-to-lowest) σ-MO that can weaken this bond. All theses states are, however, quite close in energy.

(a) For obtaining anionic potential energy curves, we applied the following method:

(b) We identify the lowest σ - orbital from a Hartree-Fock calculation of the neutral molecule using the aug-cc-pVTZ basis set.

(c) We inspect this MO graphically to see if it exhibits σ* - character at the N9-H bond.

(d) We calculate its energy by means of the outer-valence Greens' function method as a function of $r_{N9\text{-}H}$.

(e) The resulting EA curves are smooth and cross the E=0 line at $r_{N9\text{-}H}o \approx 1.4$ Å. Only positive values are physically meaningful. The negative values are replaced by polynomial extrapolation of the positive branch towards smaller distances.

(f) The total energy of the anion is obtained by adding the EA curves and the neutral potential energy curve.

The result for purine is shown in the picture to the right, together with the lowest vibrational levels. In reality, the two potential energy curves interact with each other leading to an avoided crossing. The resulting curves can in principle be obtained from the equation

$$\begin{pmatrix} E^{upper}(r) \\ E^{lower}(r) \end{pmatrix} = EV\left[\begin{pmatrix} E^{neutral}(r) & C \\ C & E^{anion}(r) \end{pmatrix}\right]$$

where C is the amount of the 'repulsion' between the curves and EV(M) is the vector of the eigenvalues of M. The dissociation probability, for example via tunneling, could then be calculated. We are presently working on this step. It is, however, difficult to get quantitative results: The neutral PE curve is only an approximation of the one for the dipole-bound state and the extrapolation method is not completely exact as well.

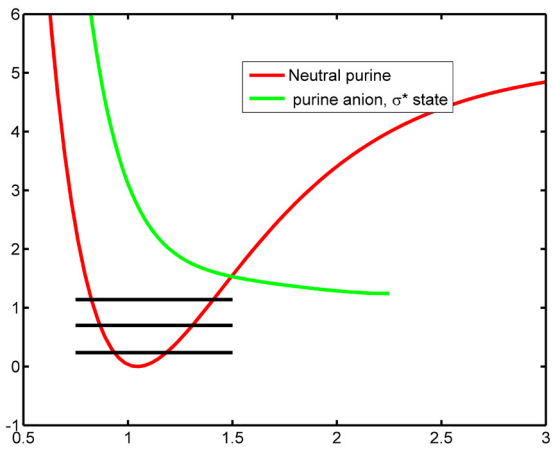

Last, we would like to mention that the electrostatic potential (ESP) of the molecule influences the shape of the diffuse anionic MO. The ESP at the N9-H region is always positive. For example, in case of adenine the only other positive region is the NH_2 group and therefore the σ* -MO density link the two regions. This explains why the remote groups cause the fine structure of the electron energy spectra to be quite different.

Conclusions

Stable and metastable anions of purine derivatives have been studied with respect to DEA experiments. The sites of H-abstraction are in perfect agreement with experiments. Potential energy curves have been calculated and an explanation of the effect of the functional groups on the observed spectra has been given in terms of the molecular ESP.

References

[1] D. Huber, M. Beikircher, S. Denifl, F. Zappa, S. Matejcik, A. Bacher, V. Grill, T.D. Märk, P. Scheier, *J. Chem. Phys*. 2006, 125, 084304-7.

P 28

Production and Nanolithography on Silicon Nanoparticle Films

S. Jaksch, F. Zappa, P. Scheier

Institut für Ionenphysik und Angewandte Physik, Leopold-Franzens-Universität Innsbruck, Technikerstrasse 25, A-6020 Innsbruck, Österreich

e-mail: stefan.jaksch@uibk.ac.at

Abstract

Films of silicon nanoparticles are formed by a magnetron sputtering and deposition onto highly oriented pyrolitic graphite (HOPG). The effect of different parameters such as the distance between magnetron and graphite surface, pressure, discharge current and deposition time is analyzed with a variable temperature scanning tunneling microscope (STM). Well defined manipulation in the nanometer regime of the films with the STM tip is demonstrated and electronic properties of the films are probed by local scanning tunneling spectroscopy (STS).

Experimental

Silicon nanoparticles are formed by magnetron sputtering of a pure silicon target and deposited onto freshly cleaved highly oriented pyrolytic graphite (HOPG). The sample preparation chamber is directly connected to a scanning tunneling microscope (STM) which enables a fast transfer into the ultra high vacuum of the analyzing part of the instrument. Thereby the contamination (oxidation) of the silicon nanoparticles is reduced to a minimum.

With the STM we are investigating the structure of the sputtered silicon nanoparticles with STM images and their electronic properties with scanning tunneling spectroscopy (STS). The presently utilized STM enables to investigate the silicon nanoparticles in a temperature range from 25K to approximately 1300K.

Results and discussion

The growth of very homogeneous silicon nanoparticle films is observed and studied. The silicon nanoparticle films are produced with a magnetron sputtering source. On HOPG the nanoparticles are deposited and investigated. We investigated the behavior of the films formed with different sputtering parameters. For the present study we analyzed the dependence on the distance / geometry, pressure, current, and also time. The distance / geometry had the strongest influence on the sputtering behavior. It was only possible to sputter in a distance regime of approximately 8cm from the sample. It's interesting to note that the influence of edges of the vacuum vessel can be neglected up to this distance.

Changes in the pressure of Ar used for sputtering affected the amount of deposited silicon nanoparticles. In addition, the sticking coefficient of the nanoparticles on the HOPG got worse with higher pressure. For very low pressure (4×10^{-3}mbar) we obtained fractal structures and decoration of defects in the HOPG substrate (see Fig. 1, left). Moreover, the overall roughness of the film increases with higher pressure.

Fig. 1 (Right) shows the initial process of film formation where a few nanoparticles are attached to each other and form isolated hillocks on the graphite surface. On the upper left corner a step in the HOPG surface is densely covered with silicon. The low roughness of this structure indicates fusion of nanoparticles into a nanorod (nanowire) [1]. Defects like steps in the HOPG are not only decorated in the first layer of nanoparticles but also in the higher layers (Fig. 4 (Right)).

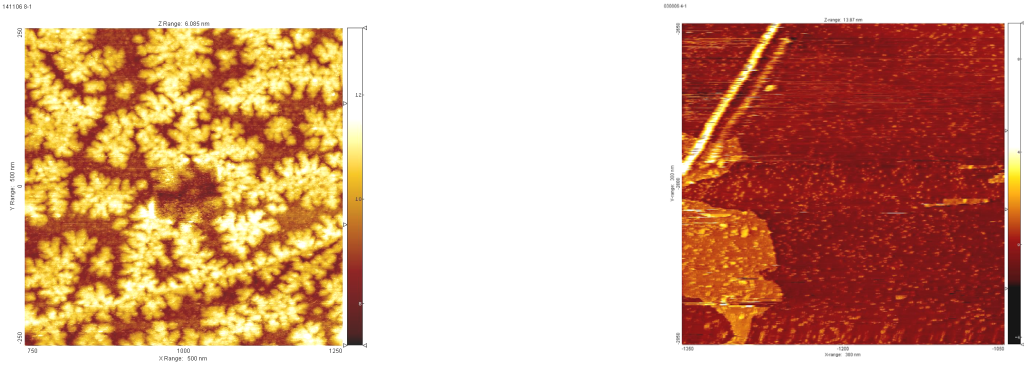

Fig. 1: Left: Fractal structure and decoration of defects; Right: Formation of silicon nanoparticle islands

Modifications like vaporization, fusion and removal of nanoparticles with the STM tip on the nanometer

scale are also possible. These techniques enable a novel kind of nanolithography and we are able to form different grey scales and patterns in the silicon film. Fig. 2 and Fig. 3 show grey scale patterns formed by different tunneling currents and different numbers of scan cycles. The right diagram shows a sectional scan for the white line in the image on the left.

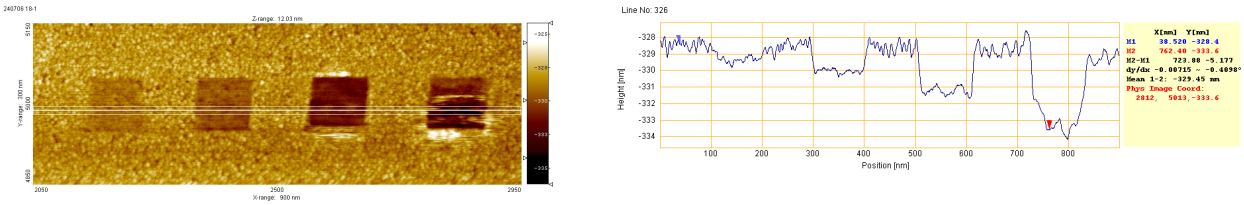

Fig 2: Greyscale series by different tunneling currents

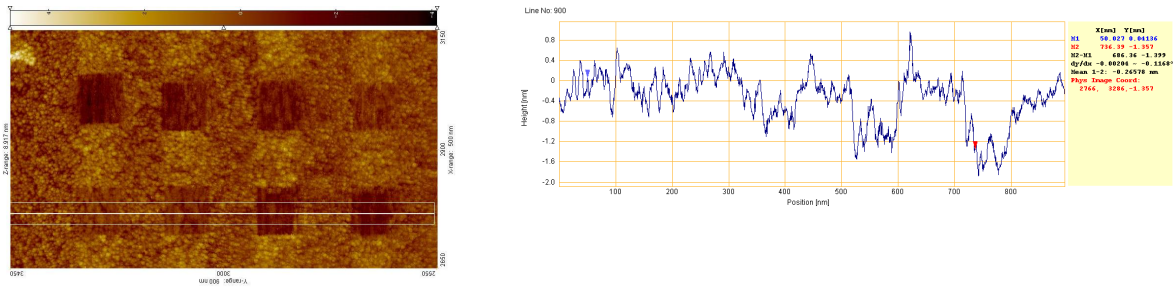

Fig 3: Greyscale series by different numbers of scan cycles

At increased bias-voltage, applied between the tip and the silicon nanoparticle film, we are able to fuse some silicon nanoparticles into larger objects. Fig. 4 (Left) shows this behavior for a 100nm × 100nm square scanned with a bias-voltage of 8V. Also the electronic density of states is changed and probed with complementary scanning tunneling spectroscopy measurements. Fig. 4 (Right) shows the removal of silicon nanoparticles on a square of 50nm × 50nm by the tip. For this effect the bias voltage was lowered down to 0.5V to dip the tip into the film and wipe away the clusters.

Fig. 4: Left: Fusion of silicon clusters; Right: Removal of silicon clusters

Conclusions

We have started to investigate in detail the growth and the properties of films of silicon nanoparticles formed by magnetron sputtering and deposition on freshly cleaved HOPG. The methods utilized are STM and STS at room temperature but with the option to perform these studies also in a wide temperature regime from 25K to 1300K. It is planned to determine the conditions for a film that has optimum properties for subsequent nanolithography as described above. A high resolution grey scale image will be imprinted on such a film. The stability of the films and the nanolithography is going to be studied at elevated temperatures in the STM.

References

[1] B. Marsen, K. Sattler, Phys. Rev. B **60**, 11593-11600 (1999)

P 29

Grafting of Hexamethyldisiloxane and Hexamethyldisilazane onto Polypropylene in Atmospheric Dielectric Barrier Discharge Nitrogen Plasma

Z. Jakubíková, M. Mikula

Department of Graphic Arts Technology and Applied Photochemistry Institute of Polymer Materials, SUT Bratislava
e-mail: zuzana.jakubikova@stuba.sk

Abstract

In our study an atmospheric dielectric barrier discharge DBD in nitrogen was used for polypropylene PP treatment in order to graft hexamethyldisiloxane HMDSO and hexamethyldisilazane HMDSZ onto the surface of PP. The surface chemistry of the treated samples was investigated using Attenuated Total Reflectance Fourier Transform Infrared Spectroscopy ATR-FTIR.

Introduction

Polymeric materials, especially PP, are widely used in various fields of industry for their excellent bulk properties, chemical inertness and also for its low cost. However, most of these polymeric materials and also PP prove insufficient surface properties required for their industrial applications such as low wettability, surface energy hence low adhesion, low barrier properties and other. These facts enforced implementation of different surface modification and treatment techniques to improve and achieve desired surface properties (printability, hardness, gas transmission, blood compatibility, etc.) requested in particular industrial applications. Among these surface treatment techniques, the most common used are corona discharge, plasmas, ion beam and UV surface modification [1]. Thin film deposition (PE-CVD), grafting of chemical groups, cross-linking (plasma treatments), and etching are the most utilized plasma processes [2]. Silicon-based monomers have been widely used in low pressure discharge processes for deposition onto various substrate surfaces [3] and some experiments have been carried out in atmospheric pressure glow discharge (APG) [4]. Polymers treated by silicon-based monomers impart specific characteristics such as hydrophobicity, reduced gas permeability, and hard transparent coatings.

Experimental

Biaxially oriented PP foils TATRAFAN ON 40μm thick were treated by barrier discharges at atmospheric pressure in industrial grade nitrogen. The barrier discharge device as shown in Fig. 1 consisted of two copper electrodes separated by an air gap (1.2 mm) and glass barriers (two 1 mm sheet glasses on both sides). One electrode was connected to the high-voltage, low-frequency source (15 kV, 5 kHz, 0.1 W/cm2) and the other was grounded. Different treatments times (ranging from 1 to 20 s) and flow rates of N_2 (2, 5, 8 l.min^{-1}) were used in our experiments. HMDSO and HMDSZ grafting were applied after plasma treatment in a chamber with a vessel (57 cm^2) filled with HMDSO and HMDSZ liquids. We assumed free evaporation to be sufficient for HMDSO and HMDSZ grafting. After treatment in DBD the sample was continuously pulled from the DBD chamber into the grafting chamber with HMDSO or HMDSZ without any exposition to air after treatment in DBD and left there for 60 s in order to allow grafting.

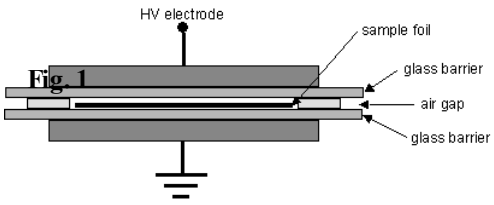

Fig. 1

The multiple ATR technique with a Ge crystal (45° and 25 reflections) of infrared absorption spectroscopy (FTIR spectrophotometer Excalibur FTS 3000 MX, Digilab) was used to elucidate the chemical changes at the surface of treated samples. The crystal was cleaned prior to every measurement to prevent a cumulative contamination from low molecular weight compounds formed during degradation reactions on the treated surface.

Results and Discussion

Infrared absorption spectra of the deposited films showed the presence of characteristic functional groups. Figures illustrate treatments at different exposure times. Fig. 2 presents formation of Si-CH_3 (1300- 1200 cm^{-1}) groups for both monomers. The peak at 1043 cm^{-1} (Fig. 3) demonstrates the formation of CH_2-O-Si (more probable for HMDSO) or wagging mode of Si-CH_2-Si (more probable for HMDSZ). Si-C bonds are well identified by an absorption bands about 700-850 cm^{-1} (Fig. 4) and are typical for both monomers. Mono-substituted amides CO-NH-R are distinguished at 1558 and 1541 cm^{-1} (Fig. 5) for

HMDSZ probably due to the presence of residual oxygen in the treatment device. The presence of air humidity is unambiguous according to wide peaks at 4000-3500 cm^{-1} and 1800-1500 cm^{-1}.

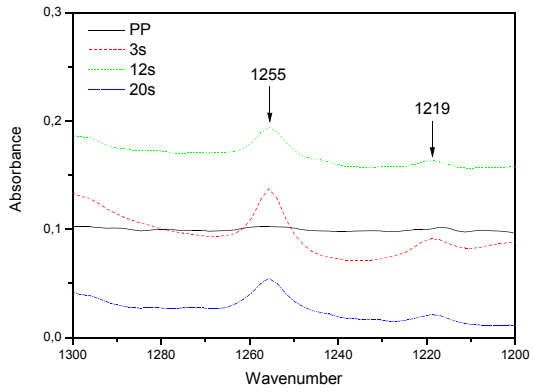

Fig. 2: Grafting of HMDSO onto PP at N_2 flow rate 8 l/min – Si- CH_3

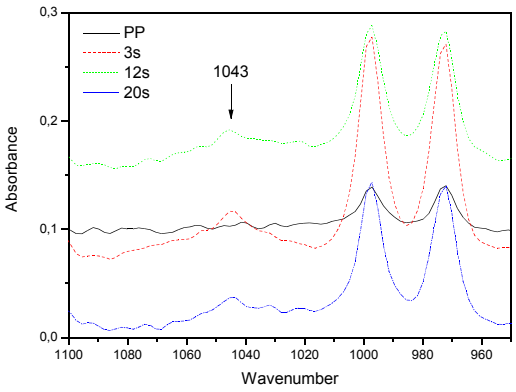

Fig. 3: Grafting of HMDSO onto PP at N_2 flow rate 8 l/min – CH_2-O-Si

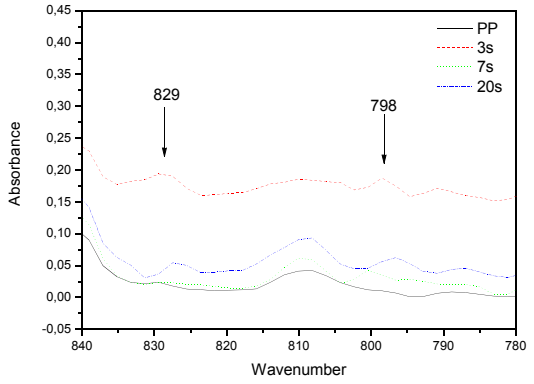

Fig. 4: Grafting of HMDSZ onto PP at N_2 flow rate 5 l/min – Si-C

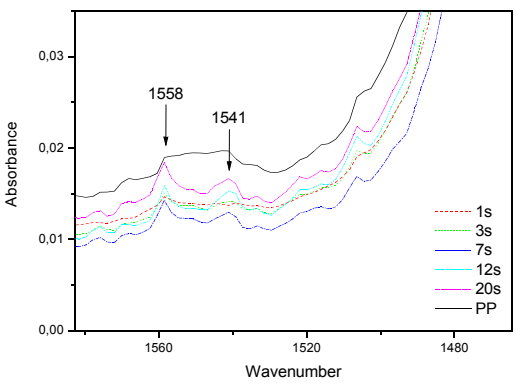

Fig. 5: Grafting of HMDSZ onto PP at N_2 flow rate 2 l/min – CO-NH-R mono-substituted amides

The N_2 flow rate, according to results, didn't influence the grafting. DBD is sufficient in grafting of thin organosilicon polymer films onto PP, however other evaluation techniques are needed.

Acknowledgement

We thank to Slovak Grant Agency for financial support (Projects Vega 1 /2454 /05).

References

[1] A. Bellel, S. Sahli, Z. Ziari, P. Raynaud, Z. Segui, D. Escaich, *Surface & Coatings Technology* 201 (2006) 129-135

[2] P. Favia, M. Creatore, F. Palumbo, V. Colaprico, R. d'Agostino, *Surface & Coatings Technology* 142-144 (2001) 1-6

[3] A. R. Denes, M. A. Tshabalala, R. Rowell, F. Denes, R. A. Young, *Holzforschung* 53 (1999) 318-326

[4] D. Trunec, Z. Navratil, P. Stahel, L. Zajickova, V. Bursikova, J. Cech, *J. Phys. D: Appl. Phys.* 37 (2004) 2112-2120

P 30

Optical Emission Spectroscopy Study of Transition Discharges in N_2/CO_2 Mixture at Atmospheric Pressure

M. Janda[1], Z. Machala[2], B. M. Rode[1], K. Hensel[2], V. Martišovitš[2]

[1]Department of Theoretical Chemistry, University of Innsbruck, Innrain 52a, Innsbruck 6020, Austria
[2]Department of Astronomy, Earth Physics and Meteorology, Comenius University, Mlynská dolina, Bratislava 842 45, Slovakia
e-mail: mario.janda@gmail.com

Abstract

The emission from new type of streamer-to-spark transition type discharge in N_2/CO_2 mixtures as a function of CO_2 concentration was studied. Emission of N_2 2nd and 1st positive systems, CN violet system, and atomic N, O and C lines were detected. The aim was better understanding of processes leading to the generation of CN.

Introduction

Chemistry induced by atmospheric pressure DC discharges burning to the water surface in N_2-CO_2-H_2O mixtures was studied recently [1, 2]. This gaseous mixture represents a model pre-biotic atmosphere of the Earth and a simplified flue gas from the stoichiometric combustion of the natural gas. The aim of these studies was the formation of organic species, especially amino acids, and the CO_2 decomposition.

For better understanding of processes leading to CN formation, we performed Optical Emission Spectroscopy (OES) study of discharges in this mixture. OES gives valuable information on excited atomic and molecular states, enables to determine the rotational and vibrational temperatures and thus gives insight in an ongoing plasma chemistry. As the first step, we analyzed the discharges in dry N_2/CO_2 mixture, which is presented here.

Experimental set-up

All experiments were carried out at room temperature in atmospheric pressure N_2/CO_2 mixtures (from 0 to 100 vol. % of CO_2), with the total gas flow from 0.08 to 0.32 l/min. The experimental set-up consisting of a discharge reactor and electric and optical circuits is depicted in Fig. 1.

DC high voltage power supply connected via a 9.82 MΩ series resistor limiting the total current was used to generate the discharge. We used filamentary discharges of transition type initiated by a streamer named 'Spontaneously Pulsing Transition Discharge' (SPTD) or 'Transient Spark' [3]. The voltage at the reactor was measured by the high voltage probe Tektronix P6015A and the discharge current was measured using the current probe Pearson Electronics 2877 (1V/A) linked to the 200 MHz digitizing oscilloscope Tektronix TDS2024. The UV-VIS spectra were obtained by a compact emission spectrometer Ocean Optics SD2000 (200 – 1100 nm, resolution 0.4 – 1.7 nm).

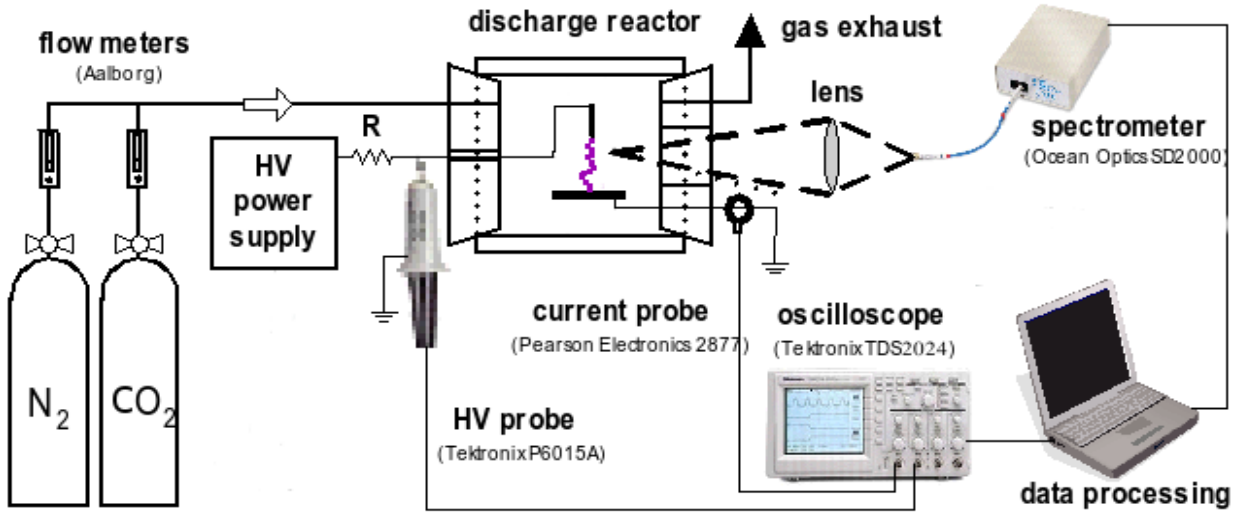

Fig. 1 – Scheme of the experimental set-up.

Results and discussion

The strongest lines observed can be attributed to the emission of N_2 2nd positive system ($C^3\Pi_u - B^3\Pi_g$) and CN violet ($B^2\Sigma^+ - X^2\Sigma^+$) system. The emission of N_2 1st positive system ($B^3\Pi_g - A^3\Sigma^+$), N_2^+ 1st negative system ($B^2\Sigma^+ - X^2\Sigma^+$), and atomic N, O and C lines were also observed, indicating plasmas with high electron temperatures with a high level of non-equilibrium. Non-equilibrium conditions were confirmed also by calculated vibrational (T_v) and rotational (T_r) temperatures (Fig. 2), obtained by fiting the experimental spectra of N_2 2nd positive system with the simulated ones (we use Specair simulation program [4]). The typical measured temperatures are: T_r = 400-800 K, T_v = 2100-2800 K.

It is possible to calculate T_v and T_r from CN violet system as well. We found that T_v and T_r of CN is much higher, around 11000 and 6000 K, respectively. Such high temperatures are unrealistic in a cold plasma and are in total disagreement with T_r and T_v measured from N_2. A possible explanation is that CN $B^2\Sigma^+$ excited state is not populated by electron impact but results from chemical reactions creating CN species. Vibrational and rotational distributions may be therefore non-Boltzmann and thus T_v and T_r are not defined.

The concentration of CO_2 (c_{CO2}) influences the intensity of individual emission lines directly (concentration of reactants), as well as indirectly, since it changes the discharge parameters. During our emission experiments, we kept the frequency of current pulses constant, but the waveforms of current and voltage changed with changing c_{CO2}. As a result, we found that in order to study the emission intensity as a function of c_{CO2} (Fig. 3), it is necessary to normalize the obtained spectra by the input energy. However, this is just an approximation, since it does not sufficiently reflect the changes of electron's energy as a function of c_{CO2} in our discharge.

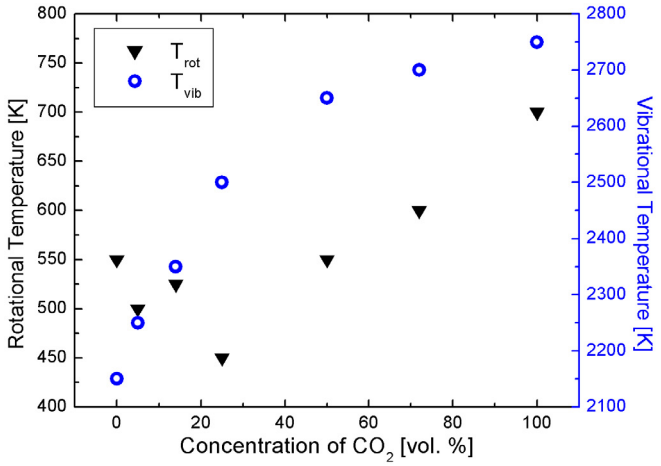

Fig. 2 – T_r and T_v as functions of c_{CO2}.

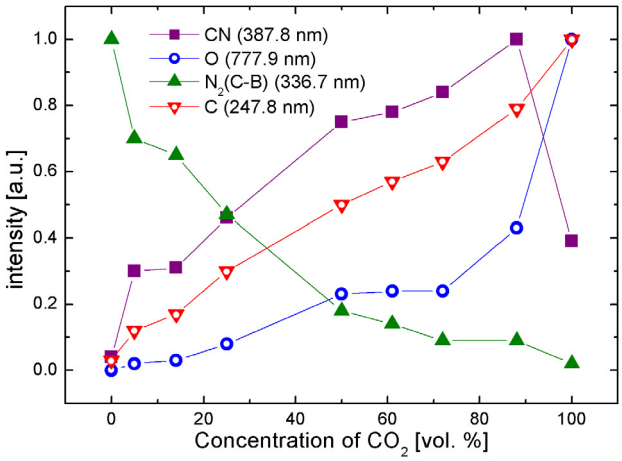

Fig. 3 – Emission intensities of selected species normalized to the input energy.

Conclusions

The transient spark discharge generates non-equilibrium cold plasma with high energy of electrons, which can dissociate N_2 and CO_2 to generate N and C species. The pathways leading to the synthesis of CN require further investigation, but they are certainly produced by more than one reaction. Moreover, CN was observed also in 'pure' CO_2 and N_2, since even minor impurities (e.g. CH_x) play an important role.

This work was carried out under the support from VEGA 1/2013/05; NATO EAP.RIG 981194, and APVT-20-032404 grants, and Project No. 45.530/0005-VI/6a/2005 of Austrian Ministry of Education, Science and Culture (bm:bwk).

References

[1] K. Plankensteiner, H. Reiner, B. Schranz, B. Rode, Angew. Chem. Int. Ed. 43 (2004) 1886.
[2] M. Janda, M. Morvova, Z. Machala, I. Morva, CO_2 Decomposition and Synthesis of Organic Species by DC Discharges Above Water Surface in CO_2 - N_2 - H_2O Mixtures, Chemosphere (submitted).
[3] Z. Machala, M. Morvova, E. Marode, and I. Morva. J. Phys. D: Appl. Phys., 33 (2000) 3198.
[4] C.O. Laux, Radiation and Nonequilibrium Collisional-Radiative Models, von Karman Institute for Fluid Dynamics, Lecture Series 2002-07, Rhode Saint-Genese, Belgium, 2002

P 31

Ion Mobility Spectrometry of the Negative Corona Discharge in Pure Oxygen and Nitrogen/Oxygen Mixtures

F. Janky[1], M. Kučera[1], Š. Matejčík[1], I. V. Prisyazhnevich[2], V. Chernyak[2]

[1]Department of Plasma Physics, Comenius University, Mlynská dolina, Bratislava 842 45, Slovakia
[2]Faculty of Radiophysics, Dept. of Physical Electronics, Taras Shevchenko Kyiv National University, Prospect Acad. Glushkova 2/5, 03127 Kyiv, Ukraine
e-mail: janky@neon.dpp.fmph.uniba.sk

Abstract

Ion Mobility Spectrometry (IMS) was used to study ions formed in negative corona discharge in pure oxygen and in pure nitrogen/oxygen mixture. The negative corona discharge in pure nitrogen is unstable, an electronegative gas is necessary to stabilize the discharge and to produce negative ions. Due to this reason nitrogen was mixed with oxygen. Analyzing the IMS spectrum in pure oxygen we have determined the presence of the negative ions O_3^- (reduced mobility 2.55 $cm^2V^{-1}s^{-1}$), O_2^- (reduced mobility 2.10 $cm^2V^{-1}s^{-1}$), and cluster ion $O_3^-(O_2)_n$ (2.35 $cm^2V^{-1}s^{-1}$). The IMS spectrum of nitrogen/oxygen mixture contains peaks, which represents ions O_2^-, O_3^- and the cluster $O_3^-(H_2O)_n$ or the ion NO_3^- with reduced mobilities 2.39, 2.24 and 2.12 $cm^2V^{-1}s^{-1}$.

Introduction

Ion Mobility Spectrometry (IMS) is an experimental technique used to measure mobilities of ions moving in a weak electric field in a carries gas. Ions are moving due to affect of homogeneous electric field and collide with neutral molecules. This kind of move is called drift. Velocity is called as a drift velocity v_d and is given:

$$v_d=\mu E, \quad (1)$$

when $[\mu]= cm^2V^{-1}s^{-1}$ is mobility, which depends on ion-molecule collisional cross-section and $[E]$=V/cm is intensity of electric field. The mobility of ions depends on temperature and pressure of drift gas (carrier gas), therefore so called reduced mobility is is introduced (ity of the ion at standard conditions):

$$\mu_0=\mu.(T_0/T).(p/p_0), \quad (2)$$

where μ_0 is the reduced mobility of the ion, $T_0=273K$ and $p_0=101kPa$.

The mobility of the O_3^- ions in pure oxygen is larger than that of O_2^- ions. This is due to the process called resonant charge transfer which has very large collisional cross section. It is typical for ions are drifting in parenth gas (3).

$$O_2^- + O_2 \rightarrow O_2 + O_2^- \quad (3)$$

This resonant charge transfer reaction is not observed when oxygen ions are drifting in pure nitrogen and therefore the mobility of O_2^- in N_2 is larger than the mobility of O_3^-.

Ions O^-,O_2^- are created in negative corona discharge in pure oxygen. Additionally O_3 is formed negative corona discharge (4,5). The ions O^- are not observed, because these ions effectively react with O_3 via charge transfer reaction and forme O_3^- ions (6) due to difference in electron affinities of O and O_3 (EA(O) = 1.461 eV and EA(O_3) = 2.103 eV [1]).

$$e + O_2 \rightarrow O(^3P) + O(^3P) + e \quad (4)$$

$$O(^3P) + O_2 + O_2 \rightarrow O_3 + O_2 \quad (5)$$

$$O^- + O_3 \rightarrow O_3^- + O \quad (6)$$

Results and discussion

Ion Mobility Spectrometer has been built at Department of Experimental Physics at Comenius University in Bratislava. The IMS consist of three parts. Ion source (negative corona discharge), reaction region (sample – oxygen is introduced) and drift tube (ions are separated due to their mobilities in the drift gas) [2]. In the negative corona region electrons are formed, which further react with ambient gas, when gas is electronegative (oxygen). Electrons which are not attached to the neutral molecules and ions are moving toward collector, which is on the end of the drift tube.

Negative ions mobility spectrum was measured in pure oxygen (fig.1) curve a). There were observed

three peaks, which correspond to oxygen negative ions. The first peak correspond O_3^- ions with reduced mobility 2.55 $cm^2V^{-1}s^{-1}$, the second one clusters $O_3^-(O_2)_n$ with mobility 2.35 $cm^2V^{-1}s^{-1}$ and last one represents ions O_2^- with mobility 2.10 $cm^2V^{-1}s^{-1}$. Negative spectrum measured in nitrogen with small admixtures of oxygen are displayed on (fig.1) plot b) and c). The plot b) represents experiment where the oxygen is mixed with the nitrogen in the reaction region and the plot c) in the corona region. Graph b, c contains three peaks, which represents negative ions formed in pure nitrogen mixed with oxygen. First peak was determined as a O_2^- ions with reduced mobility 2.39 $cm^2V^{-1}s^{-1}$ the second one was set as a O_3^- ions with reduced mobility 2.24 $cm^2V^{-1}s^{-1}$. On the basis of the known reduced mobilities, the third peak can be NO_3^- or cluster $O_3^-(H_2O)$ with reduced mobility 2.12 $cm^2V^{-1}s^{-1}$. The reduced mobilities of the ions produced in pure oxygen are in good agreement with [3,4] (tab.1).

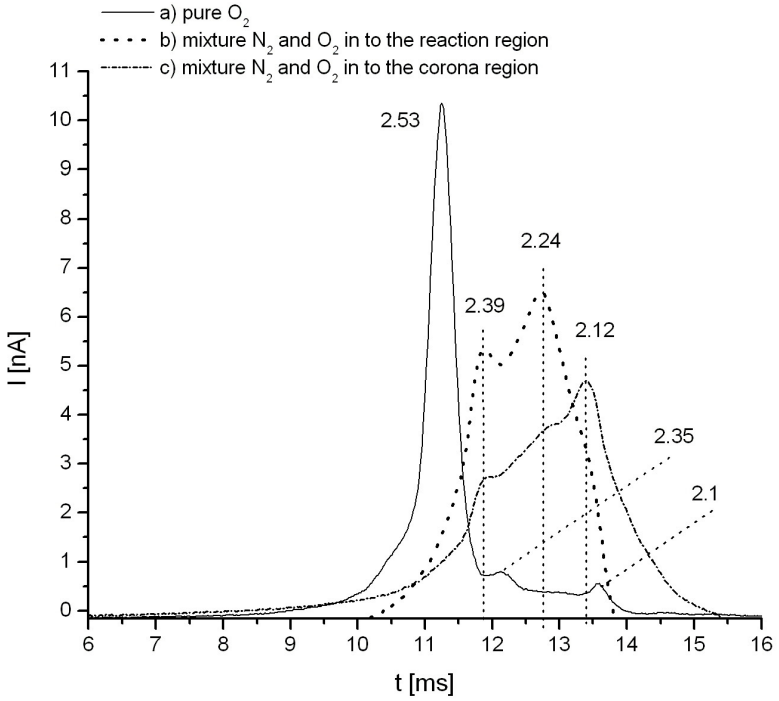

figure 1. IMS spectrum of negative corona discharge: a) in pure oxygen, b) in nitrogen with small amount of oxygen into reaction region, c) in nitrogen with small amount of oxygen into corona region

	O_3^-	O_2^-
Eliasson [3]	2,55	2,23
Snugg [4]	2,55	2,16
Present work	2,53	2,10

Table 1. Comparison measured reduced mobilities in $cm^2V^{-1}s^{-1}$. present work with other authors

Acknowledgement

This work was supported by the Slovak Research and development agency, project Nr. APVT-20-007504.

References

[1] NIST Webbook

[2] F. Janky, M. Stano, J. Husárik, Š. Matejčík, J.D. Skalný, 16th. Symposium on physics of switching arc, **1**, Brno, Czech Republic, 101, 2005

[3] Eliasson, B., *Electrical discharge in oxygen*: part 1. Basic data, rate coefficients and cross sections, Brown Boveri Forschungszentrum, Baden-Dättwil, Switzerland, 1985

[4] R.M. Snugg, D.J. Volz, E.W. McDaniel, I.R. Gatland, J.H. Schummers, D.W. Martin, *Phys. Rev. A,* **3** 1970, 477-487

P 32

Numerical Modeling of Dielectric Barrier Discharge in Neon

J. Jánský , D. Trunec

Department of Physical Electronics, Faculty of Science, Masaryk University , Kotlářská 2, Brno 611 37, Czech Republic

e-mail: jansky@physics.muni.cz

Abstract

Numerical calculations of spatio-temporal characteristics of the breakdown in the dielectric barrier discharge in neon at atmospheric pressure between parallel-plate electrodes were performed by means of one-dimensional fluid model. The hydrodynamic set of equations (continuity equations with Poisson equation) was solved using the semi-implicit Sharfetter-Gummel scheme. This algorithm allowed the simulation with high gradient of particle density in reasonable time and it is easy to convert to two-dimensional model.

Introduction

Non-thermal discharge plasma at atmospheric pressure is widely used in multiple technological applications, such as ozone production, gas cleaning, surface treatment, plasma display panel cells, etc. Central to the production of non-equilibrium plasma at atmospheric pressure lies on the dielectric barrier discharge (DBD). The annual 2005 DBD market volume was of the order of 10 billion USD. While the properties of DBD are well known for some gases (e.g. helium [1]), the character of neon DBD still remains unknown.

Many numerical methods were developed for modeling of dielectric barrier discharge. Explicit methods suffer from restricting conditions and implicit methods suffer from long computational time for one step. The semi-implicit method is used to eliminate disadvantages of previous methods [2].

Fluid model

The numerical model of the dielectric barrier discharge is based on the one-dimensional continuity equations for electrons and ions and the Poisson equation

$$\frac{\partial n_i}{\partial t}+\frac{\partial j_i}{\partial x}=S_i,$$

$$\frac{\partial^2 \phi}{\partial x^2}=\frac{-\rho}{\epsilon},$$

where n_i, j_i, S_i are the density, the flux density and the source term for the particles of i-th type. Φ is the potential of electric field, ρ is the charge density and ε is the permitivity.

The fluid model is based on equation

$$\frac{n_p^{k+1}-n_p^k}{\delta t}+\nabla \vec{j}_p(n_p^{l_n}, \vec{E}^{l_E}, \mu_p^{l_\mu}, D_p^{l_D})=S_p(n_1^{m_n}, n_2^{m_n}, \ldots, k_1^{m_k}, k_2^{m_k}, \ldots)$$

where the upper indexes indicates in which time step are the quantities considered. For explicit methods are all indexes equal to k and for implicit methods are equal to k+1. In previous work we use the explicit method for discharge modeling [3]. This method has very restrictive time step conditions. According to our numerical experiments we recognize that time condition

$$\frac{\delta t}{\epsilon_0}\sum \mu_p n_p \leq 1.$$

is the biggest problem. When the particle gradient in the front of the streamer increases the solution becomes unstable. There is also very interesting result that the solution is unstable for very short time steps which

strongly satisfy the condition. It could be explained by Von Neumann phase shift analysis. When the time step is very small compared to Courant number, the phase shift is increasing and creating numerical dispersion.

To avoid time restrictions a implicit method is supposed to use. But complete implicit treatment of the continuity equation leads to very slow computation of one time step. The semi-implicit method is constructed to eliminate these disadvantages. Continuity equation is solved implicitly in particle density, source term rate constants are treated explicitly. The main idea of semi-implicit method is in treatment of electric field strength. It was shown that implicit treatment of electric field strength is not necessary to ensure stability. In this case, Poisson's equation is solved before the continuity equation. Since the space charge density is not known yet, an estimate η_p^{k+1} is used:

$$\eta_p^{k+1} = n_p^k - \delta t \nabla \cdot \vec{j}_p(n_p^k, E^{\vec{k+1}}, \mu_p^k, D_p^k)$$

The particle flux j is calculated through Scharfetter-Gummel scheme.

$$j_{k+1/2} = \frac{D_{k+1/2}}{h_k I_0}(n_k - e^{\beta} n_{k+1}),$$

$$I_0 = \frac{e^{\beta}-1}{\beta}, \beta = \frac{\mu h_k E_{k+1/2}}{D_{k+1/2}}, h_k = x_{k+1} - x_k,$$

where D, μ and E are the diffusion coefficient, mobility and electric field strength. The lower indexes means spatial location. Densities of particles are computed at integer points. The vector quantities (electric field strength) and the direct functions of vector quantities (mobility, etc.) are computed at half-integer points. This approach is better suited for shock wave problems in fluid modeling. The main advantages are better flux conserving properties.

The equation for flux j is computed as analytical solution for continuity equation between two neighboring nodes with constant electric field strength, mobility and diffusion coefficient. The boundary conditions are the densities of particles at the integer nodes.

Our algorithm using this scheme produces some good results and it is still tested. The spatio-temporal characteristics of discharge will be presented on poster during the conference.

Conclusions

The one-dimensional fluid model of the dielectric barrier discharge in neon was developed, taking into account the primary processes of ionization and surface processes of adsorption and secondary emission. The calculations will give detailed predictions of electron and ion densities and electric field as functions of time and position.

This research has been supported by the Czech Science Foundation under contracts 202/06/1473 and 202/06/0776 and by the Research Intent from Ministry of Education of the Czech Republic under contract MSM0021622411.

References

[1] Y.B. Golubovskii, V.A. Maiorov, J. Behnke, J.F. Behnke *J. Phys .D: Appl. Phys.*, 36 (2003) 39.
[2] P.L.G. Ventzek et al. *J. Vac. Sci .Technol. B,* 12 (1994) 461
[3] J.Jánský, D. Trunec *Czech J. of Phys.,* 56(2006) B781

P 33

Bio-Decontamination by DC Discharges in Atmospheric Air with Water

I. Jedlovský[1], Z. Machala[2], V. Martišovitš[2], L. Šikurová[1]

[1]Department of Nuclear Physics and Biophysics, Faculty of Mathematics, Physics and Informatics, Comenius University, Mlynska dolina, 84248 Bratislava, Slovakia

[2]Department of Astronomy, Earth Physics and Meteorology, same address

e-mail: jedlovsky@fmph.uniba.sk

Abstract

We tested bio-decontamination effects of three types of DC electrical discharges in atmospheric air with one electrode submerged in water on selected G- and G+ bacteria in solution. A substantial decrease of bacterial concentration was observed, especially in the transient spark. Emission spectroscopy indicates the major role of radicals and active species among other inactivation mechanisms.

Introduction

Non-thermal plasmas at atmospheric pressure are nowadays widely investigated for various environmental (flue gas and water cleaning) and bio-decontamination (sterilization) applications. [1, 2] We investigate three types of DC atmospheric discharges and test their bio-decontamination effects on selected bacteria. In sterilization, it is very important to assess the role of various effects involved. [2] We attempt to do so by employing emission spectroscopy of the investigated discharges.

Experiment

Three types of DC discharges in both polarities operating in atmospheric air with or without water in the discharge chamber were investigated: a well known streamer corona, and relatively novel transient spark (TS) and glow discharge (GD). These discharges generate non-equilibrium plasmas inducing various chemical and biological effects that play role in bio-decontamination. Each discharge generates the plasma with specific properties, so each one was studied separately [3]. Since transient spark provided the highest bio-decontamination efficiency, we only describe this regime here, as shown in Figure 1. Transient spark is a DC-driven pulsed discharge with high but very short (~100 ns) current pulses, and repetitive frequency of about 0.5-5 kHz, Due to very short pulse duration (given by a small internal capacity of the discharge chamber), the plasma cannot reach LTE conditions. On the other hand, the periodic streamer-to-spark transition provides non-equilibrium conditions with fast electrons that result in efficient chemical and biological cleaning effects. [3, 4]

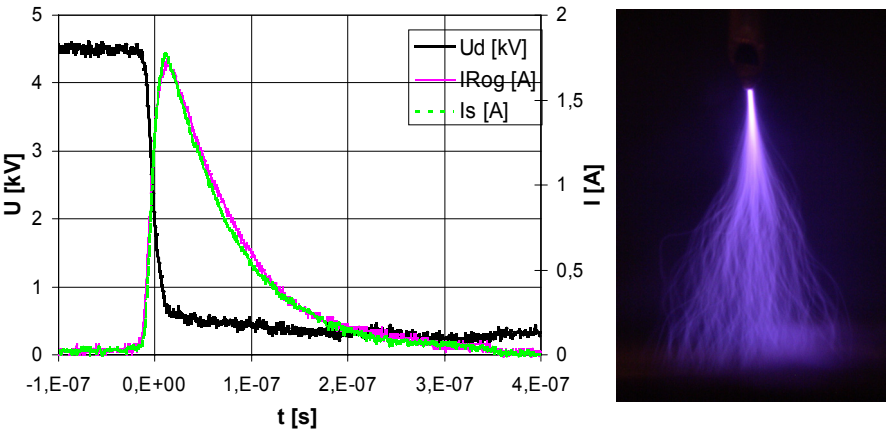

Figure 1. Transient spark typical parameters: U_d – discharge voltage, I_{Rog} - current measured by the Rogowski current monitor, I_s -measured by the current probe on a 50 Ω resistor). Photo of the discharge, gap distance 4 mm.

Biological effects of investigated DC discharges were tested on selected bacteria cultures with standard cultivation method of bacterial growth and were statistically evaluated.

1) *Salmonella typhimurium*, Gram-negative (G-) bacteria, genetically modified strain TA 98,

2) *Bacillus cereus*, Gram-positive (G+) bacteria.

S. typhi is a pathogen causing typhus diseases, and so its sterilization is important from the viewpoint of drinking water decontamination. *B. cereus* belongs to the same group as extremely hazardous *B. anthracis* (Anthrax precursor), which nowadays represents one of the highest bio-terrorism risks.

Results and discussion

The survival curves of *S. typhi* are shown in Fig. 2. The graph shows 4 experiment sets, starting at 7000 and 26 000 CFU/ml. The number of CFUs decreased with the treatment time in all discharges. We also express the relative concentration decrease, i.e. inactivation efficiency (Fig. 2, right). The highest efficiencies were obtained in the positive TS, the lowest in the coronas; GD gives fairly high efficiencies as well.

We also tested the inactivation of the G+ spore-forming *B. cereus*. It was difficult to reasonably evaluate the survival curves with these bacteria because CFUs after incubation do not form typical easily countable dots but larger stains. Nevertheless, a decrease of their concentration is demonstrated in Fig. 3: initial concentration: 12000 CFU/ml; TS (60 s): 160 CFU/ml, efficiency 98.7%.

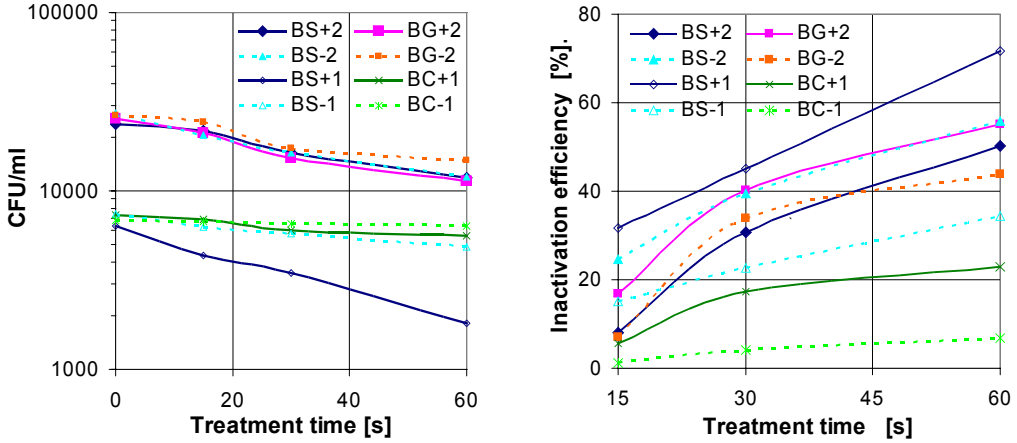

Figure 2. *S. typhi* survival curves in semi-logarithmic scale (left) and inactivation efficiency vs. treatment time (right). BS: transient spark, BG: glow discharge, BC: streamer corona, +: positive, -: negative polarity.

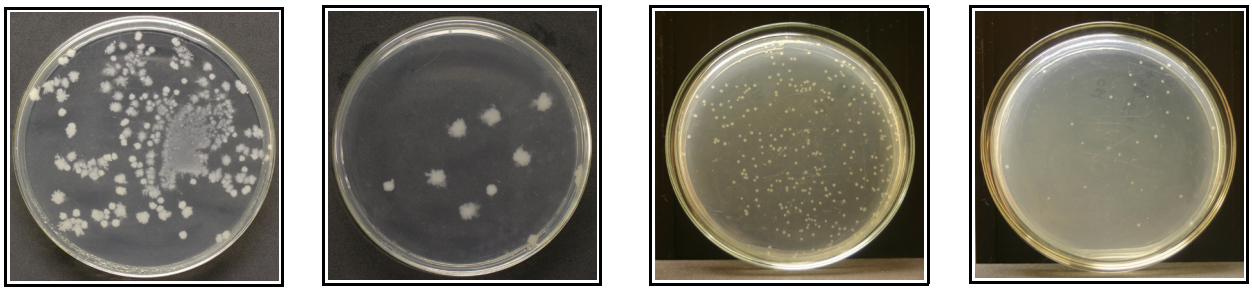

a *Bacillus cereus* ***b*** ***c*** *Salmonella typhimurium* ***d***

Figure 3. Cultivated bacteria on Petri dishes. Reference (a,c) and after-treatment (b,d) samples.

Conclusions

Bio-decontamination on selected bacteria (*S. typhimurium and B. cereus*) by three types of DC electrical discharges in atmospheric air with one electrode submerged in water was investigated. The discharges generate non-thermal plasmas with various gas temperatures and properties. Satisfactory results were obtained, with the highest efficiency in the transient spark. Spectroscopic discharge investigations enabled us to determine important bio-inactivation mechanisms, mainly the major role of radicals and active species.

This work was supported by NATO EAP.RIG 981194, VEGA 1/2013/05, and APVT-20-03240 grants. We thank Dr. Peter Polčic from Biochemistry Department of Comenius University for his assistance with bacteria cultivation.

References

[1] H.-H. Kim, Plasma Process. Polym. 1 (2004), 91-110
[2] M. Laroussi, IEEE Trans. Plasma Sci. 30 (2002) 1409-1415
[3] Z. Machala, I. Jedlovsky, K. Hensel, V. Martisovits, V. Foltin *"Biological effects of DC discharges in atmospheric air with water,"* Int. Symp. High Pres. Low Temp. Plasma Chem. HAKONE X, p. 277-283, Saga, Japan, September 2006
[4] Z. Machala, M. Morvova, E. Marode, I. Morva, *J. Phys. D: Appl. Phys.* 33 (2000) 3198-3213

P 34

Etching of Photo-Resist and Mono-Crystal Silicon in the Oxygen and CF_4 Plasmas Driven a Plasmatron

S. B. Jwa, C. J. Yim, V. Yu. Plaksin, V. A. Riaby, and H. J. Lee

Faculty of Mechanical & Energy System Engineering, Cheju National University, Jeju 690756, Korea
e-mail: hjlee@cheju.ac.kr

Abstract

An application of the arc plasma source with low anode erosion rate allowing it to generate nearly spectrally clean plasma flow at the lifetime of 10^3~10^4 hours is proposed as a tool for a plasma-chemical surface treatment.

Experimental study of the plasmatron showed that at atmospheric pressure, it could be used successfully for homogeneous plasma-chemical processes like diesel fuel reformation. But for the plasma-chemical treatment of the substrates in these conditions, it appeared hard to be realized because of the high recombination rate of the activated process gas. The experiments prompted that such heterogeneous treatment was possible only at lowered pressures. Etching was used as an example of vacuum technologic processes. Tests of this technology and their results were quite successful.

The vacuum heterogeneous processes of plasma-chemical etching of photo-resist and silicon were arranged in the following way. At first, the process of arc start-up and the conditions for the stable discharge burning were studied. After the chamber was pumped to the initial pressure of about 10^{-1} mbar, the supply of process gases - Q_{Ar}~2-4 l/min and Q_{air}~20 l/min - was switched on. As a result, the pressure in the chamber increased to 3-4 mbar. At this pressure the discharge could be excited easily but it burned at the base of the cathode rod instead of its tip. After some time the arc faded away because inter-electrode insulators melted and evaporated.

As an example of plasma-chemical processes, etching of photo-resist and mono-crystal silicon in the oxygen and halocarbon CF_4 plasmas, respectively, were tested. Initially in these experiments, a substrate was fixed at the distance of about 20 mm from the plasmatron exit; photo-resist etching (~1 μm thick film on the surface of a mono-crystal silicon wafer) in oxygen plasma was observed visually, measuring time between the moment when pressure in the chamber reached p~4 mbar and the time when the spot of clean silicon wafer sized about Ø20 mm appeared (seen by the movement of a striped photo-resist boundary); etching of mono-crystal silicon was carried out in CF_4 plasma and its rate was measured, determining time of the process and change of substrate thickness. The first process took about 45-60 s giving the etch rate of ~10^0 μm/min. In the second process, within 15 min. a mono-crystal silicon sample lost about 15-20 μm of its initial thickness δ~500 μm, showing the same level of etch rate ~10^0 μm/min.

The macroprobe current was used as an indicator of the plasma activity. The dependences of macroprobe current on chamber pressure, argon and air consumption and plasmatron power were analyzed. The reverse dependence of the probe current on chamber pressure was found. An argon flow rate in respect to current was found to have an optimal condition, but air flow effect on current is indirect. The plasma activity dependence on plasmatron power at the point of macroprobe position has a threshold character.

The correlation of etch rate or PR with process parameters was found, and basing on it we can estimate the etch rate using data of probe current and air flow rate. That gives a convenient method to assess optimal processing condition before real etching.

The estimated etch rate dependences on main process parameters were presented and discussed.

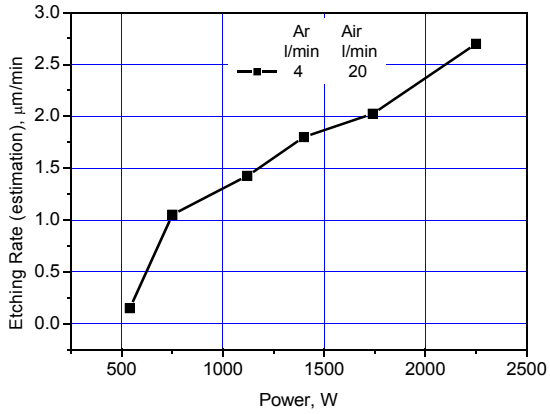

Fig. 1 Estimated etching rate dependence on power.

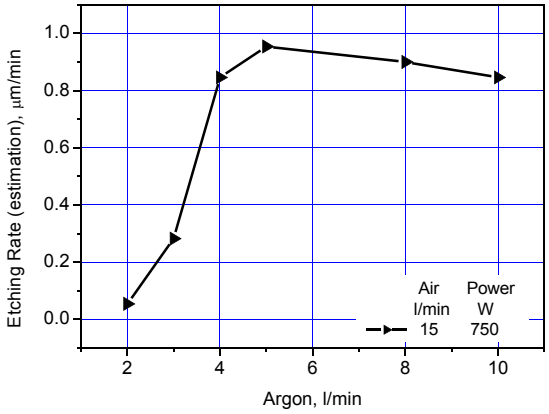

Fig. 2 Estimated etching rate dependence on Ar flow rate.

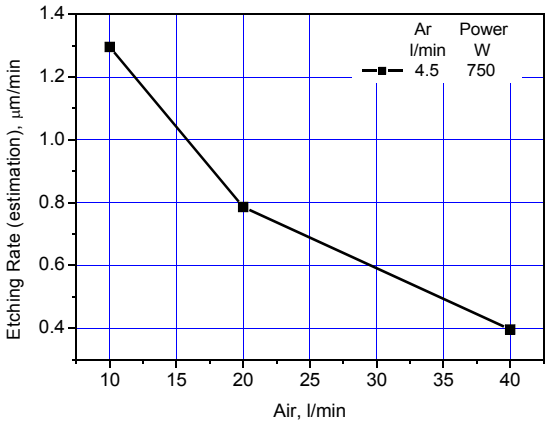

Fig. 3 Estimated etching rate dependence on air flow rate.

Acknowledgment

This work was supported by the grant R-2004-096-0-00 of the Korean Ministry of Commerce, Industry and Energy, by the grant M1-0104-00-0071 from the National Research Laboratory Program of the Ministry of Science and Technology, by the Brain Korea 21 from the Ministry of Education and Human Resources Development, Korea, and by the grant 2006-C-CC02-P-05-0-000-2006 of the Korea Energy Management Corporation.

P 35

High-Temperature Behaviour and Oxidation Resistance of Si–B–C–N Films

J. Kalaš[1], J. Vlček[1], S. Hřeben[1], J. Čapek[1], P. Zeman[1] and V. Peřina[2]

[1]Department of Physics, University of West Bohemia, Univerzitni 22, 306 14 Plzeň, Czech Republic
[2]Nuclear Physics Institute, Academy of Sciences of the Czech Republic, 250 68 Řež near Prague, Czech Republic
e-mail: jkalas@kfy.zcu.cz

Abstract

We report on temperature stability of elemental composition and mechanical properties at elevated temperatures up to 1700 °C in an inert atmosphere, and on high-temperature oxidation resistance of new quaternary Si–B–C–N coatings.

Introduction

Si–B–C–N materials possess extraordinary combination of properties such as high-temperature stability, oxidation resistance and creep resistance with superior mechanical, optical and electrical properties [1]. This unique combination leads to many potential applications in areas such as coating technologies, microelectronics or production of thermally stable fibers for composites. Recently published works dealt with preparation of Si–B–C–N ceramics using a precursor pyrolysis. To our knowledge, up to now, no effort has been made to form Si–B–C–N films using a magnetron sputtering, which allows film generation at noticeably reduced substrate temperatures and without hydrogen-containing precursors.

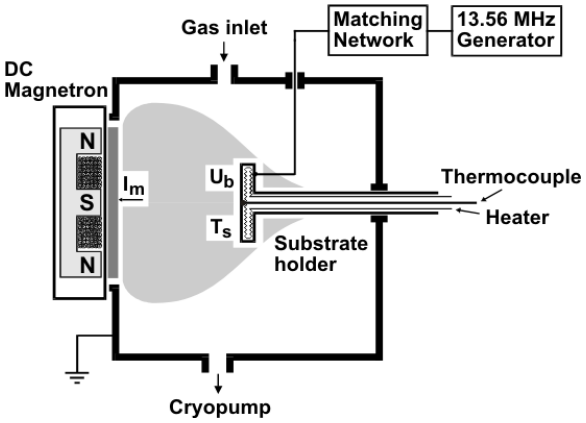

Figure 1. Schematic diagram of the experimental apparatus.

Experimental details

All the coatings were deposited on Si (100) or SiC substrates by dc magnetron co-sputtering of silicon, boron and carbon from a single C–Si–B or B4C–Si target in nitrogen-argon gas mixtures. Samples were prepared at various magnetron target compositions (60 or 75 % Si fraction in the target erosion area), gas mixture compositions (50 or 75 % Ar fraction), rf substrate bias voltage Ub = –100 V and the substrate temperature Ts = 350 °C at a constant value of the total pressure p = 0.5 Pa. To obtain results for the high-temperature behaviour of the elemental composition and mechanical properties, the coatings were post-annealed in a pure helium at the temperatures from 700 °C up to 1300 °C. The elemental composition of the coatings was determined using Rutherford backscattering spectroscopy (RBS) and elastic recoil detection (ERD) methods. Mechanical properties were measured by microindentation and the high-temperature oxidation resistance was investigated using a high-resolution thermogravimetric system in a pure air.

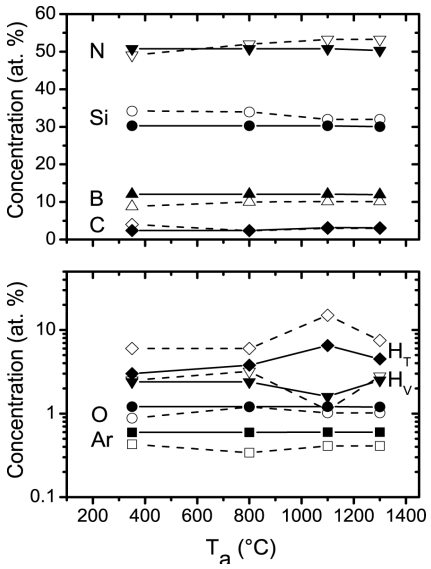

Figure 2. Temperature behaviour of elemental composition in helium for coatings prepared in a 50% N_2 + 50% Ar gas mixture with a 5%C+75%Si+20%B (full symbols) and 25%B_4C+75%Si (empty symbols) targets. Indices T and V denote top subsurface and

Results

Figure 2 shows temperature stability of the elemental composition for the coatings prepared at a constant composition of the gas mixture, 50% N2+50%Ar, substrate bias voltage Ub= –100V and different sputtered targets with a constant 75% of Si in the target erosion area. As can be seen, the annealing temperature has no or very small influence on the elemental composition, except the values of the hydrogen concentration at the temperature

Ta = 1100 °C. The N/Si concentration ratio in the films is in the range 1.4-1.7 for both the sputtered targets. Figure 3 provides information on mechanical properties (indentation hardness, effective Young's modulus and elastic recovery) as a function of the annealing temperature in helium for coatings prepared under the same deposition conditions. As can be seen, the values of indentation hardness and elastic recovery slightly increase with an increasing annealing temperature for both the targets (due to possible consequence of the changes in the bonding structure), while the values of the effective Young's modulus remain practical-ly constant. Figure 4 shows oxidation behaviour of an as-deposited Si–B–C–N film in a pure air up to a 1700 °C. In addition, the results obtained by other authors for selected hard and superhard films are also presented. From our results it can be concluded that a very thin surface layer (composed of Si and O), which is formed during oxidation, efficiently protects the films from diffusion-controlled oxidation.

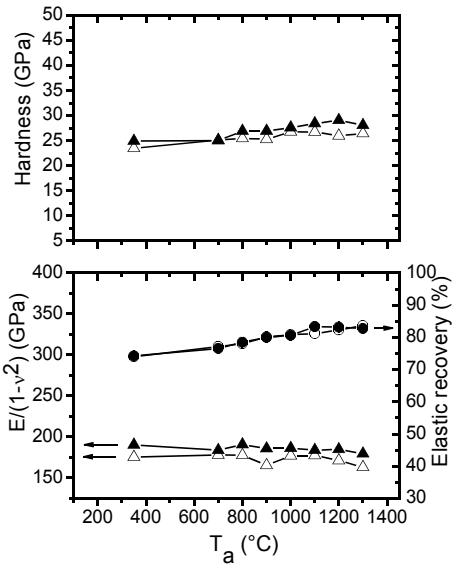

Figure 3. Temperature behaviour of mechanical properties in helium for coatings prepared in a 50% N_2 + 50% Ar gas mixture with a 5%C+75%Si+20%B (full symbols) and 25%B_4C+75%Si (empty symbols) targets.

Refrences

[1] J. Vlcek, S. Potocky, J. Cizek, J. Houska, M. Kormunda, P.Zeman, V. Perina, J. Zemek, Y. Setsuhara, S. Konuma, J. Vac. Sci. Technol. A 23 (2005) 1513

P 36

Growth Mechanisms and Some Properties of SiC Films by Plasma and Catalytic CVD

T. Kaneko[1], M. Taii,[1,2] S. Suga,[1] H. Osada,[1] N. Miyakawa[3]

[1]Depart. Appl. Phys., Science University of Tokyo, 1-3 Kagurazaka, Shinjuku-ku, Tokyo 162-8601, Japan, [2]Present address; NTT East Corp.

[3]Depart. of Mechanics and Systems, Science University of Tokyo, Suwa, 5000-1 Toyohira, Chino, Nagano pref. 391-0290, Japan

e-mail: kaneko@ap.kagu.sut.ac.jp

Abstract

SiC films grown by PE-CVD (plasma-enhanced CVD) and Cat-CVD (catalytic CVD) are compared with reference to growth conditions and specific properties. Cat-CVD was carried out in the PE-CVD chamber without plasma and a straight tungsten wire was set under the substrate at a distance. MMS (monomethylsilane) was used as the source gas with hydrogen carrier gas.

Introduction

We have already reported PE-CVD of SiC from the view-point of growth kinetics. For growth of a-SiC:H films on Si substrates by PE-CVD, the precursor in plasma was investigated using optical emission spectroscopy and optical absorption spectroscopy [1,2]. It is known that hydrogen atoms play an important role for the growth of polycrystalline Si films through hydrogen dilution [3]. In Cat-CVD (catalytic CVD) using hot-filament catalysis, much more atomic hydrogen than in PE-CVD is produced by the hot-filament catalysis [4]. Therefore, low temperature growth of μc-SiC (microcrystalline SiC) is expected by Cat-CVD in contrast to plasma CVD. μc-SiC films have been successfully grown by Cat-CVD on silicon substrates at a temperature of 300 ^{o}C [5]. From these kinetic data, growth environments of PE-CVD and Cat-CVD is considered to have SiH_2 and hydrogen, respectively, in the source of MMS (monomethylsilane) with hydrogen carrier gas.

In this article, SiC films grown by PE-CVD and Cat-CVD are compared in term of growth conditions and properties, including absorption FTIR spectra and the optical band gap. Cat-CVD was carried out in the PE-CVD chamber without plasma and a straight tungsten wire was set under the substrate at a distance, using MMS source with hydrogen. Based on this comparison, the growth kinetics of plasma CVD and Cat-CVD are discussed.

Result and Discussion

Typical absorption FTIR spectra of the PE-CVD and Cat-CVD films show a strong peak of the Si-C stretching mode but the peak of the Si-H_2 wagging mode of a-SiC:H by PE-CVD is considerably larger than that of μc-SiC (microcrystalline SiC) by Cat-CVD. The chemical bond number is calculated from the integrated absorption intensity using the reported absorption cross- section. The hydrogen content is defined as the ratio of the sum of the Si-H_n and C-H_n bonds to the total number of Si-C, Si-H and C-H bonds. Figure 1 shows the hydrogen content of a-SiC:H by PE-CVD to be about 10 at % for varying MMS concentration, while Figure 2 shows that of the films obtained by Cat-CVD having a minimum against a variation of the MMS concentration in which microcrystallites nucleate only for a minimum hydrogen content of 5 at %. The film is amorphous at other concentrations. In contrast to this the hydrogen content increases with increasing MMS concentration in PE-CVD. The nucleation of μc-SiC minimizes hydrogen content and an optimum MMS concentration is necessary for crystallization. The growth of a-SiC:H is rate-determined by the SiH_2 precursor in PE-CVD,[2] as shown in Figure 1. The growth of μc-SiC is controlled by highly concentrated atomic hydrogen originating in the Cat-CVD process, and the optimum condition is considered to be due to the fact that since for an MMS concentration of 1 % the reactive atomic hydrogen is insufficient for extraction of the terminating hydrogen but under 1 %, it is in excess and terminates again at the surface.

Since the Si (100) substrate is transparent to infrared radiation but opaque to visible light, a Corning #1737 glass substrate, which is transparent to visible light, was used for measurement of the optical band gap. The band gap was measured using a Tauc plot in indirect transition SiC. The band gap has a minimum at the lowest hydrogen content of μc-SiC by PE-CVD. The band gaps of μc-SiC and a-SiC:H films obtained by Cat-CVD and a-SiC:H films by PE-CVD change from 1.8 eV (the minimum in these runs) for μc-SiC to 3 eV for amorphous state. Therefore, we can say the optical gap can be changed from 1.8 to 3 eV by these

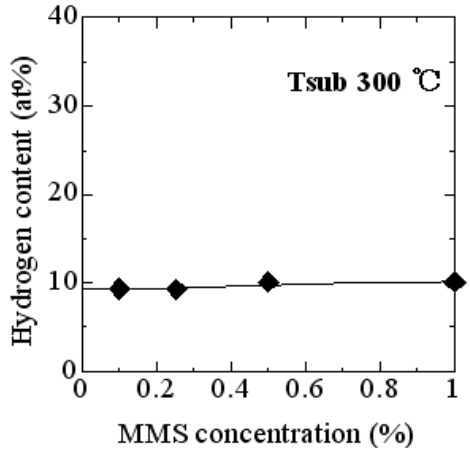

Fig.1 Hydrogen content of the films in PE=CVD of a-SIC.

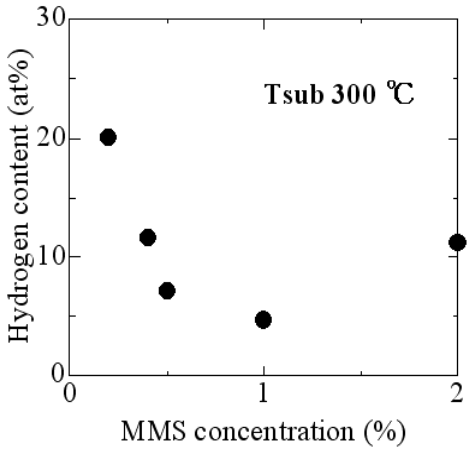

Fig.2 Hydrogen content of the films in Cat-CVD of SiC. [5]

methods.

Reference

[1] T. Kaneko, N. Miyakawa, H. Sone, H. Yamazaki, Surf. Coat. Technol. **2001**, 142-144, 360.
[2] T. Kaneko, N. Miyakawa, H. Yamazaki, Y. Iikawa, J. Cryst. Growth **2002**, 237-239, 1260.
[3] A. Matsuda, *et al.*, Jpn. J. Appl. Phys. **1980**, 19, L305.
[4] H. Umemoto, *et al*., J. Appl. Phys. **2002**, 91, 1650.
[5] T. Kaneko, Y. Hosokawa, T. Suga, N. Miyakawa, MEE **2006**, 83, 41.

P 37

Thermal Plasma Generated in Gas-Water Torch and its Utilization for Gasification of Biomass

T. Kavka, M. Hrabovsky, M. Konrad, A. Maslani

Thermal Plasma Department, Institute of Plasma Physics AV CR, Za Slovankou 3, Prague 8, 18200, Czech Republic
e-mail: kavka@ipp.cas.cz

Abstract

Thermal plasma jet generated by a gas-water DC arc torch represents an excellent source of heat for the gasification of biomass. This jet interacts very intensively with the surrounding atmosphere mixing up with ambient air and engulfing material to be gasified. High heat content of the generated plasma provides good heating conditions in the plasma gasification reactor allowing complete decomposition of the treated material into its constituents.

Introduction

The high energy content of thermal plasma accounts for why such plasma has been widely used in different industrial applications. The initial interest in thermal plasma technologies appeared in 1960's associated with aerospace programs. Since then a strong development of industrial applications has taken place in the fields of cutting, welding, spraying, waste destruction and synthesis [1]. Recently, a new application field has been introduced – plasma pyrolysis and gasification of biomass for syngas production. Biomass gasification is viewed today as an alternative to conventional fuels not only because biomass belongs to renewable energy sources, but also biofuels are more environmental friendly. In the process of gasification carbon contained material must be decomposed into its constituents, which takes place at rather high temperatures. Thermal plasma seems to provide excellent conditions for biomass gasification as at its typical temperatures any material carried into it will be decomposed. Plasma jets generated in a plasma torch represents a clean and well-controlled source of heat and can be utilized for the treatment of biomass.

A new DC plasma torch with gas-water stabilization worked out in the IPP in Prague is especially interesting for the biomass gasification [2]. This torch provides high energy throughput accompanied by the low amount of the plasma forming gas containing argon and water vapor [3]. Thus, the chemistry in the gasification reactor does not depend on the processing gas and the produced syngas consists mostly of the products of decomposition of the feedstock material. The biggest advantage of the torch is a possibility of the control of plasma parameters in the wide range providing good process control. The plasma jet generated by such a torch is fully turbulent and it mixes up intensively with the surrounding atmosphere in the process of entrainment [4]. Engulfing surrounding air the plasma jet engulfs pieces of material as well decomposing it.

This work represents analysis of the thermal plasma jet generated by the gas-water torch and its utilization for the gasification of wood in the plasma gasification reactor.

Results and discussion

Plasma jet generated by the DC arc plasma torch with gas-water stabilization is characterized by strong interaction with surrounding atmosphere. Such interaction starts right at the exit nozzle of the torch and continues alone the whole jet. Behavior of such jets and the process of entrainment of ambient atmosphere into them were experimentally studied with a number of diagnostics techniques. Properties of plasma in the upstream part of the jet were obtained by optical methods, while in the downstream by probes methods.

The results showed strong mixing of the plasma with the surrounding air. Temperature (Fig. 1 a)) and velocity of the plasma substantially decreased with a distance from the nozzle exit as a result of intensive entrainment process. Air, which was not observed in plasma at the nozzle exit, appeared first at the edges of the jet gradually penetrating into it center. Air was observed at the jet centerline at the distance about 5 nozzle diameters and its amount increased along the jet, while the jet was spreading. The enthalpy flux ρVh (ρ - density, V – velocity and h – enthalpy at the certain point of the jet) and thus the energy content was the highest at the jet centerline. It values decreased with a distance from the torch, while the profiles spread the same way as the profiles of other plasma jet characteristics (temperature, velocity, mass flux) (Fig. 1 b)). It indicates that energy (thermal as well as kinetic) was transferred from plasma to surrounding. Increase of the arc current resulted in increase of the net power of the torch and thus of the energy content in the jet. Moreover, because of higher density and velocity gradients existing at the jet fringes, interaction of the plasma jet with surrounding and entrainment rates also increased.

The plasma torch was fixed inside the plasma gasification reactor. The tested material, which was wood,

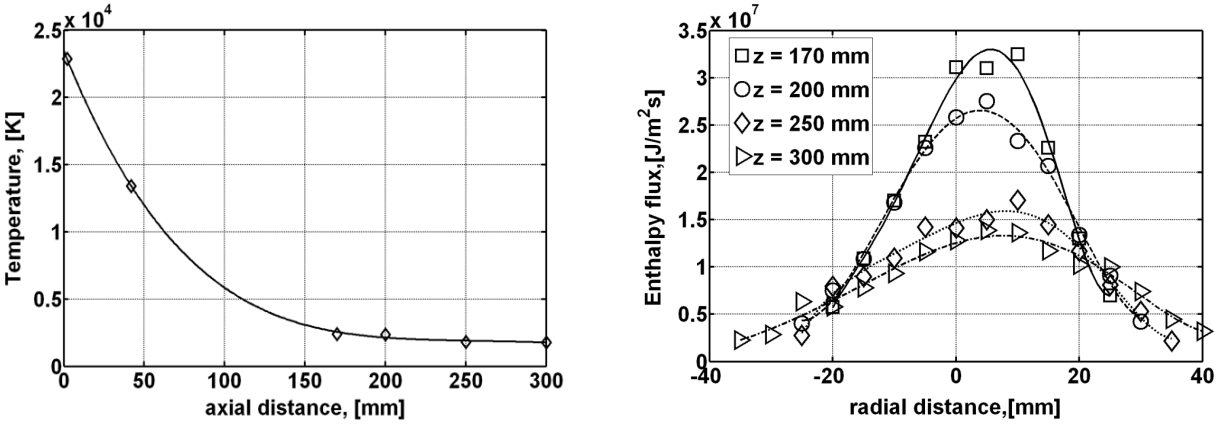

a) b)

Fig. 1 Development of the plasma properties along the jet (I = 400 A, Ar = 22.5 slm, 104 kW):a) axial temperature and b) radial profiles of the enthalpy fluxes.

was drawn continuously from the container with the help of a screw conveyer with a controlled feed rate. The material fell into the zone about 300 mm from the torch exit, i.e. into the fully developed turbulent hot flow. The composition of the produced syngas was measured with the help of the mass spectrometer at the exit tube positioned at the upper part of the reactor through which the gaseous products of wood decomposition left the reactor.

Strong interaction of the plasma jet with the surrounding provided a homogeneous heating of the reactor to the temperatures around 1300 °C. The pieces of wood were entrained into the plasma flow and almost completely decomposed. Because of surplus of carbon atoms with the respect to atoms of oxygen, CO_2 and O_2 were added to suppress the formation of solid carbon and increase CO content in the produced syngas. The obtained syngas showed a high amount of hydrogen and carbon monoxide with a very low content of other gases and tar (Table 1).

Table 1 Some results of wood gasification in the plasma gasification reactor (I = 400 A, Ar = 22.5 slm).

operation conditions					produced syngas							
Feed rate, [kg/h]	Torch power, [kW]	$T_{reactor}$, [°C]	CO_2, [slm]	O_2, [slm]	flow rate, [slm]	composition, [%]				Flow rate, [slm]		
						CO	H_2	O_2	CO_2	CO	H_2	CO_2
17	105	1323	115	-	496	61	32	0.1	3.3	304	161	17
17	106	1387	115	30	524	60	26	0.4	3.3	325	150	35
27	150	1452	115	30	655	61	32	0.1	4.7	400	210	31

Conclusions

Properties of the plasma jets generated by the gas-water DC arc plasma torch offer a good opportunity to utilize them for the gasification of biomass. The possibility of the control of the plasma jet properties provides good process control. Moreover, strong interaction of the jet with the surrounding results in good mixing of the treated material with the plasma gas and in intensive energy transfer from plasma to the material allowing its complete decomposition.

References

[1] E. Pfender, *Plasma Chem. Plasma process.*, 19 (1) (1999) 1
[2] M. Hrabovsky, M. Konrad, V. Kopecky, M. Hlina, T. Kavka, O. Chumak, *High Temp. Plasma Process.*, in press
[3] M. Hrabovsky, V. Kopecky, V. Sember, T. Kavka, O. Chumak, M. Konrad, *IEEE Transactions on Plasma Science*, 34 (4) (2006) 1566
[4] T. Kavka, V. Kopecky, V. Sember, A. Maslani, *Czech. J. Phys.*, 56 (2006) D1

P 38

Electron Impact Ionisation of the β-pinene

J. Kočišek, Š. Matejčík, D. Kubala

Department of Experimental physics, Comenius University, Bratislava, Slovakia
e-mail: kocisek@neon.dpp.fmph.uniba.sk

Abstract

The electron impact ionisation study to the β-pinene is continuation of our previous α-pinene measurements [1]. The main objective of the study is to compare the behaviour of alpha and beta pinene isomers in collisions with electrons. The study was performed using crossed electron/molecular beam apparatus [2]. Differences in the mass spectra and in the appearance energies of the ions have been observed.

Introduction

The molecules α-pinene and β-pinene are bicyclical terpenes. The terpenes are organical compounds determining odour of many plants, especialy trees. The typical examples of terpenes are citral, menthol or the studied pinenes in pine trees. The strong odour of the pinenes acts as defence to the animals. They also regulate growth of the pine trees. Also medical research with these compounds was performed [3]. More about broad application range and importance of terpenes can be found in [4].

Electron impact ionisation studies of α-pinene and β-pinene was performed using the crossed electron molecular beam apparatus established in Bratislava [2]. The electron beam was formed in a trochoidal electron monochromator (TEM). The Full Width at Half Maximum (FWHM) of the electron energy distribution function of 200 meV was measured using the retarding potential method. The pressures in the reaction chamber during the measurements achieved values around 10^{-7} mbar. Temperature of studied molecules in gas phase was around 330K. The positive mass spectra have been measured using the quadrupole mass spectrometer. The intensity of mass selected positive ions has been measured as a function of the acceleration potential, form these data, appearance energies of the ions have been estimated.

Results & discussion

Electron impact ionisation mass spectra of both α and β pinene was measured at standard energies of 70eV. The mass spectra of both molecules are very similar with one exception, the mass 69 was observed only in the case of β-pinene. We assume that it is related to position of the double bond in pinene molecules (**Fig.1**). On basis of the structural difference we expect from cyclic part of molecule formation of the ion $C_5H_9^+$ (Cyclopentyl ion 69 amu) in β-pinene and $C_5H_7^+$ (Cyclopentenyl ion 67 amu) in α-pinene.

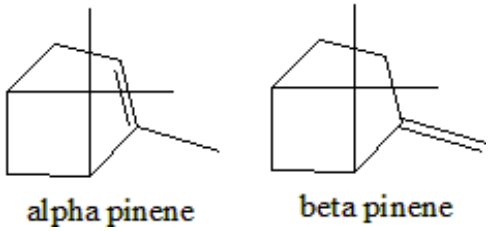

Fig.1: *Alpha and beta pinene 2D structure model*

The main results of present work are the estimated values of the appearance energies of the ions formed by electron impact to β-pinene. We are not aware of any previous EII studies to this molecule. The ion yields were measured in 6eV range around the threshold. The appearance energies were obtained from experimental data using data analysis including non linear least squares fitting procedure and deconvolution.

We compare the present values with the appearance enegies estimated for the α-pinene [1]. The results are summarised in the **Tab.1**. The values of the ionisation energies of the molecules (formation of the ion $C_{10}H_{16}^+$) are very close (within the error bars). There exist significant differences in the appearance energies of the fragment ion with the same mass to charge ratio formed by EII from α-pinene and β-pinene. Most significant differences were observed for the fragment ions $C_9H_{13}^+$ (121amu), $C_6H_5^+$ (77amu), $C_3H_5^+$(41amu) and $C_3H_3^+$(39amu). The differences are most probably result of different stability and fragmentation patters of the meastable ions formed from α-pinene and β-pinene. Quantum chemical calculations which will elucidate the differences in the structure and energetics of the positive ions formed by EII to α-pinene and β-pinene are required to be carried out in the future.

Ion mass [amu]	Expected positive ion	Appearance energy α-pinene [eV][5]	Appearance energy β-pinene [eV]
27	$C_2H_3^+$	-	13.92±0.32
39	$C_3H_3^+$	14.1±0.15	15.78±0.22
41	$C_3H_5^+$	11.5±0.15	13.12±0.08
53	$C_4H_5^+$	13.7±0.15	13.8±0.21
67	$C_5H_7^+$	11.3±0.15	11.81±0.14
69	$C_5H_9^+$	-	10.88±0.07
77	$C_6H_5^+$	10.7±0.15	12.41±0.13
79	$C_6H_6^+$	10.3±0.15	9.66±0.09
91	$C_7H_7^+$	-	11.82±0.11
93	$C_7H_9^+$	8.7±0.15	8.99±0.05
107	$C_8H_{11}^+$	-	9.76±0.11
121	$C_9H_{13}^+$	8.6±0.15	9.29±0.08
136	$C_{10}H_{16}^+$	8.3±0.15	8.48±0.04

Tab.1: *Values of ionisation treshold energies for electron impact ionisation to studied molecules at 330K.*

Acknowledgements

This work was supported by Slovak Research and Development Agency, project SK-UA-01906.

References

[1] W. Barszczewska, S. Matejcik, J. Langer, I. Martin, E. Illenberger, EPIC-EIPAM 2005 Meeting, San Martino Al Cimino, Italy

[2] S. Matejcık, V. Foltin, M. Stano, J.D. Skalny, Int. J. Mass Spect. 223–224 (2003) 9

[3] Lee, Seo; Lee, Hyun; Moon, Hyung; Kim, Dae; Park, Young; Hwang, Baek; Lee, Hyeon: Cytotechnology, Volume 49, Numbers 2-3, October 2005, pp. 87-94(8)

[4] B.Breitmaier: Terpenes, Wiley, 2006, ISBN-10: 3-527-31786-4

P 39

The Time Dependence of Gel Surface Shaping in Point-to-Plane Corona Discharge

J. Koller, V. Kříha

Department of Physics, Faculty of Electrical Engineering, Czech Technical University, Technická 2, Praha 166 27, Czech Republic
e-mail: koller@fel.cvut.cz

Abstract

The article describes the influence of corona discharge in point to plane configuration on shape of gel surface. Time and current dependencies of gel surface deformation are discussed.

Introduction

A point-to-plane corona discharge at atmospheric pressure is one of the simple discharges available for studying interactions of atmospheric ions with microorganisms such as bacteria and fungi. Such interactions come to importance in various applications including surface sterilization, improvement of seeds quality, maintaining building micro climate etc. Bactericidal or fungicidal effect of corona discharge can be studied directly on cultivating media with the gel medium surfaces serving as plane ion-conducting electrodes. This technique allows minimizing a risk of an accidental contamination of samples and makes the experiments relatively simple. However, due to ionic wind a deformation of gel surface occurs, which results in the change of corona discharge geometry. Discharge current and voltage change during the experiments in dependence on surface deformation and the gel media.

Experimental set-up

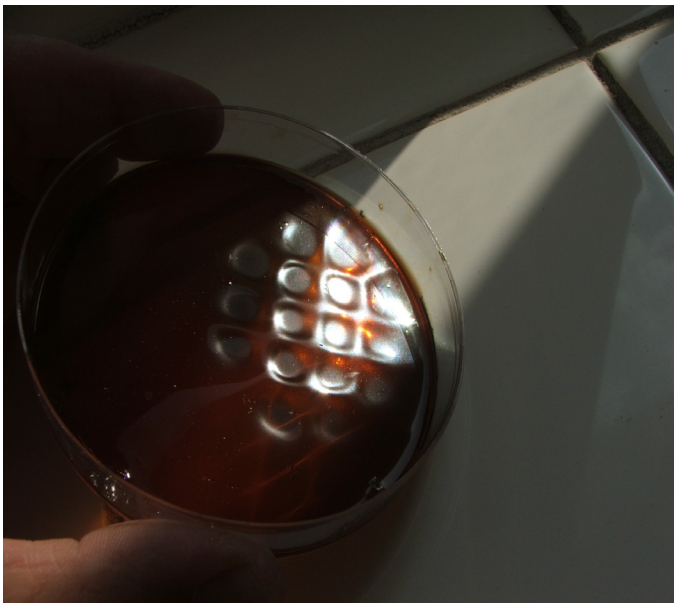

Fig. 1: The gel surface deformation after treatment.

The gel electrodes were placed in standard petri dishes 90 mm in diameter. The mean value of thickness of a gel layer for analyzed samples, was 8 mm, STD 0.7 mm. The following gel types were used: blood agar, nutrient agar, Endo agar. All samples were prepared from defined fabric substrate. Six samples of each type of agar were used; the times of sample preparation and samples storages in cooling box varied. The pin corona electrode was realized by a medicinal hollow needle with outer diameter 0.7 mm. The end of the hollow needle was cut off in 15 degrees angle. The hollow needle position was adjusted by a micrometric screw placed inside of a needle holder. The position of Petri dishes could also be changed in two perpendicular directions perpendicular to the needle movement. The position change of the hollow needle and the Petri dish was measured with the precision of 0.01 mm. The needle and the gel medium were in discharge regime connected to a high voltage source and in deformation measurement regime to an ohmmeter. The tip of the hollow needle worked in deformation measurement regime as a probe. Initially, the tip of the hollow needle was placed 6 mm above gel surface and the positions of the needle and the high voltage source set-up were not changed during corona treatment. In deformation measurements the dimple depth h was measured as a change of the distance between the pin electrodes and gel surface. The needle was moved perpendicular toward the gel surface. A contact between the needle tip and the gel surface was detected by the ohmmeter.

Results and discussion

Deformations of the gel surface caused by corona discharges are demonstrated in Fig. 1. A matrix multi-point-to-plane corona discharge was used in this case. Measurements were made with single-needle-to-gel electrode systems due to their simplicity. The dependence of a dimple depth h on the duration of the gel

surface exposition in the corona discharge is shown in Fig. 2. The corona current decreased from initial value of 50 μA accordingly to the gel electrode deformation. The dependence of the dimple depth *h* on the point-to-plane corona initial current is show in Fig. 3. Duration of the gel surface exposition in the corona discharge was 16 minutes. A diameter of 0.3 mm at a depth *D* 0.3 mm was measured as a characteristic dimension of an area affected by the point-to-plane corona discharge. The hollow needle was shifted 6.3 mm toward the gel. The diameter at 0.3 mm depth was measured by defined shift of the Petri dish in several directions. The dependence of the diameters of 0.3 mm depth on the exposition duration is shown in Fig. 4. The initial corona current was 50 μA. The dependence of the diameters of 0.3 mm depth on the initial corona current is shown in Fig. 5. The exposition duration was 16 minutes.

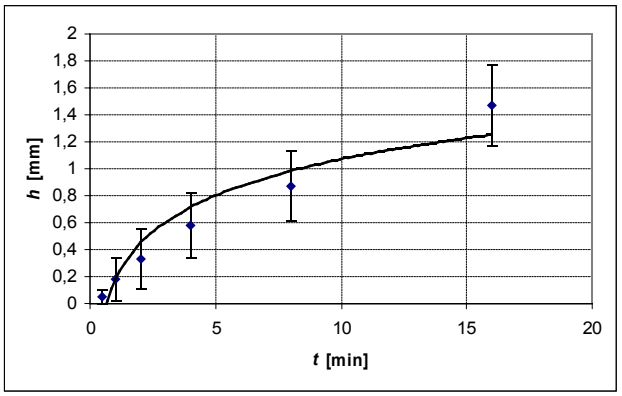

Fig. 2: Dependence of depth on time for 50 μA.

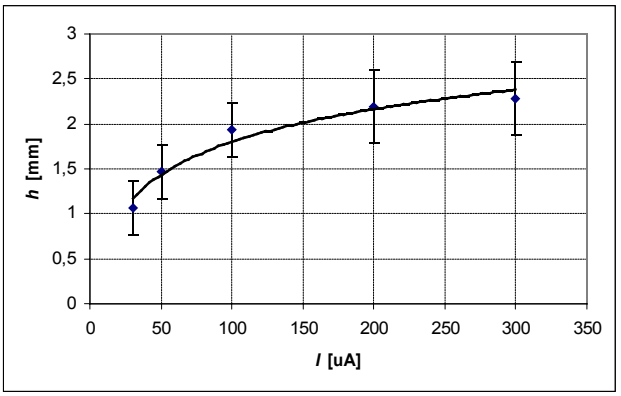

Fig. 3: Dependence of depth on current for 16 min.

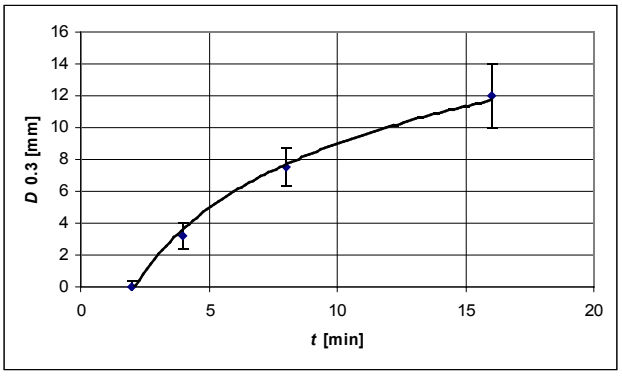

Fig. 4: Dependence of diameter on time. (50 μA)

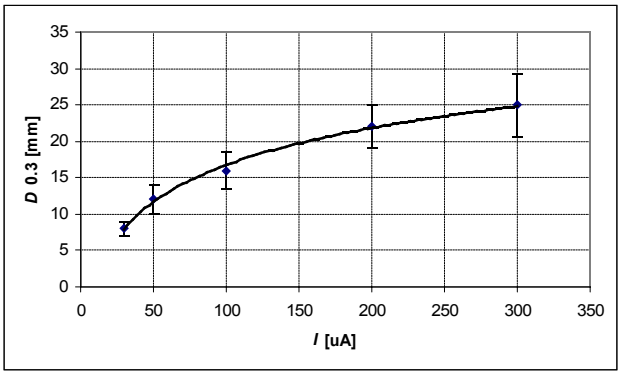

Fig 5: Dependence of diameter on current. (16 min)

Conclusions

In the pin-to-plane corona discharge with ion conducting gel electrode systems the gel surface is shaped by the stream of ions. Size of deformed gel surface is comparable to distances between electrodes used in sterilization experiments and therefore cannot be neglect. This effect leads to redistribution of corona current during gel exposition in corona due to geometry change. However described gel surface change cannot be predicted for a concrete gel. The variation of the deformation can be explained by the fact that the water content in used agar plates varies during storage and consequently a gel electrode viscosity changes.

P 40

Surface Modification of Nonwoven Fabrics by Atmospheric Pressure Plasma Generated by DCSBD Working in Continuous Regime

D. Kováčik[1], A. Zahoranová[1], J. Kubincová[1], A. Buček[1], J. Ráheľ[1, 2], M. Černák[1, 2]

[1]Department of Experimental Physics, Comenius University, Mlynská dolina, 842 48 Bratislava, Slovakia
[2]Department of Physical Electronics, Masaryk University, Kotlářská 2, 611 37 Brno, Czech Republic
e-mail: kovacik@fmph.uniba.sk

Abstract

A prototype atmospheric-pressure plasma device for continuous treatment of textile materials is described. The heart of the device is Diffuse Coplanar Surface Barrier Discharge (DCSBD) plasma source generating a thin diffuse layer of high-power-density non-equlibrium plasmas in any working gas without the use of expensive He or Ar gases. As illustrated by the results on atmospheric-pressure plasma hydrophilization of light-weigt polypropylene nonwoven fabric, other advantages of the system include the low-cost, high-speed and permanancy of the plasma treatment.

Introduction

Increased requirements on the finishing of textile products like environmental protective production, new kinds of synthetic fibers and, above all, optimized surface properties, demand innovative production technics. The advantages of the plasma treatment have been well known in the laboratories for a long time. Nevertheless, this technique is hardly used in the textile industry: the majority of applications were made at reduced pressures on the order of 10^{-3}- 10^{3} Pa, where the low-temperature plasma can easily be generated and brought into direct contact with fibres of textile materials to be treated. Several companies as, for example, *Unitika – Sando Iron Works* (Japan), *Niekmi* (Russia), *Tecnoplasma* (Russia-Italy-Switzerland), *FZM GmbH* (Germany), *Europlasma* (Belgium), and *Unitex* (Italy) have already put low-pressure plasma fabric treaters on the market and found applications in finishing of relatively small amounts of expensive textiles and other polymeric webs for special applications in, for example, medicine, military, etc.

The use of vacuum plasma systems in common textile and paper plants, however, has been discouraged by high investment costs, batch-wise processing and relatively long treatment times (on the order of minutes). For these large-area bulk products with low added value, cheap on-line surface treatments by atmospheric-pressure plasmas are required. Hence, applications of plasma reactors should allow continuous, on-line treatment of endless lengths of webs of typically 2 m or more in width at speeds up to 1000 m/min. In light of these requirements it is not surprising that, despite of significant research efforts, no actual commercially viable atmospheric-pressure plasma processing system for high-speed and cost effective on-line textile treatments has yet emerged. Apparently, the crux of plasma finishing techniques for textile industry is the availability of robust, reliable and cost-effective sources of low-temperature atmospheric-pressure plasma, able to operate in tandem with existing high-speed production lines with the plasma power density of the order of 100 W/cm^3 that is necessary to achieve exposure times less than 1 second.

The commercially available atmospheric-pressure plasma sources for the textile treatment manufactured by *Enercon* and *Dow Corning* are using helium and low plasma power densities to prevent the appearance of hot filaments or sparks that are detrimental to the textile materials. Besides the costs associate with using large amounts of helium, it also presents an unfortunate restriction of the working range.

Results and discussion

The goal of our work was to develop an atmospheric pressure plasma treater capable to fulfil the textile industry requirements without the use of helium as a costly carrier gas and operating at high plasma power densities necessary for fast in-line treatment. Fig. 1 shows the prototype of an atmospheric-pressure narrow-web plasma treater. The technique is based on the use of the DCSBD plasma source [1-3]. The device technically and economically outperforms the existing atmospheric-pressure plasma textile treaters, and can also be easily scaled-up and integrated into existing continuous manufacturing systems.

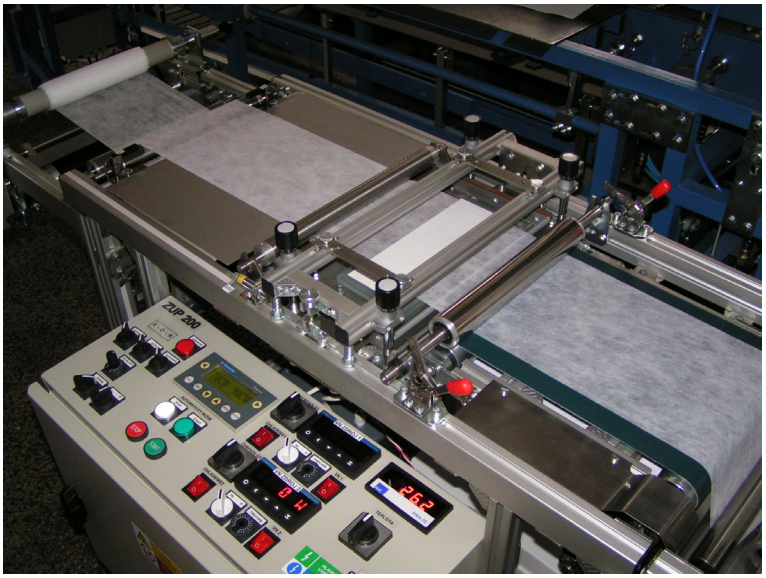

Figure 1: Prototype atmospheric-pressure treater operated in ambient air.

The unique performance characteristics of the treater are illustrated by results on ambient air-plasma hydrophization of light-weight (17 g/m^2) spun-bonded polypropylene nonwoven fabric, where the permanent fabric hydrophization was obtained also at power consumption less that 1 kWh/kg (Fig. 2).

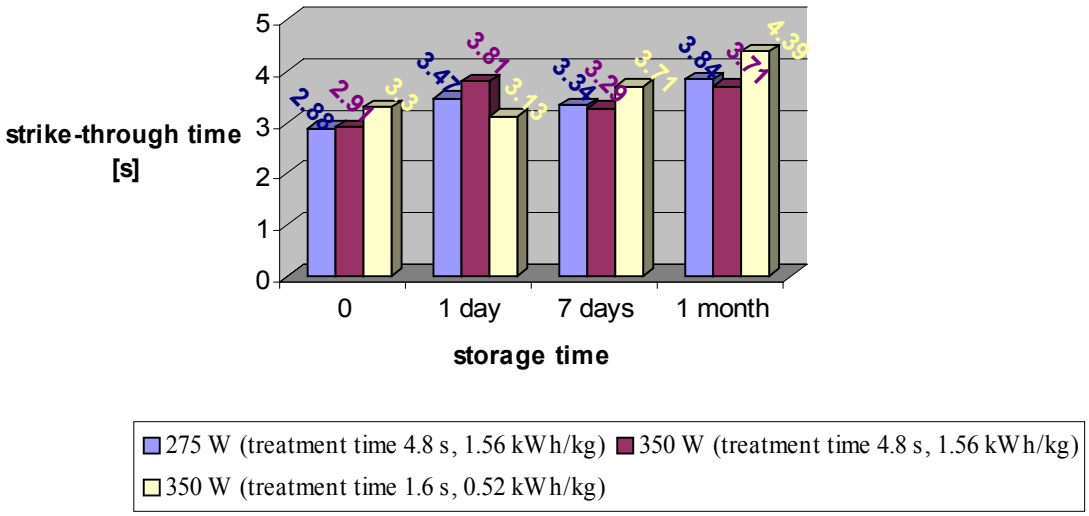

Figure 2: Ageing effect as a function of storage time for plasma treated nonwoven samples prepared at different treatment time and power. The power consumption is also listed.

Acknowledgements

This work was supported by APVV grant No. 20/P01505.

References

[1] M. Šimor, J. Ráheľ, P. Vojtek, A. Brablec, M. Černák, *Appl. Phys. Lett*. 81, No. 15 (2002), pp. 2716-2718

[2] M.Černák, J.Ráheľ, D. Kováčik, M. Šimor. A. Brablec, *Contributions to Plasma Physics* 44 (2004), pp. 492-495

[3] M. Černák, "Method and apparatus for treatment of textile materials" *US Patent Appl*. 2004/0194223

P 41

Influence of the Mercury Traces on Pure Nitrogen Post-Discharge Kinetics

F. Krčma[1], V. Kanický[2], A. Hrdlička[2]

[1]Institute of Physical and Applied Chemistry, Faculty of Chemistry, Brno University of Technology, Purkyňova 118, Brno 612 00, Czech Republic

[2]Laboratory of Plasma Physics and Plasma Sources, Faculty of Science, Masaryk University Brno, Kotlářská 2, Brno 611 37, Czech Republic

e-mail: krcma@fch.vutbr.cz

Abstract

The DC flowing post-discharge in nitrogen containing mercury traces of about 2.1 ppm was studied in Pyrex tube by emission spectroscopy. The relative populations of $N_2(B\ ^3\Pi_g)$, $N_2(C\ ^3\Pi_u)$ and $N_2^+(B\ ^2\Sigma_u^+)$ states were calculated in the dependence on the post-discharge time in the range of 3 – 40 ms. As the uncontrolled oxygen traces were recorded in the mercury flow the experiment with nitrogen-oxygen mixture was added. The results showed strong quenching of the nitrogen pink afterglow by mercury traces. The kinetic explanation should be done through strong depopulation of level $N_2(X\ ^1\Sigma_g^+, v = 20)$ (creation of mercury $^3P_1$ state) and levels $N_2(X\ ^1\Sigma_g^+, v = 28)$ or $N_2(A\ ^3\Sigma_u^+, v = 4)$ (creation of mercury $^1S_0$ state). Both mercury states are origins of UV light emission (254, resp. 185 nm) that could not be detected in our experimental set up.

Introduction

The nitrogen afterglow kinetics is a really complicated problem that is a subject of many studies during last 50 years. The mechanisms that populate various radiative states of neutral molecule as well as the molecular ion are different and many collisional quenching processes of specific states (in the ideal case vibrationally specified) must be included into the kinetic models. The traces of various species (for example carbon or oxygen) significantly change the kinetics. This study is focused on the influence of mercury atoms on the kinetic processes during the post-discharge period. It should increase the knowledge about the nitrogen post-discharge kinetics and provide a basis for further application as a new analytical technique.

Experimental set up

Active discharge was created in a Pyrex discharge tube with a 120 mm electrode distance at pressure of 700 Pa and discharge current of 150 mA. The molybdenum hollow electrodes were placed in the side arms of the main discharge tube for minimizing their sputtering. Nitrogen was of 99.999 % purity and it was further cleaned by a copper based catalyzer and a LN_2 trap. A sealed PE test tube with liquid Hg of 99.995 % purity was purged with the pure N_2 flux of 7.5 ml min^{-1} ensuring a saturated Hg vapor (0.2 μg min^{-1} Hg at 30 °C in steady state). The mercury vapor condensation was observed in the MFC valve which controls its flow into the discharge. Due to this fact we made a special procedure to verify exact mercury amount in the discharge. The working gas mixture at operating conditions without discharge was trapped for 10 hours in the LN_2 trap. After that the trap was washed by 4 ml of 50 % HNO_3 and the solution was analyzed by ICP technique. The mercury concentration in the discharge was estimated as (2.12 ± 0.02) ppm. As some oxygen traces were detected in the mercury flow, the synthetic air (80 % N_2 + 20 % O_2) was used for the verification of oxygen influence. The appropriate oxygen concentration of 528 ppm was calculated using the spectra of NO^β system. The emitted spectra were measured by Jobin Yvon TRIAX 550 (1200 gr. mm^{-1}) spectrometer with CCD using the multimode quartz optical fiber movable along the discharge tube.

Results and discussion

The influence of mercury and oxygen is substantially different on the post-discharge. It also depends on time elapsed from the decay beginning. The examples are given in Fig. 1 for two selected vibrational levels in neutral nitrogen. The strong increase of the populations with a maximum at about 6 ms corresponds to the well known nitrogen pink afterglow. It can be seen that this effect is, at given conditions, increased by oxygen presence in comparison with mercury that very efficiently quenched this effect. The pink afterglow quenching by mercury increases with increase of the vibrational level energy, thus in the molecular ion and neutral molecule $N_2(C\ ^3\Pi_u)$ state the pink afterglow is almost missing. Some rests of the "pink" can be recognized at the lowest $N_2(B\ ^3\Pi_g)$ levels, only. The vibrational population dependencies during the post-discharge are nearly the same for all observed vibrational levels ($N_2(B\ ^3\Pi_g, v = 2–20)$, $N_2(C\ ^3\Pi_u, v = 0–4)$ and $N_2^+(B\ ^2\Sigma_u^+, v = 0–7)$). The results obtained with mercury traces also show an increase of populations at

N_2 ($B\ ^3\Pi_g$, v = 10–12) levels at later decay times. This effect is more or less fully caused by uncontrolled oxygen traces because oxygen increases the atomic nitrogen concentration at later decay times.

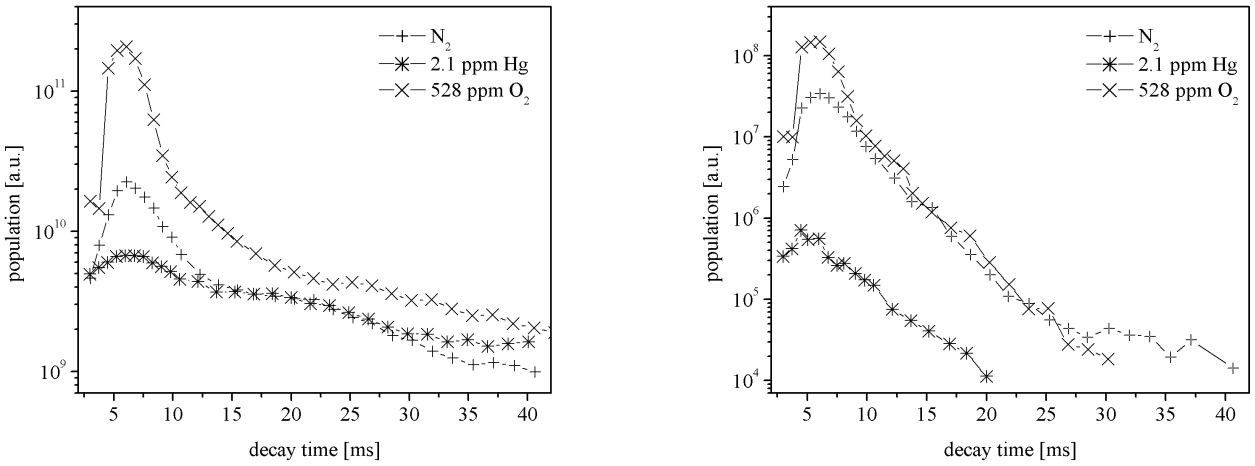

Fig. 1: Population profiles during the post-discharge in pure nitrogen and pure nitrogen containing traces of oxygen and mercury with oxygen. Left: N_2 ($B\ ^3\Pi_g$, v = 2); right: N_2^+ ($B\ ^2\Sigma_u^+$, v = 0).

The N_2 ($B\ ^3\Pi_g$) and N_2 ($C\ ^3\Pi_u$) states are dominantly created by pooling reactions of lower metastable states, especially by the vibrational excited ground state and by the lowest 8 levels of N_2 ($A\ ^3\Sigma_u^+$) state [1] that are all strongly metastable. These reactions play the main role in the creation of both these states, but they cannot explain the strong population enhancement during the pink afterglow. Therefore another process must be considered.

The kinetics of the molecular ion radiative state is more complicated and it can be explained in a two-step scheme. Before the pink afterglow the charged particles concentration is very low but during the pink afterglow it significantly increases. So, the first step must lead to the molecular ion creation. As the post-discharge is without any external energy source, a step-wise ionization process takes place here [2].

Molecular oxygen is fully dissociated in an active discharge (residence time of about 8 ms) and due to its low concentration, the NO species are formed, only. These species significantly depopulate the vibrationally excited nitrogen ground state molecules (over N_2 ($X\ ^1\Sigma_g^+$, v = 13)) and form atomic species that consequently form the NO ($B\ ^2\Pi$) radiative state. Simultaneously the highly excited nitrogen ground state molecules (over N_2 ($X\ ^1\Sigma_g^+$, v = 23)) can form the radiative NO ($A\ ^2\Sigma^+$) state.

The influence of mercury atoms on the post-discharge kinetics is more simple. The energy transfer from N_2 ($X\ ^1\Sigma_g^+$,v = 20) to the mercury ground state leads to the creation of radiative mercury $^3P_1$ state (corresponding wavelength of 254 nm) and levels N_2 ($X\ ^1\Sigma_g^+$,v = 28) or N_2 ($A\ ^3\Sigma_u^+$,v = 4) can create the excited mercury $^1S_0$ state (corresponding wavelength of 185 nm). Thus the v-v processes in nitrogen ground state are stopped at these levels and pooling reactions or step-vise ionization could not efficiently create higher electronic states of nitrogen and pink afterglow is quenched.

Conclusions

The influence of mercury traces on the pure nitrogen post-discharge kinetics was experimentally studied in DC flowing afterglow in Pyrex reactor. The mercury deexcitates by few channels the highly excited metastable nitrogen states and thus the nitrogen v-v processes and various pooling reactions are not such effective to create nitrogen pink afterglow effect. The mercury radiation is in hard UV region (186, resp. 254 nm) and thus could not be observed in our case. To confirm the proposed kinetic model the experiments will be repeated in the quartz discharge reactor.

References

[1] F. Krčma, E.T. Protasevich, *Post-discharges in Pure Nitrogen and in Nitrogen Containing Halogenated Hydrocarbon Traces*, Tomsk Polytechnic University Publishing, Tomsk, 2003, pp. 1-132.

[2] L.S. Polak, D.I. Sloveckii, A.S. Sokolov, *Opt. Spectrosc.,* 32, (1972) 247.

The work was supported by Czech Science Foundation, project No. 202/05/0111.

P 42

Electron Impact Ionization of Propane: Near-Treshold Absolute Partial Cross - Sections

D. Kubala, Š. Matejčík, J. Kočišek

Department of Plasma Physics, Comenius University, Mlynská dolina, Bratislava 842 45, Slovakia
e-mail: kubala@neon.dpp.fmph.uniba.sk

Abstract

The relative cross-sections for electron impact ionization of propane near threshold energies have been studied and reported by Denifl *et al.* [1]. The measurements have been carried out by means of the crossed electron-molecular beams technique with mass spectrometric analysis of arising fragments. Measured data were processed in this work by normalizing to the accurate values of absolute total ionization cross-section of Argon close to the threshold energy [2].

Introduction

The present investigation in the field of thermonuclear fusion shows that simple hydrocarbons rising at the low temperature plasma-wall edge of standard fusion reactor have a significant influence on the stability of fusion plasma. The relative partial electron impact ionization cross sections were measured by Denifl *et al.* and appearance energies of particular fragments were determined. This work deals with assignation of absolute cross-section values to the dataset from mentioned measurements. So called normalizing method was used for estimation of the values. The electron impact ionization measurements of Ar near the threshold energy (*15,76 eV*) were carried out immediately before everyone measurement of propane ionization. Ar data were normalized to the absolute experimental data of Rejoub *et al.* [2] and normalization constant was used to convert relative data of propane.

Experiment

The experimental setup used for measurements consists of crossed electron-molecular beams apparatus combined with quadrupole mass spectrometer. Detailed description can be found in [3]. Propane temperature was $T = 290K$ for all measurements. Pressure of measured gas, electron current and all other settings of apparatus have been kept constant during one set of measurements (Argon + Propane).

Results and discussion

Observed reaction channels are specified in [1]. The nearest measured value suitable for verification of our data is absolute total electron impact ionization cross-section of Duric *et al.* [4] at the incident energy $E = 12\ eV$. Thus we had to extrapolate our experimental data to this energy and summing all curves which contribute to the total cross-section under *12 eV* (*see fig.1*). Fitting curve *f(E)* used for extrapolation has following form:

$$f(E) = b \quad \text{if } E < AE_1$$

$$f(E) = b + c(E - AE_1)^{p_1} \quad \text{if } AE_1 < E < AE_2$$

$$f(E) = b + c(E - AE_1)^{p_1} + d(E - AE_2)^{p_2} \quad \text{if } E > AE_2,$$

where AE_1 and AE_2 are first and second ionization thresholds, b is the background signal, c and d are scaling constants and finally p_1 and p_2 are Wannier factors of ionization processes. We have compared our value also with the value [5] calculated using the Binary-Encounter-Bethe (BEB) model. Result of comparison is shown in the *Table 1*. Our value is more than one order of magnitude larger for incident energy higher than the BEB value at *12 eV*.

Table 1. : Comparison of present values, described above, and other known values of absolute total electron impact ionization cross-sections of C_3H_8 at the energy 12 eV.

σ_{BEB}(12 eV) [10^{-16} cm^2]	$\sigma_{Present}$(12 eV) [10^{-16} cm^2]	σ_{Duric}(12 eV) [10^{-16} cm^2]
0.119	0.21 ± 0.02	0.35

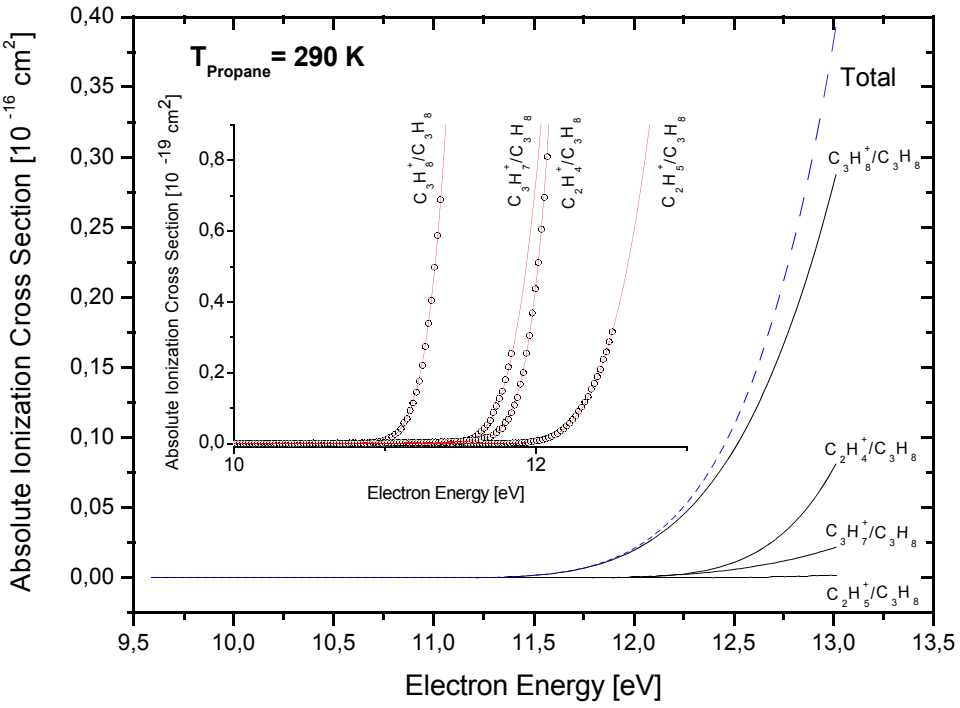

Fig.2 Cross-section curves near the ionization threshold. Normalized measured data are shown as the open circles, the fit functions are shown as solid lines inside the enclosed diagram. Outer diagram shows extrapolation till the incident energy *E = 13 eV*(solid lines), sume of this lines is shown as dashed line.

Conclusions

Absolute electron impact ionization cross section values for ionization curves measured by Denifl *et al.* were determined. The value of sume of individual partial ionization processes extrapolated to the energy *12 eV* lies between value of BEB model and reference value of Duric *et al.* (*see Table 1*).

Acknowledgement

This work was partially supported by by the Slovak Research and development agency, project Nr. APVT-20-007504, the European Comission, Brussels, Contract No 801501, the IAEA, Project No. SLR13490.

References

[1] S. Denifl, S. Matejčík, J.D. Skalný, M. Stano, P. Mach, J. Urban, P. Scheier, T.D. Märk, W. Barsczewska, *Chem. Phys. Lett*, 402 (2005) 80-87.
[2] R. Rejoub, B.G. Lindsay, R.F. Stebbings, *Phys. Rev. A*, 65 (2002) 042713.
[3] S. Matejčík, V. Foltin, M. Stano, J.D. Skalný, *Int. J. Mass Spectrom.*, 9 (2003) 223-224.
[4] N. Duric, I. Čadež, M. Kurepa, *Int. J. Mass Spectrom. & Ion Processes*, 108 (1991) R1-R10.
[5] W. Hwang, Y.-K. Kim and M.E. Rudd, *J. Chem. Phys.*, 104 (1996) 2956.

P 43

Treatment of Catalytic Iron Layer for Carbon Nanotube Growth in Microwave Plasma Torch

Z. Kučerová[1], L. Zajíčková[1], M. Eliáš[1], O. Jašek[1], J. Matějková[2], J. Buršík[3]

[1]Dept. of Physical Electronics, Faculty of Science, Masaryk University Kotlářská 2, 611 37 Brno, Czech Republic
[2] Institute of Scientific Instruments, Královopolská 147, 612 64 Brno, Czech Republic
[3] Inst.of Physics of Materials, Žižkova 22, 616 62 Brno, Czech Republic
e-mail: zus@physics.muni.cz

Abstract

Carbon nanotubes (CNT) have been prepared in atmospheric pressure microwave torch. Nanotubes have grown on colmplex substrate system with thin iron overlayer serving as a catalyst. Because the nanotubes' parameters, such as diameter and alignment are influenced by the catalyst, a careful study of the catalytic particles, occurring at the very beginning of the deposition process, has been carried out.

Introduction

Atmospheric pressure deposition techniques are less common than the low pressure ones. However, they present an opportunity to deposit carbon nanotubes without complex pumping system and usually at high deposition rate. Alike other CVD technique, plasma enhanced CVD at atmospheric pressure requires the presence of the catalyst. Most commonly used is catalyst in the form of thin film. If heated, the catalyst will decompose into tiny particles that may aggregate into bigger ones. This process is influenced by temperature, by catalyst thickness and by the heating time [1,2]. This work focuses on a preparation of catalytic particles from the iron film, on their analysis and on analysis of the carbon nanotubes grown from these particles.

Experimental

Torch is connected to the power generator via rectangular waveguide, matching unit and a coaxial line. Microwave power is 400W and the frequency is 2.45 GHz. Argon (Q_{Ar} = 1000 sccm) is used as a working gas and methane and hydrogen are used as reactive gases (Q_{CH4} = 50 sccm, Q_{H2} = 200 or 300 sccm). Iron catalytic layer varies in thickness from 5 to 20 nm. For the details on the deposition apparatus and on substrate preparation see [3]

Results and discussion

Because the torch extent is relatively small compared to substrate size, the deposites are not uniform. In [4] we discussed, that the size of iron nanoparticles decreases from the centre towards the edges, in accordance with temperature. In the sample centre particles as large as 0.35 μm^2 may be found, at the edges there are only as large as 0.1 μm^2. (Treatment conditions were: Q_{Ar} = 1000 sccm, Q_{H2} = 200 sccm, Q_{CH4} = 50 sccm, catalytic layer iron 10 nm, treatment time 30s.) Nanoparticles occure even in the absence of methane and exhibit the same size distribution, only their area is almost ten times larger. Their size ranged from 1 μm^2 at the edge to 2.5 μm^2 in the middle. Similar situation is illustrated in Fig.1. Nanoparticles preapared from the iron layer of 10 nm, Q_{Ar} = 1000 sccm, Q_{H2} = 300 sccm, with and without methane are considerably different in size. Mean diameter of particles in the sample centre prepared without methane is 0.07 μm^2 and with methane it is only 0.02 μm^2. The latter particles consist of iron core covered with amorphous carbon, as discussed in [4], so the actual area of iron particles themselves is even lower. We see that the size of particles depends strongly on the gas mixture. It is important to note, that with addition of methane we add not only carbon, but also hydrogen. The more amount of hydrogen in the discharge, the smaller the particles are. Diameter of carbon nanotubes is comparable to the iron core of the catalytic particle. The size and distribution of particles also influences the alignment of the nanotubes. In Fig.2. there are nanotubes found on the edge of the sample compared to those found in the centre. Nanotubes from the edges, where the particles are smaller and better separated, are much better aligned than nanotubes in the centre, where particles are larger and close to each other.

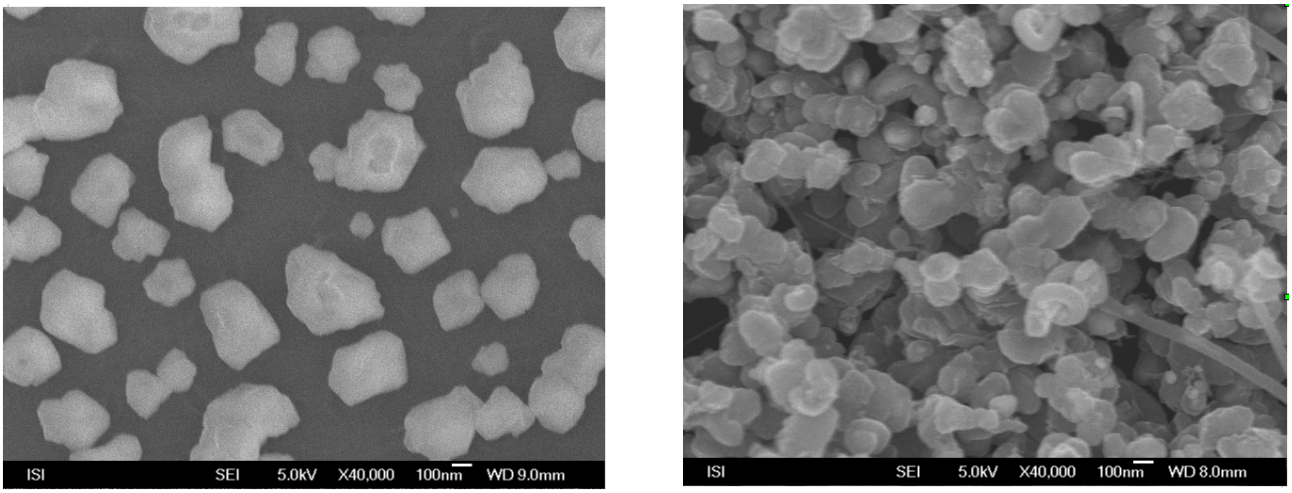

Fig.1: Iron catalytic particles prepared from the catalytic layer of 10 nm. Left) without methane. Right) with Q_{CH4} = 50 sccm. Deposition conditions were: Q_{Ar} = 1000 sccm, Q_{H2} = 300 sccm, mw power 400W, treatment time 30s.

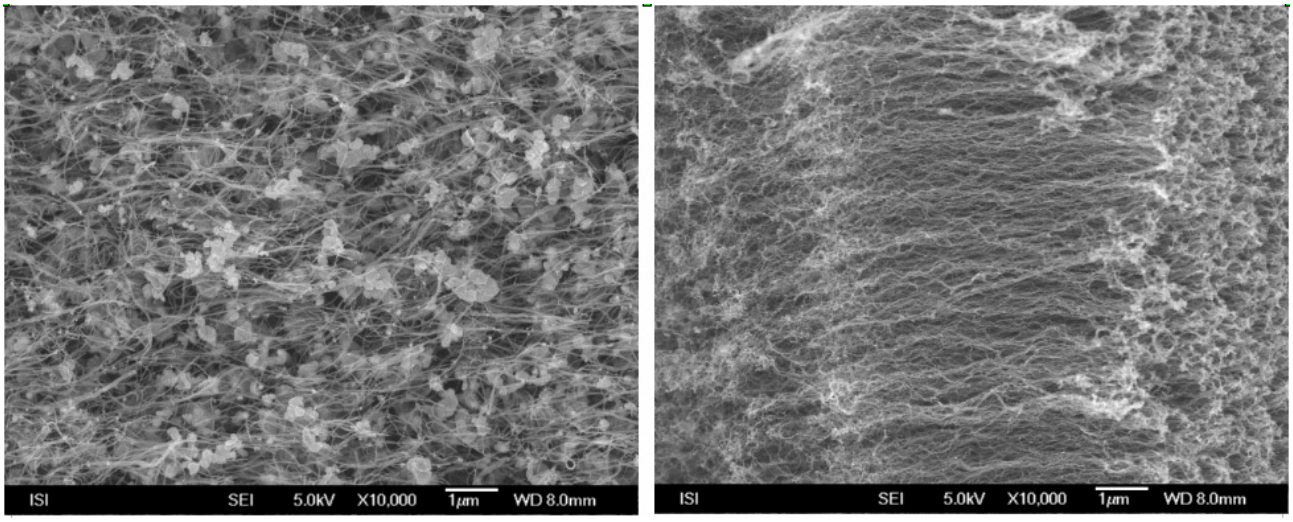

Fig.2: Carbon nanotubes found on the edge of the sample (left) and in the centre (right). Deposition conditions were: Q_{Ar} = 1000 sccm, Q_{H2} = 300 sccm, Q_{CH4} = 50 sccm, mw power 400W , original iron layer thickness 10nm, deposition time 3min.

Conclusions

Catalytic particles of iron covered with amorphous carbon have been prepared from catalytic iron film. The size and distribution of the particles has been studied in order to find out how the nanotubes' parameters are influenced by the catalytic particles.

References

[1] M. Chhowalla, et all, J. Appl. Phys., 90, 2001, 5308
[2] C. Bower, O. Zhou, W. Zhu, D. J. Werder, S. H. Jin, Appl. Phys. Lett., 77, 2000, 2767
[3] L. Zajíčková, Plasma Phys. Control. Fusion 47 (2005) 655.
[4] Z. Kucerova, *et all.* Acta Metallurgica Slovaca, *in press*

P 44

Plasmachemical Processes in Oxygen–Nitrogen Afterglow

V. Kudrle, M. Mrázková, P. Vašina, A. Tálský

Department of Physical Electronics, Masaryk University, Kotlářská 2, CZ-61137 Brno, Czech Republic
e-mail: kudrle@sci.muni.cz

Abstract

Using electron paramagnetic resonance (EPR) and optical emission spectroscopy we experimentally investigated the flowing afterglow in oxygen - nitrogen mixture.

Introduction

The discharges in oxygen, nitrogen and their mixtures are very important for the research and technology development. Especially rapidly evolving field of plasma sterilisation promotes growing interest in plasmochemical processes in oxygen – nitrogen plasmas and postdischarges. Although sophisticated models do exist, there are still experimentally observed effects[1] which remain unexplained. The most interesting regions of oxygen/nitrogen ratios are those near 0% or 100%. In such cases much higher dissociation degree is observed than in pure nitrogen or pure oxygen.

Experimental

A microwave discharge (2.45 GHz, 20 W) is produced in a quartz discharge tube with inner diameter of 13 mm passing through the surfatron cavity. Flowing afterglow may be observed in 1 m long quartz tube with inner diameter of 8 mm. Oxygen and nitrogen are mixed in given ratio and this mixture passes through the discharge. Our experiments are carried out at gas flow of 25 sccm, which corresponds to pressure of 170 Pa in a discharge area. The flow rates are measured by mass flow controllers and the pressure is set independently by throttling the pump.

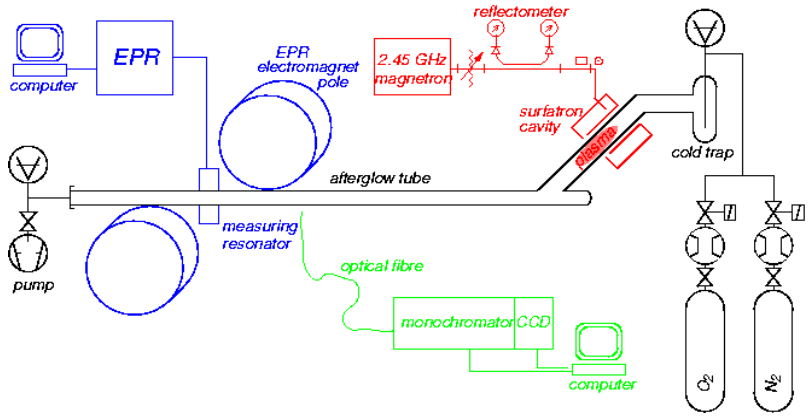

Figure 1: Experimental setup.

Afterglow tube is going through EPR spectrometer. Distance between the discharge and EPR resonator was fixed at 30 cm. We used JEOL JES 3B EPR spectrometer operating in X-band to measure the concentration of N and O atoms. This techniques is based on resonant absorption of microwave energy by the transitions between Zeeman split levels. For details about use of EPR for concentration measurements, see [2]. After a calibration by molecular oxygen (which is paramagnetic) the EPR technique gives absolute concentrations.

Results and discussion

In this work we concentrated on the case when oxygen is used as main gas and nitrogen as admixture. Results of EPR and OES are shown in Figure 2. When small amount of nitrogen admixture is added to oxygen upstream of the discharge, we observe pronounced increase in O atom concentration (10x in our case). This is quite similar to the effect described in our previous work [1] where the gases were exchanged.

We do not observe any N atoms in afterglow or optical emission of excited NO molecule. However, intensive glow of excited NO_2 permits us to estimate relative abundance of NO in fundamental state, as NO+O --> NO_2^*. Therefore the ratio of NO_2 and O intensities is shown in Figure 2, too. The NO present in the afterglow is the remain of the NO produced in the discharge which was not consumed by fast reaction

N+NO --> N_2+O, taking place in the early afterglow. This reaction, often used for titration technique [3] is also responsible for absence of N atoms in the afterglow.

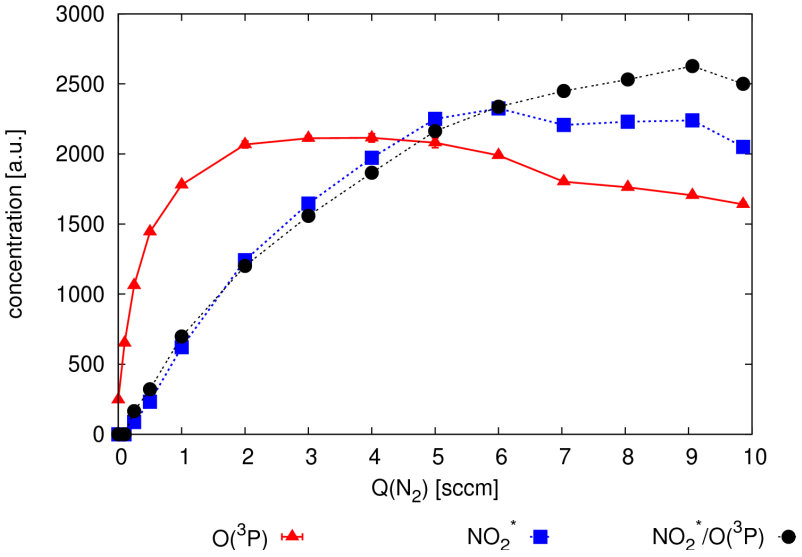

Figure 2: The relative densities of $O(^3P)$, $NO_2(A)$ as a function of nitrogen admixture. Oxygen flow was 25 sccm. Ratio $NO_2(A)/O(^3P)$ corresponds to NO(X) concentration.

Conclusions

We found that small nitrogen admixture into oxygen increases oxygen dissociation by order of magnitude. This is similar to the results with oxygen admixture to nitrogen, as discussed in [4].

However the detailed kinetics is different. In the case of oxygen as the main gas, the following species are present in the afterglow: $O(^3P)$, NO(X), $NO_2(A)$. N atoms and NO^* were not detected. In the case of nitrogen as the main gas, the $N(^4S)$, $O(^3P)$, NO(A), NO(B), $NO_2(A)$ can be found [4] depending on amount of oxygen admixture.

Acknowledgement

This work was supported by Czech Science Foundation, contract 202/05/0111 and by Czech Ministry of Education, contract MSM 0021622411.

References

[1] P. Vašina et al. *Czechoslovak Journal of Physics*, Vol. **56** (2006), Suppl. B, B877-B881
[2] A. A. Westenberg: *Prog. React. Kinet,* **7** (1973), 23
[3] P. Vašina et al: *Plasma Sourc. Sci. Tech.* **13** (2004), 668
[4] M. Mrázková et al: in this *Proceedings of SAPP XVI*

P 45

The Pretreatment Approach of Plasma Chemical Diesel Fuel Reformation Using Plasmatron

H. J. Lee, S. B. Jwa, Ch. J. Yim, V. Y.. Plaksin and V. A. Riaby

Faculty of Mechanical & Energy System Engineering, Cheju National University, Jeju 690756, Korea
e-mail: hjlee@cheju.ac.kr

Abstract

The regulation for an emission from the diesel vehicle is getting more stringent, the research in the field of the in-cylinder processing technologies (pretreatment) becomes more impertant issue as well as the catalyst after-treatment.

In this work, the pretreatment approach consisting of plasma chemical fuel reformation has been investigated. Some fraction (10…20 %) of the diesel fuel was reformed by the plasma in a high durability plasmatron and the hydrogen-rich synthesis gas, that contains of H_2, CO, CO_2, N_2 and hydrocarbons, is generated. The synthesis gas is formed by the partial oxidation of a fuel:

$$C_{12}H_{26} + 6O_2 + 22.3N_2 \rightarrow 13H_2 + 12CO + 22.3N_2 + 1000\ kJ \quad (1)$$

Here $C_{12}H_{26}$ is an average chemical formula of the diesel fuel which is a complex mixture of numerous hydrocarbons. The necessary quantity of air flow rate in order to complete the reaction (1) can be calculated. The partial oxidation of 1 mole=170 g of diesel fuel having molar volume $V_M \approx 170/0.8 \approx 212$ ml takes 28.3 mol of air that has the volume of about $28.3 \times 22.4 \approx 634$ litre at the standard condition. An ideal stoichiometric relationship between air and fuel flow rates shows very simple form as below.

$$Q_{Air}[\text{nl/min.}] \approx 3Q_F[\text{ml/min.}] \quad (2)$$

The used high durability plasmatron has the characteristics of the low plasma contamination, low anode erosion rate, low plasma temperature, and effective activation of the process gas.

In the process of fuel reformation plasmatron parameters were selected and adjusted as follows: argon flow rate in the cathode channel was $Q_{AR} \sim 1$ nl/min., arc current I=100 A, arc voltage $U \approx 12$ V, arc power $P \approx 1.2$ kW. Fuel/air flow rates were selected following experimental results of the MIT group: usually reformation of about 15-20 % of fuel consumption for an engine and supplying process products in the form of a hydrogen-rich gas (synthesis gas $CO+H_2$) allowed them to reach quite satisfactory results in cleaning engine's emission. In the present work two types of truck diesel engines (KMY-D-KA-M-03 and Kookje 3T90LT-AC) were used as experimental equipment. For both of them diesel fuel consumption could reach ~150 ml/min. So the plasma chemical reformation system had to be tuned to deal with fuel flow rate $Q_F \leq 25$ ml/min≈20 g/min≈0.12 mol/min.

Now according to (2) for Q_F = 25 ml/min stoichiometric air flow rate should be adjusted to $Q_{Air} \approx 75$ nl/min. If all 100% of this fuel quantity will be reformed into the synthesis gas then hydrogen yield of the reaction should reach $13 \times 0.12 = 1.56$ mol/min≈35 nl/min. (27%) and CO yield - $12 \times 0.12 = 1.44$ mol/min≈32 nl/min (25%). These figures are ideal limits; real results should depend on the quality of the plasma chemical process of fuel reformation.

Results of CO content measurements should characterize both qualitatively and quantitatively the hydrogen content in the reformation products because according to (1) fuel reformation must result in nearly equal relative contents of CO and H_2 at the level of about 25%.

Measurements were arranged in the following way. Engine was started and heated during some 20-30 minutes operating at idling speed. Then analyzer probe was inserted into the exhaust pipe of the engine to measure NO, NO_2 and NOx content. First initial level of these parameters without any additions was determined. Then the flow of the reformed gas from the heated and stabilized reformation system was directed into the tube supplying reformed gas into the engine. In some time gas analyzer measurements were repeated.

Initially at the trial flow rates of fuel in the range $Q_F \sim 1.0 \ldots 1.7$ cc/min it was found out that the more fuel was supplied into the plasmatron, the deeper fell NOx content in the engine exhaust flow. Then fuel flow rates were increased to $Q_F \sim 6.3$ cc/min.

The preliminary experiments with fuel reformation in the improved version of the new plasmatron at the small fuel flow rates (up to ~6 cc/min) and subsequent supply of the reformation products into a diesel

engine resulted in ~25% NOx cut in the exhaust gas flow. A simulation experiment with the pure hydrogen addition to the inlet of a diesel engine showed that both components of the synthesis gas H_2 and CO fed into the engine play significant role in cutting NOx content in the engine's emission.

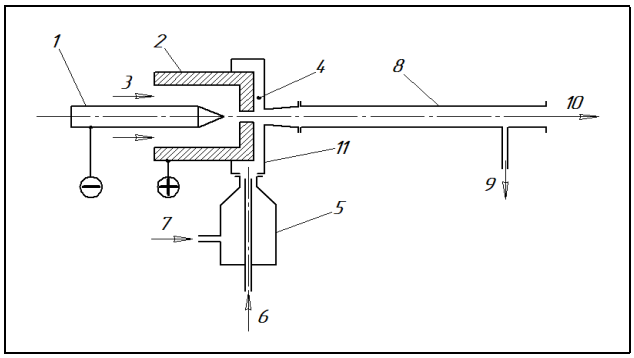

Fig. 1 Diesel fuel reformation system with the A-plasmatron

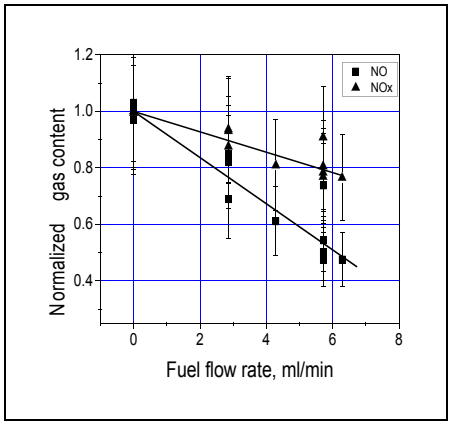

Fig. 2. Normalized NO and NOx contents versus fuel flow rate at Q_{Air}=6 - 15 nl/min

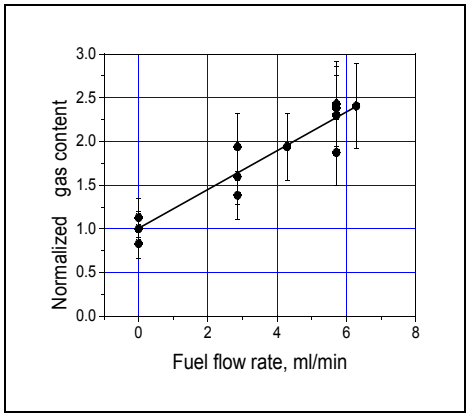

Fig. 3. Normalized NO_2 content versus fuel flow rate at Q_{Air}=6 - 15 nl/min

Acknowledgement

This work was supported by the grant R-2004-096-0-00 of the Korean Ministry of Commerce, Industry and Energy, by the grant M1-0104-00-0071 from the National Research Laboratory Program of the Ministry of Science and Technology, by the Brain Korea 21 from the Ministry of Education and Human Resources Development, Korea., and by the grant 2006-C-CC02-P-05-0-000 of the Korea Energy Management Corporation.

P 46

Carbon Benefication in Atmospheric Pressure Microwave Plasma

L. Leštinská[1], V. Foltin[2], M. Zahoran[2], Z. Machala[1]

[1]Department of Astronomy, Earth Physics and Meteorology, Comenius University, Mlynská dolina, Bratislava 842 48, Slovakia

[2]Department of Experimental Physics, the same address

e-mail: machala@fmph.uniba.sk

Abstract

We present the first tests of carbon benefication done by heating of the carbon samples in atmospheric pressure microwave plasma in nitrogen. The diagnostics of carbon samples was performed by SEM equipped with WDX element analyzer and FTIR spectroscopy.

Introduction

Atmospheric pressure microwave (MW) plasmas present considerable interest for a wide range of applications, such as air pollution control, surface treatment, or carbon nanotube growth [1]. Here we present the first tests of benefication of carbon heated in atmospheric pressure microwave nitrogen plasma. The carbon treated is a product of pyrolysis of used tyres. Its benefication is needed to get rid of the volatile components causing its bad smell, and to make it reusable for other processes.

Experimental setup

Atmospheric pressure MW plasma is generated by a Litmas Red plasma torch (2.45 GHz, 3 kW) in N_2. Experimental setup and the basic torch characteristics are described in more detail in [2]. The original carbon sample was placed on a stainless steel plate in the plasma flame about 1cm above the nozzle (Fig. 1). Approximate temperature of the plate was 1500 K. The system was closed and exhausted because of possibly dangerous gases being emitted from polluted carbon samples. The carbon samples were heated for 5 or 10 minutes in nitrogen plasma of 13 l/min flow rate and 1.4 kW generator power. After plasma being switched off, the sample was cooled at a low N_2 flow 2 l/min to avoid oxidation.

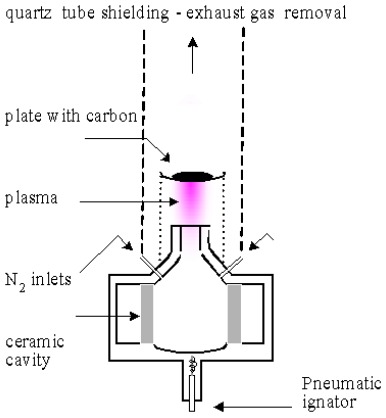

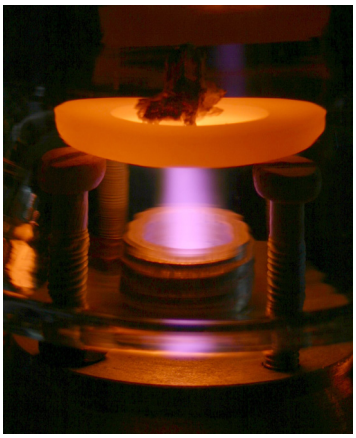

The diagnostics of carbon samples was performed directly by a scanning electron microscope (SEM) Tescan TS5136MM equipped with wavelength dispersive X-ray (WDX) INCA Wave analyzer, and on KBr pellets analyzed by Fourier-transform infrared (FTIR) spectrometer Perkin Elmer Spectrum BX.

Results and discussion

After plasma heating of the carbon samples, we first observed that the sample did not smell anymore and its mass decreased (by 27% for 5 min and 48% for 10 min heating). We assume that some volatile substances, most likely aliphatic and aromatic hydrocarbons and their –OH and ether derivates were released from the carbon, which was confirmed by FTIR spectra (Fig. 2). An apparent reduction of CH_2, C-O-C, -OH, and aromatic C-H functional groups was observed. On the other hand, new compounds were created. We assume them to be metal oxides of trace elements found by WDX analysis. Detailed interpretation of the measured FTIR spectra requires further investigation. Despite the conductivity of the carbon samples being weak, it was good enough for SEM analysis at low magnifications. Microscopic pictures showed that the carbon has an amorphous structure with pores (Fig. 3). Pictures of the treated samples revealed the steps-like shaped cleaving area (Fig. 5), which compared to the smooth shape in the original sample (Fig. 4) shows that

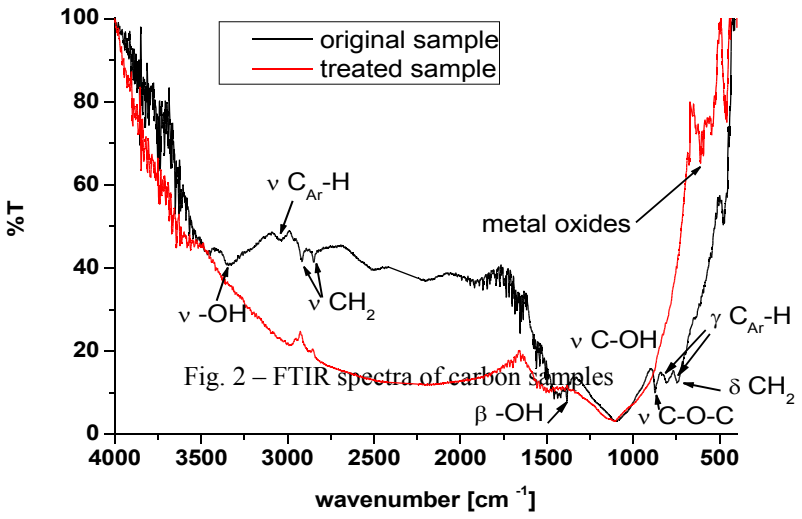

Fig. 2 – FTIR spectra of carbon samples

material became more compact.

WDX analysis of all samples demonstrated C as a dominant element. Trace amounts of S, Ca and Zn were found in the original carbon sample and decreased after the heating, but new elements, such as Fe, Al, Si, K, Mg were found. We assume that some of these metals were released from the stainless steel plate during the heating.

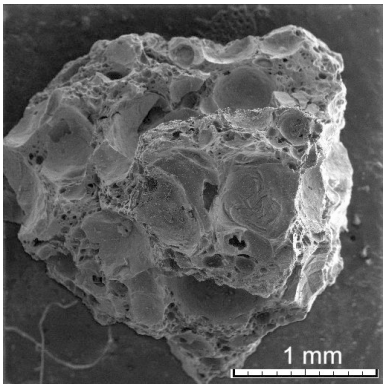

Fig. 3 – Sample shape before the heating

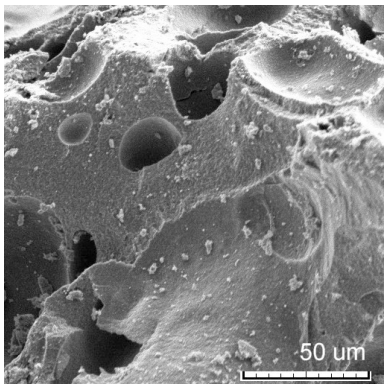

Fig. 4 – Cleaving area and pores before the heating

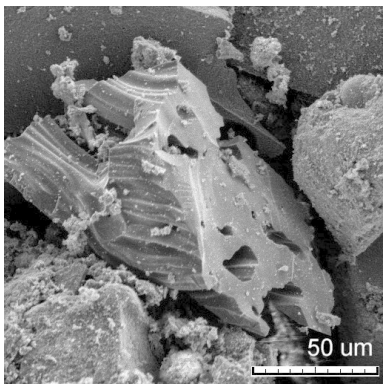

Fig. 5 – Cleaving area and pores after the heating

Summary and perspectives

Atmospheric pressure nitrogen microwave plasma was used as a heat source for used tyre carbon benefication. The plasma heat treatment causes a mass loss, a composition change and a structure change of the carbon. We are currently adapting the microwave torch system so that the carbon powder could be inserted directly into the plasma chamber, which will provide a higher temperature compared to when the sample is heated on the supporting metal plate. The new setup will turn the plasma chamber upside down to enable the collection of the treated carbon powder. Because of the presence of pores we also plan further investigations of the treated carbon, such as measuring its adsorption capacity. This could be interesting for its potential use as an active carbon.

This work was carried out under the support of the Slovak Grant Agency VEGA 1/2013/05 and 1/3043/06, and NATO EAP.RIG 981194 grants. We gratefully acknowledge Sencera, Ltd. for loaning us the MW torch.

References

[1] O. Jašek, M. Eliáš, L. Zajíčková, V. Kudrle, M. Bublan, J. Matějková, A. Rek, J. Buršík, M. Kadlečíková: "*Carbon nanotubes synthesis in microwave plasma torch at atmospheric pressure*" Materials Science and Engineering C **26** (2006) 1189–1193

[2] V. Foltin, L. Leštinská, Z. Machala: *"Spectroscopic investigations of atmospheric pressure microwave torch nitrogen plasma jet"* Czech. J. Phys. **56** (2006), B712-720

P 47

Ozone Generation by Microdischarges in Porous Ceramics

M. Leštinský, K. Hensel, V. Martišovitš

Department of Astronomy, Earth Physics and Meteorology, Comenius University, Mlynská dolina, Bratislava 842 45, Slovakia
e-mail: hensel@fmph.uniba.sk

Abstract

Plasma-chemical activity of microdischarges generated inside porous ceramics by AC high voltage was investigated. Generation of ozone in mixtures of nitrogen and oxygen were tested to evaluate the chemical efficiency of the discharges. The effects of discharge power, gas mixture composition and gas flow rate on ozone generation are described.

Introduction

The generation of microdischarges in small pores, cavities and narrow capillaries of various ceramic materials has been studied recently [1-5]. The objective of these studies was the investigation of the physical properties of such microdischarges, but also to test them for the removal of nitrogen oxides and volatile organic compounds. The microdischarges generating plasma inside porous ceramics and catalysts represent a method with very high potential for various environmental applications, especially flue gas treatment. In our previous works [4-5] we studied the generation of microdischarges by using AC and DC high voltage power. We performed various electrical and optical measurements to describe their physical properties and determine the conditions of their stable generations and distribution inside the ceramics. The objective of the presented study was to test the chemical efficiency of the microdischarges. Generation of ozone in mixtures of nitrogen and oxygen was selected as a model case. In the paper, the results of the ozone generation as the function of discharge power, gas mixture composition and gas flow rate are presented.

Experimental Setup

Figure 1 shows the experimental setup. In the discharge reactor, a porous ceramics was placed between two metal mesh electrodes. The ceramics was composed of mainly alumina and silica and had diameter and thickness of 31 and 7 mm, respectively. In the previous studies [4-5] the optimal discharge spatial distribution was observed for the ceramics of 30-80 μm pore size, therefore 80 μm ceramics selected for the tests. AC high voltage power supply connected via a 5 MΩ series resistor limiting the total discharge current was used to excite the discharge reactor. The power was measured by digital multimeter Metex 3860M. The voltage at the reactor was measured by a high voltage probe Tektronix P6015A and the discharge current was measured using a current probe Pearson Electronics 2877 (1V/A) linked to the digitizing oscilloscope Tektronix TDS1012 (100 MHz, 1 GS/s). Gas analysis was performed by FTIR absorption spectrometer Perkin Elmer Spectrum BX II. Mixtures of oxygen and nitrogen (10, 20, 50 and 100% of oxygen) with the total gas flow 0.4, 0.8, 1.2 and 2.0 were tested. The pressure drop across the discharge reactor was measured by the digital manometer PCE P-30.

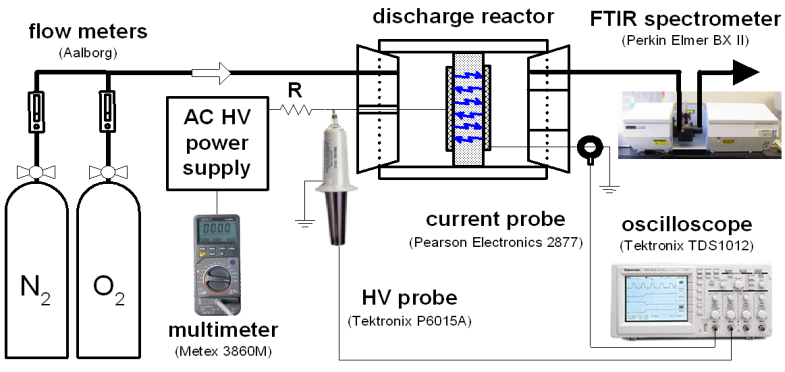

Figure 1: Schematic view of experimental setup.

Results and Discussion

The effect of the discharge power, the gas mixture composition and the gas flow rate of the discharge was investigated. The pressure drop across the reactor was negligible and ranged from 0.1 kPa to 0.8 kPa for gas flow rates of 0.4 and 2.0 l/min, respectively. In pure oxygen, the concentration of generated ozone increased with the discharge power. For the given power, the concentration of ozone was higher for smaller gas flow (Fig.2). In the mixtures of nitrogen and oxygen, a maximum of the ozone concentration was observed at a certain power. With further increase of the power the ozone concentration decreased. The power at which the maximum concentration was observed decreased with the increasing flow rate (Fig. 3). Analysis of the FTIR

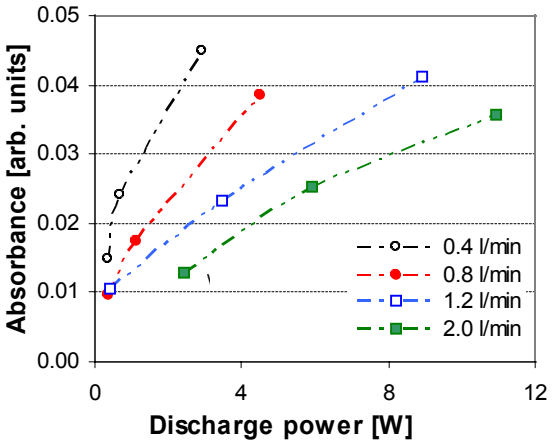

Figure 2: Ozone concentration as a function of power for various flow rate (pure O_2).

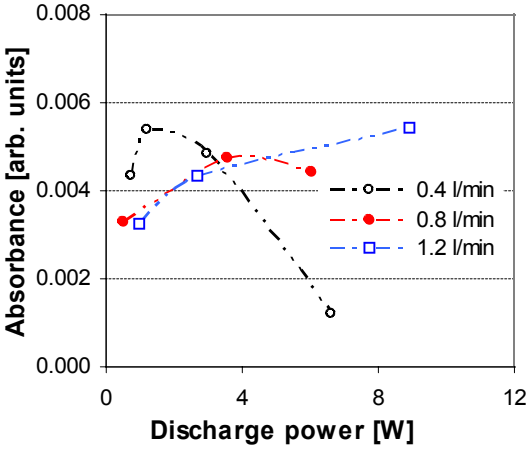

Figure 3: Ozone concentration as a function of power for various flow rates (20% of O_2 in N_2).

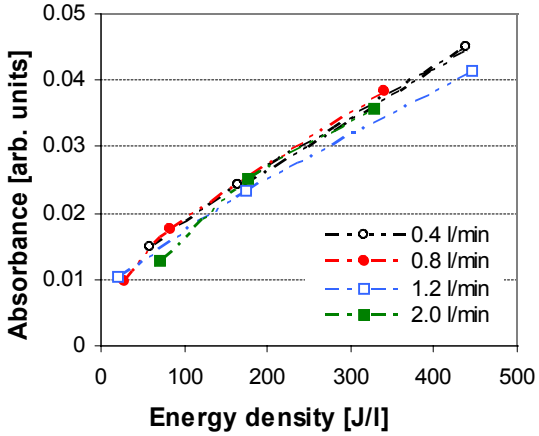

Figure 4: Ozone concentration as a function of energy density (pure O_2).

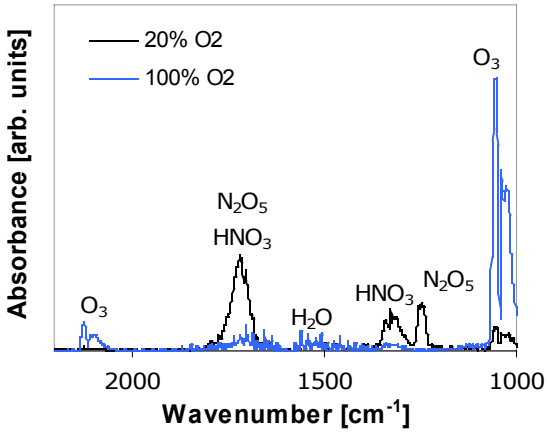

Figure 5: IR spectra of gaseous produsts in mixtures of 20% O_2 in N_2 and pure O_2 (1.2 l/min, 9.1W).

Conclusions

The plasma-chemical efficiency of microdischarges inside porous ceramics was demonstrated by the generation of ozone in various mixtures of nitrogen and oxygen. The effects of discharge power, gas mixture composition and gas flow were briefly described. We assume it may also be effectively used for flue gas treatment.

The research has been supported by Science and Technology Assistance Agency Grants APVT 20-032404 and SK-FR00506 and Slovak Grant Agency VEGA 1/3041/06.

References

[1] N. Gherardi et al., *Plasma Sources Sci. Technol.* 9 (2000) 340-346.
[2] N. Blin-Simiand et al., *Plasma Proc. Polym.* 2 (2005) 256-262.
[3] N. Jidenko, M. Petit, J-P. Borra, *J. Phys. D: Appl. Phys.* 39 (2006) 281-293.
[4] K. Hensel, S. Katsura, A. Mizuno, *IEEE Trans. Plasma Sci.*, 33 (2005) 574- 575.
[5] K. Hensel et al.: Electrical and Optical Properties of AC Microdischarges in Porous Ceramics, *10th Symposium on HP LT Plasma Chemistry HAKONE X*, Saga, Japan, September 4-8 (2006) 277-283.

P 48

RBS, XPS and AFM Study of Ag Thin Films and Polyethylene Foils Interface Modified by Plasma Treatment

A. Macková[1,3], V. Švorčík[2], Z. Strýhal[3], J. Pavlík[3],P. Malinský[3]

[1]Nuclear Physics Institute, Academy of Sciences of the Czech Republic, 250 68, Řež near Prague, Czech Republic
[2]Department of Solid State Engineering, Institute of Chemical Technology, Technická 5,166 28, Prague, Czech Republic
[3] Department of Physics, Faculty of Science, J. E. Purkynie-University, České mládeže 8, 400 96, Ústí nad Labem, Czech Republic
[4] Institute of Macromolecular Chemistry, Academy of Sciences of the Czech Republic, Heyrovského nám.2, Praha 6, Czech Republic

Abstract

In this study, the effect of plasma treatment and annealing on the diffusion of Ag in low and high-density polyethylene (LDPE and HDPE, respectively) is examined.

Introduction

Metal-polymer system prepared by metal penetration from thin metallic layers deposited on the polymer surface at increased temperature is studied. These structures find application as components e.g. of humidity sensors and optical switches [1]. For example in microelectronics this metallized films form basic structures for construction of diodes with negative differential resistance and light-emitting [2], polymer based diodes in optoelectronics. The complex processes induced by plasma treatment and annealing which take place on metal/polymer interface (metal atom diffusion, metal cluster formation and their mobility at metal/polymer interface) are far from being understood.

Experimental

Metal layers were deposited onto 50μm thick LDPE and HDPE (T_m= 115^{0}C and T_m= 137^{0}C, respectively) supplied by Goodfellow, Ltd. The Ag was deposited by diode sputtering on a BAL-TEC, SCD 050 device. The typical deposition parameters were: room deposition temperature, deposition time 65 s, total argon pressure about 4 Pa, electrode distance of 50 mm and current of 20 mA [2]. Plasma treatment and annealing were performed simultaneously in the chamber for plasma surface modification of thin film [3]. The RF discharge (13.56 MHz) was applied in "pure" argon. The sample was held on the plasma floating potential during the plasma treatment. The in situ mounted quartz lamp (20 W) in a polished stainless steel reflector was used for indirect heating of the sample holder. We obtained concentration depth profiles of the metal atoms from the RBS spectra. The beam of 2.68 MeV He^+ ions from Van de Graaf accelerator was used for RBS analysis measured at 170° laboratory scattering angle. An Omicron Nanotechnology ESCAProbeP spectrometer was used to measure the X-ray photoelectron spectra (XPS). The X-ray source was monochromated at 1486.7 eV. The exposed and analyzed area had dimensions of 2x3 mm^2. The spectra were measured stepwise with a step in binding energy of 0.05 eV.

Results and Conclusions

The data on annealing conditions and plasma treatment are summarized in Table 1. AFM roughness parameter (R_q), the diffusion coefficients and Ag integral amount extracted from RBS analysis of concentration profiles are presented. Table 1 contents the integral amount of Ag and atomic fraction of Ag determined from XPS analysis after plasma treatment. The diffusion coefficients are higher for Ag in HDPE comparing to LDPE. We observed a significant decline of the Ag integral amount with the increasing substrate temperature in Ar plasma and these results are in agreement with measurement of the metal surface fraction at Ag/LDPE. Ag surface fraction at Ag/HDPE exhibits no significant changes after plasma exposure comparing to Ag integral amount. It can be connected with the fact, that Ar plasma causes degradation of Ag and HDPE substrate also. It was studied before, that HDPE exhibits higher roughness and removal rate under Ar plasma treatment comparing to LDPE [4]. AFM analysis shows tendency to create bigger objects on the Ag/LDPE surface at lower temperatures and the higher plasma power. Ar plasma treatment at the increased temperature should support smaller metal cluster formation (see Figure 1). XPS measurement reflects the dramatic changes in the Ag/polymer surface composition. XPS measurement of Ag (core level 3d5/2) includes Ag^+ in Ag_2O (367.2 eV), Ag^0 (368.3 eV). After Ar plasma treatment (10W) at 55°C the Ag^0 is prevailing in Ag/LDPE. The third component (maximum at 369.0 eV) appears after Ar plasma treatment (10W) in case of Ag/LDPE and after plasma treatment (20W) in case of Ag/HDPE. It can be interpreted like

Ag bonded on the organic structure (Ag-C) or result of differential charging caused by Ag clusters and possible degradation of PE surface [4]. The degradation was verified from results of the C1s and O1s XPS spectra.

Plasma gas /substrate	Annealing time [min]	Temperature of substrate [°C]	Performance of plasma [W]	Coefficient of diffusion [cm^2s^{-1}]	Rq [nm]	Ag amount RBS [$10^{15}at/cm^2$]	Ag fraction XPS [atomic %]
LDPE	0	0	0	0	13,7	23,2	14,4
Ar / LDPE	20	55	10	2,44E-14	20,3	22,5	28,1
Ar / LDPE	20	65	20	2,76E-14	27,0	22,1	23,5
Ar /LDPE	20	95	10	4,66E-14	19,4	11,5	8,5
HDPE	0	0	0	0	∘	26,8	15,7
Ar / HDPE	20	55	10	5,05E-14	°	16,3	14,2
Ar / HDPE	20	65	20	5,54E-14	°	21,7	14,0
Ar / HDPE	20	95	10	6,78E-14	°	14,6	13,5

Table 1 (a) Summary of the plasma treatment conditions, diffusion coefficients and surface roughness parameter **(b)** Integral amount of metal determined using RBS and surface concentration of deposited metals determined using XPS.

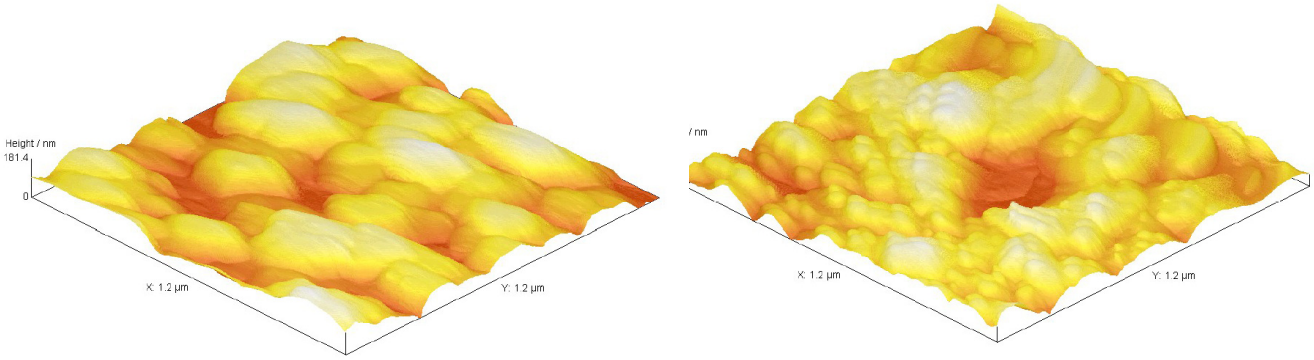

Figure 1: AFM measurement of Ag/LDPE sample after Ar plasma treatment 20 min at 55°C (left) Rq=20,3 nm and after Ar plasma treatment 20 min at 95°C (right) Rq=27 nm.

The penetration of Ag particles from metal layers deposited using a diode-sputtering technique on LDPE and HDPE substrate was studied under different plasma treatment conditions and simultaneous substrate heating. The type of polymer substrate (roughness of polymer substrate, removal rate in Ar plasma) influences Ag particles mobility at metal/polymer interface under plasma treatment. Diffusion coefficients Ag in LDPE and HDPE are higher comparing to PET polymer diffusion coefficients published in our previous paper [5].

This work was supported by the Ministry of Education of the CR under Research Programme LC 06041.

References:

[1] A. Stutzmann, T. A. Tervoort, K. Bastiaansen, P. Smith, *Nature*, (2000) 407613.

[2] V. Švorčík, J. Zehentner, V. Rybka, P. Slepička, V. Hnatowicz, *Appl Phys A,* 75 (2002) pp. 41-544.

[3] Z. Strýhal, J. Pavlík, S. Novák, A. Macková, V. Peřina, K. Veltruská, *Vacuum* 67 (2002) pp. 665-671.

[4] V. Švorčík, K. Kolářová., P. Slepička, A. Macková, M. Novotná, V. Hnatowicz, *Polymer Degradation and Stability*, 91 (2006) pp. 1219-1225.

[5] A. Macková, V. Švorčík, Z. Strýhal, J. Pavlík, *Surface and Interface Analysis*, 38 (2006) pp. 335-338.

P 49

Structure and Relative Stability of Beryllium Hydrides Be_nH_m (n=2-6, m=1-7)

P. Mach[1], J. Urban[1], M. Probst[2] , L. Horny[3]

[1]Department of Nuclear Physics and Biophysics, Faculty of Mathematics, Physics and Informatics, Comenius University, Mlynská dolina, 842 45 Bratislava, Slovakia

[2]Institute fuer Ionenphysik und Angewandte Physik, Universitaet Innsbruck, Technikerstr. 25, 6020 Innsbruck, Austria

[3]ETH Zurich , Lab. fur Phys. Chemie, Wolfgang-Pauli-Str. 10, 8093 Zurich, Switzerland

e-mail: mach@fmph.uniba.sk

Abstract

Quantum chemical calculations of the structure of beryllium hydrogen clusters of various stechiometric formulae have been performed. The influence of the number of beryllium atoms as well as number of hydrogens in the cluster on the relative stability of clusters has been calculated. Finally the ionization potentials of neutral clusters have been obtained by using of OVGF method.

Introduction

Beryllium metal has properties that make it technologically very attractive, but these advantages are severely counterbalanced by the high toxicity of inhaled beryllium dust. Just the toxicity of beryllium compounds gives the chance for investigation of beryllium containing molecules at the theoretical level. Atomic beryllium clusters have been studied at the MP4 level of the theory to obtain the structure and ionization potentials [1,2]. Accuracy and effectiveness of MP2 and CCSD(T) methods has been tested at the binding energy of these metal clusters [3]. Theoretical methods [4,5] were also applied to the description of electronic structure of beryllium atom. Significant amount of interest has been also devoted to molecular BeH_2 as the testing tool for quantum chemical methods. Hantsch et al. [6] studied at the DFT level the possible structures of this molecule with the effort to find the most stable modification. Wang et al. [7] by using of DFT with BLYP gradient correction studied structural and electronic properties of beryllium clusters up to 21 atoms. Their calculations reduced the overestimations of the binding energy and gave a look on the transitions to metalic binding. Kolchin and Hall applied the DFT and LDA to the determination of the structure of neutral and single ionized beryllium clusters. Up to now the study dealing the structure of hydrogen containing beryllium clusters has not been reported.

Results and discussion

The standard quantum chemical calculations at the MP2 level of the theory have been applied for the search of the structure of beryllium hydrogen clusters. We have used the basis set of the 6-31++G(2df,2pd) quality. Some calculations have been performed also at the DFT level of the theory. Coming out from the determined structure of beryllium clusters the structures with added hydrogen atoms were optimized. The influence of the increasing on the binding energies has been calculated. All results will be summarized and discussed.

Conclusions

The following conclusions result from the calculations:

-- - 6-311++G basis set is suitable for the determination of the structure of clusters
-- - DFT methods overestimate bond energy for this kind of clusters
-- - Trends in calculated IPare discussed**.**

References

[1] P.V. Sudhakar and K. Lamertsma, J. Chem. Phys. 99 (1993) 7929
[2] N.V. Dobrodey, A.I. Streltsov and L.S. Cederbaum, Phys. Review A, 65, 023203 (2002)
[3] J.S. Lee, Phys. Review A, 68, 043201 (2003)
[4] K. Peirs, D. Van Neck and M. Waroquier, Int. J. Quant. Chem. 91 (2003) 113
[5] S. Hirata, S. Ivanov, I. Grabowski and R.J. Bartlett, J. Chem. Phys. 116 (2002) 6468
[6] U. Hantsch, B. Winkler and V. Milman, Chem. Phys. Letters 378 (2003) 343
[7] J. Wang, G. Wang and J. Zhao, J.Phys.:Condens. Matter 13 (2001) L753-758
[8] A.M. Kolchin and R.W.Hall, J.Chem. Phys. 113(2000) 4083

P 50

Theoretical Study of Beryllium Hydrides BeH, BeH_2 (Performance Test of Various Theoretical Methods)

P. Mach[1], J. Urban[1], J. Noga[2]

[1]Department of Nuclear Physics and Biophysics, Faculty of Mathematics, Physics and Informatics, Comenius University, Mlynská dolina, 842 45 Bratislava, Slovakia

[2]Department of Physical and Theoretical Chemistry, Faculty of Natural sciences, Comenius University, Mlynská dolina, 842 15 Bratislava, Slovakia

e-mail: mach@fmph.uniba.sk

Abstract

On the basis of quantum chemical calculations systematic test of the performance of different quantum chemical methods has been performed. Starting with very cheap DFT up to the sophisticated R12 CCSD(T) method. The obtained results have been compared against the benchmark calculations.

Introduction

The simplest beryllium hydrides BeH and BeH_2 attract theoretical approaches in the study of the structure and properties. Both molecules serve also as the appropriate model and benchmark for the test of many new quantum chemical approaches to the study of the electronic and geometric characteristics. The development of new technology in the ITER project shifts the chemistry of the Be containing compounds (e.g. beryllium hydrides) into the forefront of the interest. Therefore from the point of view of the theory there is a need for the good description of the Be-H bond. It is necessary for the study of larger beryllium and hydrogen containing systems for which only less precise methods can be applied. Among many theoretical contributions the papers [1-3] give the best results concerning to the simplest beryllium hydrides. Penotti's [1] nonorthogonal single and MC calculations (highly optimized even-tempered STO basis set) of BeH_2 molecule yielded R_e=1.329Å ($D_{\infty h}$ geometry) and symmetric-stretch harmonic frequency (2053 cm^{-1}).

Martin's [3] contribution to the study of BeH systeme serves as a benchmark ab initio study (1-particle basis set calibration up to the spdfgh quality, n-particle calibration against full CI and treatment of inner shell correlation) (R_e=1.3411Å, ω_e=2062.119 cm^{-1}, $\omega_e x_e$ = 36.938 cm^{-1}). The experimental results are connected with the measuring of IR emission spectra by Bernath [4-6], BeH (R_e= 1.3424 A, ω_e= 2061.416 cm^{-1}), BeH_2 (R_e= 1.3264Å, ω_e= 2178.866 cm^{-1}, assymm.-strech)

Results and discussion

We have performed CCSD(T)-R12 explicitly correlated calculations for BeH_2 and BeH with using of basis sets for Be (19s14p8d6f4g) from the paper [7] and for H (9s,6p,4d,3f) from the paper [8] The CCSD(T) and MP2 calculations have been done in (aug)-cc-pvXZ series of basis sets. These basis sets were also augmented with core-correlation functions. Exponents for these functions for Be were extrapolated from those for B,C, and N (as a quadratic function of respective atom electronegativity).

The results obtained by DFT methods were obtained by using of B3LYP, B1LYP, B3PW91 and HCTH functionals both with cc-bases and 6-31++G(a,b) bases (a,b means different combinations of beryllium and hydrogen polarization functions). All results will be summarized and discussed.

Conclusions

The following conclusions result from the calculations:

-Core correlation functions seem to be important even for qualitative description; most sensitive are large (Roos's ANO, Ahlrichs's TZP)

-Extrapolated core functions work well

-6-311++G basis set yields acceptable results if merged with large number of diffuse functions (3d2f,3p2d)

-DFT methods are generally less sensitive to the basis sets. Inclusion of correlated functions has a minimal effect, much larger effect has a choice of functional. DFT generally overestimate bond energy of Be-H bonds.

References

[1] F. E. Penotti, Int. J. Quantum Chem. 106 (2006) 1153J
[2] R.A. Klein and M.A.Zottola, Chem. Phys. Letters 419 (2006) 254
[3] J.M.L. Martin, Chem. Phys. Letters 283 (1998) 283.
[4] P.F. Bernath, A. Shayesteh, K. Tereszchuk and R. Colin, Science 297 (2002) 1323.
[5] A. Shayesteh, K. Tereszchuk, P.F. Bernath and R. Colin, J. Chem. Phys. 118 (2003) 3622.
[6] A. Shayesteh, K. Tereszchuk, P.F. Bernath and R. Colin, J. Chem. Phys. 118 (2003) 1158.
[7] S. Kedzuch, J. Noga and P. Valiron, Mol. Phys., 103, 999-1005(2005)
[8] J. Noga, P. Valiron, Collect. Czech. Chem. Commun. 68, 340, (2003)

P 51

Can a Strongly Emitting Probe Be Used in a Low Temperature Plasma?

A. Marek[1], R. P. Apetrei[2], I. Picková[1], P. Kudrna[1], M. Tichý[1], R. Schrittwieser[3], C. Ionita[3]

[1] Faculty of Mathematics and Physics, Charles University in Prague, V Holešovičkách 2, 180 00, Prague, Czech Republic

[2] Faculty of Physics, Al. I. Cuza University, 11 Carol I Blvd., RO-700506, Iaşi, Romania

[3] Institute for Ion Physics and Applied Physics, Leopold–Franzens University of Innsbruck, Technikerstr. 25, A-6020 Innsbruck, Austria

e-mail: Ales.Marek@mff.cuni.cz

Abstract

In this contribution an experimental and theoretical study is presented on the overestimation of the plasma potential by the strongly electron-emitting probe in a low-temperature plasma which gives rise to discussions of the usability of this technique in a low-temperature plasma.

Introduction

Emissive probes are used as a suitable experimental tool for determining the plasma potential in many types of plasmas ranging from hot isothermal plasma [1,2] through low-temperature and low-pressure applications [3,4] to dense plasma [5]. Two base techniques for the plasma potential determination by the emissive probe are used – the strongly emitting probe technique and the limit of zero-emission technique. In our contribution we will focus on the strongly emitting probe technique and particularly on its applicability in a low-temperature plasma. The great advantage of this technique is that it enables direct measurements of the plasma potential and its fluctuations. It is relatively well known that the plasma potential, as determined by the strongly emitting probe technique is underestimated by approximately one kT_e/e if the temperature of emitted electrons T_{eW} can be neglected in comparison to the electron temperature T_e ($T_{eW} << T_e$), see e.g. [6]. The situation is different in low-temperature plasmas where the plasma potential, determined by a strongly emitting probe can even be overestimated, as it was observed e.g. in [7].

Results and discussion

We performed our experiments in a weakly-magnetized low-temperature argon plasma of a dc discharge in a cylindrical magnetron device [8]. Typical plasma parameters in this device are: plasma density $n_e = 10^{16}$ m^{-3}, electron temperature $T_e = 0.5$ eV and ion temperature $T_i = 300$ K at 4 Pa working argon gas pressure. The magnetic field was 20 mT. The emissive probe construction and the data acquisition technique are described in [8]. An example of the dependence of the floating potential of the emissive probe on the

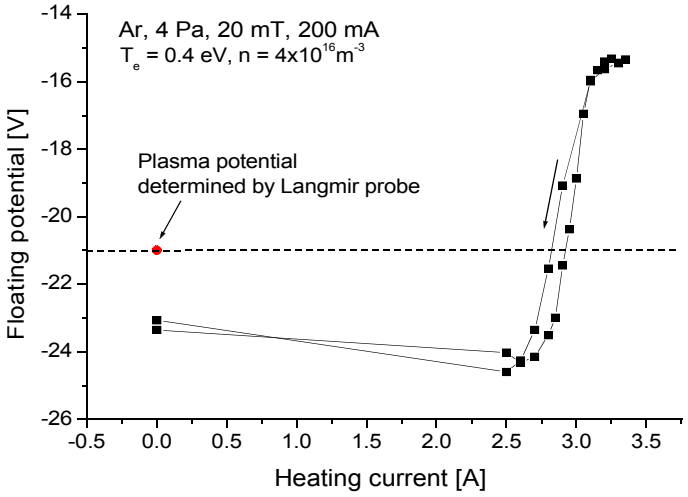

Fig 1: An example of the dependence of the floating potential of emissive probe on the probe heating current.

probe heating is shown in figure 1. It is clearly seen that the saturation value of the floating potential, which should indicate the plasma potential, rised markedly above the value determined by the Langmuir probe. In case of tungsten probes with 0.14 mm wire diameter the plasma potential overestimation was in the range of

4.1 – 6.6 V (data from 9 probe specimens) giving 5.13 V on the average. An explanation of the overestimation of the plasma potential can be found in [9]. The results of this theory, if applied to floating probe conditions (when the net current flowing through the probe should be zero), are given in figures 2 and 3.

The overestimation of the plasma potential determined by this model was found to be maximally 6 kT_e/e at our conditions and highest reachable T_{eW} (see figure 3). This is less than in our measurements, however, considering that the theory assumes an infinitely large emitting plate (in contrast to the cylindrical geometry

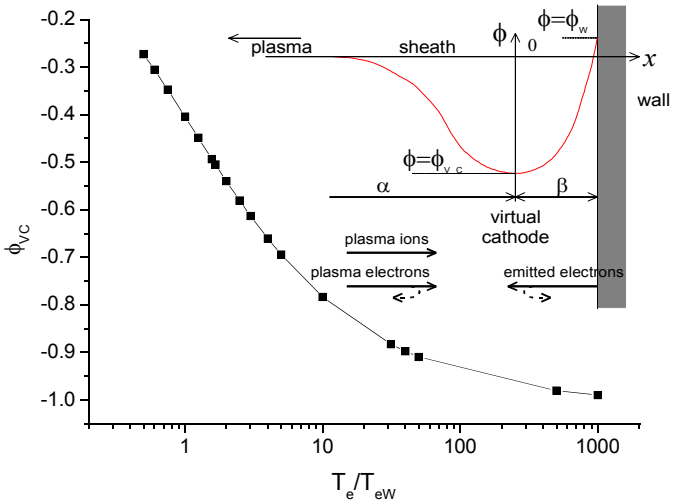

Fig. 2: Difference of normalized potential ($\phi=e\varphi/kT_e$) at the virtual cathode and the plasma potential in dependence on temperature of emitted electrons T_{eW} and schematics

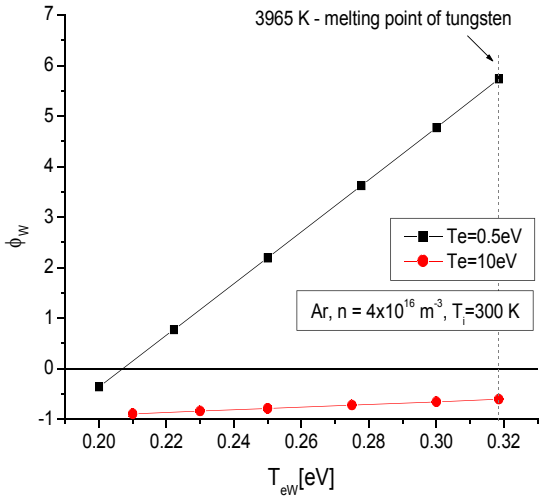

Fig. 3: Computed potential on the probe surface in dependence on increasing probe heating for two different temperatures of

of the probe) and considering the experimental error in determining the electron temperature from the second derivative of the electron retarding part of the Langmuir probe characteristic, which is very sensitive to noise, the difference between both results is acceptable.

Conclusions

The plasma potential determined by the strongly emitting probe, which depends on the plasma density and on the ratio T_e/T_{eW}, can be overestimated in a low temperature plasma. This should be taken into account if operating with a strongly emitting probe in low temperature plasma. An alternative is the limit of zero-emission technique, which is not so perturbing for the plasma and which can even be used in non-quasi neutral plasma, in sheaths in the vicinity of electrodes and even for the determination of the space potential in vacuum. However, plasma potential determination is not direct by this technique and cannot be therefore used e.g. for the study of the plasma potential fluctuations.

References

[1] P. Balan, R. Schrittwieser, C. Ionită, J. A. Cabral, H. F. C. Figueiredo, H. Fernandes, C. Varandas, J. Adámek, M. Hron, J. Stöckel, E. Martines, M. Tichý, G. Van Oost, Rev.Sci.Instrum., 74 (2003) 1583.

[2] R. Schrittwieser, C. Ionită, P. C. Balan, J. A. Cabral, F. H. Figueiredo, V. Pohoată, C. Varandas, Contrib. Plasma Phys., 41 (2001) 494.

[3] E. H. Wilson, J. Jeong, N. Hershkowitz, Rev. Sci. Instrum., 73 (2002) 2033.

[4] J. W. Bradley, S. K. Karkari, A. Vetushka, Plasma Sources Sci. Technol., 13 (2004) 189.

[5] S. Yan, H. Kamal, J. Amundson, N. Hershkowitz, Rev. Sci. Instrum., 67 (1996) 4130.

[6] M. Y. Ye, S. Takamura, Phys. Plasmas, 7 (2000) 3457.

[7] S. Ishiguro, N. Sato, Phys. Fluids B, 5 (1993) 4237.

[8] A. Marek, I. Picková, P. Kudrna, M. Tichý, R. P. Apetrei, S. B. Olenici, R. Gstrein, R. Schrittwieser, I. C. Ionită, Czech. Jour. Phys., Suppl. B, 56 (2006) B932.

[9] S. Takamura, N. Ohno, M. Y. Ye, T. Kuwabara, Contrib. Plasma Phys., 44 (2004) 126.

P 52

Electron Induced Chemical Reactions in Trifluoroacetic Acid

I. Martin[1], J. Langer[1], G. Karwasz[2], M. Orzol[1], M. Bertin[3], A. Lafosse[3], R. Azria[3] and E. Illenberger[1]

[1] *Institut für Chemie und Biochemie – Physikalische und Theoretische Chemie, Freie Universität Berlin, Takustr.3, D-14195 Berlin, Germany*

[2]*Institute of Physics, University of Torun, ul. Gagarina 11, 87-100 Torun, Poland*

[3]*Laboratoire des Collisions Atomiques et Moléculaires, CNRS-Université Paris-Sud (UMR 8625, FR LUMAT), Bât. 351, Université Paris Sud, F-91405 Orsay Cedex, France*

e-mail: martin@chemie.fu-berlin.de

Recently simple organic acids like formic acid[1,2,3,4] and acetic acid[5] have intensively been studied with respect to low energy electron interaction. Already the simplest organic acid formic acid (HCOOH) is remarkably sensitive in that interesting chemical reactions can be triggered by subexcitation-electrons (≈ 1 eV).

In this contribution we will present an overview of the results on electron interaction with trifluoroacetic acid at different states of aggregation.

Dissociative electron attachment to single molecules of the acid leads to the formation of various fragments via a low lying shape resonance around 1 eV and a core excited resonance around 7 eV[6]. The two products detected with the highest intensity are CF_3COO^- formed by dehydrogenation and CF_2COO^- produced by the loss of HF.

Going to molecular clusters of trifluoroacetic acid[7] dehydrogenation is still operative, shown in the production of the complexes $M_n \cdot (M\text{-}H)^-$. The loss of HF can be detected as well but only in weak intensity. The most efficient process is now the formation of the complex $CF_3COO^- \cdot H_2O$ at an electron energy below 1 eV via an intracluster chemical reaction. Furthermore the trifluoroacetic acid anhydride anion $((CF_3CO)_2O)^-$ was found which can be formed by condensation of two single acid molecules. In clusters energy dissipation is very effective and intact molecular anions M_n^- are generated by evaporative electron attachment.

Considering the electron induced reactivity in molecular films of CF_3COOH, two different processes could be identified by means of HREELS (High Resolution Electron Energy Loss Spectroscopy): (1) A non-resonant process with a threshold around 11 eV leading mainly to the formation of CO_2[8], and (2) a resonant process at an electron energy around 1 eV leading as well to the production of CO_2 and moreover to the formation of H_2O, which is comparable to the results obtained in the cluster experiment.

References

[1] A. Pelc, W. Sailer, P. Scheier, M. Probst, N. J. Mason, E. Illenberger, T. D. Märk *Chem. Phys. Lett.* **361** (2002), 277

[2] V. S. Prabhudesai, D. Nandi, A. H. Kelkar, R. Parajuli, E. Krishnakumar *Chem. Phys. Lett.* **405** (2005), 172

[3] I. Martin, T. Skalicky, J. Langer, H. Abdoul-Carime, G. Karwasz, E. Illenberger, M. Stano, S. Matejcik *Phys. Chem. Chem. Phys.* **7** (2005), 2212

[4] T. Sedlacko, R. Balog, A. Lafosse, M. Stano, S. Matejcik, R. Azria, E. Illenberger *Phys. Chem. Chem. Phys.* **7** (2005), 1277

[5] W. Sailer, A. Pelc, M. Probst, J. Limtrakul, P.Scheier, E. Illenberger, T. D. Märk *Chem. Phys. Lett.* **378** (2003), 250

[6] J. Langer, M. Stano, S. Gohlke, V. Foltin, S. Matejcik, E. Illenberger *Chem. Phys. Lett.* **419** (2006), 228

[7] J. Langer, I. Martin, G. Karwasz, E. Illenberger *Int. J. Mass Spec.* **249/250** (2006), 477

[8] M. Orzol, T. Sedlacko, R. Balog, J. Langer, G. Karwasz, E. Illenberger, A. Lafosse, M. Bertin, A. Domaracka, R. Azria *Int. J. Mass Spec.* **254** (2006), 63

P 53

Numerical Simulation of Trochoidal Electron Monochromator

J. Matúška, D. Kubala, and Š. Matejčík,

Department of Plasma Physics, Comenius University, Mlynská dolina, Bratislava 842 45, Slovakia
e-mail: matuska@neon.dpp.fmph.uniba.sk

Abstract

The numerical simulation of the trochoidal electron monochromator (TEM) has been carried out. The electron energy distribution function of the TEM have been studied as a function of the acceleration voltage of the electrons,. Moreover, the influence of the deflection voltage and the geometry of TEM on the width of the electron energy distribution function have been studied for variable aperture displacement.

Introduction

Many experimental studies concerning electron interaction with the molecules require electron beams with well defined and narrow energy distribution function. It can be formed with the help of electron monochromators.

There exist several types of electron monochromator, which is based on different physical principles. Most popular electrostatic monochromator has significant problem with electrostatic repulsion of the electrons on low energy. Solution of this problem is using the axial magnetic field, however the presence of the magnetic field is harmful for the operation of the electrostatic monochromator. Dispersive element is influence perpendicular homogenous electric and magnetic fields on electron.

In present paper, we discus the basic attributes of the TEM on the basis of numerical simulation of the TEM. Using the SIMION [1] program package detailed three dimensional numerical simulation of the electrostatic and magnetic fields in the TEM have been performed and trajectory calculations of the electrons with different initial conditions (energy, direction) have been carried out.

Results and discussion

The model of TEM consist of two parts, the electrode model and the model of the electron source. The electrode model is based on the geometry of the monochromator built at Comenius university [2]. The electron source was represented geometrically by a point. The kinetic energy distribution function of the emitted electrons from the source has a form of falling exponential function (thermoionic emission of the electrons). Two different angular distribution functions of the electrons have been studied, the simple model assumes isotropic angular distribution function of the electrons, the second model assumes angular distribution of the electrons according to the cosinus law:

$$I(\alpha) = I_0 \cos \alpha$$

where α is the angle between longitudinal axis of monochromator and actual velocity vector of electron, $I(\alpha)$ is the electron intensity into the angle α, I_O the relative electron intensity for the zero angle.

The trajectory calculations have been carried out for large number of the electrons with different initial parameters (velocity and angle). The number of the electrons which reach to the center of the collision chamber has been recorded and evaluated as a function of the initial conditions. The energy histogram obtained on this way corresponds to the transport function of the TEM for the electrons. The electron energy distribution function (EEDF) of the TEM have been obtained from the convolution of the EEDF of the source and from the transport function of the TEM by convolution of these two funcitions.

Present simulation has been carried out in order to evaluate three different effects in the EEDF of the electrons:

a) the effect of the acceleration potential of the electrons
b) the effect of the deflection potential
c) the effect of the geometry

The simulation of the effect of the acceleration potential of the electrons on the EEDF is presented in the Figure 1. The acceleration potential was varied in interval from 0 to 100 V. In the energy interval from 0 to 15 V the Full width at Half Maximum (FWHM) of the EEDF was practically constant. This result is particularly interesting as in this electron energy range the dissociative electron attachment reaction are measured. The variation of FWHM in this electron energy range was under 15 percent. In the electron

energy range up to 100 eV increase of the width of the EEDF up to 50% is predicted.

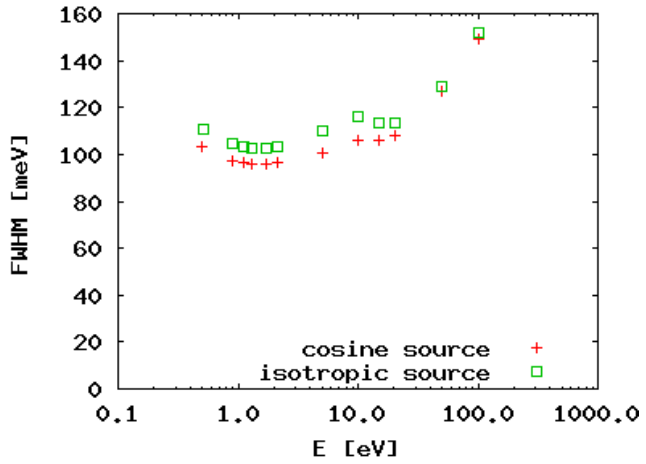

Fig. 1: dependence FWHM on energy of electrons

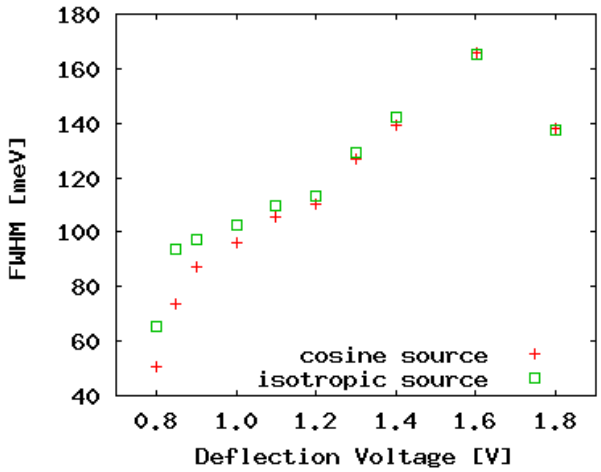

Fig. 2: dependence FWHM on deflection voltage, displacement of the apertures 2 mm

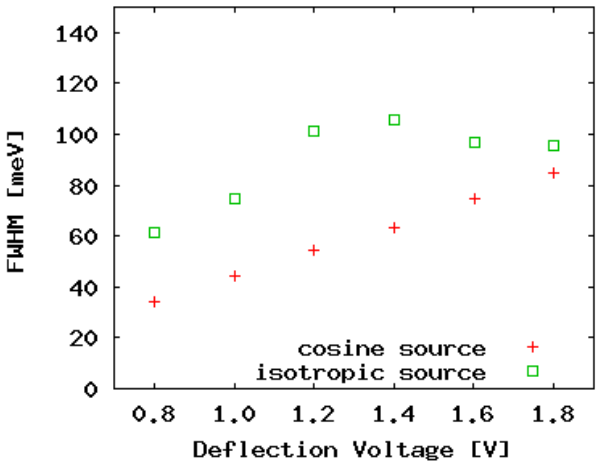

Fig.3: dependence FWHM on deflection voltage, displacement of the apertures 3 mm

The first paper about TEM [3] showed that the FWHM depends on deflection voltage. We have studied this dependence using the numerical simulation. The results are showed in Fig. 2 and Fig. 3.

Fig. 2 describes the dependence FWHM of the EEDF on deflection voltage for the TEM with the of axis displacement of the apertures 2 mm. The graph shows relatively small difference between the two models of the electron source. The major difference between the electron source models is the variation of the intensity of the electron emission with the azimuthal angle α. The transport function of TEM in this case do not pass electrons with high azimuthal angles of emission. This indicates an optimal mode of the operation of TEM. In the deflection voltage interval from 1.0 to 1.6 V linear dependence of the FWHM on the deflection voltage was observed. It indicates, according to papers[3], that major part of the increase of FWHM of EEDF is caused by the potential drop across entrance aperture of the selector. The Fig. 3 shows the dependence of the FWHM of EEDF for the TEM with of axis displacement of 3 mm. The figure shows that for this geometry the difference between two models of the electron source has been more relevant.

Acknowledgment

This work was supported by the Slovak Research and development agency, project Nr. APVT-20-007504.

References

[1] David A. Dahl, *Simion 3D version user`s manual*, Princeton Electronic Systems, Inc 1995
[2] S. Matejcik, V. Foltin, M. Stano, J.D. Skalny, *Int. J. Mass Spect.* 223-224 (2 0 0 3) 9
[3] A. Stamanovic and G. J. Schultz, *Rev. Sci. Instr.*, 41 (1970) .

P 54

Short Live Afterglow of Nitrogen Containing Oxygen Traces at Low Temperature

V. Mazánková, I. Soural, F. Krčma

Institute of Physical and Applied Chemistry, Faculty of Chemistry, Brno University of Technology, Purkyňova 118, Brno 612 00, Czech Republic
e-mail: krcma@fch.vutbr.cz

Abstract

The nitrogen short live afterglow was studied in DC flowing regime at wall temperature of liquid nitrogen as a function of oxygen traces concentration. The slight increase of populations of neutral nitrogen N_2 ($B\ ^3\Pi_g$) and N_2 ($C\ ^3\Pi_u$) states was observed more or less independently on the vibrational level, on the other hand the populations in molecular ion N_2^+ ($B\ ^2\Sigma_u^+$) state were strongly quenched by oxygen addition. The maximum of pink afterglow emission time was shifted to the later post-discharge times in the dependence on the electronic state. Besides the nitrogen molecular spectra, the spectrum of NO^β system was observed. Intensities of these bands increased with increase of decay time, as well as with the increase of oxygen concentration.

Introduction

The nitrogen afterglow kinetics is a really complicated problem that is a subject of many studies during the last 50 years. The mechanisms that populate various radiative states of neutral molecule as well as the molecular ion are different and many collisional quenching processes of specific states (in the ideal case vibrationally specified) must be included into the kinetic models. The first period of the afterglow is characterized by a strong decrease of the light emission but a few ms later, at about 5-8 ms, the strong light emission increase is observed. This effect is known as nitrogen pink afterglow. The traces of various species (for example carbon or oxygen) significantly change the kinetics and thus they have the influence on pink afterglow [1]. This study shows the influence of oxygen traces on the nitrogen pink afterglow at decreased wall temperature. The simplified kinetic model is given, too.

Experimental set up

An active discharge was created in a Pyrex discharge tube with a 120 mm electrode distance at pressure of 700 Pa and discharge current of 150 mA. The molybdenum hollow electrodes were placed in the side arms of the main discharge tube for minimizing their sputtering. Nitrogen was of 99.999 % purity and it was further cleaned by a copper based catalyzer and a LN_2 trap. Synthetic air (80 % N_2 + 20 % O_2) was used in the other input line to obtain the oxygen concentration in the discharge in the range 0 – 1900 ppm. The emitted spectra were measured by Jobin Yvon TRIAX 550 (1200 gr. mm^{-1}) spectrometer with CCD using the multimode quartz optical fiber movable along the discharge tube. Details of the experimental set up can be found in [2]. Vibrational populations at selected levels were calculated using all measured spectral band intensities in the range of 300 – 850 nm together with wavelengths and transition probabilities given by [3].

Results and discussion

The results can be divided into two groups. The first of them includes both neutral nitrogen radiative states, i.e. N_2 ($B\ ^3\Pi_g$) and N_2 ($C\ ^3\Pi_u$), the other one contains the molecular ion radiative N_2^+ ($B\ ^2\Sigma_u^+$) state. The populations at representative vibrational levels of both these groups are presented in Fig. 1 as a function of decay time at selected oxygen concentrations. The pink afterglow, i.e. the increase of populations with a maximum at about 12 ms, can be observed in both cases. This effect is less visible with the increase of the oxygen concentration in both cases but the vibrational populations show opposite dependences. The vibrational population in neutral molecule increases with the increase of the oxygen concentration while the population in molecular ion is strongly quenched by oxygen addition. The same effect is observed for all vibrational levels in both groups mentioned above with nearly the same quantity, so the vibrational distributions in all three studied nitrogen states are not significantly changed by oxygen presence.

Besides the spectra of nitrogen, the NO^β bands originating mainly at level NO ($B\ ^2\Pi$, v = 0) were observed. The intensities of these bands increase more or less linearly with the increase of decay time and it is directly proportional to the oxygen concentration. At the highest used oxygen concentration, the saturation effect of NO^β emission can be observed.

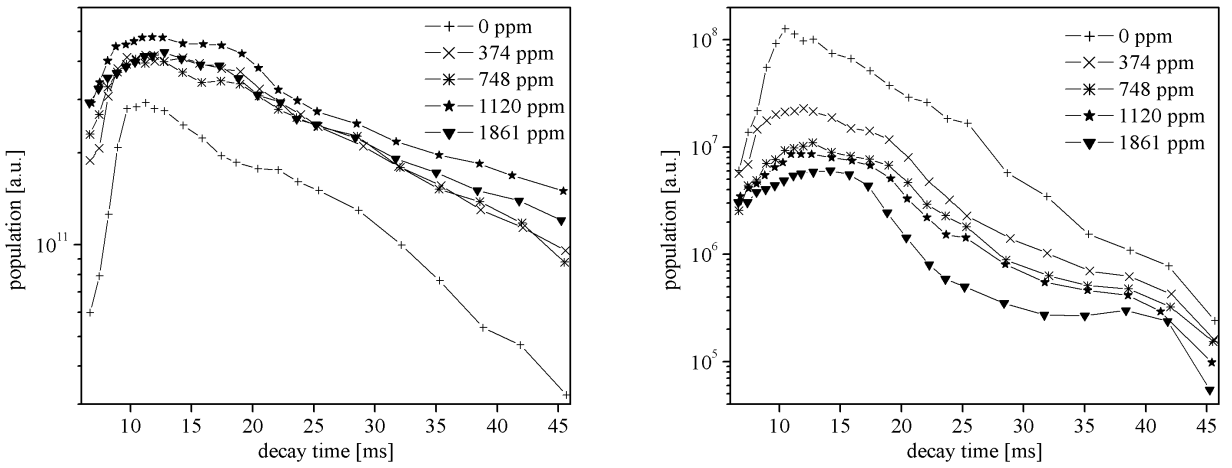

Fig. 1: An example of vibrational populations as a function of decay time at selected oxygen concentrations. Left: N_2 ($B\ ^3\Pi_g$, v = 2) level, right: N_2^+ ($B\ ^2\Sigma_u^+$, v = 0) level.

The maximal pink afterglow intensity as a function of oxygen concentration is given in Fig. 2. This figure clearly demonstrates strong quenching of nitrogen first negative system as well as the slight increase of both neutral molecule systems. The right part of this figure shows another interesting phenomenon, the shift of the maximum pink afterglow emission time to the later afterglow times. This effect is dependent on the spectral system and probably is connected with post-discharge kinetics that will be a subject of the future studies.

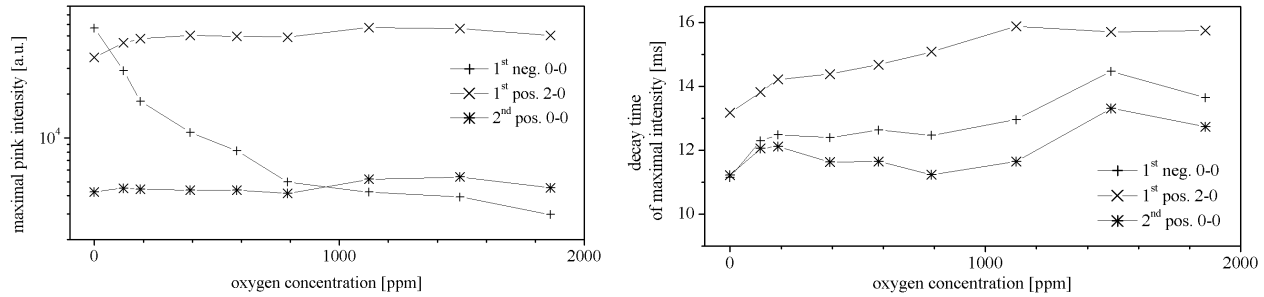

Fig. 2: Left: Maximal pink afterglow emission intensity as a function of oxygen concentration. Right: Position of the maximal pink afterglow emission intensity as a function of oxygen concentration.

Conclusions

The nitrogen short live afterglow was studied at wall temperature of liquid nitrogen in the dependence on oxygen traces concentration. The increase of populations of neutral nitrogen N_2 ($B\ ^3\Pi_g$) and N_2 ($C\ ^3\Pi_u$) states was observed more or less independently on the vibrational level, on the other hand the populations in molecular ion N_2^+ ($B\ ^2\Sigma_u^+$) state were decreased by oxygen addition. The maximum of pink afterglow emission time was shifted to the later post-discharge times in dependence on the electronic state. Besides the nitrogen molecular spectra, the spectrum of NO^β system was observed. Intensities of these bands increased with the increase of decay time as well as with the increase of the oxygen concentration. The kinetic processes will be a subject of future studies.

References

[1] F. Krčma, *Acta Phys. Slovaca*, 55 (2005) 453.
[2] F. Krčma, V. Mazánková, I. Soural, *Czech. J. Phys.*, 56 (2006) B871.
[3] F.R. Gilmore, R.R. Laher, P.J. Espy, *J. Phys. Chem. Ref. Data*, 21 (1992) 1005.

The work was supported by Czech Science Foundation, project No. 202/05/0111.

P 55

Kinetics of O(^{3}P) Species in Low-Pressure Microwave N_2-O_2 Afterglow

M. Mrázková, P. Vašina, V. Kudrle, A. Tálský

Department of Physical Electronics, Masaryk University, Kotlářská 2, Brno, 611 37, Czech Republic
e-mail: mmartina@mail.muni.cz

Abstract

In this paper, we focus our attention on concentration of O atoms in N_2-O_2 afterglow. A small amount of O_2 admixture is mixed into the main gas N_2, and in this gas mixture a microwave discharge is sustained. At a certain fixed distance from the discharge (30cm), we detect [O] as a function of the amount of O_2 admixture. In the previous paper [1] we observed an interesting behavior of O concentration when the amount of admixture is gradually increased. At the point where the measured concentration of N(^{4}S) is disappearing to zero, the concentration of O(^{3}P) starts to increase rapidly. As the effect has not been explained yet we investigated further to extend the knowledge about the kinetics of O in N_2-O_2 mixtures. The method used for detection of O(^{3}P) and N(^{4}S) was the electron paramagnetic resonance (EPR) and for NO_2(A) the optical emission spectroscopy (OES) by means of monochromator TRIAX 320 Jobin-Yvon with CCD detector.

Motivation

The N_2-O_2 discharges are used in sterilization[2,3], surface treatments and other practical applications. The chemical and plasma chemical processes, however, are still not fully understood. Such a mixture is a very complex system, containing and producing a very large number of active species, neutral and ionic molecules and atoms. There are some theoretical models[2] more or less describing only a major part of the plasma-chemical processes, however, for practical applications these models do not sufficiently cover all of the important mechanisms leading to production of the required species. Thus, still there is a need for a new experimental and theoretical studies.

Experimental set-up

The scheme of our apparatus is drafted in Fig. 1. The microwave discharge is sustained in a quartz tube of an inner diameter 13mm, by means of a surfatron cavity resonator. The surfatron is coupled to the magnetron power supply (2.45GHz), the incoming power to the resonator is about 20W. The gases are led from the gas bottles through the mass flow controllers and then mixed together and led through the LN_2 cold trap into the discharge tube surrounded by the surfatron. There the gas mixture becomes a plasma and it continues as the decaying plasma through the afterglow tube where the species can be detected by the JEOL JES-3B EPR spectrometer (X-band frequency region). The pressure is controlled independently from the flow rate by throttling the rotary pump. We are working in the low pressure ranges of about 80 to 800Pa. The cold trap is used to avoid of possible undesired impurities, such as H_2O and hydrocarbons.

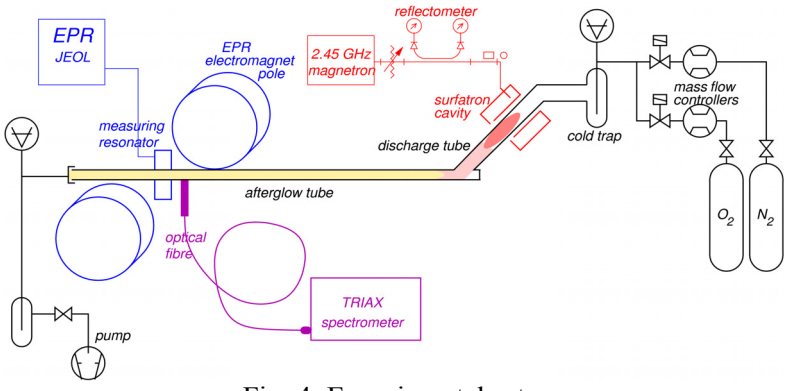

Fig. 4: Experimental set-up

Results and discussion

In the Fig. 2 and Fig. 3 there are measured concentration of N, O and $NO_2(A)$ in a semi-logarithmic scale versus added amount of O_2 for two different values of pressure. In both cases, there is a certain amount of O_2 admixture above which no N atoms were detected in the afterglow. We suppose that although the N is produced in the active discharge it is also quickly consumed by the very fast reaction N + NO --> N_2 + O.

The absence or presence of N atoms in the afterglow can be shown even without EPR. NO(B) is populated by reaction N + O + (M) --> NO(B) + (M) which produces excited NO(B) molecules. The non zero intensity of NO-beta system observed in the afterglow is a sign that both N and O atoms are present together. Similarly, simultaneous presence of O and NO in the afterglow is proved if the broad bands resulting from the de-excitation of $NO_2(A)$ are detected.

Assuming that our discharge produces a certain amount of N atoms and NO molecules, their mutual reaction causes that in the late afterglow only N or NO and only NO(B) or $NO_2(A)$ can be detected. The situation is very similar to titration process [4]. The moment where O starts to increase rapidly, corresponds well to the moment when N and NO(B) just disappear and $NO_2(A)$ appears. We suppose that in this moment the amount of NO produced by the active discharge exceeds the amount of N produced by the active discharge. Probably at this moment the subtle balance in the discharge is disturbed and plasma-chemical processes radically change.

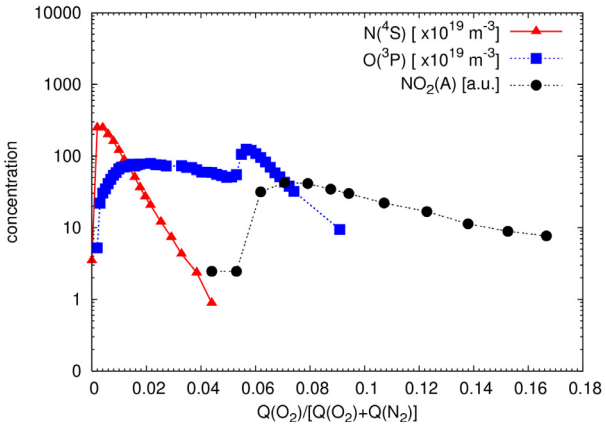

Fig. 5: High pressure (760Pa)

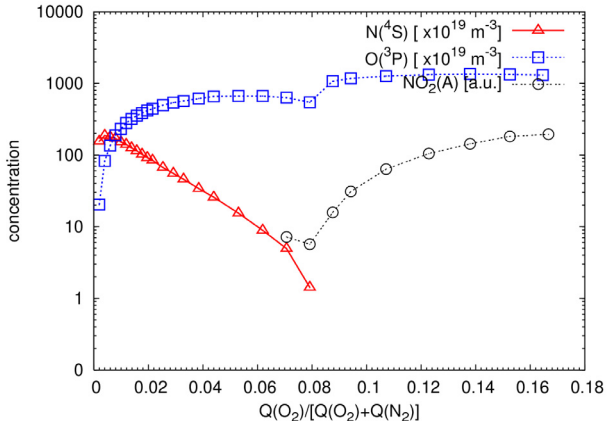

Fig. 6: Low pressure (260Pa)

In the case of the higher pressure (Fig.2), the point of sudden O increase is slightly closer to the lower percentages of admixture than in the case of lower pressure (Fig.3), however, it is always identical to the point of N disappearance. It is also evident that for the higher pressures the concentrations of O and $NO_2(A)$ with increasing O_2 admixture decrease (in measured range of percentages), while in the case of lower pressure, the O and $NO_2(A)$ concentration increases.

Conclusions

We have observed increase in O concentration connected with disappearing of N for various values of pressure. In the case of higher pressure (760Pa), the trend of concentration of O atoms (for low range of O_2 percentages) is more downward than in the case of the lower pressure.

Acknowlegment

This work was supported by Czech Science Foundation, project No.202/05/0111 and by Czech Ministry of Education, contract No. MSM 0021622411.

References

[1] P. Vašina et al., *Czechoslovak Journal of Physics,* Vol. 56 (2006), Suppl. B. B877-B881

[2] C.D. Pintassilgo et al., *J. Phys. D: Appl. Phys.* 38 No 3 (7 February 2005) 417-430.

[3] S. Villeger et al. *J. Phys. D: Appl. Phys.* 36 No 13 (7 July 2003) L60-L62.

[4] P. Vašina et al., *Plasma Sources Sci. Technol.* 13 No 4 (November 2004) 668-674.

P 56

Spatially Resolved Optical Diagnostics of Neon RF Discharge

Z. Navrátil[1, 2], D. Trunec[1], R. Šmíd[1], L. Lazar[1]

[1]Department of Physical Electronics, Faculty of Science, Masaryk University, Kotlářská 2, 611 37 Brno, Czech Republic
[2]Department of General Physics, Faculty of Science, Masaryk University, Kotlářská 2, 611 37 Brno, Czech Republic
e-mail: zdenek@physics.muni.cz

Abstract

Capacitively coupled RF discharge in neon (13.56 Mhz) was studied by spatially resolved optical emission spectroscopy and collisional-radiative model. Two discharge regimes at different pressures (10 and 80 Pa) were investigated. The measured intensities of prominent neon spectral lines in conjunction with the model were used to determine the electron temperature.

Introduction

Optical measurements in conjunction with collisional-radiative modelling represent an important way of plasma study. Using the elementary atomic data (cross sections, rate constants and transition probabilities) discharge emission of radiation over a large range conditions can be determined. These theoretical calculations, compared with the experimental data, may be used for investigation of elementary atomic data or for evaluation of the plasma parameters and processes playing role in the studied plasma.

A number of collisional-radiative models has been reported in literature [see e.g. 1-3]. In our previous work a method of determination of plasma parameters (reduced electric field strength *E/N* or electron temperature T_e) based on a collisional-radiative model was developed for neon discharge. Comparing measured spectra of the discharge with the spectra calculated by the model by least-squares method (Marquardt-Levenberg algorithm) the plasma parameters may be determined from the fit. We applied the model to the study of the positive column of low pressure DC glow discharge in order to check the possibilities and limitations of this method [4]. In [5] we investigated the electric field strength in the diffuse dielectric barrier discharge. In this paper we focused on the study of radio-frequency (RF) discharge in neon in order to extend further the applicability of our diagnostic method.

Experimental set-up

The experiments were carried out in a grounded stainless-steel vacuum chamber with inner diameter of 33 cm. In this chamber two horizontal stainless-steel, parallel plate circular electrodes with 8 cm in diameter, both movable in vertical direction, were placed 4 cm far from each other. The upper electrode (located at position 40 mm in the plots) was capacitively coupled to 13.56 MHz generator. The bottom electrode (located at position 0 mm in the plots) was grounded. The upper electrode was moreover surrounded by grounded shielding ring, which prevented the discharge from burning above the upper electrode to the walls. The chamber was filled with neon up to pressure of 10 or 80 Pa, respectively. The dicharge was sustained in flowing regime with gas flow of 10 or 30 sccm, respectively.

The optical emission spectroscopy measurements were carried out with Jobin Yvon TRIAX 550 spectrometer with CCD detector, cooled by liquid nitrogen. By moving both electrodes, while the discharge gap stayed fixed at 40 mm, the optical emission spectra in wavelength range 250 – 800 nm were measured at nine different positions over the discharge gap. The intensities of spectral lines were corrected for wavelength dependent instrument sensitivity by calibration of the device with standard Oriel tungsten halogen lamp.

Method

The collisional-radiative model being used in this paper was described in detail in [4]. However, instead of solving of Boltzmann kinetic equation for the electron distribution function in [4], Maxwell distribution was assumed in this paper as the first step. In the rate equations for concentrations of excited states various processes were taken into account (electron impact ionization of neon atoms in ground state and in metastable states, electron impact excitation and deexcitation of neon atoms, atom emission and absorption of radiation, metastable-metastable collisions, two-body and three-body collisions with neon ground state atoms, Penning ionization etc.). The system of ordinary differential equations was solved by fourth-order explicit Runge-Kutta method with adaptive step size. The calculated populations allowed to determine the optical emission spectrum.

Results and discussion

In Fig. 1 the optical emission spectra measured at two different pressures in wavelength range 580 – 760 nm are shown. The spectra measured at different positions were normalized according to the spectral line 640.2 nm. Obviously, the line ratios and spatial developments of both spectra were different. Whereas at 10 Pa the Ne line 585 nm is the highest line in the spectrum, at 80 Pa Ne line 640.2 dominates. This shows a significant presence of energetic electrons in the middle and close to the driven electrode at 10 Pa. Moreover, intensities of Ne line 585 nm at positions 20 mm (in the middle) and 32 mm are similar, but different from position 0 mm, whereas at 80 Pa the differences are not so considerable.

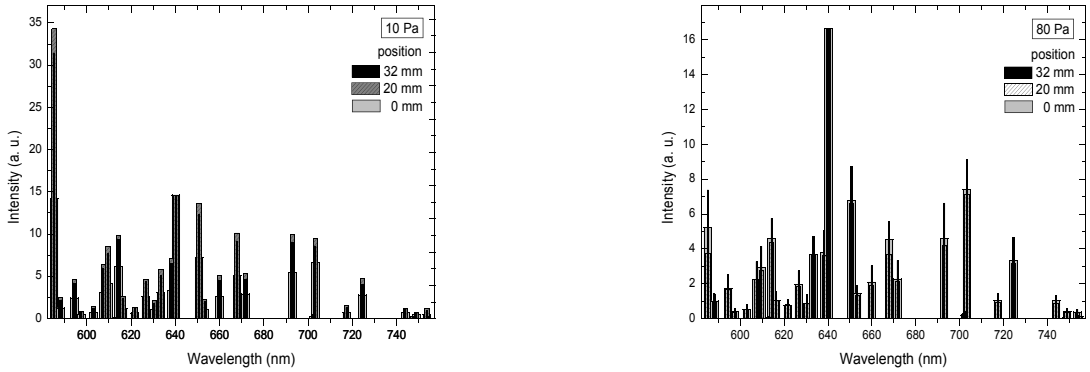

Fig. 1: Measured optical emission spectra of the neon discharge at 10 and 80 Pa at three different positions. In the plots only the spectral lines originating from the transitions between the $2p_i - 1s_i$ are shown.

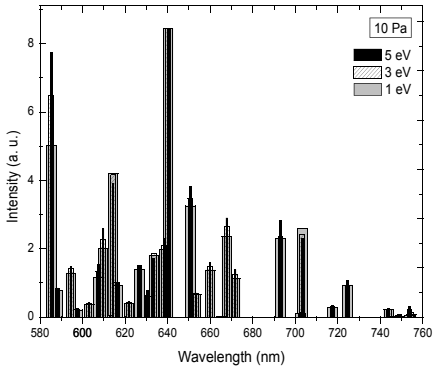

Fig. 2: Calculated optical emission spectra of neon discharge at 10 Pa for different electron temperatures. In the plots only the spectral lines originating from the transitions between the $2p_i - 1s_i$ are shown.

In Fig. 2 optical spectra calculated for discharge at 10 Pa and various electron temperatures are shown. The electron concentration was set to $4 \cdot 10^8$ cm^{-3} according to the probe measurements. The line ratios in the spectrum depended significantly on the electron temperature. Comparing the experimental and calculated spectra electron temperatures larger than 5eV may be expected in the discharge. These values may be found from the fits of the measured spectra.

Conclusions

In the model Maxwell distribution function was used to calculate the rate coefficients of electron collisions. In the following work a larger patience will be paid to the more accurate calculation of the distribution function.

References

[1] J. Vlček, *J. Phys. D: Appl. Phys.,* 22 (1989) 623.
[2] K. Kano *et al*, *Plasma Sources Sci. Technol.,* 9 (2000) 314.
[3] T. Bezanahary *et al*, *IEEE Trans. Plasma Sci.*, 31 (2003) 587.
[4] Z. Navrátil, D. Trunec, V. Hrachová, A. Kaňka, *J. Phys. D: Appl. Phys.,* 40, to be published.
[5] Z. Navrátil, D. Trunec, H.-E. Wagner, *Proceedings of HAKONE X* (2006) 71

P 57

Surface Modification of Wood Material Using Diffuse Coplanar Surface Barrier Discharge

M. Odrášková[1], J. Ráheľ[1,2], A. Zahoranová[1], M. Černák[1,2]

[1]Department of Experimental Physics, Faculty of Matematics, Physics and Informatics, Comenius University, Mlynská dolina F2, Bratislava 842 48, Slovakia

[2]Department of Physical Electronics, Faculty of Science, Masaryk University, Kotlářská 2, 611 37 Brno, Czech Republic

e-mail: cernak@gimmel.ip.fmph.uniba.sk

Abstract

Radial cuts of Pedunculate oak (*Quercus robur* L.) heartwood was activated by Coplanar Diffuse Surface Barrier Discharge (DCSBD) plasma. The plasma treatment resulted in a considerable increase of free surface energy and in the substantial reduction of 50 µl water droplet uptake time. Measurement of FTIR confirmed the formation of novel functional groups on the wood surface after the plasma treatment. The energy efficiency DCSBD plasma treatment is superior to the known volume dielectric barrier discharge treatment method.

Introduction

A main trend in the wood industry is increased bonding of wood products as a result of the use of more engineered wood products. For a bond to form, the adhesive must intimately encounter most of the wood substrate surface. Wetting is an important issue in the adhesive bond formation [1], since most wood adhesives are water-based. Even when, wood has a relatively polar surface that allows the general use of water-borne adhesives, although some woods are harder to wet. This is a particular problem for a wood surface, which was exposed to a high temperature drying [2]. In these cases a chemical treatment of the wood surface, that promotes wettability or provides new bonding sites, should improve adhesive bond performance.

Plasmas sustained at atmospheric pressure are commonly used to improve the wetting and adhesion properties of polymer materials, and have been tested also for the wood surface treatment. [3-6]. Although also low-pressure plasma processes have been studied for this purpose [7,8], atmospheric pressure processes are attractive for wood-industry applications because of their lower cost, higher throughput, and ability to operate in-line without vacuum systems.

To facilitate the high throughput and in-line operation it is desirable to enhance the concentrations of reactive species generated. This can be most conveniently approached by increasing the plasma volume power density, however without undesirable plasma filamentation and sparking. Additional requirements are low energy and equipment costs since cost efficiency is the driving force for process development in industrial chemistry.

In the present paper we report preliminary results on atmospheric-pressure plasma activation of solid wood obtained using a novel type of atmospheric-pressure plasmochemical reactor.

Results and discussion

Plasma treatment of wooden samples was done by the Diffuse Coplanar Surface Barrier Discharge (DCSBD) reactor [9]. The samples of Pedunculate oak (*Quercus robur* L.) heartwood with the dimensions of 50×15×5 mm were used during this experiment. The oak was chosen because of its known low surface energy (36.1 mJ/m^2) resulting in poor wettability by water. The surface was sanded by 150-grit before the surface energy measurement and by 100-grit before the uptake time measurement. After sanding the oak surface was blasted by air stream to remove attached dust. Plasma activation was done in air atmosphere with an average plasma power density 2 Watt/cm^2 and exposure time of 5 sec. The wood moisture content was within the range of 7-8% during whole experiment.

Table I shows the total free surface energy values and corresponding polar and dispersive parts for tested wood before and after the plasma treatment. As can be seen the total surface energy increased almost by 30 mJ/m3, mainly due to the rise of its polar part. Therefore a substantial improvement of wettability by water (as a polar liquid) is to be expected.

Tab. I Surface free energy for *Quercus robur* L. (radial section). Owens-Wendt two liquid model.

	Initial oak			Plasma treated oak		
	γ_s	γ_s^d	γ_s^p	γ_s	γ_s^d	γ_s^p
Testing liquids	[mJ/m^2]			[mJ/m^2]		
Water + Diiodomethane	40.71	39.56	1.15	74.26	45.40	28.86
Water + α-Bromonaphtalene	42.36	41.40	0.96	73.80	44.43	29.37

To verify this, we have accomplished a water uptake time measurement as described in [5], where authors employed volume dielectric barrier discharge in orders to improve the wettability of wood. A 50 µl water droplet was put on the oak surface and its uptake time was measured. The water uptake time was the time interval from the impact of the droplet to the complete penetration of the droplet in the wood surface (no optical reflection can be seen). Plasma treatment resulted in reducing the initial value of uptake time from 320 ± 94 sec to 25 ± 6 sec. The minimum observed uptake time (based on two 25 sample sets) was reduced from 114 sec to 15 sec.

Figure 1 shows a plane view of oak samples, 10 sec after the 50 µl water droplet was laid down on wood surface. As can be seen, water uptake occurs preferentially on the capillary surface of wood. This is an indication that plasma treatment modified the thin surface layer rather than bulk of wood.

The FTIR spectra analysis of oak surface confirmed the presence of polar functional groups after plasma activation. In the higher wavenumber region a marked growth of OH groups (3 600 – 3100 cm^{-1}) can be seen. Clear observable changes are in polar groups –C-O region (1320 cm^{-1}) and carbonyl region (1650 – 1700 cm^{-1}). This is in accordance with the observed increase of polar part of free surface energy.

Fig.1. Plane view on plasma treated (left) and untreated (right) oak samples.

Conclusions

Presented results of Pedunculate oak plasma activation demonstrated that the DCSBD plasma is an effective tool in enhancing the wood wettability. This is a necessary condition to promote a better adhesion with a water-based adhesives and coatings, which is currently being studied.

Comparing to the energy consumption of 0.1 kWh per m^2 for the volume barrier discharge surface declared in [5], our DCSBD system offers a considerably better efficiency, with the energy consumption of 0.03 kWh/m^2 of wood surface. In addition the involvement of planar plasma source in our case makes the quality of the plasma treatment completely independent on the thickness of wood material.

Acknowledgment

This work was financially supported by the Slovak Research and Development Agency, Project No. APVT-20-033004 "Study of atmospheric plasma surface treatment of solid wood materials "

References

[1] R. Charles, R. Frihart, *in Handbook of Wood Chemistry and Wood Composites*, Ed. R.M. Rowell, CRC Press, 215-278, Chap.9
[2] M. Sernek, F.A. Kamke, W.G. Glasser: *Holzforschung* 58 (2004)22-31
[3] I. Sakata, M. Morita et al., *J. Appl. Polym. Sci*. 49(1993)1251-1258
[4] Podgorski L., Chevet B et al., *International Journal of Adhesion and Adhesives* (2000) 103-11.
[5] P. Rehn, A. Wolkenhauer et al., *Surface and Coatings Technology* 174 –175 (2003) 515–518
[6] M. Mertens, A. Wolkenhauer, W. Viol, *Laser Physics Letters* 3 (2006) 380-384
[7] R. Mahlberg, H.E. M. Niemi et al., *Langmuir* 15 (1999) 2985-2992
[8] G.Q. Blantocas, H.J. Ramos, M. Wada, *Jap. J. Appl. Phys*. 45 (2006) 8498-8501
[9] M. Černák, D. Kováčik et al., *Proc. of 15th SAPP* (2005) pp. 139-140

P 58

The Differences between Direct and Indirect Method of Ozone Concentration Measurement

J. Országh[1], J. D. Skalný[1], N. J. Mason[2], V. Chernyak[3], I. Prisyazhnevich[3]

[1]Department of Experimental Physics, Faculty of Mathematics, Physics and Informatics, Comenius University, Mlynská dolina F-2, Bratislava

[2]Department of Physics and Astronomy, Open University, Milton Keynes, UK

[3]Radiophysics Faculty, Taras Shevchenko University, Kyiv, Ukraine

e-mail: juraj.orszagh@googlemail.com

In the experiments where ozone concentration is measured the results can be influenced by diagnostics technique. As the particular details of the experiments are often not specified in the paper the comparison of results produced by individual experiments can be problematic. In general there are two basic methods for ozone concentration measurement. The direct measurement (DM) is the technique when the O_3 concentration is measured directly in the discharge gap. The indirect measurement (IM) is technique when it is measured in the cell which inlet is connected with the outlet of the ozone generator tube by pipe. The aim of the present experiments was to compare these two methods.

In the paper [1] the negative corona discharge in carbon dioxide and its mixtures with oxygen were studied. Apart from other aims of the experiment, the ozone concentration at wide range of gas flow rates (3-300 cm^3/min) was compared. The ozone concentration was measured by IM and the dimensions of pipe were not specified in the paper. In such experiment the consideration of different ozone decomposition due to different flow rates would be useful. On the other hand there are possibilities for using the IM technique without influence upon results. In paper [2] the influence of IM is insignificant because of the same gas flow rate in individual measurements. So, the results of all the measurements contained the same error and results were not distorted. In another paper [3] the IM had insignificant effect because of very high gas flow rates. There are also other papers in which the authors used the DM technique. We have published such type of paper recently [4]. Despite the fact that the gas flow rate was low, the reliability of measurements is high. It is evident that in some cases the IM technique is reliable solution for ozone concentration measurement (high gas flow rates; short pipes). But in some experiments it is useful to prefer DM technique despite the fact that it is technically demanding. The aim of this paper is to compare these two methods and partially illustrate which one to choose for which experiment.

Ozone was generated by negative corona discharge fed by pure carbon dioxide. For DM method the reactor was placed directly into the UV spectrometer used for ozone concentration measurement. For IM the reactor was connected with the cell in the spectrometer by 1 m long Teflon pipe. The ozone concentration was found always to be higher in the case of DM. This effect is most likely caused by the decomposition of ozone by both heterogeneous (on the walls) and homogeneous (in the volume) processes in the Teflon pipe connecting the reactor and the glass cell placed in the spectrometer used for ozone concentration determination. The time needed for transport the gas from the reactor to the cell depends on the flow rate. For 5 cm^3/min it is approximately 20 minutes, for 10 cm^3/min it is 10 minutes, for 50 cm^3/min it is 2 minutes and for 100 cm^3/min it takes approximately 1 minute.

The ozone decomposition for IM in comparison to DM for different gas flow rates is shown in the table 1. The values shown in the second column were calculated as

$$\Delta = 100 - \frac{[O_3]_{IM}}{[O_3]_{DM}} \cdot 100 \qquad \{2\}$$

where $[O_3]_{IM}$ is ozone concentration measured by the IM technique and $[O_3]_{DM}$ is the ozone concentration measured by the DM technique. In the third column the difference in measured ozone concentration between IM and DM is shown.

$$\Delta_{abs} = [O_3]_{DM} - [O_3]_{IM} \qquad \{3\}$$

In the last column Δ_{abs} is divided by the time spent in the Teflon pipe according to the gas flow rate

$$\Delta_{abs/t} = \frac{[O_3]_{DM} - [O_3]_{IM}}{t} \qquad \{4\}$$

All the values shown in the table correspond to voltage 6.2 kV applied on the electrodes of discharge reactor used for ozone generation.

gas flow rate [cm³/min]	Δ	Δ_{abs} *[ppm]*	$\Delta_{abs/t}$ *[ppm/min]*
5	60%	40.9	2.05
10	60%	30.5	3.05
50	30%	5.5	2.75
100	25%	2.6	2.60

Tab. 1. Ozone concentration decrease in IM in comparison to DM.

From the values in the last column it is evident that O_3 decomposition rate is not dependent of the flow rate and initial concentration. The Reynolds number of the gas flow in the pipe is in the interval from 0.44 for gas flow rate 5 cm^3/min up to 8.8 for gas flow rate 100 cm^3/min. So the flow is strictly laminar for all gas flow rates.

In the discharge gap the processes responsible for ozone decomposition are

$$e + O_3 \rightarrow O^- + O_2 \qquad k_1 = 9 \text{ x } 10^{-12} \text{ cm}^3\text{s}^{-1} \text{ [5]} \qquad (1)$$

$$e + O_3 \rightarrow O_2^- + O \qquad k_2 = 3.78 \text{ x } 10^{-22} \text{ cm}^3\text{s}^{-1} \text{ [5]} \qquad (2)$$

$$e + O_3 \rightarrow O_2 + O + e \qquad k_3 = 5 \text{ x } 10^{-9} \text{ cm}^3\text{s}^{-1}. \text{ [5]} \qquad (3)$$

$$O(^3P) + O_3 \rightarrow O_2 + O_2 \qquad k_4 = 8.43 \text{ x } 10^{-14} \text{ cm}^3\text{s}^{-1} \text{ [5]} \qquad (4)$$

Apart from them homogenous processes are active both in the reactor and in the volume of the pipe

$$O_3 + O_2(^1\Delta_g) \rightarrow O_2 + O_2 + O \qquad k_5 = 4 \text{ x } 10^{-14} \text{ cm}^3\text{s}^{-1}. \text{ [5]} \qquad (5)$$

$$M + O_3 \rightarrow O + O_2 + M \qquad k_6 = 2.28 \text{ x } 10^{-26} \text{ cm}^3\text{s}^{-1} \text{ (M = O}_2\text{) [5]} \qquad (6)$$

Due to the de-excitation the metastable species are present just in the discharge reactor or in the beginning of the transport pipe. That is why the process (5) can be active only in this area. On the other hand the reactions with not excited species, e.g. (6) are active in whole volume of the pipe.

The heterogeneous processes are active on the wall of the reactor or pipe

$$O_3 + \text{wall} \rightarrow \text{products} \qquad k_7 = 1.71 \text{ x } 10^{-5} \text{ s}^{-1} \text{ [5]} \qquad (7)$$

The influence of ozone concentration on the discharge current was observed. This observation was in agreement with former experiments [4].

The differences in ozone concentrations and almost no differences in CV characteristics are the evidence that ozone is decomposed during transport in the Teflon pipe. For high flow rates the ozone concentration decrease is lower. Because the reaction time of the process (6) is of order 10^7 seconds the contribution of such process in ozone decomposition is negligible for transport time of order 10^3 seconds. Hence most likely only the heterogeneous depletion of ozone during the transport in the pipe is active. The DM method provides more realistic results for low gas flow rates when the difference in IM and DM can be even more than 50%. So, it is important to choose appropriate method for ozone concentration measurement according to the experimental setup to gain reasonable and reliable results that are comparable with results of other authors. With higher flow rate the difference between IM and DM methods is getting insignificant as the time needed for transport through the pipe is short. Ozone is able to capture free electrons very effectively even in the drift region of the discharge. That is why ozone concentration in the reactor influences the discharge current of negative corona very considerably.

This research project was partially supported by Slovak Grant Agency VEGA under project 1/1267/04, Slovak Research and Development Agency SK-UA-01906 and ESF projects COST P9 and EIPAM.

[1] Mikoviny, T., Kocan, M., Matejcik, S., Mason, N. J. and Skalny, J. D.: 2004, *J. Phys. D: Appl. Phys.* **37**.
[2] Yehia, A., Mizuno, A.: 2005 *IEEE/IAS Contrib. Papers Proc.*
[3] Castle, G.S.P., Inculet, I.I., Burgess, K.I.: 1969, *IEEE Transactions on Industry and General Applications* **5**.
[4] Skalný, J. D., Országh, J., Matejčík, Š., Mason, N. J., Stoica A.: 2006 *Proc. The First Central European Symposium on Plasma Chemistry and Workshop on the Plasma-Assisted Combustion and Plasma-Aftertreatment of Combustion Flue Gases of Power Industry.*
[5] Eliasson, B.: 1985, Electrical Discharge in Oxygen: Part 1. Basic Data, Rate Coefficients and Cross Sections. Report KLR 83/40 C, Brown Boveri Forschungszentrum, Baden-Dättwil, Switzerland.

P 59

Low Energy Electron Interactions with Molecules in the Condensed Phase

L. Feketeová[1], P. Cicman[1], R. Balog[1], N. Jones[1], K. Høydalsvik[1], D. Field[1], T. A. Field[2], K. Graupner[2], J. P. Ziesel[3]

[1]Department of Physics and Astronomy, University of Aarhus, Ny Munkegade, Aarhus, 8000 C, Denmark
[2]Department of Physics and Astronomy, Queen's University Belfast, Belfast, BT7 1NN, United Kingdom
[3]Laboratoire Collisions Agrégats Réactivité (CNRS UMR5589), Université Paul Sabatier, Toulouse, 31062, France
e-mail: linda.feketeova@gmail.com, dfield@phys.au.dk

Abstract

We report the first data for low energy electron collisions with solid material using our high resolution ASTRID synchrotron photoelectron source. We find that polycrystalline water ice at 130K is effectively transparent to electrons for energies between a few tens of meV and few hundred meV. Higher energies up to 8 eV display structure and are in part reflected from the material. There is no evidence of charging. This behaviour is in contrast to propanoic acid which charges strongly and shows relatively low effective electron transmission at all energies up to 7 eV.

Introduction

Our present knowledge of low energy electron scattering in condensed phases is very limited both theoretically and experimentally. To date, most experiments have been performed at high electron impact energies, typically of few eV and higher. Electron beams used in former experiments [e.g. 1,2] involved relatively high currents (~10^{-9} A) with rather poor resolution of typically more than 100 meV full-width at half-maximum (FWHM). In order to extend our knowledge of low energy electron-molecule interactions with the solid material from the tens of meV regime up, we report here the first experiments using a very high resolution electron beams with currents of a few hundred femtoamps.

There is considerable interest in this subject for fundamental reasons. The simplicity associated with gas phase very low energy scattering [3,4] may perhaps also be found in solid state systems. However no theory presently exists. One aspect is that the very high cross-sections associated with electron interactions at low energy may be mirrored in the solid state. For example, $e^- + CCl_4 \rightarrow Cl^- + CCl_3$ proceeds with very large cross-sections at low energy in the gas phase [5] and this may also be found in solid material. The interaction of low energy electrons with solids is also a process which is very widespread in nature. For example ices in planetary atmospheres and in the interstellar medium are subjected to low energy electron bombardment. This may influence the chemical evolution in polar stratospheric clouds and may trigger the formation for example of amino-acids in interstellar ices. Radiation damage is a further area of interest since electrons below 20 eV are generated by γ-rays or cosmic rays in biological systems and it is well-known that low energy electrons can create strand breaks in DNA [6,7].

Results and discussion

A new experiment has been built to study the interactions of low energy electrons with molecules in the condensed phase, with a special focus on collisions at very low electron energies down to few tens of meV. The electron source is a tried and tested synchrotron radiation photoionisation source, using the ASTRID storage ring at ISA, Aarhus, with a typical resolution of 1 meV in the incident beam [3,8]. The beam of electrons is focused onto a thin film of material deposited on tantalum. Films are prepared in a separate chamber using standard dosing techniques. The entire apparatus is UHV.

The transmitted current is measured as a function of electron energy. At present the energy scale is assigned by assuming that the onset of electron current is at zero energy. This may be in error by tens of meV.

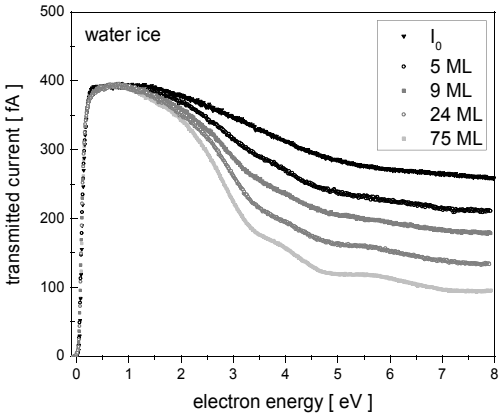

Fig. 1 Transmitted current vs electron energy for polycrystalline water ice at 130K. The top curve is for bare tantalum, and the curves refer successively to 5, 9, 24 and 75 monolayers.

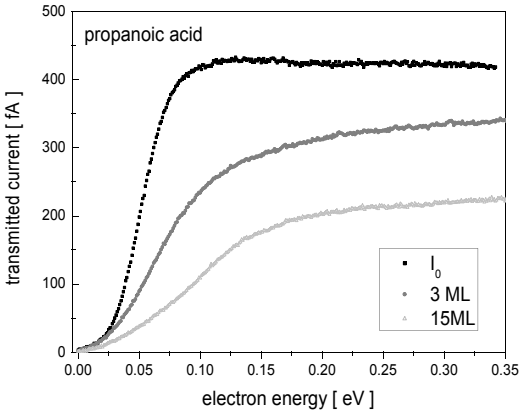

Fig. 2 Transmitted current vs electron energy for propanoic acid at 130K. The top curve is for bare tantalum, and the curves refer successively to 3 and 15 monolayers.

In Figure 1 we show data for the transmission of electrons through polycrystalline water ice at 130 K between a few tens of meV and 8 eV for 5, 9, 24, 75 ML in comparison with the bare tantalum substrate (I_0). At very low energy, below ~500 meV, we find that the electron current is only very weakly attenuated for all layers. At higher energy electrons are less efficiently transmitted through the ice. As the layer thickness is increased transmission weakens and structure in the spectrum becomes more marked. The structures are found at energies of ~4 eV and 5.7 eV. The high transmission at very low energy is believed to arise since the valence band of ice lies 0.1 eV below the vacuum level and extends into the continuum. Impinging electrons may lose energy through inelastic collisions with the ice. If sufficient energy is lost, they fall below the vacuum level and progress into the metal. This mechanism works most efficiently for very low energy electrons. The water ice does not charge, that is, the energy of inception of the curves of electron current versus energy does not change in progressive experiments.

In Figure 2 we show data for the transmission of electrons through propanoic acid (CH_3CH_2COOH) in the low energy regime for 3 ML and 15 ML layers again including data for bare tantalum. For successive experiments with the same layer of material, substantial charging takes place, with displacements of data by typically 20 meV. Returning to figure 2, data show that with increasing layer thickness there is increasing loss of electron transmission. Evidently, electron capture is taking place.

Conclusions

These first data for very low energy electron collisions with solid material show new phenomena. In particular the very high transmission of water ice is an unexpected and striking result. We are presently engaged in further experiments to discover the range of layer thickness for which this property holds. The case of propanoic acid is a somewhat extreme case of charging. Some chemistry may well accompany this charging process, but our present system is not suited to the detection of chemical change in this example since the likely product, CO_2 is not held on our surface at 130 K.

References

[1] L. Sanche, *J. Chem. Phys.* 71 (1979) 4860.
[2] R.E. Palmer, P.J. Rous, *Rev. Mod. Phys.* 64 (1992) 383.
[3] D. Field, S.L. Lunt, J.-P. Ziesel, *Acc. Chem. Res.* 34 (2001) 291.
[4] N.C. Jones, D. Field, J.-P. Ziesel, T.A. Field, *Phys. Rev. Lett.* 89 (2002) 093201.
[5] J.-P. Ziesel, N.C. Jones, D. Field, L.B. Madsen, *J. Chem. Phys.* 122 (2005) 024309.
[6] B. Boudaiffa, P. Cloutier, D. Hunting, M.A. Huels, L. Sanche, *Science* 287 (2000) 1658.
[7] J. Simons, *Acc. Chem. Res.* 39 (2006) 772.
[8] S.V. Hoffmann, S.L. Lunt, N.C. Jones, D.Field, J.-P. Ziesel, *Rev. Sci. Instr.* 73 (2002) 4157.

P 60

Dissociative Electron Attachment to Glycine, Alanine and Valine Amino Acids - Theoretical Study

P. Papp[1], J. Urban[2], P. Mach[2], Š. Matejčík[1]

[1]Department of Experimental Physics and
[2]Department of Nuclear Physics and Biophysics, Comenius University, Mlynská dolina, Bratislava 842 45, Slovakia
e-mail: papp@fmph.uniba.sk

Abstract

Dissociative electron attachment (DEA) is a process, where an extra electron attached to the molecule induces the dissociation of the molecule into a reactive radical and an anion. The temporary negative ions, which are formed by collision of low energy electrons with the molecules, have energy greater than that of the corresponding neutral molecule. The lifetimes are between 10^{-6} – 10^{-14} seconds. The resonant character of such system cannot be treated by standard quantum chemical techniques. We present the method of Nestmann and Peyerimhoff [1,2] to calculate resonant states for glycine, alanine and valine.

Introduction

The correct treatment of temporary anions cannot be done by means of standard quantum chemical methods. The electronic states of these species are resonances embedded in the continuum of scattering states. One of the simplest schemes for the calculation of the resonance energies of temporary anions is the method of Nestmann and Peyerimhoff [1,2] based on the modification of nuclear charges in the molecule. One may modify all or some of the nuclear charges

$$Z_a \rightarrow Z_a (1 + \lambda), \qquad 0 \leq \lambda \leq 0.1$$

or to add one dummy charge, e.g. in the center of the molecule

$$Z_{dummy} = \lambda, \qquad 0 \leq \lambda \leq 1.0$$

Standard quantum chemical methods are applied to calculate the energies of the states of the molecule with the modified nuclear charges. At the end it is necessary to extrapolate the energy to $\lambda \rightarrow 0$. This method was applied to three simple amino acids (glycine, alanine and valine). The resonant energies of the first two amino acids was measured by Aflatooni [3] using the electron transmission spectroscopy. They have shown that the electron attachment for this molecule is into the empty π^* orbital of –COOH group. The measured vertical electron affinities (VEA) for glycine and alanine molecules are 1.93 eV and 1.80 eV respectively. For the valine no experimental or theoretical data of the VEA were published so far, therefore we decided to calculate this property. The VEA were calculated using the Nestmann and Peyrimhoff method on different levels of theory: SCF, MP2, MP3 and the OVGF method [4].

Results and discussion

The effect of the modification of all nuclear charges is presented on the Fig.1, where the eigenvalue of S^2 and the electronic spatial extent for the glycine molecule are depicted as the functions of the modified nuclear charges. These results are obtained using the 6-311+G(2d,2p) basis set. At nuclear charge of about 2% noticeable change in the values for both characteristics occurs. At this point the bound state changes to a neutral glycine and a free electron as the perturbation parameter λ decreases. For this reason the modified nuclear charges above 102% represent the basis set for the quadratic extrapolation to $\lambda \rightarrow 0$. The extrapolation formulas and curves are presented on the Fig.2. The behavior and the extrapolated results depend on the molecule, the basis set used and the methods used. The extrapolation formulas from Fig.2 led to VEA calculated as the difference of energies for the stabilized anionic states at $\lambda \rightarrow 0$ and their neutral analogs for all the three investigated amino acids: glycine 1.895 eV (SCF), 1.539 eV (MP2), 1.331 eV (MP3), alanine 1.976 eV (SCF), 1.720 eV (MP2), 1.592 eV (MP3) and finally valine 1.837 eV (SCF), 1.258 eV (MP2), 1.348 eV (MP3). The situation is different for the OVGF method where in the same basis set a higher values for VEA are obtained: for glycine 2.512 eV, alanine 2.337 eV and valine 2.154 eV.

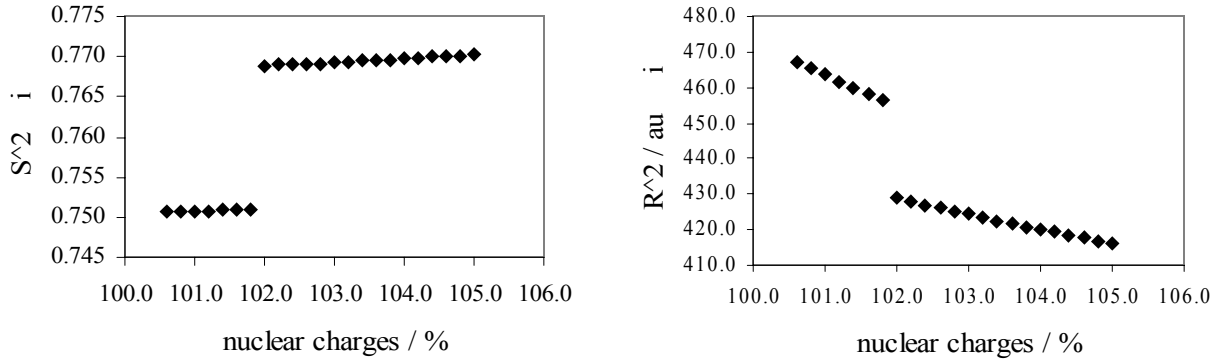

Figure 1: The total spin S^2 eigenvalue (left) and the electronic spatial extent (right) as the functions of the modified nuclear charges for the glycine amino acid in 6-311+G(2d,2p) basis set.

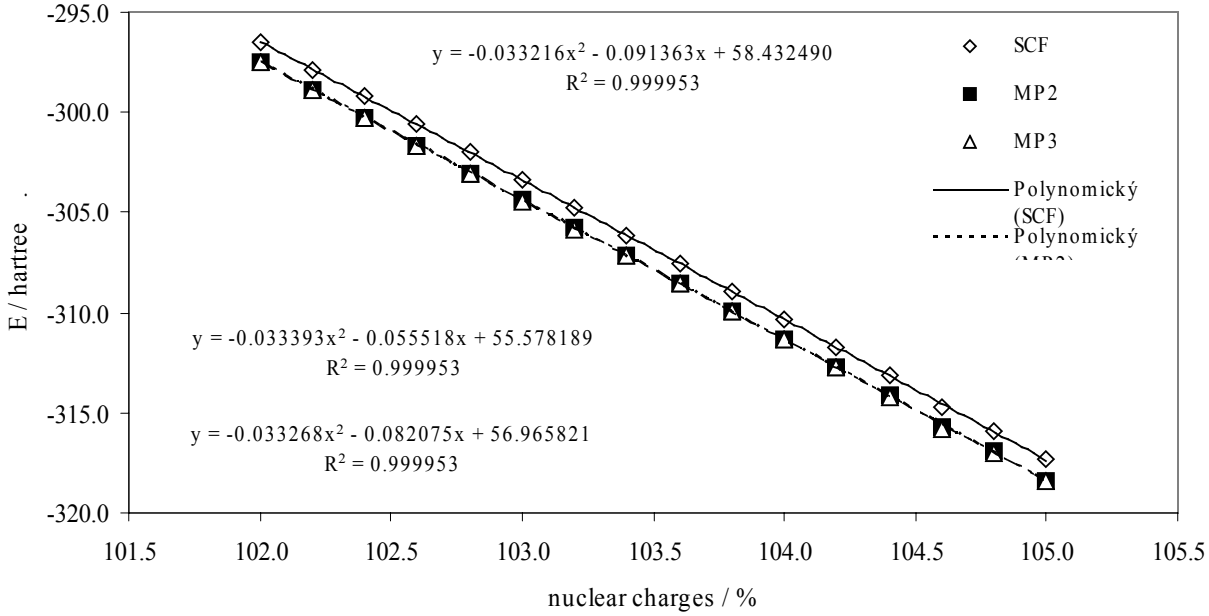

Figure 2: Polynomial extrapolation to $\lambda \rightarrow 0$ of the SCF, MP2 and MP3 energies as functions of the modified nuclear charges using the 6-311+G(2d,2p) basis set for glycine molecule. The extrapolation formulas are from the top of the graph to the bottom for SCF, MP2 and MP3 methods respectively.

Conclusions

The method of Nestmann and Peyerimhoff was applied to calculate the VEA of glycine, alanine and valine. Using four different quantum chemical methods the decrease of the VEA was observed going from glycine to valine. The *ab initio* methods MP2 and MP3 gave smaller values for VEA as the OVGF method in the same basis set. The comparison of the theoretical values with the experimental ones of Aflatooni the first two methods underestimate the reported VEA while the OVGF overestimate it. This indicates that additional diffuse functions have to be used to get the correct values for VEA.

Acknowledgment

This research project was partially supported by ESF projects COST P9 and EIPAM.

References

[1] B. Nestmann and S.D. Peyerimhoff, J. Phys. B 18, (1985) 615

[2] B. Nestmann and S.D. Peyerimhoff, J. Phys. B 18, (1985) 4309

[3] K. Aflatooni, B. Hitt, G. A. Gallup and P. D. Burrow, J. Chem. Phys. 115, (2001) 6489

[4] J. V. Ortiz, J. Chem. Phys. 89, (1988) 6348

P 61

Study of SnO_2 Thin Films Prepared by Plasma Assisted Deposition Techniques

J. Pavlik, J. Matousek, Z. Stryhal, T. Vagner

Department of Physics, J. E. Purkinje University, Ceske mladeze 8, Usti nad Labem 400 96, Czech Republic
e-mail: pavlikj@sci.ujep.cz

Abstract

Thin films of oxide materials have high potential for device applications. Development of gas sensors in last few years has shown an important interest in thin tin oxide films. The SnO_2 is one of the most widely used materials for gas sensor applications due to their good performance for a detection of oxidable gases. When SnO_2 layers are used in gas sensors, some features can depend on many layer parameters as thickness, cluster size, roughness, etc. Since the properties of the material are strongly dependent on the procedure of preparation, different techniques have been employed to obtain SnO_2 thin films [1, 2, 3, 4]. In this work we have studied surface properties and structure of SnO_2 thin films prepared both by plasma oxidation of the thin tin films [5] and by RF or DC magnetron reactive sputtering of tin target in oxygen + argon mixture atmosphere. Tin dioxide films were prepared by RF sputtering of SnO_2 target using argon or oxygen as working gas, too.

Introduction

The grain size and area of active surface are the main parameters controlling gas sensing processes in metal oxide films. The decreased grain size of tin dioxide thin films is the fundamental factor for increasing sensors sensitivity. The aim of the present work was to study the relationship between deposition parameters and tin dioxide thin films properties.

The plasma oxidation experiments were carried out in the system for the plasma surface modification of thin metal films [6]. Tin metal films were evaporated in an UHV chamber from Mo boat. The tin oxide films were then obtained by in situ plasma oxidation in the RF (13.56 MHz, power 35 W) flowing post-discharge. The RF discharge was performed in oxygen or oxygen + argon mixture (purity: argon 99.9999 %, oxygen 99.995 %) at a total mixture pressure of 50 – 100 Pa.

The magnetron sputtering deposition process was performed using set-up arrangements in a stainless steel reactor equipped with balanced magnetron (81 mm in diameter). Substrate holder was 40 mm above the magnetron. The deposition chamber was evacuated to ultimate pressure $5x10^{-3}$ Pa prior to each experiment. The total pressure was kept at 5 Pa during thin films deposition. DC current was 0.1 A. Applied RF powers to the magnetron were within the range 20 – 50 W. The surface topography was measured by the Atomic Force Microscopy (AFM - Metris – 2001A – NC, Burleigh Instruments Inc.). All AFM measurements were carried out in the non-contact mode at the ambient atmosphere and at room temperature. The scan area varied from 1.2 μm x 1.2 μm to 25 μm x 25 μm. The depth profiles were measured by the Secondary Ion Mass Spectrometry (ATOMIKA 3000 SIMS system). The chemical composition was investigated by X-ray Photoelectron Spectroscopy (based on SPECS main components).

Results and discussion

The surface morphology of the tin films prepared by vacuum thermal evaporation on SiO_2 substrates is characterized with a near flat-grain structure, which appeared on the surface with typical grain size about 500 nm. The surface morphology of the tin oxide surface after plasma oxidation is characterized by a sharper grain structure with a smaller grain size (about 100 nm) [5].

SnO_2 films prepared by DC and RF magnetron reactive sputtering of tin target in oxygen atmosphere had an average SnO_2 grain size about 45 nm. SIMS measurements indicate that the stoichiometry of SnO_2 films prepared by DC and RF magnetron reactive sputtering of tin target in oxygen atmosphere is better for thicker layers [7], too. In the XPS spectra it can be seen that Sn3d peak is shifting to the higher binding energies with increasing content of the oxygen in the working gas, see Fig. 1. It can be explained by change of SnO_x stoichiometry from SnO to SnO_2 [8]. The SIMS measurements (Fig. 2) indicate this development, too.

SnO_2 films prepared by RF magnetron sputtering of tin dioxide target in oxygen and argon atmosphere had an average grain size even smaller than 30 nm (25 nm for argon used as working gas, 15 nm for oxygen used as working gas). The typical grain size of the tin dioxide films prepared by RF magnetron sputtering of tin target in argon + oxygen mixture is dependent on the argon/oxygen ratio and it decreases upon a increase of the oxygen fraction, see Fig. 3. The AFM measurements revealed increase in typical grain size with

decreasing power delivered to the target.

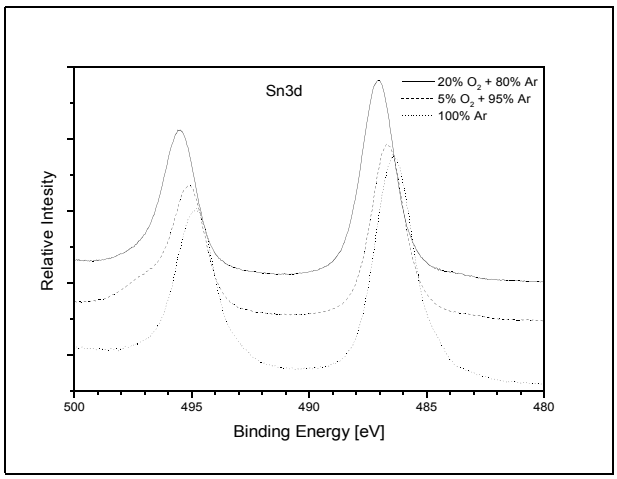

Fig. 1: The evolution of the XPS Sn3d peak of tin oxide layers prepared by RF magnetron sputtering of tin target in Ar + O_2 mixture (p_{TOT} = 5 Pa, P = 50 W). The spectra were calibrated to carbon peak at 285 eV.

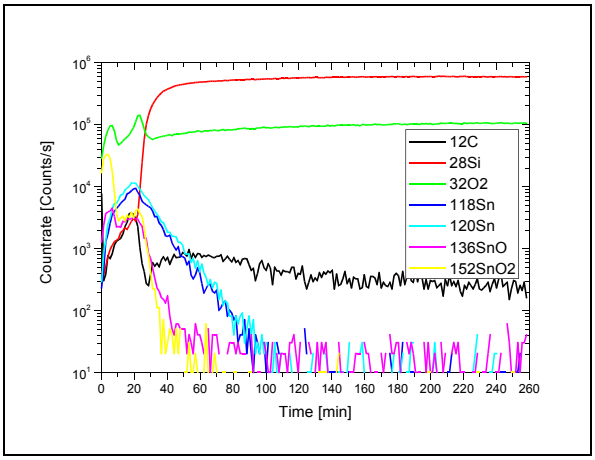

Fig. 2: Depth profiles obtained from SIMS measurements for SnO_2 thin film deposited by RF magnetron sputtering of tin target in argon + oxygen mixture (80 % Ar + 20 % O_2) atmosphere (p_{TOT} = 5 Pa, P = 50 W).

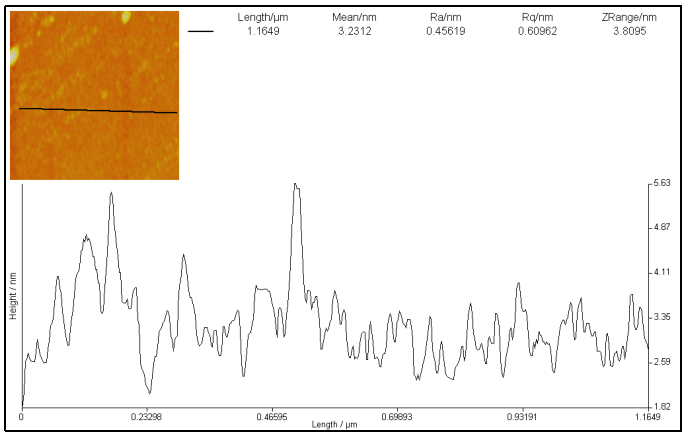

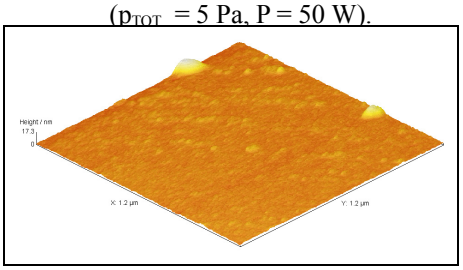

Fig. 3: The AFM image of surface of SnO_2 thin film deposited by RF magnetron sputtering of tin target in argon + oxygen mixture (80 % Ar + 20 % O_2) atmosphere (p_{TOT} = 5 Pa, P = 50 W) in top view representation and as a profile single line. The grain size was found about 20 nm.

Conclusions

In comparison with plasma oxidation [5], tin dioxide thin films prepared by magnetron sputtering are characterized by smaller non oriented grains and better stoichiometry in case of layers thicker than 100 nm.

Acknowledgement

This work was supported by The Ministry of Education of Czech Republic (Projects COST OC 143 and LC 06041).

References:

[1] B. Correa-Lozano, Ch. Comminellis, A. Battisti, *J. Electrochem. Soc.*,143 (1996) p. 203.
[2] P. Serini, V. Briois, M. C. Horrillo, A. Traverse, L. Manes, *Thin Solid Films,* 304 (1997) p. 113
[3] Y. S. He., J. C. Campbell, R. C. Murphy, M. F. Arrendt, J. S. Swinnea, *J. Mater. Res.,* 8 (1993) p. 3131
[4] S. W. Lee, P P Tsai, H Chen, *Sens. Actuator,s* B41 (1997) p. 55
[5] Z. Stryhal, J. Pavlik, S. Novak, A. Mackova, V. Perina, K. Veltruska, *Vacuum*, 67 (2002) p. 665
[6] J. Pavlik, R.Hrach, P. Hedbavny, P. Stovicek, *Superficies Y Vacio,* 9 (1999) p. 131
[7] J. Pavlik, Z. Stryhal, J. Matousek, T. Vagner, P. Hedbavny, 2006, *Europhysics Conference Abstarcts*, 30 (2006) G 493
[8] M Kwoka, L Ottaviano, M Passacantando, S Santucci, J Szuber, *Applied Surface Science,* 252 (2006) p. 7730

P 62

Immobilization of Polysaccharides onto Atmospheric Plasma Activated Polypropylene Surfaces

J. Ráheľ, V. Procházka, D. Erben

Department of Physical Electronic, Masaryk University, Kotlářská 2, Brno 611 37, Czech Republic
e-mail: rahel@mail.muni.cz

Abstract

Chitosan and *β*-cyclodextrin functionalization of polypropylene surface was done by atmospheric plasma assisted graft polymerization, with the purpose of obtaining a suitable material for high efficiency waste water filters. First results on recently completed continuous plasma-treatment reactor are presented. The chitosan coating exhibited a good resistance towards the washing effect. The *β*-cyclodextrin coating was soluble in water, which suggests a lack of strong covalent bond with the PP surface. Further research on improving the *β*-cyclodextrin coating quality is needed.

Introduction

The raising public awareness and consequent strict legislative regulations of the industrial wastewater pollution control is responsible for a systematic effort to identify and engineer novel technologies for water contaminants removal, including heavy metal ions, chlorinated phenols or textile dyes. A promising wastewater treatment candidates, meeting the high-efficiency and low-cost requirement are polysaccharide based adsorbents [1]. The *cyclodextrins* and *chitosan* obtained from the abundant natural polysaccharides – starch and chitin, are of particular interest, owing not only to their cost, but also to their high selectivity towards aromatic compounds and heavy metals.

Chitosan (deacetylated chitin) has an excellent sorption properties of heavy metal ions and organic compounds from the aqueous solutions due to its ability for the complexation (chelation) and high content of amino functional groups[2][3]. *Cyclodextrins* (or cycloamyloses) are torus-shaped cyclic oligosaccharides produced from starch. Commonly studied forms of cyclodextrins (CDs) are *α*-cyclodextrin, *β*-cyclodextrin and *γ*-cyclodextrin, consisting of six, seven and eight glucopyranoside units respectively. Cyclodextrins are able to form inclusion compounds with various molecules, especially aromatics, by trapping an apolar pollutant into the molecule interior cavity. It is interesting to note that under controlled conditions the materials functionalized with CDs may release trapped substrates, which allows e.g. a manufacturing of a long-lasting perfumed fabric with some trapped fragrances being released within a long period of time [4].

Both polysaccharide derivatives offer, in general, a low surface area due to their limited porosity. To overcome this problem a polysaccharide adsorbent thinly coated on suitable porous carrier material is desirable [2]. Low cost, large surface area and excellent flow transfer characteristics favors the use of nonwoven fabrics. Among the available nonwovens, polypropylene (PP) exhibits many advantages, such as chemical and physical stability, a good resistance to biodegradation, and low cost. What is more, the Czech Republic is the world's 3rd largest producers of PP nonwoven fabrics.

Cernakova *et al*. [5] reported a successful immobilization of chitosan directly on PP surface, using atmospheric plasma pre-activation of PP. Nevertheless the size and amount of coated samples were limited by the size of batch reactor, and the continuous plasma treatment is needed now. Le Thuaut *et al*. [4] reported a successful immobilization of CD on a PP surface, by forming the glycidyl methacrylate (GMA) graft polymer on the PP surface prior to CD immobilization. Nevertheless the GMA is an acute skin irritant and potentially genotoxic [6], therefore its use for the wastewater treatment or in the garment industry is problematic. Therefore a direct immobilization of CD onto PP surface would be preferred.

In this paper we are presenting our initial results on immobilization of chitosan and *β*-cyclodextrin on the surface of PP nonwoven fabric by using the continuous plasma treatment apparatus based on Diffuse Coplanar Surface Barrier Discharge.

Results and discussion

Spun-bonded polypropylene (PP) nonwoven fabric of 18 g/cm^2 supplied by Pegas a.s.(Czech Rep.) was activated by atmospheric pressure air plasma, generated by Diffuse Coplanar Surface Barrier Discharge (DCSBD) in the recently completed prototype of continuous plasma treatment reactor CONTI 1. The schematic of continuous plasma treater is shown in Fig.1. The plasma generator was operated at 400

Watt/200 cm^2. PP samples were treated for 5 sec in ambient air. For the immobilization of chitosan the method described by Cernakova *et al*. [5] was adopted. Immediately after the plasma activation the PP sampled was immersed into 2% of chitosan-acetic acid solution and magnetically stirred for 1 hour at 60°C. Dried sample was washed by hot distilled water to remove weekly attached coating. Afterwards the samples were dipped into the 0.1%-water-alcohol solution of the Acid red (CAS #3734-67-6) and resulting colour changes was evaluated. The plasma assisted chitosan coating sample exhibited a deeper red color, comparing to that without the plasma activation.

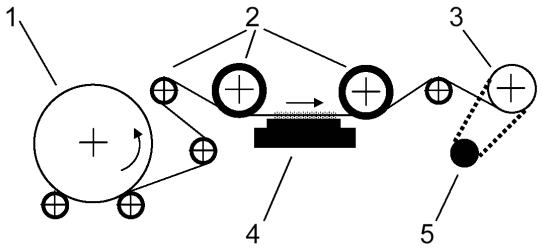

Fig.1. Schematic of continuous plasma treater CONTI 1: (1) package of PP fabric; (2) steering rolls; (3) towing and take up roll; (4) plasma reactor; (5) driving unit.

The *β*-CD coating was done immediately after the plasma treatment in the magnetically stirred saturated solution with distilled water (18 g/L at room temperature) at 60°C for 1 hour. During the course of coating bath, additional *β*-CD was supplied into the solution for several times, in order to keep the water solution saturated, as a significant portion of *β*-CD was attached onto PP surface. After drying, the samples were stained with Phenol red (CAS #143-74-8) and Acid red and resulting colour changes was evaluated. The plasma activated *β*-CD coated samples exhibited a deeper coloring comparing to none plasma-activated. Nevertheless the resulted *β*-CD was solvable in water and could be completely removed by washing in distilled water.

Conclusions

The completed prototype of continuous plasma treater demonstrated its viability with respect to the PP surface activation. Comparing to the batch DCSBD reactors employed so far, the treatment time in CONTI 1 is approx. three times higher, which can be attributed to the imperfect contact of treated fabric with the plasma and to the use of ambient air instead of nitrogen as a working gas. At the moment the solvability of *β*-CD coating prevents its use as a water contaminants absorber. The issue can be addressed either by promoting the generation of covalent bond on *β*-CD – Polypropylene interface by optimizing the plasma treatment parameters, or by inducing a crosslinking of the *β*-CD coating, which is known to reduce its water solubility [1]. Further investigation is still needed.

We gratefully acknowledge the financial support of the Czech Science Foundation, Grant No. 202/06/P337.

References

[1] G. Crini, *Prog. Polym. Sci.* 30 (2005) 38–70
[2] M.W.Wan et al., *Carbohydrate Polymers 55* (2004), 249-254
[3] V.N. Kosyakov et al., Radiochemistry 45 (2003), 403-407
[4] P. Le Thuaut et al., *J. Appl. Polym. Sci.*, 77 (2000), 2118–2125
[5] L.Cernakova et al., *Proc. of , 9th HAKONE* August 23- 27(2004), Padova, Italy
[6] http://www.chem.unep.ch/irptc/sids/OECDSIDS/106912.pdf

P 63

Ion Mobility Spectrometry in Negative Corona Discharge in Carbon Dioxide

M. Sabo[1], F. Janky[1], I. Prisazhnevich[2], J. D. Skalný[1], V. Chernyak[2], Š. Matejčík[1]

[1]Department of Plasma Physics, Comenius University, Mlynská dolina, Bratislava 842 45, Slovakia
[2]Taras Shevchenko National Univeristy, Kyiv, Ukraine
e-mail:sabo@neon.dpp.fmph.uniba.sk

Abstract

The ion mobility spectrometry (IMS) technique was applied to study the ions formed from the carbon dioxide in negative corona discharge. The measurements were carried out at room temperature and temperature *352 K*. The ions with reduced mobility *1,1* $cm^2V^{-1}s^{-1}$ and *1,0* $cm^2V^{-1}s^{-1}$ (of CO_3^- and CO_4^-) were detected in IMS spectrum. The increase in the velocity of the ions and changes in the amplitudes were observed with increasing temperature from 293 K to 352 K.

Introduction

IMS is an experimental technique used for analysis of the ions according to their mobility in a weak electric field and drift gas. The drift velocity of the ions in drift tube v_d depends on the electric field E and the mobility μ of the ions in the gas:

$$v_d=\mu E \tag{1}$$

The v_d is determined from length of the drift tube and the drift time. The ion mobility depends on the gas pressure and the temperature of the gas. For the qualitative identification of the ions is used the reduced mobility μ_0 expressed by equation:

$$\mu_0=\mu(T_0/T)(p/p_0) \tag{2}$$

where $T_0=273K$ and $p_0=101kPa$, p and T are pressure and temperature of drift gas. The mobility of the ion can be also calculated from the

$$\mu = \frac{3q}{16n}\sqrt{\frac{2\pi}{kT}}\sqrt{\frac{1}{m_r}}\frac{1}{\Omega} \tag{3}$$

where n is concentration, μ is reduced mass and Ω is collision cross-section [4].

The Ion Mobility Spectrometer consist of three parts the ions source, the reaction chamber and the drift tube [2]. The ion source is negative corona discharge in point to plain geometry. The ions and electrons formed in the ion source drift to the reaction chamber where reaction with sample gas occurs. Bunches of the negative ions (appr. 100 μs) are introduced into the drift tube by the shutter grid. The ions and electrons drift through the drift tube. The ions are in the drift tube separated according to their mobility and the ion currents is recorded as a function of the time at the collector located at the end of the drift tube.

In negative corona discharge with pure carbon dioxide will occur these reactions [1]:

$$CO_2+e^-\rightarrow CO+O^- \tag{4}$$
$$CO+e^-\rightarrow C+O+e^- \tag{5}$$
$$O^-+O\rightarrow O_2+e^- \tag{6}$$
$$O_2+e^-+M\rightarrow O_2^-+M \tag{7}$$
$$O_2^-+CO_2+M\rightarrow CO_4^-+M \tag{8}$$
$$O^-+CO_2+M\rightarrow CO_3^-+M \tag{9}$$

Results and discussions

The IMS spectra were measured at the room temperature and at temperature 352 K. As you can see on the Fig.1 with increasing temperature the decrease of the ion's drift time occurs [3]. The IMS spectra exhibit two peaks with reduced mobility $\mu_0=1,1$ $cm^2V^{-1}s^{-1}$ and $\mu_0=1,0$ $cm^2V^{-1}s^{-1}$. These peaks we tentatively assign to the ions of CO_3^- and CO_4^-. The next peak with the reduced mobility of $\mu_0=0.99$ $cm^2V^{-1}s^{-1}$ could be assigned to the CO_3^- clusters (e. g. $CO_3^-(H_2O)_n$, $CO_4^-(CO_2)_n$). The decrease of the intensity of this peak with the increasing gas temperature and the increase of the intensity of CO_3^- signal with increasing temperature supports this hypothesis. The mass spectrometric analysis of the ions detected in the IMS spectrometry is necessary in order to understand the nature of the ions with reduced ion mobility of *0.99* $cm^2V^{-1}s^{-1}$.

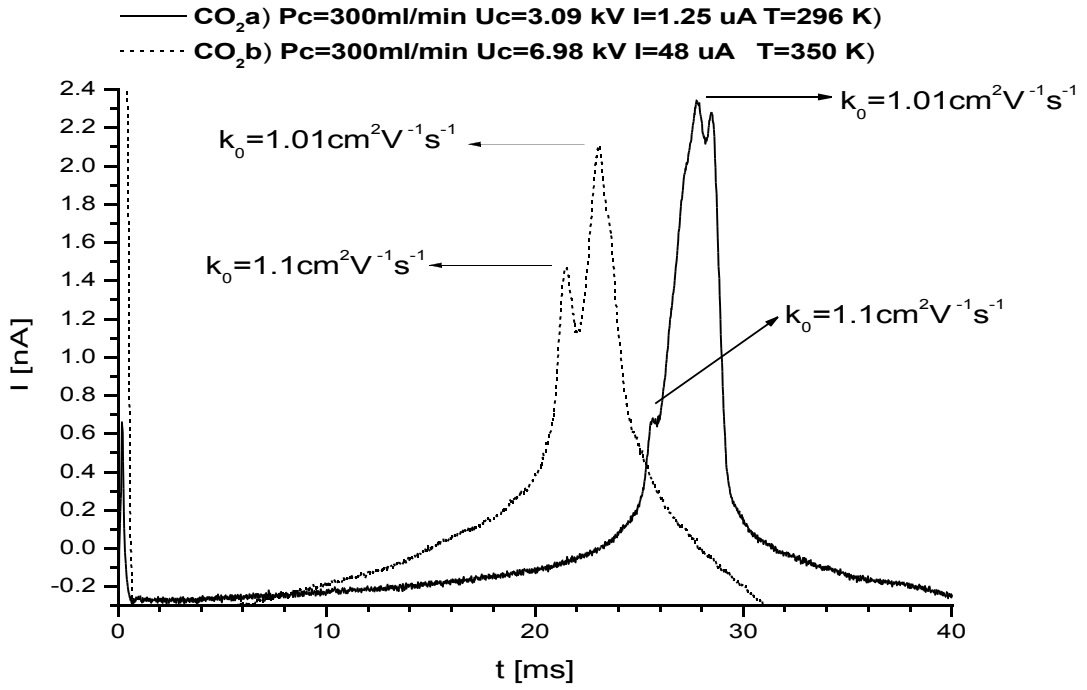

Fig. 1 IMS spectrum in negative corona in pure carbon dioxid: *a) T=296K* and U_c*=3.09 kV* ; b) *T=350 K* and U_c*=6.98 kV*

Acknowledgment

The projects has been supported by the Slovak Research and Development Agency APVV, project SK-UA 01906.

References

[1] A. Cenian, A. Chernukho, V. Borodin and G.Sliwinski, Contributions to Plasma Physics (1994)
[2] F. Janky, M. Stano, J. Husárik, Š. Matejčík, J.D. Skalný, 16th. Symposium on physics of switching arc, 1, Brno, Czech Republic, 101, 2005
[3] M. Tabrizchi, Temperature Corrections for Ion Mobility Spectrometry
[4]G.A.Eiceman and Z.Karpas Ion mobility spectrometry , CRC Press 2005

P 64

Properties of Water Solutions of Phenol after Plasma Processing in Plasma-Liquid Systems

V. Shapoval[1], V. Chernyak[1], V. Naumov[2], V. Zrazhevski[1], V. Yukhymenko[1], M. Dors[3], J. Mizeraczyk[3]

[1]Plasma Lab, Faculty of Radiophysics, Taras Shevchenko Kyiv National University, Prospect Acad. Glushkova 2/3, Kyiv 03122, Ukraine

[2]Photonics Lab, Institute of Fundamental Problems of High Technology, Ukrainian Academy of Sciences, Prospect Nauki 45, 03028 Kyiv, Ukraine

[3]Centre for Plasma and Laser Engineering, The Szewalski Institute of Fluid Flow Machinery, Polish Academy of Sciences, Fiszera 14, Gdansk 80-231, Poland

e-mail: chern@univ.kiev.ua

Abstract

The technology of the electric discharge plasma treatment of aqueous phenol solutions in the atmospheric pressure plasma-liquid systems with a secondary discharge supported by a blowing air arc is studied. The processes of degradation of aqueous phenol and their properties after the plasma treatment are analyzed.

Introduction

Phenol (C_6H_5OH) and its products in water solutions are harmful organic contaminations in human environment. Phenol molecules in water are stable and not degrade itself in natural conditions. Therefore, removal of pollutants from wastewater is an actual issue of science and technology [1]. One of most efficient approaches is the use of non-equilibrium gas discharge plasma processing of polluted water in heterophase plasma-liquid systems at atmospheric pressure [2-5]. In most works the efficiency of the plasma treatment is estimated by the measurements of phenol content in water during the treatment and after that. But in most cases the lability of plasma-treated solutions in the long term period after the treatment was not investigated.

This work presents first results of our study of the plasma-chemical degradation of phenol and its products in water solutions after the processing in the atmospheric pressure plasma-liquid reactor with a secondary discharge supported by the blowing air arc.

Results and discussion

Experiments were done for a scheme of the plasma-liquid reactor with a secondary discharge as shown in Fig. 1. The primary arc discharge was burned between two copper rod electrodes (1) in the flow of air incoming through the inlet nozzle. This blowing arc served as an auxiliary discharge for a secondary (non-self-sustained) discharge with a plasma cathode when the nozzle electrode (2) was introduced into the arc plasma column. So the voltage of a secondary discharge was applied between the electrodes (1) and (2). The treatable solution was supplied into the reactor in the form of the dispersed jet through the nozzle (2). The reference solution of phenol in concentration of 10 mM was prepared by dissolving an analytical-grade phenol in distilled water of crystal quality. Other test solutions were prepared by water diluting. In addition, a small amount of iron sulfate (0.08 mM Fe_2SO_4) was added as a catalyst to enhance the phenol decomposition. The test solutions were processed in the plasma-liquid reactor at various operational modes: with and without secondary discharge, with positive (+) and negative (-) potentials of the «liquid» electrode in respect of the air arc plasma. The discharge system was powered by the HV sources with the dropping output characteristics at the ballast resistance in a circuit. The auxiliary discharge had voltage U= 2 kV and current I= 400 mA. The secondary discharge had voltage 1.5 kV, and its current varied from 100 to 200 mA. The air flow rate was 75 ml/s, the water flow rate was 50 ml/min. The processing time varied from 2 to 10 min. The content of phenol and its products in water was analyzed by the UV optical absorption spectrophotometry using a scanning monochromator LOMO KSVU23 with the spectral resolution ~0.1 nm in the range 200-400 nm. After the plasma treatment, the test solutions were incubated at room temperature for the stabilization, and their properties were monitored during several days.

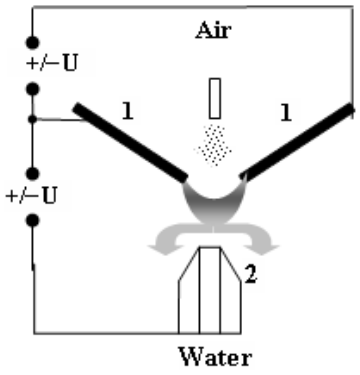

Fig. 1. Scheme of the electric discharge plasma-liquid reactor.

In running experiments, during the air plasma treatment of the test solutions the concentration of phenol

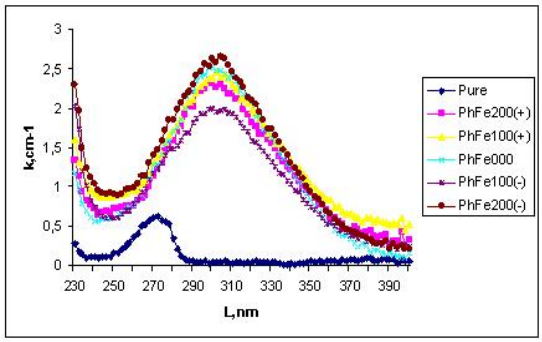

Fig. 2. Optical absorption of aqueous phenol solutions before and after plasma treatment.

I, mA	Fe(-),%	Fe(+),%	Plus,%
0	13	13	36
100	37	35	39
200	57	31	47

Table 1. Results of destruction of phenol in water after plasma treatment during 10 min.

in water decreased with the treatment time. It means that dissolved phenol was effectively oxidized by the oxidizing agents: hydroxyl radicals (OH), oxygen atoms (O), ozone (O_3) and hydrogen peroxide (H_2O_2) produced in the plasma-liquid system. Visually, the test solutions began to darken in color right after the plasma treatment. Then, during the stabilization, the plasma-treated solutions had further changes. Typical absorption spectra of the phenol solutions after the treatment by plasma of a secondary discharge at the energy consumption ~1.5 kJ/ml for the initial phenol concentration 10 mM are shown in Fig. 2. One can see that pure phenol has a clear band of UV absorption at 275 nm. The percentage of destructed phenol after the plasma treatment in different modes is given in Table 1. Here the treatment time was 10 min. But at the final stage, after 2-3 days of stabilization after the treatment, we did not see spectral marks of phenol. There was a wide spectral band near 300 nm (FWHM ≈ 50 nm) caused by the accumulation of dissolved byproducts, mainly, nitric acid (HNO_3). Its absorption index k is about 1.5 cm^{-1} for all modes of the treatment. A strong UV absorption in the range λ <230 nm belongs to H_2O_2. Thus with additions of Fe ions, initiating Fenton's reactions enhancing the phenol decomposition, the resulting products are the same in both positive and negative polarities of the solutions although their concentrations were different. This is confirmed also by the pH tests of the acidity of the solutions: due to a large amount of oxidants pH is ~3.0 in all tests irrespective of initial phenol content.

Conclusions

From our experiments with the non-equilibrium plasma processing of aqueous phenol solutions in the electric discharge plasma-liquid systems of atmospheric pressure we conclude that:

- The heterophase plasma-liquid reactor with a secondary discharge supported by a blowing air arc offers an efficient destruction of phenol in water due to the chain-branching mechanism of plasma-chemical oxidation processes induced by the generation of chemically active oxidizing agents at a well-developed plasma-liquid interface.
- The efficiency of the phenol degradation increases with the deposited discharge energy, particularly with increase of the current of a secondary discharge, and with the treatment time.
- The properties of the plasma-treated solutions are labile in time after the treatment, and their stabilization lasts several days after the treatment regardless of the treatment mode. The composition of final products and their properties are the same in all plasma-treated solutions.

Acknowledgement

This work was supported by the Taras Shevchenko Kyiv National University and by the Program of scientific cooperation between Polish Academy of Sciences and Ukrainian Academy of Sciences.

References

[1] E.M. van Veldhuizen (ed.), *Electric Discharges for Environmental Purposes: Fundamentals and Applications*, Nova Science Publishers Inc., New York (2000).
[2] D. Moussa, J.L. Brisset, *Proc. Intern. Symp. on High Pressure Low Temperature Plasma Chemistry – HAKONE V*, Milovy, Czech Republic (1996) 165; J.L. Brisset, *J. Appl. Electrochem.* 27 (1997) 179.
[3] W.F.L.M. Hoeben, E.M. van Veldhuizen, W.R. Rutgers, G.M.W. Kroesen, *J.Phys.D: Appl.Phys.* 32 (1999) L133; L.R. Grabowski, E.M. van Veldhuizen, W.R. Rutgers, *J. Adv. Oxid. Technol.* 8 (2005) 142.
[4] V. Chernyak, A. Trokhymchuk, V. Naumov, *et al.*, *Proc. Intern. Symp. on Plasma Chemistry - ISPC15*, Orleans, France, Vol. VII (2001) 3017; V.Ya. Chernyak, S.V. Olshewski, *Ukr. J. Phys.* 50 (2005) 243.
[5] M. Dors, E. Metel, J. Mizeraczyk, *Proc. 1st Central European Symp. on Plasma Chemistry*, Gdansk, Poland (2006); M. Dors, J. Mizeraczyk, Y.S. Mok, *J. Adv. Oxid. Technol.* (2006).

P 65

Statistical Description of Dissociation of Metastable Negative Ions

P. Shchukin, M. Muftakhov, R. Khatymov

Institute of physics of molecules and crystals Ufa research center of the Russian Academy of Science prospect Octyabrya, 151, Ufa, Russia

e-mail: pavel@anrb.ru

Introduction

The most accepted theories used for description of positive ion mass spectra are RRKM and QET statistical theories. They provide quantitative relationship between ions relative intensities in mass spectra and fundamental parameters characteristic to ionic structure and reactivity. Success achieved in calculation of positive ion mass spectra basing on the statistical conception had initiated the attempts in application of statistical approach to the fragmentation processes in negative ions [1, 2]. The main difficulties in such approach arise from two peculiarities of negative ions, namely, resonant nature of ion formation and their metastability with respect to electron autodetachment. This is consequence of the particular selection rules [3] controlling the processes of negative ions decomposition. Indeed, negative ion mass spectra contain few peaks and ion composition is determined mainly by simple bond cleavage reactions.

In the present work the statistical approach was applied to the negative ions undergoing metastable dissociative decay. This choice was determined by several objective reasons: i) relatively large lifetime of such ions ($\tau > 10^{-6}$ s) facilitates the more complete redistribution of the internal energy into active degrees of freedom, ii) metastable ions have strict localization in the mass spectral scale and refers to the exactly known parent ions, and possibility of overlapping of several fragmentation channels is excluded, iii) since ions are formed in the first field-free region of the mass spectrometer, it is possible to calculate precisely the time interval of their generation what is necessary for quantitative estimation of decay parameters.

The object of investigation was benzyl ester of acridanoneacetic acid (fig. 1) the fragment negative ions of which undergo further metastable fragmentation schematically shown in fig. 2.

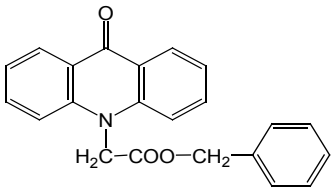

Fig. 1

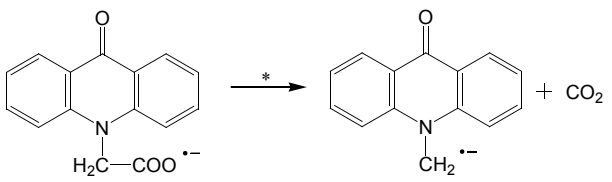

Fig. 2

Theory

Ions which undergo fragmentation are described by the monomolecular decay rate constant *k(E)* and internal energy distribution function *f(E)*. According to RRKM theory, function *k(E)* is described as follows: $k(E) = \frac{\sigma W^{\pm}(E - E_a)}{h\rho(E)}$, where σ is the number of equivalent reaction paths, $W(E–E_a)$ is the number of states of the transition state in the energy range from 0 to $(E–E_a)$, E_a is the energy of the reaction threshold, *h* – Planck's constant, and $\rho(E)$ is the density of states of the reactant. The vibrational modes required for evaluation of the functions $W(E–E_a)$ and $\rho(E)$ were obtained by quantum chemical DFT/B3LYP calculations

Dependence *f(E)* was approximated by the Boltzmann's distribution with the several variable parameters responsible for width and shape of the distribution. Resulting values for these parameters were selected by fitting to the experimental data. To this end the ratio of the intensities of metastable and parent ions vs. electron energy was calculated and compared with the analogous ratio of the experimental effective yield curves $[m^*]/[P^-]$.

Experimental

The experiments were performed using a magnetic sector mass spectrometer MI-1201 (USSR, Sumy), rebuilt for generation and detection of negative ions (the possibility to work with positive ions is retained). The sample was introduced into ionizing chamber maintained at temperature ~115°C using direct inlet probe heated up to ~ 90°C. The zero peak of SF_6^- ions from SF_6 was used for electron energy scale calibration and

measurement of electron energy resolution which was tuned to $\Delta\varepsilon \sim 0.3$ eV (FWHM) at electron current 1 μ A. The ion accelerating voltage was 3.5 kV. For more details of experimental technique see our recent review in ref. [4].

Results and discussion

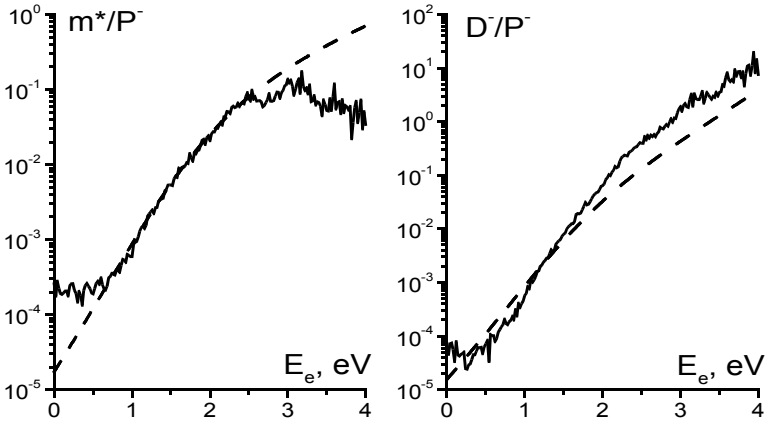

Fig. 3

Fig. 3 (left panel) shows a plot of ratio of experimental effective yield curves of metastable and parent ions $[m^*]/[P^-]$ (solid line). Such a representation makes it possible to exclude the resonant nature of negative ions formation and reflects the efficiency of the metastable decay as function of electron energy. The analogous relation calculated by RRKM theory is depicted in the same plot (dashed line). Within the middle part of the plot it is clearly seen that the calculated curve is practically coincident with the experimental one whereas in the thermal and high energy range the discrepancy is observed. The latter is obviously determined by the influence of extraneous processes which is not taken into account by the present model. In the low energy range we suppose the influence of collisional activation of ions. The capture of secondary electrons and suppression of metastable decay due to ions autoneutralization may serve as possible reasons of discrepancy at high energies. The curve of the ratio of daughter to parent ions $[D^-]/[P^-]$ (solid line) is also shown in the right panel of Fig. 3 together with corresponding calculated curve (dashed line). Observable definite disagreement between experimental and theoretical curves may be explained by partial formation of daughter ions through other (unaccounted) fragmentation channels, *e.g.* directly from molecular ion. As a result, at energies higher than 2 eV the experimental $[D^-]/[P^-]$ curve lies above the calculated one.

One of the possible applications of described statistical approach is estimation of the negative ions' internal energy distribution function what is impossible experimental task as yet. In the present instance we found the optimal shape of the distribution function *f(E)* for negative ions to be almost coincident with that of molecules (initially calculated using Boltzmann's equation), but exhibiting slight broadening, proportionally dependent on electron energy.

This work was supported by the Russian Foundation for Basic Research (№ 06-03-32412-a, 07-02-00466-a)

References

[1] Lifchitz Ch., McKenzie P., Grajover R., Weiss M. J. Chem. Phys. – 1970. – V.53. №12. – P.4605-4619.
[2] Grushina O.G., Furley I.I., Khvostenko V.I. // Teoreticheskaya I Eksperimentalnaya Khimia. – 1977. – V.14, № 4. – Pp.534-539 (in Russian).
[3] Khvostenko V.I., Rafikov S.R. // Dokl. Akad. Nauk SSSR, 1975. – V. 220. – P. 892. [Dokl. Chem., 1975 (Engl. Transl.)]
[4] Mazunov V.A., Schukin P.V., Khatymov R.V., Muftakhov M.V. // Mass Spectrometry, 2006. – V. 3(1).– P. 11 (in Russian).

P 66

High-Rate Magnetron Sputtering of Crystalline TiO2 Films

J. Šícha[1], D. Heřman[1], J. Musil[1]

[1]Department of Physics, University of West Bohemia, Univerzitni 22, 306 14 Plzen, Czech Republic
e-mail: sicha@kfy.zcu.cz

Abstract

Dual magnetron (DM) operating in asymmetric bipolar mode equipped with Ti(99.5) targets of 50mm in diameter was used for reactive magnetron sputtering of TiO_2 films in $Ar+O_2$ discharge atmosphere. The effect of repetition frequency f_r and oxygen partial pressure p_{O2} on the deposition rate a_D and hydrophilicity of TiO_2 film characterized by the water droplet contact angle (WDCA) α on the film surface after UV light irradiation has been studied in detail. Crystalline hydrophilic TiO_2 films at low substrate surface temperature $T_{surf}\approx180°C$ and high deposition rate $a_D\sim80$nm/min were prepared.

Introduction

In recent years titanium dioxide (TiO_2) has been intensively investigated due to its very good chemical stability, interesting optical properties, nontoxicity and especially due to its photoinduced superhydrophilicity and photoactivity after irradiation with UV light [1-3]. These films make it possible to convert the solar light into the chemical energy, which can be used in many applications, such as purification of water and air through the photolysis of organic and toxic compounds or killing of bacteria. Processes such as photocatalytic self-sterilization, self-cleaning or anti-fogging protection of surfaces can be realized.

This article reports on the high rate dual magnetron sputtering of crystalline hydrophilic TiO_2 films prepared at temperatures below 200°C acceptable for deposition on heat sensitive substrates and the characterization of their hydrophilic properties. The effect of time waveform evolution of sputtering pulse on properties of TiO_2 film and its deposition rate is discussed.

Experimental details

TiO_2 films with thickness h~1μm were prepared by pulsed reactive magnetron sputtering in a mixture of Ar and O_2 from Ti(99.5) targets of 50 mm in diameter. DM was operated in asymmetric bipolar mode at repetition frequency f_r ranging from 100kHz to 350kHz, average pulse discharge current $I_{da1,2}$=3A and duty cycle τ/T=0.5. Films were sputtered at substrate to target distance d_{s-t}=100mm on unheated glass substrates and maximum substrate surface temperature measured by thermostrips (Kager GmbH, Germany) was lower than $T_{surf}\leq180°C$. Photoinduced hydrophilicity was characterized by the decrease of WDCA α after 1 hour of UV light irradiation (Philips TL-DK 30W/05, W_{ir}=0.9 mW/cm^2) at the droplet volume V=4μl.

Results

The effect of f_r on the pulse waveforms of magnetron discharge and a_D of TiO_2 film was studied. It was found that the decrease of pulse period $T=1/f_r$ leads to a significant increase in a_D. In the metallic mode of sputtering a_D increases from 67nm/min to a_D=110nm/min for repetition frequencies f_r=100kHz and 300kHz at the pulse target power density 50 and 60 W/cm^2. The same effect was observed also in the oxide mode of sputtering when TiO_2 films were sputtered at p_T=0.9Pa and p_{O2}=0.15Pa. Moreover, it was observed, that increase of f_r results in the improvement of hydrophilicity of TiO_2 films, see Fig. 1. This fact is explained by the time evolution of pulse current $I_d(t)$ and voltage $U_d(t)$ waveforms of one magnetron displayed in Fig.2. The voltage waveform $U_d(t)$ can be divided into three parts: (a) plasma build-up characterized by strong increase of discharge current I_d at t<1μs (b) I_d decrease at t ranging from 1 to 3 μs due to decrease of U_d below -100 V where a very weak sputtering takes place and (c) stationary regime at t>3 μs where $U_{da}\sim400$V up to the pulse end (t=5 μs). This experiment clearly shows that the whole pulse period

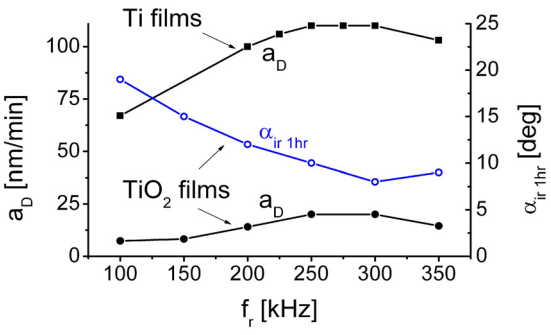

Fig.1 (i) Deposition rate a_D of Ti and TiO_2 films and (ii) hydrophilicity of TiO_2 films as a function of repetition frequency f_r.

T=10μs is very ineffectively used for sputtering of TiO_2 films. For more details see reference [4].

It means that a very simple way to increase a_D is to increase repetition frequency f_r. The increase in f_r

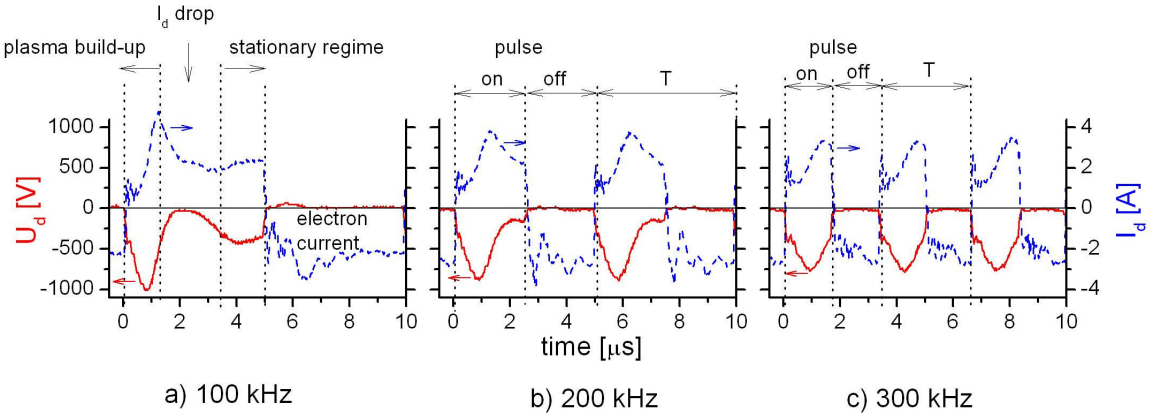

Fig.2 Time evolution of discharge voltage U_d and current I_d on one magnetron during sputtering of Ti films using dual magnetron at p_T=0.9Pa and $I_{da1,2}$=3A and three values of f_r (a) 100kHz, (b) 200 and (c) 300kHz

results in strong improvement of utilization of time due to cutting of the stationary regime of discharge and it sustaining in plasma build-up regime only, see Fig.2. Only slight increase in from 160°C to 180°C was observed when f_r was increased from 100 to 300kHz. Increase of f_r is the suitable method for improvement of a_D of photoactive TiO_2 films sputtered at T_{surf}≤180°C.

Further increase of a_D can be achieved by deposition of TiO_2 films in the transition mode of sputtering at low oxygen partial pressure p_{O2}. The effect of p_{O2} on a_D and UV induced hydrophilicity of transparent crystalline TiO_2 films sputtered at f_r=350kHz and p_T=0.75Pa is shown in Fig 3. The photoactive TiO_2 films with a_D=82 nm/min were prepared.

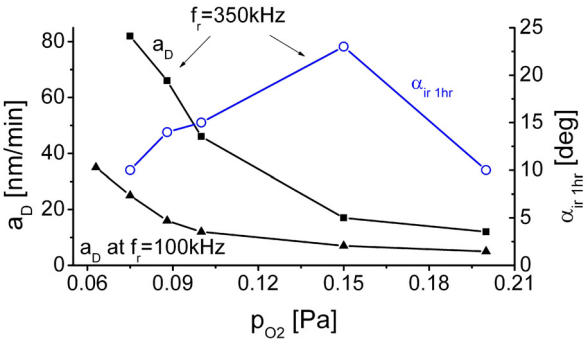

Fig.3 Deposition rate a_D and hydrophilicity of TiO_2 films sputtered at f_r=350kHz as a function of p_{O2}. a_D of films sputtered at 100 and 350 kHz are compared.

pulse
pulse
T_{surf}
thus

Acknowledgments

This work was supported by Ministry of Education of the Czech Republic (Project No. MSM 4977751302) and in part by the Grant Agency of the Czech Republic under the Project No. 106/06/0327

References

[1] A. Fujishima, K. Honda, Nature (London) 238 (1972) 37.

[2] P. Baroch, J. Musil, J. Vlcek, K. H. Nam, J. G. Han, Surf. Coat. Technol. 193 (2005) 107.

[3] J. Musil, D. Heřman, J. Šícha, J. Vac. Sci. Technol. A 24(3) (2006) 521.

[4] J.Musil, J.Sicha, D.Herman: Role of energy in low-temperature high-rate formation of hydrophilic TiO_2 thin films using pulsed magnetron sputtering, J.Vac.Sci.Technol.A (2006), submitted on November 10, 2006.

P 67

Sources of Plasma-Ion Streams for Studies of Plasma-Target Interaction

E. Skladnik-Sadowska[1], M.J. Sadowski[1-2], K. Malinowski[1], K. Czaus[1], M. Scholz[2], L. Karpinski[2], I. E. Garkusha[3], A. K. Marchenko[3] and V. I. Tereshin[3]

[1] The Andrzej Soltan Institute for Nuclear Studies (IPJ), 05-400 Otwock-Swierk n. Warsaw, Poland
[2] Institute of Plasma Physics and Laser Microfusion (IPPLM), 00-908 Warsaw, Poland
[3] Institute of Plasma Physics, NSC Kharkov Institute of Physics and Technology, 310108 Kharkov, Ukraine
e-mail: eskladnik@ipj.gov.pl

Abstract

The paper presents experimental facilities of the RPI- and PF-type, as well as results of spectroscopic- and corpuscular-measurements carried out within RPI-IBIS facility and spectroscopic studies performed within the large PF-1000.

Introduction

Studies of different materials bombarded by high-temperature plasma-ion streams are of primary importance for material engineering and for design of various technological and nuclear-fusion facilities. To perform such studies one must use experimental devices which can generate pulsed plasma-ion streams of appropriate parameters. The IPJ team developed facilities of two different types: Multi-Rod Plasma Injector (RPI) devices equipped with concentric electrodes composed of many thin rods, and Plasma-Focus (PF) devices equipped with a solid central electrode and solid or multi-rod outer one.

Experiments and results

The IBIS machine is a medium-size RPI device equipped with exchangeable coaxial electrodes made of Mo, Ti, Fe, Mg, Cu or another material. In the described experiments the inner 90-mm-dia. electrode was composed of 16 parallel Mo-rods of 2 mm in diameter, and the outer 130-mm-dia. electrode consisted of the same amount of such rods. Those rods, distributed symmetrically around the z-axis, were 200 mm in length. The discharge is powered from a 32-μF condenser bank charged usually to 30 kV. It is initiated with some delay after the injection of chosen working gas, e.g. H_2, D_2, Ar or N_2. The RPI-type facility can operate in different modes, as shown in Fig.1.

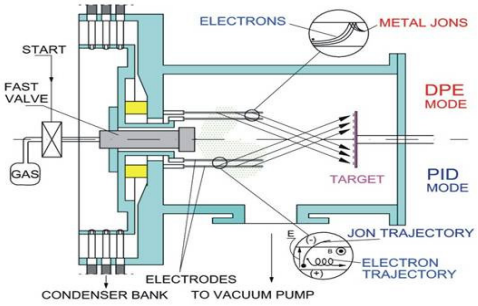

Fig.1. Scheme of the RPI-type facility and two different modes of its

If an amount of the injected gas is small one can observe the DPE mode, when a plasma stream contains ions originating mainly from the electrodes. If the gas amount is large enough one can observe the PID mode, when plasma contains ions of the working gas mainly.

The operation mode can be changed by the variation of a time delay between the gas puffing and the application of a HV pulse, as shown in Fig. 2. The RPI-IBIS facility has been used for study of the interaction of the pulsed plasma -ion streams with various targets, e.g. pure metals, alloys, semiconductors and ceramics [1]. In this machine there were recorded for the first type WI and WII spectral lines (Fig.3) emitted from a tungsten-target bombarded by the hydrogen plasma stream [2]. It is of interest for designers of fusion facilities, since tungsten is important constructional material and it is necessary to know its behavior.

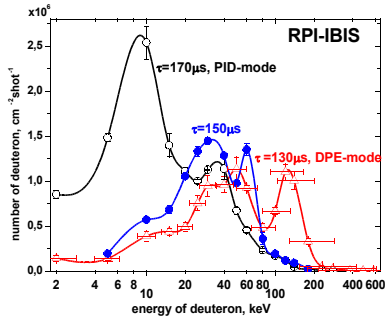

Fig.2. Energy spectra of deuterons emitted from RPI-IBIS.

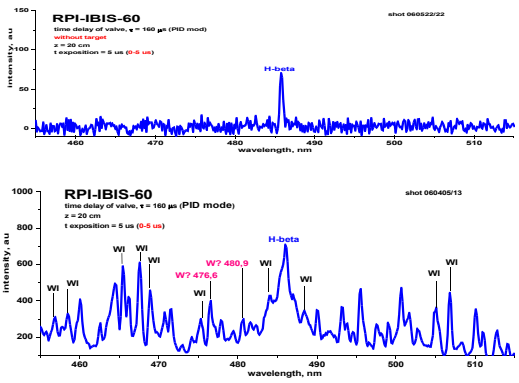

Fig.3. Optical spectra recorded in RPI-IBIS experiments without and with a W-target.

In Poland there were also constructed PF-type facilities of different energy [3]. The largest machine is the PF-1000 facility which was designed at IPJ and constructed at IPPLM [4]. During the described experiments the inner solid electrode was made of a Cu-tube of 230 mm in diameter, and the outer electrode consisted of 12 stainless-steel tubes of 80 mm in diameter, distributed symmetrically upon the cylinder of 400 mm in diameter. Those electrodes were 560 mm in length. The system was powered from a 1.32-mF condenser bank charged usually to 30 kV. The maximum current amounted to 2.3 MA.

To study behavior of different materials, various targets were placed at different distances from the PF-1000 electrode outlet, and observed with an optical spectrometer, as shown in Fig.4. Since the C- and W-based materials are of particular importance for the construction of nuclear fusion facilities, several series of measurements have been performed with C- or W-targets.

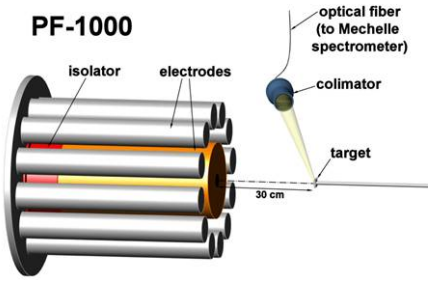

Fig.4. Scheme of coaxial electrodes and target location in PF-1000 device.

Preliminary spectroscopic studies concerned plasma streams generated by PF-1000 shots with no target. The time-resolved spectroscopic measurements showed that at the pure D_2-filling the PF-1000 facility emits first the deuterium plasma stream (one can observe intense deuterium Balmer lines), but after about 3 µs there appear intense lines (e.g. CuII, CIII, etc.) of impurities originating from the electrodes [5].

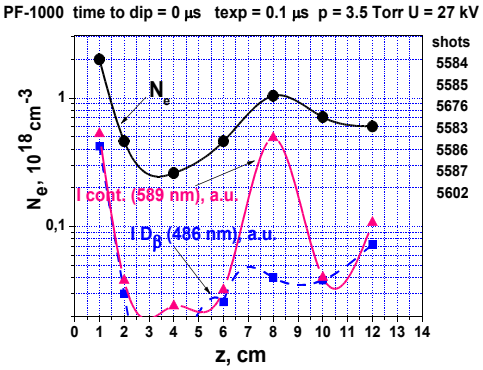

Fig.5. Axial distribution of the electron density in a deuterium plasma stream emitted from PF-1000 facility, as estimated using different spectroscopic techniques.

On the basis of the quantitative analysis of optical spectra, which were recorded at different distances from the electrode outlet, it was possible to determine the distribution of the electron concentration in the investigated plasma stream, as shown in Fig.5. It made possible to determine the proper positioning of an investigated target.

The next step was a study of plasmas formed from the chosen targets. An example of the optical spectra recorded for the composed target, consisted of a C-target upon the Cu-holder and was placed at a distance of 15 cm from the electrode outlet, is presented in Fig.6. On can easily observe that in such a case the bombarding deuterium plasma-ion stream caused first the strong erosion of the C-target (one can identify intense CI – C-IV lines), and after about 20 µs there appear CuI – Cu III lines originating from the inner electrode. The spectral analysis makes possible to compute parameters of plasmas produced from the investigated target.

Conclusions

It can be concluded that the experimental facilities of the RPI- and PF-type can be applied for research on behavior of different targets under intense corpuscular and thermal loads. It makes possible to estimate applicability of the chosen materials for harsh exploitation conditions, which appear in technological and fusion facilities.

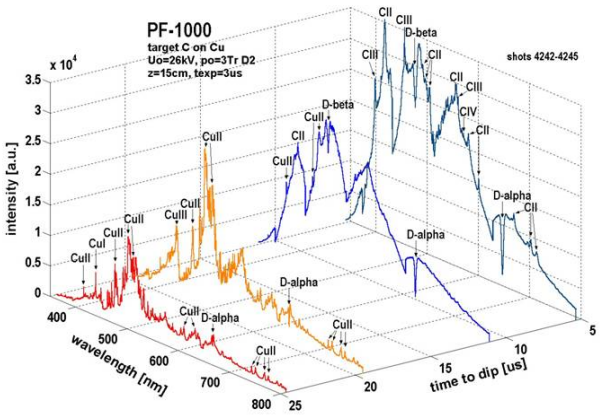

Fig.6. Optical spectra recorded during studies of the high-temperature plasma interaction with a C/Cu

References

[1] B. Sartowska, et al., *Vacuum* **78** (2005) 181-186.
[2] E. Skladnik-Sadowska, et al., *Probl. Atom. Sci. & Techn.* No. **6,** *Series: Plasma Phys.* **12** (2006) 135-137.
[3] M.J. Sadowski, M. Scholz, *Probl. Atom. Sci. & Techn.* No.**1**, *Series: Plasma Phys.* **10** (2005) 81-85.
[4] M. Scholz, et al., *Nukleonika* **51**, No.**1** (2006) 79-84.
[5] E. Skladnik-Sadowska, et al., *Czech. J. Phys.* **56**, *Suppl.* **B** (2006) B383-B388.

P 68

Comparison of Planar and Cylindrical Langmuir Probe Measurements in Low Pressure RF Helicon Reactor

R. Šmíd[1], L. Zajíčková[1], A. Granier[2]

[1]Department of Physical Electronis, Fac. of Science, Masaryk University, Kotlářská 2, 611 37 Brno, Czech Republic

[2] IMN-CNRS, UMR 6502, 2 rue de la Houssinière,B.P. 32229, 44322 Nantes cedex 3, France

e-mail: smid@physics.muni.cz

Abstract

The electron density, ion saturation current were measured in a radio frequency helicon reactor for different static magnetic field amplitude and low rf powers using cylindrical Langmuir probe, planar probe. The Different static magnetic field were applied around the and it varied from 0 to 1.4 mT in the diffusion chamber. The discharge was created in argon and oxygen at 0.7 Pa with rf powers, between 50 and 600 W. The IV characteristics from Langmuir probe were treated and electron energy probability functions (EEPFs) were finally fitted by Maxwellian distribution which was the best fit. Electron density was quantified from EEPF. We have taken ion saturation current from planar probe measurement and calculated ion density using electron temperature from Maxwellian distribution.

Introduction

Helicon generation of plasmas was first employed by Boswell [1], and were further used in material processing (e.g. [2]). Helicons are propagating whistler wave modes in a finite diameter across an insulating source wall [3] but also capacitive and inductive modes could be ignited[4]. Helicon applications to material processing utilize a process diffusion chamber downstream from the source. The present paper is focused on this type of source especially to investigation in the of plasma density which plays important role in material application. Older studies were made in the reactor with one magnetic coil around the source tube [5] and the recent one is concentrated to two coaxial coils[6].

Experimental set-up

The helicon reactor consisted of the helicon source made of a 30 cm long glass tube, 15 cm in diameter, and the stainless steel diffusion chamber with the length and diameter, both of 30 cm [5,6,7]. The source tube was surrounded by two Helmholtz coils supplied by a dc current of 0-2 A (I_B). Calculations of magnetic field amplitude in the source and diffusion chamber showed that varying the I_B in the coils from 0 to 2 A corresponded to B = 0-10 mT in the source tube and 0-1.4 mT in the diffusion chamber [7].The continuous wave rf power (13.56 MHz) in the range 50-600 W was applied to the helicon antenna through an L-type matching box. Argon or oxygen were injected through a small tube above the source directly to the source tube. Pressure was in both cases 0.7 Pa. The discharge in the diffusion chamber was investigated by a commercial cylindrical rf compensated Langmuir probe (SmartProbe, tip has 8 mm length and 0.05 mm radius (r_p))and by rf driven planar probe [8] with concentric central disc (7 mm in diameter) and an outer guard ring (16 mm in outer diameter). Both the probes had their active area in the center of the chamber, 15 cm under the source tube orifice and 4 cm above the substrate holder.

Results and discussion

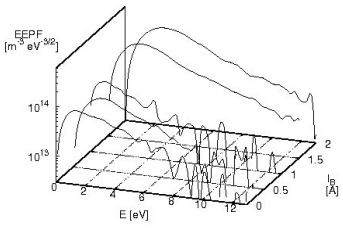

Fig. 1: Electron energy probability function for 250 W input power and different magnetic field in argon

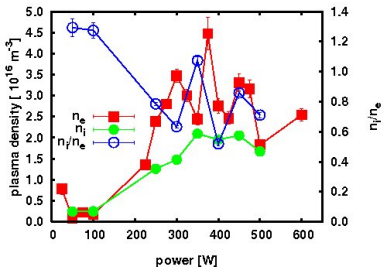

Fig. 2: Comparison of electron density from Langmuir probe with ion density by planar probe for argon discharge and I_B=2

Typical EEPFS are presented in Fig.1. Since we didn't observed two electron temperature (T_e) Maxwellian EEPFs in argon [9] typical for capacitive discharges in this pressure range we could fit them by Maxwellian distribution. This gave us reasonable value of T_e and n_e which was finally taken from integration of EEPFs.

The effect of negative ions in oxygen discharge was neglected. Electron mean free path λ_e was assumed to 12 cm in argon and 8 cm [7, 10]. Langmuir probe regimes and its reliability depends [11] on the value of λ_e, electron Debye length (λ_{De}), r_p and Larmor radius r_L [12]. The Knudsen number $K_n = \lambda_e / r_p >> 1$ for our conditions defines classical Langmuir probe. Moreover the condition for "classical" Orbital motion limited (OML) theory: $\lambda_e >> \lambda_D \geq r_p$ was also satisfied according to T_e and n_e fitted from EEPFs, since λ_D varied from 0.05 mm which is comparable with r_p to 0.4 mm [13]. Weak magnetic field influence on the IV characteristics was very well satisfied through the condition $\beta = r_p / r_L >> 1$ [11] (r_L = 4 mm). The n_e taken from Langmuir probe foregoing analysis were finally compared to the n_i taken from planar probe [8]. In this case measured ion saturation current I_{sat} is proportional to probe area A_p and its ion flux Γ_i through relation $I_{sat} = eA_p dV_{bias}/dt = eA_p \Gamma_i$. For V_{bias} around -80V we suppose that this current was predominant and electron current part was marginal. If we assume $\Gamma_i = en_i \sqrt{kT_e / M_i}$ (Bohm flux), where M_i is ion mass and n_i its density we could finally compare n_e with n_i. Since M_i in both, argon and oxygen, is more than 10^4 larger the effect of magnetic field on the ions was at least 10^2 lower. Figs. 2,3 and 4 compare n_i (planar probe) to n_e (Langmuir probe) taken from EEPF as Maxwellian fit. Presented results showed that the magnetic field could not affect the results. Ratio n_i/n_e was close to one but the calculated n_i and n_e were not the same.

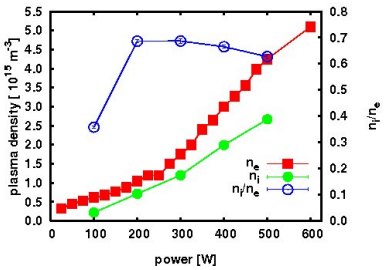

Fig. 3: Comparison of electron density from Langmuir probe with ion density from planar probe for oxygen discharge without magnetic field

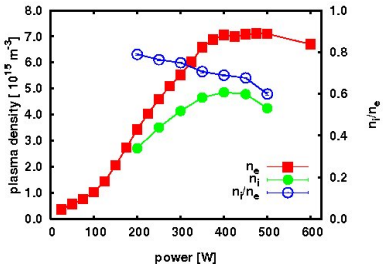

Fig. 4: Comparison of electron density from Langmuir probe with ion density from planar probe for oxygen discharge and I_B=1 A

Conclusion

We have studied plasma in the diffusion chamber of helicon reactor using cylindrical Langmuir and planar probe in the center of the diffusion chamber. Electron energy probability functions did not show two temperature Maxwellian distribution and were well fitted by one temperature Maxwellian distribution even in oxygen plasma. Langmuir probe measurements give us reasonable values of electron density which were comparable to the value of ion density taken from ion saturation current of planar probe.

References

[1] R.W. Boswell, *Phys. Lett.,* 33A, (1970) 457.
[2] A.J. Perry, D. Vender, R.W. Boswell, *J. Vac. Sci. Technol. B*, 9(2) (1991) 310.
[3] M.A. Lieberman and A.J. Lichtenberg, *Principles of Plasma Discharges and Materials Processing,* John Willey&Sons, New York, 1994, p. 434.
[4] A.W. Degeling, C.O. Jung, R.W. Boswell and A.R. Ellingboe, *Phys. Plasmas,* 3, 7 (1996) 2788.
[5] G. Borvon, *Dépot PECVD de matériaux à faible constante diélectrique*, Ph.D. thesis, Université de Nantes, 2002, in French.
[6] A. Granier, F. Nicolazo, C. Vallee, A. Goullet, G. Turban and B. Grolleau, *Plasma Sources Sci. Technol.,* 6 (1997) 147-156.
[7] R. Šmíd, A. Granier, A. Bousquet, G. Cartry and L. Zajíčková, *Czech. J. Phys.,* 56 (2006) p.B1091.
[8] N.St.J. Braithwaite, J.P. Booth and G. Cunge, *Plasma Sources Sci. Technol.,* 5 (1996) pp. 677-684.
[9] V.A. Godyak, R.B. Piejak and B.M. Alexandrovich, *Plasma Sources Sci. Technol.,* 1 (1992) pp. 36-58.
[10] L.S. Frost, A.V. Phelps, *Phys. Rev.,*136 (1964) A1538.
[11] P.M. Chung, L. Talbot, K.J. Touryan, *Electric Probes in Stationary and Flowing Plasmas:Theory and Application,* Springer-Verlag, New York, 1975.
[12] F.F.Chen, *Introduction to Plasma Physics,* Plenum Press, New York, 1984, p.33, czech translation.
[13] H.M. Mott-Smith, I. Langmuir, *Physical Review,* 28 (1926).

P 69

Space-Charge Sheaths in Atmospheric Pressure Hollow Cathodes

D. Söderström, H. Baránková and L. Bárdoš

The Ångström Laboratory, Uppsala University, P.O Box 534, 75121 Uppsala, Sweden
e-mail: daniel.soderstrom@angstrom.uu.se

Abstract

In the hollow cathode sheath, one can discern three groups of electrons: slow, fast, and secondary electrons. Usually, in the literature, only the slow electrons are taken into account when the hollow cathode sheath thickness is calculated. This gives a too thin sheath, contrary to experiments. It is shown here, that when one accounts for fast and secondary electrons in the equations for the sheath, one could get sheath thicknesses of the order of 100 μm.

Introduction

The hollow cathode effect (HCE) is the cause for the hollow cathode to be such a good source of high density plasmas. A lot of theoretical work has been done in order to understand this effect [1,2]. A generally accepted principle of the HCE can be described as the oscillation of fast electrons between the opposing space-charge sheaths in the hollow cathode. Since the dimensions and properties of the sheaths depend on the gas pressure and type of gas in the hollow cathode [3], the HCE requires an optimal width of the hollow cathode in order to allow the fast electrons to oscillate between the sheaths.

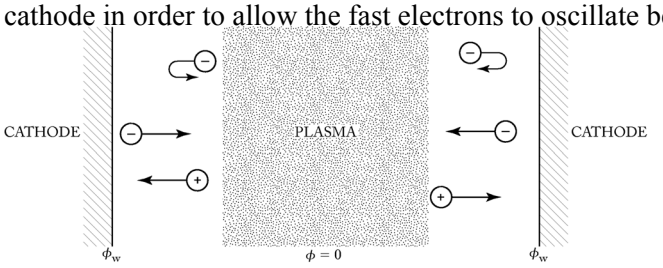

Figure 1: Schematic picture of the hollow cathode sheath region. Positive particles are ions and negative particles are electrons.

The question is then: What should the dimension of an atmospheric pressure hollow cathode be? Experiments show that the distance between the walls could be as large as 500 μm, and possibly even larger [4,5,6], particularly in radio frequency (rf) generated hollow cathodes. The structure in the hollow cathode is always wall-sheath-negative glow-sheath-wall (see Figure 1), thus the sheath dimension could be considered being of the order of 100 μm.

Sheath models based on the conventional Child-Langmuir approach gives, contrary to experiments, a sheath thickness of the order of 10 μm. Here, we will introduce a feasible model of the space charge sheath in the rf hollow cathode to show that, if we account for the characteristics of the hollow cathode, we could get a sheath thickness of the order of 100 μm.

Results and discussion

In previous works on the DC hollow cathode, the conventional Child-Langmuir approach to the sheaths has been used to support experiments [7,8,9]. However, the Child-Langmuir theory is based on a conventional DC discharge, and thus does not account for the characteristics of the hollow cathode, i.e. the fast and the secondary electrons. It has indeed been observed experimentally, that in front of a cathode, there exists a group of beam electrons [10], as well as a substantial amount of electrons in a tail extending from low to high energies. These fast electrons are thought to be secondary electrons from the cathode surface, accelerated by the sheath potential.

In total we have in the sheath region three groups of electrons: the slow, the fast, and the secondary electrons.

By using the continuity equation and the equation of motion for the ions and the secondary electrons, and assuming that the slow, as well as the fast electrons in the high-energy tail follow the Boltzmann relation

$$n_e = n_s \exp\left(-\frac{e\phi}{kT}\right), \tag{1}$$

where n_s is the density of both ions and electrons at the sheath edge, i.e. it is assumed that the plasma is quasi-neutral there, and ϕ is the electric potential. Together with the Poisson equation, we get

$$\frac{d^2\phi}{dx^2}=\frac{\epsilon_0}{e}(n_i-n_{e1}-n_{e2}-n_{e3}) \qquad (2)$$

with

$$n_i=n_s\left(1+\frac{2e\bar{\phi}}{m_i v_s^2}\right)^{-1/2}, n_{e1}=n_s(1-\beta-n_{e3_s}/n_s)\exp\left(-\frac{e\phi}{kT_{e1}}\right), n_{e2}=\beta n_s\exp\left(-\frac{e\phi}{kT_{e2}}\right),$$

$$n_{e3}=\frac{j_{e3}}{e}\left(\frac{2e}{m_e}(\phi_w-\phi)+w_c\right)^{-1/2},$$

where $T_{e2}=\theta T_{e1}$, j_{e3} is the secondary electron current at any point in the sheath, β is the ratio between the number density of fast electrons to the total number density of electrons at the sheath edge, and n_{e3_s} is the density of secondary electrons at the sheath edge. This model does not account for collisions or ionisations in the sheath. Since we are going to solve this model with an rf potential, it is assumed that the frequency of the varying potential, ω, is such that electrons are able to follow the potential but ions are only able to follow the time-average potential $\bar{\Phi}$, i.e. $\omega_{pi}\ll\omega\ll\omega_{pe}$.

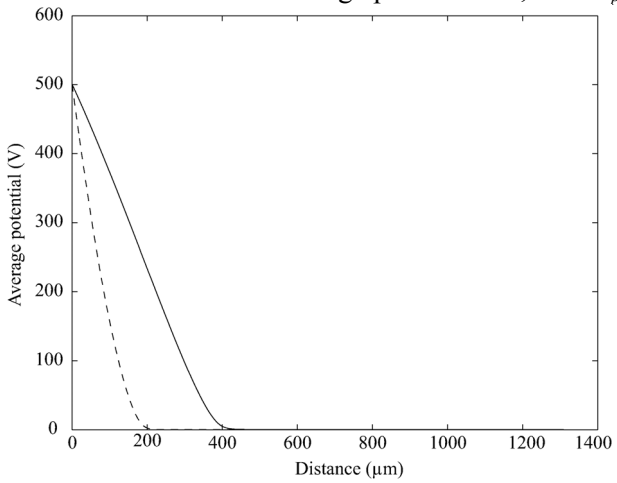

Figure 2: The sheath potential with no fast or secondary electrons, $\beta=0$, $J=0$ (normalised j_{e3}) (dashed line) and with fast and secondary electrons, $\beta=0.08$, $J=0.008$, and $\theta=80$ (full line).

Equation (2) is solved numerically with a Newton iteration method. A comparison between the sheath potentials when only slow electrons (n_{e1}) are present and when all groups of electrons are present is shown in Figure 2. The parameters given in the caption are normalised versions of the parameters in the equations above and are chosen as to resemble the distribution in [10]. As one can see, the sheath thickness is substantially increased.

Conclusions

We have introduced a simple feasible model of the space-charge sheath in an rf hollow cathode, without collisions and ionisations, to show that the sheath thickness could be of the order of 100 μm. This is due to the addition of fast and secondary electrons.

The next step would be to include collisions and ionisations in the sheath. This leads to a more complex system of equations and requires more complicated methods to solve.

Acknowledgments

Financial support from the Swedish Foundation for Strategic Environmental Research (MISTRA) is gratefully acknowledged.

References

[1] J-L. Delcroix and A.R. Trindade, in L. Marton (ed.), Advances in Electronics and Electron Physics **35**, Academic, New York (1974) 87-190.

[2] C.M. Horwitz, in S.M. Rossnagel, J.J. Cuomo, and W.D. Westwood (eds.), Handbook of Plasma Processing Technology, Noyes Publications, Park Ridge N.J. (1990) 308-335.

[3] L. Bárdos and H. Baránková and S. Berg, *Surf. Coatings Technology* **72** (1995) 174.

[4] R.H. Stark and K.H. Schoenbach, *Appl. Phys. Lett.* **74** (1999) 3770.

[5] H. Baránková and L. Bárdos, *Appl. Phys. Lett.* **76** (2000) 285.

[6] H.I. Park and T.I. Lee and K.W. Park and H.K. Baik and S-J. Lee and K.M.Song, *Appl. Phys. Lett.* **82** (2003) 3191.

[7] M. J. Kushner, *J. Phys. D: Appl. Phys.* **38** (2005) 1633-1643.

[8] K. H. Schoenbach and A. El-Habachi and W. Shi and M. Ciocca, *Plasma Sources Sci. Technol.* **6** (1997) 468-477.

[9] K. H. Becker and K. H. Schoenbach and J. G. Eden, *J. Phys. D: Appl. Phys.* **39** (2006) R55- R70.

[10] P Gill and C E Webb, *J. Phys. D: Appl. Phys.* **10** (1977) 299-311.

P 70

Investigation of Pulsed Magnetron Discharge at Different Frequencies During Deposition of TiO_x Thin Films

V. Straňák[1,2,3], Z. Hubička[2], P. Adámek[2,3], P. Virostko[2], J. Blažek[3], S. Wrehde[4], M. Tichý[1], R. Hippler[4]

[1]Faculty of Mathematics and Physics, Charles University, V Holešovičkách 2, 180 00 Praha 8, Czech Republic
[2]Academy of Science of the Czech Republic, Institute of Physics, Na slovance 2, 180 00 Prague 8, Czech Republic
[3]Department of Physics, University of South Bohemia, Jeronýmova 10, 371 15 České Budějovice, Czech Republic
[4]Institute of Physics, University of Greifswald, Domstrasse 10a, 174 89 Greifswald, Germany
e-mail: stranv00@centrum.cz

Abstract

The dc planar magnetron, used for deposition of TiO_x thin films, was operated in pulsed regime. The magnetron system was equipped by Ti target, discharge was created from mixture of Ar (19 sccm) and reactive admixture O_2 (0.3 sccm). The repetition frequency was varied from 250 Hz up to 6.3 kHz with the same length of active part T_{active} = 150 μs. The average current was kept constant in all measurements at I_{av} = 550 mA. The generated plasma was investigated by time-resolved Langmuir probe measurements and time-resolved photon counting measurements. Plasma density, plasma potential, electron temperature and discharge current were main quantities of our interest.

Introduction

In conventional magnetrons operated in continuous mode, the electron density is generally about $n_e \approx 10^{15}$–10^{16} m^{-3} [1]. One way how to achieve higher plasma density is to operate the magnetron system in pulsed regime. In such manner the instant discharge current in the active pulse can be very high while the average discharge current can be kept low; at similar magnitudes as when the system works in continuous mode. Low and mid-frequency pulsed discharges with the repetition frequency 2 – 350 kHz and duty cycles about 50% were carefully theoretically as well as experimentally studied in several works e.g. [2,3]. The measured electron density was roughly $n_e \approx 10^{16}$ m^{-3}. High power magnetron sputtering in pulsed regime, which uses peak power densities of the order of $kW.cm^{-2}$ with duty cycles of 1% at low repetition frequency 50 Hz e.g. [4,5], where $n_e \approx 8.10^{18}$ m^{-3} were studied, too. However, it was shown that despite high electron density the deposition rate in this case is lower because of short length of active part. In this work we investigated basic plasma parameters of magnetron operated in metallic mode of deposition in dependence on repetition frequency (250 Hz, 6.3 kHz). The average current was kept constant at I_{av} = 550 mA while the instant current in the active parts of pulses was changed (at frequency 250 Hz maxima peak current reached $I_{active} \approx$ 20 A). The pressure in the vacuum vessel was kept at p = 10 Pa for all measurements.

Overview of experimental results and discussion

The experiments were done using commercial magnetron of the type Vtech 75 by Gencoa. The magnetron was operated in unbalanced mode. The plasma was excited by combination of dc voltage supply working up to dc voltage -620 V (maximum dc current 1 A) and pulse modulator provided with large capacitors. In such manner it was possible to achieve high discharge current during the active pulse. This system was capable to excite dc pulse magnetron discharge with maximum average current 1A but with maximum current around 20 A at repetition frequency 250 Hz and pulse width 150 μs. In series with the discharge path, a ballast resistor (R = 3.5 Ω) was inserted in order to avoid arcing and stabilize the discharge current. Time evolution of the cathode voltage U_C measured directly on the cathode is depicted in Fig.1. For low frequency 250 Hz the U_C linearly increased during the first 30-70 μs of the modulation cycle before it reached the maximum value. Time evolution of U_C corresponds with behaviour of instant discharge current.

The generated discharge was investigated by time-resolved Langmuir probe measurements and time resolved photon-counting measurements. Hence, the Langmuir probe and optical fibre were inserted into the chamber. The emitted light from the discharge was filtered by frequency filter. After that the signal of desired spectral line (particular wavelength) was amplified and subsequently stored into RAM buffer with high resolution 10 ns. The stored data were subsequently read out and processed by computer. The time evolution of spectral lines Ti (λ_{Ti} = 518.96 nm) and atomic Ar (λ_{Ar} = 420.07 nm) are depicted in Fig.2. The intensities of Ti lines were several times higher compared to those of Ar (in Fig.2 the normalised intensities are shown). Intensities of spectral lines at higher frequency 6.3 kHz increased almost linearly during the whole period 10

μs after ignition while at frequency 250 Hz were linear or even decreased.

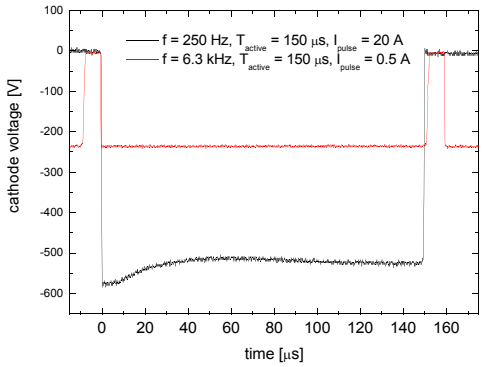

Fig.1. Time evolution of cathode voltage U_C in active pulse time p = 10 Pa, Ar 19.5 sccm, O_2 0.3 sccm, $I_{average}$ = 550 mA.

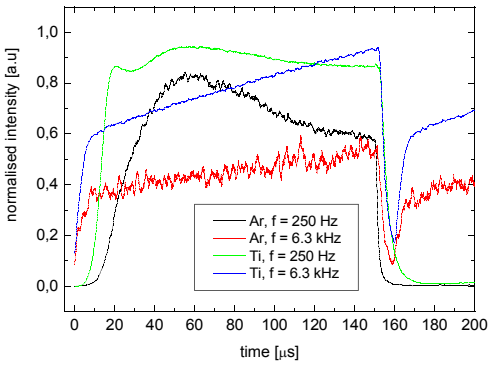

Fig.2. Time evolution of particular spectral lines Ti (λ_{Ti} = 518.96 nm) and Ar (λ_{Ar} = 420.07 nm), p = 10 Pa, Ar/ O_2 (19.5/0.3) sccm, I_{aver} = 550 mA.

The measured probe data were processed by standard ways and basic plasma parameters were determined. The electron densities n_e were strongly dependent on repetition frequency and differed by more than one order of magnitude from each other, see Fig.3 – left scale and solid lines. Decreasing of electron temperature T_e during active part of period was probably caused by ionisation of sputtered particles Ti; compare Figs.2 and 3. Plasma potential V_{pl} linearly increased during first 150 μs (active part of discharge). We attribute the negative values of V_{pl}, observed at lower frequency, to the strong electric field that appears between cathode and grounded reactor in the first instant of the active part of the modulation cycle. This field gradually relaxes because it becomes partially shielded due to the formation of the cathode fall with positive space charge of ions and $|V_p|$ decreases.

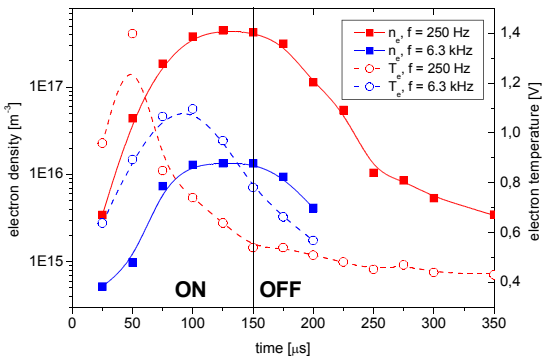

Fig.3. Time evolution of electron density and electron temperature, p = 10 Pa, Ar/ O_2 (19.5/0.3) sccm, $I_{average}$ = 550 mA.

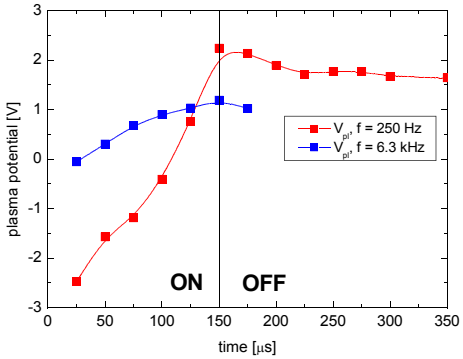

Fig.4. Time evolution of plasma potential, p = 10 Pa, Ar/ O_2 (19.5/0.3) sccm, $I_{average}$ = 550 mA.

Acknowledgment

This work was financially supported by the research plan MSM 1M06002 of MSMT of the Czech Republic, and grant GACR 202/05/2242 of Czech Science Foundation.

References

[1] V. Straňák, H. Steffen, S. Wrehde, R. Hippler, M. Tichý, *Czech. J. Phys.* Vol. 54, Suppl. **C,** (2004), 826.

[2] H. Backer, J.W. Bradley, *Plasma Sourecs Sci. Technol.* 14, (2005), 419.

[3] J. W. Bradley, H. Backer, *Surf. Coat. Technol.* 200, (2005), 616.

[4] V. Kouznetsov, K. Macák, J.M. Schneider et al, *Surf. Coat. Technol.* 122, (1999), 290.

[5] K. Macák, V. Kouznetsov, J.M. Schneider, U. Helmersson, *J. Vac. Sci. Technol.* A18, (2000), 1533.

P 71

Deposition of Protective Coatings in Surface Barrier Discharge at Atmospheric Pressure

P. Sťahel, V. Buršíková , Z. Navrátil, P. Kloc, A. Brablec, J. Čech and J. Janča

Department of Physical Electronics, Masaryk University, Kotlarska 2, 611 37 Brno, Czech Republic)
e-mail: pstahel@physics.muni.cz

Abstract

Surface barrier discharge operated at atmospheric pressure was used for deposition of thin protective hydrophobic films from mixture of nitrogen with C4F8 on the paper substrate. The plasma was investigated by means of optical emission spectroscopy. Surface properties of the deposited films were studied by means of the contact angle measurements. The colorimetric parameters such as whiteness, yellowness or brightness of samples were measured in its deposited state and also in UV exposed states.

Introduction

Recently the technologies based on plasma technology become very promising. The atmospheric pressure barrier discharges offer several advantages for the modification of low-cost materials: costly vacuum equipment is not necessary, processing times are reduced and the plasma modification of large surfaces is simpler than in low-pressure plasma reactor.

In this work the surface barrier discharge operated at atmospheric pressure was used for deposition of thin protective hydrophobic films.

The aim of this work is to demonstrate the good protective properties of films deposited by means of this technique. Variation of colorimetric parameters of samples such as whiteness or yellowness caused by plasma deposition is shown. Changes of these parameters under intensive UV radiation were studied too.

Experimental

The surface discharge was used for the deposition of teflon like films [1]. The surface power density was varied from 0.25 to 1.0 W/cm^2. In this study the deposition time 90 s was kept and the concentration of C_4F_8 in nitrogen was also kept constant in all cases. Flow rates were 0.5 slm C_4F_8 in 10 slm of pure nitrogen. Filter paper was used as a substrate. The discharge was studied by means of the optical emission spectroscopy using the Jobin-Yvon TRIAX 550 monochromator. The total surface energy of samples γ^{TOT} and its components γ^{LW}, γ^{AB}, γ^{+}, γ^{-} were investigated by means of Surface Energy Evaluation System (SEE System, http://www.seesystems.wz.cz). The samples surface free energy and its components were calculated according to Lifshitz Van der Waals/acid base approach proposed in [2]. UV degradation tests were performed in device equipped by Hg high pressure lamp 300 W with 40 mW/cm^2. The temperature of sample during degradation experiment was kept constant (40 ^{o}C). The wetting properties were studied by means of industrial permeability tests consistent with the norm ISO 9073-8:1995. Chemical composition of deposited films was investigated by means of infrared spectroscopy.

Results and discussion

The fluorinated (teflon like) materials are widely used for their low surface energy and low wettability. In Fig. 1 the dependencies of total surface energy γ^{TOT} and its components γ^{LW}, γ^{AB}, γ^{+}, γ^{-} are plotted as a function of power density. Samples deposited at power densities higher then 0.35 W/cm^2 show similar surface hydrophobic properties, however samples deposited at lower power densities exhibit high surface energy.

Fig. 2 shows power density dependencies of the whiteness *W* and yellowness *Ye* of samples. Solid lines are used as a guide of eyes. Yellowness of the sample increases and whiteness decreases with increasing power density. These colour changes include not only changes caused by creation of film on the surface but also thermal and UV degradation of substrate during the deposition. The electrodes were heated by the discharge without external cooling, i.e. electrode temperature was different for different power densities. Therefore, the electrode temperature raised with rising power density.

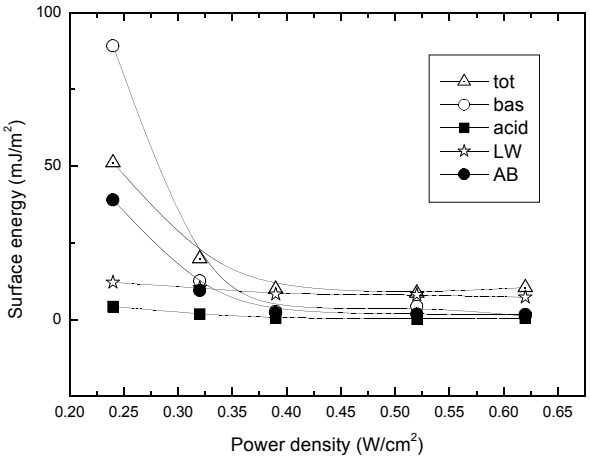

FIGURE 1. Dependence of total surface energy γ^{TOT} and its components γ^{LW}, γ^{AB}, γ^{+}, γ are plotted as a function of power density

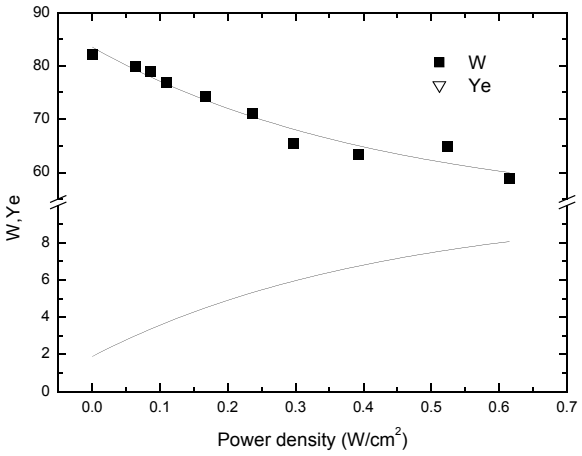

FIGURE 2.. Dependence of the whiteness *W* and yellowness *Ye* of as deposited samples on the power density.

Conclusions

Highly hydrophobic thin films were prepared by a deposition technique based on the atmospheric pressure surface barrier discharge. The thin films were prepared from mixture of octafluorcyclobutane C_4F_8 with nitrogen at different discharge power densities.

Colorimetric parameters as whiteness and yellowness of samples were studied in as deposited and also in UV exposed states. Coated samples exhibited considerably higher UV radiation resistance than uncoated samples. This type of coating is possible to use as a highly effective transparent protection of solids against UV radiation and against humidity.

Acknowledgments

This research has been supported by the grant No. 202/05/0777, Grant GAAV KAN101630651 and the Long-term intent project No. MSM0021622411, Ministry of Education, Czech Republic.

References

[1] P. Sťahel, V. Buršíková, M. Šíra, Z. Navrátil, P. Kloc, J. Janča, *J. Adv. Oxid. Technol.*, 2,(2006) p. 228
[2] M. N. Belgacem, A. Blayo, A. Gandini: Journal of Colloid and Interface Science 182 (1996) 431

P 72

Physics of Filamentary Discharges through Porous Media for Plasma Assisted Catalysis Applications

P. Tardiveau[1], A. Combe[1], C. Postel[1], S. Pasquiers[1], K. Hensel[2], Z. Machala[2]

[1]Laboratoire de Physique des Gaz et des Plasmas, Bât 210, Université Paris-Sud,
15 rue Georges Clémenceau 91405 Orsay Cedex, France
[2]Department of Plasma Physics, Comenius University, Mlynská dolina, Bratislava 842 45, Slovakia
e-mail: pierre.tardiveau@u-psud.fr

Abstract

In the context of gas treatment by catalysis oxidation assisted by non-thermal plasma, investigations on pulsed corona streamers in porous catalysis media are reported. Fast optical imaging coupled with current waveforms analysis gives precise information on streamers propagation in heterogeneous structures such as "honeycomb" ceramic monoliths or simple porous ceramics. In those cases, it is observed that space and time development of discharges is very different according to the nature and the size of the support, which lets us suppose that charge mechanisms and porosity effects are mainly involved.

Introduction

In order to treat pollutants such as volatile organic compounds (VOC), recent research showed the interest of the association of two processes: oxidation by catalysis and treatment by non-thermal plasma. This combination requires the use of catalyst supports inevitably modifying the physicochemical properties of the plasma [1,2,3]. The optimization of depollution processes involving this technique requires then the comprehension of plasma development in strongly inhomogenous structures.

Our work mainly relates to the study of a point-to-plane reactor for which plasma is created by a "bush" of filamentary discharges and where the catalyst support is a honeycomb monolith of various nature and geometry. The main objective of the study is to understand the effects of the catalyst support on the space and time development of these discharges. It is completed by the work of K. Hensel on the development of pulsed filamentary discharge inside porous ceramics with different pore sizes [4].

For that purpose, filamentary plasma is generated under short impulse high voltage allowing the use and triggering of fast opening and streak cameras. Optical measurements will be made to describe rather precisely how the filaments propagate within the support. Besides, voltage and currents waveforms treatment will give information of how energy is distributed within the support. Comparisons will be made on plasma properties when developping within or without the catalytic support. The effects of the nature and the geometry of the support will be studied. Several types of materials will be tested with various sizes of channels.

This experimental study intends to bring comprehension on the effects of catalytic support surfaces on non-thermal plasma development and reactivity. Charge mechanisms and temperature effects due to these surfaces will be discussed. Previous experiments on a plane-to-plane cordierite DBD reactor where much more streamers propagated within the structure will support our discussion.

Results and discussion

The experimental setup consists of short positive high voltage pulses (50 ns) supplied by a coaxial line generator to a point made of rhodium with a tip radius of 100 µm. The ground plane is divided into five concentric rings, each grounded through a 50 Ω resistance. Small pieces of dielectric honeycomb monoliths made of porous cordierite or mullite-zircone and with different sizes can be inserted between the two electrodes. Different support walls thickness between 150 to 500 µm can be tested and the number of channels lying between the electrodes ranges from one to four. Currents and voltage waveforms are respectively recorded through 50 Ω resistances and a voltage capacitive divider, all connected to a fast digital oscilloscope. By means of appropriated delay units, a short time integration camera (50 ns) and a high speed streak camera (2mm/ns on images), both coupled to intensifiers, are triggered. By simultaneous recordings of still and streak images of a discharge, space and time development in honeycomb monoliths can be rather precisely determined.

When a monolith is inserted between the point and the plane, the behavior of the discharge is very different from what occurs in air and it depends on the properties of the support. Using cordierite of 2.5 mm height, with two channels and a wall thickness of 150 µm, only one, two or maximum three streamers

propagate through the channels. On streak pictures as shown on Figure 1, the discharge in cordierite shows two luminous parts. The first one is its propagation from the point to the top surface of the monolith and the second one is inside the channels. One can estimate the propagation velocity of the streamers inside the channels to about 2.10^7 cm/s.

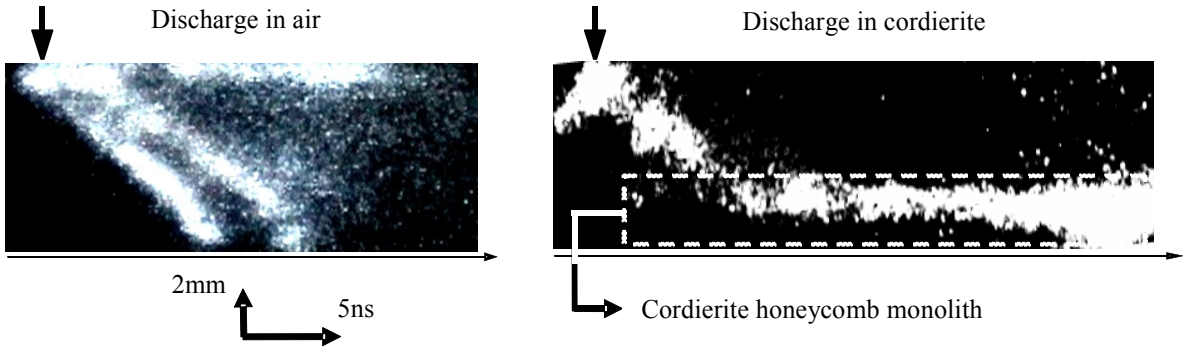

Figure 1. Streak pictures of discharges in air and in a monolith of cordierite (400 cpsi, 2 channels, 150 µm).

This two-steps process can be identified on the current waveforms where two different pulses can be observed. A first current pulse which is similar for all plane strips corresponds to a displacement current when streamers develop from the point and hit the dielectric surface. This part allows estimating the charge density deposited onto the surface, with a typical value of 200 $\mu C/m^2$, probably necessary to induce a sufficiently high electric field (about 25 kV/cm) inside the channels so that the discharge can propagate inside. The second pulse arises 20 to 30 ns later and displays the arrival of streamers at the plane electrode. When the number of channels or the wall thickness is increased, the ability for the discharge to initiate within the channels is weaker. This point does not seem so clear since the field at the surface should not depend on the geometric characteristics of the monolith. However, these observations are made with another material which is mullite-zircone, whose mechanical properties are quite different from those of the cordierite which seems to be quite much porous. The physical properties of the support such as porosity may then have an effect on the discharge development. This effect has been shown for AC discharges developing through porous ceramics of different pore sizes between two meshes [4].

Conclusions

Electrical and fast optical records are performed to analyse the propagation of streamers through the channels of a dielectric honeycomb monolith. It is observed that some streamers are able to expand through the channels with lower velocities than in the air. Their ability to cross the media seems to be correlated to the charge density deposited on its top surface, which needs to be high enough to reach the critical field for streamers development. The geometric and physical properties of the dielectric have a noticeable influence on the behavior of the discharge, with a better propagation for thin walls and porous materials.

References

[1] S. Ibuka, T. Nakamura, T. Murakami, H. Kondo, K. Yasuoka, S. Ishii, "Novel plasma reactor using honeycomb ceramics driven by a fast SI-thyristor for environmental applications", Pulsed Power Plasma Science, 2, 2001, pp. 1118-1121

[2] P. Tardiveau, C. Boyer, F. Jorand, C. Postel, S. Pasquiers, "Optical and electrical characterization of pulsed dielectric barrier discharges in heterogeneous structures", IEEE transactions on plasma science, 33, 2005, pp. 314-315

[3] N. Blin-Simiand, F. Jorand, S. Pasquiers, P. Tardiveau, "Removal of 2-heptanone by dielectric barrier discharge in air and in a monolith of cordierite", Proceedings of the 4th International Symposium on Non-thermal Plasma Technology for Pollution Control and Sustainable Energy Development, 1, 2004, pp. 254-258

[4] K. Hensel, M. Janda, M. Lestinsky, Z. Machala, V. Martisovits, P. Tardiveau, A. Mizuno, "Electrical and optical properties of AC microdischarges in porous ceramics", 10th International Symposium on High Pressure Low Temperature Plasma Chemistry, pp. 41- 46, 2006

P 73

Generation of Particles Positions for Initialization of Particle Simulation According to Schottky Theory

V. Tarjáni, J. D. Skalný

Department of Experimental Physics, Faculty of Mathematics, Physics and Informatics, Comenius University, Mlynská dolina, 842 48 Bratislava, Slovak republic
e-mail: tarjani@neon.dpp.fmph.uniba.sk

Abstract

The possibility how to generate particle position for starting up 1d particle-in-cell (PIC) simulation of a steady regime of positive column in glow discharge is discussed. The formula, which may be used for generation of particle position with distribution according to Schottky theory, was derived. This will be used in our PIC code.

Introduction

Primary aim of the study is developing of 1d3v code based on a PIC method and using this for simulation of the steady regime of positive column in glow discharge bounded by two plan-parallel non-conducting walls [1]. The direction perpendicular to the walls was simulated. To being able to start the simulation from scratch particle position (together with velocity of particles) has to be generated.

In previous PIC code [2] we have used simple particle loading with uniform distribution of positions. However it seems to be not very suitable for our purpose because such distribution is not realistic if a steady regime of positive column is analyzed. Therefore we have decided to search a distribution being able to describe particles distribution in real discharge. In the steady regime no electrical current flows to the wall and because of diffusion of charged particles to the insulating walls there is a gradual fall of concentration approaching the wall, which forms a typical diffusion shape of particles concentration *n(x)*. For this regime it is possible to start from a Schottky theory which is applicable under these conditions. On the basis of the Schottky theory we are trying to derive cumulative distribution function (CDF) for distribution of particle position and invert it (if possible) in order to obtain final expression for generation of particle position.

Results

Intuitively we expect that probability density function (PDF) will be proportional to particles concentration with factor labeled *k*, i.e.:

$$f(x) = kn(x) \quad for\, 0 \le x \le L$$

Schottky theory (see for example [1]) gives us function dependence of concentration *n(x)*. If the left wall is placed to position $x = 0$, right wall to $x = L$, then the plane of symmetry is in position $x = L/2$ and the distance between two walls is L. In this configuration we obtain from Schottky theory following expression:

$$n(x) = n_0 \sin\left(\frac{\pi}{L}x\right)$$

where n_0 is concentration in plane of symmetry. Substituting (2) to (1) we can obtain for PDF expression:

$$f(x) = k\, n_0 \sin\left(\frac{\pi}{L}x\right) \quad for\, 0 \le x \le L$$

To satisfy normalization condition [3] for this PDF, factor *k* must be

$$k = \frac{\pi}{2 n_0 L}$$

Integrating PDF in the limits $-\infty$ to x we may now obtain CDF in the form

$$F(x) = \frac{1}{2}\left[1 - \cos\left(\frac{\pi}{L}x\right)\right]$$

By inversion of this CDF the equation for particle position can be expressed as follows

$$x = \frac{L}{\pi}\arccos\left(1-2R\right)$$

This relation is used in such way that substituting R with random numbers which are uniformly distributed over interval $\langle 0,1)$ we obtaining values of particle position according to Schottky distribution – eq. (3), (5).

Conclusion

The relation (6) has been derived, which we want to use for the generation of particles position distributed according to Schottky theory. It must be noted that derived formula (6) is valid only for 1d planar model and thus for the other geometry must be modified. For example in cylindrical (radial) geometry analogous relation must be derived from concentration profile expressed by Bessel function – see for example [1].

Acknowledgments

This work was partially supported by Slovak Grant Agency VEGA under project 1/1267/04 and ESF projects COST P9 and EIPAM. This work was also supported by Science and Technology Assistance Agency under the contract No. APVT-20-007504.

References

[1] Martišovitš, V.: *Základy fyziky plazmy (Učebný text pre 3. ročník magisterského štúdia)*. Bratislava, FMFI UK, 2004.

[2] Tarjáni, V.: *Modelovanie kladného stĺpca v tlecom výboji (diplomová práca)*. Bratislava, FMFI UK, 2005.

[3] Tarjáni, V.: *Metódy generovania polôh a rýchlostí častíc použiteľné v simuláciach particle-in-cell (PIC)*. Bratislava, FMFI UK, 2006.

P 74

Surface Modification of Paper by Atmospheric DBD in N_2 with HMDSO and Chitosan to Enhance its Strength and Protection against Aging

B. Trnovec, M. Mikula

Department of Graphic Arts Technology and Applied Photochemistry, Faculty of Chemical and Food Technology, Slovak University of Technology, Radlinského 9, SK-812 37 Bratislava,
e-mail:bystrikt@gmail.com

Introduction

Aging of paper is accompanied by irreversible physical and chemical changes caused by hydrolytic and oxidative degradation leading to yellowing and embrittlement of paper [1]. Degradation processes are enhanced by humidity, higher temperature, light, by the presence of oxygen, SO_2 and NO_x emissions. Plasma treatment of paper, cellulose and nonwovens begins just recently, particularly in restoration and stabilization of old books and documents [1 ,2, 3, 4], where some strengthening, cleaning, cracks healing and even deacidification in basic (nitrogen or NH_3) plasma occurred. The aim of this work was to treat and modify papers in nitrogen plasma of dielectric barrier discharge at atmospheric pressure applying reactants, to increase its aging resistance.

Experimental

We have used newsprint paper (sheet NP, 45 gm^{-2} , thickness of 70 µm, and web NP, 45 gm^{-2}, thickness of 60 µm), reactants: chitosan (Chit) - alkalic polysaccharide with amino groups, Hexamethyldisiloxan (HMDSO) – low molecular weight linear siloxan, can make solution in water in low concentrations.

Modified papers were artificially aged by new accelerated method by Begin-Kaminska [6]: 6 g of a paper was preconditioned at relative humidity RH = 50 % (at 23 °C, 2 days), afterwards enclosed into 300 ml glass bottle, covered by Viton® (DuPontDow) sealing and heated to 100 °C for 5 days. The aging better correlates with the natural one than a dry or wet aging.

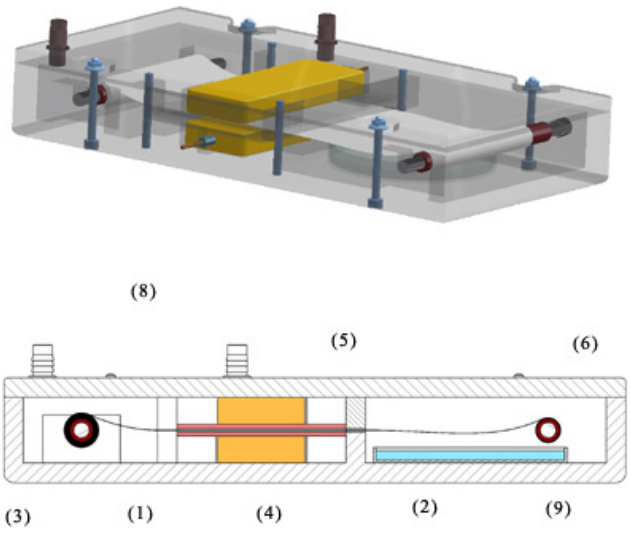

Fig. 1: DBD, 1 – discharge part, 2 – postmodification part, 3 – paper roll, 4, Cu – electrodes, 5 – barrier, 6 – papercoiling, 8 – in/out of gas, 9 – dish with HMDSO

The type of discharge arrangement was follows: dielectric barrier discharge (DBD) [5] with both side glass barriers with the treated paper moving inside 1 mm discharge gap (Fig. 1).

In one case the paper was first both side coated by a reactant from water solution of Chitosan – 2.2 wt.%, dried and afterwards treated by plasma. In other case the uncoated paper was exposed to a mixture of nitrogen and HMDSO vapor plasma in two manners: 1. Free evaporation of HMDSO from Petri dishes after plasma treatment in reactant – box ("HMDSO-after"), 2. Plasma treatment in the mixture of Nitrogen and HMDSO (N_2 was first flown through the HMDSO fluid, and then came to the discharge – box, "HMDSO-in").

Original and modified papers were tested mechanically, optically, spectroscopically and by wettingproof by: double fold test (Schopper instrument), colorimeter ELREPHO 2000, DATACOLOR by D65, 10°, spectrophotometer EXCALIBUR FTS 3000 MX (DIGILAB), sessile drop measurement of water soaking by CCD - camera (SEE – system, MU Brno).

Results and discussion

We have used atmospheric pressure. To get more diffuse and homogeneous DBD we used glass barrier on both sides of the gap between the electrodes.

Generally, the number of double folds increased after the application of modifying agent and slightly decreased after plasma treatment.

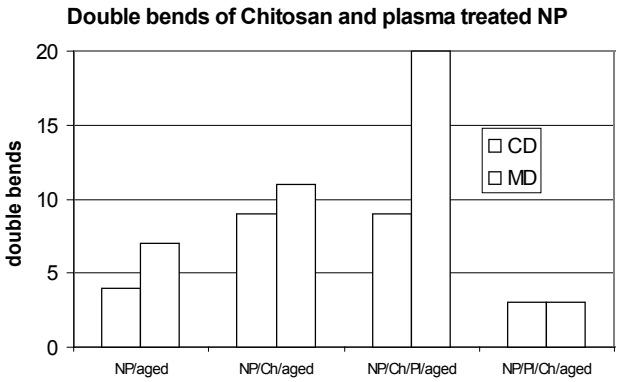

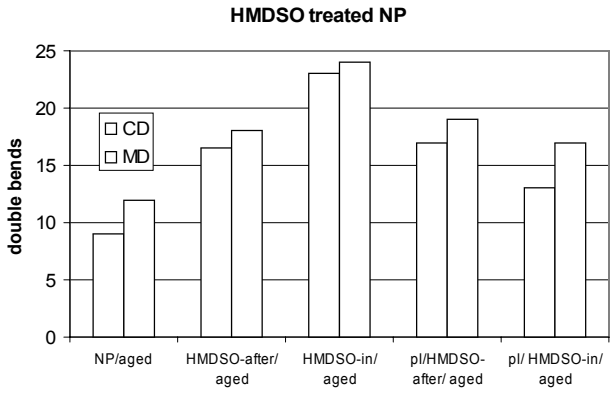

Considerable decrease occurred after ageing except the case of plasma treated paper with chitosan in the direct DBD regime. In this case the plasma induced crosslinking and grafting exceeds degradation processes caused by plasma.

As expected, considerable changes of whiteness, brightness and gloss were confirmed for coated and especially for aged papers, however, the lightness L* was changed a little.

The time of water soaking, Fig. 3, for HMDSO treated and aged paper is much longer than by clear aged paper. This is the same at both of the treatment-types.

FTIR absorption spectra of papers differ when using DRIFT or Diamond ATR techniques. DRIFT gives the information about the whole semi-transparent paper (due to IR light scattering inside the paper). This mixed reflection/absorption spectrum is useful outside the regions of high absorption, where the internal remission exceeds the influence of gloss. However, the changes with aging or plasma treatment in IR absorption are minimal. HMDSO grafts are readable at 1090 cm^{-1} (Si-O) and 1260, 800 cm^{-1} ($Si-CH_3$).

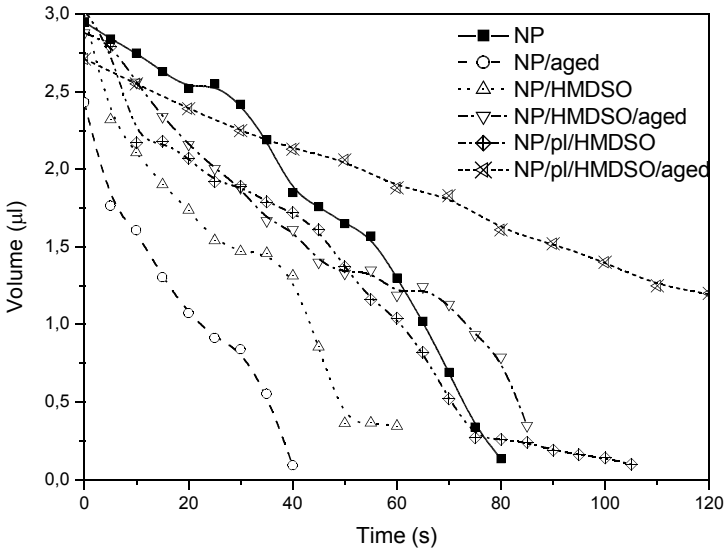

Fig. 3: Volume of water drop soaking into modified paper. HMDSO was applied after plasma treatment.

References

[1] Vohrer U., Trick I., Bernhardt J., Oehr C. and Brunner H.: *Plasma treatment - an increasing technology for paper restoration?* Surface and Coatings Technology 142-144, 1069-1073 (2001)

[2] Denes A.R., Tshabalala M.A., Rowell R., Denes F., Young R.A.: *Hexametyldisiloxane-plasma coating of wood surfaces for creating water repellent characteristics*, Holzforschung 53 (3), 318 – 326, (1999)

P 75

Interference Effect in Phase Separation of the Ni+C_{60} Composite Induced by Laser Illumination through an Array of Pinholes

J. Vacík[1], V. Lavrentiev[1], V. Havránek[1], S. Kitazawa[2], V. Vorlíček[3], L. Juha[3]

[1]Nuclear Physics Institute, Academy of Sciences of the Czech Republic, 20 68 Řež, Czech Republic
[2]Japan Atomic Energy Agency, Tokai-mura, Ibaraki 319-11, Japan
[3]Institute of Physics AS CR, Na Slovance 2, 182 21 Prague 8, Czech Republic
e-mail: vacik@ujf.cas.cz

Abstract

Phase separation of a thin film of the binary composite of Ni and C_{60} has been studied using laser illumination of the sample through an array of pinholes (with 10 micrometer large diameters and 40 micrometer spacing). The mesh with pinholes enabled splitting of the probing beam into an array of close-spaced microbeams. The simultaneous illumination of the composite with the system of microbeams resulted in a fast phase separation of the hybrid matter and an occurrence of the unusual interference effects. The results confirmed the high proclivity of the Ni+C_{60} composite to a correlated separation of the Ni and C-allotrope phases.

Introduction

In ref. [1] it was reported that using the Nd:YAG laser (with the pulse intensity of about $5x10^4$ W/cm^2) thin films of nanostructural hybrid composites, synthesized by vapor co-deposition of the transitional metal atoms and C_{60} molecules (e.g., Ni+C_{60}), undergo a fast phase separation accompanied by a massive $C_{60\ cage}$ fragmentation (and its transformation into amorphous carbon, a-C). It was shown that the defocused laser beam (illuminating the whole body of the sample) may induce both long-range as well as short-range (local) phase separations. The long-range separation resulted in the formation of large interspersed Ni and/or a-C rich areas with chaotic shape boundaries. The local separations, on the other hand, evolved coordinately into so called 'laser induced periodic surface structures' (LIPSS) formed densely in the a-C rich areas. The process of the long-range collective partitioning of the Ni+C_{60} hybrid composite was explained by an uncorrelated release of the stress accumulated in the thin film due to constrained co-existence of two immiscible phases (Ni and C allotropes) that was triggered by the laser impact. Local partitioning into LIPSS, however, could be understood by a mechanism of a multiple release-and-drift of the stress that occurs due to a sudden excess of the thermodynamic instability in the a-C rich areas. It has been realized that the process of the LIPSS formation can last only for a short time given by the laser impact duration. From this reason, the observed local LIPSS in [1] (the laser pulse duration was ~ 8 ns) have evolved only into a few micrometer-size objects that have not interfered with each other. It is supposed, however, that in case the laser illumination lasts longer, the LIPSS might be developed into larger objects with multiple domains that could collide with other LIPSS systems. This is an open issue that may deserve further experimental inspection.

In this paper, an attempt to observe the phase separation of the Ni+C_{60} composite (and possible interaction of the LIPSS systems) have been performed in a specific experimental arrangement utilizing a 100 micrometer thick metallic mesh with 10 micrometer-size pinholes (and a pinhole-pinhole spacing of about 40 micrometer) that was placed between the sample and the focusing lens of the laser beam. This set-up enabled splitting of the probing beam into a set of microbeams, each with a 10-micrometer large diameter, arranged in a form given by the pinhole array. Under such experimental conditions, the sample could be illuminated simultaneously with a multiple laser microbeams, identical in size and equidistantly spaced. Using such a closely-spaced array of the microbeams, one may anticipate specific ways of phase separation including occurrence of interference phenomena. The samples were inspected by optical microscopy and micro-Raman spectroscopy.

Results and discussion

Fig. 1 represents an optical image of the Ni+C_{60} sample surface morphology illuminated (via single shot) with a Nd:YAG laser probe (1064 nm, 8 ns, pulse intensity ~ 5 x 10^4 W/cm^2) through an array of the 10-micrometer large pinholes (with 40 micrometer spacing). One can see a complex system of spots with a dominant array of circles (with diameter of about 10 micrometer) that represent traces of the direct impact of the laser microbeams. The circles are Ni rich zones where carbon allotropes (a-C, C_{60}) have been expelled

(due to the shock-waves) to the outer regions during the laser illumination. Besides the dominant objects (circles) one can also see a complex system of concentric rings with a broad first zone of a disruptive form followed with several (up to 4) narrow rings of an irregular shape. The rings consist of separated islands (with a size of several micrometers) that are a-C (C_{60}) rich areas. The existence of the rings point out the propagation mechanism of the phase separation that obviously proceeded in waves out of the central circles (spots of the direct laser impacts). It is supposed that the surface acoustic waves of the sample (induced by a single shot illumination of the Nd:YAG laser) enabled the transport of the loosely bonded a-C (C_{60}) components and their concentration in the energetically optimal zones, i.e., the observed circles. Close look on the structure of the rings reveals also a fine system of rectangular stripe domains (consisting of the a-C (C_{60}) islands). This system is apparently a result of a complex interference of phase separation triggered by the multiple laser microbeam illuminations. The system is seen all over the Fig. 1, though it is clear only in a-C (C_{60}) rich zones.

Conclusions

The experiment confirmed results of the previous studies [1-4] that the binary composites of Ni and C_{60} possess high proclivity to a spontaneous patterning that is due to correlated phase separation of the immiscible components. In this paper, an attempt to observe a collective phase separation of the Ni+C_{60} composites has been performed utilizing a laser illumination through a system of pinholes. As a result of laser single shot impact, an interesting interference effect of the phase separation was observed.

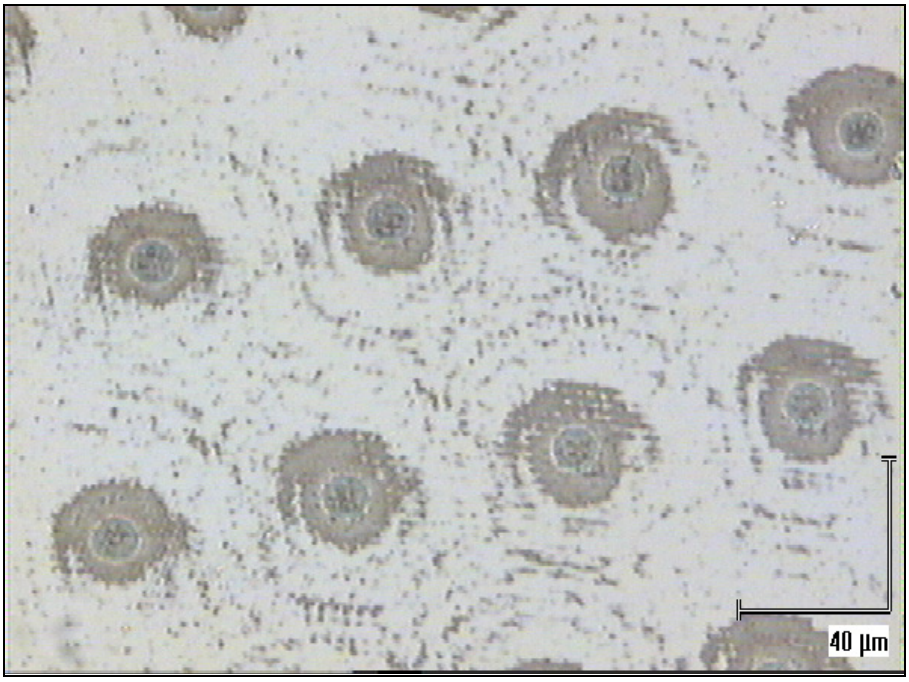

Fig. 1. Optical image of the Ni+C_{60} composite illuminated with Nd:YAG laser through an array of the pinholes.

Acknowledgement

This work was supported by Ministry of Education, Youth and Sports (Project LC06041) and Grant Agency of the Czech Republic (Grant No. 204/06/0225). Two authors (J.V. and S.K.) gratefully acknowledge the support also from the Japan Society for Promotion of Science (JSPS).

References

[1] J. Vacik, H. Naramoto, S. Kitazawa, S. Yamamoto, L. Juha, *J. of Phys. and Chem. of Sol.* 66 (2005) 581.
[2] J. Vacik, H. Naramoto, S. Yamamoto, K. Narumi, K. Miyashita, *J. of Chem. Phys.,* 114 (2001) 9115.
[3] J. Vacik, H. Naramoto, K. Narumi, S. Yamamoto, H. Abe, *Nucl. Instr. and Meth.,* B206 (2003) 395.
[4] J. Vacik, H. Naramoto, K. Narumi, S. Yamamoto, H. Abe, *Nucl. Instr. and Meth.,* B219-220 (2004) 862.

P 76

Increase of Nitrogen Dissociation Degree Due to Oxygen Admixture to Nitrogen Post-Discharge

P. Vašina[1], M. Mrázková[1], C. D. Pintassilgo[2], V. Guerra[3], V. Kudrle[1] and A. Tálský[1]

[1]Department of Physical Electronics, Kotlářská 2,Masaryk Univeristy, CZ-61137, Brno, Czech Republic

[2]Dep. Física, Faculdade de Engenharia, Univers. Porto, 4200-465 Porto, Portugal

[3]Centro de Física dos Plasmas,Instituto Superior Técnico, 1049-001 Lisboa, Portugal

e-mail: vasina@physics.muni.cz

Abstract

It is well known, that the dissociation degree of nitrogen gas can be substantially increased if a small amount of oxygen is added upstream the active discharge [1]. This phenomenon is explained by combination of following effects: increase of reduced electric field, changes of wall properties and homogeneous reactions. Surprisingly, very similar phenomenon is observed even for the oxygen added to the nitrogen late post-discharge. This increase is such well pronounced and fast that it can not be explained by the decrease of wall recombination only. The major role of some homogeneous reaction (or set of reactions), probably involving the energetic particles, is therefore clear. In this paper, we show the experimental results and we discuss probable reaction paths that can lead to the increase of nitrogen dissociation when a small amount of oxygen is added to the post-discharge.

Results and discussion

Our experimental set-up shown in Figure 1 was build in order to add the oxygen gas downstream from the microwave discharge ignited in pure nitrogen gas. The density of the nitrogen atoms in the ground state was measured by electron paramagnetic resonance technique.

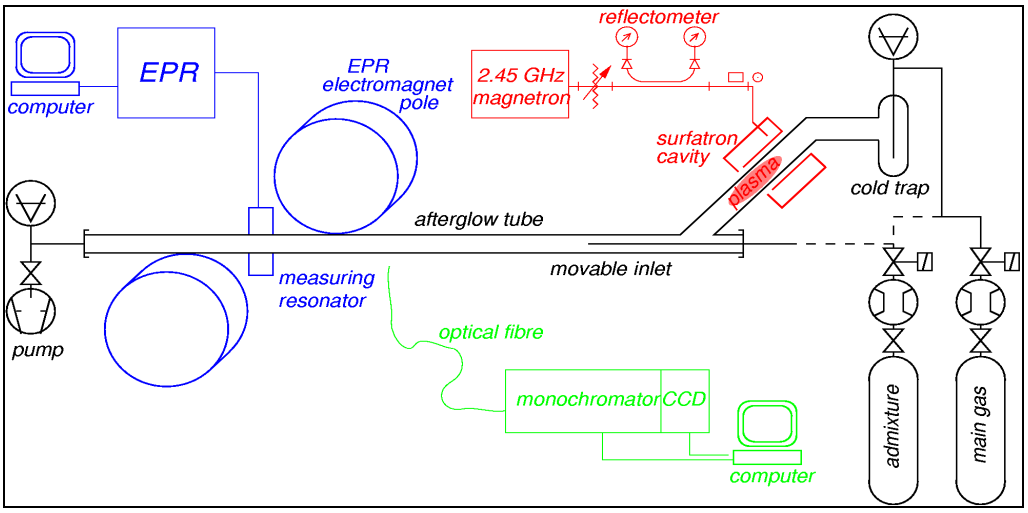

Figure 2 shows the evolution of N atom density as a function of O_2 percentage added to the nitrogen post-discharge. Pronounced increase of N atom density was observed which was followed by slower decrease. From other experiments, we concluded that observed phenomenon can be explained only by a set of homogeneous reaction with some energetic species presented in the late afterglow. In order to propose the possible reaction scheme and to determine the kind of energetic species, which can be responsible for observed phenomenon, a kinetic model [2] was modified to fit the experimental situation. Using this model, we obtained the evolution of N atom density for the case of oxygen admixture to the pure nitrogen post-discharge. For the same conditions as were in experiment, we get an increase of nitrogen dissociation degree followed by slow decrease similar to that observed experimentally. Despite the fact, that the absolute densities obtained theoretically and experimentally differ substantially, observed phenomenon was qualitatively reproduced by model. It enables us to identify the very probable reaction set responsible for observed increase. Two consequent reactions take place. The nitrogen $N_2(A^3\Sigma_u^+)$ dissociates the oxygen molecule to atoms which then react with $N_2(X^1\Sigma_g^+, v>12)$ and produce N and NO. Now, we are testing if these reaction set can explain qualitatively all measured data we have at the moment.

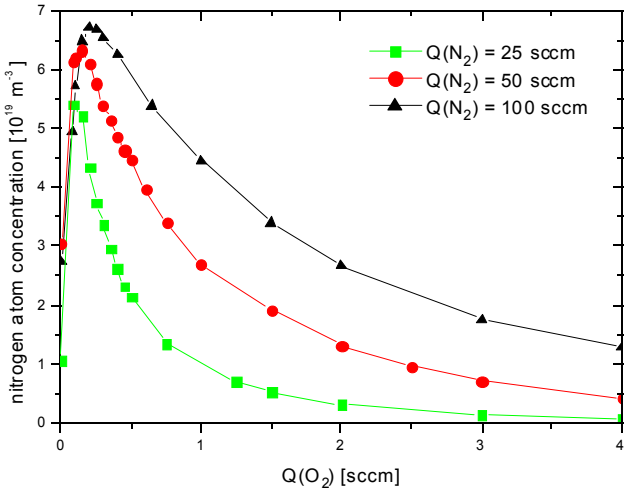

Figure 2: Influence of oxygen admixture added to the nitrogen post-discharge on nitrogen atom density. Oxygen was added via a thin capillary positioned 16 cm from the discharge, measurement of N atom density was done 24 cm farer i.g. at the distance of 40 cm from the active discharge. Symbols correspond to three experimental data sets: squares – oxygen admixture added at time t=0.14 s, nitrogen atom density measured at time t=0.33s, circles – oxygen admixture added at time t=0.07 s and nitrogen atom density measured at time t=0.17s,, triangles – oxygen admixture added at time t=0.03 s and nitrogen atom density measured at time t=0.08s.

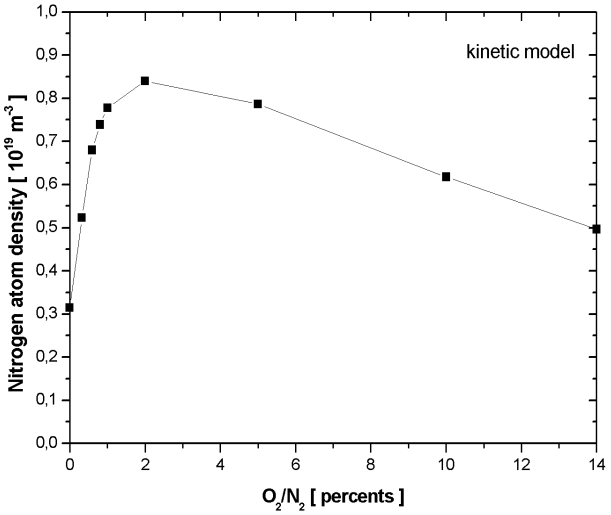

Figure 3: Results of kinetic model for experimental conditions corresponding to squares at Figure 2.

Conclusion

It was observed that the dissociation degree of nitrogen gas can be increased when a small amount of oxygen is added downstream the active discharge. It was shown that this phenomenon can not be explained by the wall processes. We proposed the set of reaction involving $N_2(A^3\Sigma_u^+)$ and $N_2(X^1\Sigma_g^+, v>12)$.

Acknowledgement

The present work was supported by projects Czech Science Foundation, contract GACR 202/05/0111 and the Ministry of Education of Czech Republic, contract MSM 0021622411.

References

[1] P. Vašina, V. Kudrle, a. Tálský, P. Botoš, M. Mrázková, M. Meško, *Plasma Source Sci. Technol.*, **13 (4)** (2004) 668

[2] C.D . Pinstassilgo, J. Loureiro, V. Guerra, *J. Phys. D: Appl. Phys.*, **38** (2005 417)

P 77

Utilization of Atmospheric Pressure Discharges for Paper Sterilization

J. Vrajová[1], Z. Rašková[2], I. Prudíková[1], F. Krčma[1]

[1] Faculty of Chemistry, Brno University of Technology, Purkyňova 118, 612 00 Brno, Czech Republic
[2] Technical Museum Brno, Purkyňova 105, 612 00 Brno, Czech Republic
e-mail: vrajova@fch.vutbr.cz

Abstract

The reduction or removal of the microbial contamination from paper using atmospheric pressure discharges has been studied. Aspergillus niger, the fungi commonly found in libraries and archives, was spread on Whatman paper no. 1. The fungi was cultivated on agar plates for five days. Aftewards the paper samples were treated in dielectric barrier discharge (DBD) in nitrogen. To observe the influence of the treatment time on the microorganisms removal, the time was varied up to 150 s. Treated samples were recultivated on agar plates in order to see the sterilisation effect of plasma. Moreover the influence of the plasma treatment on the paper mechanical properties was investigated. Positive results in microorganisms inactivation were obtained for sample treated 90 s or longer. Slight decrease of paper strength was observed for the paper contaminated with Aspergillus.

Introduction

Paper due to the influence of wide range of agents undergoes different degradation processes that result in alarming conditions of most of the historical documents [1]. One problem that has to be solved is the paper biodeterioration by microbiological agents. The Analysis of Czech National Library in Prague prooved presence of 80 different microorganisms [2]. In recent years the influence of low pressure plasma on biodeteriorat paper was studied [1, 3]. Our researched was focused on utilisation of atmospheric pressure nitrogen plasma in paper sterilisation.

Experimental

Plasma Processing

The microorganisms removal was performed by atmospheric pressure DBD plasma. The UPS 100 W plasma reactor was used to produce DBD discharge. The surface discharge is supplied by the high AC voltage with the operation frequency of 7 kHz. Plasma was generated in nitrogen. The gas flow was 2 slpm, the plasma power input was 130 W and the treatment time was varied up to 150 s. Size of samples is limited by the size of the surface electrode 10 x 10 cm.

Microbial work

Aspergillus niger F8189, the fungi which is commonly found in libraries and archives, has been chosen as a bio-indicator to evaluate the plasma microbial inactivation. The fungi was obtained in Czech collection of microorganisms (Brno Masaryk University – Faculty of Science). The culture of Aspergillus niger was cultivated on wort agar. The spore suspension was prepared by pouring 5 ml sterile water with Tween 80 into the Aspergillus culture and the surface was gently scraped with a wire. The obtained spore suspension was centrifuged three times and the supernatan was discarted [4]. The spore suspension was diluted in sterile water with Tween 80 in order to obtain suspension containing roughly 3 million spores/ ml (Bürker cell was used for spore counting). Afterward the sterilized Whatman paper no. 1 was placed on wort agar in Petri dish and 100 ml of prepared spore suspension was inoculated on the paper samples. The samples were incubated for five days at 25 °C. Before the plasma treatment, the paper samples were reached from agar medium and dried for one hour at 25 °C. Treated samples were recultivated on wort agar plates to evaluate the sterilisation effect of plasma.

Results

The nitrogen plasma used for sterilisation was created in a DBD discharge. Samples were exposed to plasma separately for different periods of time. First of all the treatment time 1, 5, 10, 20, 40, 60 and 90 s were used. Unfortunately samples treated above 40 s were damaged by the thermal heating of the surface electrodes. This was visible especially on the edge of the paper sample and on the area of the paper sample, which was exposed to the maximal plasma intensity. On these samples the microbiological inactivation was caused mainly by thermal heating. Therefore the samples were treated in a “pulse mode“, the sample was treated for 15 s and afterwards the discharge was switched off to cool down for 30 s in order to prevent

extensive sample heating. Whole period was repeated unless we reached requiered time. Using described periodical treatment, the treatment time was increased up to 150 s (10x15s).

According to our results the inactivation of microorganism occured for samples treated 90 s or longer (see Fig. 1/C below). When applying shorter treatment times the Aspergillus collonies grow again after sample recultivation (the Aspergillus micelium can be seen as a bright spots in Fig. 1/B).

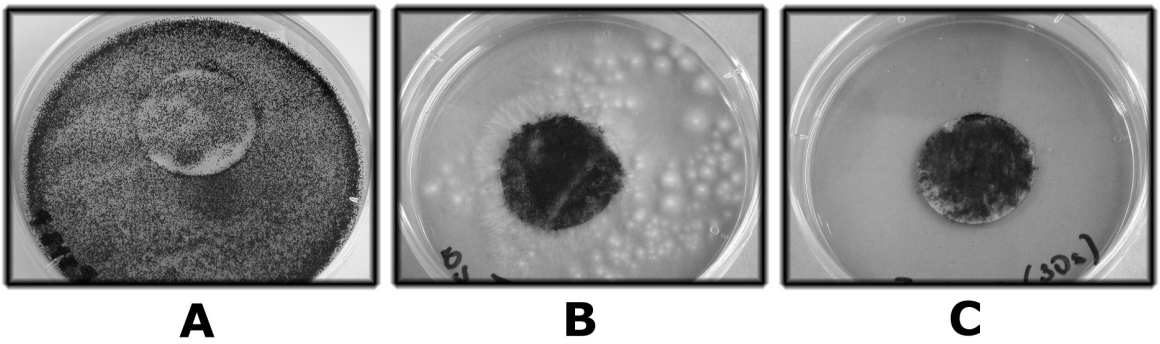

Fig. 1: Paper samples with Aspergillus niger in petri dish: A/ 5-days incubated, non-treated sample; B/ recultivated sample, after 3 days, treated for 10s; C/ recultivated sample, after 3 days, treated for 90 s (6 x 15 s, 30 s cooling between each treatment).

UV radiation and presence of ozone, that is created during the plasma treatment, are probably strongly involved in the sterilisation processes. The strong antimicrobial effect of both UV and ozone are well known [4]. The plasma was studied by optical emission spectroscopy in order to understand the processes which are involved in plasma sterilisation. The second positive and first negative nitrogen spectral bands were observed, however no other emission (as oxygen, NO or OH species) was observed. The rotational temperature of (670 ± 70) K was calculated from 0-2 second positive band and vibrational temperature of N_2 ($C\ ^3\Pi_u$) state was obtained as (1800 ± 50) K using all bands of nitrogen second positive -2 sequence.

Furthermore the influence of the plasma treatment on the paper strength was evaluated. Mechanical properties were tested by the double folds test. There are no significant changes in strength for plain Whatman paper treated in plasma. However the strength of the paper slightly decreases with treatment time for paper contaminated with Aspergillus niger.

Conclusions

The inactivation of microorganism Aspergillus niger in nitrogen plasma at atmospheric pressure was studied. According to our results the minimal treatment time for the Aspergillus inactivation is 90 s. Besides the nitrogen molecules the UV radiation, temperature and ozone, created during plasma processes are employed during the paper sterilisation.

These were just one of our first results in this field, our next investigation will be focussed on the influence of the other plasma parameters (pressure, gas flow, plasma input power) on the sterilisation processes. Furthermore we would like to extend our investigation to different microbiological agents.

Acknowledgements

This work was supported by the Czech Science Foundation, contract No. 202/03/H162.

References

[1] L. Laguardia, E. Vassallo, F. Cappitelli, E. Mesto, A. Cremona, C. Sorlini, G. Bonizzoni, *Appl. Surf. Sci.*, 252, (2005) 1159.
[2] The report of microbial analysis, Czech National Library in Prague, 2003.
[3] U. Vohrer, I. Trick, J. Bernhardt, C. Oehr, H. Brunner, *Surf. Coat. Technol.*, 142, (2001) 1069.
[4] L. Silhankova, *Microbiology for the Food Industry and Biotechnology,* Victoria Publishing, a.s., 1995 Praha.

P 78

Oscillating Hollow Cathode Discharge with Plasma Anode

M. Zahoran[1], P. Konôpka[2], J. Jašík[1], A. Labanc[3], L. Bónová[1]

[1] Department of Experimental Physics, Comenius University, Mlynská dolina, 842 45 Bratislava, Slovakia
[2] ON SEMICONDUCTOR SLOVAKIA, Vrbovská cesta 2617/102, 921 01 Piešťany, Slovakia
[3] Deutsches Elektronnen-Synchrotron, Notkestrasse 85, 22607 Hamburg, Deutschland
e-mail: zahoran@fmph.uniba.sk

Abstract

The current and light oscillations were measured in 400 kHz radio frequency discharge. The oscillations were observed in electropositive gases (Ar, N2) but no in electronegative one (SiCl4). The frequencies of oscillations were about 10 MHz. The gas pressure and rf-power dependences of current oscillations are presented. The current and light oscillations are referred to a hollow cathode effect generated in a gas outlet orifices.

Introduction

Pattern transfer by dry etching and plasma-enhanced chemical vapor deposition are two of the cornerstone techniques for modern integrated circuit fabrication [1]. In resent days radio frequency discharge with contribution of hollow cathode effect is very often applied for increasing homogeneity and throughput of technological processes [2], [3]. The main goal of this contribution is to understand the mechanism of generation of current oscillations and subsequent utilization of this effect for selective dry etching of superconductive MgB_2 layers.

Experimental

The radio frequency (rf) discharge was generated in triode type dry etcher [4]. RF generator was operated at 400kHz. Lower electrode was supplied with rf peak power up to 400W. Gas inlet and outlet was realized through upper (grounded) shower type electrode (see Fig.1.). As a gas feed nitrogen, argon and silicon tetrachlorine were used. The total gas pressure was in the range of 30-200 Pa.

The discharge voltage and current were measured with Tektronix TDS 3032 oscilloscope by high voltage divider Tektronix P 6015 A and Pearson Current Monitor (model 2877-200MHz). The light signal from rf discharge was registered by STANFORD RESEARCH SR 400 photon counter equipped with EM/9661B photomultiplier

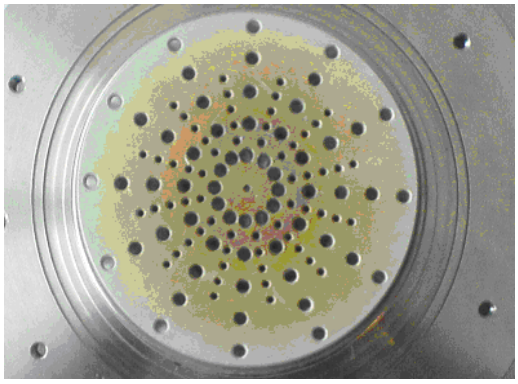

Fig.1. Upper shower type electrode (larger orifices -gas outlet, smaller orifices – gas inlet).

Results and discussion

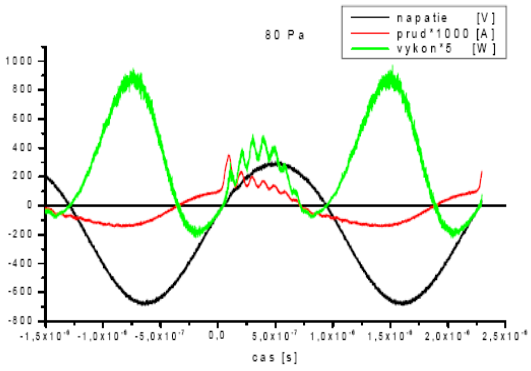

Fig. 2. Voltage, current and power waveforms measured in N_2 rf discharge at 80Pa.

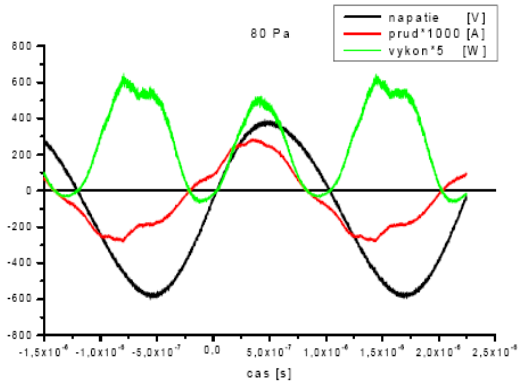

Fig. 3. Voltage, current and power waveforms measured in $SiCl_4$ rf discharge at 80 Pa.

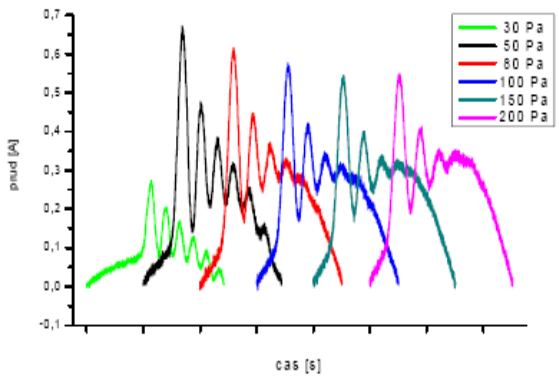

Fig. 4. Current waveforms measured in N_2 rf discharge at marked pressures.

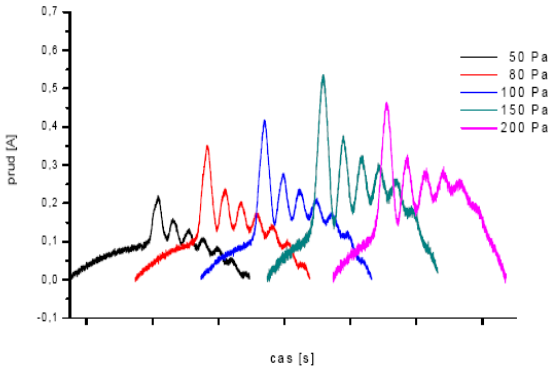

Fig. 5. Current waveforms measured in Ar rf discharge at marked pressures.

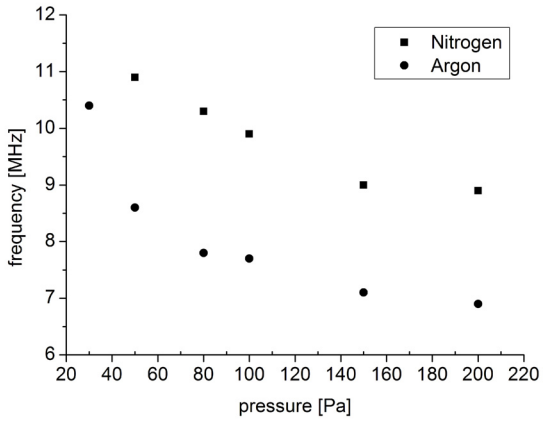

Fig. 6. Pressure dependences of oscillations frequencies, in Ar and N_2 rf discharges.

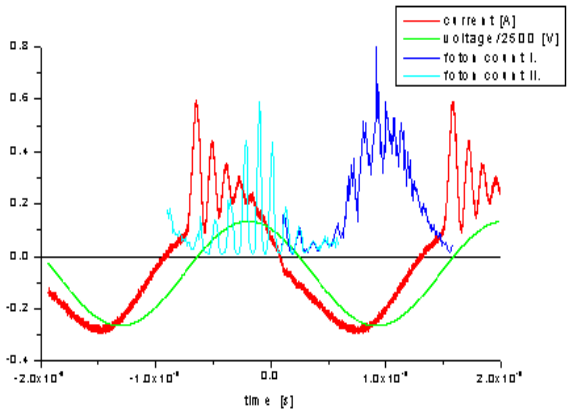

Fig. 7. Voltage, current and light waveforms measured in N_2 rf discharge at 80Pa.

Conclusions

The current and light oscillations with frequencies about 10MHz were measured in nitrogen and argon 400 kHz rf discharge at pressure ranges 30-200Pa. No oscillations were measured in $SiCl_4$ rf discharge. The peaks high in Ar rf discharge are more than tree times higher then in N_2 rf discharge. The frequencies of oscillation decrease with pressure. These oscillations were referred to hollow cathode effect generated in gas outlet orifices.

References

[1] *Handbook of Advanced Plasma Processing Techniques,* Eds.: R. J. Shul and S. J. Pearton, Springer-Verlag Berlin Heidelberg, 2000

[2] D. Zhang and M. J. Kushner, *51th Gaseous Electronics Conference & 4th International Conference on Reactive Plasmas*, Maui, Hawai'i, 19-23 Oct. 1998

[3] G. Fedosenko, D. Korzec, J. Engemann, D. Lyebyedyev, H.-C. Scheer, *Thin Solid Films,* 406 (2002) 275

[4] V.Martišovitš, J.Trnovec, R.Hajossy, V.Šurda, M.Zahoran, I.Košinár, M.Polášek, Š.Šurka: The construction of the single wafer plasmachemical etch reactor, *Research report for industrial enterprise k.p. Tesla Piešťany*, HZ 706-78/85-VČ, MFF UK, Bratislava, (1986), (44 pages).

P 79

New Laser-Nuclear Spectral Effects in a Thermalized Plasma of Multicharged Ions and Super Intense Laser Field Action on Surface with Forming the Femto-Second Laser Plasma in the Porous Materials and Possible Nuclear Fusion

A. Glushkov[1], O. Khetselius[2] and E. Gurnitskaya[1]

[1]Department of Atomic Physics, Odessa Univ., P.O.Box 24a, Odessa-9, 65009, Ukraine
[2]Institute of Applied Mathematics, Odessa Univ., P.O.Box 24a, Odessa-9, 65009, Ukraine
e-mail: glushkov@paco.net

Abstract

Within the uniform energy approach it is predicted and studied a possibility of manifestation of the new laser-nuclear spectral plasma effects in a thermalized plasma of the the O-and F-like multicharged ionswith possible using in diagnostics tasks. The modelling of the femto-second laser plasma forming in the porous materials on the basis of the energy balance equations and Green's function formalism for non-ordered materials is carried out.

Introduction

A great progress in development of laser technique and accelerators experiments resulted to a new class of problems in the plasma physics and diagnostics. It should be noted on a possibility of the using co-operative phenomena [1,2] due the interaction between photon, electron shells, nuclei nucleons for diagnostics. New approach to the multi charged ion plasma diagnostics using the new laser-electron-nuclear effects is possible. In first part of paper we consider a possibility of the experimental observation of set of the electron satellites in spectra of the electron-nuclear γ-transition of the nucleus in a multi charged ion-thermalized plasma. The second part f paper is connected with the modelling of the femto-second laser plasma forming in the porous materials on the basis of the energy balance equations and Green's function formalism for non-ordered materials. It well known that using the super short light pulses changes principally a character of interaction of the laser radiation with substance (surface) [3]. For laser intensities more than 10^{15} Wt/cm^2 during the laser pulse electrons get energy of 100-1000eV and it is realized a process of forming the femto-second laser plasma (FLP). Our paper is devoted to studying a super intense laser field action on surface and developing a consistent quantum approach to calculation of spectrum of the FLP in the porous materials.

Results and discussion

The nuclear transition in the isotope of Fe^{57} with energy 14,41 keV is considered for O-and F-like ions of Fe. The electron-nuclear lines in spectra of emission are calculated within QED energy approach [2]. System of red (blue) satellites corresponds to transitions with excitation (de-excitation) of the electron shell (fig.1.).

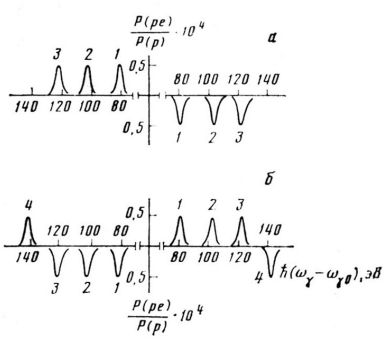

Fig.1. The positions of emission and absorption electron satellites (in a positive and negative direction of abscissa axe correspondingly) for ion FeXIX in lowest states of the ground configuration $2s^22p^4$ (a) and states of the excited configuration $2s2p^5$, $2s2p^5nl$ (b) relatively the nuclear γ-transition 14,41 keV in Fe isotope.

Calculated relative (to nuclear transition) intensities for the transitions: nl-n'l' (n=1-3, l=0-2) are~2-7(10^{-5}). It can be observed in the plasma of the O-and F-like ions and it is important that they are not overlapping by the Doppler broadening. Give some estimates. It is supposed that the K shell is significantly destroyed.

An average kinetic energy for ions in such plasma ~E_i/10~1/20c.u. (Coulomb units), where E_i is the 1s electron bond energy. The Doppler shift is $\hbar\omega_D \approx aw/(10M)^{1/2}$; here aw is connected with γ quantum energy as: E[keV] ≈4Zaw. If, say, aw=1, then $\hbar\omega_D \approx 1/200\ (Z)^{1/2}$c.u. ≈0,15 $(Z)^{1/2}$ eV. For comparison let us give the values of the 1s,2s,2p-2p transition energies for one-electron ions with Z=10-50: E(1s-$2p_{3/2}$)=1,3·10^3-2,3·10^4eV, E(2s-$2p_{3/2}$)≈E(2s-$2p_{3/2}$)==0,1-3,3·10^2eV. Obviously the transition energies have an order of the Doppler shift. In Fig.1 we present the positions of emission and absorption electron satellites for ion FeXIX in lowest states of the ground and excited configurations relatively the nuclear γ-transition in Fe isotope (14,41 keV). P(pe)/P(p) is relation of satellite intensity to nuclear transition line intensity.

Further we consider the possibilities of governing by processes, which are taken a place in the FLP in nano-structured porous materials (Si). Nano-structured porous materials consists of the separated clusters set, that forms the fractal structure or regular net. The key mechanism of the hot electrons generation in plasma is provided by oscillation of electron on the border "plasma-vacuum" or resonant absorption of laser radiation. For porous materials one may wait for the sharp increasing the hot electrons generation and X-ray radiation. Under large intensity of laser field it is observed a new type of the hydrodynamic ablation, which has the explosion character. Experimental estimates show that a velocity of the plasma flying of the strongly porous samples Si (I~10^{16} W/cm^2) is ~10^8 cm/s, that is corresponding to energy 2±1 MeV [3,4]. We carried out the modelling of the FLP forming in the porous materials on the basis of the energy balance equations and Green's function formalism for non-ordered materials. Special attention is devoted to the modelling the system: nano-structured porous material with clusters, on surface of which there is a great number of bonds with H and OH groups. In a case of the D-and OD group's one can wait for realization of the cluster explosion process and reaction D+D-alpha+n (3,8MeV) [3,4]. One can wait for appearance of the powerful flow of neutrons in plasma under intensity of the heating pulse ~ 10^{16} Wt/cm^2. In the high density plasma there is possible an excitation of the low lying isomers (level energy less 20 keV) by means of the following channels: photo excitation by own X-ray plasma radiation, electron conversion etc. We present the results of calculating the stable and long lived low lying isomers characteristics [4]. It is important to note that an experimental definition of characteristics of low lying isomers (time of life, spin, energy, decay channels etc.) of the stable and long-lived nuclei is connected with great difficulties within standard nuclear spectroscopy methods.

Conclusions

Within the uniform energy approach we have considered a possibility of manifestation of the new laser-nuclear spectral plasma effects in a thermalized plasma of the the O-and F-like multicharged ionswith possible using in diagnostics tasks. Within the energy balance equations and Green's function formalism for non-ordered materials wr have fulfilled the modelling of the femto-second laser plasma forming in the porous materials in conditions of the superintense laser field action on the corresponding surface.

References

[1]. L.N.Ivanov, V.S.Letokhov, *JETP.* 93, 83 (1987); L.N.Ivanov, E.P.Ivanova, E.V.Aglitsky, *Phys. Rep.* 166, 315 (1988); A.V.Glushkov, L.N.Ivanov, *Phys.Lett.A*. 170,33 (1992).
[2]. A.V.Glushkov, S.V. Malinovskaya, In*: New Projects and New Lines of research in Nucl.Physics*. Eds. Fazio G., Hanappe F., World Publ. Singapore, 2003,p.242-264; *Int. Journ. Quant.Chem.* 99, 936 (2004); 105, 562 (2005); A.V.Glushkov et al, *J.Phys.CS.* 178, 199 (2005); *J.Phys.CS.*35, 420 (2006); 35, 426 (2006); Recent Advances in Theory of Phys.and Chem. Systems.Eds. Julien J.-P., Maruani J., Springer: Netherlands, 2006, Vol.15, P.285-300.
[3]. *Superstrong Fields in Plasmas.* Eds. M.Lontano, AIP Ser. V.426 (1998) ; V. Gordienko, A.Saveliev, Usp.Fiz.Nauk, 169, 78 (1999); A.Andreev etal, *JETP Lett*. 66,312 (1997) ; A.V.Glushkov, L.N.Ivanov. *Preprint Inst. Spectroscopy of Russian Academy of Sciences* NAS-2, Moscow- Troitsk, 1994;
[4]. L.N.Ivanov, A.V.Glushkov, *Preprint Institute of Spectroscopy of Russian Academy of Sciences* N AS1-3, Moscow- Troitsk, 1992; A.V.Glushkov,L.N.Ivanov, *Phys. Lett. A*,170, 36 (1992); A.V.Glushkov, L.N.Ivanov, *J.Phys.B.* 26, L379 (1993); A.V.Glushkov, In: *Low Energy Antiproton Phys.,* AIP Serie.-2005. Vol. 796.-P.206-210, p.217-224; *Recent Advances in Theor. Phys. and Chem. Systems*, Eds. Julien J.-P., Maruani J., Springer, Netherlands, 2006,Vol.15,P.301-308.

P 80

Properties of a Secondary Discharge in Vapour of Ethanol as Source of Carbon Nanoparticles

Iu. Veremii[1], V. Chernyak[1], V. Zrazhevskij[1], V. Naumov[2], Eu. Safonov[1]

[1]Faculty of Radiophysics, Dept. of Physical Electronics, Taras Shevchenko Kyiv National University, Volodymyrska str. 64, 01033 Kyiv, Ukraine;

[2] Institute of Fundamental Problems for High Technology, Ukrainian Academy of Sciences, Prospect Nauki 45, 03028, Kiev, Ukraine.

e-mail: chern@mail.univ.kiev.ua, tin@mail.univ.kiev.ua

Abstract

Properties of a secondary discharge in vapour of ethanol were investigated in this work. Possibility of nanoparticles reception in plasma-discharge system with using as source material liquid hydrocarbons was considered. As a result of secondary discharge plasma treatment fine-dispersed powder was received. Power imputs on formation of one gram carbon materials amount to 1÷10 kW*h.

Introduction

There are several methods of producing carbon nanoparticles (CNP) in lab conditions [1], among them electric gas-discharge plasma methods are most commonly used [2]. They are based mainly on the sublimation of solid-phase raw materials. But recently, electrical discharge technique in liquid media has been shown to be a quite simple and inexpensive tool for a synthesis of nanostructures from different materials [3].

We propose an alternative approach to synthesis from liquid-phase materials using non-equilibrium heterophase plasma, utilizing plasma-liquid systems with secondary discharges. Under nonequilibrium plasma-liquid exposure, hydrocarbon molecules can be effectively decomposed into the carbon source radical and atomic components, which then can form the CNP. It should be noted that the carbon nanoparticle-forming material can be supplied by the electrodes as well as in result of the organic liquid decomposition [4].

In the present work, an availability nanoparticle of liquid hydrocarbons in plasma-liquid system with noncarbon electrodes was considered.

Experimental set-up and results

Treatment of organic liquid for nanoparticles generation was conducted in plasmachemical reactor on the basis of secondary discharge with continuous pumping (Fig. 1).

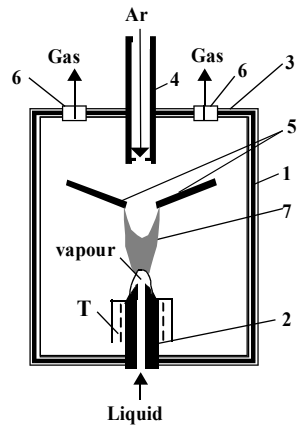

Fig. 1

Reactor consisted from the metal cylinder (1), which was closed by the cover (3). Free jet argon ran from the nozzle (4) across two opposite electrodes (5) and formed a bright crescent-shaped electric arc. The exhaust gases came out of a reactor through two holes (6). The current of secondary discharge runs through plasma (7) of arc discharge and vapour of liquid.

The power supply of arc and secondary discharges was powered by the DC sources. The polarity of secondary discharge was determined by polarity of electrode (2).

The gas was moved into the gap between two cylindrical coaxial copper electrodes, where the auxiliary discharge was burning. Liquid was put into the system through the hollow electrode (2) with the heater (T) and come into the reactor as vapour. Another electrode of the secondary discharge was plasma of auxiliary discharge.

We used ethanol as experimental substance and argon as an initiating gas.

Series of current-voltage curves (CVC) of secondary discharge in a system without ehtanol for different modes of auxiliary discharge shown on a fig.2. It is possible to relate the secondary discharge to transitive area between decaying and arc discharge by the forms of CVC. Non-self-maintained secondary discharge transformed to self-maintained when current of secondary discharge exceed 300mA.

The sharp increase in a voltage at the secondary discharge in some times takes place after filling a reactor of ethanol vapour. On a fig.3 are shown CVC of the secondary discharge before (curve 1) and after (curve 2) entering of ethanol in system, a current of auxiliary discharge was 400 mA.

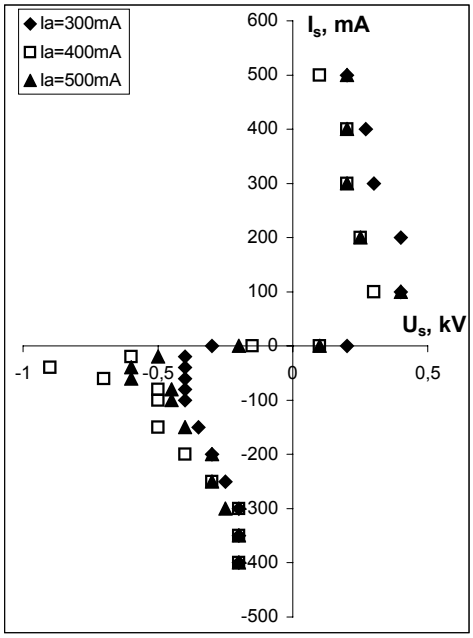

Fig.2

In the result of the plasma treatment of hydrocarbon liquids the output product was formed solid phase – carbon materials (CM).

The output products were investigated by using an atomic-force microscope, at early papers. Large and small particles, with the size 50÷300 nm and 5 ÷10 nm correspondingly, were found [5].

The average output amount to 100 mg/h from 100ml solution for all regimes with average power imputs ~ 600 watt-hour. By Raman spectrum was concluded that in a received powder contained 10 % single-wall nanotube [6].

The ethanol solution from 0.002 % by an impurity of the catalyst (ferrous acetate) was processed. The treatment of a solution was carried out after stabilization of a mode of system and characteristics of both discharges on the given meanings. The opportunity of carbon materials formation in system, effective area and conditions of their sedimentation on elements of reactor, and also expense of energy for generation of unit CM was investigated.

Operating modes of system with cooling walls of a reactor and without cooling have been realized. It was possible to find out, that the CM is more effective formed on hot elements of a reactor than on cold. So, power imputs on formation of one gram CM in system without cooling amount to 2.5 kW*h, it almost on the order is less than at mode with cooling (22 kW*h).

Polarity of the secondary discharge also essentially influences efficiency of carbon materials production. In a case of the negative polarity of secondary discharde electrode is formed in some times more BM than in case of realization of the positive polarity. Total power imputs on generation of one gram BM in case of negative polarity of secondary discharde electrode almost it is twice less (for comparison: 4.5 kW*h and 6.75 kW*h, correspondingly).

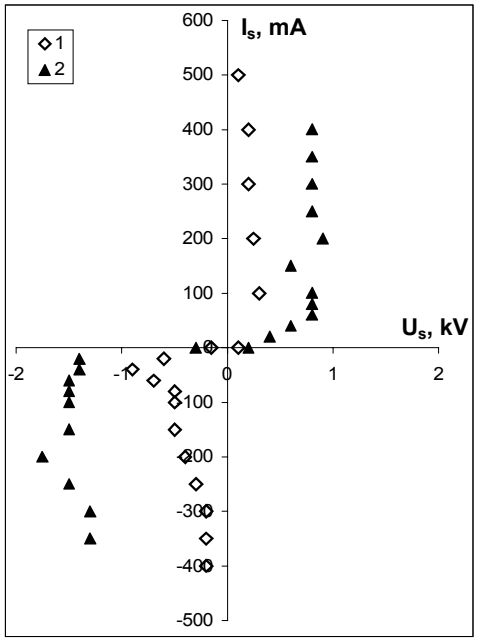

Fig.3

Conclusions

- It was emerged that efficiency of CM generation increases at rise in temperature of a substrate,
- system with the negative polarity of secondary discharde electrode much better by amount of carbon materials than system in which the positive polarity is realized,
- it was possible to achieve a level of power imputs of the order n kW*h/g received CM.

The plasma treatment of liquid hydrocarbons in the heterophase plasma-liquid system with the secondary discharge can be an effective method for producing of polymer carbon-containing nanoparticles.

References

[1] A. Eletskii, B. Smirnov, *Physics-Uspekhi* **163**:173 (1991); *Ibid.* **163**:33 (1993); *Ibid.* **165**:945 (1995).
[2] W. Kratschmer et al*, Nature* **347**:354 (1990); Iijima S, *Nature*, **354**:56 (1991).
[3] N. Sano et al., *Nature* (2001), vol.**414**, p.506-507.
[4] V.S. Burakov et al, *Noneq. Proc. in Comb. and Plasma Based Tech.,* Belarus (Minsk), 2006.
[5] V. Chernyak, et al., Electronic Proc. 17th Int. Symp. on Plasma Chem., Toronto (Canada), 2005.
[6] V. Chernyak, Iu. Veremii et al., Proc. II Int. Conf. "Electr. and App. Physics", Ukraine (Kyiv), 2006.

P 81

Application of a Plasmatron to Inactivation of Micro-Organism

Ch. J. Yim, S. B. Jwa, V. Yu. Plaksin, V. A. Riaby and H. ju Lee

Faculty of Mechanical & Energy System Engineering, Cheju National University
Email: hjlee@cheju.ac.kr

Abstract

Traditional techniques for sterilization of heat sensitive materials are using toxic gases such as ethylene oxide, but there are several problems. Some techniques for generating active species have been developed and tested in a wide range of plasma sterilizations. A plasmatron with high durability was developed. So it has a low anode erosion rate, that it can generate the pure plasma flow and has long lifetime of 103~104 hours.

In this study, Bacillus Subtilis and Aspergillus Niger which are test strains with high resistance against oxidative and UV processes respectively were exposed to a downstream plasma from a plasmatron operating with various gases such as oxygen, nitrogen and hydrogen-peroxide at atmospheric pressure. A comparative study for different parameters, e.g., gas composition, exposure time, input power which effect the inactivation are presented. In addition, possible mechanisms of the inactivation were discussed.

Acknowledgment

This work was supported by the grant R-2004-096-0-00 of the Korean Ministry of Commerce, Industry and Energy, by the grant M1-0104-00-0071 from the National Research Laboratory Program of the Ministry of Science and Technology, by the Brain Korea 21 from the Ministry of Education and Human Resources Development, Korea, and by the grant 2006-C-CC02-P-05-0-000-2006 of the Korea Energy Management Corporation.

Behavior of Polyamide 12 Modified by Barrier Discharge Plasma

M. Števiar[1], I. Chodák[1], I. Novák[1], I. Janigová[1]

Polymer Institute, Slovak Academy of Sciences, 842 36 Bratislava, Slovakia

e-mail: upolstev@savba.sk

Abstract

The effect of surface modification of polyamide 12 (PA 12) modified by barrier surface discharge (DBSD) plasma on its surface and adhesive properties has been investigated. The contact angles of the polar testing liquids decrease significantly regarding to unmodified sample. The changes in surface properties were accompanied with growth of the surface roughness of samples modified by barrier plasma.

Introduction

The low values of surface energy of polyamide 12 (PA 12) can be significantly increased by using various methods of surface modification. The higher surface energy of PA 12 is necessary for bonding or printing. The most advanced method of PA 12 surface modification is based on modification by barrier discharge plasma [1 - 3]. The surface of PA 12 was pre-treated at various times by DSBD plasma in O_2 or N_2 at atmospheric pressure. The changes in surface properties of PA 12 modified by plasma were analyzed using contact angle measurements, as well as Scanning Electron Microscopy (SEM) measurements.

Results and discussion

The dependencies of contact angles of testing liquids on the surface of PA modified by DSBD plasma

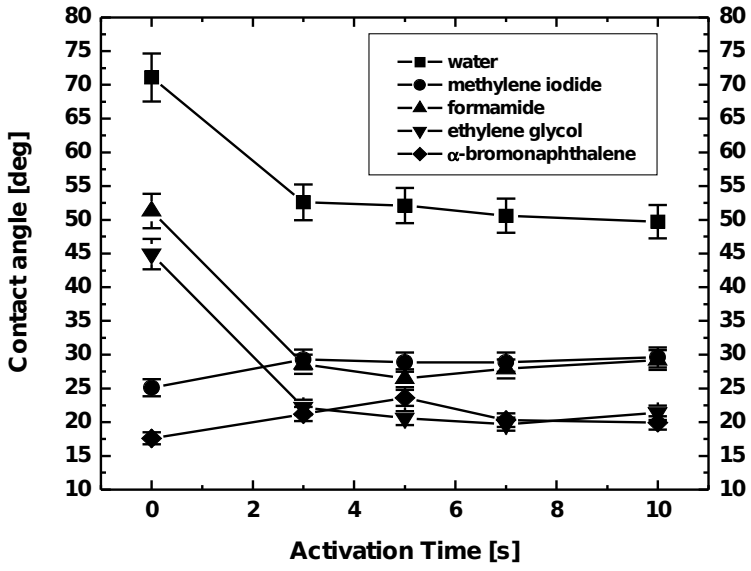

Fig. 1 Contact angles of PA 12 modified by DSBD plasma in O_2

in O_2 vs. time of activation are shown in Fig. 1. The contact angles of polar liquids (e.g. water, ethylene glycol, formamide) decrease significantly even for short time (5 s) of activation of PA 12 by DSBD plasma due to an increase of the surface polarity, for longer times of modification by plasma the dependencies in Fig. 1 were leveled off.

Fig. 2 illustrates the changes in surface roughness of PA 12 foils modified by DSBD plasma in N_2 (b), and/or in O_2(c) using SEM measurements compared to unmodified sample (a). Whilst the changes in surface topography of PA 12 modified by DSBD in O_2 were evident (increase of the roughness), in the case of modification of PA12 by DSBD in N_2 no meaningful changes were observed.

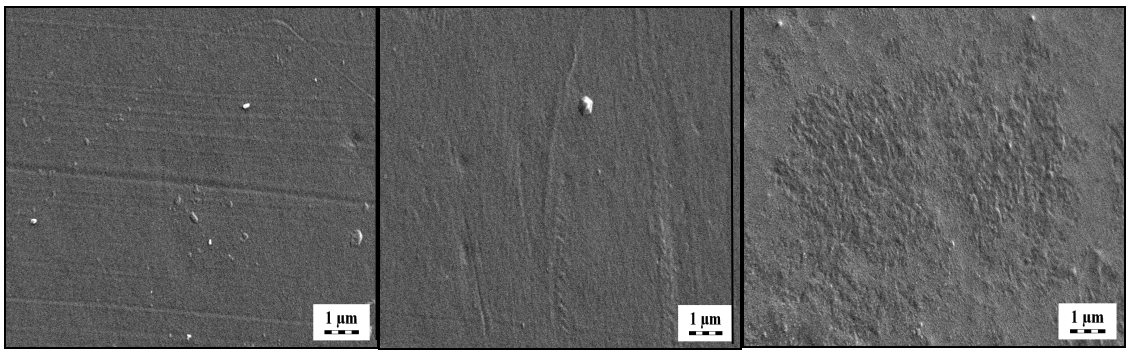

a b c

Fig. 2 SEM images of PA 12: a) reference sample, b) DSBD, 10 s, N_2, c) DSBD, 10 s, O_2

Conclusions

Surface properties PA 12 modified by DSBD plasma were substantially higher regarding to unmodified polymer due to higher polarity of the polymeric surface. SEM microphotos show the roughening of the PA 12 surface modified by DSBD in O_2 as a consequence of the DSBD plasma modification.

Acknowledgements

The authors are grateful to the Slovak Grant Agency VEGA (grant No.2/4024/04) for the support of this research.

References

[1] I.Novák, V.Pollák, I.Chodák, *Plasma Proces. Polyms.,* 3 (2006) 355.
[2] I.Novák, M.Števiar, I.Chodák, *Monatshefte für Chemie/Chemical Monthly*, 137 (2006) 943.
[3] D.J. Upadhyay, N.Y.Cui, C.A.Anderson, N.M.D. Brown, *Coll. Surf. A: Physicochem.Engn. Apects,* 248 (2004) 47.

AUTHORS INDEX

LIST OF PARTICIPANTS

Dr. Nail Asfandiarov
Institute of Molecular and Crystal Physics
Lab of Atomic Collision Physics
October Prospect, 151
450075 Ufa, Russia
nail@anrb.ru

Mr. Ilko Bald
Freie Universität Berlin
Institut für Chemie - Physikalische und
Theoretische Physik
Takustraße 3
14195 Berlin, Germany
ibald@zedat.fu-berlin.de

Dr. Wieslawa Barszczewska
University of Podlasie
Department of Chemistry
3 Maja 54
08-110 Siedlce, Poland
wbar@ap.siedlce.pl

Prof. Kurt Becker
Stevens Institute of Technology
Department of Physics
Castle Point on Hudson
7030 Hoboken, USA
kbecker@stevens.edu

Prof. Hynek Biederman
Charles University
Faculty of Mathematics and Physics
Department of Macromolecular Physics
V Holesovickach 2
180 00 Praha 8, Czech Rep.
bieder@kmf.troja.mff.cuni.cz

Prof. Marcela Bilek
University of Sydney
School of Physics
Paramatta Road
2006 Sydney, Australia
m.bilek@physics.usyd.edu.au

Mr. Zdenek Bonaventura
Masaryk University
Department of Physical Electronics
Kotlářská 2
611 37 Brno, Czech Rep.
zbona@physics.muni.cz

Mr. Petr Bruna
Jan Eavangelista Purkyně University
Faculty of Science
Department of Physics
České mládeže 8
400 96 Ústí nad Labem, Czech Rep.
pbruna@physics.ujep.cz

Mr. Oto Brzobohaty
Masaryk University
Department of Physical Electronics
Kotlarska 2
611 37 Brno, Czech Rep.
otobrzo@physics.muni.cz

Mr. Andrej Buček
Comenius University
Faculty of Mathematics, Physics and Informatics
Department of Experimental Physics
Mlynská dolina
842 48 Bratislava, Slovakia
bucek@gimmel.ip.fmph.uniba.sk

Mr. Jan Cech
Masaryk University
Faculty of Science
Physical Electronics
Kotlarska 2
61137 Brno, Czech Rep.
cech@physics.muni.cz

Prof. Mirko Cernák
Comenius University
Faculty of Mathematics, Physics and Informatics
Department of Experimental Physics
Mlynska Dolina F2
842 48 Bratislava, Slovakia
cernak@gimmel.ip.fmph.uniba.sk

Dr. Ludmila Cernakova
Slovak University of Technology
Institute of Polymer Material
Department of Plastic and Rubber
Radlinského 9
812 37 Bratislava, Slovakia
ludmila.cernakova@stuba.sk

Mr. Pavel Cerný
Jan Evangelista Purkyně University
Faculty of Science
Department of Physics
České mládeže 8
400 96 Ústí nad Labem, Czech Rep.
pav.cerny@email.cz

Dr. Martin Clupek
Acadeny of Sciences of the Czech Republic
Institute of Plasma Physics
Za Slovankou 3
182 00 Prague 8, Czech Rep.
clupek@ipp.cas.cz

Dr. Dan-Gheorghe Dimitriu
Al. I. Cuza University of Iasi
Plasma Physics
11 Carol I Blvd.
RO-700506 Iasi, Romania
dimitriu@uaic.ro

Mr. Vojtech Dolezal
Masaryk University
Department of Physical Electronics
Kotlářská 2
611 37 Brno, Czech Rep.
vojta@physics.muni.cz

Dr. Zoltan Donko
Research Institute for Solid State Physics and Optics
Department of Laser Physics
Konkoly Thege Miklos ut 29-33
H-1121 Budapest, Hungary
donko@sunserv.kfki.hu

Dr. Miroslaw Dors
The Szewalski Institute of Fluid Flow Machinery
Centre for Plasma and Laser Engineering
Fiszera 14
80231 Gdansk, Poland
mdors@imp.gda.pl

Dr. Herwig Drexel
Rho-BeSt coating
Exlgasse 20a
6020 Innsbruck, Austria
h.drexel@rhobest.com

Dr. Pavel Dvorak
Masaryk University
Faculty of Science
Department of Physical Electronics
Kotlarska 2
611 37 Brno, Czech Rep.
pavel@chemi.muni.cz

Prof. Esmaeil Farshi
University of Tennessee
Department of Electrical Engineering
TN 37996-2100 Knoxville, USA
efarshi@ece.utk.edu

Dr. Linda Feketeova
University of Aarhus
Department of Physics and Astronomy
Ny Munkegade
8000 Aarhus C, Denmark
linda.feketeova@gmail.com

Mr. Tomas Foldes
Comenius University
Faculty of Mathematics, Physics and Informatics
Departement of Experimental Physics
Mlynska Dolina
842 48 Bratislava, Slovakia
foldes.tomas@gmail.com

Prof. Juraj Glosik
Charles University in Prague
Faculty of Mathematics and Physics
Electronics and Vacuum physics
V Holesovickach 2
180 00 Prague 8, Czech Rep.
juraj.glosik@mff.cuni.cz

Prof. Alexander Glushkov
Odessa University
Applied Mathematics
P.O.Box 24a
65009 Odessa-9, Ukraine
glushkov@paco.net

Mr. Branislav Grancic
Comenius University
Faculty of Mathematics, Physics and Informatics
Department of Experimental Physics
Mlynska dolina
842 48 Bratislava, Slovakia
grancic@fmph.uniba.sk

Mrs. Hana Grossmannova
Brno University of Technology
Faculty of Chemistry
Purkynova 118
612 00 Brno, Czech Rep.
hannyg@seznam.cz

Mr. Michal Gulas
Comenius Univeristy
Faculty of Mathematics, Physics and Informatics
Departement of Experimental Physics
Mlynska Dolina
842 48 Bratislava, Slovakia
gulas@fmph.uniba.sk

Dr. Silviu Gurlui
Al I Cuza University of Iasi
Faculty of Physics
Bdul Carol I, nr 11
700506 Iasi, Romania
sgurlui@uaic.ro

Dr. Peter Hartmann
Research Institute for Solid State Physics
Laser Physics
Konkoly-Thege M. 29-33
1121 Budapest, Hungary
hartmann@sunserv.kfki.hu

Mrs. Radka Havlíková
CTU in Pragu / FNSPE
Dept. of Physical Electronics
Břehová 7
115 19 Prague, Czech Rep.
havlikov@troja.fjfi.cvut.cz

Dr. Vladimir Havranek
Nuclaer Physics Institute
Neutron Physics
250 68 Rez u Prahy, Czech Rep.
havranek@ujf.cas.cz

Mr. Michal Heinrich
Fronius International GmbH
Research & Development
Günther Fronius Straße 1
4600 Wels, Austria
heinrich.michal@fronius.com

Dr. Karol Hensel
Comenius University
Faculty of Mathematics, Physics and Informatics
Department of Astronomy, Earth Physics and Meteorology
Mlynska dolina F2
84248 Bratislava, Slovakia
hensel@fmph.uniba.sk

Prof. Zdenek Herman
J. Heyrovsky Institute of Physical Chemistry
Academy of Sciences CR
Department of Chemical Physics
Dolejskova 3
182 23 Prague 8, Czech Rep.
zdenek.herman@jh-inst.cas.cz

Mr. Tomáš Hoder
Masaryk University
Department of Physical Electronics
Kotlářská 2
611 37 Brno, Czech Rep.
hoder@physics.muni.cz

Mr. Tomáš Homola
Comenius University
Faculty of Mathematics, Physics and Informatics
Department of Experimental Physics
Mlynská dolina
842 48 Bratislava, Slovakia
homola@gimmel.ip.fmph.uniba.sk

Prof. Jiri Horacek
Charles University in Prague
Institute of Theoretical Physics
V Holesovickach 2
180 00 Praha, Czech Rep.
horacek@mbox.troja.mff.cuni.cz

Mr. Gabriel Horváth
Comenius University
Faculty of Mathematics, Physics and Informatics
Department of Experimental Physics
Mlynská dolina
84248 Bratislava, Slovakia
horesz@centrum.sk

Prof. Andrzej Huczko
Warsaw University
Department of Chemistry
1 Pasteur str.
02-093 Warsaw, Poland
ahuczko@chem.uw.edu.pl

Prof. Ivan Hudec
Slovak University of Technology
Department of Plastics and Rubber
Radlinského 9
81237 Bratislava, Slovakia
ivan.hudec@stuba.sk

Prof. Valeriy Chernyak
Kyiv National Taras Shevchenko University
Radio Physical Faculty
Physical Electronics Department
Volodymyrska st., 64
1033 Kyiv, Ukraine
chern@univ.kiev.ua

Ms. Mariya Chichina
Charles University
Faculty of Mathematics and Physics
V Holešovičkách 2
180 00 Praha 8, Czech Rep.
mchichina@yandex.ru

Prof. Ivan Chodak
Polymer Institute of the Slovak Academy of Sciences
Composite Thermoplastics
Dubravska 9
842 36 Bratislava, Slovakia
upolchiv@savba.sk

Mr. Oleksiy Chumak
IPP CAS CR
Thermal Plasma
Za Slovankou 3
18200 Prague 8, Czech Rep.
chumak@ipp.cas.cz

Prof. Eugen Illenberger
Freie Universität Berlin
Institut für Chemie und Biochemie – Physikalische und Theoretische Chemie
Takustrasse 3
D-14195 Berlin, Germany
iln@chemie.fu-berlin.de

Prof. Oddur Ingolfsson
University of Iceland, Science Institute
Chemistry
Dunhagi 3
107 Reykjavik, Iceland
odduring@hi.is

Dr. Codrina Ionita-Schrittwieser
Leopold-Franzens University of Innsbruck
Institute for Ion Physics and Applied Physics
Technikerstr. 25
A-6020 Innsbruck, Austria
codrina.ionita@uibk.ac.at

Mr. Stefan Jaksch
Univerität Innsbruck
Institut für Ionenphysik und Angewandte Physik
Technikerstrasse 25 / 3
6460 Innsbruck, Austria
stefan.jaksch@uibk.ac.at

Ms. Zuzana Jakubíková
Slovak Technical University Bratislava
Department of Graphic Arts Technology and Applied Photochemistry
Radlinského 9
812 37 Bratislava, Slovakia
zuzana.jakubikova@stuba.sk

Dr. Mario Janda
University of Innsbruck
Department of Theoretical Chemistry
Innrain 52a
6020 Innsbruck, Austria
mario.janda@gmail.com

Mr. Filip Janky
Comenius University
Faculty of Mathematics, Physics and Informatics
Department of Experimental Physics
Mlynska dolina
84248 Bratislava, Slovakia
janky@neon.dpp.fmph.uniba.sk

Mr. Jaroslav Jánský
Masaryk University
Department of Physical Electronics
Kotlářská 2
611 37 Brno, Czech Rep.
jansky@physics.muni.cz

Mr. Igor Jedlovský
Commenius University
Department of Nuclear Physics and Biophysics
Mlynská dolina
842 48 Bratislava, Slovakia
jedlovsky@fmph.uniba.sk

Prof. Antoni Jowko
University of Podlasie
Dept. of Chemistry
3 Maja 54
08-110 Siedlce, Poland
ajowko@ap.siedlce.pl

Mr. Sang Beom Jwa
Cheju National University
Faculty of Mechanical & Energy System Engineering
ara 1 dong
690756 Jeju, Korea
lajoa@cheju.ac.kr

Mr. Jiri Kalas
University of West Bohemia
Department of Physics
Univerzitni 22
30614 Plzen, Czech Rep.
jkalas@kfy.zcu.cz

Prof. Tsutomu Kaneko
Science University of Tokyo
Department of Applied Physics 1-3
Kagurazaka, Shinjuku-ku
162-8601 Tokyo, Japan
kaneko@ap.kagu.sut.ac.jp

Dr. Tetyana Kavka
IPP CAS CR
Thermal Plasma
Za Slovankou 3
18200 Prague 8, Czech Rep.
kavka@ipp.cas.cz

Mr. Jaroslav Kočišek
Comenius University
Faculty of Mathematics, Physics and Informatics
Department of Experimental Physics
Mlynská dolina
84248 Bratislava, Slovakia
kocisek@neon.dpp.fmph.uniba.sk

Dr. Andreas Kolitsch
Forschungszentrum Rossendorf
Institute of Ion Beam Physics and Materials Research
POB 510119
1314 Dresden, Germany
a.kolitsch@fz-rossendorf.de

Dr. Jan Koller
Czech Technical University in Prague
Faculty of Electrical Engineer
Department of Physics
Technická 2
166 27 Praha 6, Czech Rep.
koller@fel.cvut.cz

Mr. Dušan Kováčik
Comenius University
Faculty of Mathematics, Physics and Informatics
Department of Experimental Physics
Mlynská dolina
842 48 Bratislava, Slovakia
kovacik@fmph.uniba.sk

Dr. Frantisek Krcma
Brno University of Technology
Faculty of Chemistry
Purkynova 118
612 00 Brno, Czech Rep.
krcma@fch.vutbr.cz

Mr. Dusan Kubala
Comenius University
Faculty of Mathematics, Physics and Informatics
Department of Experimental Physics
Mlynska dolina, F2
84248 Bratislava, Slovakia
kubala@neon.dpp.fmph.uniba.sk

Mr. Marek Kucera
Comenius University
Faculty of Mathematics, Physics and Informatics
Department of Experimental Physics
Mlynska dolina
842 48 Bratislava, Slovakia
kucera@neon.dpp.fmph.uniba.sk

Ms. Zuzana Kucerova
Masaryk University
Department of Physical Electronics
Kotlarska 2
611 37 Brno, Czech Rep.
zus@physics.muni.cz

Dr. Vit Kudrle
Masaryk University
Department of Physical Electronics
Kotlarska 2
CZ-61137 Brno, Czech Rep.
kudrle@sci.muni.cz

Prof. Peter Kúš
Comenius University
Faculty of Mathematics, Physics and Informatics
Department of Experimental Physics
Mlynska Dolina
84248 Bratislava, Slovakia
kus@fmph.uniba.sk

Dr. Judith Langer
Freie Universität Berlin
Institute of Chemistry and Biochemistry
Takustr. 3
14195 Berlin, Germany
langerj@chemie.fu-berlin.de

Prof. Heon-Ju Lee
Cheju National University
Faculty of Mechanical & Energy System Engineering
ara 1 dong
690756 Jeju, Korea
hjlee@cheju.ac.kr

Ms. Lenka Lestinska
Comenius University
Faculty of Mathematics, Physics and Informatics
Department of Astronomy, Earth Physics and Meteorology
Mlynska dolina F2
84248 Bratislava, Slovakia
lele1@post.sk

Mr. Michal Lestinsky
Comenius University
Faculty of Mathematics, Physics and Informatics
Department of Astronomy, Earth Physics and Meteorology
Mlynska dolina F2
84248 Bratislava, Slovakia
catchcash@pobox.sk

Prof. Jiří Limpouch
Czech Technical University in Prague
Faculty of Nuclear Sciences and Physical Engineering
Břehová 7
115 19 Praha 1, Czech Rep.
limpouch@troja.fjfi.cvut.cz

Mr. Kethsiri Lokuliyanage
Universität Innsbruck
Institut für Ionenphysik und Angewandte Physik
Technikerstrasse 25
A-6020 Innsbruck, Austria
L.Kethsiri@uibk.ac.at

Dr. Petr Lukeš
Academy of Sciences of the Czech Republic
Pulse Plasma System, Institute of Plasma Physics
Za Slovankou 3
18200 Praha, Czech Rep.
lukes@ipp.cas.cz

Dr. Anna Mackova
Nuclear Physics Institute of ASCR
Nuclear Analytical Methods
25068 Rez near Prague, Czech Rep.
mackova@ujf.cas.cz

Prof. Tilmann D. Maerk
University of Innsbruck
Institute for Ion Physics and Applied Physics
Technikerstraße 25
A-6020 Innsbruck, Austria
tilmann.maerk@uibk.ac.at

Dr. Pavel Mach
Comenius University
Faculty of Mathematics, Physics and Informatics
Nuclear Physics and Biophysics
Mlynska Dolina
842 48 Bratislava, Slovakia
mach@fmph.uniba.sk

Dr. Zdenko Machala
Comenius University
Faculty of Mathematics, Physics and Informatics
Department of Astronomy, Earth Physics and Meteorology
Mlynska dolina
84248 Bratsilava, Slovakia
machala@fmph.uniba.sk

Mr. Petr Malinsky
Nuclear Physics Institute of ASCR
Nuclear Analytical Methods
25068 Rez near Prague, Czech Rep.
malinko@seznam.cz

Mr. Ales Marek
Charles University
Department of Electronics and Vacuum Physics
V Holešoviškách 2
18000 Prague 8 - Libeň, Czech Rep.
ales.marek@matfyz.cz

Ms. Isabel Martin
Freie Universität Berlin
Institute of Chemistry and Biochemistry
Takustr. 3
14195 Berlin, Germany
martin@chemie.fu-berlin.de

Prof. Nigel Mason
The Open University
Physics and Astronomy
Walton Hall
MK7 6AA Milton Keynes, United Kingdom
n.j.mason@open.ac.uk

Dr. Štefan Matejčík
Comenius University
Faculty of Mathematics, Physics and Informatics
Department of Experimental Physics
Mlynska dolina
84248 Bratislava, Slovakia
matejcik@fmph.uniba.sk

Mr. Ján Matúška
Comenius University
Faculty of Mathematics, Physics and Informatics
Department of Experimental Physics
Mlynska dolina
84248 Bratislava, Slovakia
matuska@neon.dpp.fmph.uniba.sk

Ms. Vera Mazankova
Brno University of Technology
Faculty of Chemistry
Purkynova 118
612 00 Brno, Czech Rep.
mazankova@fch.vutbr.cz

Ms. Emilia Metel
The Szewalski Institute of Fluid Flow Machinery
Centre for Plasma and Laser Engineering
Fiszera 14
80231 Gdansk, Poland
metel@imp.gda.pl

Prof. Jerzy Mizeraczyk
The Szewalski Institute of Fluid Flow Machinery
Centre for Plasma and Laser Engineering
Fiszera 14
80231 Gdansk, Poland
jmiz@imp.gda.pl

Ms. Martina Mrazkova
Masaryk University
Department of Physical Electronics
Kotlářská 2
611 37 Brno, Czech Rep.
mmartina@mail.muni.cz

Dr. Zdeněk Navrátil
Masaryk University
Department of Physical Electronics
Kotlářská 2
611 37 Brno, Czech Rep.
zdenek@physics.muni.cz

Prof. Stanislav Novak
J. E. Purkinje University
Department of Physics
Ceske mladeze 8
400 96 Usti nad Labem, Czech Rep.
novaks@sci.ujep.cz

Prof. Victor Novokshenov
Institute of Mathematics RAS
Mathematical Physics
Chernyshevskii street 112
450077 Ufa, Russia
novokshenov@yahoo.com

Mrs. Mária Odrášková
Comenius University
Faculty of Mathematics, Physics and Informatics
Department of Experimental Physics
Mlynská dolina
842 48 Bratislava, Slovakia
odraskova@gimmel.ip.fmph.uniba.sk

Dr. Juraj Orszagh
Comenius University
Faculty of Mathematics, Physics and Informatics
Department of Experimental Physics
Mlynska dolina F-2
84248 Bratislava, Slovakia
juraj.orszagh@googlemail.com

Dr. Peter Papp
Comenius University
Faculty of Mathematics, Physics and Informatics
Department of Experimental Physics
Mlynska dolina
842 48 Bratislava, Slovakia
papp@fmph.uniba.sk

Dr. Jaroslav Pavlik
J. Purkinje University
Faculty of Science
Department of Physics
Ceske mladeze 8
CZ - 400 96 Usti nad Labem, Czech Rep.
pavlikj@sci.ujep.cz

Dr. Vratislav Peřina
Nuclear Physics Institute of ASCR
Nuclear Analytical Methods
25068 Řež, Czech Rep.
perina@ujf.cas.cz

Ms. Irena Pickova
Charles University
Department of Electronics and Vacuum Physics
V Holešovičkách 2
180 00 Prague, Czech Rep.
irena.pickova@seznam.cz

Prof. Andrej Plecenik
Comenius University
Faculty of Mathematics, Physics and Informatics
Department of Experimental Physics
Mlynska Dolina
84248 Bratislava, Slovakia
plecenik@fmph.uniba.sk

Prof. Michael Probst
Innsbruck University
Ion Physics and Applied Physics
Technikerstrasse 25
6020 Innsbruck, Austria
michael.probst@uibk.ac.at

Mrs. Jana Prochazkova
Brno University of Technology
Faculty of Chemistry
Purkynova 118
612 00 Brno, Czech Rep.
xcprochazkova@fch.vutbr.cz

Mr. Ivan Pschenichnyuk
Charles University
Institute of Theoretical Physics
V Holesovickach 2
180 00 Prague, Czech Rep.
iapsh@anrb.ru

Dr. Jozef Rahel
Masaryk University
Faculty of Science
Department of Physical Electronics
Kotlarska 2
611 37 Brno, Czech Rep.
rahel@mail.muni.cz

Mr. Martin Sabo
Comenius University
Faculty of Mathematics, Physics and Informatics
Department of Experimental Physics
Mlynska dolina F-2
84248 Bratislava, Slovakia
martin.sabo@gmail.com

Prof. Marek Jan Sadowski
The Andrzej Soltan Institute for Nuclear Studies
Department of Plasma Physics & Technology
05-400 Otwock-Swierk, Poland
msadowski@ipj.gov.pl

Prof. Roman Schrittwieser
Leopold-Franzens University of Innsbruck
Institute for Ion Physics and Applied Physics
Technikerstr. 25
A-6020 Innsbruck, Austria
roman.schrittwieser@uibk.ac.at

Mr. Pavel Schukin
Institute of Physics of Molecules and Crystals
Laboratory of Negative Ion Mass-Spectrometry
Prospect Oktyabrya, 151
450075 Ufa, Russia
pavel@anrb.ru

Mr. Jan Sicha
University of West Bohemia
Department of Physics
Univerzitni 22
30614 Plzen, Czech Rep.
sicha@kfy.zcu.cz

Prof. Jan Skalny
Comenius University
Faculty of Mathematics, Physics and Informatics
Department of Experimental Physics
Mlynska dolina F2
84248 Bratislava, Slovakia
jan.skalny@uibk.ac.at

Dr. Elzbieta Skladnik-Sadowska
The Andrzej Soltan Institute for Nuclear Studies
Department of Plasma Physics & Technology
05-400 Otwock-Swierk, Poland
eskladnik@ipj.gov.pl

Mr. Radek Smid
Masaryk University
Department of Physical Electronics
Kotlarska 2
611 37 Brno, Czech Rep.
smid@physics.muni.cz

Mr. Daniel Soderstrom
Uppsala University
The Ångström Laboratory
The Plasma Group
P.O. Box 534
75121 Uppsala, Sweden
daniel.soderstrom@angstrom.uu.se

Dr. Pavel Stahel
Masaryk University
Faculty of Science
Physical Electronics
Kotlarska 2
61137 Brno, Czech Rep.
pstahel@physics.muni.cz

Dr. Zdenka Stara
Brno University of Technology
Faculty of Chemistry
Purkynova 118
612 00 Brno, Czech Rep.
stara@fch.vutbr.cz

Mr. Vitezslav Stranak
University of South Bohemia
Department of Physics
Jeronymova 10
371 15 Ceske Budejovice, Czech Rep.
stranv00@centrum.cz

Prof. Petra Swiderek
Universität Bremen
Institut für Angewandte und Physikalische Chemie
Leobener Strasse
28334 Bremen, Germany
swiderek@uni-bremen.de

Dr. Pierre Tardiveau
Laboratoire de Physique des Gaz et des Plasmas
Bat 210
Université Paris-Sud
91400 Orsay, France
pierre.tardiveau@pgp.u-psud.fr

Mr. Viktor Tarjani
Comenius University
Faculty of Mathematics, Physics and Informatics
Department of Experimental Physics
Mlynska dolina
842 48 Bratislava, Slovakia
tarjani@neon.dpp.fmph.uniba.sk

Dr. András Tóth
Hungarian Academy of Sciences
Chemical Research Center
Institute of Materials and Environmental Chemistry
Pusztaszeri ut 59-67
H-1025 Budapest, Hungary
totha@chemres.hu

Mr. Bystrik Trnovec
Slovak University of Technology
Printing Arts and Photochemistry
Radlinskeho 9
81237 Bratislava, Slovakia
bystrik.trnovec@stuba.sk

Dr. David Trunec
Masaryk University
Department of Physical Electronics
Kotlarska 2
61137 Brno, Czech Rep.
trunec@physics.muni.cz

Dr. Jan Urban
Comenius University
Faculty of Mathematics, Physics and Informatics
Nuclear Physics and Biophysics
Mlynska Dolina F2
84248 Bratislava, Slovakia
urban@fmph.uniba.sk

Dr. Petr Vasina
Masaryk University
Department of Physical Electronics
Kotlarska 2
61137 Brno, Czech Rep.
vasina@physics.muni.cz

Ms. Iuliia Veremii
Taras Shevchenko Kyiv National University
Physical Electronics
Volodymyrska str. 64
1033 Kyiv, Ukraine
tin@mail.univ.kiev.ua

Mr. Petr Virostko
Academy of Sciences of the Czech Republic
Institute of Physics
Department of Low-Temperature Plasma
Na Slovance 2
182 21 Prague, Czech Rep.
virostko@fzu.cz

Dr. Rodica Vladoiu
Ovidius University
Faculty of Physics
Mamaia 124
900527 Constanta, Romania
rvladoiu@univ-ovidius.ro

Prof. Jaroslav Vlcek
University of West Bohemia
Department of Physics
Univerzitni 22
CZ-30614 Plzen, Czech Rep.
vlcek@kfy.zcu.cz

Ms. Jitka Vrajova
Brno University of Technology
Faculty of Chemistry
Purkynova 118
612 00 Brno, Czech Rep.
vrajova@fch.vutbr.cz

Mr. Terry Whitmore
Hiden Analytical Ltd.
420 Europa Boulevard
WA5 7UN Warringtin, United Kingdom
twhitmore@hiden.co.uk

Mr. Chan joo Yim
Cheju National University
Faculty of Mechanical & Energy System Engineering
ara 1 dong
690756 Jeju, Korea
cjyim@cheju.ac.kr

Dr. Miroslav Zahoran
Comenius University
Faculty of Mathematics, Physics and Informatics
Department of Experimental Physics
Mlynska Dolina
842 48 Bratislava, Slovakia
zahoran@fmph.uniba.sk

Dr. Anna Zahoranová
Comenius University
Faculty of Mathematics, Physics and Informatics
Department of Experimental Physics
Mlynska Dolina F2
842 48 Bratislava, Slovakia
zahoranova@gimmel.ip.fmph.uniba.sk